Year : 2014

Post-Plutonic Magmatism: from the Source to the Emplacement of an Upper Crustal Dyke Swarm, Adamello Massif, Italy

Hürlimann Niklaus

Hürlimann Niklaus , 2014, Post-Plutonic Magmatism: from the Source to the Emplacement of an Upper Crustal Dyke Swarm, Adamello Massif, Italy

Originally published at : Thesis, University of Lausanne

Posted at the University of Lausanne Open Archive.
http://serval.unil.ch

UNIL | Université de Lausanne

Faculté des géosciences et de l'environnement

Institut des Sciences de la Terre

Post-Plutonic Magmatism: from the Source to the Emplacement of an Upper Crustal Dyke Swarm, Adamello Massif, Italy

Thèse de doctorat

Présentée à la Faculté des géosciences et de l'environnement de l'Université de Lausanne par

Niklaus Hürlimann

Master of Earth Sciences

University of Bern, Bern, Switzerland

Jury :
Président : Prof. Dr. François Bussy
Directeur de thèse : Prof. Dr. Othmar Müntener
Expert : Prof. Dr. Peter Ulmer
Expert : Dr. Tom W Sisson
Expert : Prof. Dr. Boris Kaus
Expert : Prof. Dr. Urs Schaltegger

Lausanne, 2013

UNIL | Université de Lausanne
Décanat Géosciences et de l'Environnement
bâtiment Géopolis
CH-1015 Lausanne

IMPRIMATUR

Vu le rapport présenté par le jury d'examen, composé de

Président de la séance publique :	M. le Professeur François Bussy
Président du colloque :	M. le Professeur François Bussy
Directeur de thèse :	M. le Professeur Othmar Müntener
Expert externe :	M. le Professeur Peter Ulmer
Expert externe :	M. le Professeur Tom W. Sisson
Expert externe :	M. le Professeur Urs Schaltegger
Expert externe :	M. le Professeur Boris Kaus

Le Doyen de la Faculté des géosciences et de l'environnement autorise l'impression de la thèse de

Niklaus HÜRLIMANN

Titulaire d'une
Maîtrise universitaire en Sciences de la Terre
Université de Berne

intitulée

POST-PLUTONIC MAGMATISM : FROM THE SOURCE TO THE EMPLACEMENT OF AN UPPER CRUSTAL DYKE SWARM, ADAMELLO MASSIF, ITALY

Lausanne, le 27 septembre 2013

Faculté des géosciences et de l'environnement

Professeur François Bussy, Doyen

"Wo chiemte mer hi wenn alli seite wo chiemte mer hi und niemer giengti fur einisch z'luege wohi dass me chiem we me gieng."

(Kurt Marti, rosa loui, vierzg gedicht ir bärner umgangssprach, Luchterhand 1967).

"Where will this lead us to if everybody asks where will this lead us to and nobody leads to where this will lead us to."

(Kurt Marti, rosa loui, forty poems, Luchterhand 1967).

Acknowledgements

This study was founded by the Swiss National Fonds in the context of the Prodoc 4D Adamello project that involved nine PhD students, seven supervisors and three different universities in Switzerland. The 4D Adamello project addressed questions around batholith formation in a multidisciplinary approach investigating processes such as melt generation and extraction in the upper mantle, physcial-chemical models of magma migration through the upper mantle and crust, magma differentiation during ascent and emplacement, thermal evolution of magma bodies and surroundings in contact, timescales of magma generation and differentiation processes together with aspects on style and timing of the assembly of plutonic complexes. The project also stands for a journey of several PhD students and their supervisors leading to lively exchange and discussion as well as a relaxed ground for friendship and solidarity with fellow students under both very pleasent and more difficult conditions. In this sense I am grateful for being able to take part in this project.

I would like to thank particularly Othmar Müntener and Peter Ulmer my two supervisors for giving me the opportunity to embark on this PhD and accompanying me all the way here. I don't know how I can thank you for everything. In moments of desperation your confidence and calm always helped me to bring the ship back on course. I am particularly grateful to Alexey Ulianov for giving me the opportunity to learn ICP-mass spectrometry from scratch and opening up a whole new world of analytical questions. Peter Brack is thanked for discussion, his assistance in the field with all his hints for particular outcrops, organizing sampling permits for the Adamello park and all his work to organize a memorable conference in Bagolino. Rohit is thanked for sharing many hours with me in the ICP-MS lab and pushing with me the limits of the method. I thank Benita Putliz for training me in mineral separation and for discussions. Laurent I thank for his excellent thin sections and all his help for particular sample preparation, not to mention some of the very cosy lunch hours in his atelier. Lukas Baumgartner is thanked for discussion and critical reviews, together with Benita for their hospitality at their home. Maria Ovtcharova is thanked for sample preparation and analysis for titanite and zircon geochronology. I thank David, Roel, Caroline, Cristobal, Julien and Susanne for sharing the office with me and the precious time in the field, and office talks were always very inspirational. Robert Bodner is thanked for help with numerical problems, discussions and help with the electron microprobe. I am grateful for all the time spent evolving through the 4D Adamello project together with Sylvia, Cindy, Alexandra, Katharina and Tobias, not to forget some memorable hours stuck in old World War 1 caves freezing our toes off. Urs Schaltegger, Boris Kaus and Taras Gerya are thanked for enabling me to dip into numerical and geochronolgical methods which opened up a new approach for addressing geological problems. I thank Sebastien for discussion, help in preparation for presentations and face lifting of geological french.

A special thanks goes to the Tita Secchi crew, Alda, Gino, Andrea, Lagpa, Matteo, and everyone else for making the hut our new home for several weeks and the good food that kept our moral high. Fiorella, Giacomo and Andrea of the Maria e Franco hut are thanked for their hospitality at this particular place. Giacomo is thanked for the small good night grappas and giving me insight into his collection. Andrea I thank for his assistance in carrying samples down to the valley.

I thank my family, my mother, my father and brothers for their support all the way through my thesis. My friends for their patience during all this years and all the happy moments besides work.

Then you Marcia, my fiancé and future wife and Paul Viêt, my family, I thank you for everything, all your support, patience and all the happy time I spend with you at home, in Portugal, in the mountains and where life brings us.

Abstract

Magmas of the arc-tholeiitic and calc-alkaline differentiation suites contribute substantially to the formation of continental crust in subduction zones. Different geochemical-petrological models have been put forward to achieve evolved magmas forming large volumes of tonalitic to granitic plutons, building an important part of the continental crust.

Primary magmas produced in the mantle wedge overlying the subducted slab migrate through the mantle and the crust. During the transfer, magma can accumulate in intermediate reservoirs at different levels where crystallization leads to differentiation and the heat transfer from the magma, together with gained heat from solidification, lead to partial melting of the crust. Partial melts can be assimilated and mix with more primitive magma. Moreover, already formed crystal cumulates or crystal mushes can be recycled and reactivated to transfer to higher crustal levels. Magma transport in the crust involves flow through fractures within a brittle elastic rock. The solidified magma filled crack, a dyke, can crosscut previously formed geological structures and thus serves as a relative or absolute time marker.

The study area is situated in the Adamello massif. The Adamello massif is a composite of plutons that were emplaced between 42 and 29 million years. A later dyke swarm intruded into the southern part of the Adamello Batholith. A fractionation model covering dyke compositions from picrobasalts to dacites results in the cummulative crystallization of 17% olivine, 2% Cr-rich spinel, 18% clinopyroxene, 41% amphibole, 4% plagioclase and 0.1% magnetite to achieve an andesitic composition out of a hydrous primitive picrobasalt. These rocks show a similar geochemical evolution as experimental data simulating fractional crystallization and associated magma differentiation at lower crustal depth (7-10 kbar). The peraluminous, corundum-normative composition is one characteristic of more evolved dacitic magmas, which has been explained in a long lasting debate with two different models. Melting of mafic crust or pelitic material provides one model, whereas an alternative is fractionation from primary mantle derived melts. Amphibole occurring in basaltic-andesitic and andesitic dyke rocks as fractionating cumulate phase extracted from lower crustal depth (6-7.5 kbar) is driving the magmas to peraluminous, corundum normative compositions, which are represented by tonalites forming most of the Adamello Batholith. Most primitive picrobasaltic dykes have a slightly steepened chondrite normalized rare earth elements (REE) pattern and the increased enrichment of light-REE (LREE) for andesites and dacites can be explained by the fractional crystallization model originating from a picrobasalt, taking the changing fractionating phase assemblage and temperature into account.

The injection of hot basaltic magma (~1050°C) in a closely spaced dyke swarm increases the surface of the contact to the mainly tonalitic wallrock. Such a setting induces partial melting of the wall rock and selective assimilation. Partial melting of the tonalite host is further expressed through intrusion breccias

from basaltic dykes. Heat conduction models with instantaneous magma injection for such a dyke swarm geometry can explain features of partial melting observed in the field. Geochemical data of minerals and bulk rock further underline the selective or bulk assimilation of the tonalite host rock at upper crustal levels (~2-3 kbar), in particular with regard to light ion lithophile elements (LILE) such as Sr, Ba and Rb.

Primitive picrobasalts carry an immiscible felsic assimilant as enclaves that bring along refractory rutile and zircon with textures typically found in oceanic plagiogranites or high-pressure/low-temperature metamorphic rocks in general. U-Pb data implies a lower Cretaceous age for zircon not yet described as assimilant in Eocene to Oligocene magmatic rocks of the Central Southern Alps.

The distribution of post-plutonic dykes in large batholiths such as the Adamello is one of the key features for understanding the regional stress field during the post-batholith emplacement cooling history. The emplacement of the regional dyke swarm covering the southern part of the Adamello massif was associated with consistent left lateral strike-slip movement along magma dilatation planes, leading to en echelon segmentation of dykes. Through the dilation by magma of pre-existing weaknesses and cracks in an otherwise uniform host rock, the dyke propagation and according orientation in the horizontal plane adjusted continuously perpendicular to least compressive remote stress σ_3, resulting in an inferred rotation of the remote principal stress field.

Resumé

Les magmas issus des zones de subduction contribuent substantiellement à la formation de la croûte continentale. Les plutons tonalitiques et granitiques représentent, en effet, une partie importante de la croûte continentale.

Des magmas primaires produits dans le « mantle wedge », partie du manteau se trouvant au-dessus de la plaque plongeante dans des zones de subduction, migrent à travers le manteau puis la croûte. Pendant ce transfert, le magma peut s'accumuler dans des réservoirs intermédiaires à différentes profondeurs. Le stockage de magma dans ces réservoirs engendre, d'une part, la différentiation des magmas par cristallisation fractionnée et, d'autre part, une fusion partielle la croûte continentale préexistante associée au transfert de la chaleur des magmas vers l'encaissant. Ces liquides magmatiques issus de la croûte peuvent, ensuite, se mélanger avec des magmas primaires. Le transport du magma dans la croûte implique notamment un flux de magma à travers différentes fractures recoupant les roches encaissantes élastiques. Au cours de ce processus de migration, des cumulats de cristaux ou des agrégats de cristaux encore non-solidifiés, peuvent être recyclés et réactivés pour être transportés à des niveaux supérieures de la croûte.

Le terrain d'étude est situé dans le massif d'Adamello. Celui-ci est composé de plusieurs plutons mis en place entre 42 et 29 millions d'années. Dans une phase tardive de l'activité magmatique liée à ce batholite, une série de filons de composition variable allant de picrobasalte à des compositions dacitiques s'est mise en place la partie sud du massif. Deux modèles sont proposés dans la littérature, pour expliquer la formation des magmas dacitiques caractérisés par des compositions peralumineux (i.e. à corindon normatif). Le premier modèle propose que ces magmas soient issus de la fusion de matériel mafique et pélitique présent dans la partie inférieur de la croûte, alors que le deuxième modèle suggère une évolution par cristallisation fractionnée à partir de liquides primaires issus du manteau. Un modèle de cristallisation fractionnée a pu être développé pour expliquer l'évolution des filons de l'Adamello. Ce modèle explique la formation des filons dacitiques par la cristallisation fractionnée de 17% olivine, 2% spinelle riche en Cr, 18% clinopyroxène, 41% amphibole, 4% plagioclase et 0.1% magnetite à partir de liquide de compositions picrobasaltiques. Ce modèle prend en considération les contraintes pétrologiques déduites de l'observation des différents filons ainsi que du champ de stabilité des différentes phases en fonction de la température. Ces roches montrent une évolution géochimique similaire aux données expérimentales simulant la cristallisation fractionnée de magmas évoluant à des niveaux inférieurs de la croûte (7-10 kbar). Le modèle montre, en particulier, le rôle prépondérant de l'amphibole, une phase qui contrôle en particulier le caractère peralumineux des magmas différentiés ainsi que leurs compositions en éléments en traces.

Des phénomènes de fusion partielle de l'encaissant tonalitique lors de la mise en place de filons mafiques sont observée sur le terrain. L'injection du magma basaltique chaud (~1050°C) sous forme de filons

rapprochés augmente la surface du contact avec l'encaissante tonalitique. Une telle situation produit la fusion partielle des roches encaissantes nécessaire à l'incorporation d'enclaves mafiques observés au sein des tonalites. Pour comprendre les conditions nécessaires pour la fusion partielle des roches encaissantes, des modèles de conduction thermique pour une injection simultanée d'une série de filons ont été développées. Des données géochimiques sur les minéraux et sur les roches totales soulignent qu'au niveau supérieur de la croûte, l'assimilation sélective ou totale de l'encaissante tonalitique modifie la composition du liquide primaire pour les éléments lithophiles tel que le Sr, Ba et Rb.

Un autre aspect important concernant la pétrologie des filons de l'Adamello est la présence d'enclaves feldsiques dans les filons les plus primitifs. Ces enclaves montrent, en particulier, des textures proches de celles rencontrées dans des plagiogranites océaniques ou dans des roches métamorphiques de haute pression/basse température. Ces enclaves contiennent du zircon et du rutile. La datations de ces zircons à l'aide du géochronomètre U-Pb indique un âge Crétacé inférieur. Cet âge est important, car aucune roche de cet âge n'a été considérée comme un assimilant potentiel pour des roches magmatiques d'âge Eocène à Oligocène dans les Alpes Sud Centrales.

La réparation spatiale des filons post-plutoniques dans des grands batholites tel que l'Adamello, est une caractéristique clé pour la compréhension des champs de contraintes lors du refroidissement du batholite. L'orientation des filons va, en particulier, indiqué la contrainte minimal au sein des roches encaissante. La mise en place de la série de filon recoupant la partie Sud du massif de l'Adamello est associée à un décrochement senestre, un décrochement que l'on peut lié aux contraintes tectoniques régionales auxquelles s'ajoutent l'effet de la dilatation produite par la mise en place du batholite lui-même. Ce décrochement senestre produit une segmentation en échelon des filons.

Contents

List of Figures

List of Tables

Chapter 1

Introduction and Motivation

1.1 Introduction

Subduction zones are one of the key areas for the generation of new continental crust due to major and trace element similarities between estimates of the continental crust and calc-alkaline andesites [Kay and Kay, 1985, Kelemen et al., 2003, Gill, 1981, Rudnick, 1995, Taylor and McLennan, 1985]. One of the key problems associated with formation of the continental crust and the so called "andesite model" is that that the mass flux from the mantle is described as commonly basaltic with $SiO_2 < 52$ wt%. Silica rich granitoids of the upper crust and a lower predominantly gabbroic crust can together form a bulk andesitic crust [Rudnick and Gao, 2003]. The evolution of major and trace elements of calc-alkaline differentiation suites imply that minerals such as amphibole, garnet and Ti-oxides and generally all silica-poor phases, play an important role during fractionation of the basaltic flux from the mantle [Jan and Howie, 1981, DeBari and Coleman, 1989, Alonso-Perez et al., 2009, Greene et al., 2006, Jagoutz, 2010]. High Mg# andesites, defined as an andesitic lava with Mg# > 0.3 and less than 10 wt% MgO [Kelemen, 1995], are chemically similar to the continental crust with estimates of of 55-65 wt% SiO_2, 4-7 wt% combined Na_2O and K_2O, molar Ca/(Ca+Na) of 0.4 to 0.6 and wt% Mg/(Mg+total Fe as Fe^{2+}) or Mg# 0.34 to 0.42 [e.g. Taylor et al. 1981, Weaver and Tarney 1984, Rudnick and Gao 2003]. Several authors proposed that calc-alkaline andesitic magmas can be produced as a result of reaction between ascending liquids and mantle peridotites [Fisk, 1986, Green and Ringwood, 1967, Kay, 1978, Kelemen, 1986, 1990, Quick, 1982, Arculus et al., 1983, Myers et al., 1985]. Kelemen [1995] proposed that initial liquids could be derived by small degrees of mantle peridotite melting at greater depth, or by partial melting of the downgoing slab in subduction zones. Reaction with peridotite during ascent substantially changes the silica content of derivate liquids, and will produce liquids close to saturation in mantle olivine, with high Mg# and high Ni content. The formation of high-magnesium andesite through melt-rock reaction in the upper mantle provides an alternative model for continental crust formation without extensive fractionation of silica-poor phases.

Crustal Growth in Island Arcs

Active island arcs such as the Izu-Bonin-Mariana (IBM) intraoceanic arc show the crustal structure evolution with the associated magmatism in time slices towards a mature arc crust [Kodaira et al., 2010]. Boninitic magmatism occurs in the initial stage of the subduction [e.g. Leng and Gurnis, 2011, Kodaira et al., 2010, Insergueix-Filippi et al., 2000]. The non-oceanic, increasingly mature and thicker crust was created with tholeiitic-calcalkaline andesitic magmatism after boninitic magmatism ceased [Kodaira et al., 2010]. The consequences of high-pressure cumulate formation from hydrous arc magmas on seismic velocity structure of lower arc crust are important since such studies are based on seismic refraction tomography [Kodaira et al., 2010, Müntener and Ulmer, 2006]. Müntener and Ulmer [2006] showed that at pressure exceeding 0.8 GPa (25 km), 40-60 % of ultramafic cumulates are produced by crystal fractionation to obtain andesite to dacite compositions. Out of their experimental data they calculated cumulate density values that are comparable or higher than upper mantle values. The seismic velocities vary continuously between 7.3 and 8 km/s resulting in a broad crust-mantle transition.

Deep Crustal Hot Zone

One of the key questions with regard to differentiation is at which depth fractionation occurs. The existence of shallow sub-volcanic magma chambers is widely confirmed by geophysical evidence [e.g. Iyer, 1984, Calvert, 1995, Bohrson, 2007] together with petrological and geological evidence [Annen et al., 2006]. Numerical simulations of heat transfer [Annen and Sparks, 2002] and high-temperature and high-pressure (0.8-1.5GPa) experiments [Müntener et al., 2001, Proteau and Scaillet, 2003, Alonso-Perez et al., 2009, Kägi, 2000] provide a model where silica-rich magmas are generated by incomplete crystallization of hydrous basalt at upper mantle and/or lower crustal depths. For producing rocks by fractional crystallization with more than 60 wt% SiO_2, crystallization of at least 60% or more of a typical hydrous primitive arc basalt is required [e.g. Foden and Green, 1992, Müntener et al., 2001, Alonso-Perez et al., 2009]. Huge volumes of associated mafic cumulates are required to generate large granitoid batholiths and voluminous eruptions of silicic magma involving several hundreds to thousands of km^3 [e.g Crisp, 1984, Smith, 1979, Bachmann et al., 2002]. Silica-rich residual melts from the production of the mafic cumulates in the lower crust can be extracted and ascend, either to erupt immediately or to stall and form shallow magma chambers. Large batholiths are formed in the case where the shallow magma chambers consolidate completely or to a great extent.

Formation of Corundum Normative Magmas Through Amphibole Fractionation

Amphibole occurs in many calc-alkaline volcanic and plutonic rocks with basaltic and andesitic composition [e.g Anderson, 1980, Sisson et al., 1996, Blundy and Sparks, 1992, Krawczynski et al., 2012]. Calc-alkaline intrusive and extrusive suites commonly show trends from diopside- to corundum normative composition for magmas with increasing SiO_2 that can be explained by the crystallization of hornblende from primitive hydrous basaltic magmas [Cawthorn and O'Hara, 1976, Cawthorn and Brown, 1976, Cawthorn et al., 1976, Alonso-Perez et al., 2009, Dessimoz et al., 2012, Sisson et al., 2005]. Corundum normative magmas are often interpreted as due to crustal melting for the formation of granites [e.g. Clemens et al., 2011, Clemens and Stevens, 2012]. Phase equilibrium experiments on a basaltic-andesite from Mount Shasta (N-California, Cascade Volcanic Arc) [Grove et al., 2003] showed, that at 800 MPa and 1065 °C, olivine is no longer stable and that the phase assemblage encompasses orthopyroxene, a magnesian (Mg#=0.80) pargasite amphibole and clinopyroxene. The presence of amphibole in this case was taken as high pre-eruptive H_2O ($>$ 10 wt% H_2O) contents. Further experiments on the same composition demonstrated that amphibole and olivine are coexisting above 500 MPa to at least 800 MPa between 975 and 1025 °C. The temperature difference between the liquidus of hydrous basalts and amphibole appearance decreases with increasing H_2O pressure (P_{H_2O}), causing a change in chemical composition of the first amphibole to crystallize [Krawczynski et al., 2012, Grove et al., 2003]. An experimental study by Alonso-Perez et al. [2009] explored as well the role of H_2O and pressure at lower crustal conditions on the stability of the most important phases regarding an andesitic liquid that was derived by fracitonal crystallization at 1.0 GPa from a primitive mantle derived picrobasaltic liquid. The principal phases found were garnet, amphibole, clinopyroxene and plagioclase [Alonso-Perez et al., 2009].

Dyke Emplacement and the Effect of the Regional Stress Field

Envisioned transport processes of magma in the crust include porous flow in partially molten and deformable rock [e.g. Spiegelman, 1993a,b, McKenzie, 1984, Sleep, 1974, Bercovici et al., 2001, Bercovici and Ricard, 2003], flow through fractures (dykes) in an elastic brittle rock [e.g. Taisne and Jaupart, 2009, Lister and Kerr, 1991, Murrell, 1964, Rubin, 1993a,b] and diapiric ascent through viscous rock [e.g. Rubin, 1993a, Mahon et al., 1988, Marsh, 1982]. Detailed field studies of dykes provide information about their detailed shape in the light of magma flow and overpressure in cracks, relating this process to theoretical elasticity analysis of a pressurized slit or crack [Delaney and Pollard, 1981, Kavanagh and Sparks, 2011, Poland et al., 2008, Pollard and Muller, 1976, Valentine and Krogh, 2006, Walker, 1986]. Analogue experiments provide another approach to study the propagation of a liquid filled crack [McLeod and Tait, 1999, Watanabe et al., 2002, Takada, 1990, Menand and Tait, 2002, Menand et al., 2010]. Moreover, numerical simulations address the same question [Chen et al., 2007, Gudmundsson et al., 1999, Lister and Kerr, 1991, Maccaferri et al., 2010, Rivalta and Dahm, 2004]. Dyke swarms in tonalitic to granodioritic host rocks demonstrating a high degree of mechanical isotropy [Dini et al., 2008] should provide more straightforward information about the palaeostress configuration [Pollard, 1987, Pollard and Muller, 1976] at the time of dyke emplacement than dykes within layered sediments and/or foliated metamorphic environments.

1.2 Geodynamic Context of the Field Area

During the collision of the European and the Adriatic plates, basaltic and granitoid magmatism occurred between 42 and 29 Ma [Hansmann and Oberli, 1991, Pomella et al., 2011, Schaltegger et al., 2009, Schoene et al., 2012, Fodor et al., 2008, Barth et al., 1989, von Blackenburg, 1992, Oberli et al., 2004, Del Moro et al., 1985] following the closure of oceanic basins by subduction and continental collision. Blanckenburg and Davies [1995] argue that the trace element and isotopic signature of mafic dykes suggest that they formed by low-degree partial melting of the mechanically stable lithospheric mantle. The same authors explain the almost synchronous intrusion of Alpine magmatic rocks along the Periadriatic Fault System (PFS) as an effect of rapid lateral migration of slab breakoff, resulting in a linear trace of magmatism in locally thermal weakend crust. The Adamello Batholith, the largest of the periadriatic intrusions, is located in the Central Southern Alps (N-Italy). Larger volumes of tonalite and granodiorite, together with some marginal satellite ultrabasic and basic intrusions, built up the batholith over a time interval of 42-29 Ma [Del Moro et al., 1985, Schaltegger et al., 2009, Hansmann and Oberli, 1991]. A series of late basic to intermediate, dykes are concentrated in the southern part and seem not to occur in the larger northern part of the batholith.

1.3 Thesis Structure and Key Questions

The second chapter deals with the post-plutonic dyke emplacement that follows a phase of voluminous pluton emplacement. It includes a field overview with structural and petrographical descriptions of a regional dyke swarm of mafic to intermediate composition, which intruded into the plutonic intrusive suite

of the Southern Adamello. This paper addresses questions of the interplay of dyke emplacement mechanics with the regional stress field in the light of high resolution U-Pb age dating, allowing the use of dykes as stress markers in time.

The third chapter encompasses a study on the compositional evolution of magmas in a typical arc-tholeiitic differentiation suite, forming a dyke swarm ranging from olivine-phyric mantle-derived picrobasalts to amphibole-plagioclase-phyric dacites. In this chapter, the evolution of the composition of the fractionating mineral phases are described together with the composition of the corresponding liquid. Through mass balance calculations, quantities of the required cumulates are determined to produce evolved dacitic magmas. Furthermore, the effect of the changing fractionating mineral assemblage on the trace element signatures of magmas are investigated, with general implications for the differentiation of arc-tholeiitic to calc-alkaline magmas.

The fourth chapter examines the thermal effects of the intrusion of a closely spaced composite mafic dyke swarm on the mainly tonalitic host rock. This chapter investigates the links of mafic intrusion breccias associated with these closely spaced composite dyke swarms and addresses questions concerning the thermal conditions of the host rock leading to partial melting and making such textural features observed in outcrop. Further, evidence of assimilation on the emplacement level is based on bulk rock isotopic data, bulk rock geochemistry and mineral-chemical information of both the mafic intrusives and the potential tonalitic assimilant.

The last chapter investigates the assimilation of a felsic immiscible component in a mantle derived primitive picrobasaltic to Ol-tholeiitic magma. The chapter addresses questions of how features of immiscibility and mixing behaviour between an assimilated felsic and host mafic phase can be explained on a rheological and thermal basis. Moreover, this chapter evaluates the potential high-pressure/low-temperature origin of the xenocrystic accessory phase assemblage (zircon, rutile) associated with the felsic assimilant. Such a relation would be entirely novel to document in the Eocene to Oligocene intrusives along the Periadriatic Fault System (PFS) and would have larger implications on the general structure of the Central Southern Alpine crust and its geodynamic context.

Chapter 2

Dyke Swarm Emplacement as Stress Marker for the Post-Plutonic Cooling History

2.1 Abstract

Geochronological methods, combined with a detailed structural examination of post-plutonic dykes within the southern Adamello intrusive suite, have been used to put constraints on the remote stress conditions occurring at a late plutonic stage. Magmatic dykes immediately succeeded a phase of pluton assembly in the Re di Castello intrusive suite, ranging in age from 41.67 ± 0.06 Ma to 38.62 ± 0.12 Ma. The intrusion of magma forming the dyke swarm is predating The formation of cooling joints in the large plutonic bodies in this case is predating the intrusion of magma forming the dyke swarm. The emplacement of the dykes was associated with consistent left lateral strike-slip movement along magma dilatation planes, leading to en echelon segmentation of dykes. Through the dilation by magma of pre-existing weaknesses and cracks in an otherwise uniform host rock, the dyke propagation and according orientation in the horizontal plane adjusted continuously perpendicular to least compressive remote stress σ_3, resulting in an inferred rotation of the remote principal stress field. A purely elastic analytical model yields magma over-pressure for a magma filled crack encompassing values from 19-33 MPa associated with the dyke emplacement. An asymmetrical teardrop form including a stress gradient along the strike of the dilatation plane in the elastic model provides the best approximation to the observed two dimensional shape in the present case. Such a shape is consistent with a stress gradient caused by the remote stress field along strike. Due to their rheological contrast with the host rock, the dykes act as preferential nucleation surfaces for later brittle faulting, forming cataclasites throughout the southern Adamello Batholith.

2.2 Introduction

Dyke swarms offer the potential to reconstruct stress fields at the time of their emplacement because injection occurs perpendicular to the least compressive stress σ_3 and the direction of the dilatation plane of the magma filled fractures is oriented the same way [Anderson, 1951, Spence and Turcotte, 1985]. Alternative scenarios of dyke intrusion relate injection along pre-existing fractures or joints rather than the fractures being induced through the injection of the magma [Delaney et al., 1986, Delaney and Pollard, 1981]. Magma flow and overpressure in cracks has been investigated through their shapes in detailed field studies previously relating this process to theoretical elasticity analysis of a pressurized slit or crack [Delaney and Pollard, 1981, Kavanagh and Sparks, 2011, Poland et al., 2008, Pollard and Muller, 1976, Valentine and Krogh, 2006, Walker, 1986]. Another approach to study the propagation of a liquid filled fracture or fissure is by analogue experiments [McLeod and Tait, 1999, Menand, 2010, Menand and Tait, 2002, Takada, 1990, Watanabe et al., 2002]. Furthermore, numerical simulations have been employed to address the same question [Chen et al., 2007, Gudmundsson et al., 1999, Lister and Kerr, 1991, Maccaferri et al., 2010, Rivalta and Dahm, 2004]. Syn- to post-plutonic dyke swarms are a common feature in plutonic complexes such as the Southern Adamello [Coleman et al., 2000, Creixell et al., 2009, Dini et al., 2008, Taylor and Randall, 2000]. The study of dyke swarms in tonalitic to granodioritic host rocks exhibiting a high degree of mechanical isotropy [Dini et al., 2008] should provide more straightforward information about the palaeostress configuration at the time of dyke emplacement than the same magmatic features within layered sediments and/or foliated metamorphic environments. Such a configuration of dyke emplacement into an isotropic plutonic host rock also allows the investigation of the relationship between

dyke emplacement direction and geometry in relation to pre-existing fractures (jointing) or faults [Delaney et al., 1986, Glazner et al., 1999, Tokarski, 1990]. As Glazner et al. [1999] note, tensile cracks within a shear zone initially form normal to σ_3, but bulk non-coaxial strain will cause cracks to rotate and to accommodate shear strain as finite deformation proceeds. Such relations were described for the patterns of hydrothermal veins [Alastair, 1975, Hancock, 1972, Ramsay, 1980] and according to Glazner et al. [1999], should not differ for syn-kinematic cracks. Magmatic dykes are excellent time markers [Hanski et al., 2010, Willigers et al., 1999] for the crustal evolution due to their short term activity. Crosscutting relationships among different intrusive rocks, fractures and faults can be coupled with radiometric age dating of either syn-tectonic minerals or minerals crystallizing within intrusive bodies, thereby providing a tool to reconstruct the emplacement tectonics of the succession of intrusive rock emplacement. The Adamello Batholith is the largest intrusive complex among the Oligocene plutons, which are spatially and temporally associated with the activity of the Periadriatic Fault System (PFS) [Rosenberg, 2004]. The contacts of the southern part of the Adamello Batholith, the so called Re di Castello intrusive suite [Callegari and Brack, 2002], are farthest away from the Periadriatic Fault System, whereas all other Oligocene plutonic complexes are located within 4km or less with one of their contacts from the PFS [Rosenberg, 2004]. Magmas of the southern Adamello Batholith most likely ascended independently of the PFS. In contrast, the Bergell pluton forms a 40km long steep tabular body of tonalite sub-parallel to the PFS. In this case, the tonalitic tail is part of the Periadriatic mylonite zone and the same body is considered to represent the feeder of the pluton, based on steep magmatic foliations and lineations [Berger et al., 1996]. The ages of the post-plutonic dykes occurring in the southern part (Re di Castello superunit) of the Adamello Batholith are only relatively constraint. This paper provides structural relationships between different dyke generations. For selected locations, more detailed 2D dyke geometries were recorded and compared with theoretical elastic models [Muller and Pollard, 1977, Pollard, 1987] of dyke emplacement. Furthermore, we provide new U-Pb TIMS single crystal zircon and titanite ages of these post-plutonic dykes covering the entire relative time sequence, which are combined with existing geochronological data from the individual plutonic units of the southern Adamello Batholith. A geometrical analysis of the dykes together with the new age determinations allows constraining of the relationships between magmatic and tectonic activity, since dykes act as time markers and provide information on the palaeostress distribution. The timing of the dyke emplacement is finally compared with the geochronological constraints available on the evolution along the Periadriatic Fault System.

2.3 Regional Setting

The Central Southern Alps that stretch from Lake Como in the West to the Giudicarie line in the East form part of a south-vergent fold-and-thrust belt [De Sitter and De Sitter-Koomans, 1949, Schmid et al., 2004, Carminati et al., 1997]. The Periadriatic Fault System (Fig. 2.1) is the largest fault system of the Alps and strikes more or less E-W over a distance of ~700km, extending from NW Italy to northern Slovenia [e.g. Argand, 1916, Laubscher, 1990a, Muller et al., 2001, Schmid et al., 1989]. The PFS has two characteristic bends/offsets that strike towards NE-SW. The first is the Canavese fault in the westernmost part and the other significant bend is the the Giudicarie-Mauls fault (Fig. 2.1) in the central sector [Müller et al., 2001]. East of the Bergell pluton, there is a displacement partitioning along the PFS

into a northern, intra-Austroalpine fault system, which is expressed by predominantly sinistral and N-side up vertical movement and the Tonale-Pustertal faults, where dextral deformation is dominant [e.g. Mancktelow et al., 2001, Wiedenbeck, 1986].

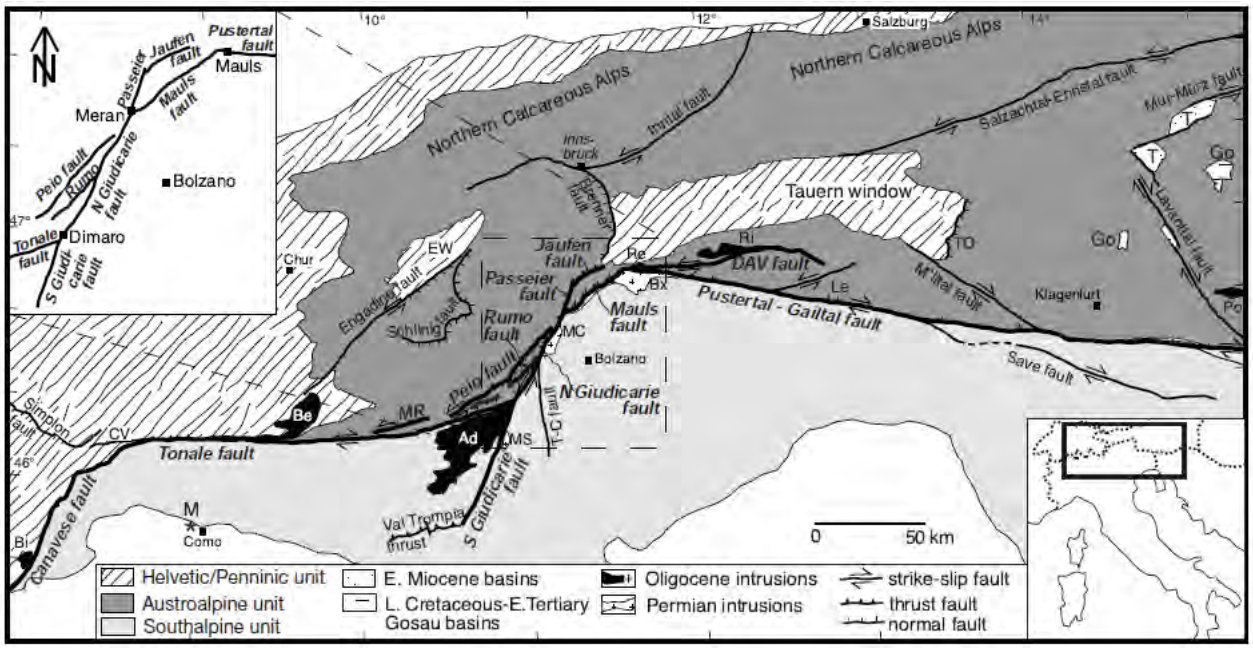

Figure 2.1: Simplified tectonic sketch map after Müller et al. [2001] of the Alps showing all major faults related to the Periadriatic fault system (PAF; thick black lines), as well as other faults (thin black lines) and major features of the Alps mentioned in the text; based on Bigi [1990] and modified after Neubauer and Genser [1990]; Ratschbacher et al. [1991]; Mancktelow [1992]; Fügenschuh [1995]; Froitzheim et al. [1997] and Prosser [1998]. Faults: CV Centovalli; MR Mortirollo; T-C Trento-Cles; DAV Defereggen-Antholz-Vals; TO Tauernostrand; plutons: Bi Biella; Be Bergell; Ad Adamello-Presanella; MS Monte Sabion; MC Monte Croce; Bx Brixen; Re Rensen; Ri Rieserferner; Le Lesachtal; Po Pohorje; basins: Go late Cretaceous-Paleogene "Centralalpine" Gosau Group basins; T Miocene basins. EW Engadine window; M Molasse with Bergell boulders.

With regard to metamorphic conditions, no significant difference between either side of the Tonale and the Pustertal fault is observed [Müller et al., 2001]. The Adamello Batholith is situated between the E-W trending Tonale Line and the southern end of the Giudicarie Line South of the junction of the Tonale Fault with the Northern and Southern Giudicarie Fault [Laubscher, 1990b, Schmid et al., 1989, 2004]. It has been proposed that the local stress field in relation to the Giudicarie Fault system has influenced the emplacement of the Adamello pluton [e.g. Laubscher, 1983]. For decades, two different models were proposed for the evolution of the N(N)E trending North Giudicarie Fault, depending on the role assigned to the Peio fault. A first model assumes that during the Neogene, the sinistral North Giudicarie fault deactivated a previously straight dextral Tonale-Pustertal-Gaital fault. This offset accumulated more than 50km and possibly up to 300km of displacement between the Tonale Fault and the Pustertal-Gailtal fault [e.g. [Frisch et al., 1998, Laubscher, 1971, Ratschbacher et al., 1991, Schönborn, 1999, Stipp et al., 2004, Werling, 1992, Schmid et al., 1996]]. The alternative model that has been put forward infers an already curved PFS. A compressional Neogene inversion reactivated Early Permian to Lower Liassic NE-

SW trending horst and graben structures. With such an interpretation, the Giudicarie-Mauls fault is at least a cogenetic part of the Oligocene (or older) PFS. Consequently, the sinistral deplacement along the whole PFS is reduced to $\leq$ 50km in the (post-) Oligocene [e.g. Castellarin et al., 2006, Castellarin and Cantelli, 2000, Muller et al., 2001, Picotti et al., 1995, Prosser, 2000, 1998, Viola et al., 2001]. Individual laser ablation $^{40}Ar/^{39}Ar$ dating of pseudo-tachylites from the Peio fault resulted in a mean apparent age of 45.8 $\pm$ 0.6 Ma. Two other pseudo-tachylites from a thin shear zone south of the Peio fault were dated by stepwise heating and the laser ablation $^{40}Ar/^{39}Ar$ method and yielded ages between 35 and 37 Ma, consistent with Rb-Sr micro-sampling analyses of mylonites. These ages suggest Late Eocene thrusting within the Tonale unit south of the Peio fault [Müller et al., 2000, Viola, 2000].

The Central Southern Alpine wedge is composed of a complex assembly of stacked thrust sheets [Brack, 1984, Forcella, 1988, Laubscher, 1985, Gaetani and Jadoul, 1979, Schönborn, 1992, Wennekkers, 1932]. The entire wedge has a basal décollement in the Pre-Permian basement that varies in depth from 5km at the wedge tip in the Po plain [e.g. Pieri et al., 1981] to a depth of about 16km close to the PFS [Montrasio et al., 1994]. Three major thrust sheets are inferred; the present exposure is limited to the upper two. Extrapolation of the lowest thrust system is inferred from surface data projected downwards, as well as by seismic data in the Po basin northwards. The uppermost, oldest thrust sheet is well exposed in the Grigne east of Lake Como. In this area, the connection between the sedimentary décollement thrusts with the basement (Orobic thrust) has been mapped [Laubscher, 1985, Schönborn, 1990, 1992]. This basement thrust (Orobic thrust) transported basement onto Permian and Triassic units of thrust sheet 2. The second thrust sheet consists of Pre-Permian basement to Permian and Middle to Upper Triassic to the lower Cretaceous lithologies and is bound laterally by strike slip faults. Thrust sheet 2 is split into a northern (2A) and southern part (2B), both with their own basement and Middle Triassic units. For the regional tectonic situation around the Adamello Batholith, this implies kinematically pre-Adamello (most likely Late Cretaceous) folding of the Cedegolo and the aligned Cabianca-Trabuchello and Orobic anticlines and post-Adamello (most likely Middle-Late Miocene) reactivation of the Orobic and Trabuchello-Cabianca anticlines, together with the Trompia structural high. The Cedegolo anticline was not active except in its westernmost part during Miocene times [Brack, 1984, Laubscher, 1990a, Schönborn, 1990, 1992]. Thrust sheet 1 is clearly sealed, deformed and overprinted by the Adamello intrusives [Brack, 1981, Cornelius, 1924]. Balanced cross-sections by Schönborn [1992] resulted in estimated shortenings of 25km for the pre-Adamello and 56-87 km for the post Adamello deformations for the western and eastern sectors of the Central Southern Alps, respectively. Roeder [1992] modelled the Southern Alps as a critical frictional wedge. In this sense, purely frictional wedges are characterized by narrow, nearly constant tapers which contrast with the topographic profiles through the Central Southern Alps. The topographic profiles from South to North are characterized by a series of slopes and plateaus. This particular topography is typical of large wedges where temperature-dependent plastic creep deformation becomes dominant in the deepest parts of the wedge, whereas brittle deformations dominate in the shallow frontal portions [Williams et al., 1994]. With regard to these differences in deformation mechanisms, Carminati and Siletto [1997] evaluated the feasibility of plastic deformations at the wedge base and within the basal décollement of the Central Southern Alps and stressed the importance of plastic processes for the Miocene to present mechanics of the belt.

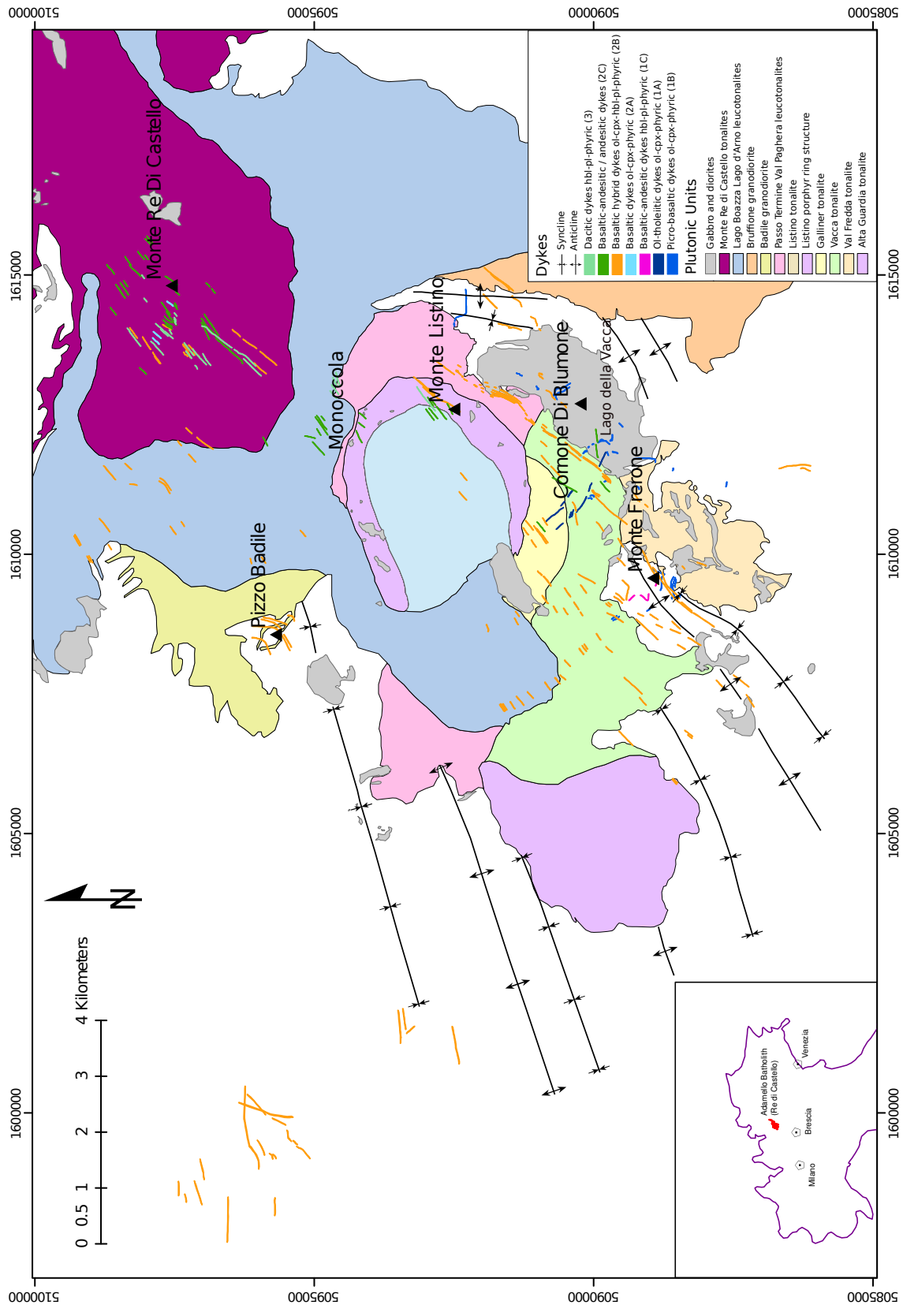

Figure 2.2: Geological map (Map datum: Monte Mario/Italy zone 1, Transverse Mercator Projection, UTM grid) of the post-plutonic dyke swarm intruding into the Re di Castello intrusive suite forming the southern part of the Adamello Batholith. Post-plutonic dykes were mapped and classified for the petrography and composition [Hurlimann 2009-2012] and further compiled [Brack, 1984, Callegari and Brack, 2002, Rösli, 1982, Ulmer, 1982]. Val Fredda Complex (VFC) includes the Val Fredda tonalite and gabbros and diorites. Lago della Vacca Complex (LVC) comprises the Vacca tonalite and Galiner tonalite. Blumone Complex builds up the Cornone di Blumone and consists mainly of a gabbroic layered sequence. Inset shows location in Italy.

The Adamello Batholith is split up into four larger intrusive suites (superunits) from oldest to youngest, Re di Castello, Adamello, Avio, and Presanella [Callegari and Brack, 2002]. Different generations of post-plutonic dykes with a large compositional range from picro-basalts to dacites [Bianchi and Dal Piaz, 1937, Callegari and Brack, 2002, Monese, 1968, Morgante, 1972, Ulmer et al., 1983, Ulmer, 1986] crosscut the Re di Castello unit, which is a composite plutonic assembly of gabbros, diorites, tonalites, granodiorites, and very minor granites. These plutons decrease systematically in age from 42.43 ± 0.05 Ma in the southwest to 39.8 Ma in the north [Hansmann, 1986, Hansmann and Oberli, 1991, Schaltegger et al., 2009] over a distance of 65 km. The different intrusive bodies are mainly tonalites and granodiorites that intruded into the Pre-Permian south-alpine basement and the overlying Permo-Mesozoic sedimentary cover [Callegari, 1983, Callegari and Brack, 2002]. Mafic sheets of gabbroic and dioritic composition occupy a marginal position in relation to the large tonalitic and granodioritic intrusions [Blundy and Sparks, 1992, Ulmer, 1986]. The contacts of the plutonic intrusives with the basement and sedimentary host rocks are vertically or steeply outward dipping [Brack, 1983]. Strong syn-intrusive deformation is expressed in sedimentary tongues that are sandwiched between neighbouring intrusions. Moreover, large scale open folds are compressed into more isoclinal forms that deviate considerably from the regional strike of antiforms further to the West due to rotation and tilting [Brack, 1983, 1984]. The extent of this syn-intrusive deformation is not quantified to date.

Hypabyssal calc-alkaline bodies, basaltic to dacitic in composition, postdate the two phases of thrust stacking in the Gandino and Presolana area in the Orobic Alps (Bergamasque Alps), east of the Southern Adamello Batholith and yielded SHIRMP U-Pb zircon ages that span between 42 ± 1 and 39 ± 1 Ma. This time span overlaps with the range of the formation of the southern part of the Adamello Batholith, Re di Castello intrusive suite [D'Adda et al., 2011]. The related dyke swarms were controlled by ENE-WSW extensional fault systems pointing towards the existence of a local extensional regime during magma intrusion. Moreover, an amphibole-gabbro forming part of a series of small intrusions along the Northern Giudicarie and Meran-Mauls fault resulted in a concordant well-defined U-Pb zircon age of 38.9 ± 0.4 Ma, close to the time range of the youngest reported ages from the Dernal granite and the Re di Castello Tonalite [Hansmann, 1986, Hansmann and Oberli, 1991, Pomella et al., 2011].

2.4 Relative Time Sequence and Structural Relationships

Local Dyke Swarm of Val Fredda-Monte Frerone and Lago della Vacca Area

The Val Fredda Complex (VFC) comprises (Fig. 2.2) the southernmost and oldest intrusive rocks of the Adamello massif. This area was mapped first by Bianchi and Dal Piaz [1937]; subsequent work was carried out on the intrusive rocks and their sedimentary host rocks by several authors [Blundy and Sparks, 1992, Brack, 1981, Ulmer et al., 1983, Ulmer, 1986]. Blundy and Sparks [1992] interpreted the VFC as a series of magma pulses that were emplaced in the following order: tonalites and granodiorites; aphyric diorite and gabbro; hornblende-phyric gabbro and diorite. Overall this complex has been interpreted as the intrusion of mafic sheets with a thickness ranging between 0.5 to >100 m into a partially solidified felsic host magma. Mafic sheets show irregular boundaries and disintegrate laterally into dense swarms of mafic inclusions. Features of mixing between the host tonalite and the mafic sheets are abundant, preserved as

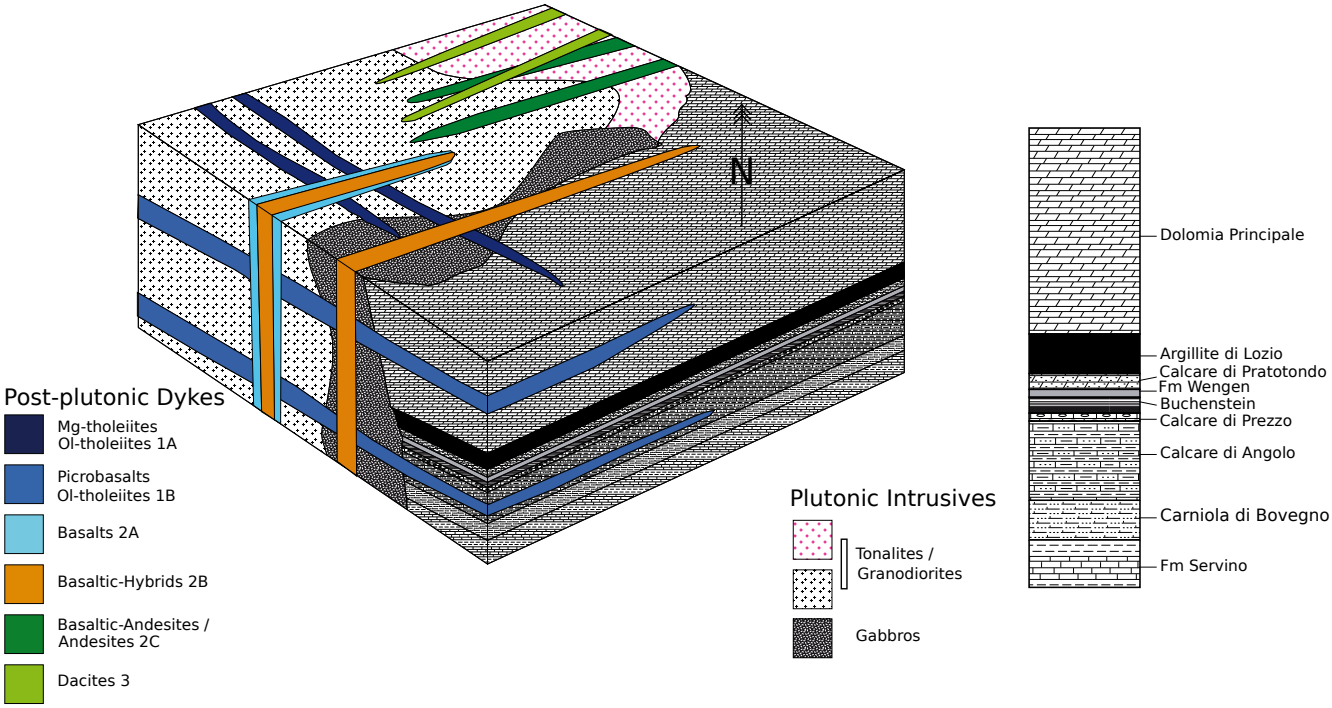

Figure 2.3: Schematic geometry of cross cutting relationships [mapping Hurlimann 2009-2012] of post-plutonic dyke generations that intruded into the Re di Castello plutonic suite. Plutonic intrusives are shown qualitatively whereas Triassic stratigraphy is drawn after Brack [1984] but is not to scale.

crystal aggregates of plagioclase, biotite and quartz in various stages of reaction inside the mafic sheets, as well as by the presence of numerous mafic inclusions [Blundy and Sparks, 1992]. The roof of the intrusion corresponds to the lower stratigraphical limit of a thick sequence of dolomites that belongs to the Breno Formation and the Dolomia Principale [Blundy and Sparks, 1992, Brack, 1981]. These dolomites are now preserved as roof pendants and stoped blocks up to 300m across, and the emplacement structure has been interpreted as a laccolith whose form was controlled by the pre-intrusive folds of the Triassic host rocks [Blundy, 1989, Blundy and Sparks, 1992], although no evidence of a floor is known.

Towards the NE, the VFC is intruded by the Lago della Vacca Complex (LVC) (Fig. 1), which forms another part of the incrementally assembled Re di Castello unit [John and Blundy, 1993, Schoene et al., 2012]. The LVC complex is comprised of high-K marginal tonalite, the low- to medium-K Vacca tonalite and the Galiner granodiorite. The Blumone Complex situated at the southeastern border of the LVC is built by an older stratified gabbroic sequence which now forms the Cornone di Blumone and the Scoglio di Laione [Ulmer et al., 1983, Ulmer, 1986]. This gabbroic sequence was later disrupted by the intrusion of hydrous gabbroic and tonalitic rocks. The Blumone Complex comprises various rock types, encompassing plagioclase-bearing wherlites, granular olivine-gabbros, granular gabbros, granular cpx-bearing anorthosites to anorthositic gabbros, coarse grained magnetite and hornblende ultramafic cumulates. The entire Blumone Complex is crosscut by younger pegmatitic hornblende gabbros [Rösli, 1982, Ulmer et al., 1983, Ulmer, 1986]. The emplacement model of John and Blundy [1993] suggests an early phase with brittle fracturing and stoping of country rocks [Brack, 1983] with a transition to incremental, forceful intrusion

through inner magma pulses, creating a margin-parallel foliation and increasing cumulative magmatic strain towards the margins. Brack [1984] noted the apparent dextral offset of the anticline-syncline pair of Triassic sediments between the Val Fredda and the Val Caffaro and related this movement to the eastward translation of the Blumone Complex due to the forceful emplacement of the LVC.

Two different sets of post-plutonic dykes were already described by Bianchi and Dal Piaz [1937] and Ulmer [1986]. The older generation, here designated as picro-basalts and olivine-tholeiites (1B), are blackish green coloured dykes, 0.5 to 2.5 m thick. They are sub-horizontal (Fig. 2.2, 2.4a, 2.6) sill-like features with micro-gabbroic texture with fine-grained apophyses. The chilled margins are fine-grained (<2 mm) and exhibit pseudomorphs of olivine (12%) and sparser clinopyroxene (5%) phenocrysts. The central parts of these dykes are micro-gabbroic with abundant greenish hornblende and interstitial plagioclase. Felsic plagioclase-rich lenses or schlieren like features are observed within these dykes. They are present across 5km from the Frerone area in the Val Fredda to the Lago della Vacca-Blumone area and extend as far NE as the Scoglio di Laione. Particularly along the crest from the Passo della Vacca to the Cima Terre Fredde and within the cliffs of Cornone di Blumone, these picro-basaltic and Ol-tholeiitic dykes (1B) occur at different levels of altitude. Ulmer [1986] described these dykes (1B) as flat lying intrusions in the central part and increasingly steeply dipping towards the peripheral in the area of the Passo della Vacca and around the Cresta di Laione, and potentially also in the area of Monte Frerone, forming a cupola-like structure. This dyke generation clearly crosscuts the VFC, Blumone Complex, and LVC (Fig. 2.2) plutonic units, constraining their relatively younger age. The SW-face of the Monte Frerone reveals well exposed crosscutting relationships between these dykes (1B) and the Triassic sediment sequence. Brack [1981] described the rheological inversion of the regularly bedded multi-layered sequence of the Calcare di Angolo during contact metamorphism that led to recrystallization of marls to hornfels and limestone to calcite marbles. The hornfels layers typically exhibit boudinage within the marbles within the contact metamorphic zones. Where flat-lying dykes (1B) show sharp steps, the layered hornfels facies displays folding (Fig. 2.5a) in accordance with these abrupt dyke margins. Slight shortening of these flat-lying dykes is observed in the SW-flank of Monte Frerone.

These sub-horizontal picro-basalts and Ol-tholeiites (1B) are clearly crosscut by younger sub-vertical dyke generations (2A, 2B) (Fig. 2.2, 2.3) that extend much further to the northeast (15 km) towards the Re di Castello-Passo di Campo area. At the highest levels, close to the peak of Monte Frerone, a 2m wide sub-horizontal, pyroxene-hornblende-plagioclase phyric andesite dyke slightly dipping to the NW is encountered. This dyke occurs isolated and has previously been described [Brack, 1981, De Lucchi, 1938/39] to be crosscut by the regional dyke swarm of generation (2A, 2B).

A distinct generation of Ol-tholeiitic dykes (1A) strikes N70W to N30W (Fig. 2.6) with sub-vertical dips ranging from 81° to 55°. The strike direction of these Ol-tholeiitic dykes differs clearly from the structural setting of basaltic (2A) and basaltic hybrid dykes (2B) present in the same area that are described subsequently. These Ol-tholeiitic dykes are confined to the Lago della Vacca area from where they reach out about 1.5 km further to the SW (Fig. 2.2). The strike orientation of these Ol-tholeiitic dykes is perpendicular to the regional fold axes (Fig. 2.2). Chilled margins are fine grained and 1 to 5cm thick. Central parts of these dykes are characterized by abundant pseudomorphs of coarse-grained olivine (13%) and clinopyroxene (12%) phenocrysts. In rare instances, cores of olivines are preserved and yield a

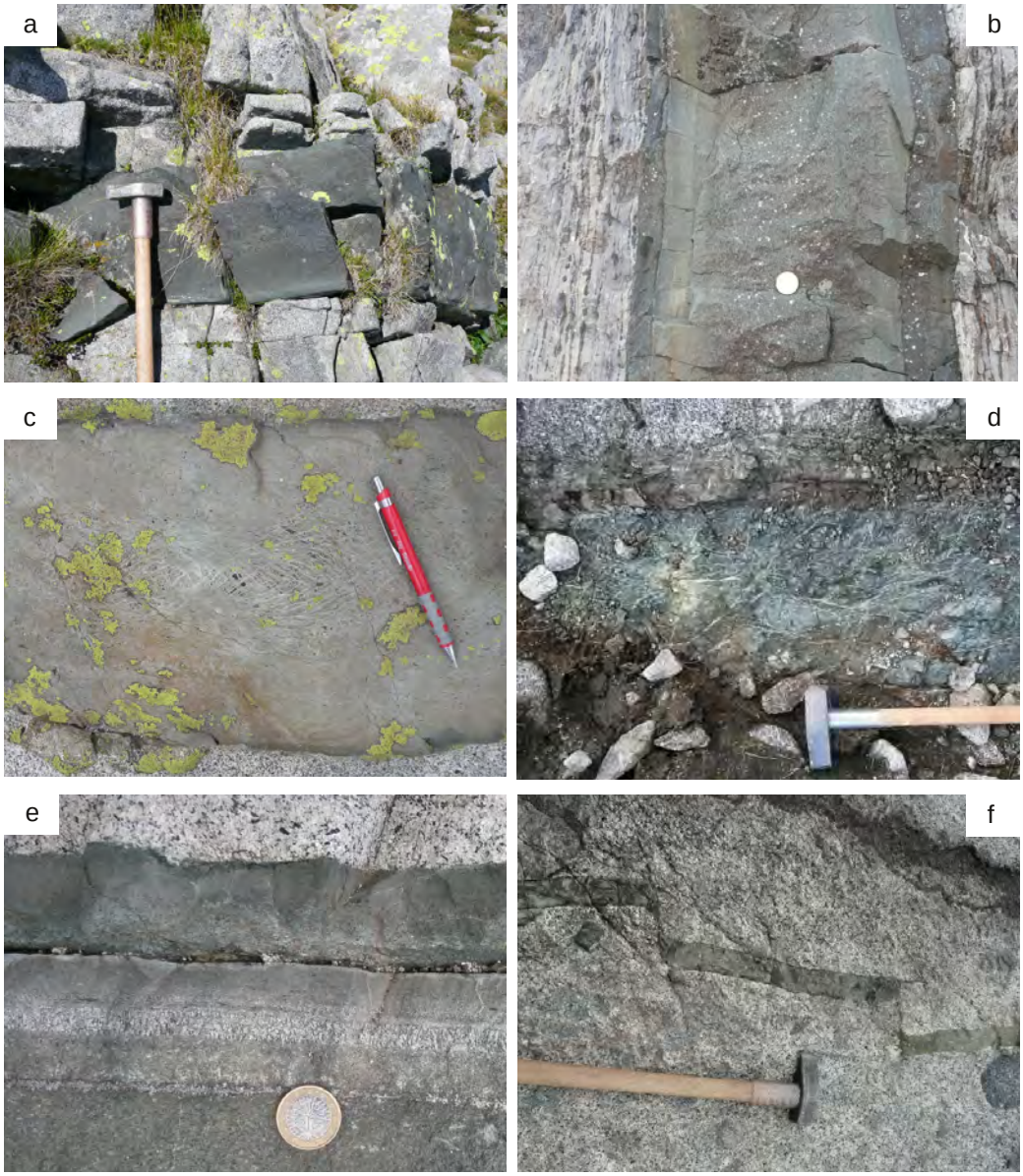

Figure 2.4: Field photographs of post-plutonic dykes: *(a)* Sub-horizontal Olivine-tholeiite dyke of generation (1B) in the Lago della Vacca area. *(b)* Basaltic and hybrid basaltic dykes of generation 2B show common composite structures built-up by multiple injections. *(c)* Brighter coloured conjugate shear bands are identified as melt-rich zones associated with left slip movement along magma filled fracture plane during emplacement. *(d)* Late brittle shearing focalized along a basaltic dyke (2A) at Passo Dernal (Re di Castello). *(e)* Comb-layering developed along dyke margin with alternating clinopyroxene-amphibole and plagioclase combs. *(f)* En echelon dyke segments of basaltic-hybrid dyke (2B) at NE-side of Cima Sablunera.

rusty orange colour. Coarse-grained crystals are sorted and concentrated in the middle part of the dykes to form aggregates or clumps. Common felsic plagiolcase-rich schlieren and lenses are interpreted as partly digested assimilated material. These felsic zones partially form internal channel structures. Many (1B) dykes branch en echelon along strike.

Regional Dyke Swarm Val Fredda to Re di Castello

A continuous dyke swarm of several generations (2A, 2B, 2C, 3) spreads over the entire Re di Castello intrusive suite (18 km) (Brack, 1984) and reaches into the adjacent Triassic sedimentary host rock sequence as well. Overall, this dyke swarm encompasses a large compositional range from basalt to dacite. The mean value of strike of this dyke swarm spreads from N30E to N47E with near-vertical dips ranging as shallow as 65° to 76° over the different generations (Fig. 2.6). The northernmost members of this dyke generation crop out in the Bissina quarry at the Lago di Bissina [Ulmer, 1986] close to the contact with the Adamello superunit (Western Adamello tonalite). To the west, these dykes have previously been traced to the Concarena [Brack, 1984] on the west side of the Val Camonica. A possible continuation is present by the dykes and associated gabbroic and tonalitic stocks of the Orobic Alps (Bergamasque Alps) [D'Adda et al., 2011, De Michele and Zezza, 1979, De Michele et al., 1983]. The dykes in the Orobic Alps were assigned by De Michele et al. [1983] to an arc-tholeiitc and calc-alkaline magmatism and were correlated with the Gandino leucogabbro stock. The eastward limit of the present regional dyke swarm (2A, 2B, 2C, 3) was located in the Passo del Frate-Cima Uzza area (22km from SW end of dyke swarm), between Val Daone and Val Breguzzo (22km from SW end of dyke swarm), where an olivine-clinopyroxene-phyric-basaltic dyke containing various types of crustal xenoliths and an amphibole-plagioclase-phyric andesitic dyke containing mafic enclaves and xenoliths were observed. An additional dyke was reported by Ulmer [1986] in the northern flank of Val Danerba (24km from SW end of dyke swarm).

The compositions of these dykes, described in an accompanying paper, range from Ol-tholeiites to dacites. Composite dyke structures are common, expressed as multiple internal contacts (Fig. 4b). The Val Fredda-Monte Stabio-Monte Frerone area and further northeast to the Val Braone-Lago della Vacca-Cima Laione area is dominated by dark green, fine-grained dykes exhibiting larger (1-3mm) phenocrysts of olivine-pseudomorphs, clinopyroxene and amphibole. These dykes can be subdivided into Ol-tholeiitic to basaltic dykes (2A), with phenocrysts of olivine-pseudomorphs and clinopyroxene. The same dykes (2A) have micro-phenocrysts of clinopyroxene and plagioclase. Dyke type (2B) is characterized by the same phenocryst assemblage but shows abundant coarse-grained, rounded xenocrysts of quartz and coarse grained plagioclase crystals with resorbed cores or partial resorption textures, which indicate assimilated materials. Moreover, (2B) dykes often contain coarse-grained amphiboles with resorbed cores rimmed by a fresh, brown-red overgrowth. In the vicinity of these dykes, commonly increased dyke-parallel jointing is observed towards the dyke contacts within the host rock (Fig. 2.5d-f). This feature is particularly well expressed at the dyke tips (Fig. 2.5d, f) or bridges where an alteration front (5-15 cm) (Fig. 2.5d, e) of the tonalitic wall-rock exists. These alteration zones appear to indicate the exsolution of fluids from the dyke magma during brittle fracture opening in the course of dyke propagation. Within these alteration zones, brown amphibole in the tonalitic wall-rock is replaced by chlorite, and plagioclase is replaced by sericite.

Amphibole-plagioclase-pyhric andesites (2C) and amphibole-plagioclase-pyhric dacites (3) are confined to a 8 km span between Monte Listino to Re di Castello-Passo di Campo, including Val di Dois and parts of Val Daone. They are characterized by a green to light-green, fine-grained matrix with coarse-grained euhedral homogeneous plagioclase and amphibole phenocrysts to 15 mm. Plagioclase exhibits thin, more albite rich overgrowths. In some instances, comb-layering (Fig.2.5e) projects in a symmetrical way from the

dyke margins. This comb-layering is composed of alternating layers of brown-green amphibole, plagioclase and clinopyroxene where the comb minerals are set in a matrix of lath-shaped plagioclase and amphibole. The latter dacites (3) crosscut the basaltic-andesites and andesites (2C) (Fig. 2.5c), as revealed around Monte Re di Castello. The regional dyke swarm (2A, 2B, 2C, 3) is clearly younger than the previously described plutonic VFC, Blumone Complex and the LVC clearly shown by crosscutting relationships. Furthermore, these dykes intrude into the Listino Ring Structure (Fig. 2.2), which was first described by Brack [1983, 1984] as a mechanically syn-intrusive, strongly deformed ring-shaped structure with a massive internal, fine-grained homogeneous tonalitic core, 2.5km in diameter. This sub-vertical or steeply inwards dipping zone is inferred to have a cylindrical structure. Petrographically, its external zone comprises a heterogeneous suite of fragments of mafic, ultramafic and sedimentary rocks, syn-plutonic mafic dykes and mafic enclaves set in a matrix of medium-grained porphyritic tonalite and granodiorite [John and Blundy, 1993]. Dykes of generation 2C and 3 crosscut the Lago Boazza-Lago D'Arno fine-grained, leucocratic and massive, hornblende-biotite granodiorite (extent: 16 x 28km). In the north, this dyke swarm intruded into Badile granodiorite (extent: 4 x 5.5km), the fine-grained biotite-hornblende tonalite of the Monte Re di Castello (extent: 10 x 28 km) and an associated, small leucocratic mass of garnet-bearing biotite leucogranite at Passo Dernal [Brack, 1984, Callegari and Brack, 2002].

Crosscutting relationships between the various dyke generations are summarized in Figure 2.3. Basaltic-andesites and andesites (2C) and dacites (3) are more abundant in the northeastern part of the Re di Castello superunit (Fig. 2.2).

2.5 Structural Features of Dykes

Detailed Form of Dykes in Mapview

About 1.5 to 2km southwest of the Re di Castello summit, two parts of en echelon basaltic-andesitic dyke (2C) were mapped in detail to record thickness changes along the strike of these dyke segments (Fig. 2.9a). An overview map of the two dyke segments within the Conca del Gellino at the top of Val di Leno is displayed in Figure 2.7. The map clearly reveals the pervasive direction of jointing as measured in the field along a traverse. Lineaments were mapped remotely with the aid of orthophotos. These lineaments were recognized clearly as jointing surfaces due to their correspondence with actual measurements in the field (Fig. 2.7). For the two dyke segments, the mean strike is N51E with a mean dip of 81° and the mean strike of measured regional jointing is N46E with a mean dip of 80 (Fig. 8). From a structural point of view, these measurements indicate that these features are to the extent of 5-10° discordant to each other. The two dyke segments step en echelon to the SE (Fig. 2.9a). Continuous thickness measurements were taken along the strike of the two dyke segments (Fig. 2.9b, c). The two histograms of the frequency of the thickness measurements in Figure 2.9d reflect well the limitations of such measures with regard to outcrop conditions. Dyke thickness from these measurements ranges from 0.12 to 1.35m.

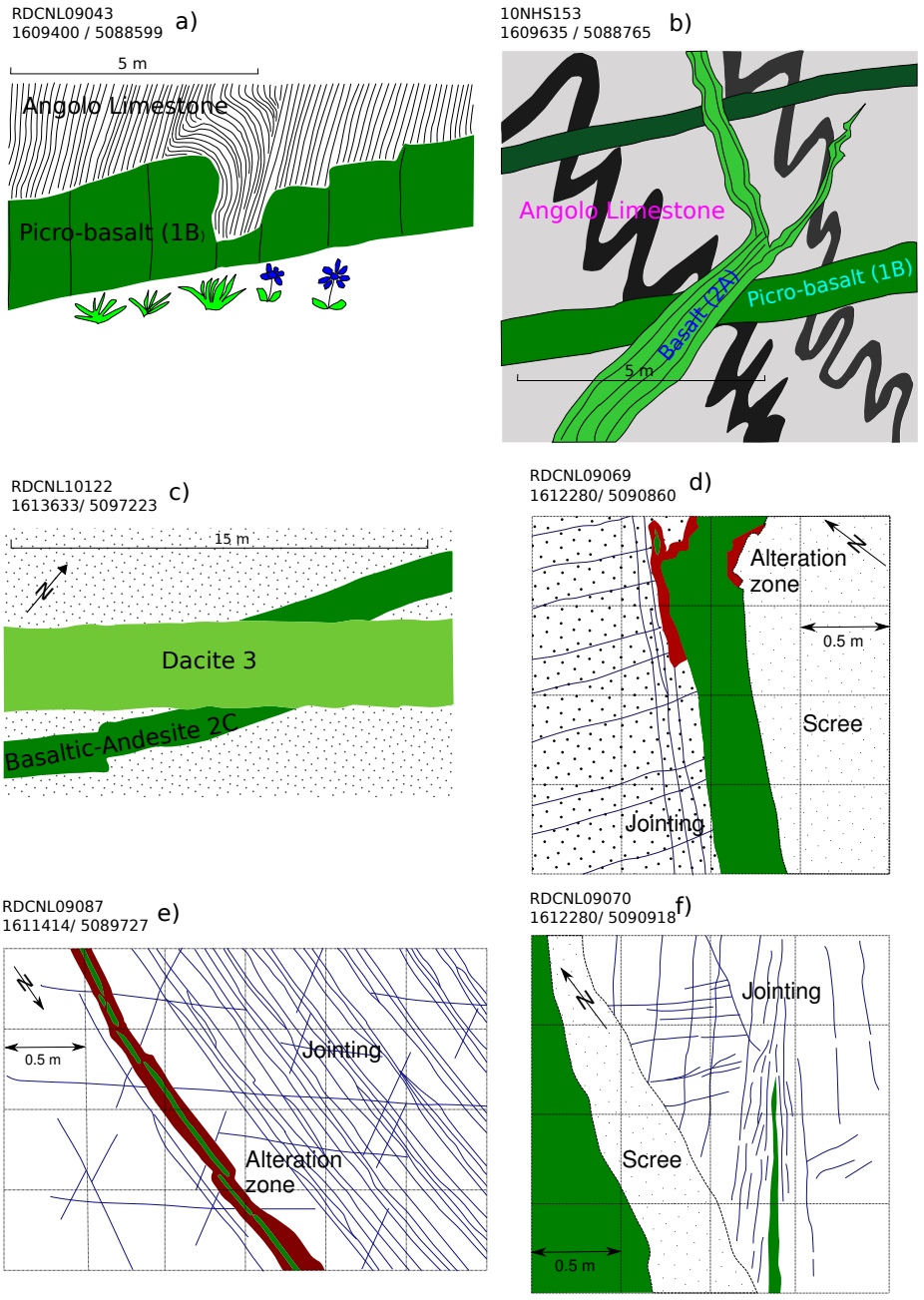

Figure 2.5: Field sketches of post-plutonic dykes (Map datum for coordinates: Monte Mario/Italy zone 1, Transverse Mercator Projection) *(a)* Along flat-lying picro-basalt dyke (1B), folding of the metamorphic hornfels facies of the Calcare di Angolo occurs towards depressions of dyke steps, indicating higher temperature conditions of the wallrock due to contact metamorphism during emplacement of the dyke. *(b)* Crosscutting relationships between subhorizontal picro-basalts/Ol-tholeiites (1B) and later basaltic dykes (2A). *(c)* Differentiated dacites (3) cut earlier basaltic-andesites/andesites (2C). *(d)* Dyke bridge with associated alteration of the wallrock indicates fluid exsolution processes at the tip during propagation. Close spaced dyke parallel jointing is associated with the dyke emplacement and crosscuts other joint set in the tonalitic host rock. *(e)* Dyke strand that displays similar alteration zone as observed in *(d)*, together with abundant parallel jointing associated with dyke propagation. *(f)* Dyke tip that stopped during propagation and clearly shows the forgoing fracturing linked to dyke propagation.

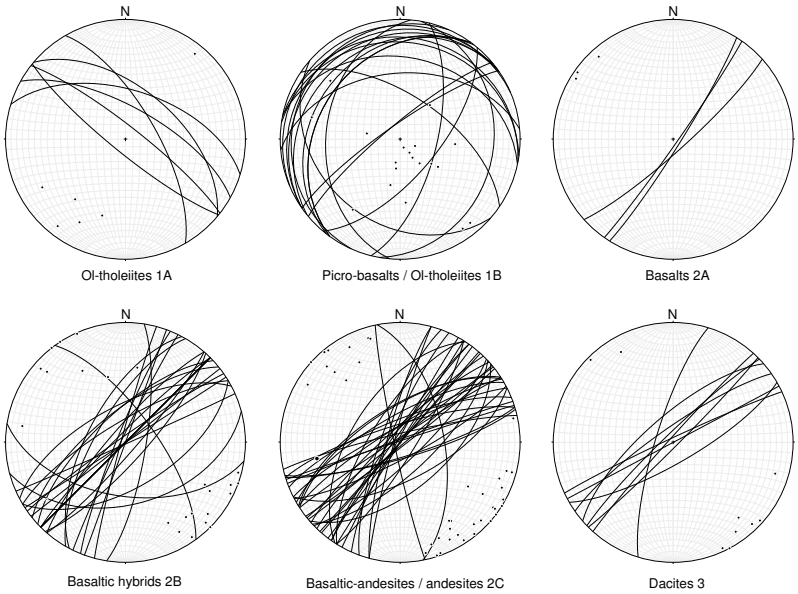

Figure 2.6: Stereographic projections of dyke planes and according poles within an equal area stereographic projection (Schmidt net, lower hemisphere projection) for all the different dyke generations (1A, 1B, 2A, 2B, 2C, 3) distinguished in Figure 2.3. Generations (2A, 2B, 2C, 3) belong to the same regional dyke swarm that intruded into the Re di Castello intrusive suite and therefore display, very similar orientation in general.

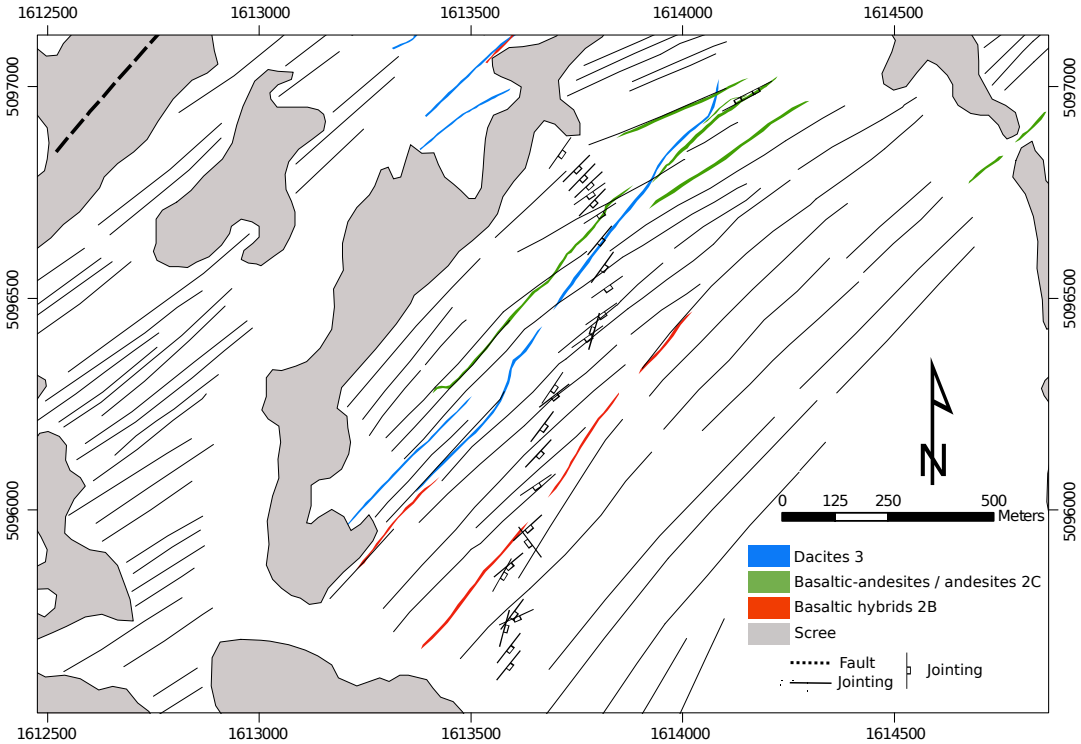

Figure 2.7: Detailed map of dyke segments from the Conca del Gelino, located on the S-side of Monte Re di Castello. Lines that indicate jointing were traced on orthophotos. Ground proof of jointing was established through a measurement traverse shown on the map.

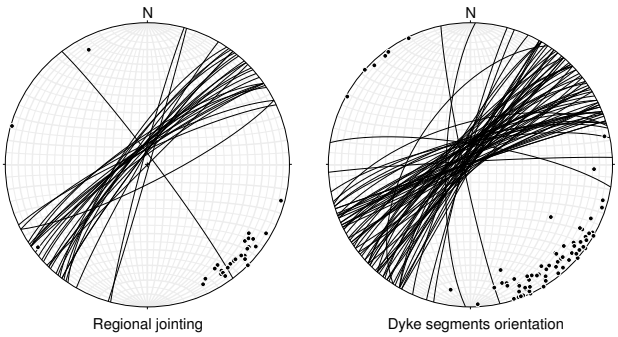

Figure 2.8: Equal area stereographic projection of regional jointing surfaces (planes, poles) indicated on the map in Figure 2.7. For comparison, dyke planes and poles are shown in a similar projection displaying good correspondance in orientation in relation to regional jointing.

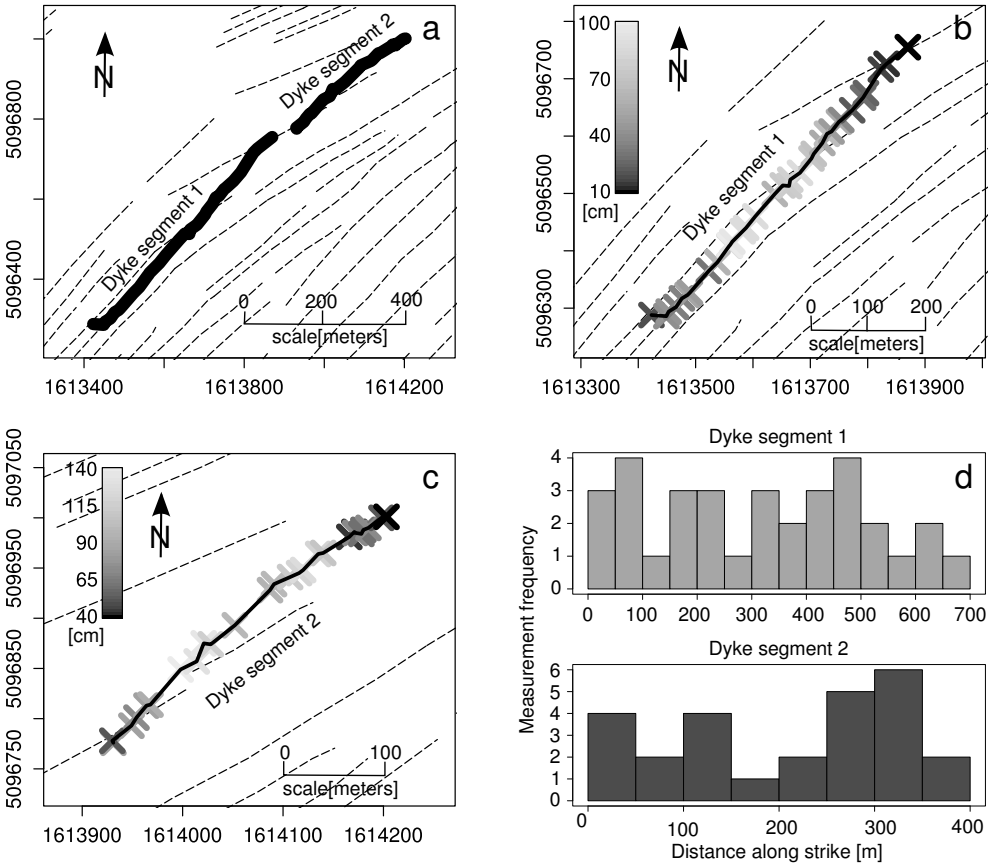

Figure 2.9: *(a-c)* Detailed maps of the two dyke segments of Figure 2.7, recorded for their geometry along the strike. *(b)* Thickness distribution for dyke segment 1 (for thickness values see greyscale bar). *(c)* Thickness distribution for dyke segment 2 (for thickness values see greyscale bar). *(d)* Histograms of the density distribution for the number of measurements along the strike of each segment in *(b)* and *(c)*.

En Echelon and Shearing Structures

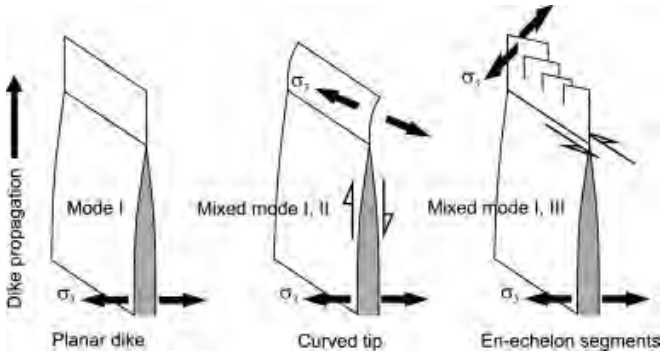

Figure 2.10: Sketch of different propagation paths for dykes related to the spatial change in orientation of the least compressive stress and the modes of fracture, modified after Pollard [1987]. Mode I fracture is induced by a least compressive stress acting perpendicular to the dyke plane and produces a planar dyke. Mixed mode I and II fracture is induced by a spatial rotation of the least compressive stress about an axis parallel to the dyke periphery. This produces a curved dyke. Mixed mode I and III fracture is induced by a spatial rotation of the least compressive stress about an axis parallel to the propagation direction. Mixed mode I and III produces segmented dyke with en echelon array (see Figure 2.11).

En echelon bridging of dykes (Fig. 2.4f) is particularly common in the regional dyke swarm extending over the entire Re di Castello superunit. The geometry of such en echelon structures was recorded in the field according to the parameters described in Figure 2.11. Parameters that are notably of interest are the dyke segment length b and the dyke center spacing c, as well as variations in the twist angle ω. Additional parameters determined in the field are the overlap o of the dyke segments in relation to each other, the separation s of the segments, the thickness δ of the individual segments, array width 2B and the center spacing k measured parallel between the different segments [Nicholson and Pollard, 1985, Pollard et al., 1982]. Arrays of en echelon dyke segments were examined in detail at four different locations (Fig. 2.12a-c) around the Re di Castello peak and in adjacent areas of good continuous outcrops, such as the Conca del Gellino. Out of the four locations (Fig. 2.12a-d), three show a general southwest stepping of the dyke segments and indicate a sinistral shear component during dyke opening perpendicular to σ_3 (Fig. 2.10). For the most part, these en echelon segments appear to be straight throughout these arrays and do not show extensive curvature against each other. The morphology of the array resembles straight propagation paths during dyke emplacement. The measurements lead to the description of two ratios; the bridge aspect ratio, R_a, and the crack tip ratio, R_0. The bridge aspect ratio, R_a for the en echelon segments is defined as

$$R_a = (b - k)/s; (b > k) \tag{2.1}$$

The condition b > k assures that neighbouring crack tips have overlapped to create an actual bridge between two en echelon segments. The crack tip ratio R_0 is the relative length of the rectilinear and curved parts of crack walls. It is defined as

$$R_0 = (b - k)/k; (b > 0) \tag{2.2}$$

and the condition b > 0 assures that the crack have some finite length [Nicholson and Pollard, 1985]. Larger values of aspect ratios are associated with larger values of overlap ratios when higher twist angles

are attained. The relationship between twist angle, aspect ratio and overlap ratio is given by

$$R_0 = R_a tan(\omega) \tag{2.3}$$

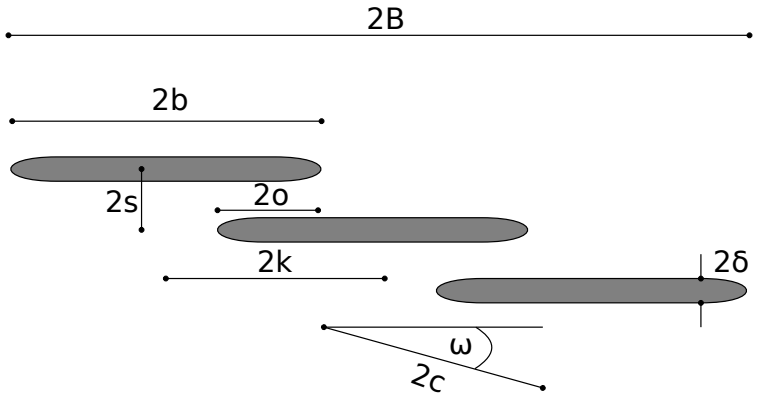

Figure 2.11: Geometric features after Nicholson and Pollard [1985] of an array of three rectilinear en echelon cracks before significant dilation: crack width is *2b*: overlap is *2o*: separation is *2s*: dilation is *2δ*: center spacing measured parallel to cracks is *2k*: center spacing measured parallel to array is *2c*: twist angle is ω: array width is *2B*.

Locality	**[b/c] (mean)**	**[b/c] 1SD**	R_a	**(R_a) 1SD**	R_0	**(R_0) 1SD**	**ω°(twist)**
10NHS122	0.85	0.45	0.65	0.30	0.07	0.02	8.00
10NHS116	2.17	0.95	5.88	0.37	1.08	0.11	7.00
RDCNL10145	1.01	0.74	0.23	0.03	0.02	0.00	7.00
RDCNL11192	1.91	0.93	3.27	1.17	0.76	0.24	10.00

Table 2.1: *b* is half the dyke breadth length of the en echelon segments according to Figure 2.11. Whereas *c* is the dyke segment center spacing of the en echelon array (Fig. 2.11). R_a is the bridge aspect ratio defined as: R_a*=(b-k)/s* for *(b>k)*. R_0 is the crack tip overlap ratio defined as: R_0*=(b-k)/k* for *(b>0)*. *(1SD)* corresponds to one standard deviation of the sample population. ω is the twist angle of the en echelon array according to Figure 2.11. After Nicholson and Pollard [1985].

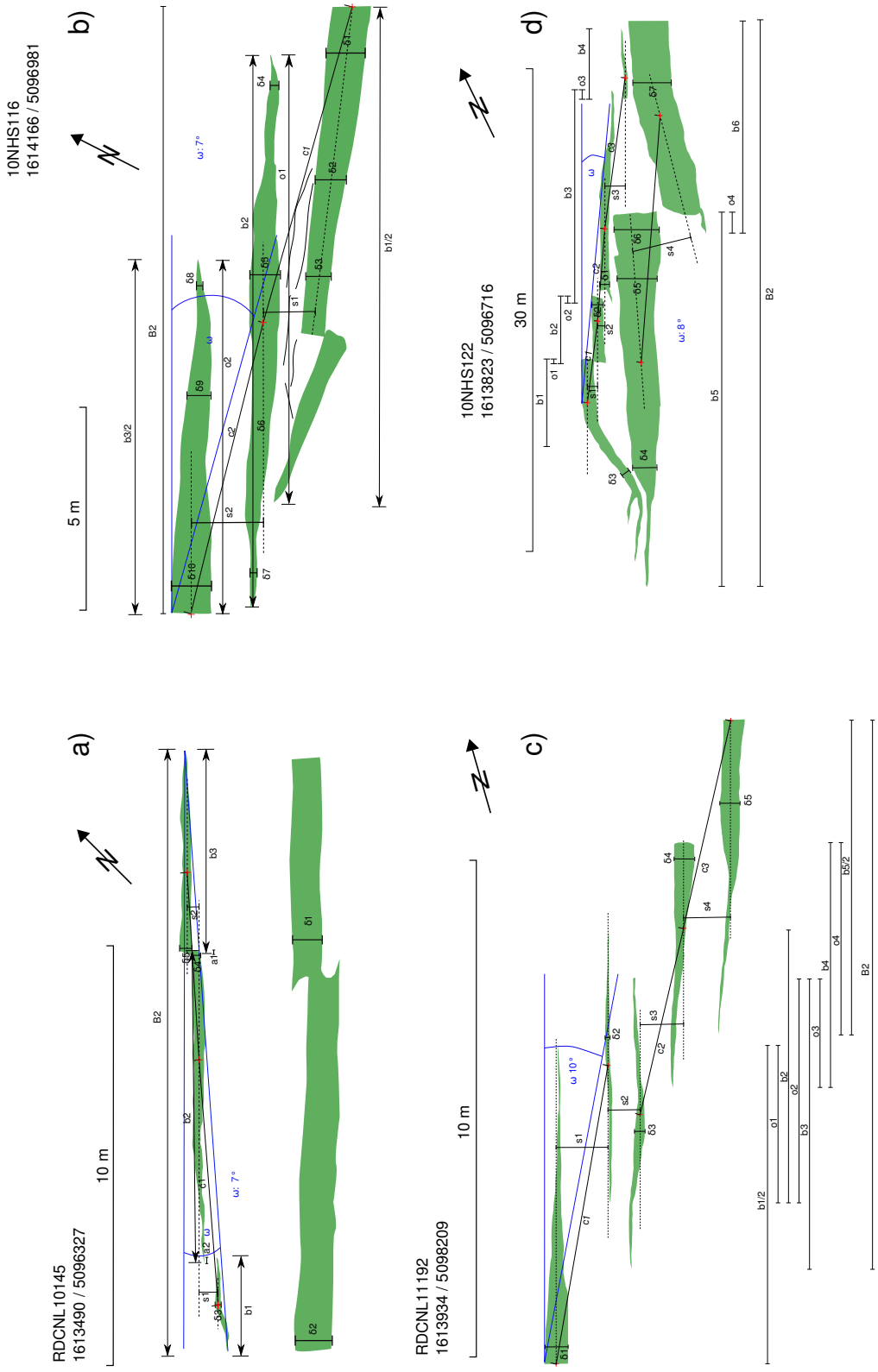

Figure 2.12: Sketch maps of different localities *(a-d)* displaying en echelon dyke segment arrays from the area between Passo di Campo and Passo Rossola. For actual localities see coordinates for the according outcrop maps (Map datum: Monte Mario/Italy zone 1, Transverse Mercator Projection).

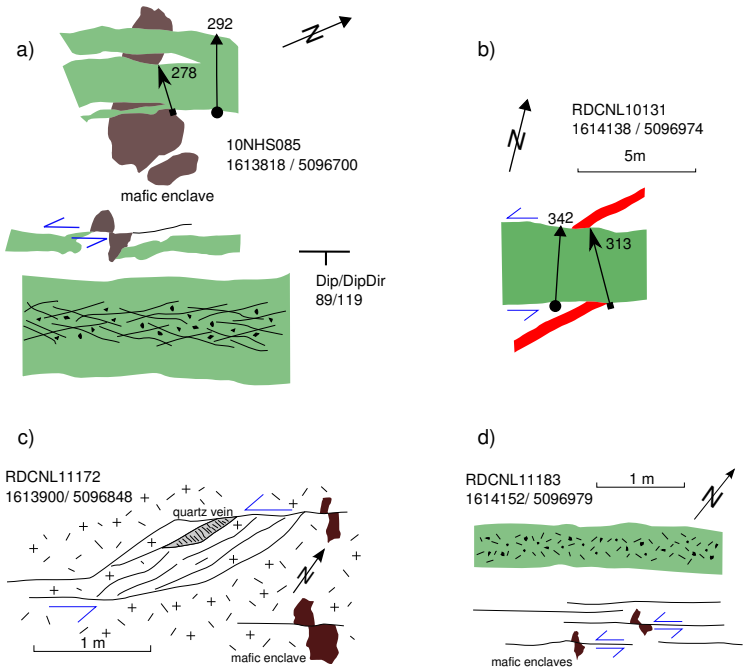

Figure 2.13: Different outcrop maps of the area between Passo di Campo (Mt. Re di Castello) and Passo Dernal (Mt. Re di Castello) along the strike of the dyke swarm (2A, 2B, 2C, 3). *(a)* Enclaves indicate left lateral slip on dyke cogenetic fracture at emplacement conditions. *(b)* Basaltic-andesitic dyke (2C) crosscuts aplite within the tonalitic host rock. Aplite as a passive marker indicates a mixed mode I and III fracture opening during emplacement of the dyke. *(c)* Dyke parallel regional jointing associated with tensional fractures partially infilled by quartz veins together with enclaves as left-lateral slip markers. *(d)* Enclaves show, as in (a) and (c), left lateral slip associated with dyke cogenetic fractures or joints.

Arrays of higher twist angle can be described as stiffer with respect to dilation, where the stiffness is a direct result of the smaller aspect ratio of bridges. Results of the field measurements are given in Table 2.1. As seen in Figure 17, the twist angle does not show considerable variation and ranges between 7° and 10°. Two of the en echelon arrays show practically no overlap between the individual segments, hence the overlap ratio R_0 is very small, between 0.02-0.07. These two arrays further show a smaller bridge aspect ratio R_a in the range of 0.23-0.65. At several places (Fig. 2.13a-c), dykes show associated displacement features with passive markers such as enclaves (Fig. 2.13a, d) or aplitic dykes (Fig. 2.13b) in the tonalitic or granodioritic wall-rock. These features mark displacement associated with the intrusion and emplacement of the dykes and indicate a sinistral shear component during dyke opening perpendicular to σ_3. Similar sinistral shear displacement is observed through enclaves as markers along dyke parallel jointing. Quartz veins are further developed in tension gashes of arrays of the same dyke parallel jointing, indicating left-lateral slip.

2.6 Topography, Tectonics Structures and Dykes

A digital elevation model (DEM) is the basic element for deriving morphometric maps that are then compared to tectonic features and the described dyke swarm. Such an analysis should reveal if and to what extent topographic lineaments, such as valley depressions and drainage, are controlled by tectonic

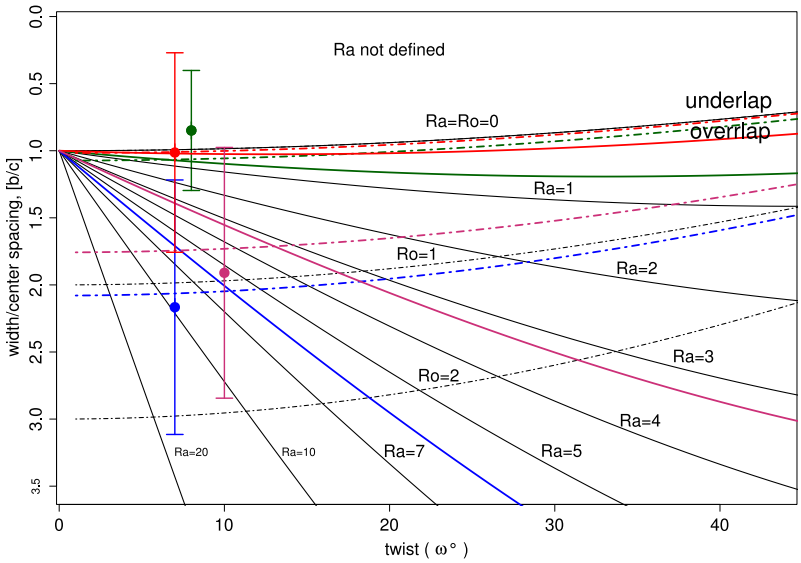

Figure 2.14: Modified after Nicholson and Pollard [1985] of crack width normalized by center spacing *[b/c]* plotted vs twist angle ω. Solid curves are for constant bridge aspect ratio, R_a. Dashed curves are for constant crack overlap ratio, R_0. Plotted values with different colours are as follows from Table 2.1: red is RDCNL10145, green is 10NHS122, blue is 10NHS116, purple is RDCNL11192. Lines are for constant values of R_a and R_0 determined from field measurements of the according parameters of equations 2.1 and 2.2. Points plot the mean of the crack width normalized by center spacing *[b/c]* vs the measured twist angle for each of the four en echelon arrays of Figure 2.12, with error bars of one standard deviation for *[b/c]* for each of the arrays.

features such as faults. Furthermore, the dyke orientation is compared to the direction of prevailing fault systems to investigate if dykes acted as nucleation surfaces in the development of fault planes [D'Alessio and Martel, 2005]. The topographic digital raster basis used here is the DEM from the NASA's Shuttle Radar Topographic Mission (SRTM) with a 90m resolution for the current area [Marian, 2001, Rabus et al., 2003]. The SRTM data was further analysed in the GIS open-source project, Geographic Resources Analysis Support System (GRASS-GIS). A first step included a spline interpolation algorithm applied to the SRTM raster to fill occurring null values in the SRTM data. The south vergent fold-and-thrust belt of the Central Southern Alps [e.g. De Sitter and De Sitter-Koomans, 1949] is truncated and delimited in this region by the right lateral strike slip, Tonale Fault and the left lateral strike-slip, Giudicarie Fault (Fig. 2.1, 2.15).

The area covered by the Adamello Batholith covers a range of pre- and post-intrusion tectonic features. In close vicinity to the Adamello batholith occurs the south vergent Gallinera thrust that belongs to the Pre-Adamello belt of the Central Southern Alps [e.g. Cassinis and Castellarin, 1988, Castellarin et al., 2006, Cornelius, 1924] associated to thrust sheet 1 [Laubscher, 1985, Schönborn, 1990, 1992] (Fig. 2.15). The Gallinera thrust is cut and overprinted by contact metamorphism through the Western Adamello- and Avio-tonalites [Brack, 1984, Cornelius, 1924]. Another example of a thrust belonging to the overall imbricate structure of the Central Southern Alps is the Poggio la Croce on the east side of the Val Camonica adjacent to the Val Camonica. To the south of the Adamello batholith, the Valsugana and Val Trompia system

(Fig. 2.1) comprises structures related to both the Insubric-Helvetic (early post-collisional Oligocene-Miocene) and the Valsugana (Serravallian-Tortonian) compressional phases [Castellarin et al., 2006]. This belt is a continuous wide arcuate southeast of the Adamello batholith and pre-Adamello tectonic belt. The Giudicarie fault system corresponds to the northeast continuation of this arcuate structure. The Giudicarie system is defined by a style of NNE trending sinistral lateral ramps connecting short east-oriented frontal thrusts [Castellarin et al., 1993, Picotti et al., 1995, Trevisan, 1939]. In the northwestern part of the Adamello batholith within the Central Peak- and the Avio tonalite, the Gole Larghe Fault (GLF) and the Lares Fault Zone (LFZ) which are right lateral strike fault zones, associated with pseudo-tachylites on which deformation is focussed; their ages are constrained by ^{39}Ar–^{40}Ar determination yielding ~30 Ma [Pennacchioni et al., 2006, Di Toro and Pennacchioni, 2005, Di Toro et al., 2005a, Di Toro and Pennacchioni, 2004]. The post-magmatic deformation in this zone is characterized by joints that developed during earliest stages of pluton cooling. These joints experienced high temperature (~500°C), ductile overprinting which produced lineations, defined by aligned biotite and hornblende, on the joint surfaces and highly localized mylonites. Pseudo-tachylites and cataclasites of the GLF and LFZ formed during the main phase of faulting that occurred at ~250°C and was associated with extensive fluid infiltration [Pennacchioni et al., 2006]. This sequence documents the nucleation of the GLF and the LFZ on precursor joints, formed in the course of the cooling of the plutonic masses. Such a behaviour should be expected elsewhere in the Adamello batholith close to the depth of the ductile-brittle transition.

Aspect and Slope Angle

The aspect slope is the direction slopes are facing and includes the azimuth ranging from 0-360°N. The aspect processing on the SRTM DEM was classified into four categories, as revealed in Figure 2.15 for the identical region: 0-90°(NE); 90-180°(SE); 180-270°(SW); 270-360°(NW). The slope values are calculated from the DEM as degrees of inclination from the horizontal [Hofierka et al., 2009]. The four aspect-class raster maps were then multiplied by the calculated slope raster map [Grohmann, 2004], which covers the identical region with r.mapcalc implemented in GRASS-GIS (Fig. 2.15a-c). The slope variations for the four different aspect-classes are as follows: NE: 0-68.8°; SE: 0.1-66.8°; SW: 0-66.3; NW: 0.1-70°. Thus the slope range appears to be similar for all the four aspect classes. The aspect to slope product is displayed in the form of density distribution (Fig. 2.16) for the same four aspect-classes. The four classes show a similar density distribution with a maximum in the range of of 27-30° for the slope angle. However, aspect classes SE and NW have a very equal distribution and are attaining similar values, whereas the two other classes, NE and SW, show differences in the density distribution, particularly in the peak region with a flatter distribution for the NE class. Based on these aspect-classes, the distribution of the slope density does not show any additional difference.

Topographic Lineaments

Lineaments were drawn on shaded relief maps for the same defined region of the DEM as in Figure 2.15. The advantage of shaded relief maps over satellite imagery for drawing lineaments is the possibility to set up the position and scene of illumination (azimuth and inclination) [Grohmann, 2004]. This approach allows the description and drawing of several existing lineaments due to the enhancement of directions

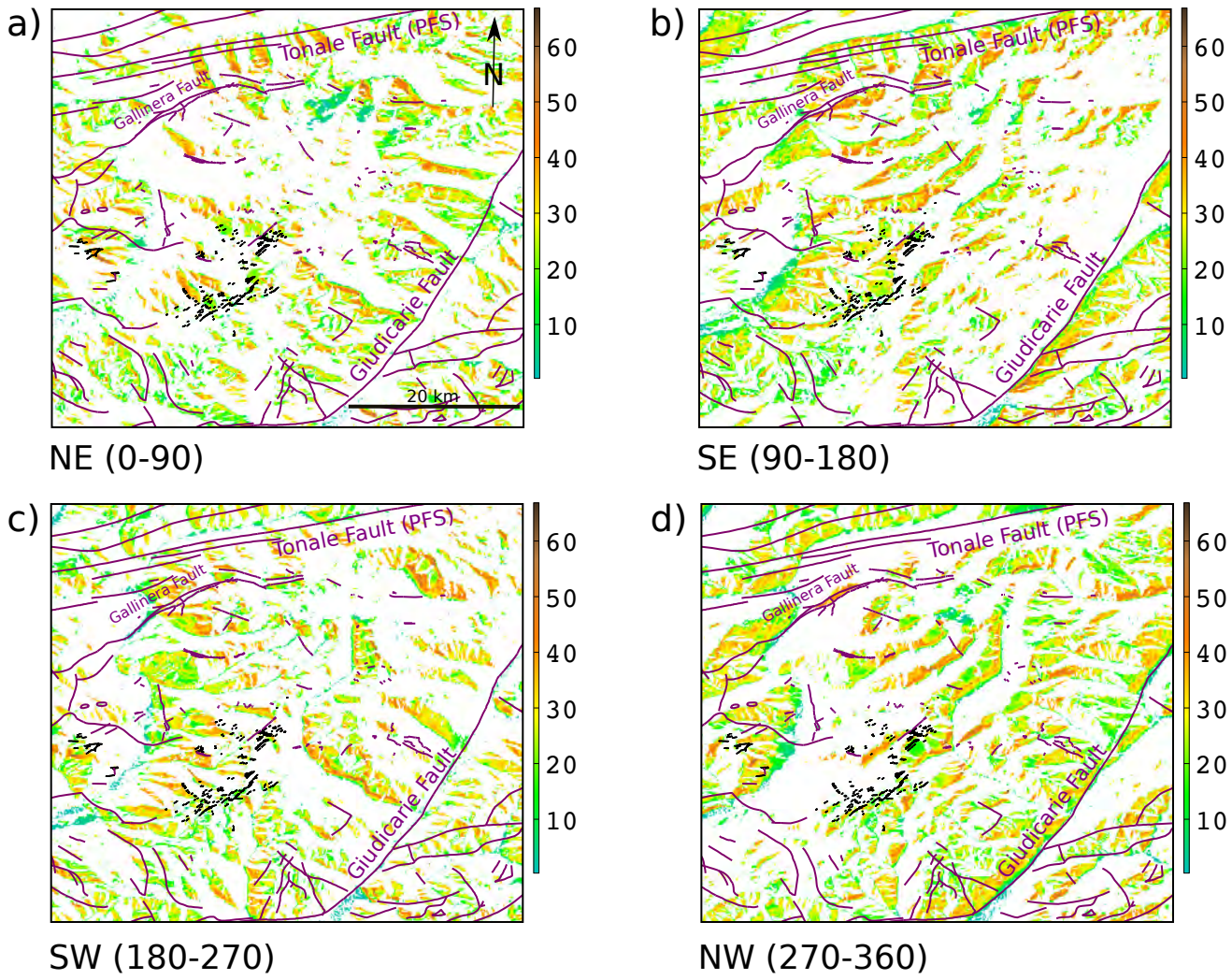

Figure 2.15: Slope-aspect (colour-ramp for slope angle in degrees) maps after the method of Grohmann [2004] for the Adamello Batholith area, together with tectonic features in purple. Digital elevation model (DEM) is based on the SRTM raster data set with a grid resolution of 90m [Marian, 2001, Rabus et al., 2003]. Slope-aspect maps for four azimuth quadrants: *(a)* NE(0-90°); *(b)* SE(90-180°); *(c)* SW(180-270°); *(d)* NW(270-360°).

perpendicular to lighting, used in the different shaded relief maps [Grohmann, 2004, Riccomini and Cróstal, 1988]. An 45° inclination above the horizon for the lightning at N90°, N45°, N00° and N315° was used for the creation of the different shaded relief maps. Lineaments were subsequently digitized manually (Fig. 2.17a) into a vector layer and all of the four different shaded relief maps were considered, when drawing the vector lines. The orientation (azimuth) and the length of each lineaments was determined by the GRASS script v.to.db (vector to database) [Mandelbrot and Blumen, 1989], which updates this information into the according attribute table of the vector file. Topographic lineaments with an extent of 4000m in length and greater are displayed in a rose diagram (Fig. 2.17b). The same Figure shows the orientation of the regional dyke swarm in a rose diagram for comparison, comprising dyke generations: 2A; 2B; 2C;

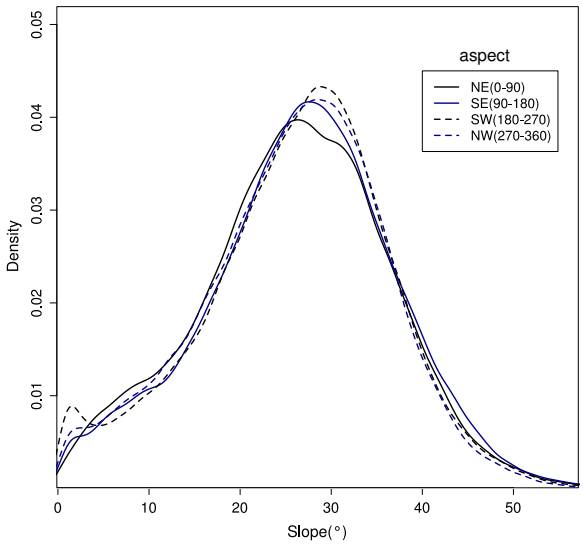

Figure 2.16: Density plot of slope variations comparing the four different aspects of Figure 2.15 for the topography of the region within and around the Adamello Batholith.

3. Azimuth orientation for lineaments of 4000m and greater ranges between 31°N and 229°. Though the directions in the range between 40-50°N show the highest frequency and the orientation around 80-100° follows with the second highest frequency. These lineament trends reflect major topographic depressions such as the lower part of the Val Camonica, the Val Giudicarie with the in line adjoining Val di Chiese. These valleys clearly coincide with the Giudicarie Fault (Fig. 2.1, 2.15) and its extension to the SE. In addition, within the Adamello batholith, glacial valleys such as the Val Adamé, the Val Salarno, the area around Lago Baitone, the Val Gallinera and parts of the Val di Fumo have a similar drainage orientation. Within the dyke swarm of the Re di Castello unit, the lineament reflecting the topographic depression of the Val di Dois to Passo Dernal has the same general orientation and is associated with a fault that created cataclasites within the Re di Castello tonalite clearly evident on the NE side of Passo Dernal. This fault deformed basaltic dykes of generation (2A, 2B) within the saddle SE of the Monte Frerone to cataclasites [Brack, 1984]. Moreover, as illustrated in Figure 2.4d, shearing along this fault on Passo Dernal in immediate vicinity of the Rifugio Maria e Franco is concentrated and localized on a plane along a dyke of generation (2A), which shows conjugate carbonate shear fractures sets in the interior. The potential extension of the Val di Dois-Passo Dernal line to the NE is the NE-SW oriented Val di Fumo heading towards NE from Lago Bissina. The second prominent E-W lineament orientation coincides with the orientation of the valley leading down from Passo Aprica to Edolo, the uppermost Val Camonica (Ponte di Legno and Temu area), the Val di Sole and Val Genova. The first three valleys are aligned with the Tonale Fault (Fig. 2.1, 2.15), which is part of the Periadriatic Fault System (PFS).

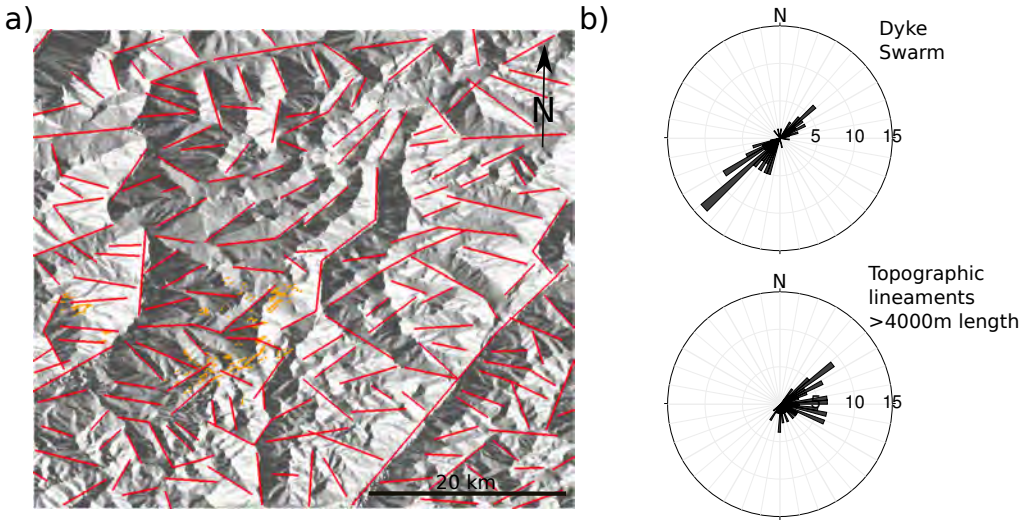

Figure 2.17: *(a)* Shaded relief map created from SRTM-DEM with 90m raster resolution. Illumination of the relief from N90 with an inclination angle of 45°; *(b)* Rose diagram for strikes of dyke swarm (2A, 2B, 2C, 3) in comparison to a similar diagram for lineaments with length in excess of 4000m drawn onto the shaded relief *(a)*.

2.7 High-Precision Time Constraints on Dyke Emplacement

Methods U-Pb Titanite and Zircon Data

Mineral separation started with crushing 2-5cm sized precut blocks of the sample under a hydraulic press. The resulting gravel was subsequently disintegrated with a tungsten carbide mill, employing short bursts of 12s. The product was sieved to a size fraction 125-250 μm and a fraction of <125 μm. The remaining coarser fraction was milled again until everything passed through the sieve (<250 μm). The two size fraction were then pre-panned to be processed through diiodomethane (3,2 g cm^{-3}) heavy liquid. Magnetite was removed from the heavy mineral separate using a Frantz magnetic separator. Individual titanite and zircon grains were hand-picked under a binocular microscope; grains exhiting inclusions were avoided. A total of 13 titanite and 8 zircons grains were analysed for their U-Pb isotopic composition using high precision ID-TIMS techniques (see Broderick et al., in prep for analytical details) for three different samples. Zircons were chemically abraded after Mattinson [2005]. Titanite and zircon grains were spiked using the EARTHTIME (http://www.earth-time.org) ^{202}Pb-^{205}Pb-^{233}U-^{235}U-tracer solution and dissolved following procedures modified after Krogh [1973]. For zircons, all common Pb was assumed to be blank. For titanites, 0.8pg common Pb was assumed to be blank and corrected with the according isotopic compositions: ^{206}Pb/^{204}Pb = 18.30 ± 0.71%;^{207}Pb/^{204}Pb = 15.47± 1.03%; (all uncertainties 1-sigma). The remaining excess common Pb in titanite was considered as initial Pb and corrected using the age corrected Pb isotope ratios (for 40Ma) of the whole rock: ^{206}Pb/^{204}Pb = 18.08 ± 0.80%; ^{207}Pb/^{204}Pb = 15.62± 0.32%; ^{208}Pb/^{204}Pb = 37.93 ± 0.74% (all uncertainties 1-sigma). All measurements were performed at the University of Geneva on a Thermo-Scientific TRITON thermal ionization mass spectrometer, equipped with a MasCom discrete dynode electron multiplier operated in ion counting mode. The initial statistical analysis was done using the TRIPOLI program followed by data reduction and age calculation using the

U-Pb Redux software [Bowring et al., 2011], applying the algorithms of McLean et al. [2011]. The data was corrected for mass fractionation with the ET2535 tracer composition, using a $^{202}Pb/^{205}Pb$ ratio of 0.99924 and a $^{235}U/^{205}Pb$ ratio of 100.23. All uncertainties are reported at the two-sigma level. The uncertainties are propagated using the algorithms of Schmitz and Schoene [2007] and Crowley et al. [2007].

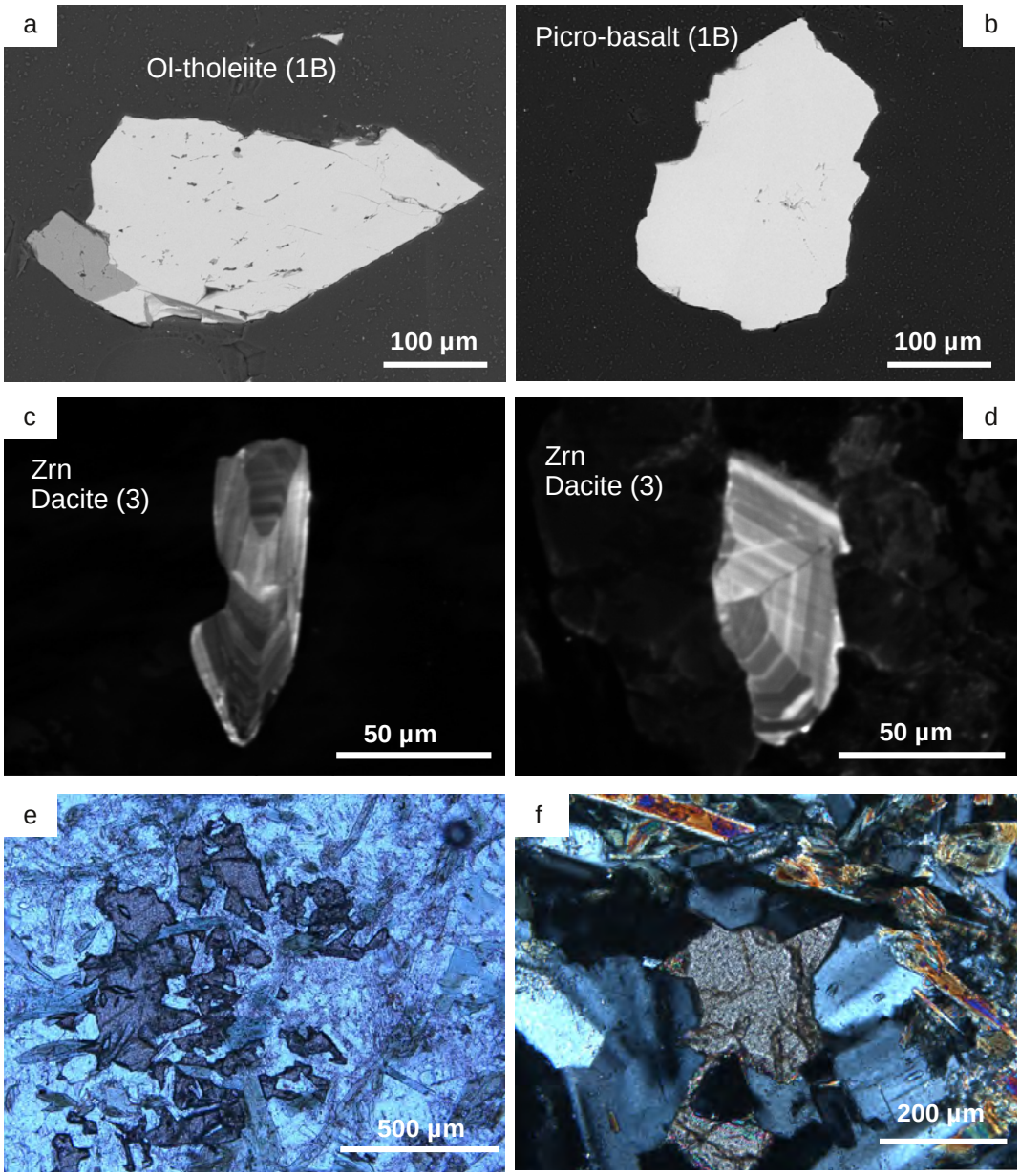

Figure 2.18: *(a)* and *(b)* Back-scattered electron images illustrating titanites of picro-basalt and Ol-tholeiite (1B) from sample NHS011 used for U–Pb geochronology. *(c)* and *(d)* Zircons from dacite (3) sample NHS083 showing concentric regular oscillatory zoning. *(e)* Interstitial titanite within felsic plagioclase-rich zone of Ol-tholeiite in plane polarized light (1B). *(f)* Similar titanite as in *(e)* in cross polarized light.

High-precision dating addresses a key question when a zircon or titanite grain actually precipitates within a magmatic context [Miller et al., 2007]. Coleman et al. [2004] and Schaltegger et al. [2009] for

example suggested that the youngest age cluster represents the best approximation to the emplacement age and older ages might potentially be influenced by earlier crystallization episodes leading to antecrystic or xenocrystic zircons. An essential first step is to establish a profound petrographic description of the sample containing the titanites and zircons. It should also be considered that dykes are small in dimension in outcrop compared to large plutonic masses, therefore their cooling time is considerably shorter than for large plutons, which inhibit dissolution and re-precipitation processes of zircon at emplacement level. Titanite clearly reveals an interstitial textural position (Fig. 2.18e, f) within the amphibole-plagioclase micro-gabbroic texture in the sampled picro-basalts and Ol-tholeiites (1B). Sub-horizontal dykes of this type (1B) with a thickness not exceeding 1m are expected to cool within days, considering the inferred ambient temperature around ~400° of the Vacca tonalite [Caricchi et al., 2012]. In back-scattered electron images (BSE), titanites reveal (Fig. 2.18a, b) no apparent zoning and are often associated with apatite. Within picro-basalts and Ol-tholeiites (1B), titanites are concentrated in plagioclase-rich lenses or bands. Analysed zircons from a dacite (3) in general show concentric oscillatory zoning in CL images (Fig. 2.18c, d) acquired at conditions of 10 kV on a CamScan SEM at the University of Lausanne. Zircons are euhedral and occur in textureal relationship, commonly together with ilmenite and apatite in an otherwise amphibole-plagioclase-phyric dacite with a fine-grained greenish-grey matrix. The propagated errors in ages for titanite are higher than for zircons, partly due to the correction of the remaining excess common Pb with age corrected isotopic ratios for $^{206}Pb/^{204}Pb$ and $^{207}Pb/^{204}Pb$ from the according bulk rocks.

Zircon and Titanite Geochronology

Results of U/Pb age dating of titanites and zircons for the Southern Adamello post-plutonic dyke rocks are given in Table 2.2. The terms xenocrystic, inherited, antecrystic and autocrystic zircon are used according to Miller et al. [2007]. Two samples are from the earliest dyke generation comprising picro-basalts and Ol-tholeiites of (1B). A third sample is from the latest and most differentiated dacitic (3) dyke generation. The chosen samples represent the entire age range established through crosscutting relationships in the field (Fig. 2.3). All five titanite grains that have been dated from sample NHS011, a sub-horizontal Ol-tholeiite (1B) result $^{206}Pb/^{238}U$ ages that vary from 41.81 ± 0.70 Ma to 41.397 ± 1.21 Ma (Fig. 2.19); the youngest titanite is still within error of the oldest one. The weighted mean age for titanites of sample NHS011 yields a value of 41.72 ± 0.09 Ma with a MSWD of 1.5. The picro-basalt NHS161 of the same generation (1B) that occurs on the small plateau adjoining the Lago della Vacca yields an oldest $^{206}Pb/^{238}U$ age for a titanite of 42.04 ± 0.42 Ma (Fig. 2.19) and is within the error of other 5 titanites from the same sample . The youngest titanites (t2, t6) of this picro-basalt yield and $^{206}Pb/^{238}U$ age of 40.88 ± 0.89 Ma and 41.17 ± 0.21. Both of these titanites (t2, t6) have considerably higher Th/U ratios ranging from 1.34-3.94 than the other six titanites with a range of 0.20-0.68. The weighted mean average $^{206}Pb/^{238}U$ age for titanites of the sample NHS161 results in a value of 41.68 ± 0.04 Ma with a MSWD of 2.1, excluding the two youngest titanites (t2, t6). This sample (NHS161) corresponds to picro-basalt RC158c that was used as a starting composition for hydrous fractional crystallization experiments at both 1.5 GPa [Alonso-Perez, 2006] and 1.0 GPa [Kägi, 2000]. The original sample was collected by Ulmer [1986] who described this composition as the most primitive and potential primary magma. Later Ulmer [1988] performed high-pressure, multiple saturation experiments to constrain mantle separation conditions

Sample	Wt. [mg]	U [ppm]	$\frac{Th}{U}$	Pb [ppm]	$\frac{Pb^*}{Pb_c}$	Pb_c [pg]	$\frac{206Pb}{204Pb}$	$\frac{207Pb}{206Pb}$	% err	$\frac{207Pb}{235U}$	% err	$\frac{206Pb}{238U}$	% err	corr. coef.	$\frac{207Pb}{204Pb}$	±	$\frac{207Pb}{235U}$	±	$\frac{206Pb}{238U}$	±
(a)	(b)	(c)	(d)	(c)	(e)	(e)	(f)	(g)	(h)	(g)	(h)	(g)	(h)		(i)	(h)	(i)	(h)	(i)	(h)
Ol-tholeiite NHS011 (1B)																				
NHS011/t6	0.1001	27	1.35	0.34	2	12.51	104	0.04495	3.83	0.04007	3.99	0.006466	0.52	0.37	-58.62	93.38	39.89	1.56	41.55	0.21
NHS011/t7	0.0657	9	4.74	0.22	1	7.25	50	0.04068	17.82	0.03612	18.52	0.006441	1.22	0.60	-307.72	456.28	36.03	6.56	41.39	0.50
NHS011/t9	0.0346	19	2.58	0.35	1	5.14	69	0.04822	8.08	0.04323	8.34	0.006503	0.60	0.47	110.01	190.66	42.97	3.51	41.78	0.25
NHS011/t10	0.0532	15	2.30	0.26	1	6.11	71	0.04736	11.37	0.04249	11.72	0.006506	0.70	0.52	67.45	270.47	42.25	4.85	41.80	0.29
NHS011/t12	0.0415	23	2.05	0.34	2	4.95	97	0.04785	4.96	0.04287	5.12	0.006498	0.38	0.46	91.98	117.36	42.62	2.14	41.75	0.16
Picro-basalt NHS161 (1B)																				
NHS161/t1	0.0509	125	0.26	0.97	4	9.07	306	0.04694	1.01	0.04218	1.52	0.006517	1.10	0.74	46.25	24.19	41.95	0.62	41.88	0.46
NHS161/t2	0.0445	11	3.94	0.16	6	1.07	199	0.04559	7.96	0.04028	8.22	0.006407	0.50	0.53	-24.04	192.74	40.09	3.23	41.17	0.21
NHS161/t3	0.0441	13	0.68	0.17	1	3.46	86	0.04669	7.35	0.04180	7.59	0.006493	0.47	0.53	33.60	175.97	41.58	3.09	41.72	0.19
NHS161/t4	0.0644	4	0.54	0.08	1	3.29	53	0.04788	16.94	0.04319	17.49	0.006542	1.00	0.57	93.21	400.81	42.93	7.35	42.04	0.42
NHS161/t5	0.0751	78	0.41	0.68	3	12.77	204	0.04716	1.29	0.04213	1.34	0.006480	0.18	0.33	57.20	30.85	41.90	0.55	41.64	0.07
NHS161/t6	0.0495	11	1.34	0.17	1	3.73	78	0.04753	18.02	0.04168	18.58	0.006361	0.89	0.64	75.70	427.92	41.47	7.55	40.88	0.36
NHS161/t7	0.0441	55	0.31	0.51	2	6.91	161	0.04760	2.31	0.04262	2.39	0.006493	0.21	0.41	79.48	54.81	42.38	0.99	41.72	0.09
NHS161/t8	0.0886	57	0.20	0.47	3	10.74	209	0.04684	1.35	0.04186	1.40	0.006482	0.16	0.35	41.07	32.27	41.64	0.57	41.65	0.07
Dacite NHS083 (3)																				
NHS083/z1	0.0026	76	0.74	0.61	5	1.04	294	0.04672	2.48	0.03871	2.57	0.006008	0.12	0.78	35.05	59.27	38.56	0.97	38.62	0.05
NHS083/z2	0.0017	111	0.87	0.85	12	0.67	653	0.04686	1.09	0.04004	1.13	0.006197	0.10	0.52	42.05	26.00	39.86	0.44	39.82	0.04
NHS083/z3	0.0054	214	0.62	1.45	25	0.55	1501	0.04690	0.51	0.03946	0.54	0.006102	0.05	0.61	44.13	12.26	39.29	0.21	39.21	0.02
NHS083/z4	0.0026	137	0.92	1.08	8	1.18	459	0.04683	1.59	0.03943	1.66	0.006106	0.11	0.64	40.69	38.12	39.27	0.64	39.24	0.04
NHS083/z5	0.0022	68	0.70	0.51	8	0.58	461	0.04687	1.61	0.03888	1.68	0.006016	0.10	0.73	42.56	38.58	38.73	0.64	38.67	0.04
NHS083/z6	0.0039	87	0.68	0.63	10	0.58	587	0.04683	1.32	0.03885	1.38	0.006016	0.09	0.71	40.55	31.54	38.70	0.52	38.67	0.03
NHS083/z7	0.0032	93	0.78	0.68	11	0.58	621	0.04687	1.24	0.03907	1.30	0.006045	0.08	0.68	42.85	29.65	38.91	0.49	38.85	0.03
NHS083/z8	0.0018	98	0.88	0.77	8	0.82	474	0.04684	1.59	0.03938	1.66	0.006097	0.10	0.75	41.29	37.96	39.22	0.64	39.18	0.04

Table 2.2: (a) z1, z2 etc. and t1, t2 etc. are labels for single zircon and titanite grains or fragments. (b) Nominal weights measured (zircons are chemically abraded, after Mattinson [2005]. (c) Nominal U and total Pb concentrations subject to uncertainty in weighting zircons and titanites. (d) Model Th/U ratio calculated from radiogenic $^{208}Pb/^{206}Pb$ ratio and $^{207}Pb/^{235}U$ age. (e) Pb^* and Pb_c represent radiogenic and common Pb respectively; mol % $^{206}Pb^*$ with respect to radiogenic, blank and initial common Pb. (f) Measured ratio corrected for spike and fractionation only. Mass fractionation correction for Pb and U was applied using the EARTHIME ^{202}Pb-^{205}Pb-^{233}U-^{235}U tracer ($^{202}Pb/^{205}Pb$ = 0.999239 and $^{235}U/^{205}Pb$=100.23). (g) Corrected for fractionation, spike, and common Pb; All common Pb was assumed to be procedural blank in zircons. $^{206}Pb/^{238}U$ and $^{207}Pb/^{206}Pb$ ratios corrected for initial disequilibrium in $^{230}Th/^{238}U$ using Th/U [magma] = 4. (h) Errors are 2-sigma, propagated using the algorithms of Schmitz and Schoene et al. [2012] and Crowley et al. [2007].

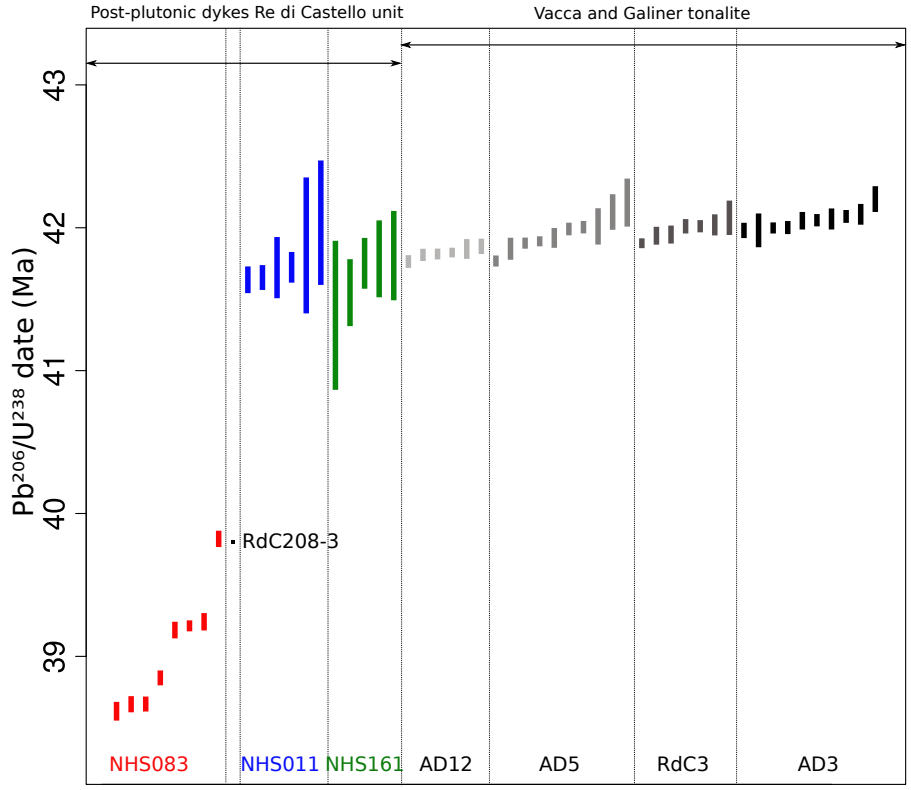

Figure 2.19: U–Pb geochronology: $^{206}Pb/^{238}U$ ages for individual titanite (NHS011: blue, NHS161: green) and zircon (NHS083: red) grains. An individual analysis is represented by a bar; the height of the vertical bars include ±2-sigma uncertainties for each analysis. Samples are separated by vertical dashed lines. Systematic uncertainty in titanite dates arises from unknown common Pb composition and produces a systematic error larger than that of zircon ages. In grey are $^{206}Pb/^{238}U$ ages from Schoene et al. [2012]. Samples: AD12 Galliner tonalite; AD5, RdC3 and AD3 are all from different localities within the Vacca tonalite (for details see Schoene et al. [2012]). RdC208-3 is a $^{206}Pb/^{238}U$ zircon age from Hansmann and Oberli [1991] for the Dernal Granite (Re di Castello).

for this composition at 28 kbar, 1370°C in equilibrium with a garnet-lherzolite residue. A weighted mean $^{206}Pb/^{238}U$ age of 41.68 ± 0.04 with a MSWD of 1.7 results from all titanites of samples NHS011 and NHS161 together representing the same dyke generation (1B), excluding the two youngest titanites (t2, t6), from samples NHS161. The dacitic dykes (3) yields a youngest $^{206}Pb/^{238}U$ zircon age of 38.62 ± 0.05 Ma. Three of the analysed zircons from the dacite (NHS083) lie within error yielding $^{206}Pb/^{238}U$ ages ranging from 38.67 ± 0.04 Ma to 38.62 ± 0.05 Ma (Fig. 2.19). The weighted mean $^{206}Pb/^{238}U$ age for these three zircons (z1, z5, z6) results 38.66 ± 0.02 with a MSWD of 1.8. One zircon results an age of 38.85 ± 0.03 Ma and is considered to be an antecryst. Another group of three zircons yield $^{206}Pb/^{238}U$ ages ranging from 39.24 ± 0.04 Ma to 39.18 ± 0.04 Ma and are interpreted to be xenocrysts. The oldest zircon of this sample (NHS083) results a $^{206}Pb/^{238}U$ age of 39.82 ± 0.04 Ma and is considered to be a xenocryst as well. This xenocryst has a similar $^{206}Pb/^{238}U$ age as a mutliple zircon grain analysis for the Dernal granite (RdC208) [Hansmann and Oberli, 1991, Hansmann, 1986] yielding a $^{206}Pb/^{238}U$ age of 39.8 ± 0.2.

2.8 Discussion

Magma Overpressure in Dykes and Regional Stress Field

For dykes, the intrusion driving pressure, defined as the difference between the magma pressure and the horizontal stress perpendicular to the dyke plane, is a key element for the propagation and the resulting form of the sheet intrusion [Poland et al., 2008]. The thickness of the dyke is directly related to the driving pressure within a dyke [Delaney and Pollard, 1981, Pollard and Muller, 1976]. Analytical solutions were proposed by Pollard and Muller [1976] and Delaney and Pollard [1981] that relate dyke thickness to the driving pressure of the magma. These analytical solutions based on the principles of Linear Elastic Fracture Mechanics (LEFM) describe a dyke as a fluid-filled fracture that intrudes into a brittle, elastic material. The propagation is controlled by both, fluid mechanics and fracture mechanics [Lister and Kerr, 1991, Menand and Tait, 2002, Muller et al., 2001, Takada, 1990, Watanabe et al., 2002]. The orientation and geometry of a dyke is controlled by the product of magma over-pressure and buoyancy forces driving the flow and the environment in the form of the elastic properties of the host-rock and interface strength of layers [Menand, 2011] resisting the propagation [Lister and Kerr, 1991, Rubin, 1995]. The dyke shape is thus determined by a simple elastic deformation control at fixed overpressure. The dyke shape in two dimensions is approximated here by the continuous measurements of the dyke thickness as shown in Figure 9. The observed dyke cross-section is then compared with the analytical elastic model in order to estimate the magma driving pressure or overpressure and potential stress gradients during emplacement [e.g. Delaney and Pollard, 1981, Kavanagh and Sparks, 2011, Poland et al., 2008, Pollard and Muller, 1976]. Numerical models by Buck et al. [2006] found that the propagation distance is dependent on the initial distribution of the tectonic stress but they also infer that the dyke intrusions can effect the tectonic stress distribution as well.

A theoretical model describes the dyke as tabular sub-vertical magma body that cuts discordantly across the host rock. Dykes are, in general, very thin in relation to their breadth. Under uniform stress conditions, the ideal cross-sectional form is elliptical (Fig. 2.20a). The assumption of a host rock behaving as homogeneous, elastic solid is justified regarding the uniform tonalite host in which the dyke described in Figure 2.9 intruded into. For a blade-shaped dyke associated with constant driving pressure, the thickness *(t)* is described by [Delaney and Pollard, 1981, Poland et al., 2008, Pollard and Muller, 1976]:

$$t = (P - S)(a^2 - x^2)^{(1/2)}(\frac{1-\nu}{\mu}) \tag{2.4}$$

In this relationship P is the magma pressure, S is the dyke normal stress perpendicular to the dyke plane, which is in general the least compressive stress σ_3 under a given crustal environment; a is the half dyke thickness, x is the distance from the along-strike midpoint of the dyke. Elastic moduli for the assumed homogeneous isotropic tonalite are μ, the elastic shear modulus, and ν, the Poisson's ratio. The driving pressure is defined by *P-S* [Delaney and Pollard, 1981, Poland et al., 2008, Pollard and Muller, 1976, Pollard, 1987, Reches and Fink, 1988]. Previously, detailed geometrical analysis of dykes in the field however revealed teardrop forms of dykes [Hoek, 1995, Poland et al., 2008, Pollard and Muller, 1976] rather than ideal elliptical forms in several cases. To account for this observed teardrop form, Weertman [1971] suggested for the asymmetry of a fluid-filled crack to consider the effect of a gradient in stress or

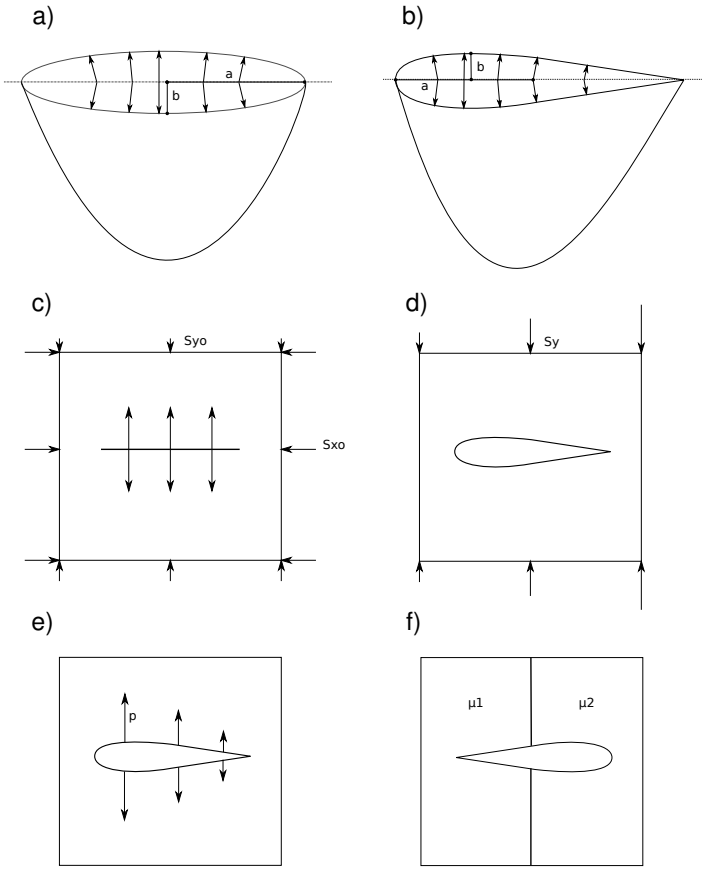

Figure 2.20: Analytical solutions for an elastic dyke model modified after Pollard and Muller [1976]. *(a)* and *(c)* Ideal elliptical model for elastic analytical model with dyke constant overpressure and no stress gradient along strike. *(b)* Teardrop form of a dyke taking into account a stress gradient along strike. Working hypotheses to explain origin of teardrop form of blade like dyke. *(d)* Regional stress gradient: $s_y = s_{y0} + \Delta s_y$. *(e)* Magma pressure gradient: $p = p_0 + \Delta p$. (f) Change in host rock stiffness: $\mu_1 > \mu_2$.

pressure acting along the fracture. For dykes, Pollard and Muller [1976] and Delaney and Pollard [1981] described a teardrop-shaped dyke with its thickness distribution as a function of uniform driving pressure, together with a driving pressure gradient. Poland et al. [2008] proposed the following equation for this relationship:

$$t = (P - S)(a^2 - x^2)^{(1/2)}(\frac{1-\nu}{\mu}) + \nabla(P - S)x(a^2 - x^2)^{(1/2)}(\frac{1-\nu}{\mu}) \tag{2.5}$$

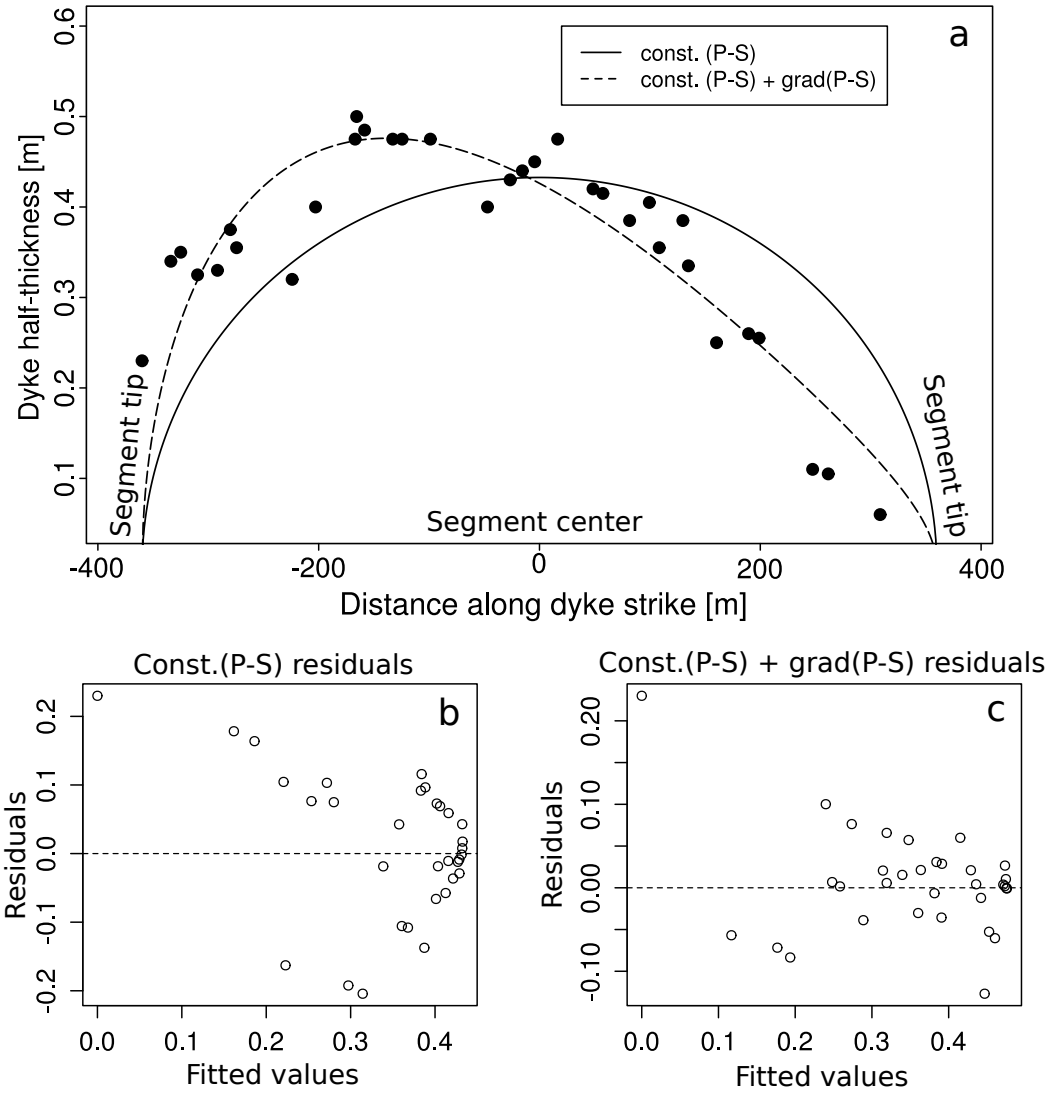

Figure 2.21: Results of least square linear inversion for analytical solutions of purely elastic dyke emplacement after [Delaney and Pollard, 1981, Poland et al., 2008, Pollard and Muller, 1976] relating dyke thickness to driving pressure (magma over-pressure). *(a)* Thickness distribution along strike of dyke segment 1, with an analytical solution for uniform driving pressure 2.4 and uniform driving pressure + pressure gradient along strike 2.5. *(b)* Residuals for fitted thickness values for uniform driving pressure model. *(c)* Residuals for fitted thickness values for uniform driving pressure + pressure gradient model.

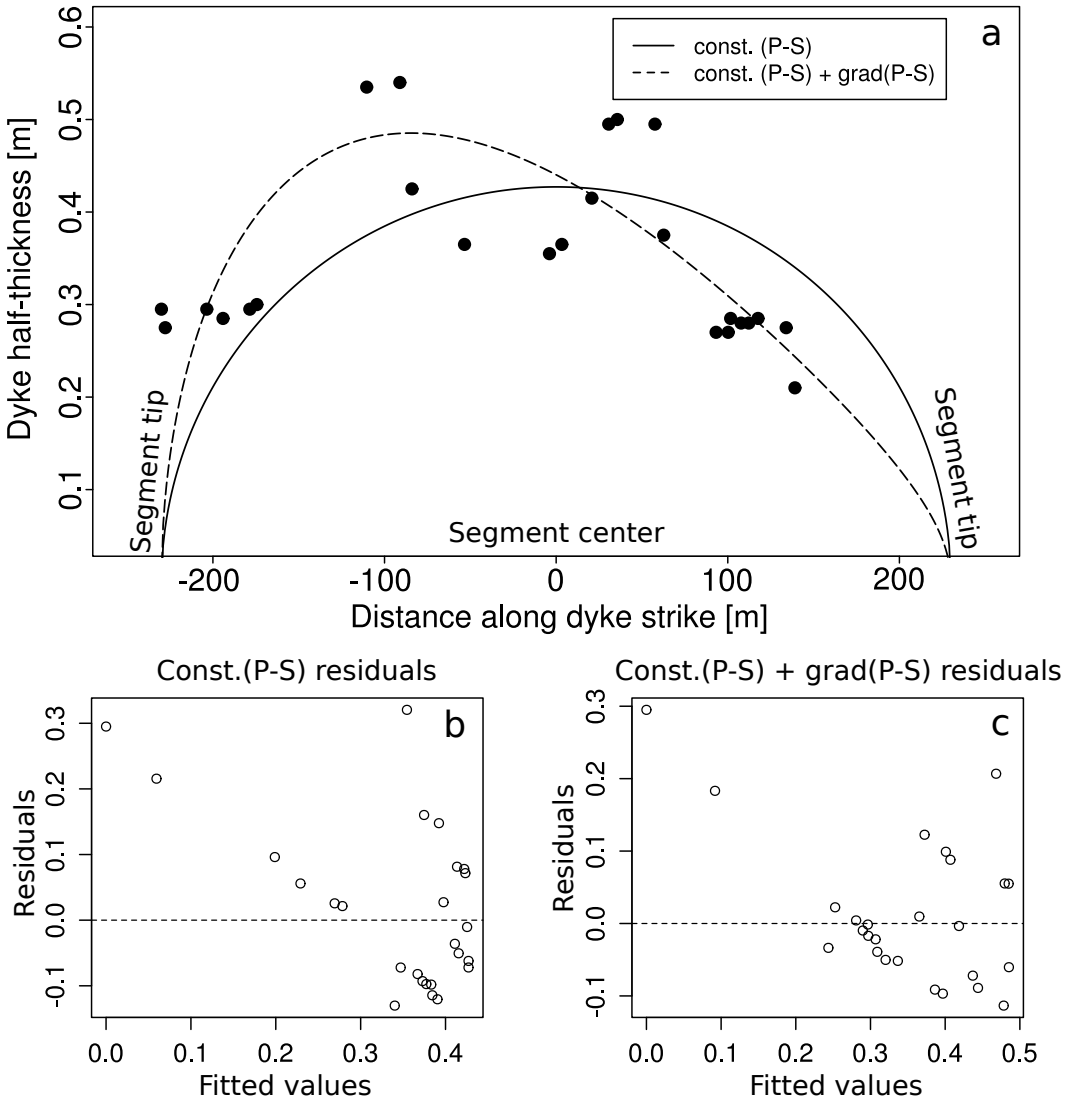

Figure 2.22: Results of least square linear inversion for analytical solutions of purely elastic dyke emplacement after [Delaney and Pollard, 1981, Poland et al., 2008, Pollard and Muller, 1976] relating dyke thickness to driving pressure (magma over-pressure). *(a)* Thickness distribution along strike of dyke segment 2, with an analytical solution for uniform driving pressure 2.4 and uniform driving pressure + pressure gradient along strike 2.5. *(b)* Residuals for fitted thickness values for uniform driving pressure model. *(c)* Residuals for fitted thickness values for uniform driving pressure + pressure gradient model.

The first part is identical to Equation 2.4 whereas $\nabla(P - S)$ is the pressure gradient term along the dyke [Pollard, 1987]. Examined dyke segments display chilled margins that are simple and non-composite which excludes the intrusion style of multiple pulses. Xenoliths and xenocrysts are rare within the dykes at this particular locality in contrast to dykes in the Lago della Vacca area about 8km south. Therefore wall rock erosion by mechanical disintegration is considered to be of minor importance. The third dimension of these dykes is difficult to assess at this locality; nevertheless dykes of the same swarm in the Concarena at the E-side of the Val Camonica show vertical extents up to 1km.

The driving pressure is then modelled through a least square inversion to determine both a model with uniform driving pressure and another model with a combination of uniform driving pressure and driving pressure gradient (Fig. 2.21, 2.22). Such a model assumes a static fluid-filled crack in equilibrium with an elastic host-rock. The least square inversion was centered about the origin, which is the along-strike midpoint of the dyke. Non-elastic processes can affect the thickness distribution along the strike of the dyke, such as plastic deformation of the host rock [Sleep, 1988], thermal erosion [Huppert and Sparks, 1985] or rock erosion through mechanical disintegration, intrusion along pre-existing fractures [Delaney et al., 1986], ground surface topography in the case of shallow intrusions and structural features such as folding of strata [Pollard and Muller, 1976] and multiple phases of dyke growth or transient pressure changes due to eruptions in a volcanic setting [Valentine and Krogh, 2006]. For the present case, features for shallow intrusions such as topographical effects and effects related to actual eruption are less likely, assuming that these dykes intruded at a depth range of 9-11km with an ambient pressure of 0.2 to 0.35 GPa [John and Blundy, 1993, Stipp et al., 2004, Pennacchioni et al., 2006]. Thermal erosion is additionally dependent on the host rock temperature at the time of intrusion. The host is a homogeneous tonalite; therefore changing material properties through layering can be excluded. As Kavanagh and Sparks [2011] noted, driving pressure estimates from dyke thickness measurements are minimum values as the final preserved thickness of the dyke is determined by late-stage conditions when driving-pressure, has already declined, taking into account chilling effects as well. The applied approach here is simplified but nevertheless provides an example of the emplacement conditions of dykes occurring throughout the entire post-plutonic dyke swarm episode of the Southern Adamello.

A value of 26 GPa for the elastic shear modulus μ for the host tonalite [Rzevskij et al., 1971] results from the computation of a theoretical dynamic stress field around propagating fractures, which was applied by Di Toro et al. [2005a] for the Gole Larghe Fault (GLF) in the Central Peak- and the Avio-tonalite. A Poisson's ratio ν of 0.25 is reasonable for the scale of kilometre long dykes and was used by both Pollard [1987] and Schultz [1993].

dykesegment	$a(m)$	n	**Model**	$P_o = (P-S)$ (MPa)	$grad(P-S)$ $(kPam^{-1})$	$err.P_0$	$err.grad(P-S)$	RSS	$res.st.err.$	DF
I	360	33	Ellipse	20.83		1.05		0.35	0.1047	32
			Teardrop	20.52	62.21	0.64	8.36	0.13	0.0650	31
II	230	26	Ellipse	32.19		2.26		0.41	0.1285	25
			Teardrop	33.18	145.52	1.85	38.44	0.26	0.1038	24

Table 2.3: Results are shown for a non-linear least square inversion of dyke thickness with a constant driving pressure ($P_0 = (P-S)$) for a predicted elliptical form [Poland et al., 2008, Pollard and Muller, 1976]. For the teardrop form in cross-section, a driving pressure $\nabla(P-S)$ is added to the uniform driving pressure. This analysis was performed on two different adjacent dyke segments (I) + (II). Error P_0 and error $\nabla(P-S)$ are the estimated standard error variance s_2. RSS stands for residual sum of squares from the non-linear regression. $DF(n-k)$ stands for degrees of freedom.

Results of the least square inversion for both (1) a uniform driving-pressure and (2) uniform driving-pressure plus a driving-pressure gradient are provided in Table 2.3. The dyke segments mapped in detail for their thickness and other structural properties have lengths of 230m and 380m respectively. The measurement density along strike is higher for the first, longer dyke segment (Fig. 2.9, 2.21) than for the second dyke segment (Fig. 2.9, 2.22), as apparent from the histograms displayed in Figure 2.9d. Particularly for the longer and better constrained first dyke segment, the driving pressure plus gradient model yields the best model to describe the measured thickness distribution as evidenced by the distribution of residuals (Table 2.3, Fig. 2.21, 2.22). Residuals are generally smaller for the teardrop shaped dyke described by the driving pressure plus gradient model. The second dyke segment is less well constrained through the number of measurements, but for most of the measurements along the strike, residuals are smaller for the composite model, leading to a teardrop form taking into account a driving pressure gradient. Potential error sources in this least square inversion include particularly the incomplete exposure of dykes, whereas the actual measurement error of the thickness is negligible.

Modelled driving pressure with the combined driving pressure plus gradient model for the two dykes is 21 MPa for the first dyke segment and 33 MPa for the second dyke segment. These driving-pressure values are within the range reported by other studies [Geshi et al., 2010, Kavanagh and Sparks, 2011, Poland et al., 2008, Pollard and Muller, 1976]. Pollard and Muller [1976] for comparison modelled driving-pressures for the Walsen dyke of the Spanish Peak radial dyke swarm and obtained values in the range of 3.5 to 48MPa and Poland et al. [2008] obtained similar values in the range of 3.5 to 148 ($\mu = 4\ GPa$) for a radial dyke swarm of the Summer Coon volcano in southern Colorado. These studies were carried out in shallow volcanic environments that are not necessarily comparable to the examined dykes in this study, which intruded at considerably greater depth of 9-11km. As Kavanagh and Sparks [2011] noted, calculated magma pressures should be considered minimum estimates, as the dyke thickness during magma intrusion may have been up to twice the actual size of the measured thicknesses in the dyke profile. The dyke over-pressure is generally required to overcome the fracture toughness (K_c) [Pollard, 1987], which was estimated to be ~2-100$MPa{\cdot}m^{1/2}$ [Delaney and Pollard, 1981, Di Toro et al., 2005a]. The overpressure has to be larger than ~$K_c/L^{1/2}$, where L is the length of the dyke [Daniels et al., 2012]. The calculated stress gradients $\nabla(P-S)$ for the two dykes range from 62-146$kPa{\cdot}m^{-1}$ where the latter, higher value is less well constrained due to less favorable outcrop conditions of the second dyke segment (Fig. 2.9). These stress gradients are comparable with values obtained for the Summer Coon volcano [Poland et al., 2008] that range from 3 to 133$kPa{\cdot}m^{-1}$, whereas driving pressure stress gradients determined by Pollard and Muller [1976] for the Walsen dyke are lower, ranging from 0.052-0.71$kPa{\cdot}m^{-1}$. For a magma source over-pressure of 20MPa, which is the magma pressure in excess of the regional, compressive tectonic stress, a dyke propagating 1km from its source region would experience a regional stress gradient of $<$20$kPa{\cdot}m^{-1}$ [Jaupart and Allègre, 1991], which is lower than encountered in the model results of this study. However, magmatic chamber over-pressures at the source are expected to be higher, in the range of ~20-100MPa for magma sources $\geq$20 km [Karlstrom et al., 2009]. Such over-pressures are obtained by balancing the elastic propagation of a dyke and the gradual solidification at the dyke walls due to thermal considerations [Jellinek and DePaolo, 2003, Karlstrom et al., 2009, Rubin, 1995]. Petrological constraints place the magma source that feeds the southern Adamello post-plutonic dyke swarm at depth level of

15-20km [Hürlimann et al., in prep.a]. The obtained model results for the driving pressure are consistent with magma over-pressures at such depth.

The Effects of External Stress on the Dyke Geometry and Regional Structures

The crustal level where the dyke swarm is exposed is close to the ductile to brittle transition zone, constrained at ~10km by Pennacchioni [2005] and Pennacchioni et al. [2006], through the formation of joints in the Central Peaks- and Avio-tonalite and the subsequent development and nucleation of faults along the same features. The timing of joint formation is important since these structures represent fractures or more generally, surfaces of weaknesses along which magma can invade to form dykes [Currie and Ferguson, 1970, Delaney et al., 1986]. Magma pressure occurs in excess of the compressive stress that acts across dyke planes to generate tension that is sufficient to propagate a new fracture that the magma can invade [Anderson, 1938, 1951]. The latter situation assumes that the least compressive stress σ_3 is, in general, perpendicular to the along strike direction of the magma filled crack or dyke [Anderson, 1938, 1951, Spence and Turcotte, 1985]. The occurrence of abundant dyke-parallel to sub-parallel jointing (Fig. 2.7, 2.8) and the later development of faults and the formation of cataclasites of dykes (2A, 2B) Brack [1984] raises the question of the relative timing of the development of all these structural features. Moreover, dykes exhibit en echelon structures (Fig. 2.12, 2.1) that reveal some influence of rotation of the regional or local stress field [Nicholson and Pollard, 1985, Pollard et al., 1982] during dyke intrusion. The preferential directions of dykes can serve as principal loci for shear zone and fault nucleation [Christiansen and Pollard, 1997, D'Alessio and Martel, 2005, Mancktelow and Pennacchioni, 2005].

The formation of cooling joints is a common feature in plutons [e.g. Segall and Pollard, 1983, Segall et al., 1990, Bergbauer and Martel, 1999]. Joint formation is closely related to the cooling of the tonalitic host rock in the present case. The latest dacitic dykes (3), which intruded mainly within the Re di Castello tonalite in close vicinity to the location of the detailed map in Figure 2.7, have a $^{206}Pb/^{238}U$ age that is ~1.2 Ma younger than the Dernal Granite (39.8 Ma) [Hansmann, 1986], which intruded at the latest stage into the Re di Castello tonalite. In experimental studies, Piwinskii (1968) confirmed the solidus temperatures for tonalite (15 wt% H_2O, excess) in the range of ~700-720° C for the depth level at ~9-11km (0.2-0.3 GPa). In the Avio- and Central Peak-tonalite of the Adamello Batholith, Pennacchioni et al. [2006] described the nucleation of ductile shear zones along precursory cooling joints. Biotite and plagioclase are recrystallized in these ductile shear zoners or mylonites, which places the formation of these zones into the amphibolite facies. Temperatures of ~500°C are further inferred from dynamically recrystallized quartz [Mancktelow and Pennacchioni, 2005, Pennacchioni et al., 2006]. In addition, precursor cooling joints display high-temperature lineation of hornblende and biotite that Pennacchioni et al. [2006] used to argue that these fractures developed at a very early stage of cooling of the plutonic bodies most likely due to thermal contraction and differential solidification of magmatic bodies, as described by Bergbauer and Martel [1999] for the Sierra Nevada. The age relationship between the formation of the pluton and the emplacement of the dykes in the Re di Castello tonalite provides a maximum time frame of ~1.2 Ma for potential precursor cooling joint formation, predating the intrusion of the dykes in Figure 2.7. This would imply a required cooling of ~200 °C for the observed joint formation. The present regional joint surfaces however bear mainly a phase paragenesis of epidote + K-feldspar ± chlorite, which is consistent

with a temperature of ~250°C [e.g. Guilbert and Park, 2007]. This slightly discordant (5-10°) regional jointing further commonly shows a bleached alteration haloes. Prevailing regional joints, in this case (Fig. 2.7), postdate the dyke intrusion due to their low temperature mineral paragenesis, together with the discordance of the joints in relation to the general dyke strike. Such a relation validates the assumption of a homogeneous elastic tonalitic host rock in excluding considerable pre-existing jointing or fracturing at the time of the dyke intrusion.

Other distinct structural features are the en echelon segments of the dykes, which are associated with left lateral shearing observed with independent markers such as enclaves or aplitic dykes (Fig. 2.10). The en echelon stepping associated with larger overlaps of the segments (Fig. 2.12, 2.14) is in accordance with a left lateral slip movement during dyke intrusion. Furthermore, basaltic-andesitic (2C) dykes show brighter coloured melt-rich shear bands (Fig. 2.4c) that are an additional indication of shearing processes operating during emplacement. En echelon segmentation of dykes results from mixed mode I and III fracturing (Fig. 2.10) during intrusion of the magma, which is caused by a spatial or temporal rotation of the least compressive stress σ_3 that has axis about parallel to the propagation direction [Pollard et al., 1982, Pollard, 1987]. As each segment propagates, it twists to attain an orientation perpendicular to the local least compressive stress. The breakdown into en echelon segments is independent of σ_2 of all the principal stresses $(\sigma_1, \sigma_2, \sigma_3)$, since σ_2 acts within the propagation direction (Fig. 2.10). The magma filled crack initially dilates in a plane perpendicular to σ_3 that changes spatially or temporally its direction. In the applied model, σ_3 changes the orientation with an angle α uniformly over the entire region [Pollard et al., 1982]. The path that a dyke follows after rotation of the remote stress field is dependent on parameters such as orientation and magnitude of the remote stresses, magma pressure and the elastic properties of the host rock in which the dyke propagates. Pore pressure and the stress field conditions are commonly combined into the stress ratio, R. The stress ratio is the difference between the internal magma pressure within the dyke and the remote mean horizontal stress, divided by the remote shear stress [Pollard et al., 1982].

$$R = \frac{2P_i + \sigma_1^r + \sigma_3^r}{\sigma_1^r - \sigma_3^r}, P_i > -\sigma_3^r \tag{2.6}$$

The inequalitiy relating P_1 and σ_1 is required to ensure that the magma filled crack remains open during propagation of the dyke. The twist angle β measured in outcrop (Fig. 2.12, 2.1) is a function of the stress ratio, R, the Poisson's ratio, ν, and the angular change of the remote stress orientation, α [Pollard et al., 1982].

$$\beta = 0.5 tan^{-1}[\frac{sin2\alpha}{(R + cos2\alpha)(0.5 - \nu)}] \tag{2.7}$$

The rotation angle α of the remote stress field can be determined through this relation with known R and β. The level of dyke emplacement is constrained to 9-10km, with a confining pressure of 0.2-0.35 GPa mainly constrained by metamorphic phase assemblages in the contact aureole [Stipp et al., 2002, Werling, 1992]. Di Toro et al. [2005b] determined $\sigma_1^r = 256$ MPa, $\sigma_2^r = 160$ MPa and $\sigma_3^r = 64$ MPa for all three principal stresses for the Gole Larghe strike slip fault in the Central Peak- and Avio-tonalite. With a pore-fluid factor of $\lambda = 0.4$, the effective vertical stress is $\sigma_\nu^{'} = \varrho g z(1 - \lambda) = 160$MPa at a depth of 10km. The effective vertical stress is equal to σ_2^r . These conditions appear feasible for dyke emplacement

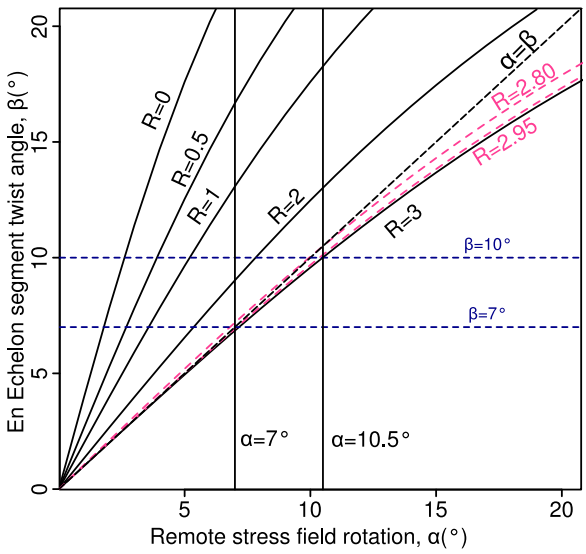

Figure 2.23: Incipient crack angle β plotted versus angular rotation α of the remote principal stresses. Poisson's ratio is held constant at $\nu = 0.25$ and the stress ratio R calculated after 2.6 (see text) is varied. Relation for given stress ratio R between β and α is given by 2.7. The two stress ratios are calculated for modelled magma over pressure at 32 MPa – $R = 2.95$ (2nd dyke segment, Table 2.3) and at 19 MPa – $R = 2.80$ (1st dyke segment, Table 2.3). Principal stresses ($\sigma_1^r = 256$ MPa, $\sigma_2^r = 160$ MPa, and $\sigma_3^r = 64$ MPa, see text for details) are according to fault slip conditions of the Gole Larghe strike slip fault in the Central Peak- and Avio-tonalite, taken as an approximation after Di Toro et al. [2005b].

that occurs with a given Poisson's ratio $\nu = 0.25$ and a magma over-pressure of 32MPa; the resulting R value amounts to 2.95. With the same principal stress conditions with a magma over-pressure of 21MPa, R results in a value of 2.80 (Fig. 2.23). Under these conditions the rotation of the remote stress field gives values for α in the range of 7-10°, which are identical with β since the curves evolve along $\alpha = \beta$ in the α versus β plot (Fig. 2.23). The well constrained asymmetrical teardrop form (Fig. 2.20b) of the first dyke segment (Fig. 2.9, 2.21) can be explained either through a regional stress gradient (Fig. 2.20d) or through a magma pressure gradient (Fig. 2.20e) [Pollard and Muller, 1976]. An abrupt change in host rock stiffness can be excluded since the tonalitic host rock is isotropic and homogeneous over several kilometers. An asymmetry of the dyke shape along the strike is similar to some observed fault slip distribution along faults [Bürgmann et al., 1994]. A regional stress gradient along the dyke dilatation plane goes along with observed left lateral slip movement during emplacement, leading eventually to the observed dyke shape. In this sense, the propagating dyke attempts to adjust in the form of en echelon structures to the regional remote stress field rotation.

Regional Implications

Colinearity of dykes with younger faults crosscutting the Re di Castello plutonic intrusive suite is prominent. Nucleation of succeeding fault planes is prominent in a few outcrops, as in the case of the Val di Dois to Passo Dernal line that does not exhibit large displacement. Other, larger continuous

(>4000m) topographic lineaments display colinearity with the orientation of the post-plutonic dyke swarm covering the southern Adamello (Re di Castello). However, these topographic depressions are related to younger structures post-dating the intrusive history. Nevertheless, the direction of all these features in time probably indicates an inheritance of previously active basement structures which turn into a roughly NE-SW alignment towards the Southern Giudicarie Fault.

Within the time frame of emplacement the post-plutonic dykes are markers for the build-up of two larger plutonic suites (Fig. 2.24) in the southern Adamello. The first suite comprises the Val Fredda-, Lago della Vacca- and Alta Guardia-tonalite and confirms the crosscutting relationships observed in the field [Schaltegger et al., 2009, Schoene et al., 2012]. The second plutonic building block of the southern Adamello plutonic suite comprising all the other remaining units of the Re di Castello suite (Fig. 2.2,2.24b), is terminated by the intrusion of the regional dyke swarm that shows a preferred orientation with respect to the remote regional stress field. The left lateral slip associated with the emplacement of the later dyke swarm cannot directly be correlated with the Oligocene ages (29-32 Ma) [Müller et al., 2001] of the mylonites and pseudotachylites of the North Giudicarie Fault that document the top-to-(E)SE thrusting along this fault. Older Eocene activity from shear zones south of the Peio Fault are characterized by top-to-(W)NW thrusting and these mylonite and pseudotachylite ages (35-37 Ma) are overlapping. This activity is much closer in the time range of the emplacement of the post-plutonic dyke swarm. However, the confined age (38.9 ± 0.4) of an amphibole gabbro [Pomella et al., 2011] among the periadriatic intrusion situated along the Northern Giudicarie Fault falls clearly within the age range of the emplacement of the regional dyke swarm into the Re di Castello plutonic suite. The relation to actual movement along the fault plane associated with the intrusion of this gabbro remains, however, unresolved. Documented movement along the Southern Giudicarie Fault is younger [Castellarin et al., 1987, 2006] of Servallian-Tortonian age than dyke U-Pb ages but does not exclude any earlier older movements. Nevertheless, observed left lateral strike-slip movement associated with the emplacement of the dyke swarm within the southern Adamello coincides with the same slip direction documented along the Giudicarie Fault.

2.9 Conclusions

Over time the post-plutonic dyke swarm marks two phases in the pluton assembly of the Re di Castello suite and U-Pb ages confirm the crosscutting relationships documented in the field. An early assemblage of plutonic rocks composing the southernmost part (Val Fredda, Alta Guardia, and Vacca tonalites and associated mafic intrusions) is cut by the most primitive magmatic rocks found in the entire Adamello Batholith. They reveal emplacement under the control of rather localized stresses. A second phase is marked by a regional post-plutonic dyke swarm (2A, 2B, 2C, 3) that succeeds a last voluminous phase of intermediate tonalitic intrusions (Monte Re di Castello tonalites and Dernal granite). Compositions of the dyke swarm range from primitive basalts (2A) to the most evolved homogeneous dacites (3). This phase of dyke emplacement has a prominent clear orientation that can be linked with left lateral slip movements during emplacement. The following proposed model reconciles the shape of dykes and the associated structures that go along or succeed the intrusion of the dykes. The intrusion of magma forming the dyke swarm predates the formation of cooling joints in the large plutonic bodies, in this case and low temperature joint formation (~ 250°C). A maximum time frame of ~1.2 Ma between the last plutonic

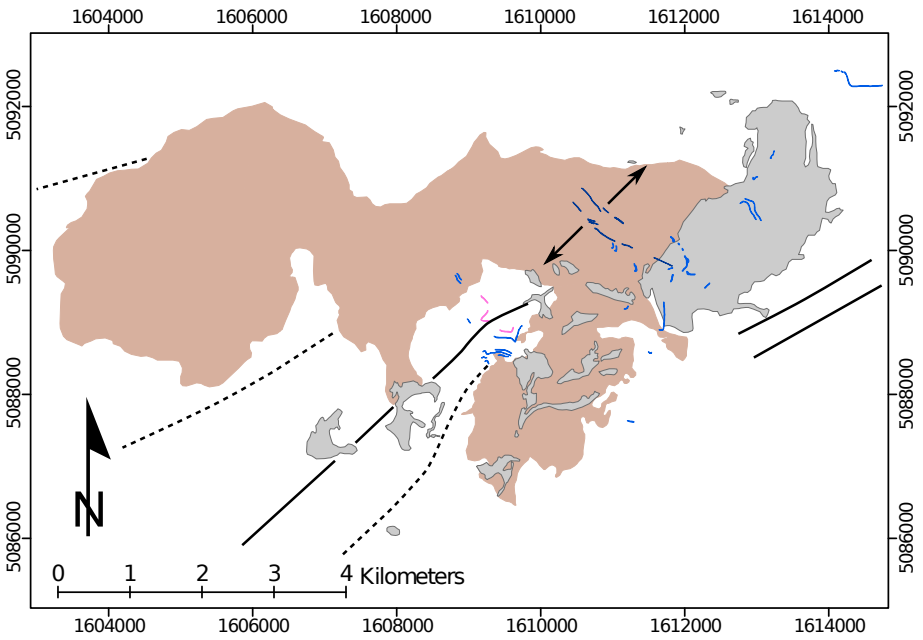

(a)

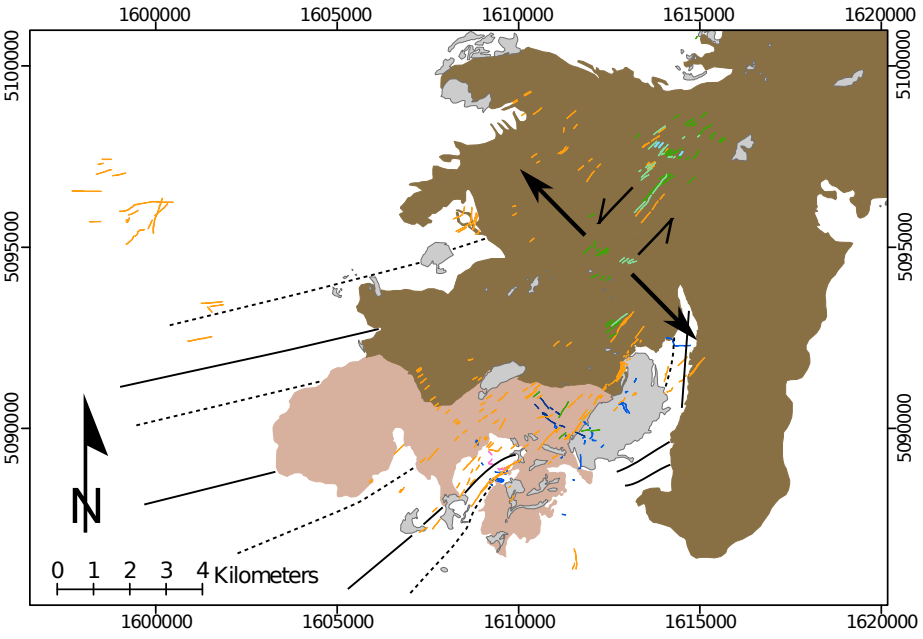

(b)

Figure 2.24: *(a)* Earliest plutonic phase comprising Alta Guardia tonalite, Val Fredda Complex and Vacca Complex including gabbroic Blumone Complex is terminated by the intrusion of picro-basaltic/Olitholeiitic dykes (1A, 1B). *(b)* Regional dyke swarm ranging from basalts (2A), basaltic-hybrids (2B), basaltic-andesites/andesites (2C) to dacites (3) intrudes after the build-up of the entire Re di Castello intrusive suite.

intrusion and the dyke intrusion appears to be insufficient to cool to these low temperatures associated with the joint formation. Left lateral slip movement associated with the dyke emplacement, caused by a clockwise rotation of the remote stress field, caused an adjustment of the main mode I dilatation surface

direction of the dykes and formation of en echelon segments stepping preferentially to the SE, consistent with observed slip directions. The two dimensional asymmetrical teardrop shape of the few dykes examined in detail could be explained with a gradient in the remote stress field along the strike, which underlines that the dilatation surfaces of the magma filled cracks are not perfectly oriented perpendicular to the least compressive stress σ_3^r in an otherwise homogeneous tonalitic host. Younger fault planes do in some cases develop and nucleate along these post-plutonic dykes, forming a clear rheological contrast in the uniform tonalite. Regional fault controlled valleys have the same lineament as the regional dyke swarm and document the erosion and drainage processes caused through uplift.

Chapter 3

Fractionation of Primitive Arc-tholeiitic Magmas to Corundum Normative Dacites

3.1 Abstract

Fractional crystallization has long been evoked as one of the key processes with regard to magma differentiation in middle to deep crustal levels. Geochemistry of a series of post-plutonic dykes from the southern part of the Adamello Batholith ranges from very primitive hydrous picro-basalts, including intermediate basalts, to andesites and dacites. The Adamello Batholith (44-33 Ma) is located in the Northern Italian Alps. It intruded into the South Alpine basement and its Permo-Triassic cover. In the Southern part, a series of late dykes intruded into gabbroic and mainly tonalitic plutonic bodies. The primary picro-basalts are constrained through multiple saturation experiments to be consistent with mantle-separation conditions of 28kbar and 1370°C. More differentiated andesites and dacites lie along the liquid line of descent of fractional crystallization experiments simulating differentiation in middle to deep crustal levels. These andesites and dacites have a primitive $^{87}Sr/^{86}Sr_i$ (0.7032-0.7038) and $^{143}Nd/^{144}Nd_i$ (ϵNd_{CHUR}: 3.5-3.2) isotopic signature. In particular, the trace element chemistry of amphiboles from basaltic-andesite and andesite dykes reflects a primitive liquid in equilibrium with this phase crystallizing in such hydrous magmas. Barometric constraints for the same amphiboles results in 6 and 7.5kbar with Am-Pl temperatures ranging up to ~1050°C, going towards the high-temperature limit of stability of amphibole in such magmas. The absence of an Eu-anomaly in the mineral chemistry of these amphiboles indicates the late appearance of plagioclase in the crystallization sequence. The crystallization of amphibole drives the more differentiated magmas to peraluminous, corundum-normative compositions, which are common for tonalites building the bulk part of the Adamello Batholith. The least squares fractionation model results in the cumulative crystallization of 17% olivine, 2% Cr-rich spinel, 18% Cpx, 41% amphibole, 4% plagioclase and 0.1% magnetite, to achieve an andesitic composition out of a primitive hydrous picro-basalt. Cumulates that are formed in association with fractional crystallization in the middle to deep crust are ultramafic dunites and wherlites and at a more evolved stage, cumulates are comprised of hornblendites and hornblende-gabbros. Trace element signatures of andesites can be aquired through fractionation processes in the described depth level of the crust in active continental margin settings. Crustal assimilation or considerable input of sediments in the mantle source region is not necessarily the main factor to attain the observed trace element signatures of more evolved andesitic magmas.

3.2 Introduction

Crystal fractionation has been proposed as one of the processes leading to the formation of an average andesitic continental crust, accompanied by considerable volumes of ultramafic and mafic cumulates below and above the seismic Moho [Kay and Kay, 1985, Kelemen, 1995]. An alternative process was put forward for the formation of bulk averaged andesitic crust and the formation of upper crustal tonalitic complexes and granitoids by crustal anatexis of basaltic lower crust, produced previously by differentiation of mantle-derived primary basaltic magmas [Takahashi et al., 2007, Tatsumi, 2000]. Furthermore, the crystallization and differentiation of (primary) high magnesium (Mg#) andesites has been suggested to generate a considerable amount of the continental crust [Kelemen, 1995]. The production of such andesitic magmas through reaction between ascending basaltic magma and peridotite in the upper mantle appears to be a feasible process to reach the geochemical characteristics of high magnesium (Mg#) andesites [Kelemen,

1990, Kelemen et al., 1990, 1992]. Experiments by [Sisson and Grove, 1993a,b] were able to reproduce a calc-alkaline liquid-line of descent at H_2O-saturated conditions at 2 kbar at the Ni-NiO (NNO) oxygen fugacity buffer equilibrium. These experiments addressed the phase relations of natural high-alumina basalts and intrusive equivalents. With respect to phase relations, the appearance of Fe-rich spinel near or at the liquidus in a basaltic melt can produce calc-alkaline derived liquids for moderate-to-high H_2O contents. Here we specifically address the possibility of continuous differentiation through crystal fractionation as a process to produce slightly peraluminous dacitic magmas in lower to middle crustal magma reservoirs.

Intrusive and extrusive suites of calc-alkaline magmas appear to frequently show a trend from diopside- to corundum-normative composition with increasing SiO_2 [Cawthorn and Brown, 1976]. Several experimental equilibrium and fractional crystallization liquid-line of descents (LLD) [Alonso-Perez et al., 2009, Müntener et al., 2001, Müntener and Ulmer, 2006, Ulmer, 2007, Sisson and Grove, 1993a] at different pressures produced peraluminous derivative liquids from an initial metaluminous magma in a restricted pressure range of about 0.7-1.2 GPa. The fractionation of amphibole is thereby the major factor controlling the liquid evolution towards peraluminous, corundum-normative compositions. At higher-pressure garnet inhibits the evolution to peraluminous liquids, whereas at lower pressure in hydrous magmas, An-rich plagioclase and decreased modal cpx-crystallization has as similar effect on liquid evolution [Alonso-Perez et al., 2009]. Such phase-relations during crystal fractionation are crucial for predictive trace-element modeling and evolution of liquid compositions during fractional crystallization. Alternatively, these phase-relations and proportions during fractional crystallization can be determined by thermodynamic modeling of phase-equilibria with the program MELTS [Ghiorso and Sack, 1995, Asimow and Ghiorso, 1998]. According to these authors, phase-equilibria involing hornblende (amphibole) are not well predicted in the current state of the MELTS program. As a consequence, the evolution of intermediate and silica-rich calc-alkaline systems starting from a primitive, mantle-derived parental magma is not recommended, which exemplifies the need to incorporate of more recent data in MELTS, in particular step-wise fractional crystallization experiments that approximate the natural conditions of magma differentiation more closely [Ulmer, 2007].

A suite of dyke rocks with a large compositional range represents an ideal case to quantify the amount of continuous crystal fractionation starting from a picrobasalt to achieve dacitic magma compositions. Such dyke rocks show (near) volcanic textures and are chemically close to liquid compositions. The investigated dyke rock suite varies in composition from primitive picro-basalt to dacites and follows a liquid line of descent during differentiation [Ulmer, 2007, 1986, Ulmer et al., 1983]. A pure fractional crystallization model, based on natural dyke rock compositions along the liquid line of descent, was choosen to quantify the inferred formation of cumulates and the changing modes of involved solid phases. The most primitive end-member of such a model is a picrobasalt that was separated from the mantle at 28 kbar and 1370°C [Ulmer, 1988], determined by multiple saturation conditions experiments. Obviously hybrid magmas are avoided from this study based on petrographic and geochemical characteristics. The dyke suite is cogenetic with larger volume plutonic magmatism, comprising predominantly dioritic, tonalitic and granodioritic rocks in the southern Adamello, but crosscuts these plutonic rocks. The fractionation model includes the geochemical evolution of trace-element concentrations and pattern to demonstrate the compositional range created by this particular magmatic process.

3.3 Geological Overview

An array of different generations of dykes with a large compositional range, from picro-basalts to dacites, cross cuts the Re di Castello superunit [Callegari and Brack, 2002], the southernmost plutonic intrusive suite of the Adamello Massif. The Adamello Batholith in northern Italy builds up the largest Tertiary intrusive complex in the Alps and is split into four superunits; Re di Castello, Adamello, Avio, and Presanella. Regarding its geographical position, the Adamello is the only larger tertiary intrusive complex located south of the periadriatic lineament [Schmid et al., 1989]. The Re di Castello superunit is composed of gabbros, diorites, tonalites, granodiorites and very minor granites and ulramafic rocks. The plutonic assembly of the Re di Castello shows a systematic age progression from 42.43 ± 0.05 Ma in the very south, to 39.8 Ma in the north [Hansmann, 1986, Hansmann and Oberli, 1991, Schaltegger et al., 2009, Schoene et al., 2012]. The principal plutonic lithologies are tonalites and granodiorites that intruded into the South-Alpine pre-Permian polymetamorphic basement and its non-metamorphosed Permo-Mesozoic sedimentary cover [Callegari, 1983, Callegari and Brack, 2002]. The more mafic rock types form intrusive sheets of gabbro and diorites particularly, at the margin of the large tonalitic and granodioritic intrusions. Mafic inclusions and dykes are very common within tonalites [Blundy and Sparks, 1992, Ulmer, 1986]. Ultramafic and mafic rocks such as olivine-pyroxene wherlites, hornblendites and hornblende gabbros [Blundy and Sparks, 1992, Ulmer, 1986] from the southern part of the Re di Castello unit reveal Sr_i and $\delta^{18}O$ ratios close to mantle values [Cortecci et al., 1979, Kagami et al., 1991]. $^{87}Sr/^{86}Sr$ initial ratios exhibit a rough, but systematic increase northwards from 0.7036 to 0.7120 [Del Moro et al., 1985]. The $^{18}O/^{16}O$ ($\delta^{18}O$) ratio demonstrates a similar northwards increase, from +5.9 for the Southern Adamello, Monte Mattoni Gabbro, to +9.4 for the Avio quartz-diorite in the Northeast [Cortecci et al., 1979]. The country rock contacts of the Adamello igneous complex are largely intrusive. Pre-Adamello deformation of the country rock is described by D'Adda et al. [2011] for the Gandino and Presolana area in the Orobic Alps (Bergamasque Alps). The late Cretaceous to early Paleocene evolution is marked first by stacking of Middle to Upper Triassic units. A second thrusting event is probably related to out-of-sequence southward propagation of the Orobic anticlines. During this second event, emplacement of the Orobic Anticlines belt caused uplift and back-thrusting of the Upper Triassic units, over Middle Triassic along the Clusone fault between Middle and late Eocene. Brack [1984] described the entire contact of the plutonic intrusives against the basement and sedimentary rocks as vertical or steeply dipping outwards. The country rock contact is accompanied by a continuous metamorphic contact aureole. In some cases, deformation of the wallrock within areas overprinted by high-temperature contact metamorphism is deformed by the ascending magma, leading to the formation of isoclinal folds in dolomite marble. Much stronger effects of syn-intrusive deformation at the contact is expressed in sedimentary tongues situated between two neighbouring intrusions. Large scale folds are compressed into more isoclinal forms and deviate considerably from the regional strike due to rotation and/or tilting, as is clearly visible in the Upper Val Caffaro for instance.

This study concentrates on the petrological evolution of dyke swarms of ultramafic (picro-basalts) to intermediate (dacite) composition that intruded in a relative time sequence after the emplacement of previous larger volume plutonic rocks in the Re di Castello superunit. Overall, the examined dyke swarm covers an area of 338 km^2 and reaches into the bordering country rocks of the intrusion at the western and southern sectors respectively. The post-plutonic dykes do not occur towards the northeast in the

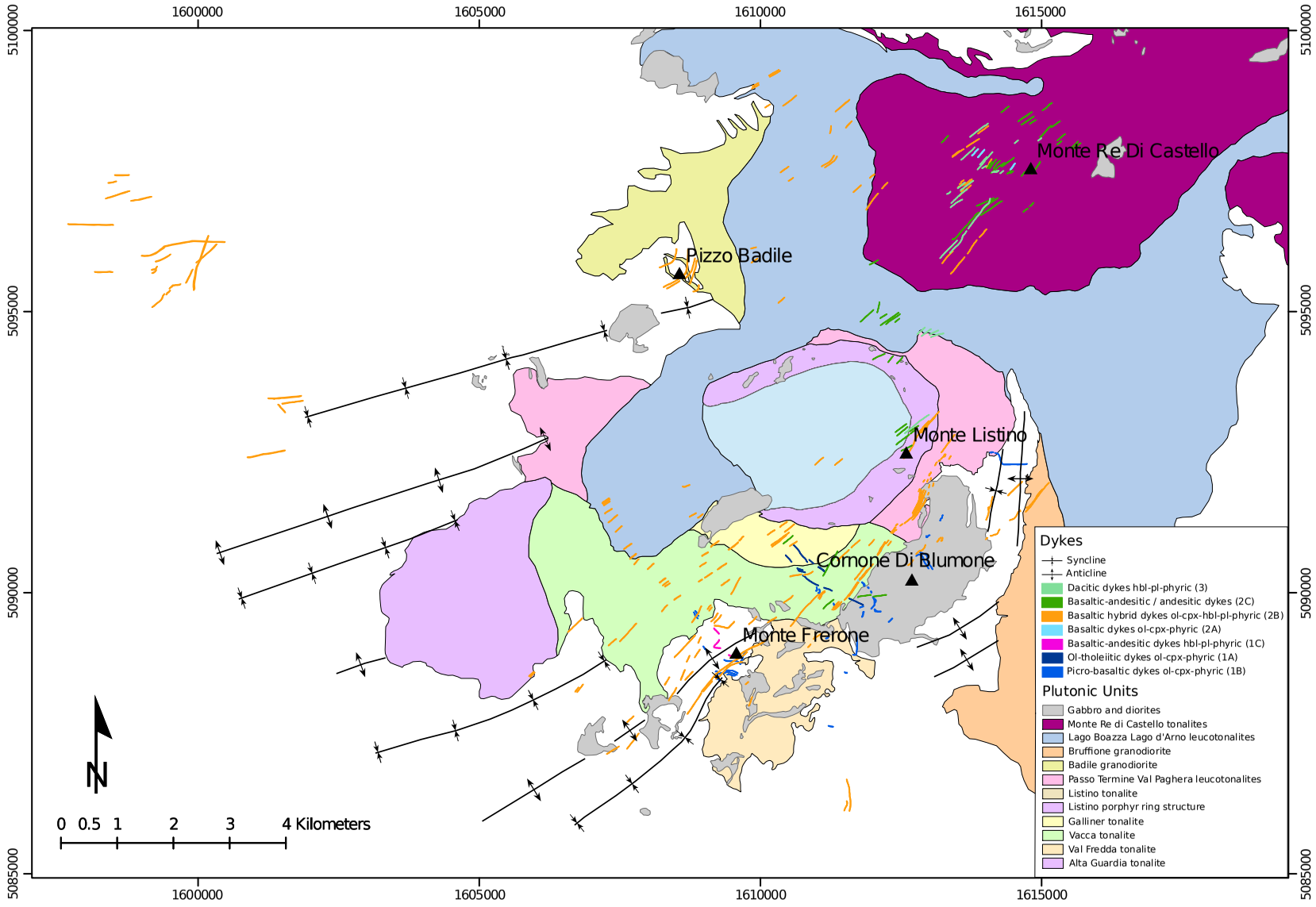

Figure 3.1: Occurrence of ultramafic to intermediate dykes in the southern part of the Adamello Batholith within the Re di Castello superunit. All different dyke generations crosscut the tonalitic to granodioritic plutonic rocks. Earliest generations of dykes of picrobasaltic to olivine-tholeiitic composition are subhorizontal and steeply dipping with NW-SE strike respectively and are concentrated in the Lago della Vacca and Monte Frerone area. Later subvertical dyke generations crosscut early more primitive dykes in the southwestern part and strike pervasively NE-SW over the entire southern part of the batholith and into the adjacent sedimentary country rocks. (Map datum: Monte Mario/Italy zone 1, Transverse Mercator Projection)

younger superunits of the Adamello batholiths, but are confined to the Re di Castello superunit and its surrounding Permo-Triassic country rocks [Callegari and Brack, 2002, Ulmer, 1986].

3.4 Field Relations and Petrography

Sample:	**NHS136**	**NHS158**	**NHS065**	**NHS051**	**NHS106**	**NHS116**	**NHS083**
Rock:	**Picro-basalt**	**Mg-tholeiite**	**Ol-tholeiite**	**Basalt**	**Basaltic-andesite**	**Andesite**	**Dacite**
Ol	12	13	13	15	0	0	0
Cpx	5	6	12	15	0	0	0
Am	0	0	0	0	20	22	7
Pl	0	1	1	0	15	14	30
Spl / Mt / Ilm	1	1	1	1	2	2	3
Matrix	82	78	73	69	63	62	60

Table 3.1: Mineral modal abundances of post-plutonic dyke rocks of the Southern Adamello. Estimated modal percentages of principal phenocryst mineral phases from typical dyke rocks obtained by thin section analysis. Phenocrysts phases are: Ol, olivine; Cpx, clinopyroxene (high Ca-clinopyroxene); Am, amphibole; Pl, plagioclase; Spl, spinel; Mag, magnetite; Ilm, Ilmenite.

The earliest dyke generation of picro-basalts and olivine-tholeiites (1B) (Fig. 3.1) cross cuts the Val Fredda Complex (granodiorite, tonalite, quartz-diorite and gabbro [Blundy and Sparks, 1992, John and Blundy, 1993, Ulmer, 1986]), Blumone Complex (hornblende-gabbro and ultra-basic rock [Ulmer, 1986], and Lago della Vacca Complex (granodiorite, tonalite and diorite [John and Blundy, 1993]). These subhorizontal picro-basaltic dykes (1B) show slight deformation, generally expressed by shortening of small amounts within the country rocks they intruded (lower to middle Triassic silici-clastics and carbonates). A second olivine-tholeiite dyke generation (1A) cross cuts the Vacca Complex as well. A wider basaltic dyke swarms (2A, 2B) crop out over at least 10km from southwest to northeast and extends further northward within the Re di Castello superunit; this dyke suite is distinctly younger than the pircobasalts and olivine-tholeiites of generation (1A, 1B). Basaltic-andesitic and andesitic dykes (2C) strike along the same direction(s), but are confined to more northern areas of the Re di Castello, Monoccola and Listino regions. Dacitic dykes (3) cross-cut these basaltic-andesitic and andesitic dykes and are confined to the same area.

Picrobasalts to Ol-tholeiites

Early picro-basaltic to olivine-tholeiitic dykes (1B) were emplaced after the intrusion of the Vacca tonalite . These dykes have intruded sub-horizontally on different altitude levels forming a dome-shaped structure [Ulmer, 1986], which dips downward to the sides, with a center located in the Lago della Vacca and Monte Frerone area (Fig. 3.1). Thickness ranges from 2.5m to 0.5m for the dykes at different levels. Apophyses are limited in length and have thickness of only a few centimeters. Within chilled margins, olivine pseudomorphs and pyroxene phenocrysts are visible. Otherwise, these dykes consist of massive equigranular amphibole and interstitial plagioclase, which form a dense dark green matrix (Fig. 3.2a).

Figure 3.2: Photographs of *(a)* Chilled margin of subhorizontal picrobasaltic dyke from Lago della Vacca that contains olivine and clinopyroxene phenocrysts. Internal part of dyke is composed of a massive green-bluish groundmass, consisting of amphibole and interstitial plagioclase. *(b)* Idiomorphic olivine phenocrysts now pseudomorphosed that consist of chlorite and tremolite with magnetites, which replace former Cr-spinel within bluish-green massive olivine-tholeiitic matrix. Idiomorphic clinopyroxene is present as pseudomorphs of green amphibole. *(c)* Amphibole-phyric basaltic-andesite shows a greenish massive fine-grained matrix. Brown idiomorphic amphibole, together with less abundant idiomorphic plagioclase, are coarse-grained and constitute up to 15-20 modal % of the whole rock. *(d)* Coarse-grained plagioclase phenocrysts set in light-green dacitic matrix, together with finer grained partially acicular brownish amphibole. These dacitic dykes can include minor fine-grained, darker, slightly amphibole-richer centimeter scale enclaves in centimeter scale.

In the Lago della Vacca area, a set of closely spaced olivine-tholeiitic dykes (1A) intruded in NW-SE direction (Fig. 3.1). These dykes are olivine- and clinopyroxene- phyric (Fig. 3.2b), though most of these phenocrysts are pseudomorphs. In rare cases, cores of olivine are still preserved within the very fine-grained chilled margins of these dykes.

Microscopically, olivine phenocrysts (Fig 3.3a, 9a) within chilled margins of picro-basalts and olivine-tholeiites are comprised by different secondary phases. Various amounts of chlorite, epidote, brucite, talc, tremolite, haematite and magnetite build up olivine pseudomorphs. Preserved olivine is found only in the cores and is mantled by talc and magnetite, overall mimicking the originally idiomorphic crystal shapes. Brownish Cr-spinel or picotite is often preserved within olivine pseudomorphs and high temperature al-

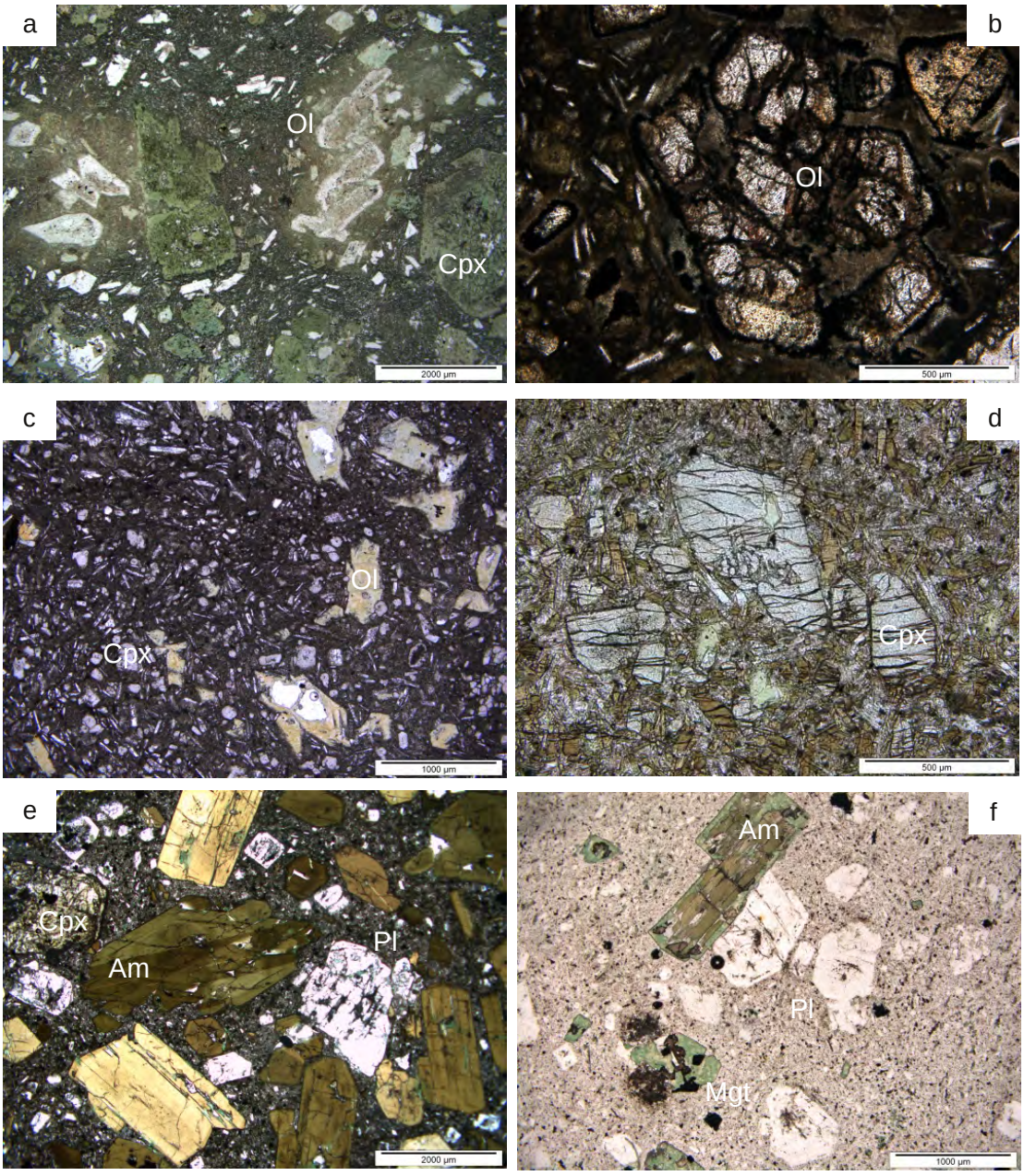

Figure 3.3: Photomicrographs of different dyke lithologies. *(a)* Chilled margin of a picrobasaltic dyke with fine-grained aphyric matrix consisting of amphibole and plagioclase. Pseudomorphosed olivine phenocrysts are comprised of chlorite and epidote and contain brownish spinel inclusions. Clinopyroxene is partly to completely replaced by green amphibole. *(b)* Preserved olivine phenocrysts of outermost dyke tip within basalt. *(c)* Finer grained clinopyroxene micro-phenocrysts are set in a basaltic aphyric matrix, together with olivine pseudomorphs consisting of chlorite. *(d)* Clinopyroxene phenocrysts set in a basaltic matrix of amphibole microlites and interstitial plagioclase. *(e)* Coarse-grained brown homogeneous amphibole phenocrysts, together with plagioclase within a fine-grained matrix (amphibole plagioclase) in basaltic-andesites and andesites. Opaques are magnetites. *(f)* Coarse-grained brownish amphibole partly replaced by chlorite, together with plagioclase, are set in a fine-grained matrix, mainly composed of plagioclase and quartz with minor amphibole in dacite. Opaques are magnetite and ilmenite.

teration is indicated by the presence of magnetite.

Clinopyroxene is generally much better preserved and forms large single crystals or crystal clots. Clinopyroxene often exhibits skeletal growth or sieve textures (Fig. 3.3a), expressed by embayments within the crystals that are filled with fine-grained phases composing the matrix. Complete or partial pseudomorphic replacements of clinopyroxene consist of green amphibole. Slightly brownish spinels occur in core zones of clinopyroxene.

Plagioclase is present in the form of microphenocrysts (Fig. 3.3a) and occurs only in more evolved olivine-tholeiitic compositions. These microphenocrysts show Karlsbad and albite polysynthetic twinning. The plagioclase lacks apparent zoning and is in general very homogeneous. They exhibit a euhedral shape and show some flow alignment parallel to the dyke margins. Group of plagioclases build actual crystal clots.

The matrix consists of acicular green to olive zoned amphibole and plagioclase, forming together a microlithic fluidal texture at the margins in sub-horizontal dykes. Central parts of the same dykes show acicular amphiboles as well, but larger interstitial strongly zoned plagioclase are indicative for slower cooling of this part of the sub-horizontal dykes. Opaque minerals within the matrix are ulvospinel and magnetite forming anhedral to subhedral grains.

Basalts

Basaltic dykes (2A, 2B) are steeply dipping and reveal an overall NE-SW striking pattern on a regional scale (Fig. 3.1). They spread over the entire Southern part of the Re di Castello superunit of the Adamello Batholith, from the Val Fredda in the South, to the area further NE around the Monte Re di Castello summit. These dykes reach out into the Permo-Mesozoic wallrocks of the Adamello massif. Their thickness ranges from a few tenths of a meter (0.2m) to over a meter and commonly features a chilled margin of a few centimeters.

These basaltic dykes build up dyke swarms ranging up to 15 to 20m in width. Individual dyke widths range from a few tenths of a meter to coalescened dykes of up to 5m in width. Such dyke swarms are accompanied by intense fracturing, parallel to sub-parallel to their margins. Internal chilled margins within dykes further indicate a complex emplacement history through multiple injections. Tonalitic and dioritic xenoliths are abundant, together with very crystal-rich zones within the dykes. Branching of small crystal-rich apophyses is common, together with small drag folds at the dyke margins. Dyke contacts range from very sharp to diffuse, particularly in the case of thick specimens where mechanical disaggregation is apparent in the form of breccia textures between wallrock and basaltic dyke.

Euhedral pseudomorphs of olivine phenocrysts (Fig. 3.3c) are replaced by chlorite, epidote and calcite on a microscopic scale within the central parts these dykes. Brownish euhedral Cr-spinel is commonly preserved as inclusions withinin these pseudomorphs. In rare cases within quenched margins or smallest dyke apophyses, olivine (Fig. 3.3b) is preserved. Clinopyroxene is present as phenocrysts and micro-phenocrysts that range from sieve textures to pristine porphyritic grains (Fig. 3.3d). Brownish amphibole phenocrysts and micro-phenocrysts are common and exhibit faint zoning in brown shades. Crystal-rich zones contain abundant amphibole and plagioclase crystals that exhibit resorption textures of entire cores to zonation bands of single crystals. Sieve-textured amphiboles are filled either by fine grained matrix

or ophitic clinopyroxene. These amphibole xeno-crystals exhibit pristine dark-brown overgrowth rims. Quartz xenocrysts are additionally abundant and often show rims of a network of acicular clinopyroxene that indicates reaction due to disequilibrium between a single crystal and basaltic melt. Plagioclase crystals exhibit, like amphibole, similar signs of resorption, with sieve texture cores or distinct bands within the zoned crystals. The micro-gabbroic matrix is composed of microlitic acicular amphibole, fine grained spinel and interstitial plagioclase.

Basaltic-Andesites and Andesites

Homogeneous amphibole-plagioclase-phyric basaltic-andesites (2C) (Fig. 3.2c) and andesites (2C) occur as sub-vertical dykes, concentrated in the Monte Re di Castello and Monoccola area to the NE of the Southern part of the Adamello Batholith (Fig. 1) These dykes are generally thicker (0.5m-3m) than their basaltic counterparts. There is a distinct chilled margin of less than 1cm width. Abundant porphyritic amphibole and plagioclase have no gradient in crystal size distribution across dyke width which if often thought to be caused by differences in flow regime across a dyke channel. Overall, these dykes are non-composite, single intrusions that belong to the larger dyke swarm striking NE-SW, which is comprised as well by basaltic dykes of generation (2A, 2B).

Brownish, homogeneous, coarse-grained prismatic pargasitic amphibole phenocrysts (Fig. 3.3e) are abundant and locally reach up to 25-30 modal#%. Euhedral amphibole phenocrysts commonly show irregular voids that are filled with quartz, plagioclase and alkali-feldspar. These voids most likely represent former melt inclusions. Coarse- to medium-grained plagioclase phenocrysts are rather homogeneous and occasionally show sieve textures in the cores and distinct small concentric overgrowth rims. Pseudomorphs comprised entirely of epidote minerals (Fig. 3.3e) are interpreted on the basis of their euhedral crystal-shapes as former clinopyroxene phenocrysts. The fine grained matrix is build up by microlites of brown amphibole and interstitial plagioclase. Magnetite is present mainly within the matrix as subhedral to euhedral opaque phase, often displaying prismatic shapes in cross section.

Dacites

Like basaltic-andesites and andesites, plagioclase- and amphibole-phyric dacitic dykes (3) (Fig. 3.2d) are constrained to the area of Monte Re di Castello and Monoccola. In relative chronology, these dykes crosscut earlier basaltic and basaltic-andesitic to andesitic dykes. Therefore, the last stage in temporal evolution coincides with the most evolved magma composition, ranging from basaltic to dacitic. These dykes are rather crystal-rich, with a dense light-green to greyish matrix and are part of the overall larger dyke swarm trending NE-SW comprising dyke generations (2A, 2B, 2C).

Coarse-grained, euhedral plagioclase is microscopically continuously zoned (Fig. 3.3f). Sieve textures in plagioclase are confined to the core zone of individual grains. Medium- to coarse-grained, slightly elongated, brown amphibole (Fig. 3.3f) is commonly partially replaced by chlorite and titanite inclusions that indicate the former presence of ilmenite (exsolutions) within these amphiboles. Euhedral to subhedral magnetite and ilmenite pairs dispersed throughout the matrix are coarser grained than the overall matrix. Some primary ilmenite is preserved otherwise it is replaced by titanite. The matrix consists of microlites of amphibole, which is almost entirely replaced by chlorite. Other matrix phases are lathshaped plagio-

clase and interstitial quartz. Fine-grained subhedral to anhedral magnetites are dispersed throughout the matrix. Abundance of secondary phases such as epidote and chlorite points towards auto-alteration processes, caused by late-stage fluids during cooling of these dykes.

3.5 Analytical Techniques

Whole Rock Chemistry

After initial size reduction by a hydraulic press, all samples were first ground to a fine powder in an agate mill. Thereafter, an aliquot was heated to 1050°C in a furnace to determine the loss of ignition by mass difference. The fired product was then mixed with the appropriate amount of $Li_2B_4O_7$ (1.2121 : 6) and fused for five minutes in a Pt-crucible and subsequently poured in a Pt-casting dye and quenched to a glass. Major element compositions of whole rock samples were determined on glass beads by X-ray fluorescene (XRF) on a PANalytical Philips PW2400 spectrometer at the University of Lausanne. BHVO-1, NIM-N, NIM-G and SY-2 standards were used for quality control. Uncertainties for XRF analyses are in the range of 0.5 wt.% (2 sigma) for major components such as SiO2 and 0.006% for a minor component such as NiO. The trace-element concentrations of bulk rocks were measured on the same XRF glass beads with a Geolas 200M 193nm ArF excimer laser ablation system, interfaced with an Elan 6100 DRC quadrupole spectrometer (LA-ICP-MS) at the University of Lausanne. The performance of the LA-ICP-MS was optimized with the NIST SRM 612 glass in order to improve the sensitivity (Mg $>$ 10000 cps and La $>$ 40000 cps). During this optimization doubly charged ions ($Ba^{++}/Ba^{+} < 2\%$) and oxide production rates (ThO^{+}/Th^{+}) were minimized. Three repeat measurements were performed on the glass beads with a laser pit size of 120μm, using a laser frequency of 10Hz and energy of 160mJ, which is equivalent to 12 J/cm^2. Helium was used as a cell gas carrier. Background and ablation interval acquisition times were 70 and 30-35 seconds respectively. Dwell times for different isotopes range from 10 to 20ms employing a peak hoping mode. Absolute trace-element concentrations were determined using CaO wt% (determined by XRF) as an internal standard and NIST 612 or NIST 610 as an external standard. The average elemental abundances are taken from Pearce et al. [1997] and data was reduced with LAMTRACE [Jackson, 2008, Longerich et al., 1996] software.

Mineral Chemistry

Major element compositions of minerals were measured by wavelength-dispersive analysis, using a JEOL JXA-8200 electron microprobe equipped with five spectrometers at the University of Lausanne. Samples were polished and carbon coated thin-sections; standards employed are natural minerals and synthetic glasses. Measurements were corrected with the PRZF [Armstrong, 1995] method. The beam current was set to 15nA with an acceleration voltage of 15keV and beam size was varied between 1μm and 4μm. Major elements on the respective mineral phase were measured for 20s on peak and 10s on background on both sides of the peak. Most minor- and trace-elements were measured for 30s on peak and 15s on background each side of the peak. Trace-elements such as Mg and Sr in plagioclase were measured for 60s on peak and 50s on the background. Trace-element analysis was performed on the same polished thin-sections using an ELEMENT XR sector field ICP-MS coupled with an UP193-FX ArF 193nm excimer

laser ablation system at the University of Lausanne. The LA-ICP-MS system was optimized using NIST SRM 612 glass standard to maximize the sensibility ($La^{139+} > 3.5*106$ cps and $Th^{232+} > 4.5*10^6$cps). At the same time, doubly charged ions ($Ba^{++}/Ba^{+} + < 2\%$) and oxide production ($ThO^{+}/Th^{+} < 0.0$ 5%) was minimized. Helium was used as cell gas (1.00 [l/min]) and Ar was used as sample gas (ranging from 0.690-0.735 [l/min]).The pit size during laser ablation was chosen according to grain size and mineral texture and varied between 25μm and 100μm. Repetition rate was varied between 5Hz and 15Hz and the laser energy was varied to achieve 5.2-5.8 J/cm^2 depending on analysed mineral phase. Acquisition times for background and ablation interval were 120s and 60s respectively for each laser spot. According to expected concentrations, dwell times for measured masses were varied between 10 and 20ms. Absolute trace-element concentrations were likewise determined for glass beads using CaO wt% or alternatively Al_2O_3 (determined by EMPA) as an internal standard and NIST 612 as an external standard. The data were reduced with LAMTRACE [Jackson, 2008, Longerich et al., 1996] and average elemental abundances for the NIST 612 standard were taken from Pearce et al. [1997].

Radiogenic Isotopes

A representative selection of eight samples for the different dyke rock types were analysed for whole rock Sr, Nd and Pb isotopic compositions at the Department of Mineralogy, University of Geneva. Approximately 160mg of powdered rock was dissolved in closed Teflon vessels for seven days on a hot plate at 140°C, within a mixture of 4ml of concentrated HF and 1ml HNO_3 15M, following the procedure described by Chiaradia [2009] and Chiaradia et al. [2011]. Samples were subsequently dried on a hot plate and then redissolved with 3ml of 14 M HNO_3 in Teflon vials at 140°C and desiccated again.

The Sr, Nd and Pb separation was performed using stacked columns with Sr-spec, TRU-spec and Ln-spec resins. The applied method is modified after Pin et al. [1994]. Purification for Pb was further achieved through AG-MP1-M anion exchange resin in a hydrobromic medium. Sr, Nd and Pb isotope ratios were analysed using a Thermo TRITON mass spectrometer, using Faraday cups in static mode. Pb was loaded onto Re filaments using the silica gel technique and all samples (and standards) were measured at a pyrometer-controlled temperature of 1220°C. Using the standard values of Todt et al. [1996], Pb isotope ratios were corrected for instrumental fractionation by a factor of 0.07% per a.m.u. based on more than 90 measurements of the SRM981 standard. External reproducibility of the standard ratios are 0.05 % for $^{206}Pb/^{204}Pb$, 0.08 % for $^{207}Pb/^{204}Pb$ and 0.10% for $^{208}Pb/^{204}Pb$.

Sr was loaded onto single Re filaments with a Ta oxide solution and measured at a pyrometer-controlled temperature of 1480°C in static mode, using the virtual amplifier design to cancel out biases in gain calibration among amplifiers. $^{87}Sr/^{86}Sr$ values were internally corrected for fractionation using an $^{88}Sr/^{86}Sr$ value of 8.375209. Raw values were further corrected for external fractionation by a value of + 0.03‰, determined by repeated measurements of the SRM987 standard ($^{87}Sr/^{86}Sr = 0.710248$). External reproducibility of the $^{87}Sr/^{86}Sr$ ratio for the SRM987 standard is 7μg g^{-1} (1σ). Nd was loaded onto double Re filaments with 1 M HNO_3 and measured in static mode with the virtual amplifier design. $^{143}Nd/^{144}Nd$ values were internally corrected for fractionation using a $^{146}Nd/^{144}Nd$ value of 0·7219 and the^{144}Sm interference on ^{144}Nd was monitored on mass ^{147}Sm and corrected by using a $^{144}Sm/^{147}Sm$ value of 0·206700. External reproducibility of the JNdi-1 standard [Tanaka et al., 2000] is <5μg g^{-1} (1σ). $^{87}Sr/^{86}Sr$ and

143Nd/144Nd whole-rock compositions were corrected for time-integrated decay of ^{87}Rb and ^{147}Sm using Rb, Sr, Sm and Nd concentrations determined by LA-ICP-MS on bulk-rock glass beads and an age of 41.7 Ma [Hürlimann et al., in prep.b], 39.8 Ma [Hansmann, 1986, Hansmann and Oberli, 1991] and 38.6 Ma [Hürlimann et al., in prep.b] for picro-basalt (1B) and olivine-tholeiite (1A) dykes, basaltic-andesite and andesite (2C) dykes, dacite (3) dyke, respectively. The resulting time-integrated corrections are small (less to much less than 500ppm for ^{87}Sr/^{86}Sr and less to much less than 100ppm for ^{143}Nd/^{144}Nd).

Composition	**picro-basalt**	**Mg-tholeiite**	**Ol-tholeiite**	**basalt**	**basaltic-andesite**	**andesite**	**dacite**
Sample	**NHS136**	**NHS158**	**NHS065**	**NHS051**	**NHS106**	**NHS116**	**NHS083**
Generation	**1B**	**1B**	**1B**	**2A**	**2C**	**2C**	**3**
SiO2	45.83	47.43	47.68	48.96	53.53	58.48	65.7
TiO2	0.71	0.71	0.77	0.84	0.75	0.57	0.35
Al2O3	13.13	13.67	15.47	16.25	18.29	17.97	17.1
Fe2O3	9.8	7.81	9.38	8.7	7.99	7.55	3.8
MnO	0.17	0.14	0.23	0.17	0.16	0.14	0.15
MgO	15.38	13.11	10.68	8.43	4.31	2.81	1.45
CaO	10.01	10.64	10.62	10.56	8.71	7.23	5.03
Na2O	1.1	1.86	1.56	1.76	2.68	2.93	3.51
K2O	0.42	0.74	1.21	0.78	0.75	0.92	0.88
P2O5	0.09	0.16	0.13	0.16	0.14	0.12	0.18
LOI	2.57	2.76	1.28	2.92	2.06	0.94	1.24
Cr2O3	0.16	0.11	0.1	0.07	0.01	b.l.d	b.l.d
NiO	0.04	0.03	0.02	0.01	b.l.d	b.l.d	b.l.d
Total	99.4	99.16	99.13	99.6	99.38	99.66	99.38

Table 3.2: Representative analyses of different post-plutonic dyke rock suites of the Southern Adamello (Re di Castello superunit). Major elements and Cr2O3 and NiO were determined by XRF analysis (all in [wt%]).

Composition	**picro-basalt**	**Mg-tholeiite**	**Ol-tholeiite**	**basalt**	**basaltic-andesite**	**andesite**	**dacite**
Sample	**NHS136**	**NHS158**	**NHS065**	**NHS051**	**NHS106**	**NHS116**	**NHS083**
Generation	**1B**	**1B**	**1B**	**2A**	**2C**	**2C**	**3**
Be	0.693	$\leq$ 1.164	$\leq$ 3.115	1.583	1.316	1.03	1.732
Sc	52.8	46.2	44.1	33.1	36.8	23.8	6.0
V	291	259	271	242	301	236	66
Cr	1180	832	621	549	95	64	64
Co	55.0	30.0	35.3	31.3	21.1	19.2	6.1
Ni	336.2	249.7	137.7	90.5	20.1	18.0	13.4
Cu	31.1	6.3	19.1	92.2	49.4	50.8	11.3
Zn	150.6	142.1	167.5	145.5	195.5	169.8	218.8
Ga	12.3	13.4	15.2	15.7	16.9	16.4	17.1
Ge	2.1	2.3	3.0	1.7	2.5	2.3	2.0
As	2.1	2.7	1.3	2.2	$\leq$ 1.8	2.0	$\leq$ 2.0
Rb	9.6	24.3	47.1	24.9	15.0	23.1	22.2
Sr	186	620	282	368	596	508	476
Y	13.1	14.3	15.4	15.3	18.9	13.5	12.3
Zr	33	47	51	73	76	57	92
Nb	2.3	4.7	3.9	5.5	3.9	3.7	6.1
Mo	2.5	2.3	1.5	2.2	1.9	3.2	2.3
Cs	1.16	0.75	3.89	0.29	0.27	0.50	0.44
Ba	62	120	106	168	204	256	346
La	6.5	18.0	10.4	15.4	16.0	14.9	24.6
Ce	13.6	31.0	20.1	31.4	31.1	28.4	43.1
Pr	1.73	3.31	2.35	3.65	3.59	2.95	4.54
Nd	8.0	12.6	10.7	15.0	14.7	12.2	16.1
Sm	2.12	2.69	2.59	3.16	3.10	2.43	2.63
Eu	0.66	0.84	0.97	0.95	0.99	0.70	0.85
Gd	1.97	2.50	2.39	2.88	3.09	2.13	2.36
Tb	0.363	0.382	0.483	0.406	0.479	0.320	0.272
Dy	2.60	2.41	2.63	2.83	3.18	2.47	2.28
Ho	0.506	0.548	0.614	0.566	0.687	0.517	0.396
Er	1.46	1.49	1.65	1.65	1.92	1.44	1.09
Tm	0.196	0.213	0.262	0.241	0.292	0.217	0.166
Yb	1.46	1.61	1.72	1.59	2.02	1.55	1.44
Lu	0.215	0.238	0.297	0.238	0.330	0.249	0.230
Hf	1.01	1.38	1.54	1.99	1.86	1.60	2.30
Ta	0.18	0.29	0.32	0.34	0.21	0.25	0.43
Pb	0.64	1.53	1.12	3.61	4.86	7.98	11.19
Th	1.74	4.70	2.43	3.11	4.59	4.85	7.96
U	0.35	1.52	0.76	0.76	1.01	1.04	1.78

Table 3.3: Representative analyses of different post-plutonic dyke rock suites of the Southern Adamello (Re di Castello superunit). Trace elements were analyzed by LA-ICP-MS analysis (all in [ppm]).

3.6 Geochemistry of Dyke Rocks Southern Adamello

A total of 143 analyzed dykes (Tab. 3.2) of the southern part of the Adamello Batholith range from primitive picro-basalts to dacites and all plot within the sub-alkaline field (Fig. 3.4). Bulk rock compositions range from the arc-tholeiitic to calc-alkaline series (Fig. 3.5a), with no apparent compositional gap within the differentiation suite. Early picro-basalts and olivine-tholeiites together with later basalts, basaltic-andesites and andesites are all metaluminous (Fig. 3.5b), with a continuous transition to peraluminous compositions for dacitic dykes. Changes in the mineral assemblages, together with the textures of these rocks define rather distinct groups reflected through their bulk rock compositions (Fig. 3.5a-d). Bulk rock analyses of dykes are taken here as an approximation for liquid composition throughout the different differentiation stages.

Bulk Rock Major- and Trace-Elements

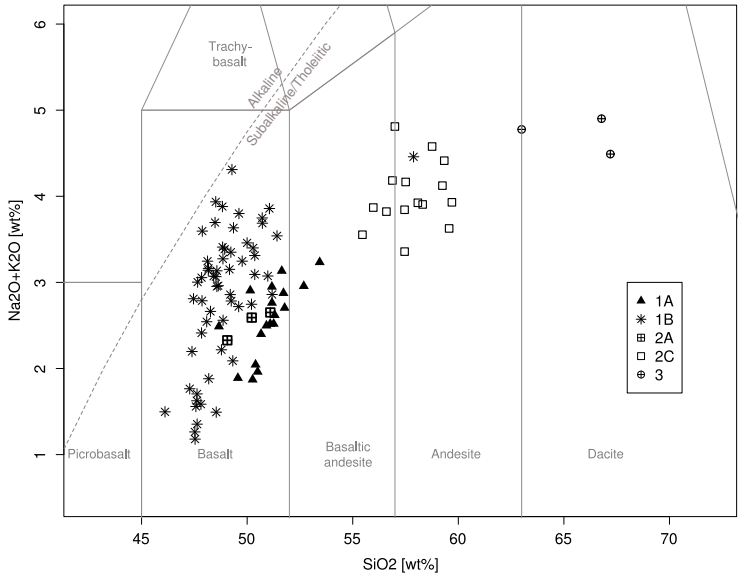

Figure 3.4: A portion of the total alkali (Na_2O+K_2O) vs. silica (SiO_2) diagram TAS [Le Bas et al., 1986] illustrating the compositions of the dyke rocks of the Southern Adamello Batholith. These dykes span the compositional range from picro-basalts to dacites on an anhydrous basis. Dyke generations: picrobasalts, Mg-tholeiites, olivine-tholeiites (1B), Mg-tholeiites, olivine-tholeiites (1A), basalts (2A), basaltic-andesites, andesites (2C), dacites (3).

Scattered over a regional extent of about 216km^2, major elements such as TiO_2 (Fig. 3.5c) reveal some distinct variation throughout the differentiation range from 5 to 17 MgO wt%. This is expressed by higher TiO_2 concentrations for a given MgO-content for picro-basalts, Mg-tholeiites (intermediate between picro-basalts and olivine-tholeiites), olivine-tholeiites and basalts (dyke generations 1B, 2A) and a lower TiO_2 series for Mg-tholeiites and olivine-tholeiites (1A). The decrease of TiO_2 at MgO-contents lower than 5 wt% goes along with the appearance of Ti-magnetite and illmenite in more evolved basaltic-andesites, andesites and dacites in the course of magma differentiation. Within the same compositional range (MgO 5-17 wt%), a continuous enrichment of Al_2O_3 is observed for picro-basalts, Mg-and olivine-tholeiites and

basalts, where the dominant phenocryst mineralogy ranges from olivine to pyroxene with a transition to the beginning of crystallization of amphibole and concomitant plagioclase. Al_2O_3 is decreasing in low-MgO basaltic-andesites, andesites and dacites, which are strongly amphibole-plagioclase-phyric rocks.

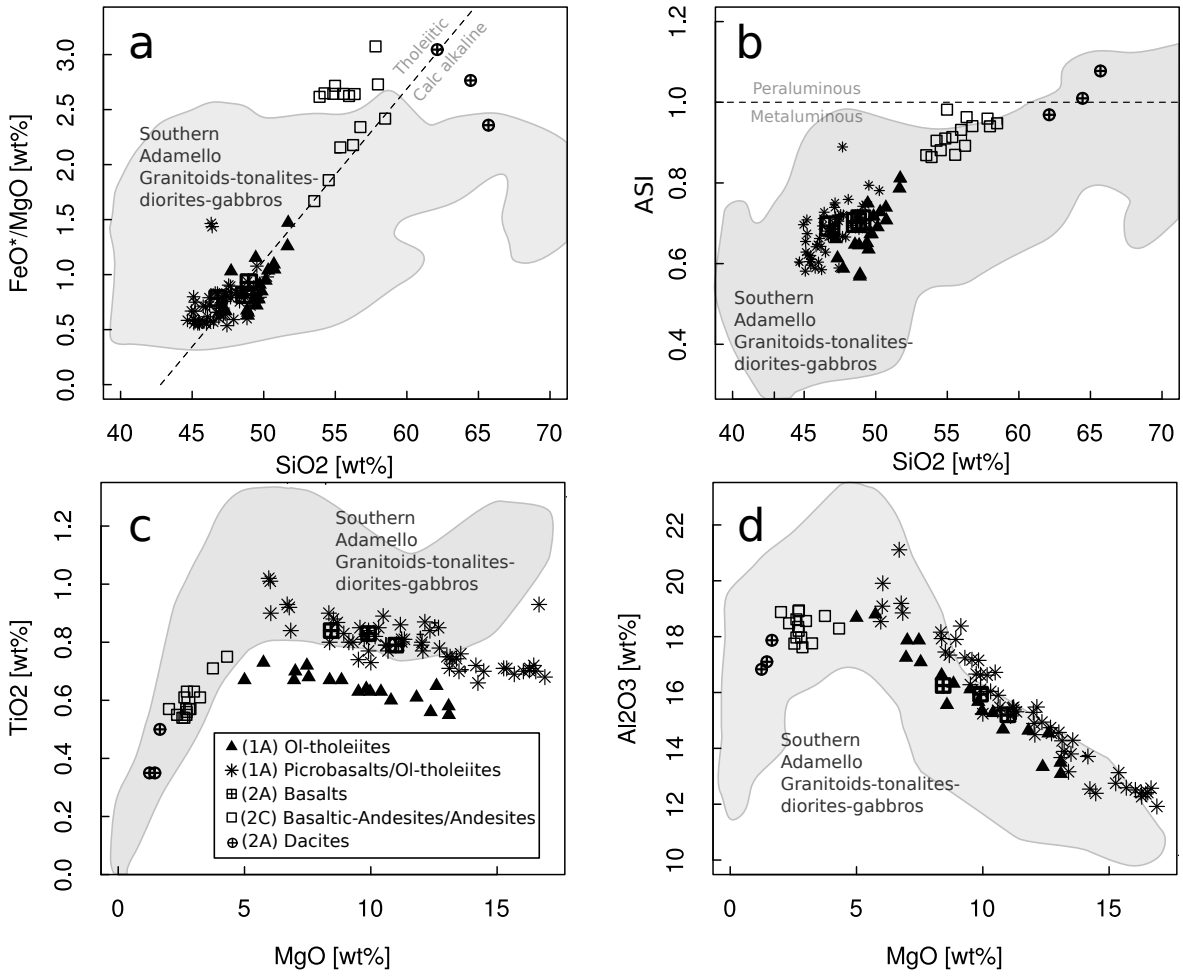

Figure 3.5: Late stage dyke rocks reveal arc-tholeiitic and calc-alkaline trends in *(a)* FeO*/MgO vs. SiO_2 diagram of Miyashiro [1974]. Throughout the differentiation suite, bulk rock compositions change to the calc-alkaline field for dacitic dykes. *(b)* Bulk compositions are metaluminous for picro-basalts to andesites with a continuous transition to peraluminous for dacites in the ASI [Al/(2Ca + Na + K)] vs. SiO_2 diagram. *(c)* TiO_2 vs. MgO variation diagram clearly identifies two distinct trends for higher MgO concentrations, i.e. for ultramafic to mafic compositions. *(d)* In the range primitive picro-basalts to basaltic compositions, an enrichment of Al_2O_3 is observed with decreasing MgO until Al_2O_3 starts to decrease for basaltic-andesites, andesites and dacites. The grey field in diagrams represents the composition of Southern Adamello granitoids-tonalites-diorites-gabbros [Ulmer, 1982, 1986, Blundy and Sparks, 1992].

Trace element variations of bulk rock compositions are summarized in Figures 3.6a-g. For the large ion lithophile elements (LILE) such as Sr, Rb and Ba (Fig. 3.6a-c) and the light rare earth elements (LREE) such as Ce (Fig. 3.6e), a uniform variation for the Mg- and olivine-tholeiites of dyke generation 1A, basaltic-andesites and andesites (2C), together with the most evolved dacites (3), is evident: Sr

systematically increases with decreasing MgO content from about 350 to over 600ppm, followed by a sharp bend and decreasing Sr content at the onset of plagioclase appearance; Ba and Ce concentrations show a systematic increase with decreasing MgO that appears to accelerate for basaltic-andesites, andesites (2C) and dacites (3); Rb behaves likewise but shows larger scatter. In contrast, partially very primitive subhorizontal dykes of generation 1B from the Lago della Vacca area show a large scatter in Sr, Ba, Rb and Ce at a given MgO, Zr varies by a factor of 4.8 over the entire compositional range with some larger variation in the case of basaltic-andesites to dacites. Ni and Cr are positively correlated with MgO (Fig. 3.6f, g), decreasing from highest values of 1360 ppm for Cr for picro-basalts (1B) down to values of ~35 ppm for dacites (3) and andesites (2C). Ni decreases likewise from 340ppm to ~ 15ppm over the same compositional range of MgO.

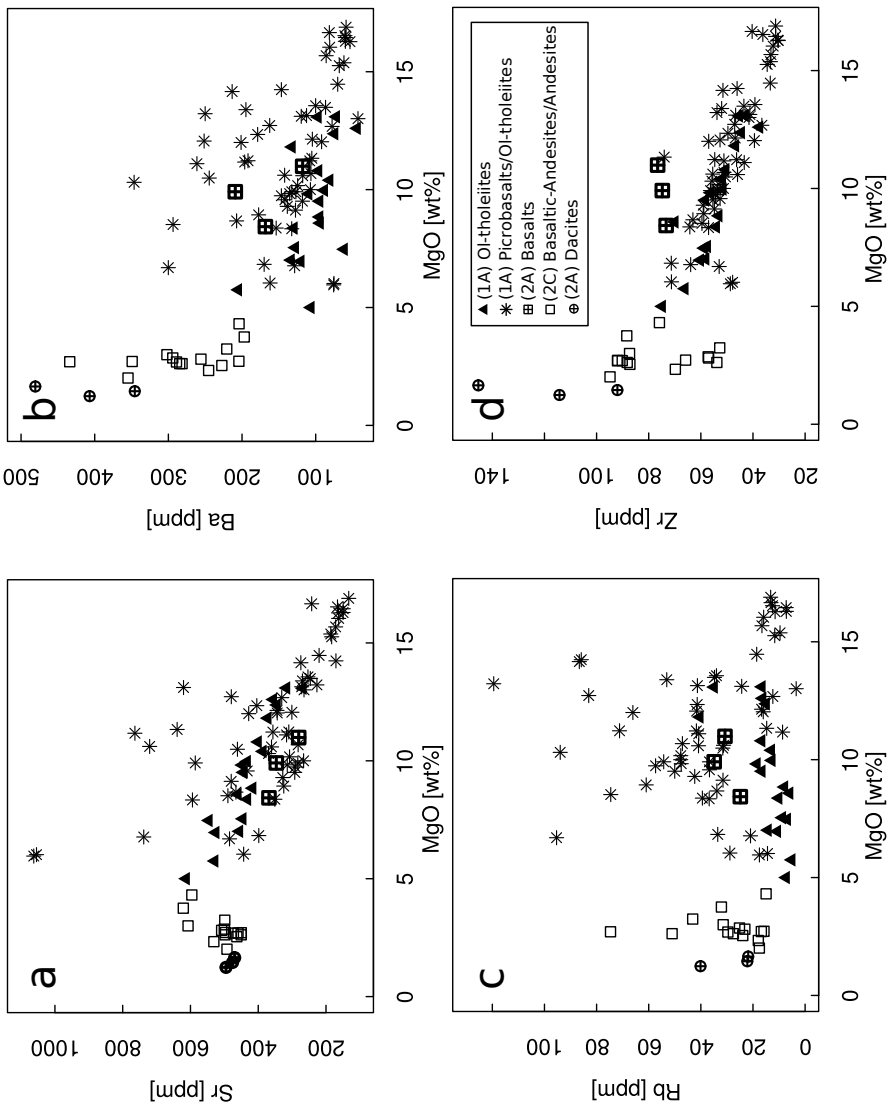

Figure 3.6: Trace element variation diagrams for Sr, Ba, Rb and Zr as a function of MgO (increasing degree of differentiation). *(a)* Sr vs. MgO shows enrichment of Sr towards basaltic-andesites with subsequent decrease towards dacite and andesites. Scatter for dyke generation 1B is much larger than for any other dyke generation. *(b)* Ba vs. MgO reveals a rather pronounced increase for basaltic-andesites (2C) to dacites (3) Dykes of generation 1B show again a similar scatter as for Sr. *(c)* Rb vs. MgO reveals small variation with increasing concentrations for andesites, except for generation 1B that scatters widely. *(d)* Zr vs. MgO indicates two different evolutions towards more evolved basaltic-andesite / andesites (2C) and dacites (3).

Figure 3.7: Trace element variation diagrams for Ce, Ni, Cr and K_2O as a function of MgO (increasing degree of differentiation). *(a)* Ce vs. MgO shows constant increase from basalt (1A) to basaltic-andesites (2C) to dacites (3), with more scattered data for dykes 1B. *(b)* Ni vs. MgO; and *(c)* Cr vs MgO both exhibit a continuous decrease from primitive picro-basalts to evolved basaltic-andesites (2C) and dacites (3). (d) K_2O shows a slight increase for basaltic-andesites (2C) to dacites (3) with decreasing MgO, whereas values for picro-basalts to Ol-tholeiites (1B) are very scattered.

The slope of the chondrite-normalized rare earth elements (REE) patterns for olivine-tholeiite dykes of generation (1A) (Fig. 3.8a) is less inclined towards the light REE in comparison with all other dyke generations. Picro-basalts and olivine-tholeiites of generation (1B) (Fig. 3.8b) reveal two subgroups: one with a similar REE pattern to (1A) and a larger group that approaches the LREE patterns of dacites (3) (Fig. 3.2d). Basaltic-andesites and andesites of generation (2C) (Fig. 3.8c) exhibit distinctly higher light REE than (1A) olivine-tholeiites. REE patterns of basalts (Fig. 3.8c) are in the range of basaltic-andesites and andesites. Dacites (3) (Fig. 3.8d) show very steep slopes from LREE to middle REE (MREE) for two samples and one sample has overall higher REE. The averge La/Yb ratios increase from 3.5 for picro-basalts (1A) to over 10 for dacites (3).

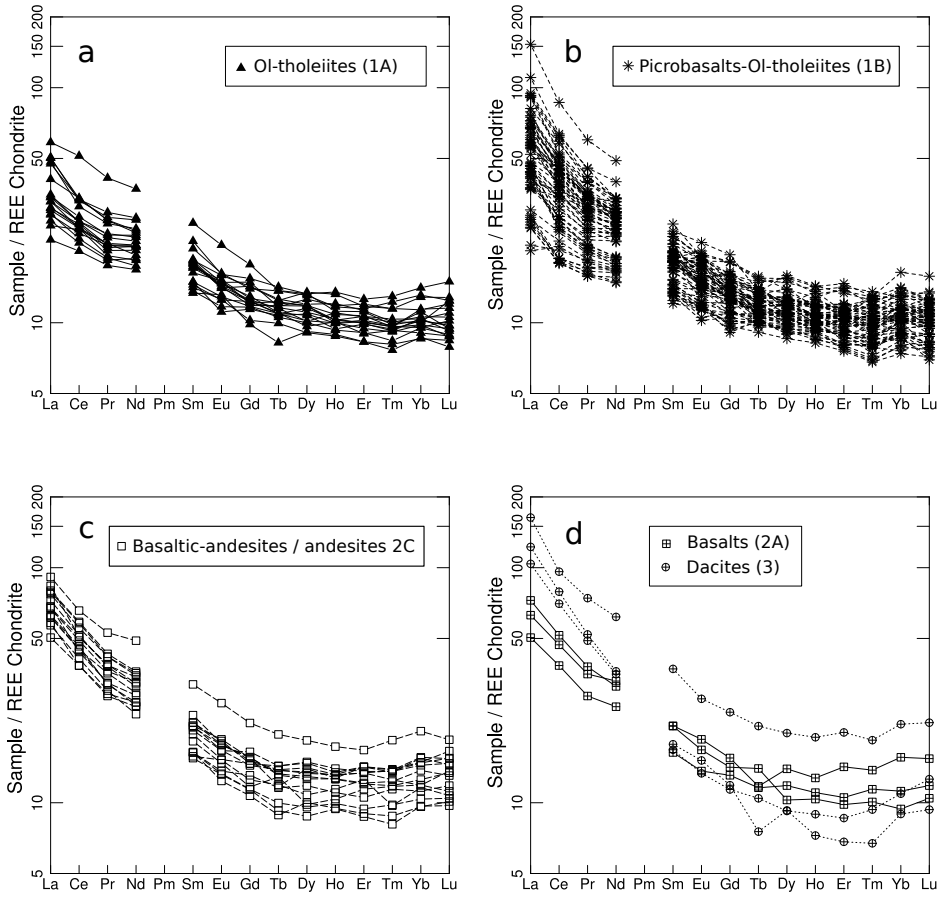

Figure 3.8: CI Chondrite-normalized Rare Earth element (REE) patterns [McDonough and Sun, 1995] of different dyke generations : *(a)* Olivine.tholeiites (1A) ; *(b)* picro-basalts and olivine-tholeiites (1B); *(d)* basalts (2A); *(c)* basaltic-andesites and andesites (2C); *(d)* dacites (3). REE patterns *(a)* of olivine-tholeiites (1A) in general reveal flatter slopes than *(b)* picro-basalts and olivine-tholeiites (1B), which exhibit a much larger spread for light REE. *(c)* Basaltic-andesites and andesites (2C) build a homogeneous group. *(d)* Basalt (2A) REE patterns resemble the pattern of basaltic-andesites and andesites (2C). Dacites (3) show the steepest REE patterns, with depletion of middle to heavy REE for two samples.

Larger variations occur for incompatible elements such as Cs and Rb between different dyke generations as well as within single groups (Fig. 3.9). General characteristics include distinct negative Nb and Ta

anomalies typical for arc-basalts [Tatsumi, 2005, Pearce and Stern, 2006, Arevalo and McDonough, 2010]. La/Nb ratios increase from 3 for picro-basalts and olivine-tholeiites (1A, 1B) to >4 for basaltic-andesites, andesites and dacites. The Ba/Th ratio ranges from 68 for olivine-tholeiites (1A) to 43 for dacites (3). The Th/La ratio used as well to trace the sediment input in subduction zone magmas [Plank, 2005] results in 0.18 for olivine-tholeiites (1A), 0.24 for picro-basalts and olivine-tholeiites (1B) and 0.20 for basalts (2A). In particular, basaltic-andesites and andesites (2C) and dacites (3) show a positive Pb anomaly. A negative Ti-anomaly is faintly expressed for basaltic-andesites and andesites (2C) and thoroughly developed for dacites.

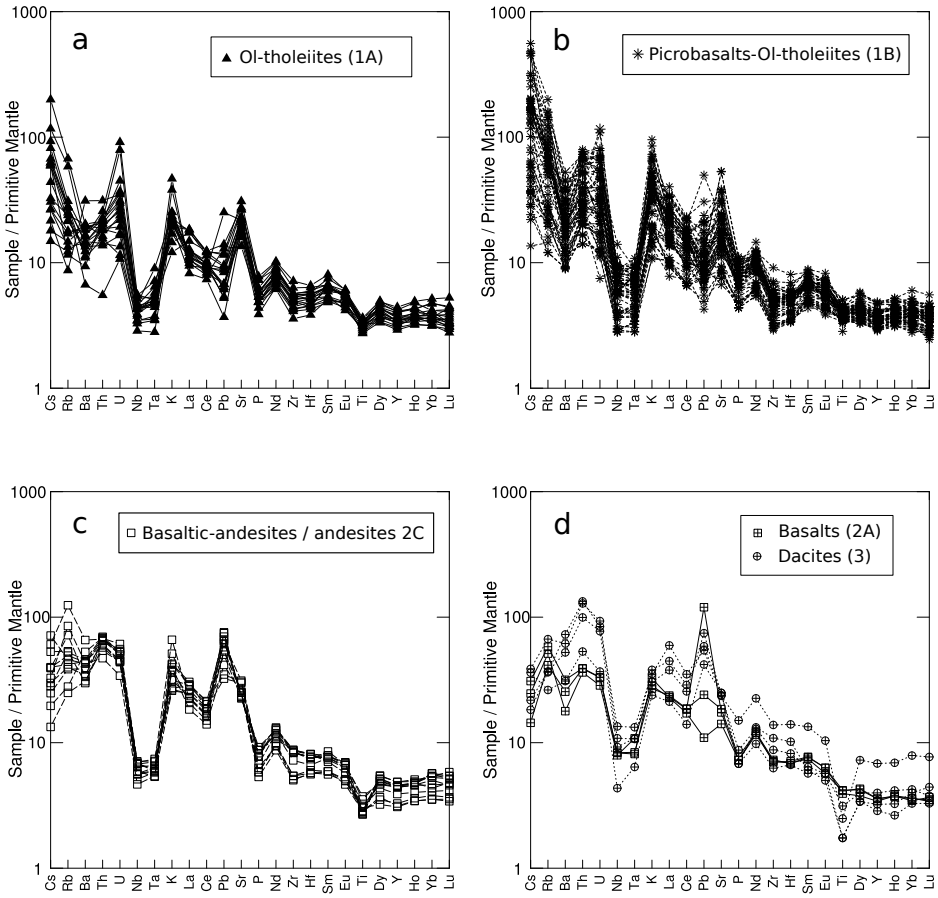

Figure 3.9: Primitive mantle normalized trace element patterns [McDonough and Sun, 1995] for different dyke generations and groups: *(a)* Olivine-tholeiites (1A) ; *(b)* picro-basalts and olivine-tholeiites (1B); *(d)* basalts (2A); *(c)* basaltic-andesites and andesites (2C); *(d)* dacites (3). All different generations exhibit a negative Nb and Ta anomaly. Basaltic andesites and andesites (2C) and dacites (3) feature a positive Pb anomaly. *(c)* Basaltic-andesites and andesites (2C) show a moderate negative Ti-anomaly. *(d)* For dacites (3) this negative Ti-anomaly is much more pronounced.

Composition	Sample	Generation	$^{87}Sr/^{86}Sr$	$^{143}Nd/^{144}Nd$	ϵNd	$^{206}Pb/^{204}Pb$	$^{207}Pb/^{206}Pb$	$^{208}Pb/^{204}Pb$
picro-basalt	NHS136BR1	1B	0.703961	0.512718	1.6	18.336	15.649	38.437
Ol-tholeiite	NHS002BR1	1B	0.704674	0.512636	0.0	n.d.	n.d.	n.d.
Ol-tholeiite	NHS003BR2	1B	0.704467	0.512641	0.1	18.066	15.615	37.901
Ol-tholeiite	NHS066BR2	1A	0.703971	0.512575	-1.2	18.501	15.639	38.649
basalt	NHS079BR1	2A	0.705114	0.512513	-2.4	18.538	15.657	38.779
basaltic-andesite	NHS106BR1	2C	0.703355	0.512816	3.5	18.485	15.637	38.583
andesite	NHS116BR1	2C	0.703237	0.512820	3.5	18.416	15.629	38.478
dacite	NHS083BR1	3	0.703803	0.512801	3.2	18.287	15.614	38.341

Table 3.4: Bulk rock radiogenic isotope data for Sr, Nd and Pb.$^{87}Sr/^{86}Sr_i$, $^{143}Nd/^{144}Nd_i$, $^{206}Pb/^{204}Pb_i$, $^{207}Pb/^{204}Pb_i$ and $^{208}Pb/^{204}Pb_i$ are initial values recalculated to the following ages: picro-basalts and olivine-tholeiites (1B), olivine-tholeiite (1A) to 41.7 Ma; basalt (2A), basaltic-andesite and andesite (2C) and dacite (3) to 39.8 Ma; according to titanite ages (41.7 Ma) and zircon ages (38.7 Ma) determined by [Hürlimann et al., in prep.b]. ϵNd was calculated according to a present-day CHUR value of $^{143}Nd/^{144}Nd$ of 0.512638 [Jacobsen and Wasserburg, 1980].

Bulk Rock Isotopic Composition

The Sr, Nd and Pb isotopic compositions (Fig. 3.10) of the post-plutonic dyke rocks from the Southern Adamello region result in a negative correlation for $^{87}Sr/^{86}Sr_i$ and $^{143}Nd/^{144}Nd_i$, together with a slightly positive correlation between $^{207}Pb/^{204}Pb_i$ and $^{206}Pb/^{204}Pb_i$ that varies from 18.06-18.54 in $^{206}Pb/^{204}Pb_i$ and from 15.61-15.65 in $^{207}Pb/^{204}Pb_i$. Compared to a series of plutonic rocks from the Re di Castello superunit, whole rock $^{87}Sr/^{86}Sr_i$ and $^{143}Nd/^{144}Nd_i$ (Fig. 3.10a) of post-plutonic dyke rocks lie mostly in the range of the more primitive Val Fredda group [Kagami et al., 1991] which consists of coarse-grained olivine-pyroxene-hornblendites, porphyritic hornblende-gabbros and medium-grained hornblende-bearing biotite leucotonalite. Coarse-grained olivine-clinopyroxenites, clinopyroxene-magnetite-hornblende-leucogabbros, and medium-grained biotite-bearing hornblende quartz diorites of the Blumone group occupy a similar but more restricted range for whole-rock $^{87}Sr/^{86}Sr_i$ and $^{143}Nd/^{144}Nd_i$. The basaltic-andesite and andesite (2C), together with the dacite sample (3), have very similar $^{87}Sr/^{86}Sr_i$ and $^{143}Nd/^{144}Nd_i$ isotopic signature as the hornblendites from Monte Mattoni (Val Fredda group; Tiepolo et al., 2011, Ulmer et al., 1983, Blundy and Sparks, 1992). Different groups of rocks, encompassing picro-basalts together with Mg- and olivine-tholeiites (1B) and basaltic-andesites together with andesites (2C) and dacites (3) appear to form two distinct groups in terms of $^{87}Sr/^{86}Sr_i$ and $^{143}Nd/^{144}Nd_i$ variations (Fig. 3.10b): The most evolved rocks, basaltic-andesites, andesites (2C) and dacites (3) reveal the most primitive isotopic signatures of the entire dyke rock suite. Chemically primitive picro-basalts and olivine-tholeiites show increased $^{87}Sr/^{86}Sr_i$ that coincide with the range determined for Blumone and Val Fredda plutonic rocks. The dyke bulk rock data shows a variation for both $^{207}Pb/^{204}Pb_i$ vs. $^{206}Pb/^{204}Pb_i$ values (Fig. 3.10c) and $^{208}Pb/^{204}Pb_i$ vs. $^{206}Pb/^{204}Pb_i$ values (Fig. 3.10d), that plot within the data range obtained from sulfides [Cumming et al., 1987] of the lower crustal, Permian, Mafic Igneous Complex of the Ivrea-Verbano Zone. One sample of the picro-basalts to olivine-tholeiites (1B) in figure 3.10d is closet to the depleted MORB mantle (DMM) reservoir value of Rehkämper and Hofmann [1997].

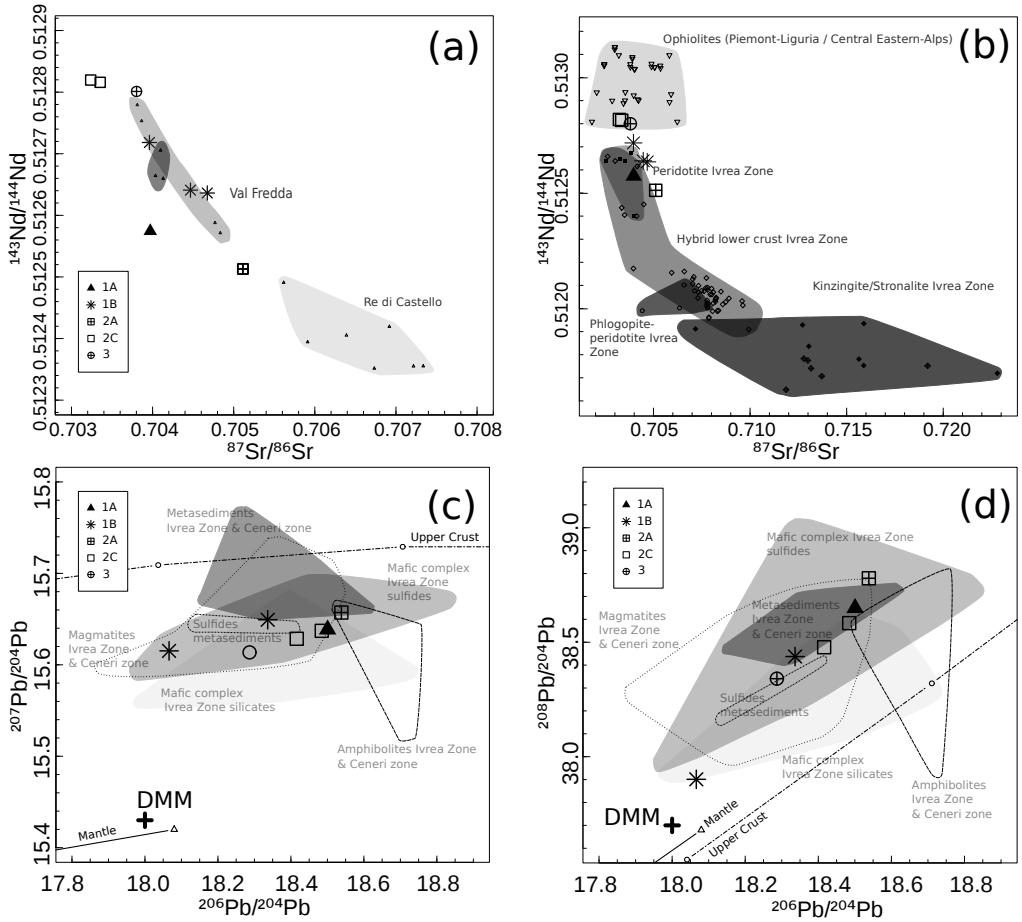

Figure 3.10: *(a)* Whole rock radiogenic $^{87}Sr/^{86}Sr$ and $^{143}Nd/^{144}Nd$ isotopes from Val Fredda, Blumone and Re di Castello intrusives [Kagami et al., 1991] are compared with data from dykes rocks of this study. *(b)* Comparison with different parts of the upper mantle and lower crustal section exposed in the Ivrea Zone [Voshage et al., 1987, 1990] further west along the Periadriatic lineament indicates the relatively primitive character of the Southern Adamello dyke rocks in terms of $^{87}Sr/^{86}Sr$ and $^{143}Nd/^{144}Nd$ isotopes. *(c)* and *(d)* Pb whole rock radiogenic isotopes ($^{207}Pb/^{204}Pb$, $^{206}Pb/^{204}Pb$, $^{208}Pb/^{204}Pb$) for dyke rocks are compared with a compilation of data from the Ivrea upper mantle and lower crustal sequence. Data is taken from Boriani et al. [1995] and Cumming et al. [1987], comprising whole rock data from metasediments, sulfides of the Mafic Complex, igneous rocks of the Ivrea and Ceneri zone and amphibolites of the Ivrea and Strona-Ceneri zone. DMM represents the depleted MORB mantle [Rehkämper and Hofmann, 1997]. Pb radiogenic isotope evolution curves for the mantle and the upper crust are from Zartman and Doe [1981].

3.7 Mineral Chemistry and Textures

Porphyritic textures of basalts, basaltic-andesites, andesites and dacites are a common feature. Major phenocryst phases include olivine, clinopyroxene, amphibole and plagioclase. The latter only occurs as a phenocryst phase in the more differentiated andesites and dacites. Basaltic-andesites, andesites and dacites can be highly crystalline, with up to 40% phenocrysts (Tab. 3.1). Phenocrysts have a size $>300\mu$m, whereas microphenocrysts are in the size range of 100-300μm. Plagioclase micro-phenocrysts commonly exhibit a more anorthite-rich composition than microlites and correspond to the composition

of overgrowths rims of larger phenocrysts. Microlites are generally $<100\mu$m and can be oriented forming pilotaxitic and fluidal textures. The picro-basalts and Mg- or olivine-tholeiites contain about 12-13 modal % (Tab. 3.1) of olivine phenocrysts. The other phenocryst phase is clinopyroxene with a modal percentage of 5-12% and Cr-rich spinel inclusions within phenocrysts that have a modal abundance of around 1%. More evolved basalts have similar phenocryst assemblage like olivine-tholeiites with 15% olivine and 15% clinopyroxene together with 1% spinel. Plagioclase in basalts and olivine-tholeiites is only present as a micro-phenocryst phase. Intermediate basaltic andesite and andesites are characterized by the appearance of amphibole (20-22%) and plagioclase (14-15%) as phenocrysts and about 2% of magnetite as the opaque phase forming micro-phenocrysts. Most evolved dacites are characterized by increased modal concentrations of plagioclase phenocrysts, with a modal abundance of 30%, lower amphibole contents of 7% and the occurrence of both Fe-Ti-oxides, magnetite and ilmenite, with an abundance of about 3%.

Phase	Sample	Generation	SiO2	TiO2	Al2O3	Cr2O3	FeO	MnO	MgO	CaO	Na2O	K2O	NiO	Total
Ol	Ol001-1	1A	40.57	0.01	0.02	0.05	9.43	0.18	50.25	0.19	0.01	0.01	0.22	100.94
Ol	Ol167-1	1B	40.88	0.00	0.01	0.02	8.93	0.13	50.11	0.16	0.00	0.00	0.27	100.51
Ol	Ol144-9	2A	40.16	0.00	0.03	0.04	9.75	0.17	49.32	0.15	0.00	0.00	0.37	99.99
Cpx	Px053-31	2A	53.01	0.24	1.98	0.57	4.45	0.20	16.94	21.98	0.12	0.00	0.00	99.50
Spl	Spl001-1	1A	0.04	0.01	0.02	48.51	29.57	1.63	6.51	0.03	n.a.	n.a.	0.07	100.27
Spl	Spl167-9	1B	0.12	0.35	13.09	48.67	25.35	0.79	10.47	0.00	n.a.	n.a.	0.09	99.18
Spl	Spl144-5	2A	0.13	0.31	20.82	42.76	21.41	0.56	13.17	0.04	n.a.	n.a.	0.18	99.70
Hbl	Am106-2	2C	40.59	1.63	15.07	0.02	9.85	0.10	14.65	12.35	2.49	0.50	n.a.	97.26
Hbl	Am086-4	3	43.84	1.62	11.32	0.00	13.41	0.40	13.32	11.37	1.73	0.23	n.a.	97.25
Pl	Pl106-1	2C	45.33	0.00	34.50	n.a.	0.46	0.01	0.00	18.66	0.79	0.00	n.a.	99.93
Pl	Pl086-6	3	45.71	0.00	33.85	n.a.	0.44	0.00	0.00	18.23	1.05	0.00	n.a.	99.34
Mag	Mag083-12	3	0.05	3.57	0.09	0.02	85.95	0.81	2.50	0.04	n.a.	n.a.	0.00	93.57

Table 3.5: Major and minor element compositions (EMPA) (all in [wt%]) of mineral phases that were used to constrain fractional crystallization. These are representative compositions of each phase. Phenocrysts phases are the following Ol, olivine; Cpx, high-Ca clinopyroxene; Am, amphibole; Pl, plagioclase; Spl, spinel; Mag, magnetite. (n.a.: not analyzed)

Olivine

Olivine is present throughout the more primitive post-plutonic dyke rocks of the Southern Adamello and shows rather primitive compositions covering a very small range of Fo_{87}-Fo_{91}. Fresh olivine is rare. This phase is most typically identified by its idiomorphic shape and the near ubiquitous presence of brownish Cr-rich spinel inclusions. Typically only the core of olivine phenocrysts is preserved and analysed; potentially present core-rim zoning features, were therefore not accessible. Magnetite reaction rims are commonly associated with the transformation of pristine olivine to its pseudomorphs. These pseudomorphs exhibit different phase assemblages such as chlorite + epidote + calcite, chlorite + brucite + hematite, chlorite + tremolite + hematite, epidote + hematite + chlorite or talc + magnetite. Pseudomorphs with a preserved core (Fig. 3.11a) commonly reveal a "schlieren-like" distribution of secondary magnetite that is concentrated in distinct alteration zones.

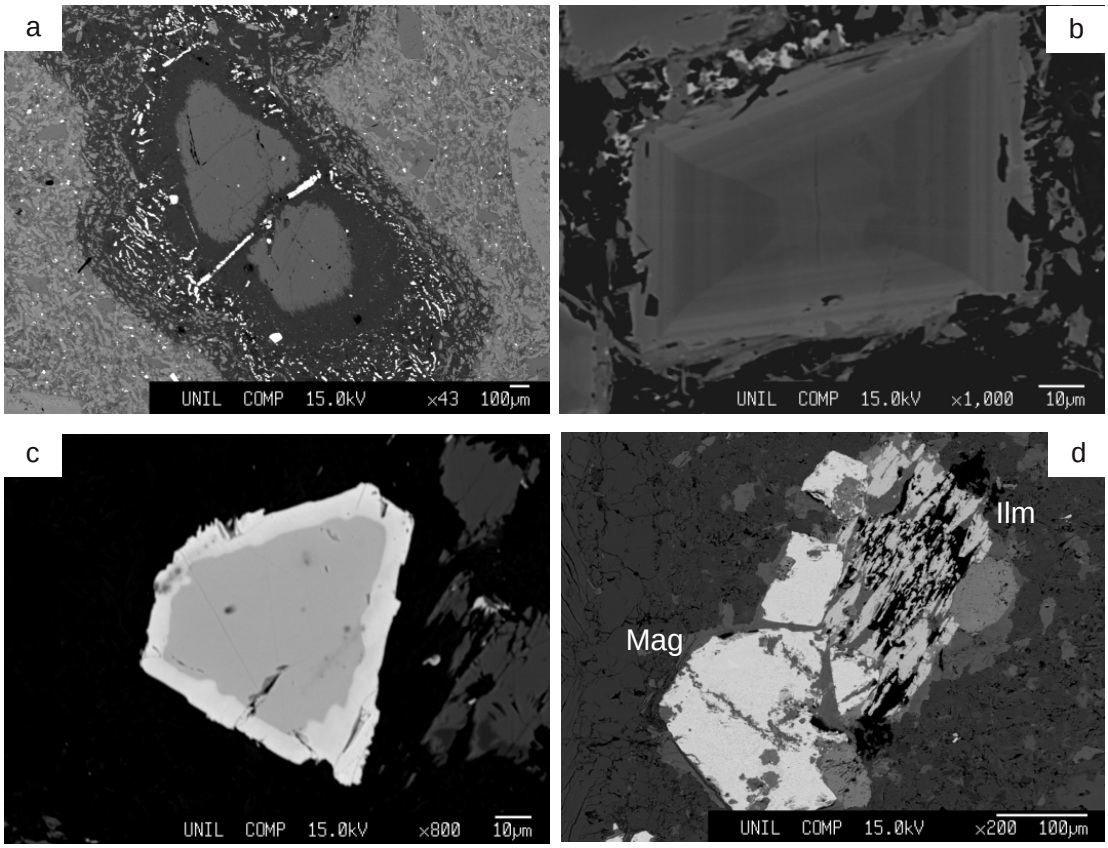

Figure 3.11: Backscattered electron (BSE) images of: *(a)* Olivine phenocryst in an olivine-tholeiite (1A) with Cr-rich spinel inclusions that has a preserved core whereas borders are pseuomorphs, consisting of talc, tremolite, hematite and magnetite; *(b)* Clinopyroxene microphenocryst within basalt (2A) that shows sector zoning throughout the grain; *(c)* spinel within olivine pseudomorph from a picrobasalt (1B) that exhibits a darker grey Cr-rich core and a brighter rim, representing magnetite that formed through diffusive exchange during cooling of the magma; *(d)* dacites (3) commonly contain distinct magnetite-ilmenite pairs, with ilmenite exhibiting some replacement to titanite.

Clinopyroxene

In primitive picrobasalts, Mg-tholeiites and olivine-tholeiites, clinopyroxene is widely replaced by greenish pseudomorphs composed of actinolitic hornblende, whereas in more evolved basalts clinopyroxene is commonly pristine. Some of the larger phenocryst cores show sieve textures and some clinopyroxene microphenocrysts display well-developed sector zoning, as indicated by the variations of AlIV and Cr as a function of Mg# in Figure 3.12a, b. Sector zoning is well preserved (Fig. 3.11b). Characteristic X-ray mapping and detailed electron microprobe analysis of experimentally grown enstatite showed that {010} sectors have the highest concentrations of Al, Cr and Ti [Schwandt and McKay, 2006]. The model of Schwandt and McKay [2006] interprets sector zoning of Al, Cr and Ti as a result of rapid crystal growth in their experiments. Rapid growth along the crystal's c-axis results in Si-depleted melt along the more slowly growing prism faces. This melt, in turn, is enriched in Al and other impurity elements that can act as charge compensating cations for Al incorporated in tetrahedral sites. The {100} sectors show less

Tschermak-type substitution enrichment relative to {010} sectors because tetrahedral and octahedral sites lie parallel to {100}. As a consequence, only tetrahedral or octahedral sites are alternately exposed for new growth at any instance. Within the {010} sectors, tetrahedral and octahedral sites are exposed simultaneously, which allows the substitution of tetrahedral and octahedral cations as charge-compensating couples, including elements such as Ti and Cr [Hollister and Hargarves, 1970, Hollister et al., 1971]. Observed clinopyroxene textures and zoning imply rather rapid phenocryst growth of crystals, potentially related to super-cooling of the magma. Overall, clinopyroxenes major element compositions vary from 0.48 to 0.35 for $Mg_2Si_2O_6$ (enstatite component) and from 0.43 to 0.32 for $Ca_2Si_2O_6$ (wollastonite component). The sum of all the pyroxene tschermaks components ($CaAl_2SiO_6$; $CaFe^{3+}AlSiO_6$; $CaCrAlSiO_6$; $CaTiAl_2O_6$) ranges from a maximum of 0.221 to a minimum of 0.044.

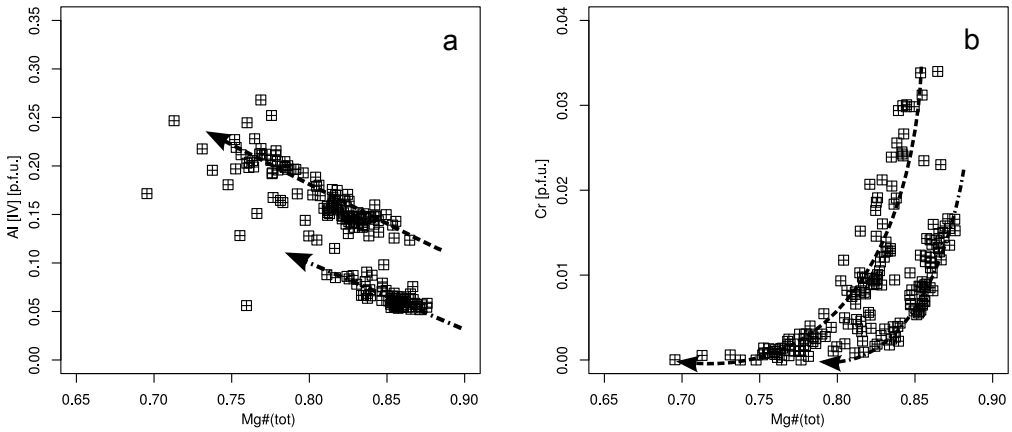

Figure 3.12: *(a)* and *(b)* Tetrahedral Al and Cr cations in clinopyroxene show two distinct variations against Mg#(tot) (Mg/Mg+Fe^{2+} +Fe^{3+} cations (apfu)). This co-variation of Cr and Al results from coupled substitution of ${}^{VI}Cr^{3+}$+ ${}^{IV}Al^{3+}$= ${}^{VI}Mg^{2+}$ + ${}^{IV}Si^{4+}$. The offset of trends is related to sector zoning in clinopyroxene, as illustrated in Fig. 3.11b.

The chondrite normalized [McDonough and Sun, 1995] rare earth element (REE) patterns (Fig. 3.13c) are homogeneous for clinopyroxenes occurring within basalts (2A). These REE patterns show a systematic (negative) Eu anomaly, indicating concomitant crystallization of plagioclase. This Eu anomaly however is not expressed in whole rock geochemistry of the basalts (2A). The lack of the Eu anomaly thus indicates that plagioclase crystallizes mainly during ascent of the basaltic magmas together with clinopyroxene. Light REE patterns are characteristically inclined with highest concentrations for Nd and Sm. Most variable trace-elements are Th, U, Nb, Ta and Pb (Fig. 3.13a) that are, with the exception of Pb, probably most affected by variable Tschermak´s components related to sector zoning and/or rapid crystallization.

Amphibole

Amphibole chemical formulae based on microprobe major and minor element wt. % oxide data were calculated to 13 cations per formula unit (apfu), with the cummingtonite component not taken into account [Hawthorne and Oberti, 2007, Hawthorne, 1983]. This method assumes that the $M(4)$-site only contains Ca and Na, remaining Na and K are allocated on the A-site. Euhedral and prismatic amphiboles are in general very homogeneous for basaltic-andesites and andesites (2A) and dacites (3) respectively, as evident from

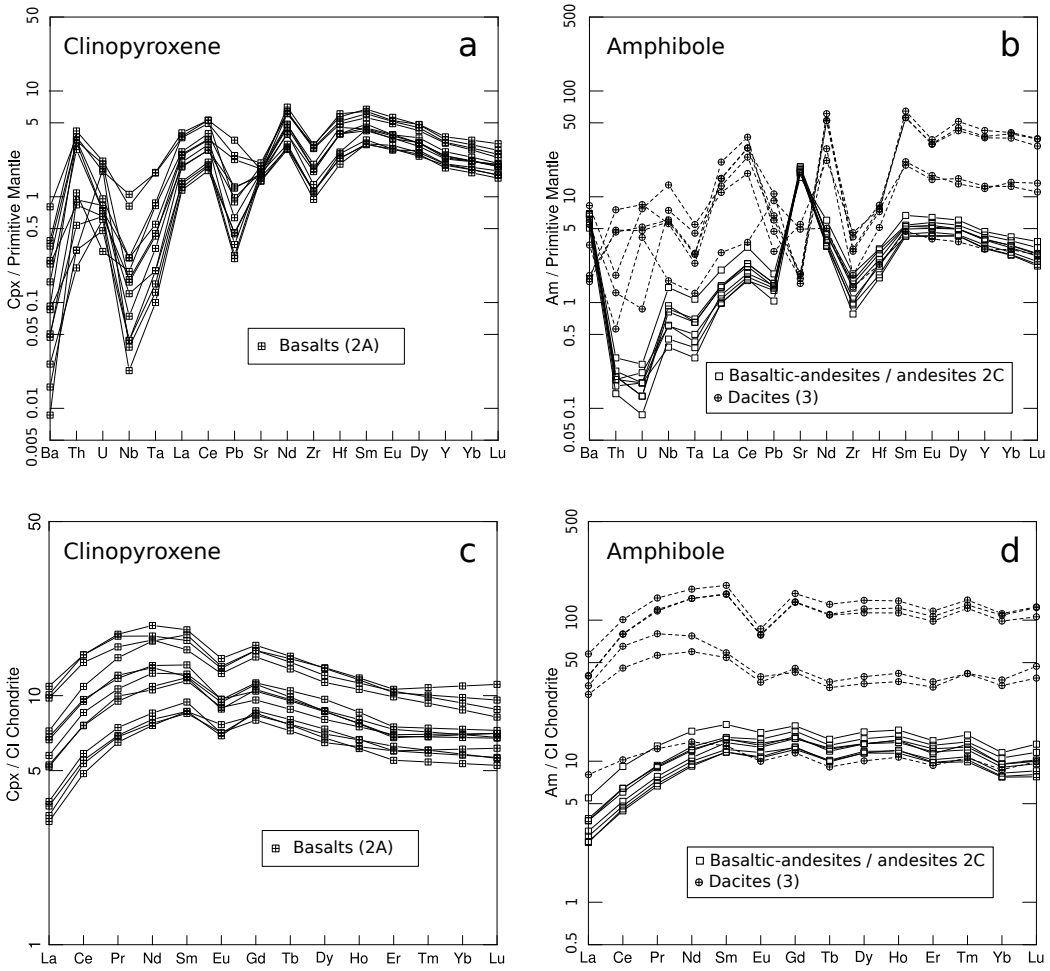

Figure 3.13: *(a)* and *(b)* present primitive mantle-normalized [McDonough and Sun, 1995] trace-element variation diagrams for *(a)* clinopyroxene from basalts (2A) and *(b)* amphiboles from basaltic-andesites/andesites (2C) and dacites (3). Figures *(c)* and *(d)* are chondrite-normalized Rare Earth element (REE) patterns for *(c)* clinopyroxene from basalts (2A) and *(d)* amphiboles from basaltic-andesites/andesites and dacites.

the compositional variation in Figure 3.14. Amphiboles from basaltic-andesites and andesites are pargasitic (Fig. 3.14a), whereas amphiboles from dacites stretch towards the compositional field of edenite [Leake et al., 1997]. In general, amphiboles exhibit very limited compositional zoning in major and minor elements and therefore form distinct groups for different bulk-rock compositions. High temperature pargasitic amphibole from basaltic-andesites and andesites have higher Mg#(tot) at rather constant but high Al^{IV} contents (Fig. 3.14b). Furthermore, these amphiboles cover some variation in Mg#(tot). Somewhat more edenitic amphiboles from dacites in contrast show some significant variation in Al^{IV} at rather constant Mg#(tot) (Fig. 3.14b). The variation between Al^{IV} and Na on the A-site ($Na(A)$) (Fig. 3.14c) reveals the effect of the combined Tschermak's and edenite substitutions that in the present case is actually about 1 : 1 edenite to Tschermak's substitution, resulting in a 0.5 slope in the diagram($NaAl^{VI}Al_2^{IV}{}_{O-1}OMg_{-1}Si_{-2}$) for Na versus Al^{IV}. Indication for high temperature formation of amphiboles within basaltic-andesites

and andesites is further provided by higher Ti content per formula unit (Fig. 3.14d), compared to edenitic amphiboles occurring in dacites. Amphiboles from basaltic-andesites and andesites have a K_2O range from 0.54 to 0.27 wt.%, whereas amphiboles from dacites show lower concentrations in the range of 0.28 to 0.09 wt.%.

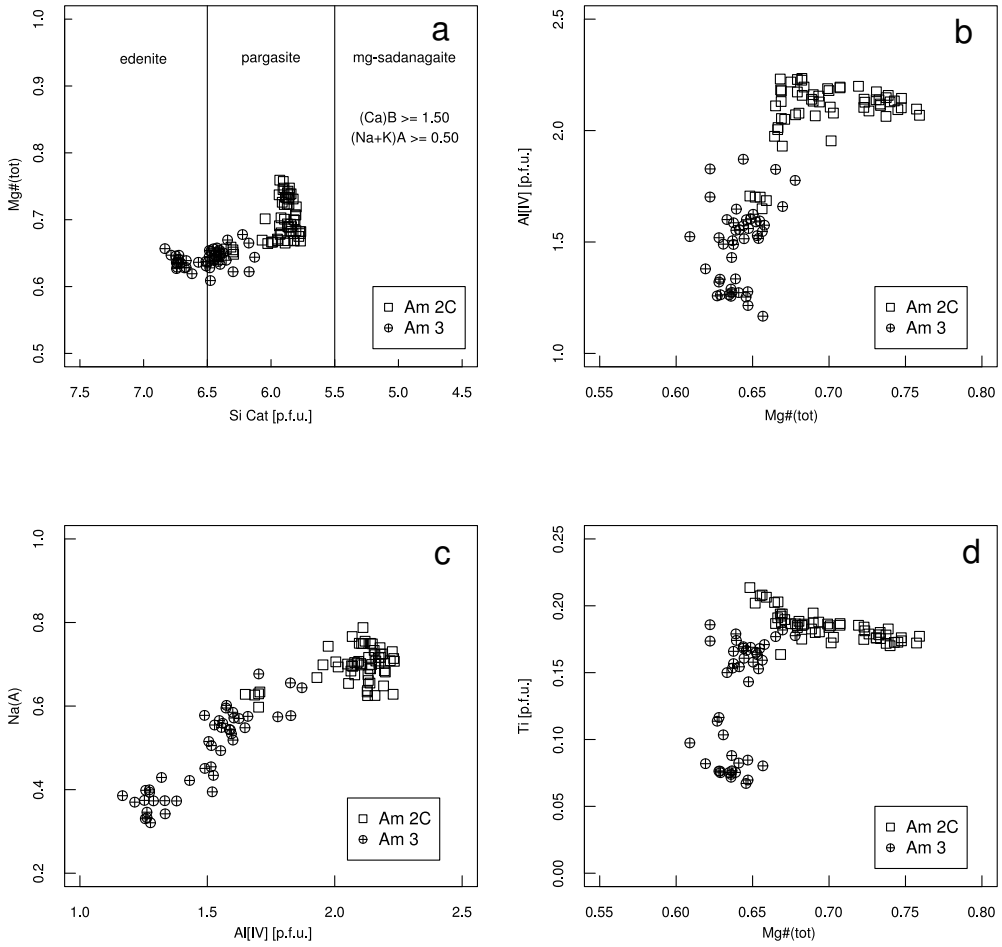

Figure 3.14: Amphibole geochemistry: *(a)* Amphibole classification for calcic amphiboles based on the parameters: CaB >1.50; (Na+K) A>0.50 after Leake et al. [1997]. *(a)* to *(d)* Cations per formula unit (apfu), calculated on the basis of 13 cations (Cations-Ca-Na-K=13) where $M(4)$ only contains Ca and Na and remaining Na and K goes on the A site. Assumes that all Na either occurs on the $M(4)$-site or on the A-site [Hawthorne and Oberti, 2007]. *(b)* and *(c)* Pargasitic amphiboles from more primitive basaltic-andesites and andesites (2C) reveal higher Al^{IV} (apfu) and Na(A) contents related to pargasite substitution ($NaAl^{VI}Al^{IV}_2{}_{O-1}Mg_{-1}Si_{-2}$), which is a composite of the edenite and the Tschermak exchange vectors. *(d)* Higher Ti (apfu) content of paragsitic amphiboles from basaltic-andesites and andesites indicate higher temperature conditions during crystallization of this mineral phase.

The amphiboles from basaltic-andesites and andesites (2C) show relatively low values for chondrite-normalized [McDonough and Sun, 1995] REE concentrations (Fig. 3.13d), with progressively lower values for light REE and a flat pattern towards heavy REE. These low REE concentrations indicate crystallization of amphiboles from a melt relatively depleted in REE and/or crystallization at higher temperature with lower partition coefficients for REE. Edenitic amphiboles from dacites (3) are more enriched in REE and exhibit an evolution towards increasing relative depletion of light REE pattern, with increasing REE con-

centrations and the development of a more pronounced negative Eu anomaly (Fig. 3.13d), consistent with the co-precipitation of plagioclase at this stage of magma differentiation. Such a crystallization relationship is further supported by decreasing Sr concentrations of amphiboles, with increasing REE concentration in dacites (Fig. 3.13b) from primitive mantle normalized trace element distribution [McDonough and Sun, 1995], compared to pargasitic amphiboles from basaltic-andesites and andesites. Decreasing Sr concentrations are the result of the compatible behaviour of Sr in plagioclase [Blundy and Wood, 1991], which leaves concomitant crystallizing amphibole with a relative depleted signature in Sr. However, whole rock data of dacites does not show an Eu anomaly, which shows that plagioclase is not a major cumulate phase in the differentiation process. In general, Th and U contents of edenitic amphiboles from dacites (3) (Fig. 3.13b) are more variable than in the pargasitic amphiboles from basaltic-andesites and andesites (2C) and are possibly related to additional accessory phases, in particular zircon and apatite.

Plagioclase

Cations per formula unit and endmember proportions of plagioclase were calculated based on 5 cations and 16 negative charges [Wood and Banno, 1973]. Plagioclase is present as micro-phenocrysts in basalts (2A), together with clinopyroxene that exhibits concomitant crystallization of the phases based on negative Eu-anomalies present in the latter (Fig. 3.13c). Anorthite (An) content of these micro-phenocryst plagioclases ranges from An_{98} to An_{46}. In basaltic-andesites/andesites (2C) (Fig. 3.3e) and dacites (3) (Fig. 3.3f), plagioclase becomes a dominant phase in the crystallizing solid assemblage. Zoning patterns in plagioclase from basaltic-andesites/andesites reveal rather constant compositions (Fig. 3.15a, b), with an abrupt change at the edge of each crystal in the range of tenths of a micrometer. In these rims, anorthite content changes from An_{95} in the core to An_{65} in the marginal zone. More albite-rich, thinner overgrowths over the anorthite-rich central part formed at a very late stage of mineral growth. Two different types of zoning patterns are present in plagioclase from dacites. Either single crystals are continuously zoned (Fig. 3.15d) or they show the same step-like zoning pattern as in the case of plagioclases from basaltic-andesites/andesites. Anorthite content in dacites ranges from An_{95} to An_{50}. In more detail, electron backscattered images further reveal oscillatory growth stages of crystals on a smaller scale, in the range of up to 5 units in the anorthite number. The large Sr and Ba ions are accommodated as trace elements in plagioclase; their partitioning with coexisting melt is pre-dominantly governed by relative lattice strain [Blundy and Wood, 1991]. Sr ranges from a maximum of 1629ppm to a minimum of 865ppm (Fig. 3.15) along zoning profiles in basaltic-andesites/andesites. For dacites, concentrations of Sr in plagioclase are lower and range from 1364ppm down to 612ppm. In fact, the trace element signal of Sr and Ba along a measurement profile of a plagioclase represents an integrated value due to limiting laser-spot size between 25 to 50μm which contrasts with the detailed growths zones revealed by microprobe analysis in the range of a few micrometers. Zoning of Ba and Sr is generally correlated with decreasing anorthite content as predicted by Blundy and Wood [1991]. Therefore, highest concentrations of Ba and Sr are obtained in the albite-rich overgrowths of individual plagioclase crystals. In basaltic andesites/andesites and dacites, plagioclase partly exhibit sieve textures that are related to resorption processes and potential interaction with surrounding melt during growth due to convection in a magma chamber [Couch et al., 2001], or they are due to rapid decompression during ascent [Blundy et al., 2006]. Amphiboles from dacites have lower

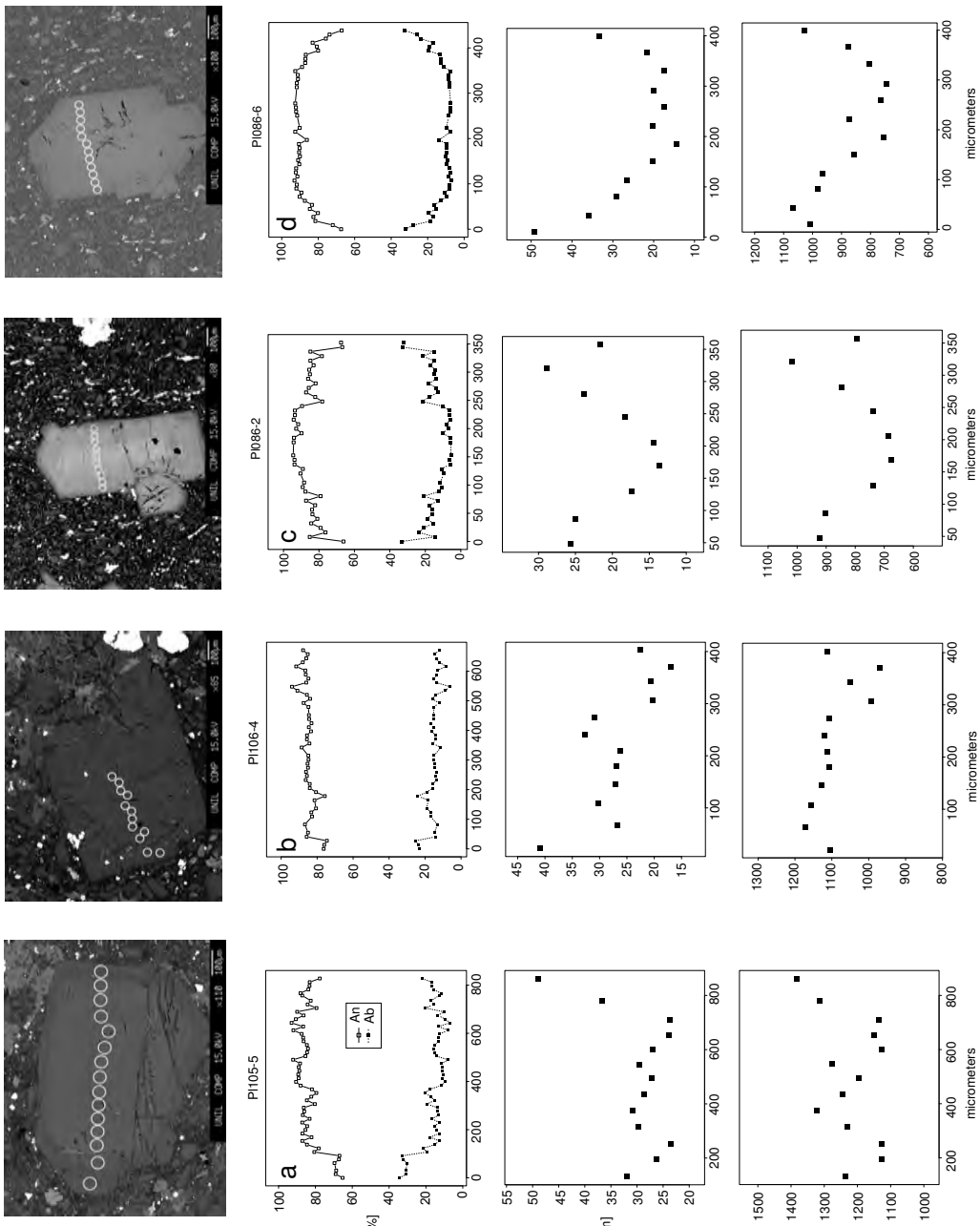

Figure 3.15: BSE images and detailed compositional profiles of anorthite and albite contents [%], Ba and Sr [ppm] concentrations of plagioclases from basaltic-andesites/andesites *(a)* and *(b)* ; the backscattered electron images show the laser-ablation pit location and size for the profiles; *(a)* Laser-spot diameter is $35\mu m$ for Pl105-5; for Pl106-4 *(b)*, Pl086-2 *(c)* and Pl086-6 *(d)* laser-spot size is $25\mu m$. Due to its size, laser-ablation-ICP-MS analysis along the profiles integrates the actual trace-element signal of partially very thin growth zones revealed by microprobe analysis. Compositional profiles Pl086-2 *(c)* and Pl086-6 *(d)* are from plagioclases from dacites (3).

concentrations of Sr and Ba (Fig. 3.16) than amphiboles from basaltic-andesites/andesites. In contrast, plagioclases from basaltic-andesites/andesites are somewhat more enriched in Sr than plagioclases from dacites.

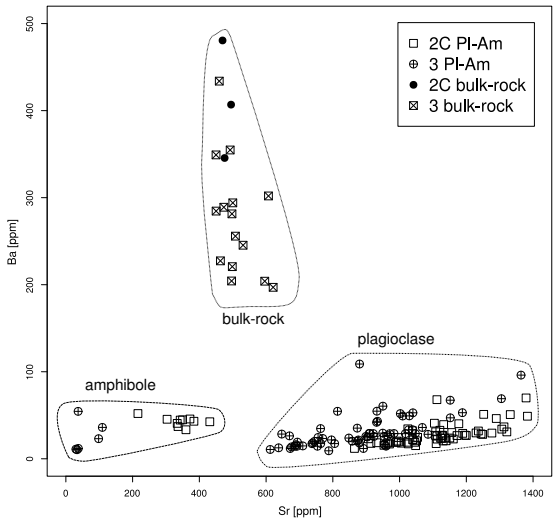

Figure 3.16: Bulk-rock, amphibole and plagioclase Ba versus Sr [ppm] variation diagram. Bulk-rock Ba scatters in the range 197 to 480ppm and Sr covers the range 450 to 621ppm. Amphiboles from dacites (3) are less enriched in Sr than amphiboles from basaltic-andesites/andesites (2C). Plagioclases from basaltic-andesites/andesites (2C) are on average more enriched in Sr than plagioclases from dacites (3). Ba and Sr concentration in plagioclases shows an overall positive correlation.

Spinel and Fe-Ti Oxides

Spinel chemical formulas were calculated based on 3 cations and 8 negative charges. The ratio of ferrous to ferric iron (Fe^{2+}/Fe^{3+}) was calculated based on the method from Lindsley and Andersen [1983]. Oxides of the spinel group are present throughout all different rock types present in this dyke suite. Within primitive picro-basaltic to olivine-tholeiitic compositions, pristine spinels are generally Cr-rich that are found as idiomorphic, brownish inclusions within olivine and clinopyroxene, or they are pseudomorphs. Spinel inclusions in olivine are affected by later alteration to magnetite-rich spinel, as shown in a backscattered electron image (Fig. 3.11c): the brighter rim corresponds to a magnetite-rich composition whereas the darker grey core corresponds to Cr-rich spinel. The compositional change between these zones is further expressed by strongly decreasing MgO contents from core to rim that is, at least partly, attributed to the relatively rapid diffusive Fe^{2+}-Mg^{2+} exchange [Liermann and Ganguly, 2002, Ozawa, 1983, 1984] of these spinel inclusions with olivine, which is the surrounding host phase. Spinel from picro-basalts (1A) and olivine-tholeiites (1A, 1B) are classified as magnesio-chromites (Fig. 3.17a), whereas spinels from basalts (2A) are classified either as chromites or hercynites. Spinels from basalts occur as inclusions within clinopyroxene and are in general richer in Al_2O_3 (Fig. 3.17b) than spinels from picro-basalts (1B) and olivine-tholeiites (1A,1B). TiO_2 has a similar range for spinels from picro-basalt/olivine-tholeiites (1A, 1B) and basalts (2A). Spinels within clinopyroxenes in basalts (2A) exhibit higher NiO concentrations (Fig. 3.17c) than spinel inclusions in olivines from picro-basalts and olivine-tholeiites (1A, 1B). Ni is very

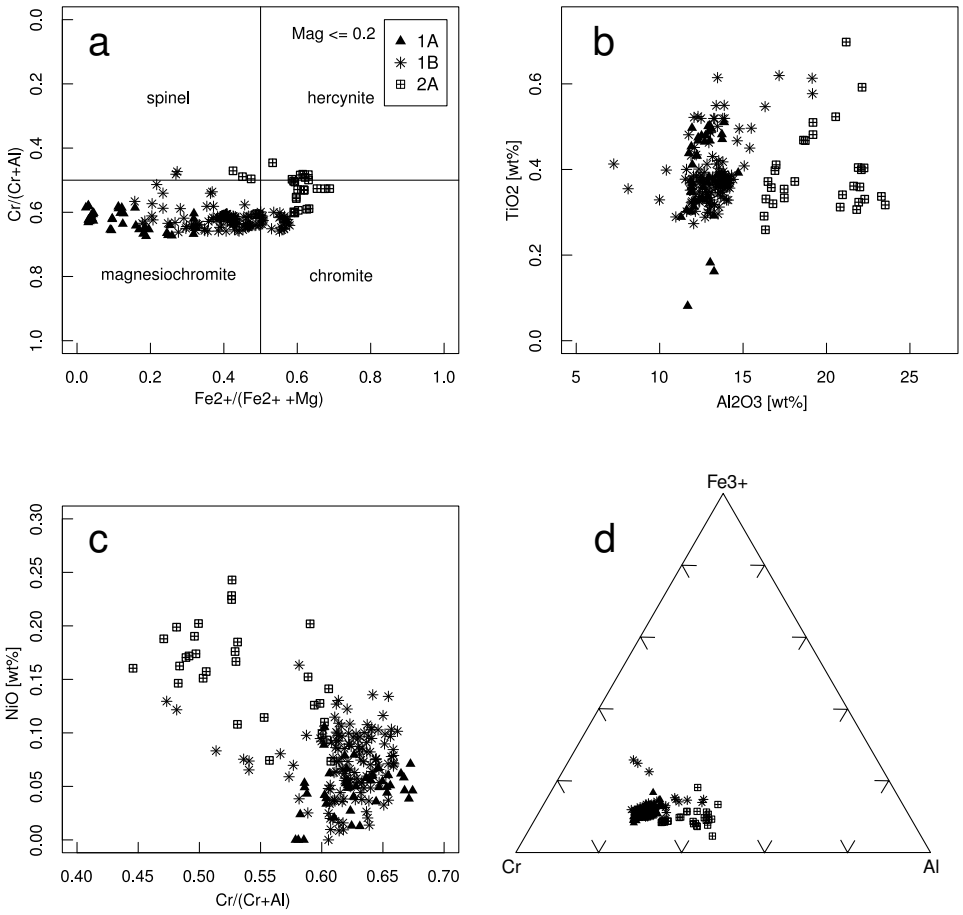

Figure 3.17: Compositions of Cr-rich spinels. Spinels with magnetite (Fe_3O_4) component >0.2 are excluded because they represent non-primary, re-equlibrated oxide phases in primitive dyke rocks. (a) Classification of spinel based on Cr/(Cr+Al) and Fe2+/(Fe^{2+}+Mg), all (apfu), for the different endmembers: chromite ($FeCr_2O_4$), magnesiochromite ($MgCr_2O_4$), hercynite ($FeAl_2O_4$) and spinel ($MgAl_2O_4$) [Dana et al., 1944, MacGregor and Smith, 1963]. (b) Spinels from basalts (2A) have higher Al_2O_3 concentrations than spinels from dyke generations (1A and B) and are commonly included in clinopyroxene. (c) Spinel inclusions in olivine from picro-basalts and olivine-tholeiites (1A, 1B) contain less NiO than spinel inclusions in clinopyroxenes from basalts (2A). (d) Ternary diagram displaying the compositional space for Cr^{3+}, Al^{3+} and Fe^{3+} (apfu) for primitive Cr-rich spinels.

compatible in olivine [Kinzler et al., 1990], thus co-crystallizing spinel will typically be depleted in NiO. Spinels within basalts (2A) show lower Cr concnetration (apfu) that is counterbalanced by increasing Al (apfu) (Fig. 3.17d). Oxide phases in basaltic-andesites/andesites (2C) are magnetite. Euhedral magnetite occurs throughout the matrix of these rocks as well as inclusions in amphibole. Ilmenite-magnetite pairs (Fig. 3.11d) occur only in differentiated dacites (3). Ilmenite commonly shows alteration to titanite. Zircon and apatite are primary phases associated with magnetite-ilmenite pairs. Ilmenite is TiO_2 rich Fe-Ti-oxide thermo-oxy-barometry results too low temperatures below 700°C, which indicates reequilibration during cooling. The determination of fO_2 conditions with such low temperatures has a large uncertainty on the determined oxygen fugacity (fO_2) and is not considered reliable.

Sample	Am105-1	Am105-2	Am105-3	Am105-4	Am106-1	Am106-7	Am106-2	Am106-6	Am106-3	Am106-5
Rock Type	**Basaltic-andesite**	**Basaltic-andesite**	**Basaltic-andesite**	**Basaltic-andesite**	**Basaltic-andesite**	**Basaltic-andesite**	**Basaltic-andesite**	**Basaltic-andesite**	**Basaltic-andesite**	**Basaltic-andesite**
Generation	**2C**	**2C**	**2C**	**2C**	**2C**	**2C**	**2C**	**2C**	**2C**	**2C**
Sc	80.3	166.3	95.1	120.0	167.7	141.8	176.6	145.1	208.8	161.6
V	467	703	576	674	773	746	742	815	719	790
Ni	4.4	33.6	10.1	16.4	35.1	26.6	61.1	27.3	112.4	41.7
Zn	81.7	29.5	53.2	37.4	40.8	45.2	38.4	49.5	35.5	46.6
Sr	216	360	303	334	384	343	350	431	336	372
Y	33.2	13.9	20.2	15.1	16.9	18.7	16.7	28.5	14.1	17.1
Zr	35	10	20	10	16	17	11	18	8	14
Nb	2.8	0.3	0.9	0.4	0.5	0.6	0.4	0.6	0.3	0.6
Ba	52	33	45	41	43	44	45	43	37	46
La	4.0	0.6	1.3	0.7	0.9	0.9	0.8	8.1	0.6	0.9
Ce	14.5	2.8	5.6	2.9	3.7	3.9	3.2	17.4	2.7	3.9
Pr	2.66	0.62	1.15	0.66	0.81	0.84	0.70	2.45	0.60	0.83
Nd	15.9	4.4	7.5	4.6	5.5	5.8	4.9	12.5	4.2	5.6
Sm	5.02	1.74	2.73	1.82	2.15	2.21	2.03	3.65	1.74	2.14
Eu	1.56	0.63	0.96	0.69	0.78	0.86	0.75	1.36	0.64	0.80
Gd	5.77	2.42	3.56	2.49	2.99	3.27	2.90	4.56	2.53	2.91
Tb	0.946	0.402	0.572	0.406	0.471	0.519	0.486	0.704	0.396	0.495
Dy	6.61	2.86	4.03	2.94	3.31	3.61	3.32	4.93	2.86	3.33
Ho	1.352	0.569	0.831	0.591	0.706	0.756	0.678	1.077	0.599	0.701
Er	3.73	1.56	2.24	1.64	1.96	2.08	1.86	2.93	1.57	1.81
Tm	0.501	0.198	0.307	0.215	0.252	0.274	0.241	0.431	0.205	0.263
Yb	3.26	1.23	1.84	1.32	1.53	1.69	1.45	2.68	1.25	1.52
Lu	0.453	0.155	0.264	0.171	0.204	0.231	0.192	0.374	0.161	0.200
Hf	1.61	0.66	0.90	0.51	0.81	0.88	0.62	0.80	0.48	0.72
Ta	0.12	0.02	0.04	0.02	0.03	0.03	0.02	0.03	0.01	0.03
Pb	1.36	0.16	0.28	0.21	0.21	0.23	0.22	11.55	0.20	0.23
Th	0.06	0.01	0.02	0.02	0.02	0.02	0.02	0.74	0.01	0.02
U	0.24	0.00	0.01	0.01	0.00	0.00	0.00	2.95	0.00	0.00

Table 3.6: Trace element compositions (all in [ppm]) of amphiboles (hornblende) obtained by LA-ICP-MS analysis. Trace element analyses of amphibole phenocrysts from basaltic-andesites (2C) and dacites (3). Internal standard for data reduction in LAMTRACE is CaO (wt.%) determined by electron microprobe. External standard is NIST SRM 612.

Sample	Am083-5	Am083-6	Am083-8	Am083-9	Am086-2	Am086-5
Rock Type	**dacite**	**dacite**	**dacite**	**dacite**	**dacite**	**dacite**
Generation	**3**	**3**	**3**	**3**	**3**	**3**
Sc	99.3	116.9	119.2	126.7	81.1	47.9
V	525	329	327	298	354	265
Ni	54.0	8.2	12.6	8.6	4.6	7.4
Zn	227.3	321.0	406.7	281.7	149.3	39.2
Sr	37	30	37	33	109	98
Y	51.4	155.1	159.8	182.2	54.1	13.7
Zr	19	34	44	32	48	15
Nb	8.5	3.7	4.0	3.8	4.9	1.1
Ba	54	11	12	10	36	23
La	8.2	9.7	9.6	13.8	7.1	1.9
Ce	39.8	48.7	48.4	61.5	27.9	6.2
Pr	7.21	10.68	10.45	12.92	5.07	1.10
Nd	35.6	65.5	65.6	76.3	27.5	6.3
Sm	8.80	23.06	22.82	26.46	8.15	1.93
Eu	2.39	4.70	4.75	5.21	2.18	0.60
Gd	8.53	26.72	26.98	30.87	9.11	2.29
Tb	1.330	4.344	4.397	5.183	1.460	0.364
Dy	8.86	28.16	30.03	34.57	9.95	2.51
Ho	1.833	5.624	6.089	6.846	2.099	0.534
Er	5.36	15.72	17.01	18.55	5.85	1.49
Tm	0.839	2.426	2.561	2.778	0.834	0.211
Yb	6.03	15.77	17.34	17.82	5.50	1.39
Lu	0.941	2.113	2.453	2.485	0.777	0.198
Hf	1.43	2.17	2.33	2.02	2.13	0.64
Ta	0.22	0.09	0.12	0.11	0.18	0.05
Pb	0.90	1.60	0.99	0.71	0.46	1.38
Th	0.15	0.60	0.37	0.39	0.10	0.05
U	0.18	0.19	0.12	0.11	0.02	0.10

Table 3.7: Trace element compositions (all in [ppm]) of amphiboles (hornblende) obtained by LA-ICP-MS analysis. Trace element analyses of amphibole phenocrysts from basaltic-andesites (2C) and dacites (3). Internal standard for data reduction in LAMTRACE is CaO (wt.%) determined by electron microprobe. External standard is NIST SRM 612.

Sample	Px053-5	Px053-6	Px053-7	Px053-8	Px051-3	Px051-4	Px051-5	Px051-6	Px051-7	Px051-8	Px051-9	Px051-11	Px051-12	Px051-13
Rock Type	basalt	basalt	basalt	basalt	basalt	basalt	basalt	basalt	basalt	basalt	basalt	basalt	basalt	basalt
Generation	2A	2A	2A	2A	2A	2A	2A	2A	2A	2A	2A	2A	2A	2A
Sc	139.1	146.2	118.8	134.0	129.5	139.5	137.9	162.0	133.8	130.5	138.8	123.6	131.6	131.6
V	284	283	216	182	308	308	287	318	227	323	246	295	173	198
Ni	162.8	131.4	185.2	165.3	133.1	133.6	139.7	125.3	148.5	123.8	125.8	139.1	153.4	150.0
Zn	44.2	20.8	19.6	22.5	40.7	26.2	42.3	25.3	22.9	29.6	18.3	21.0	20.1	20.6
Sr	34	34	33	31	75	39	42	33	31	36	34	36	28	28
Y	10.0	10.5	8.0	8.5	13.0	14.1	13.8	15.8	10.4	14.9	9.8	11.5	8.8	8.7
Zr	21	19	12	12	36	31	30	32	14	33	18	19	10	12
Nb	0.1	0.0	0.0	0.0	1.1	0.5	0.7	0.1	0.1	0.2	0.1	0.2	0.0	0.0
Ba	1.65	0.06	0.33	0.57	32.36	2.54	5.30	0.31	1.04	0.61	1.53	2.26	0.17	0.11
La	1.6	1.4	0.9	0.8	3.9	2.6	2.3	1.7	1.3	2.4	1.2	1.6	0.8	0.9
Ce	5.8	5.2	3.6	3.3	11.0	8.9	8.3	6.6	4.6	8.9	4.6	5.9	3.0	3.4
Pr	1.09	0.96	0.67	0.62	1.64	1.56	1.41	1.28	0.86	1.59	0.90	1.06	0.59	0.62
Nd	6.0	5.7	3.9	3.6	8.3	8.0	7.7	7.6	5.0	8.8	4.9	6.1	3.5	3.7
Sm	1.79	1.83	1.41	1.27	2.37	2.50	2.29	2.63	1.77	2.76	1.72	1.99	1.30	1.30
Eu	0.56	0.58	0.42	0.43	0.64	0.77	0.74	0.79	0.53	0.85	0.54	0.58	0.41	0.46
Gd	2.22	2.09	1.70	1.59	2.62	3.04	2.86	3.04	2.11	3.19	1.92	2.25	1.74	1.67
Tb	0.333	0.338	0.257	0.282	0.404	0.424	0.434	0.509	0.332	0.481	0.307	0.337	0.268	0.265
Dy	2.16	2.16	1.69	1.62	2.63	3.01	2.83	3.24	2.18	3.22	2.01	2.42	1.84	1.75
Ho	0.458	0.451	0.319	0.348	0.548	0.572	0.567	0.647	0.445	0.633	0.405	0.453	0.378	0.371
Er	1.09	1.10	0.88	0.96	1.46	1.67	1.58	1.70	1.17	1.65	1.12	1.20	0.96	1.00
Tm	0.137	0.153	0.116	0.132	0.212	0.211	0.200	0.252	0.153	0.221	0.149	0.173	0.135	0.139
Yb	1.00	0.93	0.81	0.77	1.35	1.26	1.42	1.48	0.91	1.52	0.93	1.07	0.79	0.79
Lu	0.141	0.135	0.105	0.113	0.199	0.176	0.164	0.222	0.136	0.192	0.141	0.145	0.123	0.112
Hf	1.27	1.10	0.72	0.65	1.47	1.45	1.37	1.71	0.74	1.60	1.10	1.10	0.57	0.64
Ta	0.02	0.01	0.01	0.01	0.09	0.07	0.07	0.03	0.01	0.04	0.02	0.02	0.00	0.01
Pb	0.10	0.05	0.04	0.04	1.22	0.13	0.37	0.18	0.19	0.51	0.15	0.34	0.07	0.07
Th	0.27	0.08	0.04	0.03	0.88	0.34	0.30	0.09	0.22	0.28	0.07	0.26	0.02	0.03
U	0.05	0.02	0.02	0.04	0.11	0.05	0.04	0.01	0.02	0.02	0.02	0.02	0.01	0.01

Table 3.8: Trace element analyses (all in [ppm]) of clinopyroxenes in basalts (2A) obtained by LA-ICP-MS. Trace element analyses of clinopyroxene phenocrysts from basalts (2A). Internal standard for data reduction in LAMTRACE is CaO (wt.%) determined by electron microprobe. External standard is NIST SRM 612.

Sample	Pl105-5	Pl105-5	Pl105-5	Pl105-5	Pl105-5	Pl105-5	Pl105-5	Pl105-5	Pl105-5	Pl105-5	Pl105-5	Pl105-5	Pl105-5
Rock Type	basaltic-andesite	basaltic-andesite	basaltic-andesite	basaltic-andesite	basaltic-andesite	basaltic-andesite	basaltic-andesite	basaltic-andesite	basaltic-andesite	basaltic-andesite	basaltic-andesite	basaltic-andesite	basaltic-andesite
Generation	2C	2C	2C	2C	2C	2C	2C	2C	2C	2C	2C	2C	2C
Rb	<0.047	0.1	0.1	<0.047	<0.052	<0.053	<0.038	<0.050	0.2	0.1	0.1	<0.045	1.1
Sr	1236	1128	1126	1229	1321	1244	1196	1277	1128	1151	1136	1313	1383
Y	0.2	0.1	0.1	0.2	0.1	0.2	0.2	0.1	0.1	0.1	0.1	0.2	0.3
Zr	0.14	0.17	0.07	0.11	0.03	<0.028	0.12	0.10	0.31	0.05	0.09	0.03	0.37
Nb	0.023	0.015	<0.011	<0.012	<0.010	<0.011	<0.010	0.012	<0.009	<0.009	<0.008	<0.007	0.016
Ba	32	26	23	30	31	29	27	30	27	24	24	37	49
La	2.0	1.6	1.4	1.9	2.0	1.9	2.1	2.1	1.6	1.6	1.7	2.3	2.6
Ce	2.9	2.3	2.2	2.8	2.9	2.9	2.9	3.0	2.3	2.4	2.6	3.5	3.9
Pr	0.25	0.21	0.19	0.24	0.26	0.27	0.27	0.28	0.22	0.23	0.23	0.33	0.35
Nd	1.0	0.9	0.7	0.9	0.9	1.0	0.9	1.0	0.8	0.8	0.9	1.0	1.2
Sm	0.09	0.09	0.08	0.12	0.13	0.15	0.11	0.13	0.12	0.12	0.12	0.13	0.16
Eu	0.36	0.31	0.26	0.29	0.34	0.33	0.31	0.35	0.28	0.28	0.31	0.35	0.42
Gd	0.10	0.09	0.06	0.06	0.05	0.06	0.07	0.09	0.04	0.09	0.06	0.09	0.16
Tb	0.010	0.004	0.006	0.008	0.008	0.006	0.008	0.011	0.009	0.007	0.009	0.008	0.009
Dy	0.03	0.03	0.03	0.04	0.02	0.06	0.04	0.04	0.03	0.05	0.03	0.03	0.11
Ho	0.008	0.007	0.006	<0.010	0.006	0.009	0.008	0.006	0.007	0.007	0.005	0.012	0.020
Er	0.01	0.02	0.01	0.01	0.02	0.01	0.02	0.01	0.01	0.01	0.01	0.02	0.05
Tm	<0.002	<0.002	0.003	<0.002	<0.002	0.002	<0.001	<0.002	0.001	0.002	0.002	<0.001	0.007
Yb	0.02	<0.010	0.01	0.01	<0.009	0.01	0.01	<0.008	0.01	<0.010	0.01	0.01	0.07
Lu	<0.002	<0.002	<0.002	0.003	<0.002	<0.002	<0.002	0.002	<0.002	<0.002	0.002	<0.002	0.014
Pb	0.81	0.68	0.65	0.84	0.84	0.80	0.76	1.63	0.63	0.72	0.75	0.97	1.30
Th	0.03	0.04	0.01	0.01	<0.005	<0.004	0.01	0.02	0.04	0.01	0.01	0.01	0.11
U	0.02	0.04	0.01	0.01	<0.002	0.00	<0.001	0.01	0.05	0.01	0.00	0.00	0.20

Table 3.9: Representative data: trace element (all in [ppm]) profile for a plagioclase phenocryst from basaltic-andesite (2C). Internal standard for data reduction in LAMTRACE is CaO wt% determined by electron microprobe. External standard is NIST SRM 612.

Sample	**Pl086-1**	**Pl086-1**	**Pl086-1**	**Pl086-1**	**Pl086-1**	**Pl086-1**	**Pl086-1**	**Pl086-1**	**Pl086-2**	**Pl086-2**	**Pl086-2**	**Pl086-2**	**Pl086-2**
Rock Type	**dacite**	**dacite**	**dacite**	**dacite**	**dacite**	**dacite**	**dacite**	**dacite**	**dacite**	**dacite**	**dacite**	**dacite**	**dacite**
Generation	**3**	**3**	**3**	**3**	**3**	**3**	**3**	**3**	**3**	**3**	**3**	**3**	**3**
Rb	0.5	<0.352	<0.263	<0.333	0.3	<0.367	<0.291	<0.352	<0.297	<0.246	<0.287	<0.242	<0.299
Sr	1039	899	931	1305	873	909	950	921	923	903	738	676	686
Y	0.3	0.1	0.1	0.2	0.2	0.2	0.1	0.1	0.1	0.1	0.1	0.1	0.1
Zr	1.09	<0.371	<0.305	<0.343	<0.349	0.38	<0.337	<0.282	<0.350	<0.289	<0.275	<0.244	<0.333
Nb	<0.054	<0.033	0.034	<0.049	0.054	<0.048	0.048	0.040	<0.034	<0.032	<0.040	<0.029	<0.038
Ba	33	26	42	69	35	29	29	29	26	25	17	14	14
La	4.0	2.8	2.9	3.9	2.8	2.9	3.6	3.5	3.5	2.8	1.2	1.0	1.2
Ce	5.2	3.7	3.6	5.2	3.7	3.8	4.6	4.9	4.4	3.9	1.7	1.5	1.8
Pr	0.60	0.29	0.31	0.45	0.42	0.30	0.40	0.34	0.39	0.39	0.14	0.13	0.15
Nd	1.6	1.2	1.0	1.6	1.0	0.9	1.8	1.3	1.6	1.1	0.7	0.7	0.5
Sm	0.05	0.12	0.18	0.39	0.17	0.15	0.18	0.18	0.20	0.12	<0.025	0.10	0.08
Eu	0.45	0.38	0.39	0.55	0.43	0.35	0.39	0.40	0.37	0.38	0.28	0.20	0.30
Gd	<0.228	0.08	<0.127	<0.259	<0.052	<0.151	<0.112	<0.217	0.12	0.12	<0.093	0.11	<0.114
Tb	<0.005	<0.004	<0.018	<0.024	<0.014	<0.009	0.016	<0.020	0.010	<0.007	<0.017	<0.008	0.011
Dy	<0.064	0.12	<0.058	<0.111	0.04	0.04	<0.096	<0.068	0.07	<0.080	0.04	0.10	<0.063
Ho	0.015	0.003	0.019	0.017	0.016	<0.080	0.019	0.000	<0.019	<0.009	<0.019	<0.017	0.022
Er	<0.098	0.01	0.02	0.07	<0.069	0.02	<0.028	0.02	<0.013	0.02	<0.019	0.01	0.02
Tm	<0.020	0.000	<0.010	<0.014	<0.013	<0.007	<0.011	<0.011	<0.006	<0.009	<0.010	0.007	<0.007
Yb	0.06	0.01	0.00	<0.029	0.04	<0.023	<0.019	<0.040	<0.037	<0.013	<0.079	<0.035	0.02
Lu	<0.014	<0.008	<0.013	<0.006	<0.007	<0.009	<0.011	<0.005	<0.006	<0.013	<0.005	0.012	<0.009
Pb	1.85	1.24	1.09	1.54	1.22	1.25	1.53	1.75	1.39	1.22	0.68	0.59	0.66
Th	0.11	0.00	0.01	<0.009	0.05	0.03	<0.008	0.02	<0.010	<0.004	0.01	0.00	0.01
U	0.03	<0.005	0.01	0.01	0.01	0.01	<0.016	0.01	0.00	0.00	0.00	<0.004	0.00

Table 3.10: Representative data: trace element (all in [ppm]) profiles for plagioclase phenocrysts from dacites (3). Internal standard for data reduction in LAMTRACE is CaO wt% determined by electron microprobe. External standard is NIST SRM 612.

3.8 Discussion

Magmatic Differentiation History

The different rock types presented here present homogeneous magmatic textures and phenocryst assemblages. The phenocryst textures of plagioclase and amphibole reveal no clear features indicative for extensive magma mingling or mixing. The large compositional range covered by the various rock types investigated bears general bulk-rock chemical and mineral chemical characteristics that are consistent with a general island-arc-tholeiitic type magma evolution (Fig. 3.5a). Because magmas in an island-arc setting have been inferred to be important contributors in the formation of continental crust [Kay and Kay, 1985, Kelemen, 1995], such a wide compositional rock suite allows testing of the fractional crystallization model. Such a model comprises all major crystallizing mineral phases and ultimately leads to the formation of most differentiated end-members; in the present case, these are dacites (3). Despite the fact that the various subgroups of the investigated rock suite cannot be linked directly to genesis from a single parental magma based on relative age relations and isotope geochemistry, it is evident from field relations, textures and geochemistry that they form a closely linked series of magmas on a regional scale that reflect the evolution from similar if not identical primary magmas. The evolution to either an island-arc tholeiitic series or to a calc-alkaline series is based on a relative iron enrichment for the former and iron depletion for the latter [Kushiro, 1972, Zimmer et al., 2010]. Arc magmas are inferred to be more oxidized than average arc mantle [Lee et al., 2012]. However, where and how arc magmas acquire this signature is a highly debated issue. One view is that the oxidized state of arc magmas is inherited during melting of the sub-arc mantle, previously metasomatized by subducted fluids and/or melts originating from deeply subducted sediments and/or basaltic oceanic crust [Arculus, 1985, Carmichael, 1991, Kelley and Cottrell, 2009, Lee et al., 2012, Mungall, 2002]. An alternative view of the evolution from less iron-rich to iron-richer magmas is provided through magmatic differentiation associated with crystallization and chemical interaction with preexisting crust [Dauphas et al., 2009, Jenner et al., 2010, Lee et al., November 2005, 2010]. Mass balance calculations and associated trace-element partitioning between minerals and melt through crystallization may provide further insight into magmatic differentiation and potential FeO(tot) enrichment or depletion relative to MgO. Fractionation-driven differentiation is necessarily associated with the formation of cumulates resulting from the separation of crystallizing phases. Recently, major and trace element models have been presented that integrate actual cumulate compositions found in the lower crustal arc sections, such as in the case of the Kohistan arc (1 - 1.5GPa) [Jagoutz, 2010] and the Chelan Complex (Cascades, Washington) (~ 1.0GPa) [Dessimoz et al., 2012], to produce upper crustal granitoids by hydrous fractional crystallization of primitive mantle-derived melts. A straightforward fractional crystallization mass-balance model is presented here to trace the evolution from primitive mantle-derived picro-basalts (1B) to the most evolved dacites (3) that bear a primitive radiogenic isotopic signature (Sr, Nd). The proposed model does, of course, not account for the actual magma dynamics that are potentially marked by several magmatic recharge episodes at the base of crust or within the lowermost crust. Nevertheless, such a model allows quantitative assessment of phase proportions to be fractionated to generate evolved magma compositions such as dacites, which are equivalent to tonalites and granodiorites building the bulk part of the upper-crustal Adamello Batholith.

Hydrous Fractional Crystallization and the Role of Oxide Phases

A striking feature of the compositional suite represented by the dyke rocks is the Al_2O_3 enrichment with decreasing MgO contents down to ~ 5 wt% (Fig. 3.5d). The transition to andesites (2C) and dacites (3) is marked by the change to decreasing Al_2O_3. Furthermore amphiboles from basaltic-andesites and andesites reveal rather primitive trace element signatures (Fig. 3.13b, d), identifying them as important cumulus phases, crystallizing from primitive magmas not yet enriched in incompatible trace elements. This relationship is, for example, underlined by low Rb, Ba and Ce contents (Fig. 3.6b, c and e) for basaltic-andesites/andesites (2C) and dacites (3). Some amphiboles do not reveal any Eu anomaly and are pargasitic with relatively high Ti (apfu), which results from formation at higher temperatures. This data indicates that plagioclase was not an early crystallizing phase during differentiation, which is supported also by textural relations that show increased plagioclase phenocrysts only at advanced stages of differentiation in andesitic and dacitic magmas. Very low Ni contents (~13 ppm) (Fig. 3.6f) of basaltic-andesites/andesites and dacites are consistent with early fractionation of olivine and clinopyroxene from a primary, primitive, picro-basaltic composition with high Ni content (~339 ppm). The transition from a moderate relative FeO(tot)/MgO enrichment trend towards a relative depletion trend is observed in the compositional range of basaltic-andesites (2C) to dacites (3). At this stage in magma differentiation, magnetite and later ilmenite begin to crystallize. These observations are consistent with a popular model that attributes calc-alkaline differentiation to increased magmatic water content as one of the principal reasons for enhancing magnetite saturation on the liquidus [Gill, 1981, Grove et al., 2003, Sisson and Grove, 1993a,b, Zimmer et al., 2010, Osborn, 1959] and permitting early amphibole crystallization [Cawthorn and Brown, 1976, Grove et al., 2003, Sisson and Grove, 1993a,b]. Fe-rich, ferric iron-bearing phases such as magnetite require elevated oxygen fugacity and/or H_2O content of the magma. Amphibole saturation on the other hand requires high H_2O and Na_2O. Based on the mineral chemistry of amphiboles, the textural information of phenocrysts and Fe-Ti oxide phases, magnetite appears to exert a more important role in driving the magmas from the tholeiitic to the calc-alkaline field. The relatively late onset of pronounced magnetite crystallization in the present case might be due to lower oxygen fugacity in the early stage of magmatic differentiation [Osborn, 1959, Sisson and Grove, 1993a,b].

Isotopic Source Constraints

Isotopic bulk composition in terms $^{87}Sr/^{86}Sr_i$ and $^{143}Nd/^{144}Nd_i$ (Fig 3.10b) reveal that rocks with highest SiO_2 such as basaltic-andesites, andesites (2C) and dacites (3) are isotopically the most primitive among the present dykes. The isotopic characteristics of these rocks overlap with Mesozoic ophiolites from Piemont-Liguria and the Central Eastern-Alps zone, representing a N-MORB type mantle [Borsi et al., 1996, Rampone et al., 1998, Schaltegger et al., 2002]. Bulk rocks analysed for $^{87}Sr/^{86}Sr_i$ and $^{143}Nd/^{144}Nd_i$ from the Central Eastern Alps are represented by gabbroic intrusions in the Platta nappe, ranging from Mg-rich to Fe-rich and were emplaced into a cold mantle at a depth less than 8km below the sea floor. Additionally, the same basalts for the Platta nappe were analysed as well [Schaltegger et al., 2002]. Bulk rock samples from the Voltri Group, Sestri-Voltaggio Zone and the Braco unit from the Northern Apennines [Borsi et al., 1996] analysed for Sr and Nd isotopes are plagiogranites. The sample from the Braco unit has a typical rodingite mineral paragenesis, resulting from chemical exchange between plagiogranite dykes and

serpentinite host rock. Additional samples from the Internal Liguride [Rabinowicz et al., 2002] ophiolite comprise ultramafic cumulates in the form of plagioclase-clinopyroxene-dunites, olivine-gabbro and pillow lavas. Three basalts in the form of dykes from External Liguride complement this data set and overall represent a MORB-type depleted mantle source [Schaltegger et al., 2002]. The more primitive dyke rock samples encompassing picro-basalts, Mg- and olivine-tholeiites and basalts (Fig 3.10b) exhibit isotopic ratios in the range found in residual peridotites from Balmuccia and Baldissero in the Ivrea Zone which coincide to some extent with $^{87}Sr/^{86}Sr_i$ and $^{143}Nd/^{144}Nd_i$ values determined for the hybrid lower crust of the Ivrea Zone overlying upper mantle lithologies. They occur as ultramafic cumulates such as websterites and peridotites, together with gabbros of basal and intermediate section [Voshage et al., 1987, 1990] of the lower crustal mafic complex of the Ivrea-Verbano Zone. Their $^{87}Sr/^{86}Sr_i$ and $^{143}Nd/^{144}Nd_i$ isotopic ratio coincides with the range of values of picro-basaltic, olivine-tholeiitic (1A, 1B) and basaltic (2A) dyke rocks of the Southern Adamello. The entire lower to middle crustal assembly of lithologies encountered in the well-exposed Ivrea-Verbano Complex potentially provides a close analogue of the lower Adriatic (Southern Alpine) crust further east along the Periadriatic Line, at the stage of the pluton assembly and subsequent dyke intrusions in the southern part of the Adamello Batholith. Lower crustal rocks such as Kinzingites (qtz + or + sil + grt + crd + bt + gr) and Stronalites (grt + fsp + qtz ± bt ± crd ± ky ± sil) represent paragneisses with signs of extended partial melting [Hunziker and Zingg, 1980, Schmid, 1978/79, Schmid and Wood, 1976, Sighinolfi and Gorgoni, 1978]. Extensive partial melting of late to post-Hercynian time (270-310 Ma) [Köppel, 1974, Pin, 1990, Wright and Shervais, 1980] leaves a crustal residue that is not particularly fertile with regard to potential crustal assimilation processes associated with subsequent Tertiary arc-type magmatism.

Dyke bulk rock radiogenic Pb-isotope data plots conspicuously in the range of sulfides in ultramafic layers of the basal part of the Mafic Complex of the Ivrea-Verbano Zone [Cumming et al., 1987]. The $^{207}Pb/^{204}Pb$ data from the post-plutonic dykes of the southern Adamello and the Ivrea-Verbano Complex are all elevated with respect to the depleted MORB mantle (DMM) value [Rehkämper and Hofmann, 1997]. Such a relation appears to indicate some contribution of an upper crustal component according to the growth curves of Zartman and Doe [1981]. On the other hand the $^{208}Pb/^{204}Pb$ signature of primitive Ol-tholeiite (1B) is much closer to the DMM value. Moreover, large middle-to upper crustal granitoid plutons and many basic to intermediate dykes and stocks formed during Permian magmatism in the Serie de Laghi [Pinarelli et al., 1993] have a similar range of $^{207}Pb/^{204}Pb$ vs. $^{206}Pb/^{204}Pb$ and $^{208}Pb/^{204}Pb$ vs. $^{206}Pb/^{204}Pb$ as the post-plutonic dykes of the southern Adamello Batholith [Boriani et al., 1995, Pinarelli et al., 1993]. Very similar rocks formed in the same early Permian time interval are found in close vicinity of the Adamello; the volcanic products of the Collio Basin [Breitkreuz et al., 2002, Cassinis et al., 2007] are characterized by calc-alkaline rhyolitic to rhyodacitic ignimbrites and the Dasdana Beds, volcaniclastics that have been deposited in a shallow-water alluvial to lacustrine environment [Breitkreuz et al., 2002]. Relatively extensive infill of Permian volcanic products within the Collio basin provided material for potential assimilation during magma ascent through the crust. Partial melting and assimilation of such siliceous material composed of plagioclase, quartz and alkali feldspar with devitrified matrix could produce restitic plagioclase or quartz, depending on the original mode and melting reaction, which could potentially be present and identified in hybrid magmas [Johannes and Holtz, 1996] produced by the interaction

of ascending magma with local partial melt. However, field relationships of hybrid basaltic magmas investigated in an accompanying paper rather testify for partial melting and entrainment of crystals such as plagioclase and amphibole from the dominates tonalitic and granodioritic plutonic host rocks at emplacement level, rather than uptake of residual phases from a granitic or pelitic crustal source.

Constraints on Fractionation Depth and Temperature Conditions

Sample	RockType	Am	Pl	$P(kbar)^1$	$P(kbar)^2$	$P(kbar)^3$	$T°C^4$	$Al^{[VI]}(apfu)$
NHS105	Hbl-Pl-phyric basaltic-andesite (2C)	Am105-1	Pl105-4	4.94	3.42	4.94	1005	0.376
NHS105	Hbl-Pl-phyric basaltic-andesite (2C)	Am105-2	Pl105-5	6.63	7.27	6.39	1060	0.526
NHS106	Hbl-Pl-phyric basaltic-andesite (2C)	Am106-1	Pl106-1	7.10	7.34	7.10	1026	0.544
NHS106	Hbl-Pl-phyric basaltic-andesite (2C)	Am106-3	Pl106-1	7.20	7.67	7.20	980	0.549
NHS106	Hbl-Pl-phyric basaltic-andesite (2C)	Am106-2	Pl106-2	7.32	8.07	7.32	972	0.567
NHS106	Hbl-Pl-phyric basaltic-andesite (2C)	Am106-4	Pl106-2	7.05	7.48	7.05	1002	0.551
NHS106	Hbl-Pl-phyric basaltic-andesite (2C)	Am106-5	Pl106-4	7.65	7.72	7.65	981	0.573
NHS106	Hbl-Pl-phyric basaltic-andesite (2C)	Am106-6	Pl106-4	6.99	7.89	6.99	998	0.547
NHS086	Hbl-Pl-phyric dacite (3)	Am086-1	Pl086-1	6.89	3.25	6.89	961	0.484
NHS086	Hbl-Pl-phyric dacite (3)	Am086-2	Pl086-2	7.69	4.05	7.69	1024	0.523
NHS086	Hbl-Pl-phyric dacite (3)	Am086-3	Pl086-4	6.08	3.04	6.08	1072	0.438
NHS086	Hbl-Pl-phyric dacite (3)	Am086-4	Pl086-5	6.87	3.45	6.87	1032	0.479
NHS086	Hbl-Pl-phyric dacite (3)	Am086-5	Pl086-7	6.24	3.23	6.24	999	0.449

Table 3.11: The cores of adjacent hornblende (amphibole) and plagioclase were selected for thermobaromteric calculations. *(1)* Empirical calibration, based on experiments on high-Mg basalts employing the correlation between pressure and octahedral coordinated AlVI after Larocque and Canil [2010]. *(2)* Pressures obtained by the calibration of Ridolfi et al. [2010] that is based on compositional components such as Si*, Al^T, Mg*, ^{VI}Al*. *(3)* Recalibrated barometer of Larocque and Canil [2010] by Krawczynski et al. [2012], adding additional experiments. *(4)* Temperature constraints are obtained by the edenite-richterite thermometer after Holland and Blundy [1994]. $Al^{VI}$is the octahedrally coordinated Al in amphibole used in the calculations.

The depth of formation of primitive amphiboles from basaltic-andesites/andesites (2C) based on mineral chemistry can be inferred from the barometric calibration established by Ridolfi et al. [2010] for the stability and chemical equilibrium of amphibole in calc-alkaline magmas. This empirical thermobarometric formulation should be applicable on a single phase such as amphibole. An independent pressure estimate was obtained by employing the empirical barometer of Larocque and Canil [2010], based on the correlation of octahedral Al^{VI} in amphibole with pressure from liquidus experiments of high-Mg basalts. Pressures of ~7-8kbar (Tab. 3.11) for basaltic-andesites/andesites (2C) and ~3-4kbar for dacites (3) were obtained by the barometric formulation of Ridolfi et al. [2010]. For the empirical calibration of Larocque and Canil [2010], the estimated pressure range is slightly lower, between 6.5 and 7.5kbar for basaltic-andesites/andesites (2C), but much higher for the dacites (3), resulting between 6 and 7.5kbar. An extended calibration of the same compositional relation of amphibole correlated to pressure, as in Larocque and Canil [2010], was established by Krawczynski et al. [2012] and gives almost identical results as the original calibration. These barometric constraints infer >20km as a rough depth estimate for the formation of basaltic-andesites/andesites (2C) and >10km for the dacites (3), using the barometric constraints of

Ridolfi et al. [2010]. Temperature estimates were obtained by the thermometric calibration for hornblende and plagiolcase after Holland and Blundy [1994]. Due to rapid quenching within dykes, the mineral phases should not have experienced extensive post-emplacement reequilibration. For the present case, the edenite-richterite thermometer was preferred over the edenite-tremolite thermometer, which requires the presence of quartz, which is absent as a phenocryst phase in basaltic-andesites/andesites (2C). The pressure applied in the thermometric calibration was taken from the determination of Ridolfi et al. [2010]. Hornblende (amphibole) and plagioclase analyses were taken from the cores of adjacent phenocryst pairs (Table 5) for thermometric calculations. Plagioclase composition in cores is constant and anorthite-rich. Average temperature for several mineral pairs result 1004 ± 29°C (Tab. 3.11) for basaltic-andesites/andesites (2C) and 1018 ± 41°C for dacites (3).

Major Fractionating Phases and Resulting Cumulate Proportions

Phases	**Mg-tholeiite**	**Ol-tholeiite**	**Basalt**	**Basaltic-Andesite**	**Andesite**	**Dacite**
Liq	0.911	0.777	0.725	0.268	0.183	0.075
Ol	0.070	0.127	0.172	0.172	0.172	0.172
Spl	0.019	0.019	0.019	0.019	0.019	0.019
Cpx		0.077	0.084	0.176	0.176	0.176
Hbl				0.353	0.408	0.457
Pl				0.012	0.040	0.090
Mag					0.001	0.012
RSS	3.903	2.686	1.608	2.080	0.011	0.151

Table 3.12: Cumulative mineral proportions obtained by least square fractionation modelling. Tabulated data of modal proportions for the different mineral phases occurring in the crystallization sequence, which are determined through least square analysis [Bryan et al., 1969] between two fractionation steps. For the least square approach, starting and derivative liquid composition are known together with the compositions of the fractionating mineral phases. Major and minor elements in least square regression are SiO_2, TiO_2, Cr_2O_3, Al_2O_3, FeO, MgO, MnO, NiO, CaO, Na2O and K_2O. FeO is equivalent to FeO*(tot), which includes all Fe_2O_3. Mineral modes correspond to accumulated solids fractionated over the entire fractionation interval from picro-basalt (1B) to dacite (3). *RSS* stands for residual sum of squares from the linear regression.

A crystal fractionation model was constructed to trace the liquid evolution during the crystallization of the principal mineral phases. The sequence of the mineral phases appearing on the liquidus was determined mainly from petrographic observation of the present rock suite, in combination with their bulk rock compositions that were utilized as liquid compositions. The picro-basalt (1B) is taken as the starting, primary magma for the fractionation model that leads to a final dacitic (3) composition. Such a relation covers all the intermediate compositions that were identified and described under field constraints and petrography. The crystallizing phase proportions between two liquids, i.e. fractionation steps, were determined through least square analysis [Bryan et al., 1969], knowing parental and derivative liquid composition of the fractionation step, together with the composition of the crystallizing minerals (Tab. 3.12). The least square analysis was performed on major and minor element composition, employing SiO_2, TiO_2, Cr_2O_3,

Al_2O_3, FeO, MgO, MnO, NiO, CaO, Na_2O and K_2O. An Mg-tholeiite (~13 MgO wt.%) was additionally introduced with an intermediate composition, apart from rock types discriminated in the field. In the case of olivine (Fo-rich) and plagioclase (An-rich), the phenocryst core compositions were taken for the calculations. Amphiboles are very homogeneous and almost devoid of zoning, whereas clinopyroxene shows sector zoning. Averaged mineral chemical values were used over the different sectors for clinopyroxene. The crystallization sequence from a picro-basalt to Mg-tholeiite involves olivine and spinel crystallization. The differentiation to an olivine-tholeiite is characterized by the appearance of clinopyroxene on the liquidus. Olivine and clinopyroxene continue to crystallize and the liquid evolves to a basaltic composition. In the petrographic analysis, spinel is present throughout and the composition shifts from Cr_2O_3 rich to increasingly Al_2O_3 rich compositions in basaltic magmas with advanced magma differentiation. Within picro-basalts, Mg-tholeiites and Ol-tholeiites spinel is very Cr rich (Fig. 3.17a) and least square analysis is very susceptible to the total Cr budget of the starting composition. The magnetite-rich spinel composition at the margins of grains was avoided for the least square analysis, as they generally reflect low-temperature or even sub-solidus requilibration. Thus, after the first fractionation step including spinel, the entire Cr budget is exhausted and no further Cr-spinel fractionation is considered in subsequent steps. The transition to basaltic-andesitic compositions occurs through considerable crystallization of amphibole (hornblende), accompanied by clinopyroxene and plagioclase. The further evolution to an andesite is characterized by the disappearance of clinopyroxene from the liquidus and the appearance of magnetite. With the same crystallizing assemblage, the magma evolves to a dacitic composition. As common in least square analysis, the right hand side approximation $\hat{y}$ [Bryan et al., 1969], representing the residual liquid computed in each fractionation step, is compared to the actual residual liquid composition; the sum of the square of residuals (Tab. 3.12) is the indicator for the goodness of the approximation. They range from 3.90 to 0.01 (Tab. 3.12) for the various fractionation steps. The results of the least square analysis of the fractionation model are shown in Figure 3.18a. The temperature axis was established by comparing the liquid compositions of the different fractionation stages with the LLD obtained experimentally at 7kbar, consistent with the pressure estimates based on the thermobarometry (Tab. 3.11) [Larocque and Canil, 2010, Ridolfi et al., 2010]. According to this model, melt fractions representing liquid mass/initial liquid mass (Fig. 3.18a) do not decrease linearly as a function of temperature during fractionation-driven differentiation. The largest drop in melt fraction during fractionation occurs at the onset of amphibole fractionation, around 1020°C and 1050°C, at 7 and 10kbar respectively. This value marks the high-temperature stability of amphibole on the liquidus according to the experiments of Kägi [2000] and Nandekar [2013]. At this point, the melt fraction modeled by the least square approach of the dyke suite drops from 0.725 to 0.268, with the evolution from a basalt (2A) to a basaltic-andesite (2C). Amphibole (hornblende) constitutes the major constituent of the inferred cumulates, with a modal fraction of 0.457 at the final step of the differentiation when a dacite (3) is obtained. The early differentiation is characterized by the formation of ultramafic cumulates in the form of dunites and wherlites (Fig. 3.18). In a more evolved stage, cumulates are comprised of hornblendites (hornblende) and hornblende-gabbros. In particular, hornblendites and amphibole-rich gabbros of the Val Fredda pluton of the Southern Adamello show amphibole with olivine inclusions of Fo_{88}, which were interpreted by various authors applying different methods and approaches as cumulus phase originating from a deep seated reservoir located in the lower crust around 30km depth

(7-10kbar) [Blundy and Shimizu, 1991, Blundy and Sparks, 1992, Ulmer, 2007, 1986, Ulmer et al., 1983]. Crustal sections exposed in the island-arc terrains in places such as the Kohistan-arc in Pakistan [Burg et al., 2005, Jagoutz, 2010], the Tonsina-Talkeetna-arc in Alaska [DeBari and Coleman, 1989, Greene et al., 2006] and the Chelan Complex [Dessimoz et al., 2012] in Washington State (North Cascades) in the United States show a cumulate rock association of dunites, olivine websterite, wehrlites, pyroxenites, hornblendites, hornblende gabbro and gabbronorites. Garnet is stable at higher pressures, depending as well on the amount of dissolved water (H_2O wt%) within the silicate liquids [Alonso-Perez et al., 2009] forming garnet-bearing ultramafic cumulates and gabbros [DeBari and Coleman, 1989, Jagoutz, 2010]. In a crystal fractionation model for the Aleutian island-arc crust [Kay and Kay, 1985], 65%-70% of the initial liquid mass of primitive tholeiite had crystallized to form an andesitic composition, which is equivalent to a diorite. Least square analysis in the present case leads to crystallization of approximately 75% to 80% of the initial liquid mass to form basaltic-andesitic/andesitic compositions. The common occurrence of amphibole-rich gabbros, wherlites, pyroxenites and dunites in the different known crustal sections of the Kohistan-arc [Jagoutz, 2010], Tonsina-Talkeetna-arc [DeBari and Coleman, 1989, Greene et al., 2006] and the Chelan Complex [Dessimoz et al., 2012], associated with hydrous arc-magmas, supports the inferred cumulus rocks for the formation of higher differentiated magmas such as dacites (3).

Comparison with Prediction from Thermodynamic Model (MELTS)

The present crystal fractionation model proposed for the generation of the entire compositional range of the dyke suite is compared with the predictions of the thermodynamic model MELTS [Asimow and Ghiorso, 1998, Ghiorso and Sack, 1995]. Fractional crystallization calculations with MELTS were performed isobarically at 7kbar (Fig.3.18b), starting from the same picro-basaltic parental magma (1B) (NHS136). An initial H_2O content of 3wt% was assumed and the Fe_2O_3/FeO ratio was constrained by the Ni-NiO oxygen buffer integrated in MELTS under the given hydrous conditions of the parental magma. MELTS determined a liquidus temperature for the picro-basalt (1B) of 1376°C at a $\log_{10}(fO_2)$ of -5.76 with olivine as the liquidus phase (Fig. 3.18b). In Figure 3.18b, the olivine-in (Ol-in), spinel-in (Spl-in) and clinopyroxene-in (Cpx-in) reactions characterize the appearance of these phases on the liquidus during fractional crystallization determined by MELTS. The appearance of amphibole at a temperature around 1020°C is constrained by fractional crystallization experiments (Fig. 3.19) at 10 kbar [Kägi, 2000] and 7 kbar [Nandekar, 2013]. The dashed line in Figure 3.18b represents the evolution of the melt fraction, obtained by fractional crystallization modeling using the least square approach. The dotted trace in Figure 3.18b represents the melt fraction evolution modeled with MELTS. During the initial stage when olivine (Ol) and spinel (Spl) are liquidus phases, the melt fraction decreases in a similar fashion. After the appearance of clinopyroxene (Cpx) on the liquidus, the melt fractions develop very differently and the traces diverge considerably for the two different approaches. The melt fraction stays much higher in the least square approach and only strongly decreases when amphibole appears on the liquidus, whereas the MELTS model describes a much more rapid decrease of the melt fraction. In the present case, MELTS fails to predict the saturation of amphibole on the liquidus in the temperature range constrained by fractional crystallization experiments for this starting composition and the natural dyke suite present here. Petrography and mineral chemistry of amphiboles clearly indicate an early appearance of amphibole on

Phase	Generation	n	SiO2	TiO2	Al2O3	Cr2O3	FeO	MnO	MgO	CaO	Na2O	K2O	NiO	Total
			[wt%]	[wt%]	[wt%]	[wt%]	[wt%]	[wt%]	[wt%]	[wt%]	[wt%]	[wt%]	[wt%]	[wt%]
Ol	1B	n=47	40.84	0.00	0.02	0.04	8.90	0.15	49.95	0.15	0.01	0.00	0.26	100.34
			(35)	(1)	(2)	(3)	(9)	(2)	(23)	(1)	(2)	(0)	(3)	(49)
Ol	2A	n=41	39.98	0.01	0.03	0.03	10.52	0.18	48.29	0.15	0.02	0.00	0.30(5)	99.52
			(20)	(1)	(4)	(2)	(53)	(2)	(2)	(3)	(2)	(0)		(45)
Cpx	2A	n=193	50.43	0.65	4.30	0.32	5.80	0.14	15.39	21.84	0.22	0.01	n.a.	99.11
			(188)	(35)	(188)	(26)	(107)	(5)	(130)	(61)	(6)	(1)		(57)
Spl	2A	n=12	0.09	0.39	17.48	46.32	22.51	0.58	12.53	0.04	n.a.	n.a.	0.12	100.07
			(4)	(8)	(115)	(207)	(158)	(4)	(134)	(5)			(4)	(30)
Spl	1B	n=21	0.07	0.43	12.92	49.17	24.99	0.57	11.91	0.02	n.a.	n.a.	0.08	100.41
			(3)	(7)	(65)	(129)	(74)	(4)	(30)	(2)			(2)	(41)
Hbl	2C	n=58	40.40	1.68	14.68	0.02	10.91	0.14	14.20	12.24	2.45	0.42	n.a.	97.12
			(90)	(9)	(107)	(2)	(115)	(6)	(66)	(25)	(15)	(6)		(32)
Hbl	3	n=44	44.35	1.18	11.32	0.01	13.55	0.51	13.60	10.77	1.70	0.19	n.a.	97.19
			(145)	(39)	(86)	(1)	(71)	(24)	(43)	(91)	(35)	(6)		(60)
Pl	2C	n=81	46.50	0.01	33.68	n.a.	0.51	0.01	0.03	17.72	1.24	0.02	n.a.	99.83
			(104)	(1)	(68)		(4)	(2)	(2)	(76)	(39)	(1)		(28)
Pl	3	n=261	47.04	0.14	33.23	n.a.	0.44	0.02	0.02	16.85	1.71	0.02	n.a.	99.56
			(137)	(35)	(88)		(8)	(2)	(2)	(102)	(55)	(1)		(52)
Mag	3	n=10	0.31	4.71	0.02	0.03	84.72	1.14	0.98	0.08	n.a.	n.a.	0.00	92.36
			(33)	(87)	(2)	(2)	(217)	(42)	(139)	(5)			(1)	(186)

Table 3.13: All the mineral phases (Ol, Spl, Cpx, Hbl, Pl, Mag) used for the fractional crystallization model, established through least square analysis between starting (NHS136), intermediate and end (NHS083) composition, which are documented in Table 3.2. n is the number of replicate microprobe analyses. In brackets reported one standard deviation of replicate analyses is reported in terms of the least unit cited. Thus, 40.84 (35) represents 40.84 $\pm$ 0.35.

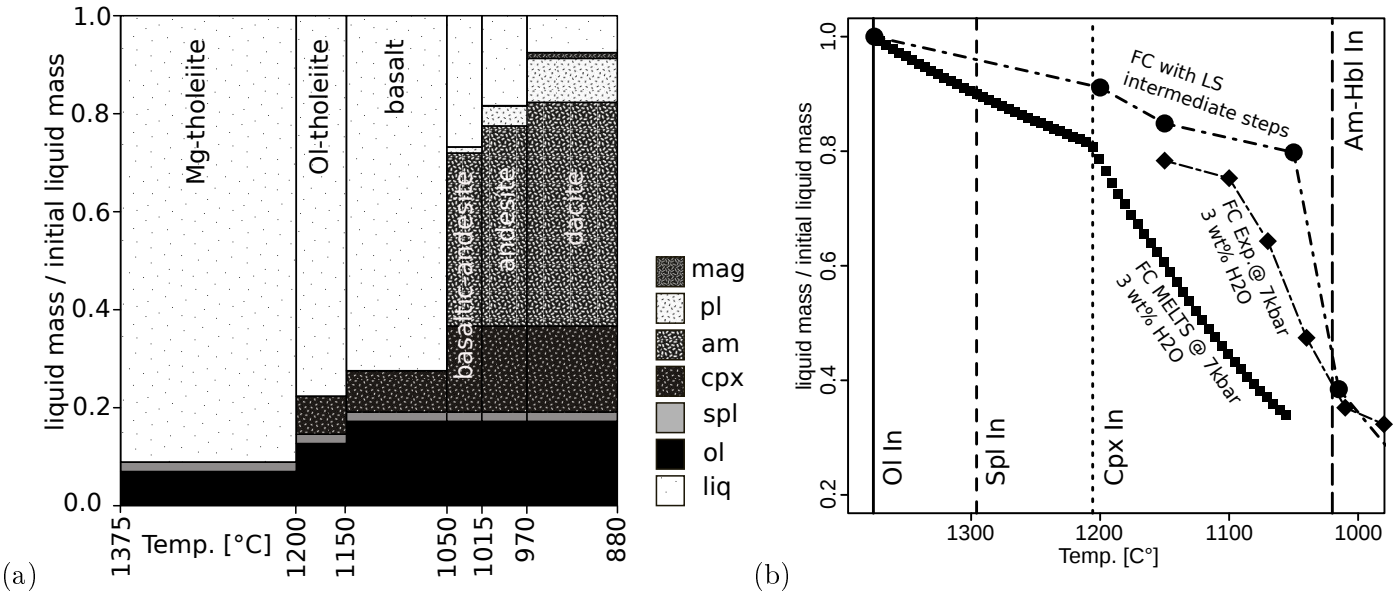

Figure 3.18: *(a)* Bar diagram illustrating mineral and liquid phase proportions obtained from fractional crystallization modelling, starting from a picrobasalt (1B) to dacite (3); phase proportions are listed in Table 3.12. Fractional crystallization is modelled by a least square approach [Bryan et al., 1969], employing measured bulk rock compositions for each fractionation step, together with measured solid (phenocryst) composition of the fractionating solid phases. The fractional crystallization produces initial ultramafic cumulates such as dunites and wherlites. Subsequent steps generate considerable amounts of hornblendites and hornblende-gabbros and smaller amounts of dioritic rocks with the evolution towards residual dacite. Temperatures of the fractionation steps are inferred from hydrous fractional crystallization experiments at 7kbar [Nandekar, 2013]. *(b)* Evolution of the melt fraction (liquid mass/initial liquid mass) during fractional crystallization using the thermodynamic approach (MELTS) and the least square mass-balance approach based on the natural dyke rock suite. The thermodynamic approach is modelled with fractional crystallization at 7kbar with MELTS [Asimow and Ghiorso, 1998, Ghiorso and Sack, 1995], with an initial H_2O content of 3 wt%. Oxygen fugacity is constrained to the Ni-NiO buffer for MELTS. The saturation of olivine (Ol-in) at 1376°C, spinel (Spl-in) at 1296°C and clinopyroxene (Cpx-in) at 1206°C on the liquidus is constrained by the thermodynamic calculations with MELTS. The saturation of amphibole on the liquidus at 1020°C and 1050°C is constrained by fractional crystallization experiments at 7 kbar [Nandekar, 2013] and 10 kbar [Kägi, 2000] respectively. Temperatures for the least-square mass-balance approach are inferred from the pseudoternary phase-diagram Ol-Cpx-Qtz of Figure 17, based on the fractional crystallization experiments [Kägi, 2000, Nandekar, 2013] and the respective LLDs.

the liquidus during the differentiation of the parental magma to basaltic-andesitic and andesitic compositions. This apparent failure of the MELTS code most likely reflects the fact that hydrous phases such as hornblende are less well-constrained in the MELTS thermodynamic model [Asimow and Ghiorso, 1998, Ghiorso and Sack, 1995] and thus, questions the use of MELTS for modelling fractionation of arc magmas at moderate to high pressures where amphibole is an early and important fractionating phase.

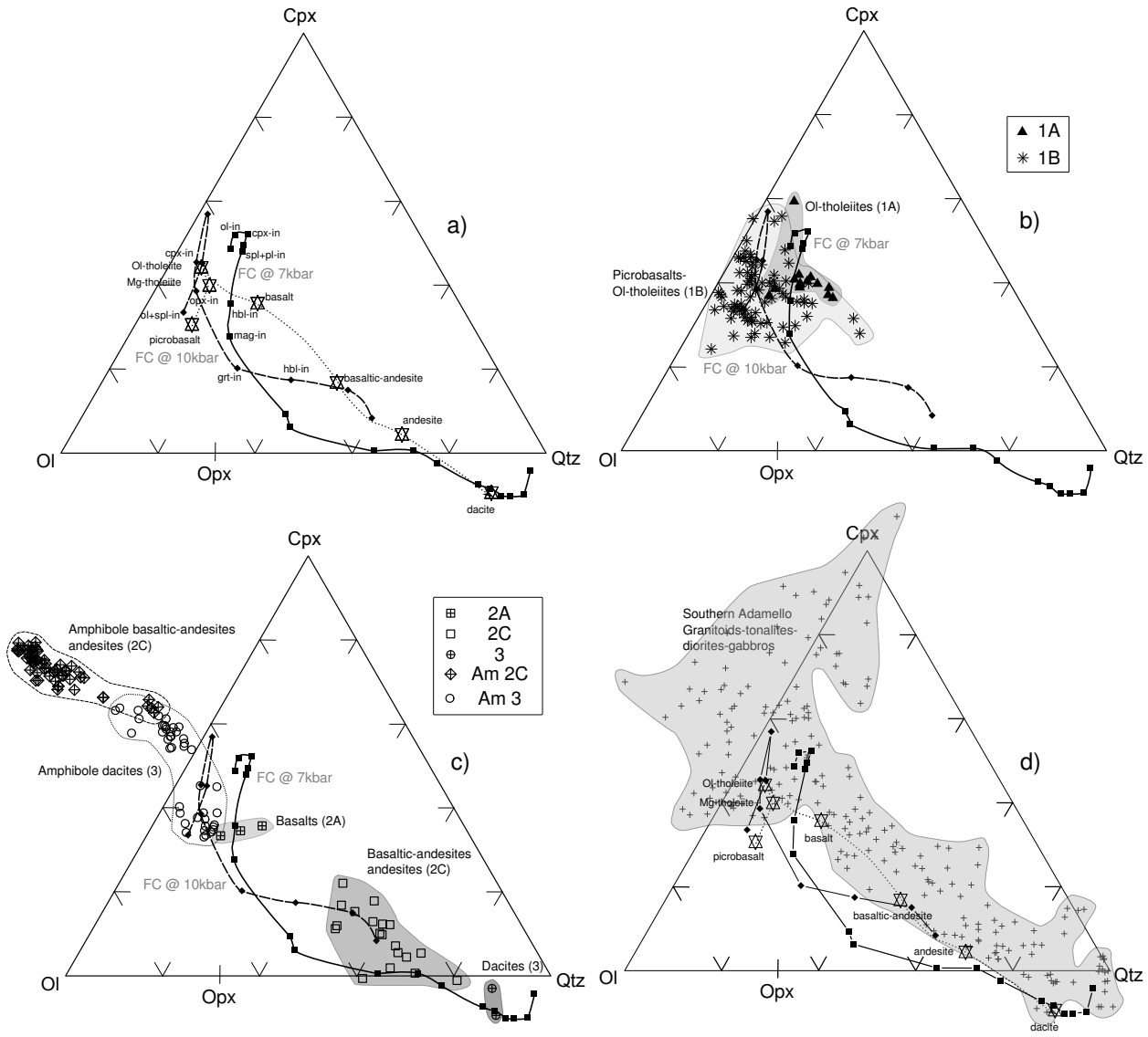

Figure 3.19: Pseudoternary projection Ol-Cpx-Qtz, which is part of the basalt-classification tetrahedron of Yoder and Tilley (1962). Liquid and mineral (amphibole) compositions are recalculated according to the scheme of Grove [1993], Grove et al. [1982, 1983] and Tormey et al. [1987] into olivine (Ol), plagioclase (Pl), clinopyroxene (Cpx), quartz (Qtz), orthoclase (Or), apatite (Ap) and ilmenite-hematite-chromite (IHC). *(a)* Projection of two different liquid lines of descents from fractional crystallization experiments at 10 kbar [Kägi, 2000] and 7 kbar [Nandekar, 2013]. Bulk rock compositions representing the liquid compositions used in the least square analysis for determination of the phase proportions between different fractionation steps are shown. *(b)* Bulk rock compositions for picro-basalts/olivine-tholeiites (1B) and olivine-tholeiites (1A). *(c)* Projections of compositions of basalts (2A), basaltic-andesites/andesites (2C) and dacites (3). Amphibole compositions of basaltic-andesites/andesites (2C) and dacites (3) are included. *(d)*

Trace Element Modelling

A trace-element evolution model was developed based on the major-element fractional crystallization model. Trace-element partition coefficients (Kd's) for phases such as clinopyroxene, amphibole and plagioclase were chosen to account for temperature and mineral chemical changes of fractionating phases. Partition coefficients for clinopyroxene were taken from the experimental fractional crystallization study of Alonso-Perez [2006] and different fractionation stages from a primitive to a more evolved composition were correlated based on temperatures between the natural and the experimental composition suite. Unmeasured REE were fitted with a non-linear regression of the lattice-strain model [Wood and Blundy, 1997]. For amphibole, Sisson [1994] established a parametrization for REE, Y, Ti, V and Cr as a function of the distribution of Ca between amphibole and melt, which gives an expression to predict amphibole-melt trace element partitioning. In the case here, this parametrization was used for basaltic amphibole and missing REE were fitted again with the lattice-strain model [Wood and Blundy, 1997]. For andesitic and dacitic amphiboles used partition-coefficients were determined experimentally for an andesite by Alonso-Perez [2006]. Missing REE partition-coefficients were determined as before by the lattice-strain model. Partition coefficients for plagioclase were calculated based on a parametrization by Bédard [2006] that takes anorthite content, temperature and $XSiO_2$ of the liquid into account. Trace element partition-coefficients for olivine were taken from McKenzie and O'Nions [1991]. A detailed list for the partition-coefficient data applied here is displayed in Table 7.15. A bulk partition-coefficient (Fig. 3.20b) was calculated based on the changing phase proportions fractionating in each step. This allows the tracing of the partitioning behaviour of certain elements during fractional crystallization, as in the case of Sr, from incompatible behaviour in primitive compositions to more or less compatible behaviour for very evolved andesitic and dacitic compositions. In Figure 3.20a, the melt fraction is 0.08 for a single step in the course of fractional crystallization, represented as dashed lines for primitive mantle [McDonough and Sun, 1995] normalized trace element patterns. An averaged starting composition in terms of the modeled trace element was used for picrobasalts with MgO higher or equal to 15 wt%. Within Figure 3.20a an averaged andesitic (2C) composition is displayed as target differentiated magma composition. For light REE and the high field strength elements (HFSE) such as U, Th and Nb, a model with a residual melt fraction around 0.24 appears to reflect the averaged basaltic (2C) trace element composition. However, the Sr and the Ba content of the andesitic magma appears to be more elevated than the modeled value. The model shows a gradual increase of the heavy REE, whereas the middle and light REE such as Gd, Tb, Dy and Ho show a slight decrease over the course of increased fractionation. This behaviour is reflected in the slope of the heavy REE for the averaged andesitic (2C) composition in Figure 3.20a. What is remarkable is the development of a negative Ti anomaly with increased fractionation, which is reflected as well in the averaged andesitic (2C) composition. The trace element model includes the partitioning behaviour of Ol, Cpx, Am and Pl and in particular, amphibole appears to influence the partitioning of Ti towards compatible behaviour, thus causing the expression of a negative Ti anomaly. The fractionation of magnetite is not accounted for in this trace element fractional crystallization model. With some exceptions, the primitive mantle normalized trace element pattern can be rather well reproduced by a simple fractional crystallization model down to melt fraction of 0.24.

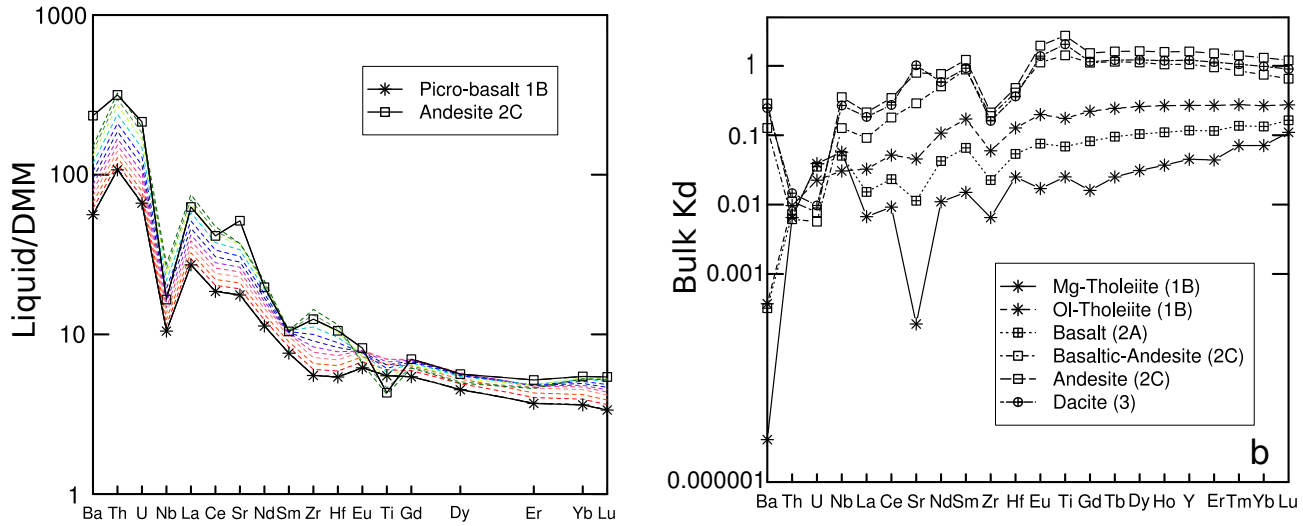

Figure 3.20: *(a)* Trace element evolution by fractional crystallization, with the removal of cumulates proportions determined through the least square approach. Changing partition-coefficients used in this model are listed in table 7.15. Trace element concentrations are normalized to the depleted morb mantle DMM after Workman and Hart [2005]. Fractionation steps are displayed in the form of coloured dashed lines from red to green, with a step size for df: 0.08. *(b)* Changing bulk partition-coefficients (Kd) are displayed throughout the fractionation series, ranging from a picro-basalt to a dacite.

Implications for Magmatic Differentiation in the Crust

The parental picro-basaltic (1B) magma with inferred mantle separation conditions of 28 kbar and 1370°C [Ulmer, 1988] and the more differentiated magmas in the form of basalts (2A), basaltic-andesites/andesites (2C) and dacites (3) provide direct constraints on intra-crustal differentiation processes of such magmas when mineral phase assemblage and chemistry, together with isotopic and bulk rock geochemical information, are thoroughly evaluated and combined. The magmatic differentiation model here is modeled as a fractional crystallization process at lower crustal level (>20 km) below the Conrad Discontinuity, based on thermobarometric constraints [Krawczynski et al., 2012, Larocque and Canil, 2010, Ridolfi et al., 2010] (Tab. 3.11). A bulk rock geochemical indication for deeper crustal differentiation processes is the enrichment of Al_2O_3 (>18 wt%) (Fig. 3.5d) at intermediate basaltic-andesites/andesites (2C). High pressure crystallization, together with elevated H_2O concentrations of parental mafic magma, is inferred by the lack of plagioclase as an early liquidus phase, causing the Al_2O_3 enrichment towards intermediate compositions. The generation of the dyke suite from the southwestern sector towards the northeastern sector of the Re di Castello superunit is related to a continuous evolution in time [Hürlimann et al., in prep.b] at a late stage, succeeding the formation of plutonic rocks in the Re di Castello superunit. This implies that in time sequence and geographical relation, the dykes occurring in the southwest and the northeast (Fig. 3.1) might not be directly genetically related to each other. Nevertheless, a fractional crystallization model starting from an averaged primitive picro-basaltic (1B) composition reproduces to a considerable extent the trace element composition of a more differentiated andesitic (2C) composition. This means that the source characteristics did not change dramatically in time and over the regional extent that is covered

by these post-plutonic dykes. The enrichment of light-ion-lithophile-elements (LILE) and lesser amounts of LREE for primitive picro-basalts and olivine-tholeiites can be explained by a flux of these elements supplied by the slab [McCulloch and Gamble, 1991].

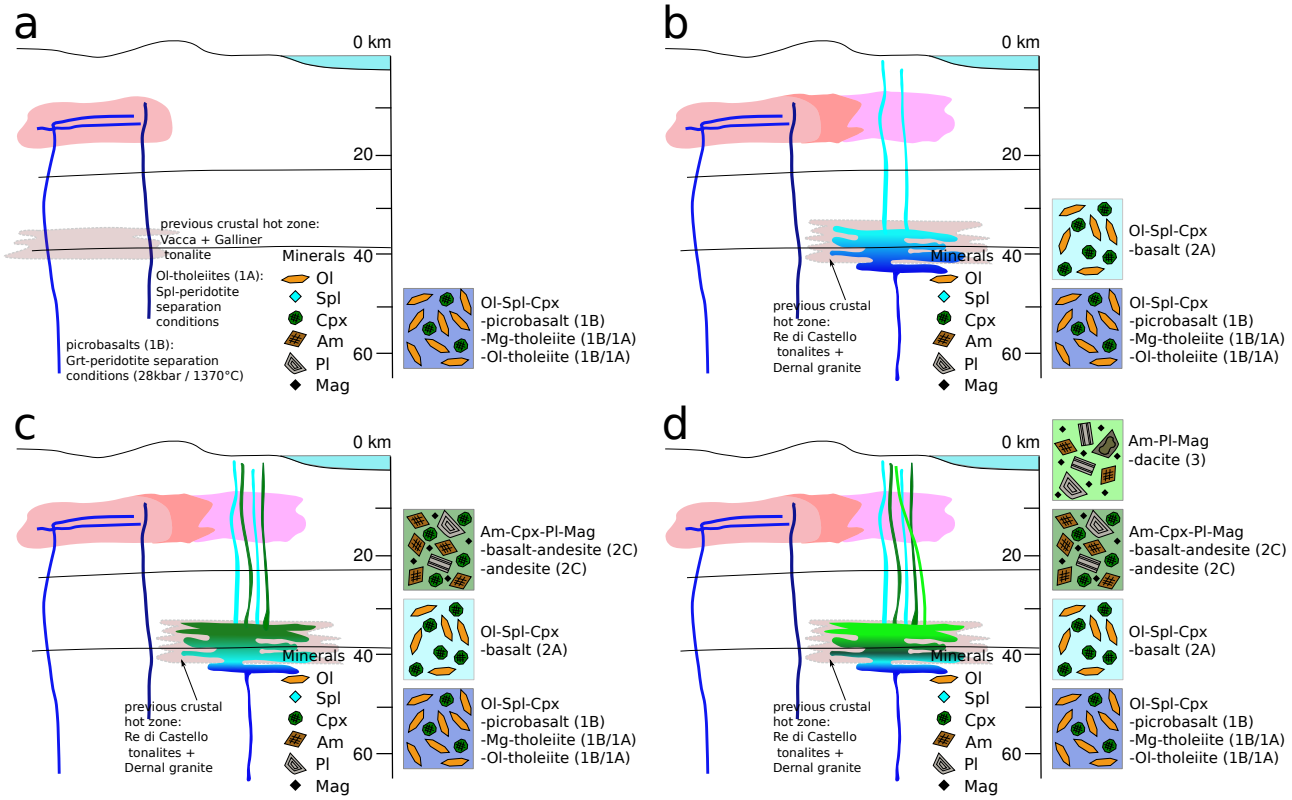

Figure 3.21: Intra-crustal magmatic differentiation model for the evolution of the S-Adamello dyke rock suites with fractional crystallization as the dominating process to produce intermediate magmas such as basaltic-andesites / andesites and dacites in lower crustal magma reservoirs (> 20km) below the Conrad Discontinuity. (a) Picro-basalts and olivine-tholeiites (1B) magmas are primary magmas with mantle separation conditions of 28 kbar and 1370°C. Ol-tholeiites (1A) are mantle melts at shallower conditions (Spl-peridotite). Major element compositions of these magmas experienced only very minor modification in the transit through the crust. (b) The regional dyke swarm is associated with increased differentiation (fractional crystallization) at lower crustal depth. The isotopic signatures $^{87}Sr/^{86}Sr_i$ and $^{143}Nd/^{144}Nd_i$ of crustal assimilation is decreasing, with increasing SiO_2 content from basalts (2A) to (c) basaltic-andesites/andesites (2C) and (d) dacites (3). For discussion see text.

During the transfer through the continental crust, in particular, the primitive picro-basalts and Ol-tholeiites (1B) experienced some crustal assimilation, which is indicated by increased values of highly incompatible elements such as Rb and Ba (Fig. 3.6b, c), as well as for radiogenic isotopes $^{143}Nd/^{144}Nd_i$ and $^{87}Sr/^{86}Sr_i$ (Fig. 3.10a, b). Picro-basalts and olivine-tholeiites dykes appear to have the thermal capacity for assimilation within parts of the crust by thermal erosion [Huppert and Sparks, 1985, Thompson et al., 2002] along the conduit walls of the dyke during ascent. Olivine-tholeiites (1A) are an exception to all the encountered generation and units here, on the grounds that they have distinct minor and trace element chemistry, reflected in distinct REE patterns (Fig. 3.8a) and in a plot using MgO as differentiation index against TiO_2 (Fig. 3.5c). Some of these features could be interpreted as reflecting

differences in source characteristics, regarding H_2O content of the source and/or degree of partial melting in the source [Kelley et al., 2006]. If so, olivines-tholeiites (1A) could either originate from a different mantle source and/or experience further compositional modification of the magma at lower crustal levels during differentiation (Fig.3.21). More evolved basalts (2A) on the other hand clearly show effects of differentiation and to some extent assimilation regarding incompatible trace elements (Rb, Ba) (Fig.3.6b, c) and bulk rock radiogenic isotopes ($^{143}Nd/^{144}Nd_i$ and $^{87}Sr/^{86}Sr_i$) (Fig.3.10a). This differentiation occurs at high pressure at lower crustal levels (>20km) (Fig.3.21) as testified by late plagioclase saturation reflected in increasing Al_2O_3 concentration (Fig. 3.5d) during differentiation to intermediate compositions (basaltic-andesites/andesites). In the present case, basaltic-andesites/andesites (2C) and dacites (3) have the most primitive radiogenic isotope signature of all Adamello magmatic rocks in terms of $^{143}Nd/^{144}Nd$ and $^{87}Sr/^{86}Sr$ (Fig.3.10a), typical for MORB type mantle. Primitive amphibole trace-element chemistry and the lack of co-crystallization of plagioclase places the differentiation of these rocks to a lower crustal level (>20km) (Fig.3.21). Previous intrusion of the Re di Castello tonalite and the small Dernal granite (39.8 Ma, Hansmann, 1986, Hansmann and Oberli, 1991) imply extensive fractionation and assimilation processes at lower crustal levels, in the same region as the later intrusion of basaltic-andesites/andesites (2C) and dacites (3). Such processes lead to a preheating of the lower crust and to the consumption of fertile material for assimilation. Later magma intrusion and reservoir formation at this level that feeds the more differentiated dykes (2C, 3) are much less affected by crustal contamination which explains their primitive isotopic signature. Primitive amphiboles (hornblendes) phenocrysts indicate the actual extraction of a cumulate mineral phase, originating from lower crustal level.

3.9 Conclusions

The present post-plutonic dyke suite of the Southern Adamello documents the largest compositional range over the whole Adamello Batholith that can be approximated as an actual series of differentiated liquids achieved through fractional crystallization. Peraluminous dacitic dykes can be produced through fractional crystallization without partial melting and assimilation of parts of the continental crust. The primitive isotopic signature of dacites and andesites exemplifies that these compositions do not originate from crustal melts. Moreover, inferred intermediate and more differentiated liquids are in very good correspondance with the evolution of the composition of the LLD of fractional crystallization experiments (7-10kbar). Mineral chemistry of cumulate forming amphibole and barometric constraints, inferred from the same mineral phase, indicate the importance of fractional crystallization in the genesis of andesitic and dacitic magmas at middle to lower crustal depth from a primitive mantle derived hydrous basaltic magma. Results of a fractional crystallization model, taking into account the calculated inferred cumulates, show that the trace element signature difference between a parental picrobasalt and andesites are to a great extent aquired through fractionation at middle to deep crustal level (20-40km). However, the initial enrichment of the LILE and to a lesser extent the LREE is attributed to a slap component replenishing these elements in the mantle wedge. There is no need to explain the trace-element signature through different mantle source characteristics for the regional extent covered by the present post-plutonic dyke swarm intruded into a whole sequence of previously emplaced plutonic units. Amphibole fractionation in these hydrous magmas is in many aspects of great importance, for a realistic model of the trace element

evolution during differentiation to evolved dacitic composition and potential plutonic equivalent, such as granodiorites. Furthermore, amphibole fractionation is driving the magmas eventually to peraluminous corundum-normative magma compositions. Radiogenic isotopic data reflects well the thermal capabilities for the different magma compositions in terms of assimilation processes with the hottest and most primitive picro-basalt as one of the most contaminated here. As a field and geochemical study, combined with recent fractional crystallization experiments, this contribution should help in understanding to what extent arc-tholeiitic to calc-alkaline magmas aquire the geochemical characteristics in the middle to lower crust in continental margin settings. This is important since these magmas are building in larger volumes whole batholiths, which overall contribute to the formation of the continental crust.

Chapter 4

Partial Melting, Assimilation and Hybridisation Processes During Dyke Emplacement

4.1 Abstract

This contribution constrains the effects of assimilation of immediate tonalitic host rock on the composition of basaltic hybrid magmas in a dyke swarm intruding into the shallow crust (2-3kb). The study encompasses detailed petrological and structural description of basaltic to basaltic hybrid, 10 to 15m wide dyke swarms, occurring within the Re di Castello intrusive suite building the southern part of the Adamello Batholith in Northern Italy. These intrusive zones are part of a regional dyke swarm intruding into larger volumes of tonalitic and granodioritic bodies that are thermally still hotter than the Permo-Triassic host rock sediments of the Central Southern Alps, distant from the batholith at the time of the dyke swarm formation. On a macroscopic scale, outcrops of these dyke swarms reveal intrusion breccias, formed by the injection of basaltic magma into partially molten tonalite. In microscopic textures, partially molten tonalite is present in the form of transparent and brownish glass, located in between grain boundaries. Biotite and interstitial K-feldspar were completely consumed in many cases by melting reactions. Partial melting of the tonalitic host rock represents a selective assimilation process, with melting reactions controlling the phase proportion and composition of the assimilant added to a primitive basaltic magma. In contrast, abundant xenocrysts of plagioclase with sieve textures and reverse zoning bearing more evolved albitic cores, in combination with amphibole xenocrysts with lower temperature cores and high temperature overgrowths, imply bulk assimilation through the disaggregation of tonalite host rock xenoliths. Based on trace element geochemistry and bulk rock radiogenic, $^{87}Sr/^{86}Sr$ and $^{143}Nd/^{144}Nd$ isotopic ratios obtained on closely examined dykes quantifies assimilation of the adjacent Vacca tonalite host rock at the emplacement level. A static conduction thermal model emphasizes the importance of increased host rock to intrusive magma contact surface for numerous closely spaced single primitive basaltic dykes and enables the generation of partial melting in the host rock tonalite. Basaltic magma intrusion temperature was estimated by trace element partitioning of amphibole microphenocrysts, in conjunction with experimentally determined partition coefficients at high temperature (~1050°C) close to the thermal stability limit of amphibole in calc alkaline magmas. Observed trace element assimilation behaviour of the immediate wallrock of basaltic hybrid dykes, complemented by field observation, bulk rock compositions and mineral chemistry and textures, provide insight into the crustal assimilation processes operating during the intrusion of high density dyke swarms at shallow, but preheated crustal environment through preceding pluton generation.

4.2 Introduction

Mantle derived basaltic magmas that intrude into the crust constitute an important source of heat for heating parts of the continental crust [Sawyer et al., 2011, Kaczor et al., 1988, Annen and Sparks, 2002]. Assimilation of crustal rocks by primitive basaltic magmas has been invoked in numerous geochemical models, in the context of assimilation and fractional crystallization, AFC [DePaolo, 1981] models and mixing, assimilation, storage and hybridization, MASH [Hildreth and Moorbath, 1988] processes, together with thermally constrained models for arc-related magmas [Annen et al., 2006]. Partial melting of the crust has been considered extensively regarding the generation of intermediate andesites and more evolved dacites within the concept of the deep crustal hot zone that builds upon underplating of mantle derived

mafic magmas at the base of the crust [Raia and Spera, 1997, Huppert and Sparks, 1988, Bergantz, 1989] and includes magma differentiation at high pressure [Grove et al., 2002, Alonso-Perez et al., 2009, Müntener et al., 2001], together with AFC and MASH. The integration and partial melting of xenoliths [Daly, 1933, Green, 1994] during the transfer and storage of basaltic magma in intermediate reservoirs in the crust is yet another process associated with assimilation and the resulting geochemical magma characteristics. Huppert and Sparks [1985] considered thermal erosion along dyke conduits due to turbulent ascent of magma and the accompanied geochemical changes for primitive magmas such as komatiites and picrites. Energy-constrained open system magmatic processes describing the thermal potential of crustal assimilation during fractionation of hydrous mantle derived magmas and its influence on the geochemical evolution of the differentiating magma were described by Spera and Bohrson [2002] andThompson et al. [2002]. Moreover, textural evidence from xenocrysts, such as reserved zoning and partially resorbed crystals [Gerlach and Grove, 1982, Green, 1994, Kaczor et al., 1988], are a key feature in recognizing mixed magmas that were affected by assimilation processes. The presence of a glass fraction in xenoliths or wallrocks [Petcovic and Grunder, 2003, Kaczor et al., 1988] is an unequivocal feature of the thermal effect of hot primitive basaltic magma on crustal rocks.

A mafic post-plutonic dyke swarm of the southern Adamello Batholith (Fig. 4.1) reveals ample evidence for mechanical desintegration and partial melting of a mainly tonalitic wallrock in outcrop, which is accompanied by crystal textures indicating hybridisation of basaltic magmas. The investigated rocks represent an example of shallow (9-11km depth; [John and Blundy, 1993, Stipp et al., 2004]) crustal assimilation where evidence can directly be inferred from the field relationships. Basaltic dyke swarms of up to 15m in width across strike show a closely spaced network of single dykes that partly coalesce to thicker dykes. The close spacing of multiple and composite dykes creates an extended surface at the dyke margins against the tonalitic host rock. Furthermore, xenoliths are commonly present, indicating mechanical shattering and incorporation of the host rock into the moving magma.

This contribution examines the thermal effect of such a dyke swarm, comprised of a primitive mantle derived basaltic magma with closely spaced single dykes over tenths of meters on the host rock and its implications on the geochemical evolution of such a magma. Due to the relatively fast transfer of magmas in such a setting with practically no residence time, the mechanism for assimilation is rather different than in the case of proposed more sustained assimilation in the EC-RAFC process [Spera and Bohrson, 2002]. Thus, major element composition is not expected to change considerably through the proposed crustal assimilation process at relatively shallow level. Trace element concentrations and radiogenic isotope ratios that fingerprint magma sources and contaminants can however be modified to a larger extent, even though the magma retains a primitive character in terms of major elements.

4.3 Geological Setting

The Adamello Batholith [Rath, 1864, Salomon, 1908] is located in the Northern Italian Alps, north of Brescia and has an extent along its central axis of several tenths of kilometers, from the southernmost oldest plutonic units in the area of Passo Croce Domini between Val Camonica and Val Sabbia/Val di Chiese, to the northernmost plutonic units in the area of Dimaro where the Tonale and the Giudicarie Line form a triple junction. In the southern part of the Batholith, a continuous dyke swarm composed of several

generations (Fig. 4.1: 2A, 2B, 2C, 3) spreads over the entire Re di Castello intrusive suite [Brack, 1984] and ranges as well into the adjacent Triassic sedimentary wall rock sequence. The entire dyke swarm spans a large compositional range from basalts to dacites. The compositional and petrographic characteristics of dykes are described in more detail in an accompanying paper [Hürlimann et al., in prep.a] and reveals a large range from olivine-tholeiites (Ol-tholeiites) to dacites. This contribution focuses on basaltic (2A) and basaltic-hybrid (2B) dykes (Fig. 4.1) building an important part of this regional dyke swarm. Composite intrusive structures (Fig. 4.2) of these dykes are a common feature expressed by multiple magma injections into each other. These types of dykes (2A, 2B) extend from the Val Fredda-Monte Stabio-Monte Frerone area in the SW to the Monte Re di Castello-Cima Sablunera area at the northeastern termination (Fig. 2.2). Petrographically, the rock types range from olivine-clinopyroxene-plagioclase-phyric basalts (2A) to hybrid-basalts (2B), containing coarse-grained amphibole, quartz and plagioclase xenocrysts indicating input of assimilated material. In relative time sequence, the regional dyke swarm crosscuts earlier picro-basaltic and Ol-tholeiitic dykes of generation (1B) (Fig. 4.1).

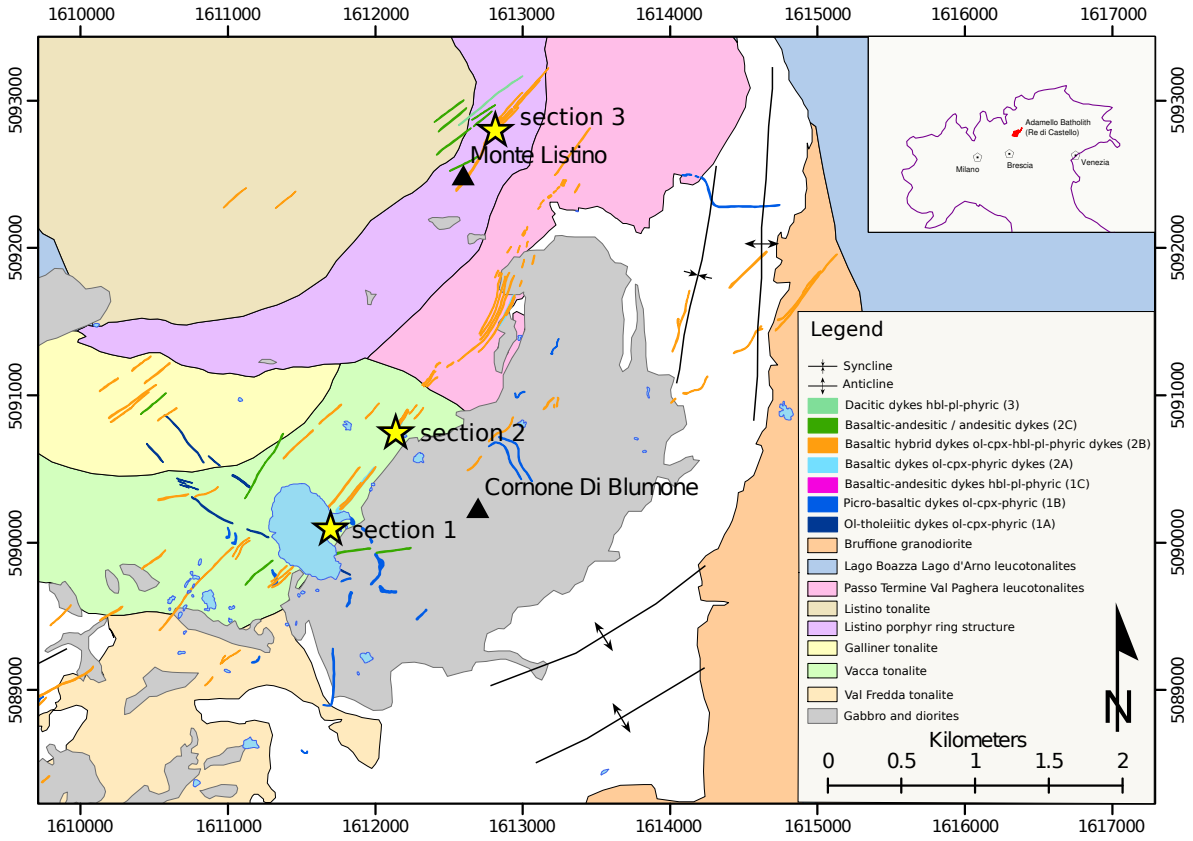

Figure 4.1: The southern part of the Adamello Batholith, located in the central southern Alps north of Brescia. Yellow stars indicate locations of detailed cross sections of Fig. 4.3 and Fig. 4.5. Val Fredda Complex (VFC) in the SW corner, comprised by Val Fredda tonalite intruded by dioritic and gabbroic intrusives. The Lago della Vacca Complex (LVC) includes the Vacca tonalite and Galliner tonalite. The Blumone Complex is a gabbroic stratified sequence, composed of a range of rock types including plagioclase-bearing wherlites; granular olivine-gabbros; granular gabbros; granular clinopyroxene-bearing anorthosites to anorthositic gabbros; coarse-grained magnetite and hornblende ultramafics.

The Val Fredda Complex (VFC), together with the Lago della Vacca Complex (LVC) and Blumone Complex [Blundy and Sparks, 1992, Brack, 1981, Ulmer, 1986, Ulmer et al., 1983, Schoene et al., 2012, Bianchi and Dal Piaz, 1937] as part of the plutonic host rock of the regional dyke swarm builds the southernmost and oldest (42-43 Ma [Schoene et al., 2012, Schaltegger et al., 2009]) intrusive complex of the Adamello Batholith. The VFC has been interpreted as intrusion of mafic sheets into a partially solidified felsic tonalitic and granodioritic host, comprising dioritic and gabbroic intrusives [Blundy and Sparks, 1992]. The LVC is bordered by the high-K marginal tonalite, the Vacca tonalite and the Galiner granodiorite [John and Blundy, 1993]. East of the LVC is the older gabbroic, stratified Blumone Complex that is composed of a range of rock types including plagioclase-bearing wherlites; granular olivine-gabbros; granular gabbros; granular clinopyroxene-bearing anorthosites to anorthositic gabbros; coarse grained magnetite and hornblende ultramafics [Ulmer et al., 1983, Ulmer, 1986]. John and Blundy [1993] proposed an emplacement model for the VFC, LVC and the Blumone Complex with an early phase of brittle fracturing and stoping of country rocks [Brack, 1983], which goes over to an incremental forceful intrusion through inner magma pulses into partially solidified preceding plutonic masses. The regional dyke swarm comprising basalts (2A) and basaltic hybrids (2B) is clearly younger than VFC, Blumone Complex and LVC revealed through crosscutting relationships [Hürlimann et al., in prep.b]. Moreover, basalts (2A) and basaltic hybrids (2B) intrude into the Listino Ring Structure [Brack, 1983, 1984] and the Passo Termine and Val Paghera leucotonalites [Callegari and Brack, 2002]. The ring-shaped structure of Listino is comprised of a steeply inwards dipping zone that Brack [1983, 1984] interpreted overall as a cylindrical structure. A heterogeneous suite of fragments of mafic, ultramafic and sedimentary rocks, synplutonic mafic dykes, and mafic enclaves within a medium-grained porphyritic tonalite and granodiorite [John and Blundy, 1993] characterize this ring zone.

The three examined cross sections across a dyke swarm of basalts (2A) and basaltic-hybrids (2B) are located either within the Vacca tonalite (section 1&2: Fig.4.3) or the Listino porphyry ring structure (section 3: Fig. 4.5) as located in figure 4.1.

4.4 Field Relations and Petrography

Three different cross sections reveal details in dyke thickness and spacing across strike in a zone that was intruded by an extensive network of closely spaced single dyke threads. These zones further display extensive parallel to subparallel fractures or jointing associated with these dyke networks. Outcrops of these 10 to 15m wide intrusive zones (Fig. 4.3, 4.5) exhibit different stages of the thermo-mechanical interaction of the intruding basaltic magma and the brittle elastic response of the mainly tonalitic host rock in the detailed examined localities.

Particularly for section 1 and 2 (Fig. 4.1) situated within the Vacca tonalite, an early stage of intrusion is characterized by the advancement of extensive fracturing in front, in the tip region during propagation of dykes as described by Pollard [1987]. In dyke tip regions, an accumulation of several stringer-like dykelets adjoining each other is commonly associated with chills on a millimeter scale, depicted in Figure 4.2b, forming in some cases small sheeted dykes on a centimeter scale. Thicker dyke strings in the range of $>$0.3m concentrate crystals towards the central part, with abundant coarse- to medium-grained crystals. These thicker dykes though still preserve the aphyric to fine-grained chills that are similar to the texture

and phase assemblage found in the accumulation of thin dyke stringers. At a later stage, the dyke network is intruded by a distinctively different generation of a basaltic hybrid (2B) (Fig. 4.2).

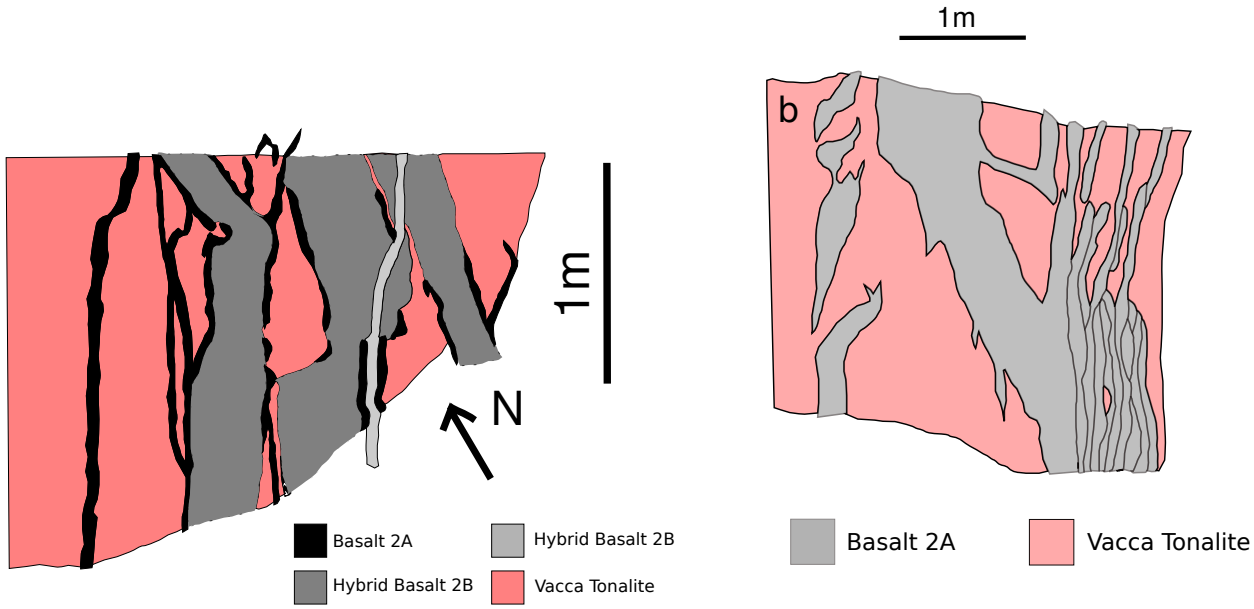

(a) (b)

Figure 4.2: (a) Detailed outcrop map of dyke swarm shown in Figure 4.3, which intruded into the Vacca tonalite. Margins of larger dykes are olivine-clinopyroxene-plagioclase phyric basalts (2A). Thick dykes have a crystal-rich basaltic-hybrid (2B) partly with abundant amphibole and plagioclase xenocrysts, apart from olivine, clinopyroxene and plagioclase phenocrysts and microphenocrysts. These basaltic-hybrids show multiple generations. (b) Accumulations of small basaltic olivine-clinopyroxene-phyric basaltic (2A) adjoining dykelets with millimeter scale internal chilled margin are a common texture in dyke tip regions observed in locations of Fig. 4.3.

Some different macroscopic textures are present in section 3 from a dyke swarm that intruded into the Listino ring structure. This locality shows a 4-5m wide dyke zone of which 1-2m are composed of an intrusion breccia of a basaltic-hybrid dyke (2A, 2B), as seen in figure 4.7, which is set in the partially molten tonalite of the Listino porphyry ring structure. In a similar way as in section 1 and 2, multiple succeeding injections into each other characterize this zone.

Dyke Cross Sections

The detailed cross sections record swarms with close spacing of individual basaltic dykes that in an alternating way coalesce and split again. These swarms were mapped over a width of up to 20m in cross section across the dyke strike. Detailed thickness measurements of the individual dykes and the spacing between were obtained (Fig. 4.3, 4.5). Additionally, all fractures and jointing present for section 1 and 2 (Fig. 4.3) were recorded. Moreover, the different sections represent different levels of altitudes for the same intrusive zones along the strike.

Section 1 is situated inside the Lago della Vacca (altitude: 2359m), a hydropower lake, that is normally submerged by water and section 2 is located at higher altitude in the trough between Cima Laione and

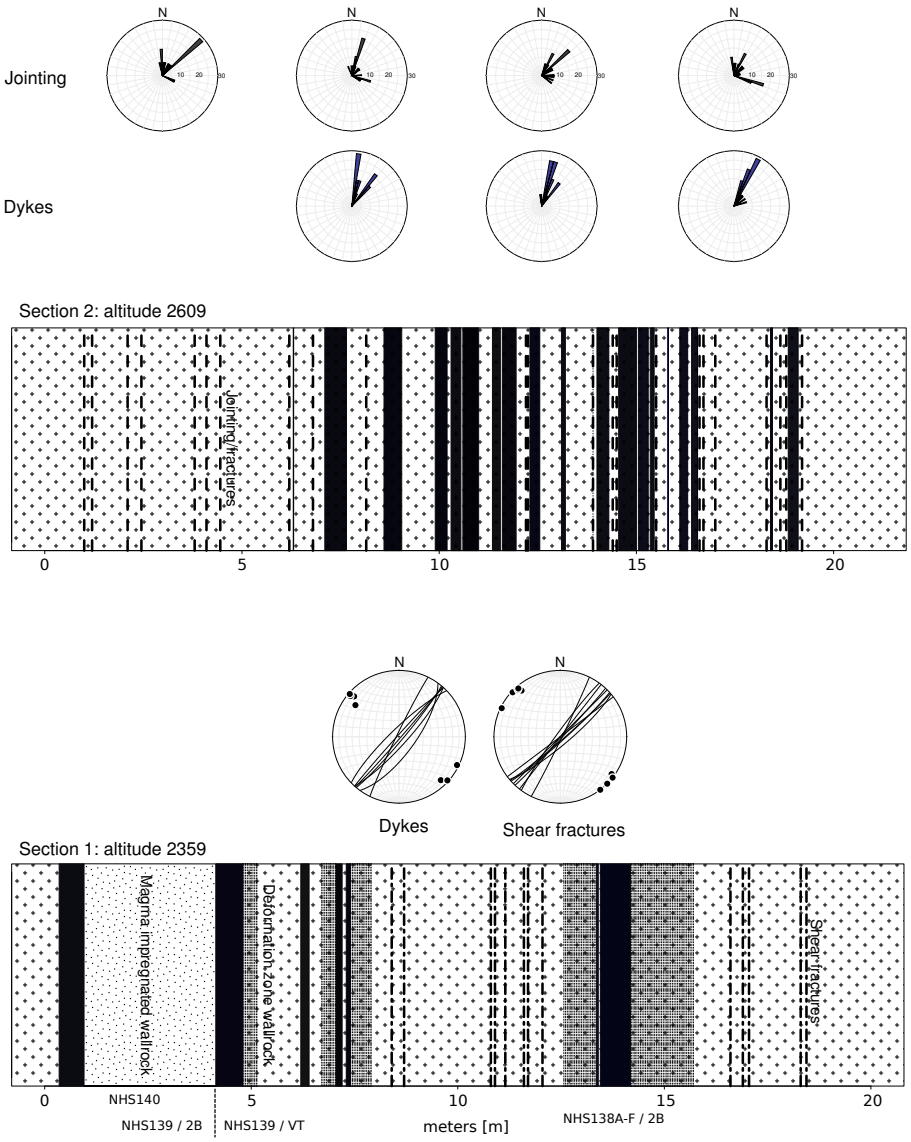

Figure 4.3: Two cross sections exhibiting the record of dyke thickness and dyke spacing of a swarm that can be followed from the Lago della Vacca over the ridge between Cima Laione and Passo Blumone. Section 1 is located inside the Lago della Vacca and normally submerged by water. Section 2 is higher in altitude, located in trough between Cima Laione and Cornone Blumone.

Cornone Blumone. Section 2 shows a closely spaced network of dykes commonly not exceeding >0.5m. Dyke parallel jointing is frequent and the spacing of these fractures decreases in the vicinity of the individual dyke margins. Parallel to subparallel jointing prevails in the different distinguished 5m wide zones with a high frequency of dykes. On a more regional perspective (Fig. 4.4), not all jointing is parallel to

sub-parallel to the dyke swarm containing the basalts (2A) and basaltic-hybrids (2B). Two dominant sub-vertical to vertical sets of joints are present, with one striking NE-SW and the other NW-SE. Section 1, located at lower altitude of the same intrusive zone along the strike, shows some thicker dykes and an up to 4m wide zone (Fig. 4.7a) where the single dykes from section 2 appear to coalesce to one single dyke. This zone is characterized by zones of partial melting of the Vacca tonalite (Fig. 4.7c) host rock at dyke margins (Fig. 4.3) and is further characterized by diffuse impregnation of the tonalite by a basaltic magma, which gives the host a light green colour. High frequency of jointing parallel to the dyke margins results in deformation zones similar to section 2. These deformation zones fade out away from the margin into the non-intruded tonalitic host. Based on the difference in altitude (~250m), a thick dyke splits up higher up and laterally along the strike towards NE into several individual thinner dykes (<0.5m).

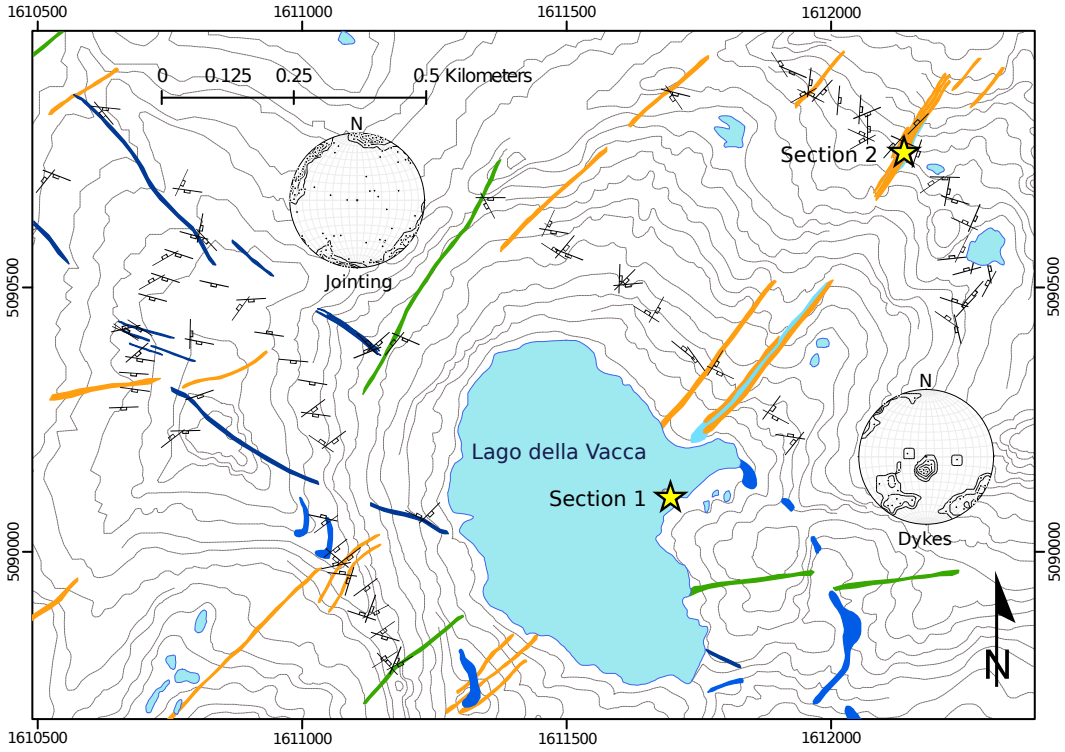

Figure 4.4: Structural map of the Lago della Vacca area displaying the measured planes (stereographic projection: Schmidt net) of all the different jointing surfaces (black symbols) in the rather homogeneous Vacca tonalite. Measurements of planes of dyke margins are shown for comparison in a stereographic projection. For the legend for dykes, see Figure 4.1.

Section 3 is a composite of several sections (Fig. 4.5a,b,c) at slightly different altitudes (difference between individual sections: ~25m). At the highest point on the NE-side of Monte Listino, a 5m thick basaltic-hybrid (2B) dyke is present that splits up into a number of single dykes towards NE, which for the bulk part are again <0.5m in thickness. This relationship can be traced on well-polished rock slabs along the strike and is comparable to the pattern observed between section 1 and 2 in the Lago della Vacca area. This splitting of a thick dyke into individual thinner ones appears to be a lateral effect along the strike and not related to different depth levels in the crust. The intrusion breccia is characterized by

sharp chilled margins of breccia clasts against the tonalitic host rock in the internal brecciated zone (Fig. 4.5, 4.7b,f). The form of the clasts consisting of basaltic-hybrid magma (2B) is angular to sub-angular. Partially molten tonalitic host rock of the Listino porphyry ring structure builds up the matrix of this brecciated zone. In sections b) and c), the individual dykes are characterized by sharp chilled margins with 1-2cm thickness in contact with host rock tonalite. Sections b) and c) are devoid of intrusion breccias within the individual dykes. In contrast to earlier generations of syn-plutonic mafic and felsic dykes within the Listino ring structure described in Brack [1984], these younger basaltic hybrid dykes (2B) show no deformation features at all.

A data set recording dyke-thickness and -spacing is available from the detailed cross sections of the three localities. Detailed measurements of dyke spacing are scarce [Menand, 2010], despite the fact that they provide crucial information. In the present case, both thickness and spacing measurements (Fig. 4.6) show a log-normal distribution. Dyke thickness and spacing are non-fractal distribution or scale-invariant [Mandelbrot and Blumen, 1989]. This is a common characteristic of such mafic dyke swarms reported in previous studies [e.g. Walker et al., 1995, Jolly and Sanderson, 1995, Glazner et al., 2008]. The mean thickness is 0.28m and the median amounts to 0.25m, though a more useful measure for such a distribution is the geometric mean [Glazner et al., 2008] with a value of 0.20m. For the spacing of the dykes the summary statistic measurements are as follows: 0.44m for the mean, 0.25m for the median and 0.25m for the geometric mean. In general, the thickness and spacing measurements of dykes do not conform to a power-law distribution in these cumulative frequency plots and there is a flattening off of the cumulative frequency for thicknesses $<$0.1m, as reported by Jolly and Sanderson [1995] for the Mull dyke swarm. As noted already by Jolly and Sanderson [1995], dykes with thicknesses of 0.01 to 0.1m would easily be recognized under continuous outcrop conditions, as is the case with the glacially polished slabs on the NE-side of Monte Listino and in the trough between Cima Laione and Cornone Blumone. The scarcity is a real feature of the distribution and not a bias due to sampling. The poor fit to a power-law model for thickness and spacing of the dykes further suggests a relation with characteristic length scale, which is best described by the median or the geometric mean [Menand, 2010, Jolly and Sanderson, 1995, Glazner et al., 2008].

Petrography of Basaltic Dykes and Wallrock Tonalites

Within the recorded sections, basaltic magmas can be divided into four different types based on petrography. An early basaltic generation (2A) occurs at dyke margins and as accumulations of thin dyke stringers (Fig. 4.2b). This generation or early, non-hybrid basaltic phase is characterized by olivine and clinopyroxene phenocrysts, which are set in a cryptocrystalline matrix at the outermost dyke tips. Micro-phenocrysts of clinopyroxene and plagioclase partially indicate a fluidal texture. In non-completely quenched zones, the matrix consists of microlites of plagioclase. In rare cases, as displayed in Figure 4.8b, olivine is pristine in the quenched parts such as the very thin outermost dyke tips. In the more massive, less rapidly cooled parts of the dyke, olivine is present mainly as chlorite-epidote-calcite pseudomorphs. Medium-grained euhedral clinopyroxene phenocrysts exhibit partially sieve textures in the core regions. These early basalts (2A) display the effect of mechanical shattering during emplacement and the incorporation of anhedral quartz and subhedral plagioclase at the extreme dyke-tip region.

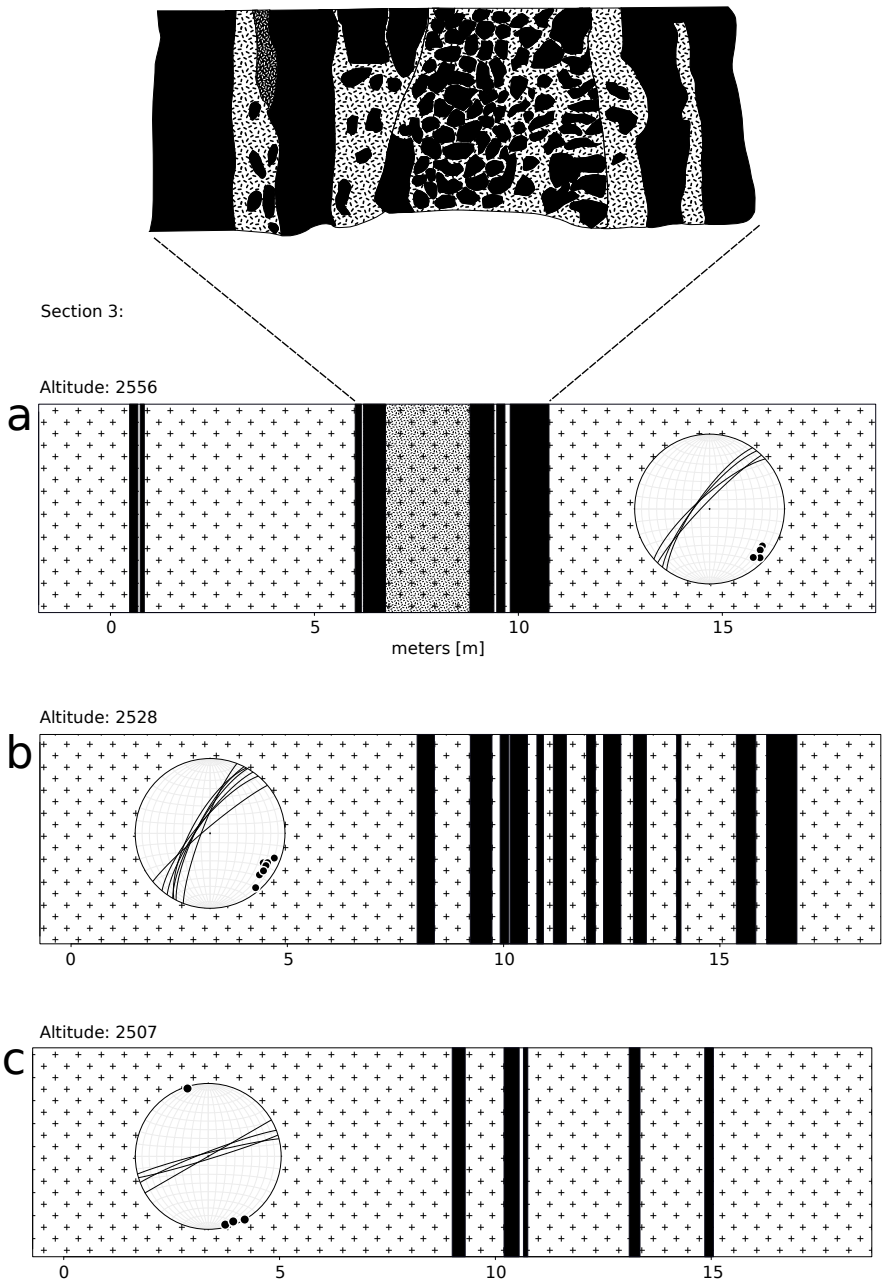

Figure 4.5: (a-c) Intrusive zone comprised by either an up to 5m thick dyke or split up into a number of individual dykes with <0.5m thickness. (a) In the thick portion of this intrusive zone, an intrusion breccia occurs, with sharp chilled margins towards the tonalitic host rock of the Listino porphyry ring structures. (b) and (c) The thick dyke gradually splits up laterally towards NE into individual dykes and stereographic projections (Schmidt net) indicate a slight deflection of the orientations of the dykes, leading to a more ENE-WSW strike.

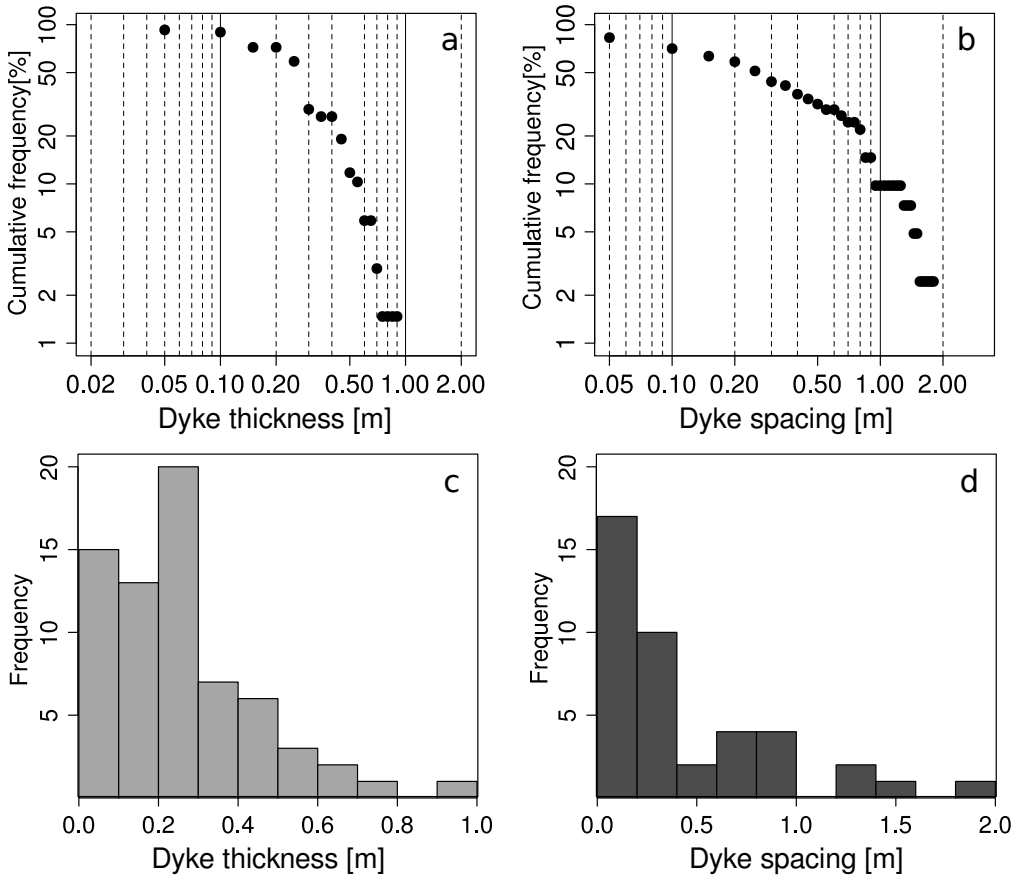

Figure 4.6: Dyke-thickness (a) and -spacing (b) from sections 1, 2 and 3 (Fig. 4.3, 4.5) are plotted in cumulative frequency diagrams to assess their spatial configuration. Histograms of thickness (c) and spacing (d) of dykes follow an overall log-normal distribution.

Thicker dykes commonly occur as a composite structure with an early, thinner marginal zone composed of quenched basalts (2A) (Fig. 4.9a). The central part is characterized by abundant coarse-grained amphibole (Fig. 4.9d) and plagioclase xenocrysts. Medium- to coarse grained clinopyroxene, brownish amphibole, and plagioclase are present as well. Euhedral pseudomorphs of olivine consist of similar phase assemblages, as in the case of basalts (2A). Clinopyroxene is euhedral and contains slightly brownish spinel inclusions. Plagioclase exhibits polysynthetic albite and carlsbad twinning for euhedral grains. Amphibole and plagioclase occur, as well as medium- to fine-grained microphenocrysts. Amphibole xenocrysts (Fig. 4.9a, b, d) are characterized by cores that show resorption sieve textures with abundant magnetite inclusions and have later overgrowths that correspond to the pristine amphibole pheno- and microphenocrysts. Similarly, plagioclase xenocrysts display sieve textures cores or outer bands that indicate partial resorption. As for amphibole xenocrysts, these xenocrystic plagioclases exhibit a later overgrowths corresponding to pheno- and micro-phenocrysts. Coarse- to medium-grained quartz crystals show reaction textures at their borders with acicular clinopyroxene bordering them. The matrix of such basaltic-hybrid (2B) dykes containing abundant xenocrysts is comprised of amphibole microlites set in interstitial plagioclase. Pheno- and

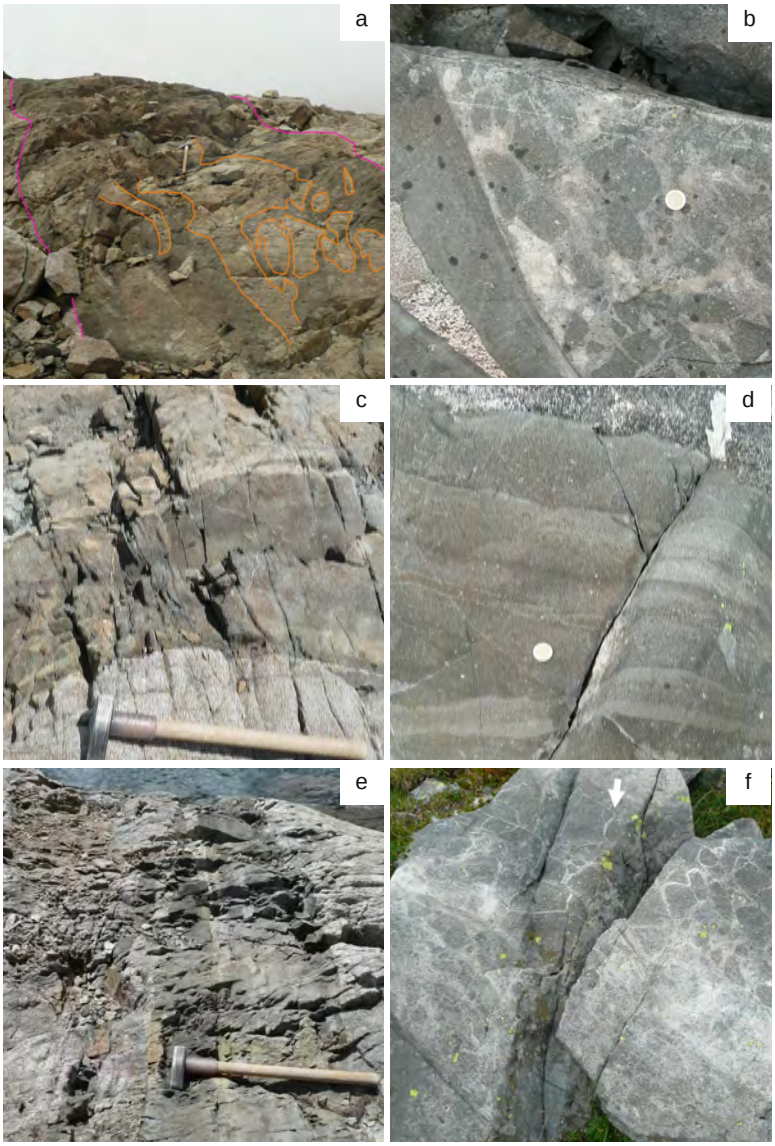

Figure 4.7: (a),(c) and (e) Basaltic hybrid dyke swarm of section 1 and 2 (Fig.4.3) that intruded into the Vacca tonalite in the Lago della Vacca-Cima Laione area. (b), (d) and (f) Basaltic-hybrid dyke swarm (section 3) intruded into the Listino porphyry ring structure and the Passo Termine and Val Paghera leucotonalites. (a) Up to 10m wide zone shows a network of dykes that alternates coalesce and split, including large blocks of the tonalitic host rock. (b) Up to 5m thick basaltic hybrid dyke with an internal part that displays brecciated dark green basaltic magma in a partially molten tonalitic matrix. (c) Partially molten tonalitic host rock in contact with a basaltic hybrid dyke. Note back veining of the molten tonalitic host into the basaltic dyke and absence of extensive melting of the tonalitic host on the opposite dyke margin. (d) 4m wide zone exhibiting multiple basaltic dyke injections into each other with internal chilled margins. (e) Deformation of the host rock in the form of dyke parallel to sub-parallel fractures. (f) Intrusion breccia as in (b) of a basaltic-hybrid set in partially molten tonalite.

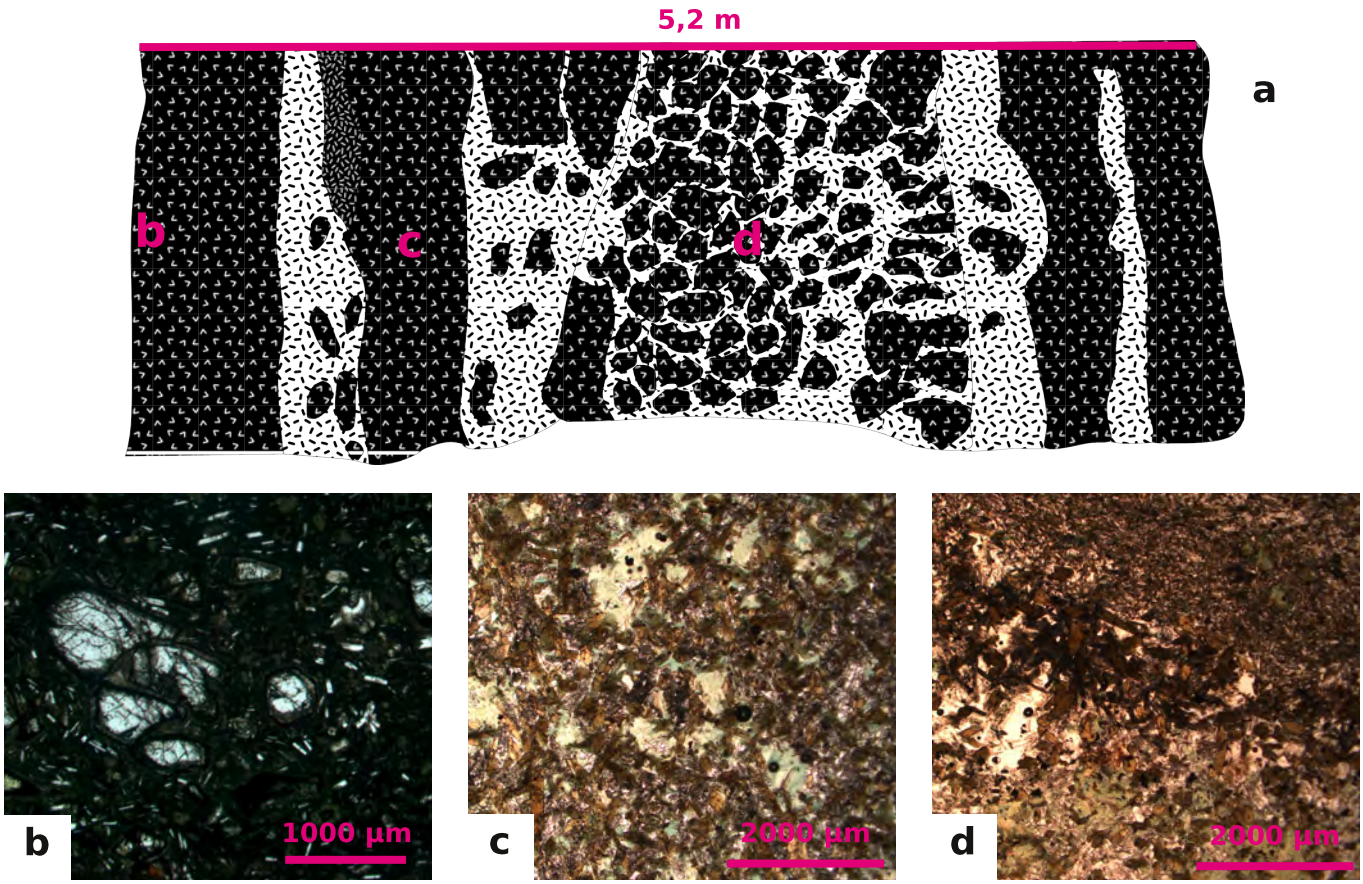

Figure 4.8: (a) Intrusion breccia of section 3 (Fig. 4.5, 4.7b) mantled by basaltic (2A) and basaltic hybrid (2B) dyke. (b) In the outermost dyke tips within the quenched parts, olivine phenocrysts are preserved. (c) Massive basaltic hybrid parts of the dyke (thickness: >5m) where olivine is pseudomorphosed, comprised of chlorite, epidote and hematite. Inclusions of brownish Cr-rich spinel are common in pristine olivine and olivine pseudomorphs. The matrix consists of medium-grained brown euhedral amphibole micro-phenocrysts and subhedral to interstitial plagioclase. (d) Contact of a basaltic intrusion breccia clast against the partially molten host tonalite of the Listino porphyry ring structure. The inside of the basaltic breccia clasts composed of coarse- to medium-grained phenocrystic olivine pseudomorphs and a similar matrix as in (c). Medium-grained, brownish amphibole micro-phenocrysts concentrates at immediate contact with the more felsic magma. The brighter felsic matrix of the breccia is characterized by fine-grained microlites of amphibole and interstitial plagioclase and quartz. Alignment of amphibole microlites indicate a fluidal texture.

microphenocrysts are aligned sub-parallel to dyke margins in the rapidly quenched parts. On a small scale as depicted in Figure 4.2a, a second basaltic hybrid generation (Fig. 4.2a bright coloured basaltic hybrid (2B)) displays enrichment in amphibole and plagioclase phenocrysts or xenocrysts. This generation shows increased modal abundance of pristine amphibole pheno- and micro-phenocrysts (15%), together with abundant coarse-grained amphibole xenocrysts (5%) (Fig. 4.9d). Furthermore, coarse-grained xenocrystic plagioclase (5%) is present, apart from euhedral olivine pseudomorphs (2%) and euhedral clinopyroxene (2%).

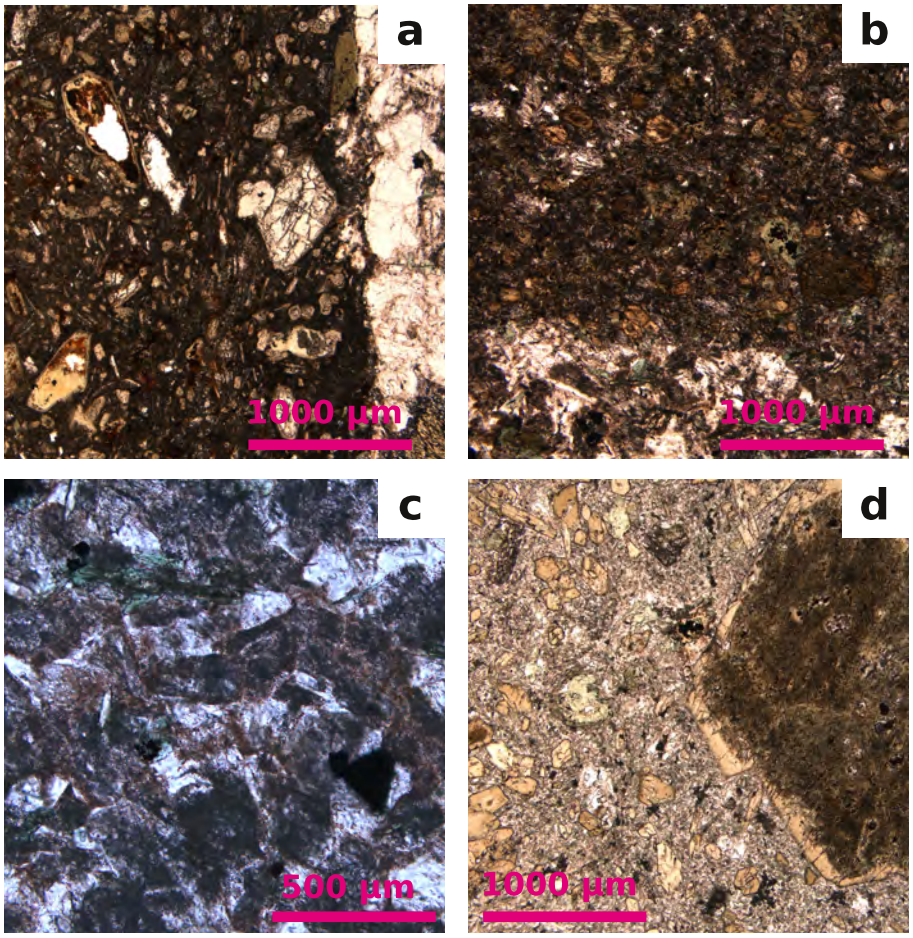

Figure 4.9: (a) Cryptocrystalline chilled margin of basaltic hybrid (2B) dyke in contact with host tonalite. Phenocrysts are euhedral clinopyroxene and pseudomorphs of olivine, consisting of chlorite and calcite together with pristine brownish Cr-spinel inclusions. (b) Basaltic-hybrid (2B) with abundant amphibole micro-phenocrysts (15%) in contact with tonalitic host rock. This diffuse contact corresponds to the juxtaposition of patially molten or melt impregnated tonalite with the actual basaltic hybrid (2B) dyke (Fig. 4.3, section 1). (c) Partially molten Vacca tonalite (Fig. 4.3) with decomposed plagioclase and amphibole with a brownish glass between grain boundaries. (d) Latest amphibole-plagioclase-phyric basaltic hybrid dyke (2B) generation of outcrop in figure 4.2a. Euhedral olivine occurs as pseudomorphs in the form of chlorite and calcite.

The intrusion breccia of the thick (~5m) dyke found in the Listino ring structure shows the juxtaposition of olivine-phyric basaltic clasts against (Fig. 4.8d) a more felsic matrix, consisting entirely of partially molten host tonalite or a mixture of the partially molten tonalite with primitive basaltic magma. The basaltic clasts are enriched in coarse-grained olivine (10-15%), in comparison to the much finer-grained felsic matrix, with a fluidal texture of amphibole microlites set in mainly interstitial plagioclase.

The melt impregnated zone of the Vacca tonalite in section 1 (Fig. 4.3) is characterized by features of partial melting, in the form of brownish to bright glass located between grain boundaries of plagioclase (Fig. 4.9c) and pseudomorphs of amphibole. Plagioclase cores commonly exhibit sieve textures.

4.5 Analytical Methods

Bulk Rock Chemistry

After initial size reduction employing a hydraulic press, all samples were first ground to a fine powder in an agate mill. Thereafter, an aliquot was heated to 1050°C in a muffle furnace to determine the loss of ignition by mass difference. The fired product was mixed with the appropriate amount of $Li_2B_4O_7$ (1.2121:6) and fused for five minutes in a Pt-crucible and subsequently poured in a Pt-casting dye and quenched to a glass blead. Major element compositions of whole rock samples were determined on glass beads by X-ray fluoresence (XRF) analysis, using a PANalytical Philips PW2400 spectrometer at the University of Lausanne. BHVO-1, NIM-N, NIM-G and SY-2 standards were used for quality control. Uncertainties of XRF analyses are in the range of 0.5 wt.% (2 sigma) for major components such as SiO_2 and 0.006% for a minor component such as NiO. The trace-element concentrations of bulk rocks were determined on the same XRF glass beads with a Geolas 200M 193 nm ArF excimer laser ablation system, interfaced with an Elan 6100 DRC quadrupole mass spectrometer (LA-ICP-MS) at the University of Lausanne. The performance of the LA-ICP-MS was optimized with the NIST SRM 612 glass in order to improve the sensitivity (Mg>10000cps and La>40000cps). During this optimization, doubly charged ions ($Ba^{++}/Ba^{+} < 2\%$) and oxide production rates (ThO^{+}/Th^{+}) were minimized. Three repeat measurements were performed on the glass beads with a laser pit size of 120μm using a laser frequency of 10Hz and energy of 160mJ, which is equivalent to 12 J/cm2. Helium was used as a cell gas carrier. Background and ablation interval acquisition times were 70 and 30-35 seconds respectively. Dwell times for different isotopes range from 10 to 20ms employing a peak hopping mode. Absolute trace-element concentrations were determined using CaO wt% (determined by XRF) as an internal standard and NIST 612 or NIST 610 as an external standard. The average elemental abundances are taken from Pearce et al. [1997] and data was reduced with LAMTRACE [Longerich et al., 1996, Jackson, 2008] software.

Mineral Chemistry

Major element compositions of minerals were determined by wavelength-dispersive analysis using a JEOL JXA-8200 electron microprobe equipped with five spectrometers at the University of Lausanne. Samples were polished and carbon coated thin-sections; standards employed are natural minerals and synthetic glasses. Measurements were corrected with the PRZF [Armstrong, 1995] method. The beam current was set to 15nA with an acceleration voltage of 15KeV and beam size was varied between 1μm and 4μm. Major elements on the respective mineral phase were measured for 20s on peak and 10s on background on both sides of the peak. Minor-elements were measured for 30s on peak and 15s on background each side of the peak. Trace-element analysis was performed on the same polished thin-sections using an ELEMENT XR sector field ICP-MS coupled with an UP193-FX ArF 193nm excimer laser ablation system at the University of Lausanne. The LA-ICP-MS system was optimized using NIST SRM 612 glass standard to maximize the sensibility ($La^{139+} > 3.5 \cdot 10^6$cps and $Th^{232+} > 4.5 \cdot 10^6$cps). At the same time, doubly charged ions ($Ba^{++}/Ba^{+}<2\%$) and oxide production ($ThO^{+}/Th^{+} <0.05\%$) were minimized. Helium was used as cell gas (1.00 [l/min]) and Ar was used as sample gas (ranging from 0.690-0.735 [l/min]). The pit size during laser ablation was chosen according to grain size and mineral

texture and varied between 25μm and 100μm. Repetition rate was varied between 5Hz and 15Hz and the laser energy was varied to achieve 5.2-5.8J/cm^2 depending on analysed mineral phase. Acquisition times for background and ablation interval were 120s and 60s respectively for each laser spot. According to expected concentrations, dwell times for measured masses were varied between 10 to 20ms. Absolute trace-element concentrations were determined likewise for glass beads using CaO wt% or alternatively Al_2O_3 (determined by EMPA) as an internal standard and NIST 612 as an external standard. The data was reduced with LAMTRACE [Longerich et al., 1996, Jackson, 2008] and average elemental abundances for the NIST 612 standard were taken from Pearce et al. [1997].

Radiogenic Isotopes

A representative selection of 8 samples for the different dyke rock types was analyzed for whole rock Sr, Nd and Pb isotopic compositions at the Department of Mineralogy, University of Geneva. Approximately 160mg of powdered rock was dissolved in closed Teflon vessels for 7 days on a hot plate at 140°C within a mixture of 4ml of concentrated HF and 1ml HNO_3 15M, following the procedure described by Chiaradia [2009] and Chiaradia et al. [2011]. Samples were subsequently dried on a hot plate, and then redissolved with 3ml of 14 M HNO_3 in Teflon vials at 140°C and desiccated again. The Sr, Nd and Pb separation was performed using stacked columns with Sr-spec, TRU-spec and Ln-spec resins. The applied method is modified after Pin et al. [1994]. Purification for Pb was further achieved through AG-MP1-M anion exchange resin in a hydrobromic medium. Sr, Nd and Pb isotope ratios were analysed using a Thermo TRITON mass spectrometer using Faraday cups in static mode. Pb was loaded onto Re filaments using the silica gel technique and all samples (and standards) were measured at a pyrometer-controlled temperature of 1220°C. Using the standard values of Todt et al. [1996], Pb isotope ratios were corrected for instrumental fractionation by a factor of 0·07% per a.m.u. based on more than 90 measurements of the SRM981 standard. External reproducibility of the standard ratios are 0.05% for $^{206}Pb/^{204}Pb$, 0.08% for $^{207}Pb/^{204}Pb$ and 0.10% for $^{208}Pb/^{204}Pb$. Sr was loaded onto single Re filaments with a Ta oxide solution and measured at a pyrometer-controlled temperature of 1480°C in static mode, using the virtual amplifier design to cancel out biases in gain calibration among amplifiers. $^{87}Sr/^{86}Sr$ values were internally corrected for fractionation using an $^{88}Sr/^{86}Sr$ value of 8·375209. Raw values were further corrected for external fractionation by a value of + 0·03‰, determined by repeated measurements of the SRM987 standard ($^{87}Sr/^{86}Sr = 0{\cdot}710248$). External reproducibility of the $^{87}Sr/^{86}Sr$ ratio for the SRM987 standard is 7 μg^{-1} (1σ). Nd was loaded onto double Re filaments with 1 M HNO_3 and measured in static mode with the virtual amplifier design. $^{143}Nd/^{144}Nd$ values were internally corrected for fractionation using a $^{146}Nd/^{144}Nd$ value of 0·7219 and the ^{144}Sm interference on ^{144}Nd was monitored on mass ^{147}Sm and corrected by using a $^{144}Sm/^{147}Sm$ value of 0·206700. External reproducibility of the JNdi-1 standard [Tanaka et al., 2000] is $<5\mu g\ g^{-1}$ (1σ). $^{87}Sr/^{86}Sr$ and $^{143}Nd/^{144}Nd$ whole-rock compositions were corrected for time-integrated decay of ^{87}Rb and ^{147}Sm using Rb, Sr, Sm and Nd concentrations determined by LA-ICP-MS on bulk-rock glass beads and to an age of 39.8 Ma [Hansmann, 1986, Hansmann and Oberli, 1991] for basaltic (2A) and basaltic-hybrid dykes (2B). The resulting time-integrated corrections are small (less to much less than 500ppm for $^{87}Sr/^{86}Sr$ and less to much less than 100ppm for $^{143}Nd/^{144}Nd$).

4.6 Bulk Rock Chemistry

Major Elements

XRF analyses for basaltic, basaltic-hybrid dykes and the Vacca tonalite host in section 1 and 2 (Fig. 4.3) are reported in tables 4.1, 4.5 and 4.6. Basalts (2A) of the early intrusive phase have SiO_2 contents between 46.8 and 49.0 wt%. MgO ranges between 12.0 and 8.4 wt% (Fig. 4.10a), whereas the hybrid dykes reveal a considerable range in SiO_2 (45-51 wt%) and MgO (11.7-1.7 wt%). TiO_2 (Fig. 4.10b) and CaO (Fig. 4.10d) show distinctively lower contents for the Vacca tonalite (VT) of 0.4-0.65 wt% and 4.41-6.68 wt%. Al_2O_3 (Fig. 4.10c) exhibits a slight enrichment trend among basalts (2A) and basaltic-hybrids (2B). K_2O (Fig. 4.10e) shows a remarkable enrichment for basaltic-hybrid (2B) dykes with values of up to 2.37 wt%. Similarly Na_2O attains higher values for basaltic hybrids with values up to 3.78 wt%. Higher values for K_2O can be partly associated with secondary mobility due to aqueous fluids [Zack and John, 2007] that are present in altered zones of the host rock around dyke tips and bridges [Hürlimann et al., in prep.b]. Though the similarity of the highest Na_2O values of basaltic-hybrid dykes with the content of the Vacca tonalite appears to be an effect influenced by the tonalitic host rock.

Trace Elements

All analyzed trace elements are reported in tables 4.1, 4.5 and 4.6 for basalts (2A), basaltic-hybrids (2B) and the Vacca tonalite host rock of section 1 and 2 (Fig. 4.3). In general trace elements show a larger variability with regard to basaltic-hybrid rocks. In particular, the light-ion-lithophile-elements (LILE) such as Sr, Rb and Ba show a larger scatter (Fig. 4.11a, b, c) that ranges up to values corresponding to the Vacca tonalite host rock.

In the Ni versus Ba diagram (Fig. 4.11c), basaltic hybrids (2B) indicate two different trends; one follows a curved evolution with a distinct bend at very low Ni concentrations, whereas the other trend describes a straighter line between two end members. The two end members are in this case the basalt (2A) on one hand and the Vacca tonalite (VT) on the other hand.

Composition	basalt	basaltic-hybrid	basaltic-hybrid	basaltic-hybrid	basaltic-hybrid	basaltic-hybrid	basaltic-hybrid	basaltic-hybrid
Sample	**NHS079**	**NHS138A**	**NHS138B**	**NHS138C**	**NHS138D**	**NHS138E**	**NHS138F**	**NHS139A**
Generation	**2A**	**2B**	**2B**	**2B**	**2B**	**2B**	**2B**	**2B**
SiO2	48.65	48.33	47.76	48.18	49.32	49.79	50.42	48.73
TiO2	0.83	0.84	0.81	0.81	0.83	0.84	0.85	0.94
Al2O3	15.94	15.71	15.44	15.59	15.7	16.03	16.51	16.91
Fe2O3	8.99	9.1	8.55	9.6	9.37	8.95	8.85	9.38
MnO	0.18	0.17	0.18	0.17	0.18	0.19	0.18	0.21
MgO	9.91	9.43	8.61	9.5	9.04	8.91	8.01	8.09
CaO	10.51	9.96	9.5	9.1	8.84	9.17	8.9	8.99
Na2O	1.57	1.86	2.02	1.88	1.9	1.96	1.85	2.58
K2O	0.94	0.6	1	1.01	1.17	1.01	1	1.26
P2O5	0.15	0.15	0.16	0.14	0.15	0.16	0.16	0.18
LOI	2.31	3.41	5.38	3.37	2.63	2.42	2.39	2.03
Cr2O3	0.09	0.08	0.07	0.08	0.08	0.07	0.07	0.06
NiO	0.02	0.01	0.01	0.01	0.01	0.01	0.01	0.01
Total	100.08	99.65	99.49	99.46	99.23	99.5	99.19	99.37

Table 4.1: Major elements and Cr2O3 and NiO (all in [wt%]) were determined by XRF analysis. Samples NHS138A-F are part of a section across strike of basaltic hybrid (2B) dyke section 1 (Fig. 4.3), with a total thicknesses of 0.73 m.

Composition	basaltic-hybrid	basaltic-hybrid	basaltic-hybrid	basaltic-hybrid	basaltic-hybrid	basaltic-hybrid	basaltic-hybrid	basaltic-hybrid
Sample	**NHS045A**	**NHS045B**	**NHS045C**	**NHS045D**	**NHS045E**	**NHS045F**	**NHS078A**	**NHS078B**
Generation	**2B**	**2B**	**2B**	**2B**	**2B**	**2B**	**2B**	**2B**
SiO2	48.43	46.44	48.78	50.74	50.31	49.04	49.84	50.1
TiO2	0.98	0.95	0.98	1.03	0.96	0.92	0.87	0.84
Al2O3	17.25	17.44	17.48	17.61	17.17	16.81	16.32	17.05
Fe2O3	9.34	9.61	9.07	8.98	8.77	9.04	8.5	8.15
MnO	0.18	0.19	0.16	0.13	0.15	0.18	0.15	0.14
MgO	7.43	8.17	6.47	5.41	6.07	7.73	6.96	6.75
CaO	10.61	10.83	9.33	8.08	8.47	9.4	8.25	7.47
Na2O	2.39	1.96	3.1	3.78	3.53	2.86	2.69	2.98
K2O	0.6	1	1.84	2.3	2.18	1.23	2.28	2.24
P2O5	0.17	0.17	0.18	0.18	0.18	0.16	0.15	0.17
LOI	1.64	2.42	1.69	1.01	1.26	1.88	3.12	3.21
Cr2O3	0.06	0.08	0.05	0.03	0.04	0.06	0.03	0.03
NiO	0.01	0.01	0.01	0	0	0.01	0.01	0.01
Total	99.1	99.25	99.13	99.27	99.09	99.32	99.18	99.15

Table 4.2: Major elements and Cr_2O_3 and NiO (all in [wt%]) were determined by XRF analysis. Samples NHS045A-F and NHS078A-C (Fig. 4.2) are sections across strike of basaltic hybrid (2B) dykes, with thicknesses of 0.2m and 0.08m respectively.

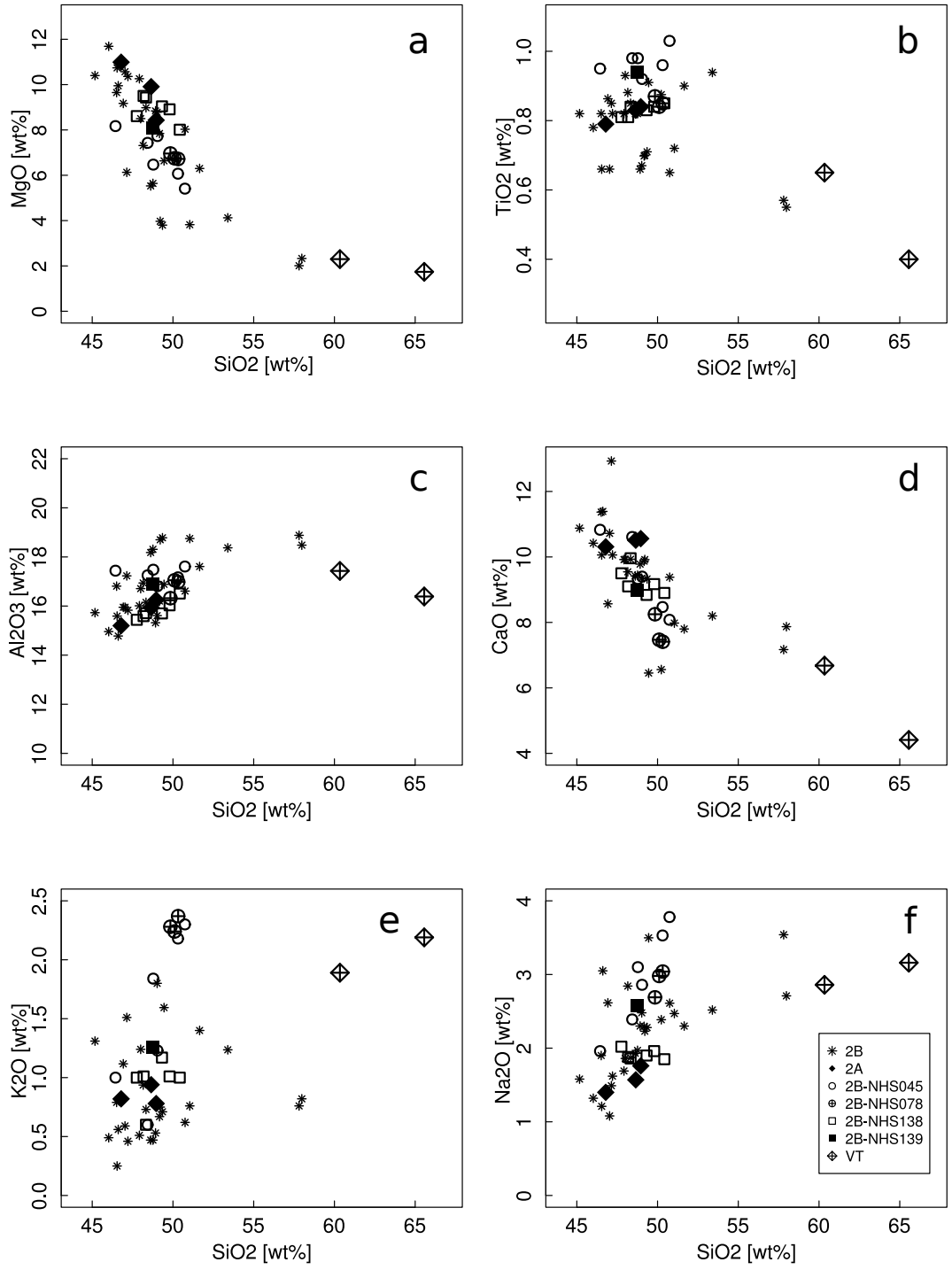

Figure 4.10: Harker diagrams displaying variation of SiO_2 vs. MgO (a), TiO_2(b), Al_2O_3(c), CaO (d), K_2O (e) and Na_2O (f) (all in wt%). Basalt (2A) is ol-cpx-pl-phyric and is devoid of amphibole, plagioclase and quartz xenorcrysts. NHS045 is a 0.2m thick section across a basaltic-hybrid (2B) dyke (Fig. 4.2). NHS078 is a 0.08m thick section across latest generation of basaltic hybrid (2B) dykes in figure 4.2. Sample NHS139 is the part of a basaltic hybrid (2B) dyke in immediate contact with the Vacca tonalite host rock indicated in section 1 (Fig. 4.3). VT stands for Vacca tonalite, the host rock for section 1 and 2 (Fig. 4.3).

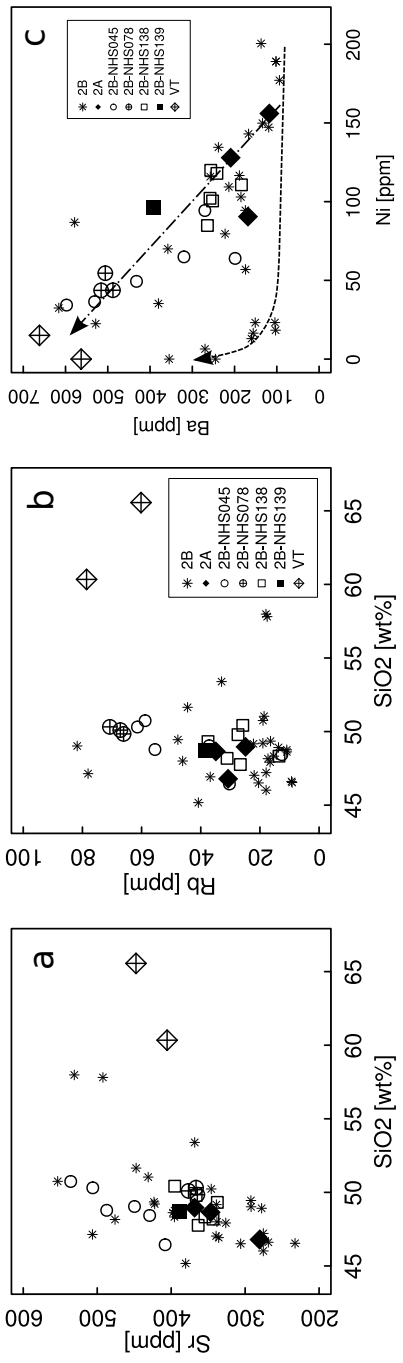

Figure 4.11: Trace element variation diagrams for (a) Sr [ppm] vs. SiO_2[wt%] and (b) Rb [ppm] vs. SiO_2[wt%]. (c) Variation between Ni [ppm] and Ba [ppm] shows two distinctive trends. A curved pure crystal fractionation trend and mixing trend between basalt (2A) and Vacca tonalite (VT). For further details see text.

Composition	**basaltic-hybrid**	**melt impregnated tonalite**	**partiallly molten tonalite**	**tonalite**	**basaltic-hybrid bulk rock**	**recal. Matrix (chilled margin) = liquid**
Sample	**NHS078C**	**NHS140**	**NHS139B**	**RDC3**	**NHS053**	**NHS053**
Generation	**2B**	**2B**	**2B**	**Vacca Tonalite**	**2B**	**2B**
SiO2	50.32	51.65	65.56	60.34	48.00	49.63
TiO2	0.85	0.90	0.40	0.65	0.93	0.96
Al2O3	16.98	17.61	16.39	17.43	16.71	17.14
Fe2O3	8.07	8.34	4.13	1.28	9.41	10.04
MnO	0.14	0.16	0.10	0.13	0.18	0.19
MgO	6.72	6.30	1.74	2.30	8.50	8.65
CaO	7.41	7.80	4.41	6.68	9.93	9.83
Na2O	3.04	2.30	3.16	2.86	1.86	1.95
K2O	2.37	1.40	2.19	1.89	1.24	1.34
P2O5	0.17	0.17	0.18	0.23	0.16	0.17
LOI	3.12	2.79	1.39	n.a.	2.16	n.a.
Cr2O3	0.03	0.02	0.00	n.a.	0.07	0.07
NiO	0.01	0.00	0.00	n.a.	0.01	0.01
Total	99.23	99.45	99.63	98.54	99.15	100

Table 4.3: Major elements and Cr2O3 and NiO (all in [wt%]) were determined by XRF analysis. Sample NHS078C is part of a section across strike of a dyke with a thickness of 0.08m. The matrix or chilled margin of the basaltic hybrid (2B) NHS053 consists of a recalculation based on bulk rock XRF analysis explained in the text and a LA-ICP-MS laser scan of the same chilled margin.

Composition	basalt	basaltic-hybrid	basaltic-hybrid	basaltic-hybrid	basaltic-hybrid	basaltic-hybrid	basaltic-hybrid	basaltic-hybrid
Sample	**NHS079**	**NHS138A**	**NHS138B**	**NHS138C**	**NHS138D**	**NHS138E**	**NHS138F**	**NHS139A**
Generation	**2A**	**2B**	**2B**	**2B**	**2B**	**2B**	**2B**	**2B**
Be	1.777	n.a.	n.a.	n.a.	n.a.	n.a.	n.a.	n.a.
Sc	36.1	38.1	33.2	36.2	36.3	34.6	34.9	36.1
V	244	250	240	260	255	257	259	273
Cr	668	607	563	649	591	560	516	498
Co	38.5	37.0	32.6	36.4	35.2	34.6	32.3	34.7
Ni	127.9	110.7	102.1	117.9	119.9	100.4	84.8	96.5
Cu	61.4	16.1	15.4	17.2	16.9	20.5	24.0	21.4
Zn	189.9	162.3	174.7	185.0	221.6	185.7	194.4	186.1
Ga	15.4	16.5	15.5	16.2	16.6	16.9	17.3	17.6
Ge	2.2	2.4	1.6	2.7	2.6	2.5	2.5	2.6
As	2.263	n.a.	1.838	n.a.	n.a.	n.a.	1.365	1.828
Rb	34.9	13.5	26.6	31.1	37.6	27.4	25.8	38.4
Sr	347	354	363	343	338	366	395	388
Y	15.4	16.0	15.7	15.0	15.6	15.6	16.1	20.5
Zr	75	76	76	70	71	76	81	85
Nb	5.5	5.8	5.8	5.1	5.7	5.8	6.5	6.5
Mo	1.9	1.8	2.0	2.0	1.8	1.7	2.5	2.0
Cs	0.62	0.31	0.61	0.63	0.68	0.46	0.45	1.09
Ba	209	184	258	242	256	252	264	393
La	15.0	15.6	15.9	14.7	15.6	16.1	17.7	16.2
Ce	31.1	31.9	32.2	29.6	30.9	32.3	35.4	40.7
Pr	3.73	3.72	3.78	3.53	3.81	3.72	4.09	4.21
Nd	14.5	15.8	15.4	14.3	14.8	15.6	17.3	17.3
Sm	3.05	3.16	3.13	2.91	3.04	3.12	3.53	3.58
Eu	0.85	1.00	0.93	0.88	0.91	0.93	1.01	1.08
Gd	2.85	2.768	3.014	2.938	3.332	2.946	3.145	3.51
Tb	0.450	0.469	0.438	0.409	0.448	0.477	0.497	0.529
Dy	2.88	3.04	3.00	2.76	2.77	2.93	2.90	3.69
Ho	0.553	0.599	0.581	0.552	0.574	0.595	0.587	0.759
Er	1.61	1.71	1.74	1.61	1.63	1.70	1.64	2.34
Tm	0.274	0.233	0.243	0.229	0.224	0.225	0.247	0.334
Yb	1.58	1.72	1.61	1.57	1.58	1.58	1.67	2.27
Lu	0.245	0.240	0.234	0.226	0.222	0.238	0.235	0.358
Hf	1.93	2.09	2.07	1.84	1.96	2.08	2.14	2.43
Ta	0.33	0.33	0.35	0.33	0.33	0.41	0.38	0.38
Pb	17.99	4.89	4.73	10.20	32.10	17.53	8.90	5.07
Th	3.13	3.18	3.13	2.85	2.98	3.28	3.51	4.09
U	0.77	0.81	0.82	0.84	0.84	0.95	1.10	0.71

Table 4.4: Trace elements (all in [ppm]) were determined by LA-ICP-MS analysis (n.a.: not analyzed). Samples NHS138A-F are part of a section across strike of basaltic hybrid (2B) dyke section 1 (Fig. 4.3), with a total thicknesses of 0.73m.

Composition	**basaltic-hybrid**	**basaltic-hybrid**	**basaltic-hybrid**	**basaltic-hybrid**	**basaltic-hybrid**	**basaltic-hybrid**	**basaltic-hybrid**	**basaltic-hybrid**
Sample	**NHS045A**	**NHS045B**	**NHS045C**	**NHS045D**	**NHS045E**	**NHS045F**	**NHS078A**	**NHS078B**
Generation	**2B**	**2B**	**2B**	**2B**	**2B**	**2B**	**2B**	**2B**
Be	n.a.	n.a.	n.a.	n.a.	n.a.	n.a.	n.a.	n.a.
Sc	35.4	35.9	34.7	32.3	33.3	34.6	32.3	29.4
V	247	257	266	272	263	252	242	220
Cr	391	479	305	195	266	399	198	179
Co	30.1	33.5	27.3	27.3	25.2	29.7	28.9	26.8
Cu	59.6	85.9	47.1	44.5	56.5	48.6	185.1	59.1
Zn	217.0	188.6	179.5	194.4	228.6	159.4	176.9	159.7
Ga	17.4	17.5	16.1	16.3	16.1	16.5	17.2	16.3
Ge	2.6	2.5	2.7	1.9	2.4	2.5	2.6	2.4
As	1.666	1.775	1.492	2.284	1.312	1.99	7.249	6.096
Rb	12.6	30.3	55.5	58.8	61.4	37.1	66.1	67.2
Sr	429	408	487	536	506	450	365	377
Y	18.5	18.1	19.3	19.6	18.2	17.8	18.4	18.0
Zr	84	88	89	94	90	83	101	108
Nb	5.7	5.6	5.8	5.9	5.7	5.2	6.6	7.1
Mo	1.5	1.4	1.4	3.1	1.5	0.7	1.2	1.0
Cs	0.49	0.65	0.96	0.82	0.94	0.76	0.56	0.49
Ba	199	270	432	598	531	320	506	488
La	16.3	16.2	17.3	17.4	17.7	15.9	23.7	24.0
Ce	31.6	31.4	33.5	34.1	33.8	30.4	42.4	45.0
Pr	3.87	3.65	3.96	3.97	3.96	3.52	4.73	4.78
Nd	16.5	15.7	17.1	17.2	16.6	16.1	19.2	20.0
Sm	3.68	3.33	3.69	3.89	3.58	3.48	4.15	3.93
Eu	1.08	1.08	1.14	1.06	1.10	1.02	1.17	1.09
Gd	3.193	3.275	3.29	3.487	3.3	3.362	3.377	3.71
Tb	0.524	0.469	0.553	0.577	0.539	0.487	0.536	0.583
Dy	3.15	3.21	3.40	3.53	3.34	3.09	3.30	3.29
Ho	0.719	0.654	0.724	0.735	0.698	0.671	0.754	0.676
Er	1.80	1.72	1.96	1.88	1.93	1.78	1.82	1.89
Tm	0.292	0.258	0.278	0.281	0.281	0.274	0.309	0.296
Yb	1.78	1.80	1.90	1.94	1.94	1.77	1.98	1.83
Lu	0.276	0.258	0.280	0.278	0.293	0.265	0.285	0.283
Hf	2.09	2.11	2.15	2.37	2.23	2.27	2.59	2.56
Ta	0.49	0.38	0.34	0.35	0.38	0.28	0.43	0.45
Pb	2.61	3.55	5.28	6.26	6.68	5.41	6.81	5.36
Th	3.25	3.24	3.50	3.51	3.41	3.16	5.13	5.80
U	0.67	0.63	0.59	0.63	0.59	0.56	0.95	0.97

Table 4.5: Trace elements (all in [ppm]) were determined by LA-ICP-MS analysis (n.a.: not analyzed). Samples NHS045A-F and NHS078A-C (Fig. 4.2) are sections across strike of basaltic hybrid (2B) dykes, with thicknesses of 0.2m and 0.08m respectively.

Composition	**basaltic-hybrid**	**melt impregnated tonalite**	**partiallly molten tonalite**	**tonalite**	**basaltic-hybrid bulk rock**	**recal. Matrix (chilled margin)**
Sample	**NHS078C**	**NHS140**	**NHS139B**	**RDC3**	**NHS053**	**NHS053**
Generation	**2B**	**2B**	**2B**	**VT**	**2B**	**2B**
Be	n.a.	n.a.	n.a.	n.a.	n.a.	n.a.
Sc	29.5	32.8	8.5	12.0	33.9	29.9
V	218	244	69	196	250	268
Cr	169	193	62	32	429	n.a.
Co	26.9	26.7	8.2	12.0	33.2	n.a.
Ni	43.6	35.3	15.1	n.a.	94.5	47.6
Cu	51.2	35.0	26.2	n.a.	31.9	n.a.
Zn	157.9	195.8	208.1	69.0	194.0	122.6
Ga	16.1	19.3	19.6	11.0	16.7	n.a.
Ge	2.1	2.2	3.6	n.a.	5.3	n.a.
As	4.661	2.466	2.305	n.a.	4.212	n.a.
Rb	70.7	44.5	60.2	78.6	46.1	n.a.
Sr	366	447	448	406	338	335
Y	18.4	22.1	19.3	12.0	18.9	22.4
Zr	108	126	216	100	79	104
Nb	7.2	9.3	15.1	n.a.	5.2	4.6
Mo	1.0	1.7	1.9	n.a.	0.7	n.a.
Cs	0.52	0.70	1.11	n.a.	0.46	n.a.
Ba	516	380	662	563	174	214
La	24.1	29.4	54.7	35.1	16.5	14.9
Ce	44.8	56.9	98.2	69.1	31.4	35.7
Pr	4.81	6.40	9.55	n.a.	3.77	4.73
Nd	20.5	24.3	33.0	26.5	16.3	20.4
Sm	3.85	4.70	4.84	4.20	3.64	4.24
Eu	1.08	1.21	1.13	1.05	1.23	1.06
Gd	3.277	4.223	3.695	n.a.	3.292	4.045
Tb	0.561	0.609	0.461	0.517	0.591	0.647
Dy	3.20	3.96	3.36	n.a.	3.28	4.07
Ho	0.716	0.816	0.669	1.920	0.743	0.818
Er	1.89	2.31	1.94	0.30	1.97	2.41
Tm	0.274	0.348	0.312	2.700	0.303	0.361
Yb	1.88	2.37	2.40	16.27	2.04	2.53
Lu	0.275	0.353	0.373	2.400	0.347	0.386
Hf	2.69	3.16	4.92	n.a.	2.15	2.81
Ta	0.43	0.54	0.95	n.a.	0.47	0.30
Pb	5.52	5.59	10.78	16.81	1.45	n.a.
Th	5.69	7.24	15.48	16.76	6.16	3.19
U	0.95	1.19	2.53	3.27	3.47	4.89

Table 4.6: Trace elements (all in [ppm]) were determined by LA-ICP-MS analysis. For RDC3, REE were analyzed by INAA/RNAA. (n.a.: not analyzed). Sample NHS078C is part of a section across strike of a dyke with a thickness of 0.08m. The matrix or chilled margin of the basaltic hybrid (2B) NHS053 consists of a recalculation based on bulk rock XRF analysis explained in the text and a LA-ICP-MS laser scan of the same chilled margin.

Whole Rock Radiogenic Isotopes

Values for radiogenic $^{87}Sr/^{86}Sr$, $^{143}Nd/^{144}Nd$, $^{206}Pb/^{204}Pb$, $^{207}Pb/^{204}Pb$ and $^{208}Pb/^{204}Pb$ of a basalt (2A) and several basaltic-hybrid (2B) dyke bulk rocks are given in table 4.7. In terms of $^{87}Sr/^{86}Sr$ and $^{143}Nd/^{144}Nd$ whole rock ratios (Fig. 4.12), the early basaltic phase (2A) is the most primitive among the compositions present in the described sections 1, 2 and 3 (Fig. 4.3, 4.5). The central, crystal-rich (abundant xenocrysts) part (NHS045D, Tab. 4.5) of the 0.2 m thick section across a basaltic hybrid (2B) dyke has the highest radiogenic $^{87}Sr/^{86}Sr$ and lowest $^{143}Nd/^{144}Nd$ values of all samples across the section. In terms of radiogenic $^{87}Sr/^{86}Sr$ and $^{143}Nd/^{144}Nd$ ratios, the samples of the basalt (2A) and basaltic-hybrids (2B) plot between the values of all the other dykes comprising Ol-tholeiites (1A), picro-basalts/Ol-tholeiites (1B), basaltic-andesites/andesites (2C) and dacite (3) and the Re di Castello intrusive suite [Kagami et al., 1991] consisting of hornblende-gabbros, tonalites and granites.

Composition	Sample	Generation	$^{87}Sr/^{86}Sr$	$^{143}Nd/^{144}Nd$	ϵNd	$^{206}Pb/^{204}Pb$	$^{207}Pb/^{204}Pb$	$^{208}Pb/^{204}Pb$
basalt	NHS079BR1	2A	0.705114	0.512513	-2.4	18.538	15.657	38.779
basaltic-hybrid	NHS042BR2	2B	0.705391	0.512498	-2.7	18.478	15.653	38.722
basaltic-hybrid	NHS078BR2	2B	0.705646	0.512422	-4.2	18.540	15.665	38.780
basaltic-hybrid	NHS045BR2	2B	0.705138	0.512511	-2.5	18.511	15.640	38.695
basaltic-hybrid	NHS045BR4	2B	0.705170	0.512519	-2.3	18.574	15.691	38.860

Table 4.7: $^{87}Sr/^{86}Sr$, $^{143}Nd/^{144}Nd$, $^{206}Pb/^{204}Pb$, $^{207}Pb/^{204}Pb$ and $^{208}Pb/^{204}Pb$ are all initial values re-calculated to the following age: basalt (2A), basaltic-hybrids to 39.8 Ma; according to zircon ages (39.8 Ma) from Hansmann [1986], Hansmann and Oberli [1991]. ϵNd was calculated according to a present-day CHUR value of $^{143}Nd/^{144}Nd$ of 0.512638 [Jacobsen and Wasserburg, 1980].

4.7 Mineral Chemistry

Olivine and Clinopyroxene

Olivine (Tab. 4.8) that is only rarely preserved in basalts (2A) at the outermost parts of dyke tips varies from $Fo_{89}$to Fo_{87}. Euhedral spinel inclusions are common in olivine phenocrysts. Olivine phenocrysts in contact with fine-grained crypto-crystalline matrix exhibit a magnetite reaction seam (Fig. 4.13a). Spinel inclusions are Cr-rich.

The major element composition of clinopyroxene (Tab. 4.8) varies from 0.48 to 0.35 for $Mg_2Si_2O_6$ (enstatite component) and from 0.43 to 0.32 for $Ca_2Si_2O_6$ (wollastonite component). The sum of all the pyroxene Tschermak's components ($CaAl_2SiO_6$; $CaFe^{3+}AlSiO_6$; $CaCrAlSiO_6$; $CaTiAl_2O_6$) ranges from a maximum of 0.221 to a minimum of 0.044. Crystal chemical variations associated with sector zoning and the detailed trace element chemistry of clinopyroxenes of basalts (2A) are described in Hürlimann et al. [in prep.a] under the description for clinopyroxene.

Plagioclase

Cations per formula unit and endmember proportions of plagioclases were calculated based on 5 cations and 16 negative charges [Wood and Banno, 1973]. For plagioclase, two distinct compositional ranges (Tab.

Mineral	**Ol**	**Cpx**	**Am**	**Am**	**Am**	**Pl**	**Pl**	**Pl**
Generation	**2A**	**2A**	**2B**	**2B**	**2B**	**2B**	**2B**	**2A**
Label	**Ol144-7**	**Px079-31**	**Am037-2**	**Am041-7**	**Am037-24**	**Pl037-17**	**Pl037-17**	**Pl053-13**
Grain zone	core	core	core	innerrim	outerrim	core	rim	microphenocryst
SiO2	39.85	49.96	40.78	42.12	41.71	55.87	47.19	45.65
TiO2	0.01	0.68	1.75	1.83	2.64	0.01	0.03	0.02
Cr2O3	0.04	0.43	n.a.	0.06	0.01	n.a.	n.a.	0
Al2O3	0.02	4.80	14.23	14.57	13.19	27.80	33.43	33.73
FeO	10.02	5.46	14.08	8.74	11.47	0.15	0.58	0.82
MnO	0.17	0.08	0.18	0.06	0.17	0.01	0.02	0
MgO	48.49	15.11	11.31	16.12	14.53	0.00	0.08	0.06
NiO	0.36	n.a.	0.00	0.02	0.01	n.a.	n.a.	0
CaO	0.13	22.26	11.53	12.11	11.65	10.26	17.32	17.73
Na2O	0.011	0.26	2.29	2.33	2.47	5.51	1.6	1.30
K2O	0.01	0.00	0.48	0.48	0.42	0.28	0.03	0.04
Total	99.11	99.07	96.62	98.43	98.26	100	100.37	99.35

Table 4.8: Different phenocryst (Ol: olivine, Cpx: clinopyroxene, Pl: Plagioclase) and xenocryst (Am: amphibole, Pl: plagioclase) phases present in basalts (2A) and basaltic hybrids (2B). Analyses are all in [wt%] for the different oxides.

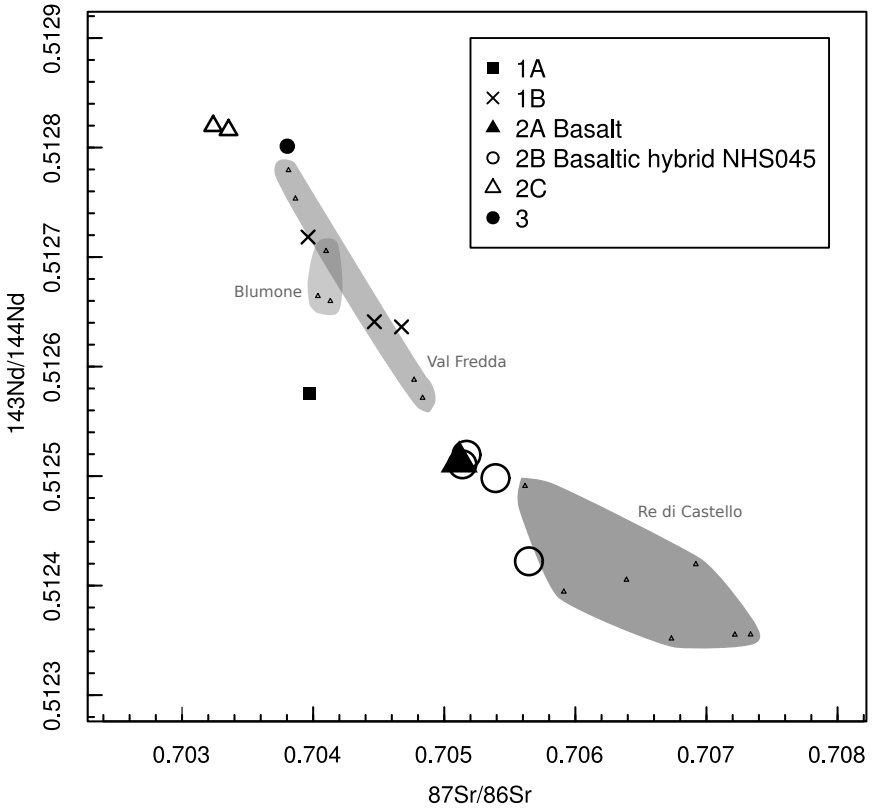

Figure 4.12: Whole rock radiogenic $^{87}Sr/^{86}Sr$ and $^{143}Nd/^{144}Nd$ isotopes from Val Fredda, Blumone and Re di Castello intrusives [Kagami et al., 1991] are compared with data from basaltic (2A) and basaltic hybrid (2B) dyke rocks of this study. $^{87}Sr/^{86}Sr$ and $^{143}Nd/^{144}Nd$ data for Ol-tholeiites (1A), picro-basalts/Ol-tholeiites (1B), basaltic-andesites/andesites (2C) and dacite (3) provided in Hürlimann et al. [in prep.a].

4.8) can be distinguished throughout the basaltic (2A) and basaltic-hybrid (2B) dyke rocks. These compositional ranges are closely associated with crystal textures in these rocks, which are coarse- to medium-grained xenocrysts with resorption features and finer grained micro-phenocrysts respectively. Cores of xenocrysts anorthite content vary mainly between An_{44} to An_{58} (Fig. 4.14a). The same xenocrysts reveal later overgrowth textures following bands of previous dissolution or resorption (Fig. 4.13d) with an anorthite content that ranges between An_{82} and An_{88}. Micro-phenocrysts of basalts (2A) and basaltic hybrids (2B) have an anorthite content that varies from An_{90} to An_{79} and corresponds to the compositional range covered by late anorthite-rich overgrowths of plagioclase xenocrysts of hybrid magmas. The orthoclase component of the different plagioclase textures and textural domains provides an additional crystal-chemical distinction (Fig. 4.14a). Micro-phenocrysts and late overgrowths of plagioclase xenocrysts reveal an orthoclase component that ranges between 0.0081 and 0.0007, whereas the cores of the plagioclase xenocrysts have a considerably higher orthoclase content varying from 0.0183 to 0.0118. Moreover late xenocryst overgrowths and micro-phenocrysts are enriched in MgO and FeO compared to the xenocryst cores.

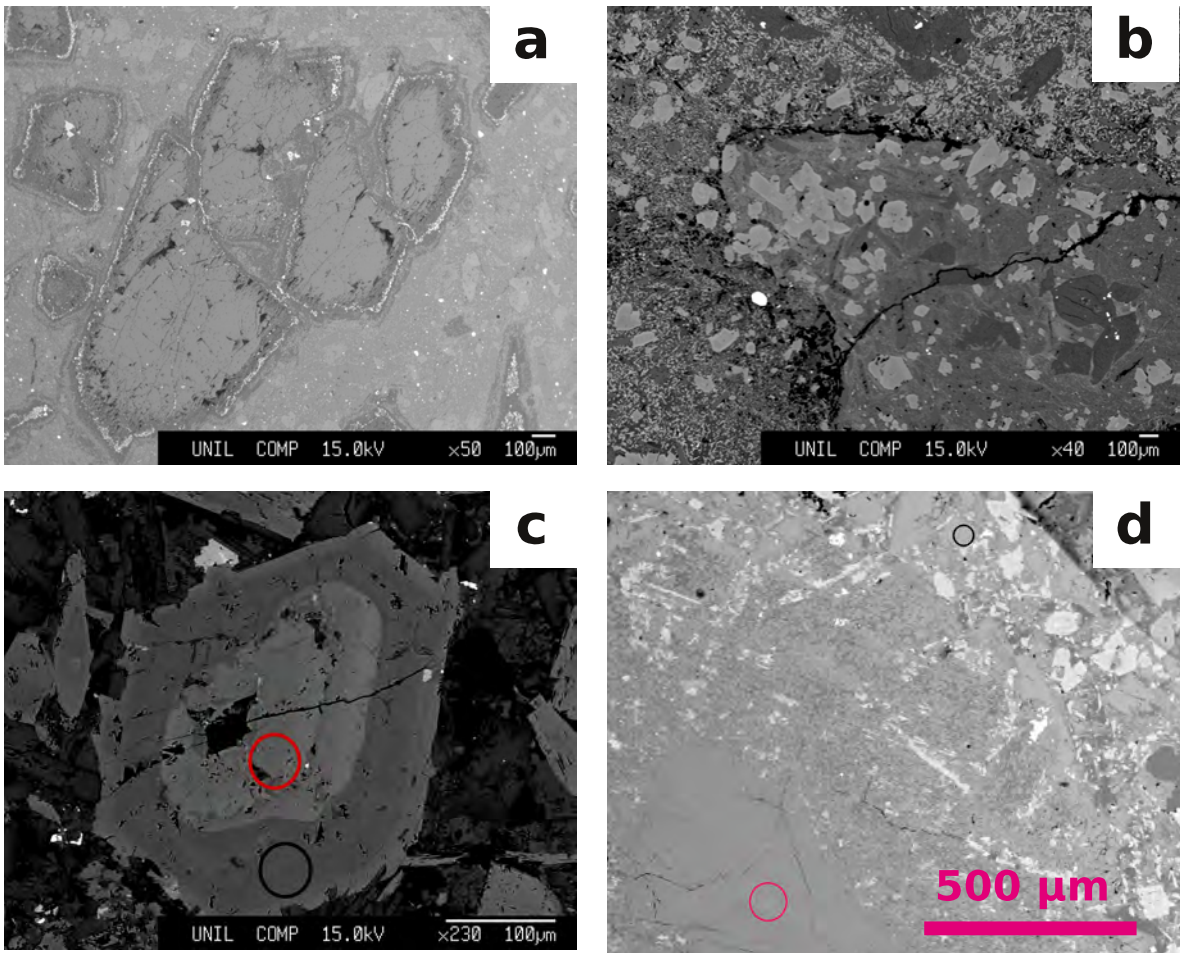

Figure 4.13: Back scattered electron (BSE) images of phenocryst and xenocryst phases occurring in basalts (2A) and basaltic hybrids (2B) (a) Olivine phenocryst set within cryptocrystalline matrix of outermost basaltic (2A) dyke tip. Olivine has euhedral Cr-spinel inclusions and a magnetite reaction rim. (b) Juxtaposition of glassy fragments of a basalt (2A) with micro-phenocrysts of darker olivine pseudomorphs and brighter clinopyroxene adjacent to a cryptocrystalline part of the matrix. (c) Amphibole xenocryst in a basaltic hybrid (2B) with a rounded core with magnetite inclusions overgrown by a later phase with a darker innerim and a brighter outerim (circles are LA-pits). (d) Plagioclase xenocryst with a preserved core and a sieve or sponge textured band with a fresh later overgrowth corresponding to plagioclase microphenocryst in the basaltic hybrid (2B).

Mineral	**Pl**	**Pl**	**Pl**	**Pl**	**Pl**	**Pl**	**Pl**	**Pl**	**Pl**
Label	**Pl042-3**	**Pl042-4**	**Pl042-4**	**Pl041-1**	**Pl041-2**	**Pl037-14**	**Pl037-14**	**Pl037-16**	**Pl037-17**
Generation	**2B**	**2B**	**2B**	**2B**	**2B**	**2B**	**2B**	**2B**	**2B**
Grain zone	**core**	**core**	**core**	**core**	**core**	**core**	**core**	**core**	**core**
Rb	0.34	0.47	0.36	0.39	6.75	0.24	1.55	0.35	0.23
Sr	1150	1095	1081	1200	1150	1042	1906	1164	1132
Y	0.08	0.12	0.06	0.08	0.12	0.05	0.14	0.09	0.06
Zr	<0.090	<0.057	<0.042	<0.046	<0.070	0.03	0.37	0.16	<0.041
Nb	<0.006	<0.004	<0.003	<0.004	0.014	0.009	0.07	0.074	<0.004
Cs	<0.024	0.016	<0.014	<0.022	0.3	<0.006	0.035	0.027	<0.014
Ba	219	280	206	194	7 137	315	204	128	
La	12.5	15.9	12.8	7.7	2.6	12.6	31.8	13.9	12.4
Ce	13.6	16.2	11.8	7.9	3.7	12.2	32.2	14.3	12.5
Pr	0.95	1.00	0.70	0.56	0.30	0.77	2.00	0.91	0.81
Nd	2.2	2.3	1.6	1.3	1.2	1.8	5.1	2.1	1.8
Sm	0.10	0.16	0.11	0.13	0.15	0.10	0.33	0.14	0.12
Eu	0.74	0.79	0.56	0.71	0.27	0.70	1.68	0.76	0.74
Gd	0.09	0.06	0.03	0.04	0.06	0.05	0.14	0.04	0.06
Tb	0.011	0.005	0.006	0.005	0.008	0.004	0.011	0.004	0.004
Dy	<0.012	0.026	0.028	0.033	0.033	0.016	0.018	0.019	0.023
Ho	0.007	0.008	0.005	<0.002	0.005	0.001	0.004	0.002	0.002
Er	0.011	0.011	0.006	0.004	0.007	0.003	0.02	0.005	0.008
Tm	<0.003	<0.001	<0.002	<0.001	0.003	<0.001	<0.002	<0.001	0.001
Yb	<0.010	0.008	<0.009	<0.004	0.008	0.004	0.005	0.007	0
Lu	<0.002	0.001	0.001	<0.002	0.003	0.001	<0.002	0.002	<0.000
Hf	<0.010	<0.002	<0.003	<0.003	<0.008	0.003	0.016	0.007	<0.003
Ta	<0.005	<0.003	<0.003	<0.003	<0.004	0.001	0.009	0.007	<0.002
Pb	18.07	14.11	18.91	19.43	31.70	19.99	30.76	15.21	18.95
Th	0	0	0	0.001	0.006	0.011	0.127	0.08	0
U	0	0.001	0	0.002	0.013	0.028	0.041	0.032	0

Table 4.9: Trace element analysis (all in [ppm]) of cores of (Pl) plagioclase xenocrysts from basaltic hybrids (2B). Internal standard for data reduction in LAMTRACE is CaO wt% determined by electron microprobe. External standard is the NIST SRM 612.

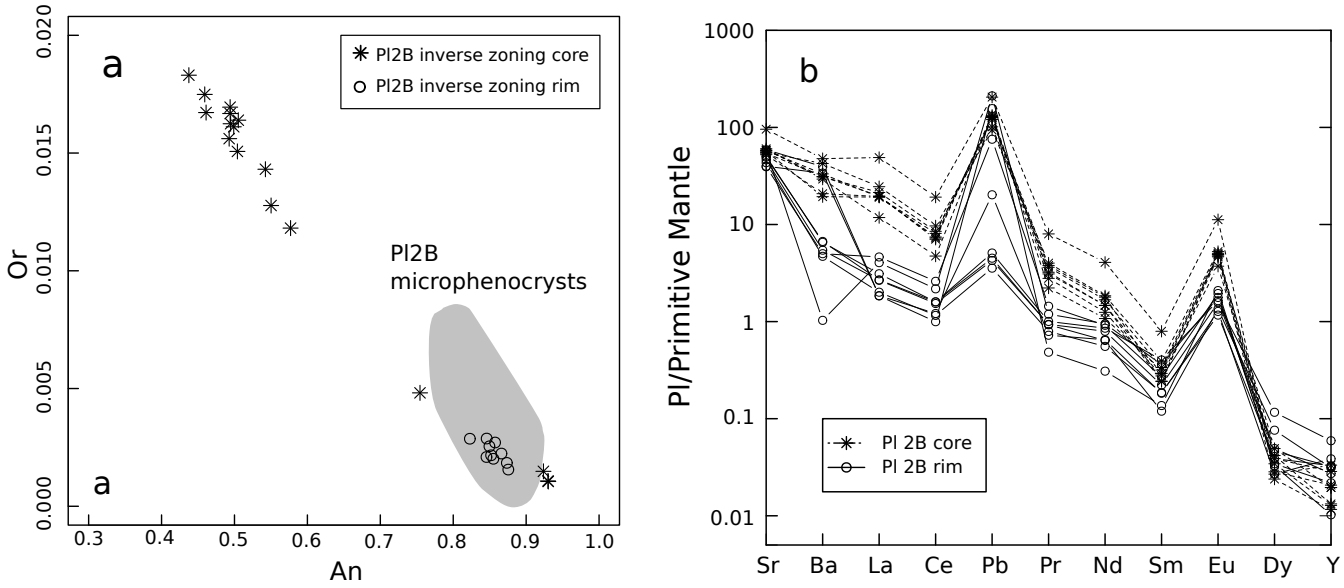

Figure 4.14: (a) Anorthite vs. orthoclase content of different textural zones such as late overgrowths and cores of plagioclase xenocrysts of basaltic-hyrbids (2B), microphenocrysts of basalts (2A) and basaltic-hybrids (2B). (b) Chondrite normalized [McDonough and Sun, 1995] trace element patterns of the core and late overgrowths (rim) zones of of plagioclase xenocrysts in basaltic hybrids (2B).

Trace element compositions of core and late overgrowth domains of plagioclase xenocrysts of basaltic hybrids (2B) are reported in tables 4.9 and 4.10. With regard to trace element compositions, the plagioclase xenocryst cores from the basaltic hybrids (2B) are enriched in Ba and light rare earth elements (LREE) (Fig. 4.14b) (chondrite normalized basis [McDonough and Sun, 1995]) in comparison to the late overgrowths (rims) of the same xenocrysts. For the two different textural domains of these xenocrysts, Sr, however does not differ considerably (Fig. 4.14). The heaviest detected rare earth elements (HREE) are slightly enriched in late overgrowths (rims) of the xenocrysts, compared to the still preserved core domain of the same crystals.

Amphibole

Amphibole chemical formulae based on major and minor element wt% oxide data from microprobe analysis were calculated to 13 cations per formula unit (apfu), excluding Ca, Na and K which neglects any potential cummingtonite component [Hawthorne, 1983, Hawthorne and Oberti, 2007]. With this normalization scheme, the M(4) site only contains Ca and Na and any Na and K exceeding 2.0 are allocated on the A site. A representative data set for the different textural domains observed for amphibole xenocrysts of basaltic hybrids (2B) encompassing core, innerrim and outerrim (Fig. 4.13c) is provided in table 4.8.

Overall, all analyses from the different textural domains (core, innerrim, outerrim) of amphibole xenocrysts fall within the pargasite field after Leake et al. [1997] (Fig. 4.15a). Xenocryst cores show a scatter in the K (apfu) versus Mg#(tot) variation diagram (Fig. 4.15b) with lowest Mg#(tot) of ~0.55;

Mineral	**Pl**	**Pl**	**Pl**	**Pl**	**Pl**	**Pl**	**Pl**	**Pl**
Label	**Pl041-1**	**Pl041-2**	**Pl037-16**	**Pl037-17**	**Pl053-1**	**Pl053-2**	**Pl042-3**	**Pl041-2**
Generation	**2B**	**2B**	**2B**	**2B**	**2B**	**2B**	**2B**	**2B**
Grain zone	**rim**	**rim**	**rim**	**rim**	**rim**	**rim**	**rim**	**rim**
Rb	<0.070	2.90	0.10	0.17	0.13	51.08	0.40	6.75
Sr	982	783	922	1005	863	791	1173	1150
Y	0.13	0.09	0.26	0.14	0.14	0.17	0.04	0.12
Zr	<0.126	<0.114	0.342	<0.078	<0.047	0.086	<0.060	<0.070
Nb	<0.007	<0.007	0.032	<0.008	<0.009	<0.018	<0.005	0.014
Cs	<0.031	0.062	<0.026	<0.030	31.036	223.259	<0.014	0.300
Ba	44.2	33.0	35.9	43.2	1.3	1.2	260.4	6.8
La	1.75	3.01	1.73	2.02	1.95	2.04	1.20	2.63
Ce	2.68	4.37	2.58	2.68	0.20	0.18	1.68	3.65
Pr	0.23	0.36	0.23	0.25	0.69	0.81	0.12	0.30
Nd	0.80	1.15	0.99	1.07	0.08	0.08	0.39	1.19
Sm	0.05	0.11	0.09	0.17	0.18	0.19	0.06	0.15
Eu	0.20	0.29	0.24	0.25	0.07	0.07	0.31	0.27
Gd	0.12	0.06	0.13	<0.050	0.01	0.01	0.03	0.06
Tb	0.008	0.009	0.011	0.006	0.026	0.018	<0.002	0.008
Dy	0.051	0.023	0.078	0.031	0.005	0.009	0.022	0.033
Ho	0.005	0.002	0.007	<0.002	0.019	<0.010	0.001	0.005
Er	0.014	0.008	0.041	0.015	<0.001	<0.002	0.004	0.007
Tm	0.001	<0.002	0.004	<0.002	0.009	<0.016	<0.001	0.003
Yb	0.012	0.010	0.021	0.012	<0.003	<0.007	0.004	0.008
Lu	<0.002	<0.002	<0.004	<0.002	0.533	3.035	<0.001	0.003
Hf	0.000	0.003	<0.013	<0.006	0.005	0.000	<0.002	<0.008
Ta	<0.005	<0.005	<0.005	<0.005	0.008	0.045	<0.002	<0.004
Pb	0.675	11.333	0.639	0.763	0.533	3.035	23.435	31.697
Th	0.058	0.000	0.003	0.005	0.005	0.000	0.000	0.006
U	0.009	0.014	<0.001	0.009	0.008	0.045	0.000	0.013

Table 4.10: Trace element analysis (all in [ppm]) of rims (late overgrowths) of (Pl) plagioclase xenocrysts from basaltic hybrids (2B). Internal standard for data reduction in LAMTRACE is CaO wt% determined by electron microprobe. External standard is the NIST SRM 612.

innerrim and outerrim domains reveal lower K (apfu) contents and are much more confined in terms of Mg#(tot). The variation and scatter between Na(A) and Al^{IV} (apfu) (Fig. 4.15) for amphibole xenocrysts cores shows the effect of coupled Tschermak's and edenite substitution. In the present case both innerrim and outerrim of the amphibole xenocrysts are confined to higher Na(A) and Al^{IV} (apfu) values. The innerrim domain of amphibole xenocrysts contains the most Ti (apfu) (Fig. 4.16d) of all the different xenocryst zones, indicative of higher temperature conditions during the formation of this part of the late overgrowth. The outermost rims of amphibole xenocrysts have lower Ti (apfu) and indicate most likely a later phase of crystal growth during cooling. Ti (apfu) content for amphibole xenocryst cores scatters from higher, equivalent to innerrims, to lower values below the Ti (apfu) level for outerrims.

Label	**Am041-1**	**Am041-3**	**Am041-8**	**Am041-1**	**Am041-10**	**Am037-17**	**Am037-21**
Generation	**2B**	**2B**	**2B**	**2B**	**2B**	**2B**	**2B**
Grain Zone	**core**	**core**	**core**	**core**	**core**	**core**	**core**
Sc	38.4	34.5	80.6	42.2	84.3	54.1	88.8
V	348	408	421	334	440	397	325
Cr	110.5	9.6	92.0	104.8	55.4	45.3	14.4
Ni	35.3	18.6	61.0	34.3	46.1	27.6	28.6
Zn	102.3	92.7	141.0	108.5	153.4	200.3	157.2
Rb	4.37	10.09	22.95	4.45	2.76	6.11	2.10
Sr	156	285	164	149	143	70	92
Y	81.5	21.4	53.0	67.1	70.9	44.1	84.6
Zr	122	90	28	87	36	26	35
Nb	2.4	4.8	16.3	2.1	19.3	10.4	18.6
Ba	74	135	251	75	63	102	52
La	3.2	5.3	4.7	3.0	8.7	7.2	15.6
Ce	15.9	18.9	19.9	14.4	39.2	31.6	67.5
Pr	3.77	3.16	4.18	3.26	7.91	5.86	12.07
Nd	26.8	17.2	26.2	23.1	44.6	31.8	63.3
Sm	11.12	4.40	10.02	9.51	13.83	8.31	16.07
Eu	2.63	1.37	2.28	2.45	3.02	2.33	3.17
Gd	13.97	4.65	10.44	12.05	13.84	7.83	15.59
Tb	2.218	0.672	1.573	1.896	2.055	1.204	2.336
Dy	15.11	4.09	9.74	12.53	13.12	7.96	15.83
Ho	3.103	0.828	1.987	2.655	2.758	1.566	3.272
Er	8.90	2.39	5.52	7.66	7.58	4.58	9.14
Tm	1.303	0.323	0.832	1.052	1.126	0.691	1.338
Yb	9.38	2.24	5.72	7.60	7.64	4.79	8.77
Lu	1.316	0.334	0.850	1.150	1.160	0.699	1.258
Hf	5.88	2.63	1.49	4.09	2.15	1.24	2.00
Ta	0.11	0.39	0.63	0.09	0.68	0.26	0.70
Pb	0.94	0.98	2.20	0.90	2.22	1.27	1.55
Th	0.23	0.55	0.49	0.26	0.66	0.29	0.79
U	0.07	0.05	0.13	0.07	0.11	0.12	0.15

Table 4.11: Trace element analysis (all in [ppm]) of cores of (Am) amphibole xenocrysts from basaltic hybrids (2B). Internal standard for data reduction in LAMTRACE is CaO wt% determined by electron microprobe. External standard is the NIST SRM 612.

Label	**Am037-22**	**Am037-3**	**Am037-30**	**Am037-31**	**Am037-32**	**Am037-21**	**Am037-21**
Generation	**2B**	**2B**	**2B**	**2B**	**2B**	**2B**	**2B**
Grain Zone	**core**	**core**	**core**	**core**	**core**	**core**	**core**
Sc	66.4	99.4	86.5	116.1	80.4	86.7	86.7
V	447	448	435	522	358	361	361
Cr	457.0	47.7	57.8	360.3	90.5	16.3	16.3
Ni	72.3	21.7	49.5	160.7	35.7	38.5	38.5
Zn	222.2	190.3	100.5	46.2	175.1	148.8	148.8
Rb	4.76	6.49	2.24	2.04	7.20	1.76	1.76
Sr	73	70	227	269	82	77	77
Y	35.7	101.1	33.0	18.2	68.8	62.9	62.9
Zr	23	33	85	32	30	49	49
Nb	10.5	12.6	4.2	2.1	19.1	14.4	14.4
Ba	116	59	76	70	132	48	48
La	4.6	9.6	6.7	2.2	7.1	11.1	11.1
Ce	24.7	41.7	24.3	8.1	32.0	48.6	48.6
Pr	5.11	8.68	4.49	1.59	6.93	8.51	8.51
Nd	27.4	49.6	24.9	9.3	41.3	43.9	43.9
Sm	7.75	16.34	6.31	2.98	13.05	11.39	11.39
Eu	2.41	3.74	1.81	0.99	2.94	2.14	2.14
Gd	6.86	17.45	6.40	3.69	12.95	11.59	11.59
Tb	0.989	2.747	0.940	0.551	2.000	1.749	1.749
Dy	6.22	18.28	6.20	3.67	13.09	11.91	11.91
Ho	1.287	3.770	1.277	0.761	2.591	2.508	2.508
Er	3.78	10.61	3.62	1.96	7.51	7.01	7.01
Tm	0.626	1.632	0.525	0.262	1.084	1.021	1.021
Yb	4.80	10.98	3.66	1.57	7.26	7.26	7.26
Lu	0.737	1.577	0.529	0.232	1.059	1.000	1.000
Hf	1.17	1.90	3.71	1.71	1.90	2.08	2.08
Ta	0.26	0.49	0.24	0.13	0.78	0.57	0.57
Pb	3.88	2.78	1.06	0.38	2.85	1.02	1.02
Th	0.14	0.38	0.32	0.07	0.53	0.81	0.81
U	0.12	0.12	0.09	0.03	0.15	0.05	0.05

Table 4.12: Trace element analysis (all in [ppm]) of cores of (Am) amphibole xenocrysts from basaltic hybrids (2B). Internal standard for data reduction in LAMTRACE is CaO wt% determined by electron microprobe. External standard is the NIST SRM 612.

Label	**Am053-11**	**Am053-13**	**Am042-1**	**Am042-1**	**Am042-2**	**Am042-3**	**Am042-4**
Generation	**2B**	**2B**	**2B**	**2B**	**2B**	**2B**	**2B**
Grain zone	**rim**	**rim**	**rim**	**rim**	**rim**	**rim**	**rim**
Sc	63.7	86.5	151.3	63.2	74.8	126.6	94.7
V	474	519	625	531	578	608	590
Cr	n.a.	n.a.	467.9	56.2	171.6	331.8	389.6
Ni	83.8	117.1	187.2	97.8	93.4	141.7	155.2
Zn	58.1	59.8	56.6	75.6	69.5	52.6	60.1
Rb	n.a.	n.a.	2.06	2.09	4.18	2.02	2.92
Sr	277	232	297	278	246	297	263
Y	21.4	19.6	22.5	29.7	22.8	22.0	21.5
Zr	40	17	37	43	38	36	38
Nb	1.9	2.0	2.7	3.6	1.8	3.2	2.8
Ba	71	116	88	97	86	97	99
La	2.7	1.5	2.5	4.4	2.9	3.4	3.6
Ce	9.3	6.7	9.5	16.4	11.0	11.8	12.7
Pr	1.70	1.36	1.88	3.03	2.11	2.15	2.29
Nd	9.6	8.7	10.4	17.1	11.6	11.7	12.8
Sm	3.27	2.99	3.66	5.03	3.55	3.44	3.84
Eu	1.05	0.94	1.16	1.54	1.20	1.16	1.17
Gd	3.93	3.60	4.50	6.00	4.46	4.34	4.54
Tb	0.623	0.558	0.706	0.911	0.663	0.659	0.695
Dy	4.21	3.98	4.49	6.32	4.68	4.45	4.68
Ho	0.865	0.793	0.952	1.252	1.006	0.925	0.897
Er	2.50	2.12	2.41	3.39	2.52	2.31	2.32
Tm	0.378	0.305	0.344	0.449	0.350	0.300	0.368
Yb	2.24	1.89	1.97	2.86	2.50	1.95	2.09
Lu	0.286	0.257	0.300	0.403	0.327	0.292	0.277
Hf	1.83	0.95	1.99	2.26	1.88	1.73	1.73
Ta	0.12	0.11	0.16	0.22	0.13	0.18	0.15
Pb	0.46	0.84	0.56	0.55	0.73	0.99	0.59
Th	0.12	0.05	0.05	0.08	0.11	0.09	0.10
U	0.020	0.018	0.022	0.012	0.011	0.018	0.022

Table 4.13: Trace element analysis (all in [ppm]) of rims (late overgrowths) of (Am) amphibole xenocrysts from basaltic hybrids (2B). Internal standard for data reduction in LAMTRACE is CaO wt% determined by electron microprobe. External standard is the NIST SRM 612.

Label	Am042-5	Am041-3	Am041-7	Am041-8	Am041-10	Am041-1	Am037-17
Generation	**2B**	**2B**	**2B**	**2B**	**2B**	**2B**	**2B**
Grain zone	**rim**	**rim**	**rim**	**rim**	**rim**	**rim**	**rim**
Sc	113.9	110.0	100.9	127.0	81.1	116.7	88.9
V	630	561	550	537	511	504	496
Cr	88.4	217.8	232.6	90.6	139.7	374.0	92.1
Ni	141.6	161.6	164.9	150.1	152.2	173.0	111.5
Zn	52.5	51.8	52.3	50.0	65.7	49.3	68.1
Rb	2.00	2.27	2.07	2.08	2.20	1.82	2.33
Sr	274	272	274	297	255	255	277
Y	23.2	19.4	18.8	20.0	23.1	19.0	23.1
Zr	35	38	32	39	57	45	77
Nb	2.2	2.2	2.5	3.3	3.8	3.1	4.5
Ba	83	89	92	85	94	76	81
La	2.5	2.9	3.0	2.4	3.9	2.5	3.3
Ce	9.9	10.9	11.1	9.0	14.4	9.4	12.9
Pr	1.88	1.95	1.97	1.65	2.51	1.70	2.26
Nd	11.1	10.9	11.2	9.4	13.7	9.7	13.1
Sm	3.80	3.43	3.34	3.09	4.02	3.10	4.10
Eu	1.16	1.04	1.04	1.06	1.21	1.04	1.28
Gd	4.69	3.80	4.01	3.90	4.53	3.72	4.61
Tb	0.691	0.608	0.594	0.598	0.665	0.550	0.696
Dy	4.85	3.77	3.90	3.96	4.51	3.61	4.69
Ho	1.012	0.770	0.756	0.818	0.874	0.741	0.994
Er	2.61	2.20	2.00	2.10	2.55	2.01	2.65
Tm	0.349	0.275	0.259	0.281	0.300	0.269	0.351
Yb	2.15	1.79	1.64	1.88	2.21	1.70	2.25
Lu	0.281	0.246	0.227	0.273	0.301	0.239	0.312
Hf	1.69	1.78	1.43	1.98	2.50	2.04	3.38
Ta	0.14	0.16	0.13	0.16	0.23	0.18	0.26
Pb	0.40	0.50	0.44	0.56	0.58	0.36	0.82
Th	0.06	0.16	0.08	0.08	0.16	0.06	0.09
U	0.009	0.017	0.010	0.012	0.016	0.008	0.019

Table 4.14: Trace element analysis (all in [ppm]) of rims (late overgrowths) of (Am) amphibole xenocrysts from basaltic hybrids (2B). Internal standard for data reduction in LAMTRACE is CaO wt% determined by electron microprobe. External standard is the NIST SRM 612.

Label	**Am037-18**	**Am037-20**	**Am037-22**	**Am037-23**	**Am037-24**	**Am037-3**	**Am037-30**
Generation	**2B**	**2B**	**2B**	**2B**	**2B**	**2B**	**2B**
Grain zone	**rim**	**rim**	**rim**	**rim**	**rim**	**rim**	**rim**
Sc	75.0	129.0	103.5	120.1	107.6	95.2	112.6
V	509	550	533	541	503	505	539
Cr	129.4	97.3	148.8	458.7	598.0	291.1	370.6
Ni	193.4	148.5	139.5	177.4	176.6	209.7	225.2
Zn	57.1	49.6	56.8	50.7	51.3	51.2	45.3
Rb	1.44	1.80	2.41	2.18	9.21	2.56	1.87
Sr	321	295	291	301	253	250	252
Y	22.0	21.2	21.5	19.1	17.1	20.2	18.4
Zr	55	50	40	34	124	40	31
Nb	2.9	3.0	3.6	2.5	2.0	3.3	1.8
Ba	79	85	94	88	75	75	70
La	4.0	2.8	3.4	2.6	2.5	3.0	2.2
Ce	14.5	10.4	12.3	9.3	8.7	11.1	8.6
Pr	2.51	1.88	2.21	1.75	1.63	1.93	1.58
Nd	14.3	11.2	12.6	9.9	9.2	11.5	8.8
Sm	4.18	3.42	3.83	2.95	2.91	3.47	3.19
Eu	1.26	1.10	1.18	1.01	0.97	1.10	0.97
Gd	4.53	4.34	4.43	3.66	3.39	3.95	3.74
Tb	0.667	0.637	0.690	0.585	0.530	0.615	0.519
Dy	4.48	4.17	4.45	3.80	3.55	4.11	3.85
Ho	0.883	0.863	0.940	0.791	0.677	0.817	0.756
Er	2.35	2.24	2.64	2.07	1.92	2.14	1.84
Tm	0.327	0.300	0.303	0.285	0.271	0.291	0.254
Yb	2.10	1.87	1.98	1.78	1.70	1.79	1.53
Lu	0.282	0.254	0.290	0.241	0.226	0.253	0.226
Hf	2.76	2.91	2.07	1.79	5.45	2.14	1.46
Ta	0.20	0.18	0.20	0.14	0.11	0.19	0.13
Pb	0.41	0.50	0.68	0.51	0.39	0.45	0.29
Th	0.18	0.07	0.23	0.07	0.10	0.07	0.06
U	0.010	0.006	0.041	0.018	0.020	0.007	0.008

Table 4.15: Trace element analysis (all in [ppm]) of rims (late overgrowths) of (Am) amphibole xenocrysts from basaltic hybrids (2B). Internal standard for data reduction in LAMTRACE is CaO wt% determined by electron microprobe. External standard is the NIST SRM 612.

Label	Am037-32	Am037-33	Am042-1	Am042-2	Am042-4	Am042-5	Am053-11
Generation	**2B**	**2B**	**2B**	**2B**	**2B**	**2B**	**2B**
Grain zone	**rim**	**rim**	**rim**	**rim**	**rim**	**rim**	**rim**
Sc	74.7	110.3	78.0	106.2	70.4	130.6	88.9
V	518	567	681	594	485	598	554
Cr	149.9	97.3	93.2	534.4	153.2	947.9	n.a.
Ni	111.8	109.3	100.9	130.4	99.7	188.5	84.4
Zn	56.6	59.6	84.0	49.3	73.5	44.8	54.1
Rb	2.67	1.84	21.23	3.37	2.89	2.56	n.a.
Sr	247	276	251	236	272	262	295
Y	22.2	24.5	26.6	18.9	28.1	18.6	25.5
Zr	42	38	29	31	79	25	54
Nb	2.9	4.2	4.6	1.5	6.4	1.9	1.8
Ba	93	97	222	78	154	79	74
La	3.6	3.7	6.5	2.2	3.3	1.9	2.2
Ce	13.4	13.4	23.3	8.3	13.2	7.5	8.7
Pr	2.46	2.49	4.27	1.59	2.54	1.54	1.72
Nd	13.7	14.0	23.4	9.0	16.9	9.0	10.4
Sm	4.13	4.28	5.65	2.91	5.15	3.06	3.73
Eu	1.21	1.32	1.68	0.90	1.43	0.97	1.23
Gd	4.31	5.06	5.93	3.65	5.94	3.95	4.70
Tb	0.678	0.766	0.870	0.570	0.851	0.574	0.730
Dy	4.59	4.73	5.53	4.03	5.84	4.06	5.09
Ho	0.916	0.966	1.041	0.835	1.110	0.812	1.015
Er	2.53	2.55	2.77	2.04	3.03	2.18	2.71
Tm	0.328	0.341	0.387	0.293	0.416	0.330	0.398
Yb	2.15	2.25	2.53	1.83	2.93	2.01	2.72
Lu	0.301	0.299	0.348	0.257	0.360	0.237	0.372
Hf	1.87	1.78	1.33	1.72	3.31	1.26	2.53
Ta	0.16	0.24	0.30	0.11	0.33	0.13	0.14
Pb	0.73	0.50	1.43	0.45	0.66	0.49	0.43
Th	0.14	0.08	0.36	0.07	0.08	0.06	0.10
U	0.030	0.010	0.060	0.011	0.029	0.014	0.014

Table 4.16: Trace element analysis (all in [ppm]) of rims (late overgrowths) of (Am) amphibole xenocrysts from basaltic hybrids (2B). Internal standard for data reduction in LAMTRACE is CaO wt% determined by electron microprobe. External standard is the NIST SRM 612.

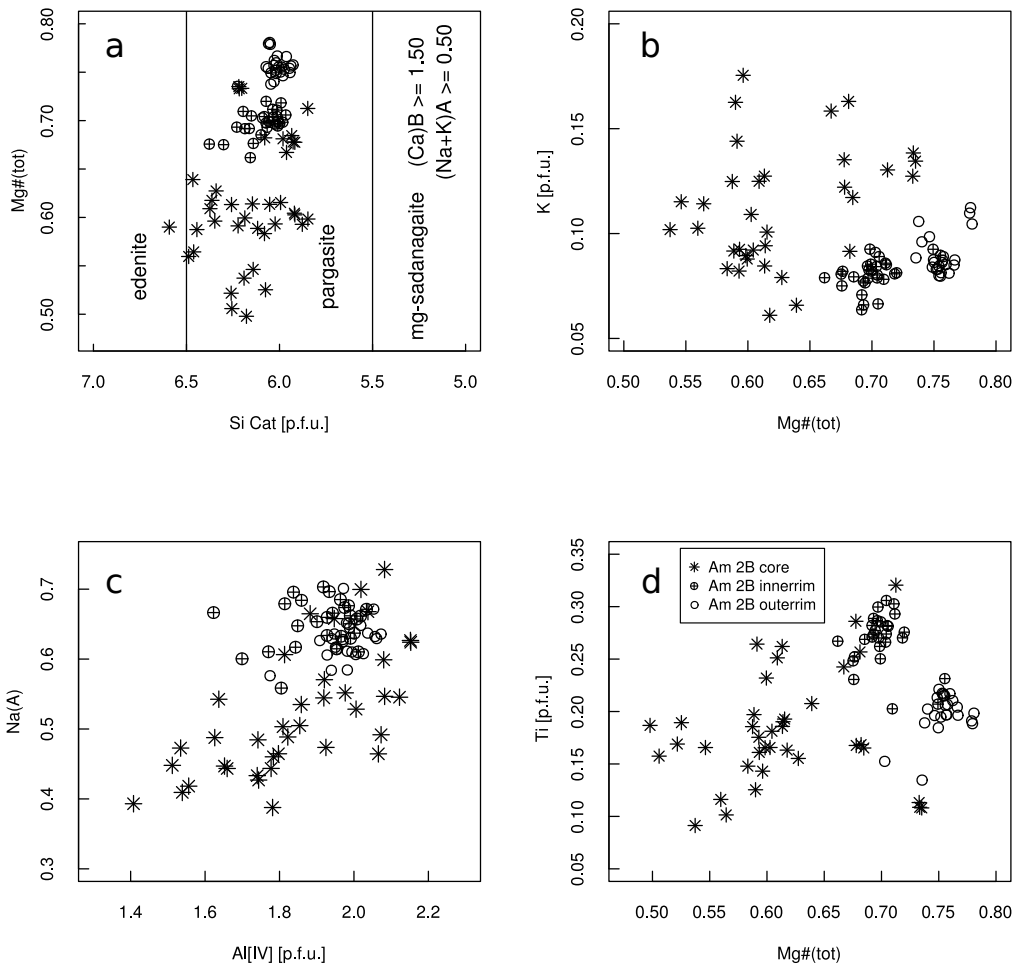

Figure 4.15: Amphibole crystal-chemistry: (a) Amphibole classification for calcic amphiboles based on the parameters: (Ca)B >1.50; (Na+K)A>0.50 after Leake et al. [1997]. (a) to (d) Cations per formula unit (apfu) calculated on the basis of 13 cations (Cations-Ca-Na-K=13), where M(4) only contains Ca and Na and remaining Na and K assigned to the A-site. (b) Innerrims and outerrims of amphibole xenocrysts have distinctly lower K (apfu) contents whereas cores show a larger scatter in both Mg#(tot) and K [p.f.u.]. (c) Amphibole xenocryst cores show a scatter to lower values of Na(A) and Al^{IV} (apfu) than the inner- and outerrims of the same xenocrysts that are very confined in composition and reveal higher Al^{IV} (apfu) and Na(A) contents related to pargasite substitution ($NaAl^{VI}Al^{IV}_2{}_{O-1}Mg_{-1}Si_{-2}$), which is a composite of the edenite and the Tschermak's exchange vectors. (d) Ti (apfu) varies among different textural zones of xenocrysts and is highest for the innerrim domain, indicating higher temperature conditions during amphibole precipitation at this stage.

The chondrite-normalized [McDonough and Sun, 1995] rare earth element (REE) diagram of amphibole xenocryst cores reveals distinctly higher concentrations and more evolved composition than the corresponding rim (late overgrowth) composition (Fig. 4.16a) of the same xenocrysts. The core REE patterns possess a negative Eu-anomaly that accentuates for higher REE concentrations, indicating the co-precipitation of plagioclase under appropriate oxygen fugacity (fO_2) conditions. This is coupled with

Label	Am053-12	Am053-13	Am053-15	Am037-20	Am037-18	Am041-7
Generation	**2B**	**2B**	**2B**	**2B**	**2B**	**2B**
Grain zone	**rim**	**rim**	**rim**	**rim**	**rim**	**rim**
Sc	116.9	73.0	75.3	36.2	56.1	98.3
V	519	485	470	460	452	571
Cr	n.a.	n.a.	n.a.	93.5	125.6	260.0
Ni	140.4	129.8	122.2	83.7	149.2	94.3
Zn	44.1	55.0	95.4	123.9	55.9	56.9
Rb	n.a.	n.a.	n.a.	4.17	1.61	67.15
Sr	317	279	269	212	312	198
Y	21.8	22.7	30.6	16.6	20.1	20.9
Zr	30	32	91	53	48	29
Nb	1.8	2.5	4.0	12.0	2.5	1.4
Ba	83	81	114	237	82	73
La	1.8	2.3	4.9	2.9	4.2	1.6
Ce	7.3	9.0	17.6	11.0	15.4	6.7
Pr	1.32	1.73	3.08	1.96	2.61	1.22
Nd	7.9	9.9	17.1	10.0	14.3	7.6
Sm	2.88	3.24	4.82	3.10	4.11	2.78
Eu	0.96	1.08	1.41	1.19	1.22	0.88
Gd	3.70	4.08	5.34	3.52	4.34	3.52
Tb	0.624	0.681	0.871	0.507	0.631	0.555
Dy	4.29	4.30	5.91	3.05	4.04	3.91
Ho	0.915	0.909	1.203	0.667	0.800	0.825
Er	2.30	2.56	3.22	1.77	2.23	2.39
Tm	0.338	0.352	0.490	0.261	0.313	0.335
Yb	1.99	2.13	3.04	1.64	1.89	2.23
Lu	0.287	0.315	0.433	0.265	0.245	0.302
Hf	1.59	1.54	3.70	1.61	2.14	1.81
Ta	0.10	0.16	0.24	0.30	0.20	0.09
Pb	0.48	0.58	1.55	1.32	0.41	0.75
Th	0.05	0.07	0.41	0.23	0.17	0.07
U	0.007	0.007	0.079	0.153	0.012	0.074

Table 4.17: Trace element analysis (all in [ppm]) of rims (late overgrowths) of (Am) amphibole xenocrysts from basaltic hybrids (2B). Internal standard for data reduction in LAMTRACE is CaO wt% determined by electron microprobe. External standard is the NIST SRM 612.

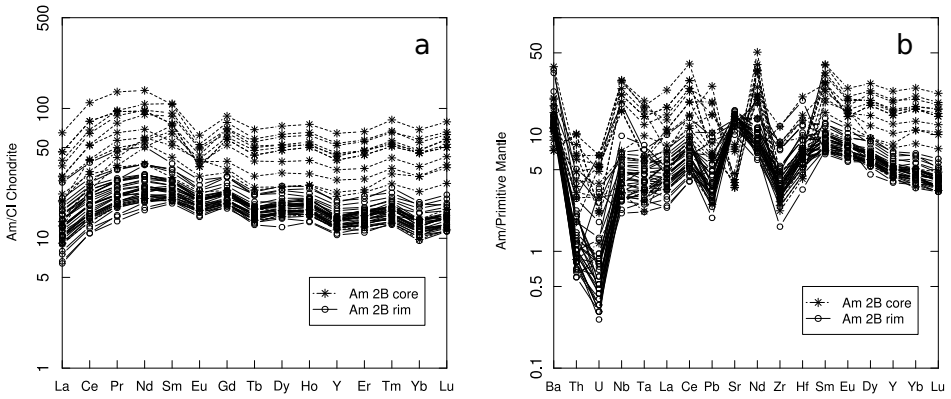

Figure 4.16: (a) Chondrite normalized [McDonough and Sun, 1995] rare earth element (REE) pattern of different amphibole xenocryst domains (core; rim/overgrowth) of basaltic hybrids (2B). (b) Primitive mantle normalized [McDonough and Sun, 1995] trace element patterns of the same amphibole xenocrysts domains (core; rim/overgrowth) as in (b).

a well visible depletion of Sr for the cores of amphibole xenocrysts, as shown in the primitive mantle normalized [McDonough and Sun, 1995] trace element patterns (Fig. 4.16b), since Sr is very compatible in co-crystallizing plagioclase [Blundy and Wood, 1991]. Rims or late overgrowths on the other hand reveal a relative enrichment in Sr compared to cores. High field strength elements such as Th, U, Nb and Ta mark (Fig. 4.16b) an enrichment for amphibole xenocryst cores relative to the corresponding late overgrowths (rims).

4.8 Discussion

Geochemical Constraints on Wallrock Assimilation

Bulk rock geochemical and crystal chemical properties of the basaltic (2A) and basaltic hybrid (2B) dykes, together with the Vacca tonalite host rock presented in sections 1 and 2 (Fig. 4.3), indicate wallrock assimilation and mixing processes of an initial basaltic magma. Textural features of amphibole, plagioclase and quartz xenocrysts underline this relation in conjunction with textures of partial melting of the tonalitic host rock (Fig. 4.9c) in all of the examined sections (Fig. 4.3, 4.5). Moreover, the occurrence of tonalitic wallrock xenoliths within the basaltic hybrid (2B) dykes provides another aspect of the assimilation process.

The assimilation process in magmatic open systems is either a bulk or a selective process [Edwards and Russell, 1996b]. In the case of bulk assimilation, the material being assimilated by a given melt is added in proportions equal to the bulk xenolith composition. In contrast, selective assimilation is described as a process where the composition of the added assimilant is not equal to the bulk xenolith composition. In open magmatic systems both processes have been recognized (e.g. Doe et al., 1969, Watson, 1982, Kitchen, 1989, Blichert-Toft et al., 1992, Philpotts and Asher, 1993, Reiners et al., 1995). The selective assimilation

process stresses the importance of kinetic aspects, such as different dissolution rates of different mineral phases, which is a question of the reaction kinetics [Edwards and Russell, 1996a, Donaldson, 1985, 1990, Brearley and Scarfe, 1986].

Major elements such as SiO_2 do not change considerably in the course of the assimilation process, as exemplified by the relation of the basaltic hybrids in section 1 relative to the host Vacca tonalite (Fig. 4.10a-f). However, the K_2O and Na_2O contents of some basaltic hybrids (2B) are significantly elevated and approach the range of concentrations of the Vacca tonalite host rock. In contrast to the potential secondary modification of K_2O due to fluid mobility, the increased values of Na_2O for the more evolved basaltic hybrids indicates preferential dissolution of Na-rich phase, such as albite-rich plagioclase of the tonalitic host rock, as documented by plagioclase xenocrysts and partial melting tin the host rock.

Trace elements generally more susceptible to assimilation processes such as Sr and Rb that, in the present case, show a larger variation over the confined SiO_2 content of the basaltic hybrids attaining the concentration levels of the Vacca tonalite host rock. The Ni versus Ba diagram (Fig. 4.11c) suggests the presence of two different differentiation evolutions. The first, curved evolution characterized by a rapid initial decrease in Ni followed by an enrichment in Ba can be ascribed to a pure fractional crystallization trend, as inferred by Hürlimann et al. [in prep.a] in their fractional crystallization model. A second major evolution trend consists of a mixing trend between a basalt (2A) and the Vacca tonalite (VT). Some of the basaltic hybrids (2B) plot along the evolution assigned to pure fractional crystallization whereas the 0.2m thick cross section of sample NHS045 with 0.02m intervals shows a large scatter between a basalt and the Vacca tonalite host rock. Sample NHS045 however has a very low content of coarser- and medium-grained xenocrysts (amphibole, plagioclase, quartz) and exhibits only the occurrence of abundant fine- to medium-grained micro-phenocrysts of clinopyroxene, amphibole and plagioclase, potentially growing during ascent and decompression. These magmas do not show any isolated felsic liquid phase in the form of lenses. This implies homogenization and actual mixing of the assimilated melted material with an intitial basaltic (2A) composition. The latest phase of a sequence of injections of dykes (NHS078, Fig. 4.9d) displayed through the field relations plots in the Ni versus Ba diagram (Fig. 4.11c) in close vicinity to the tonalitic host rock (VT) along the mixing trend. Radiogenic $^{87}Sr/^{86}Sr$ and $^{143}Nd/^{144}Nd$ whole rock ratios further constrain a significant contribution of the Vacca host tonalite during assimilation processes, due to the intermediate position of the basaltic hybrid values between the primitive source reflected by basaltic-andesites/andesites (2C) and dacites (3) [Hürlimann et al., in prep.a] and the analyzed Vacca tonalite (Fig. 4.12).

The trace element patterns of the core domains of plagioclase (Fig. 4.14b) and amphibole (Fig. 4.16) xenocrysts provide another indication of a more differentiated composition of the assimilant. For both mineral phases, trace elements are enriched indicating protracted differentiation and in particular, the Eu anomaly associated with amphibole xenocryst cores reveals concomitant crystallization of plagioclase. Anhedral quartz crystals with acicular clinopyroxene reaction seams at the grain margins add further constraints on the phase assemblage of the tonalitic host rock assimilant. Biotite, another phase of the tonalitic host rock, is absent among the xenocrysts, which implies that biotite started melting at the very beginning of the dissolution process and has completely been consumed. This process is reflected in enrichment of K_2O content (Fig. 4.10e) of basaltic-hybrid (2B) magmas and implies a selective assimilation process. A comparable dissolution scheme has been shown by Kaczor et al. [1988] between a trachyandesite

and a partially molten granite and by Knesel and Davidson [1996] in fusion experiments on Proterozoic biotite granite.

Olivine exhibits most primitive compositions of Fo_{89} in basalts (2A) and together with Ni bulk rock values of up to ~200ppm infers that these magmas fractionated minor olivine and clinopyroxene prior to intrusion into shallow levels and thus represent near primary melts. This consideration takes the picro-basalt (1B) described in a companion paper [Hürlimann et al., in prep.a] as primary mantle-derived liquid. On a chemical basis, this picro-basalt (1B) shows olivine with highest values of $Fo_{91}$and Ni concentration of over 300ppm for the most primitve and MgO (~16 wt%) rich magmas.

Trace Element Partioning at Emplacement Levels

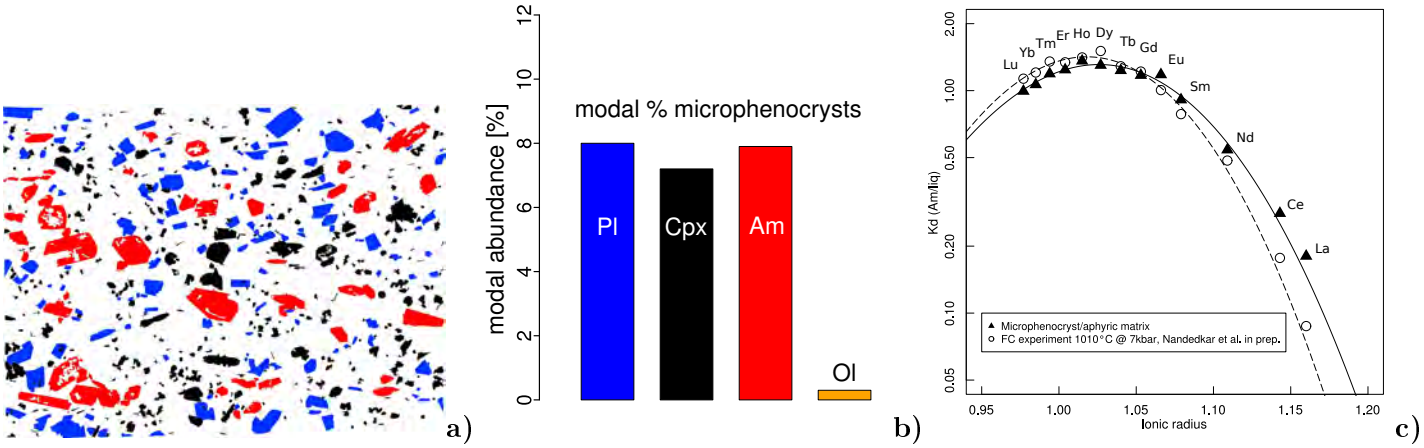

Figure 4.17: (a) Visualization of micro-phenocryst phases based on thresholding of stitched back scattered electron (BSE) images within the chilled margin of a basaltic hybrid (2B) dyke, with (Cpx) clinopyroxene (black), (Am) amphibole (red) and (Pl) plagioclase (blue). (b) Modal abundances of microphenocryst phases that were determined by image analysis of a chilled margin of basaltic hybrid (2B) magma. Modes: Cpx (7.2%), Am (7.9%), Pl (8%) Ol (0.3%). (c) Onuma plot for calculated amphibole REE partition coefficients (DAm_{REE}) reported in table 4.18. For details of partition coefficient calculation see text. For comparison, are given the partition coefficients for amphibole from a fractional crystallization experiment at 1010°C at 7kbar from Nandedkar et al. [in prep.] are given.

DAm_{La}	DAm_{Ce}	DAm_{Pr}	DAm_{Nd}	DAm_{Sm}	DAm_{Eu}	DAm_{Gd}	DAm_{Tb}	DAm_{Dy}	DAm_{Ho}	DAm_{Er}	DAm_{Tm}	DAm_{Yb}	DAm_{Lu}
0.180	0.281	0.392	0.542	0.910	1.180	1.172	1.232	1.301	1.360	1.241	1.191	1.065	0.994

Table 4.18: Displayed are partition coefficients for amphibole microphenocrysts in basaltic hybrids (2B). For the data treatment of scan LA-ICP-MS analysis of the cryptocrystalline matrix, the bulk rock XRF-analysis was corrected by the subtraction of the according microphenocryst phases (Ol,Cpx,Am,Pl) to obtain a corrected CaO wt% value serving as an internal standard. External standard is the NIST SRM 612.

Trace element partitioning for amphibole microphenocrysts within basaltic hybrids (2B) and in particular partition coefficients for REE result in an indirect temperature constraint for the saturation temperature of amphibole. The calculation of these REE partition coefficients reported in table 4.18 is based

on the following method. Fine-grained microp-henocrysts of 100 to 200μm in size are interpreted as the product of crystallization upon decompression of the magma during ascent within the present dykes and, thus do not necessarily represent cumulate building phases entrained in the dyke. The cryptocrystalline matrix in the chilled margins of basaltic hybrid (2B) dykes represents the liquid composition and, together with the respective composition of amphibole micro-phenocrysts set in this matrix, provides information on the partitioning of trace elements between amphibole and liquid.

In practice, the cryptocrystalline chilled margin was measured in laser-scan mode with the LA-ICP-MS technique. The bulk rock analysis of sample NHS053 reported in table 4.6 was recalculated by subtracting present micro-phenocrysts phases, using their model abundances in order to obtain a corrected CaO wt% value used for the data reduction of the LA-ICP-MS scan data. The recalculated liquid composition for major and minor elements reported in element wt% oxides is provided in table 4.6. Modes of micro-phenocrysts (Fig. 4.17a, b) in the chilled margin were obtained by image analysis, applying a thresholding technique to stitched backscatter images. The entire data reduction yielded a trace element composition for the cryptocrystalline chilled margin representing the liquid at the emplacement stage of the dyke. The amphibole micro-phenocryst REE concentration divided by the REE concentration of the recalculated liquid results directly in the respective mineral-liquid (DAm_{REE}) partition coefficients.

Amphibole-liquid partition coefficients for a variety of trace elements were determined by Nandedkar et al. [in prep.] in a series of isobaric fractional crystallization experiments at 7 kbar for a calc-alkaline differentiation suite, with an olivine-tholeiite derived from a primitive picro-basalt (1B) as a starting composition. These experiments saturate amphibole at the fractionation step at 1010°C. Additional fractional crystallization experimental studies on similar starting material in the light of hydrous calc-alkaline magma differentiation, carried out by Kägi [2000] at 10 kbar and Alonso-Perez [2006] at 15kbar place the high temperature stability of amphibole around ~1050°C. In the case of Kägi [2000] the appearance of amphibole is marked by a peritectic reaction involving clinopyroxene and liquid, whereas in the case of Nandedkar et al. [in prep.], amphibole appears through a peritectic reaction involving orthopyroxene, plagioclase and liquid. Comparison of the amphibole partition coefficients determined for basaltic hybrid (2B) dykes with the experimentally derived partition coefficients from Nandedkar et al. [in prep.], in an Onuma diagram (Fig. 4.17c) based on the lattice strain model [e.g.Wood and Blundy, 1997, Blundy and Wood, 1994] expressed by the Brice equation [Brice, 1975], reveals close accordance with the experimental values obtained at 1010°C and at 7 kbar. The first appearance of amphibole in these experiments at 1010°C implies for basaltic hybrids (2B) temperature conditions close to the first occurrence (saturation) of amphibole (~1010-1050°C).

Thermal Constraints on Partial Melting of Wall Rock

Textural features in the host rocks in immediate vicinity to the dyke margins display partial melting of the tonalitic host (Fig. 4.9c) and the formation of related basaltic intrusion breccias for dyke swarms extending up to 15m in width (Fig. 4.3,4.5) with close spacing of the single dykes. The observed partial melting zones constitute a record of the thermal history of the observed magma intrusion and offer the possibility to model the basalt injection and the cooling history of the dyke swarm and the adjacent tonalite host rock. For comparison with the field observation of partially molten host rock and intrusion

breccias, static conduction diffusion simulations were carried out to establish a thermal model. Section 2 and section 3b with closely spaced single dykes were directly simulated with such a static conduction heat diffusion model in order to put constraints on partial melting of the host rock tonalite by instantaneous injection of basaltic dyke swarms. The quantitative approach was chosen to test the potential extent of partial melting within these 10 to 15m wide zones with a high frequency of dykes with small spacing. An additional process that needs to be considered is the effect of partial melting on the decrease of the aggregate strength [Rosenberg and Handy, 2005, Rutter and Neumann, 1995, Molen and Paterson, 1979, Arzi, 1978] by the increasing melt-interconnectivity between the crystal grains of the host rock.

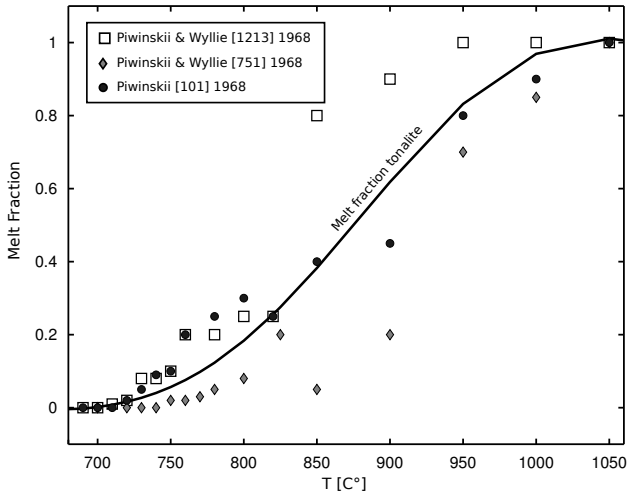

Figure 4.18: Melt fraction as a function of temperature for the tonalite wall rock (Vacca tonalite (VT), tonalite of the Listino ring structure), based on melting experiments of Piwinskii [1968] and Piwinskii and Wyllie [1968]. The two border zone tonalites (1213, 751) [Piwinskii and Wyllie, 1968] from the Needle Point Pluton from the Wallowa Batholith, Oregon have the following modes: 1213-quartz (17.4%), K-fsp (0.1%), plagioclase (50.7%), biotite (16%), hornblende (amphibole) (15.3%), Fe-Ti-oxides (0.1%), accessory phases (0.4%); 751-quartz (12.3%), K-fsp (0%), plagioclase (60.5%), biotite (9.5%), hornblende (amphibole) (15.2%), Fe-Ti oxides (1.5%), accessory phases (1.0%). The tonalite (101) [Piwinskii, 1968] from the Central Sierra Nevada Batholith, California has the following mineral modes: quartz (13.1%), K-Fsp (4.4%), plagioclase (58.9%), mafic minerals (amphibole, biotite, Fe-Ti oxides) (23.6%). Melting experiments were performed at 3 kbar and 15 wt% H_2O in the case of Piwinskii [1968] and 15-25 wt% H_2O for Piwinskii and Wyllie [1968]. This implies H_2O saturation for all these experiments.

The thermal model formulation is based on a basic thermal conduction simulation and the model starts with an instantaneous injection of the basaltic magma. The reported and described profiles of section 2 and section 3b were directly implemented into the thermal simulation to obtain the thermal conduction effect of closely spaced single dykes in 10 to 15m wide zones on the tonalitic host rock and the related partial melting of the host. Injection of the basaltic magma was assumed to be vertical in the absence of field-measured flow indicators.

The model formulation is based on a 1D finite difference implicit solution for the static heat diffusion equation:

$$\rho c_p \frac{\partial T}{\partial t} = \frac{\partial}{\partial x}\left(k \frac{\partial T}{\partial x}\right) \tag{4.1}$$

The discretized form of equation (4.1) for an implicit thermal 1D finite difference model scheme is ($\kappa = \frac{k}{\rho c_p}$):

$$\frac{T^{n+1} - T^n}{\Delta t} = \kappa \frac{T_{i+1}^{n+1} - 2T_i^{n+1} + T_{i-1}^{n+1}}{\Delta x^2} \tag{4.2}$$

In the 1D finite difference model scheme, i represents the node location along the x axis and n stands for the time step. Applied properties and their values, such as thermal conductivity k, heat capacity c and the density ρ are reported in table 4.19. The melt fraction of the tonalite host rock in each of the two modeled cases (section 2, section 3b) was calculated on a nonlinear melt fraction to temperature relationship displayed in figure 4.18. This nonlinear melt fraction to temperature relationship was established on a 10th order polynomial regression, based on fusion experiments of Piwinskii and Wyllie [1968] and Piwinskii [1968] (Fig. 4.18) on different tonalites from the Wallowa Batholith, Oregon and the Central Sierra Nevada Batholith, California respectively. In thermal model calculations, the soldius temperature for the tonalite host rock was fixed to 700°C whereas the liquidus temperature was fixed to 1050°C [Piwinskii, 1968, Piwinskii and Wyllie, 1968]. The thermal diffusivity κ was varied between that of basaltic magma and tonalite host rock (table 4.19). These calculations do not include latent heat of fusion or crystallization. Initial host rock temperature was set to 300°C, 400°C and 500°C respectively and was held constant during the thermal simulations. Results of 1D geochemical modeling of burial and the thermal history for Upper Triassic and Lower Jurassic strata of the Iseo W location by Carminati et al. [2010] resulted in temperatures of 150°C to 200°C for variable heat flow at 40 Ma. The host rocks are however expected to have higher temperatures than the ones resulting from burial alone, due to the previous emplacement of the Vacca tonalite (youngest zircon ages for different concentric zones of the tonalite: 41.85 ± 0.06 and 41.98 ± 0.03 from Schoene et al. [2012]) and the tonalite of the Listino porphyry ring structure. Particularly in the light that basaltic (2A) and basaltic hybrid (2B) dykes are closely associated with the Re di Castello plutonic suite with a youngest zircon age U-Pb of 38.62 ± 0.12 Ma [Hürlimann et al., in prep.b] supports elevated host rock temperatures. Intrusion temperature of the basaltic magma was set to 1050°C based on the high temperature stability of amphibole and the implications from trace element partitioning between micro-phenocrysts and melt composition constraining emplacement conditions.

Results of the temperature evolution for the thermal model for the two cross sections considered are depicted in Figure 4.19a, b. The evolution of the temperature profile shows the thermal conduction over time for an instantaneous injection of closely spaced basaltic dykes as found in section 2 (Fig. 4.3) and 3b (Fig. 4.5b) at an initial host rock temperature of 400°C. These temperature evolution profiles show the importance of the close spacing of the single dykes in the cooling history of both the dyke and the tonalite wall rock. At a distance of 4m away from the outermost dyke contact for these 10 to 15m wide dyke swarms, the thermal effect of the intrusion becomes negligible.

Resulting tonalite host rock melt fractions obtained through the static conduction model with instantaneous basaltic magma injection for the dyke swarm of cross section 2 are displayed in figure 4.20 for different time steps (0.5d, 1d, 5d, 10d) and for a variation of host rock temperatures (300°C, 400°C and 500°C). Similar results for section 3b are provided in figure 4.20. Model results clearly confirm that a host

symbol	parameter	numerical value	units
t	time		s
k_t	thermal conductivity tonalite	3 .0	$W(mK)^{-1}$
k_b	thermal conductivity basalt	1.7	$J(kgK)^{-1}$
c_t	heat capacity tonalite	1100	K
c_b	heat capacity basalt	1150	K
T	temperature		K
ϕ	melt fraction		
ρ_t^s	tonalite solid density	2650	kgm^{-3}
ρ_b^l	basalt liquid density	2600	kgm^{-3}

Table 4.19: Symbols of parameters and values used in the 1D finite difference thermal model for section 2 and 3b. Thermal conductivity of tonalite k_t and basalt k_b are taken from Touloukian et al. [1981]. Values for the solid density of the tonalite ρ_t^s and the basalt liquid density ρ_b^l are reported in Dobran [2012]. The heat capacity for tonalite c_t and basalt c_b are values from Barboza and Bergantz [1996].

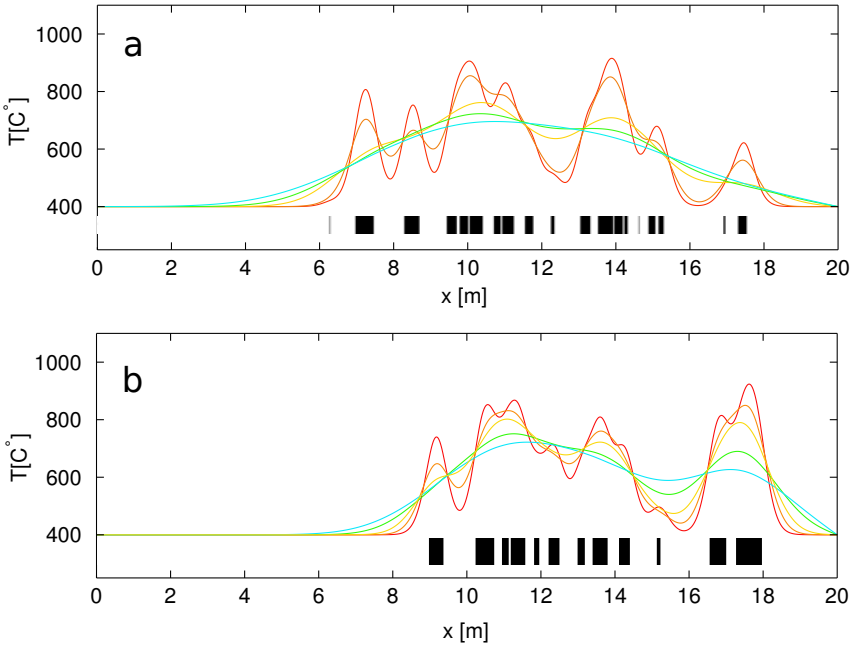

Figure 4.19: Temperature profiles as a function of time for section 2 (a) and 3b (b) (Fig. 4.3, 4.5). Intervals of the temperature records are 0.5, 1, 5, 10 and 20 days. Dyke spacing and thickness are all to scale. Colour coding goes from red (hot) to blue (cold).

rock temperature of 300°C is not capable of creating a partially molten zone over wider extent (>2m) and up to 4m wide as observed in the field (Fig 4.3, 4.5) with such static thermal conduction simulations. Additionally the melt connectivity transition (MCT) for granitic rocks [Rosenberg and Handy, 2005] defined by melt fraction ϕ >0.07, which is the boundary of a dramatic strength drop, are indicated in Figures 4.20 and 4.21. Melt interconnectivity implies that deformation is distributed but localized along an interconnected network of melt on the grain scale. The liquid to solid transition (LST) or rheological critical melt

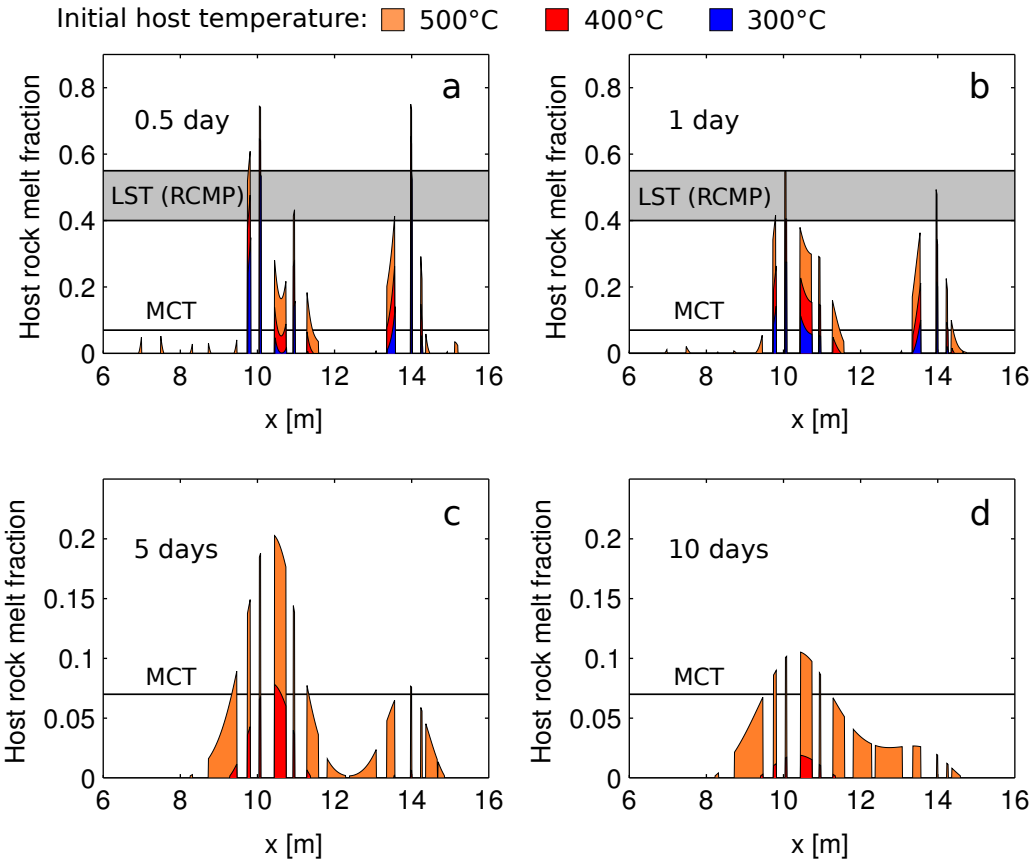

Figure 4.20: Results of the melt fraction evolution as a function of time for the ~10m wide dyke swarm of section 2 (Fig. 4.3), based on 1D static thermal conduction simulations for different initial tonalite host rock temperatures (300°C, 400°C, 500°C). Displayed are the evolutions of the melt fractions in the tonalite host rock at different times in the cooling history (a) 0.5 day, (b) 1 day, (c) 5 days and (d) 10 days. A host rock temperature of 300°C does not allow the creation of wider zones (>2 m) of partially molten tonalite and after 5 days the partially molten wall rock disappeared due to cooling below the solidus temperature of the tonalite. In contrast, host rock temperatures of 400°C and 500°C are suitable to create wider zones (> 2m) of partially molten tonalitic host rock by instantaneous magma injection.

percentage (RCMP) (Fig. 4.20,) appears between a melt fraction ϕ of 0.4 and 0.6 for partially molten granitic rocks. The LST reflects the drop in strength where the solid framework breaks down [Molen and Paterson, 1979, Arzi, 1978, Rosenberg and Handy, 2005].

In particular, models with initial host rock temperatures at 500°C produce up to 4m wide zones where the tonalite is partially molten with melt fraction above the MCT where deformation of the host localizes along the interconnected network of melt after a time frame of several days (1-5d). For the formation of 1-2m wide basaltic intrusion breccias in the present dyke swarms, the tonalite host must to pass the LST zone, which is the case immediately after injection (0.5d) for zones that only reach up to 1m. The occurrence of intrusion breccias in the interior of up to 5m thick basaltic hybrid dykes implies rheological inversion [Sparks and Marshall, 1986]. Mafic magmas tend to have higher solidi temperatures and thermal equilibration leads to initially increased crystallization in the basaltic magma that is injected into the cooler

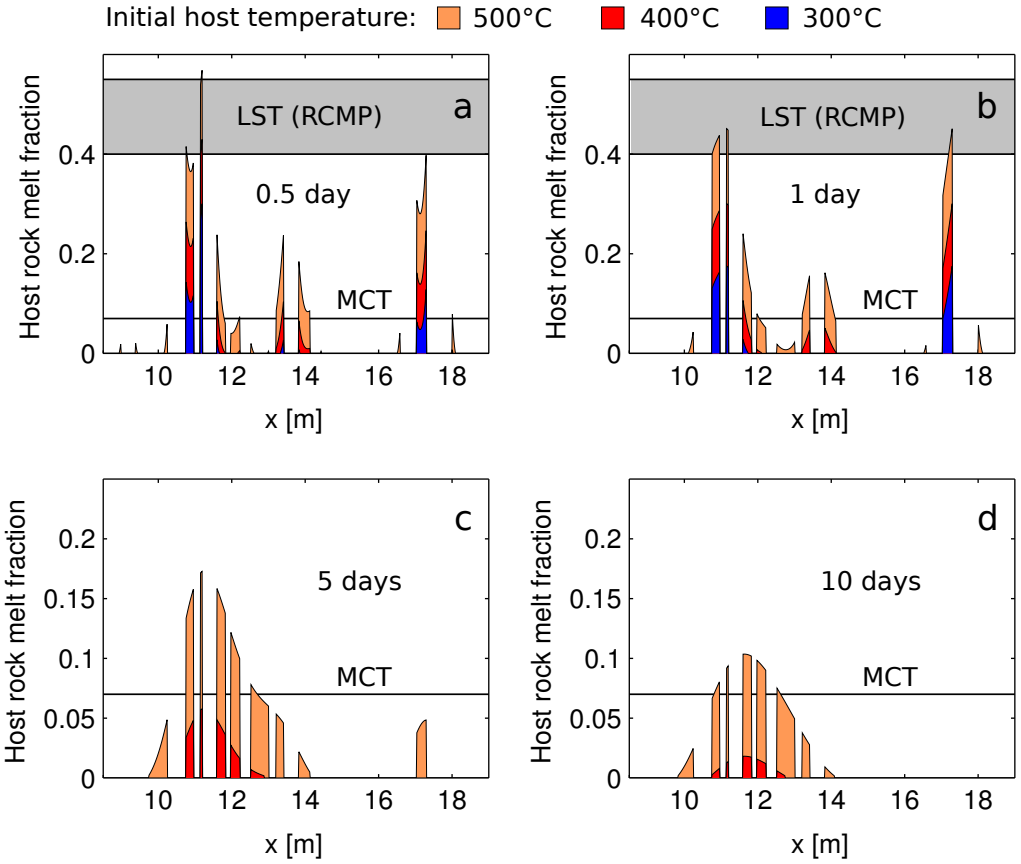

Figure 4.21: Results of the melt fraction evolution as a function of time for the ~10m wide dyke swarm of section 3b (Fig. 4.5). Displayed are the evolutions of the melt fractions in the tonalite host rock at different times in the cooling history (a) 0.5 day, (b) 1 day, (c) 5 days and (d) 10 days. A host rock temperature of 300°C does not allow the creation of wider zones (>2m) of partially molten tonalite and after 5 days the partially molten wall rock disappeared, as in the case of section 2 (Fig. 4.20). Host rock temperatures of 400°C and 500°C are however suitable to create wider zones (> 2m) of partially molten tonalitic host rock by instantaneous magma injection.

tonalitic magma. Injection leads to disaggregation of the mafic magma into enclaves [e.g. Caricchi et al. 2012, Turner and Campbell 1986, Hodge et al. 2012, Snyder and Tait 1995]. The increased crystallinity of the mafic enclaves leads to higher viscosity relative to the tonalitic host magma than at the start of injection, thus a rheological inversion occurs. Back-veining of partially molten tonalite of widths of <0.5m into the basaltic hybrid (2B) dyke (Fig. 4.7c) can be explained by such a static conduction thermal model with a host temperature of at least 500°C.

4.9 Conclusions

Partial melting textures of the tonalite host rock in immediate contact or close vicinity of dykes within 10 to 15m swarms and the abundance of tonalitic host rock xenoliths imply both selective and bulk assimilation. Plagioclase xenocrysts exhibiting inverse zoning, more albitic cores with fresh anorthite-rich

overgrowth and amphibole xenocryst with a lower temperature (less Ti (apfu)) cores and high temperature overgrowths (higher Ti (apfu)) underline the process of bulk assimilation. The tonalitic host rock assimilation source was identified based on bulk rock geochemical relations between the basaltic magma and the tonalite. In particular, trace elements such as Ni and Ba of post plutonic basaltic hybrid (2B) dykes demonstrate a mixing relationship of more primitive basalts (2A) with a Vacca tonalite end member in one of the cases. Whole rock radiogenic isotope ratios of $^{87}Sr/^{86}Sr$ and $^{143}Nd/^{144}Nd$ further reinforce the hypothesis of the Vacca tonalite as an assimilant to generate the basaltic hybrid (2B) dykes.

Trace element partitioning between amphibole micro-phenocrysts and the basaltic hybrid melt constrains the temperature of amphibole formation and emplacement to the high temperature stability ($\tilde{}$1050°C) of amphibole in calc-alkaline magmas. Temperature constraints are based upon comparison with partition coefficients obtained for amphiboles from fractional crystallization experiments at 7 kbar Nandedkar et al. [in prep.].

Closely spaced relatively thin dykes with a thickness for the bulk part of $<$0.5 m show alternating coalescence to dykes of up to 5 m in thickness and splitting again into thinner single dykes along strike. Coalescence of dykes in a swarm is furthermore associated with increased partial melting of the tonalite host rock, forming features like melt impregnated tonalite, basaltic intrusion breccias, and back veining of the molten host tonalite into the basaltic hybrid (2B) dyke.

The close spacing of relatively thin dykes in 10 to 15m wide swarms considerably increases the contact surface to the tonalite host rock and thus, boosts the heating effect of the host by the intrusion of the relatively hot, primitive basaltic magma. 1D static heat conduction models that were scaled to the recorded dyke swarm cross sections reproduce partial melting of the tonalite host rock, based on the instantaneous intrusion of closely spaced single basaltic (2A) and basaltic hybrid (2B) dykes, as observed in the field. A host rock temperature of at least 500°C at the time of dyke intrusion is required in order to reproduce observed 1 to 2m wide basaltic intrusion breccias through a static thermal conduction model.

Chapter 5

Immiscible Assimilation Processes in Picrobasaltic Dykes (Adamello Massif, Italy)

5.1 Abstract

Primitive picrobasaltic to Ol-tholeiitc dykes from the southern part of the Adamello Batholith (N-Italy) give insight into thermal erosion processes associated with arc-tholeiitic magmatism. These picrobasalts are the latest phase within a sequence of plutonic rocks, ranging from layered gabbros to different tonalitic to granodioritic intrusives. These primitive intrusions contain various features of felsic assimilants brought up from crustal depth with refractory rutile and zircon with textures typically found in plagiogranites or high-pressure/low-temperature metamorphic rocks. Picrobasalts with liquidus temperatures of up to 1375°C and estimated emplacement temperature conditions >1100°C carry these suspended plagioclase rich enclaves in the form of immiscible felsic liquids inside the host mafic liquid. Slow cooling within subhorizontal flat-lying thin sills allows in cases some mixing, leading to the observed gradational contacts in the field between the felsic and the mafic phase in the form of banding or layering. Compositional and temperature dependent viscosity model calculations for the felsic enclave liquid composition and the picrobasaltic composition show differences in viscosity that explain that the two phases did not mix at high temperatures and do preserve these textures in rapidly quenched chilled margins. Field evidence further shows that felsic liquids are concentrated towards the top of these sill like structures. This indicates that the lower density felsic liquids moving towards the top of the flat-lying magmatic bodies floating in the denser mafic liquid phase. Rutile and zircon with the according textural features and thermal constraints could represent a high-pressure/low-temperature (~470°C) origin of the assimilant, which so far has not been described in the Central Southern Alps. U-Pb ages of zircon show an early Cretaceous inherited component so far not described for the intrusives of the Adamello Batholith.

5.2 Introduction

Primitive mantle derived basaltic magmas such as picrobasalts bear the potential to melt and assimilate material during their transfer through the crust [Huppert and Sparks, 1985]. The present study focuses on such mantle derived picrobasaltic melts [Ulmer, 1988] that intruded immediately after a more voluminous phase of gabbroic, tonalitic and granodioritic plutonic intrusives in the southernmost part of the Adamello Batholith (N-Italy).

Such primitive picritic magmas bear features such as spherical to elliptical felsic structures also termed ocelli, which have been interpreted as immiscible parts of assimilated crust [Appel et al., 2009]. These spherical to elliptical phases within these ultramafic magmas have been described for Archean greenstone belts [Coltorti et al., 1987, Polat et al., 2007, 2008, Gelinas et al., 1976]. Occurrences of such structures are also reported from non-Archean volcanic and intrusive rocks [Philpotts, 1979, Freestone, 1978, Elthon et al., 1984, Mauger, 1988]. Fowler et al. [2002] give an overview of the different description terms comprising varioles, spherulites, spinifex and ocellis. The origin of such elliptical felsic structures has been much debated and the discussion has been confused by different names for similar structures and the same name for different structures [Fowler et al., 2002]. The origin and genesis of these features has been the subject of discussion and Gelinas et al. [1976] described felsic varioles as immiscible splitting of a tholeiitic magma from the Archean Abitibi Metavolcanic belt (Canada). The proposed genesis of these varioles has been later challenged based on petrographic features by other authors [Philpotts, 1979, Fowler et al.,

1987, 2002]. Appel et al. [2009] state that, due to their diverse compositional and textural characteristics, it is likely that more than one petrogenetic process is responsible for the formation of felsic spheroidal structures in mafic flows.

In the present case, the term ocelli is used entirely as a descriptive term for plagioclase rich lenses with a diameter ranging from 0.5 to 2 cm set in micro-gabbroic amphibole rich matrix. These felsic textural features are commonly associated with actual plagioclase rich banding containing quartz and accessory phases such as allanite, titanite, zircon and rutile. Furthermore, the felsic phase is expressed as banding or larger blobs. Accessory zircon and rutile with their inclusions provide crucial information of previous geological conditions [Spandler et al., 2004, Finch and Hanchar, 2003]. Zircon as a container is stable over a very large P-T range [Hermann et al., 2001, Katayama et al., 2001] and is used to constrain geochronological information. Spandler et al. [2004] showed the preservation of low-temperature alteration of oceanic crust by seawater, in the form of exsolution assemblage of thortveitite, yttrialite and xenotime withtin zircon.

So far, these felsic textural features have been described by Ulmer [1986] on petrographical and first order compositional basis. This study is the first to describe the associated accessory mineral assemblage based on detailed textures and composition. Further field relations and detailed compositional and petrographical description of the felsic textures together with the picrobasaltic host are provided. New U-Pb data on xenocrystic zircon indicates a lower Cretaceous age, of which the implications are discussed.

5.3 Geological Setting

The Adamello Batholith is located in the Alps in Northern Italy. Large volumes of tonalite and granodiorite, together with some marginal satellite ultrabasic and basic intrusions, built up the batholith over a time interval of 42-29 Ma [Del Moro et al., 1985, Schaltegger et al., 2009, Hansmann and Oberli, 1991]. An array of different dyke generations ranging from picro-basalts to dacites intruded into the Re di Castello superunit [Callegari and Brack, 2002], the southernmost plutonic intrusive suite of the Adamello Batholith.

The most primitive are picrobasaltic to Ol-tholeiitic dykes (1B) (Fig. 5.1) with inferred mantle separation conditions of 28 kbar and 1370°C [Ulmer, 1988] determined by multiple saturation experiments. The dyke suite is cogenetic, with larger volume plutonic magmatism comprising predominantly dioritic, tonalitic and granodioritic rocks in the southern Adamello but crosscuts these plutonic rocks. Picrobasalts and Ol-tholeiites intruded into the Lago della Vacca Complex (LVC) (41.98 ± 0.03 to 41.76 ± 0.03 Ma) and the Blumone Complex (42.07 ± 0.04 to 42.06 ± 0.02 Ma). The LVC complex is comprised of high-K marginal tonalite, the Vacca tonalite and the Galiner granodiorite, which together form an incrementally assembled pluton [John and Blundy, 1993, Schoene et al., 2012]. At the SE border of the LVC is the Blumone Complex, an older stratified gabbroic sequence that now forms the Cornone di Blumone and the Scoglio di Laione [Ulmer et al., 1983, Ulmer, 1986]. Various rock types build up the Blumone Complex encompassing: plagioclase-bearing wherlites; granular olivine-gabbros; granular gabbros; granular cpx-bearing anorthosites to anorthositic gabbros; coarse grained magnetite + hornblende ultramafics. The whole complex is crosscut by younger pegmatitic hornblende gabbros [Rösli, 1982, Ulmer et al., 1983, Ulmer, 1986]. Picrobasalt and Ol-tholeiites of generation (1B) have titanite ages for two samples with

weighted average means of 41.70 ± 0.16 Ma and 41.67 ± 0.06 Ma respectively [Hürlimann et al., in prep.b]. These ages appear to confirm the crosscutting relationships with regard to the LVC and the Blumone Complex and stress the close association with the slightly older plutonic suite.

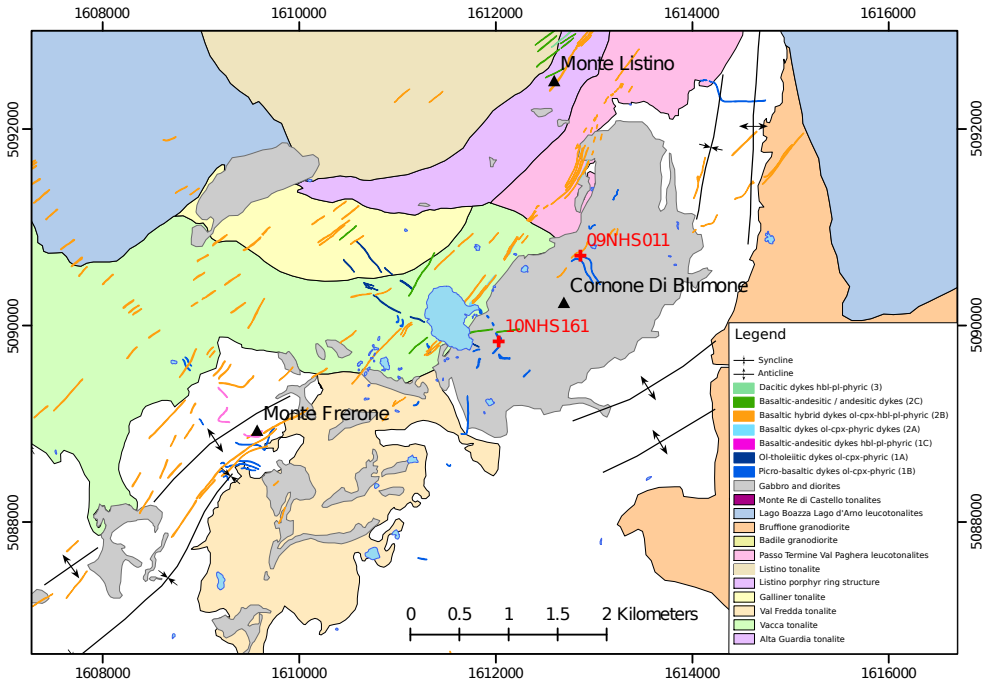

Figure 5.1: Geological map of the Val Fredda and Lago della Vacca area with a sequence of plutonic intrusives belonging to the southernmost part of the Re di Castello intrusive suite [Callegari and Brack, 2002] of the Adamello Batholith (N-Italy). An earlier phase of post-plutonic dykes are subhorizontal flat-lying picrobasalts to Ol-tholeiites (1B) that contour on different levels of altitude from Monte Frerone (SW) towards Cornone di Blumone (NE).

5.4 Field Relations and Petrography

Picrobasalts and Ol-tholeiites of the generation (1B) are subhorizontal, flat-lying, small scale, sill-like features. These subhorizontal dykes range in thickness from 0.5 to 2.5m and have been emplaced on different level of altitudes, which is best seen as intrusion into the layered gabbroic Blumone Complex and the LVC. These picrobasalts further reach into the Triassic wallrock sedimentary sequence, where they are exposed prominently in SE and SW cliff faces of Monte Frerone. Ulmer [1986] interpreted them as dome-shaped structures, of which one is located in the Lago della Vacca area whereas the other is lying in the area of Monte Frerone. Apophyses have a limitation in length and their thickness reaches down to only a few centimeters.

Within chilled margins, pseudomorphs of olivine and clinopyroxene phenocrysts are abundant. Throughout the whole thickness, these dykes consist otherwise of equigranular amphibole set in interstitial plagioclase, which form in general a dense massive green matrix. Olivine phenocrysts are replaced by different secondary phases. Various amounts of chlorite, epidote, brucite, talc, tremolite, haematite and magnetite

build up olivine pseudomorphs. In rare cases, cores of olivine are preserved and mantled by secondary talc and magnetite. Within olivine pseudomorphs of brownish Cr-spinel or picotite and high temperature alteration is indicated by the presence of magnetite. Clinopyroxene is generally much better preserved and forms large single crystals or crystal clots. Skeletal growth or sieve textures of clinopyroxene are common and embayments are filled with fine-grained phases composing the matrix. Pseudomorphic replacements of clinopyroxene consist of green amphibole and light brownish spinels occur in the core zones of clinopyroxene. Plagioclase occurs in olivine-tholeiites in the form of microphenocrysts. These microphenocrysts show polysynthetic twinning. The plagioclase lacks apparent petrographicaly zoning and is in general homogeneous. Euhedral plagioclase microphenocrysts are flow aligned, parallel to the dyke margins. The matrix consists of acicular green to olive zoned amphibole and plagioclase. A microlithic fluidal texture at dyke margins consists of acicular green to olive zoned amphibole and plagioclase. Central parts of the same dykes show acicular amphiboles and interstitial strongly zoned plagioclase that are indicative for slower cooling of this part of the dyke. Opaque minerals within the matrix are ulvospinel and magnetite forming anhedral to subhedral grains.

A striking textural feature in outcrop and microscopic scale is the occurrence of a separate felsic bright white zones in the form of lenses (Fig. 5.2a) or bands (Fig. 5.2a, c) at the top part of these picrobasalts and Ol-tholeiites (1B). This felsic phase is plagioclase with minor greenish zoned amphibole, alkalifelspar and quartz in larger bands or blobs. Anorthite rich cores of plagioclase are in cases replaced by sericite or epidote minerals. Accessory phases, including euhedral to subhedral zircon (Fig. 5.2b) and anhedral rutile are concentrated in these plagioclase rich parts. Rutile exhibits a reaction rim to secondary titanite as shown in figure 5.2f. Allanite occurs interstitially between green amphibole and plagioclase and is commonly strongly zoned (Fig. 5.2d). Interstitial titanite (Fig. 5.2b) is another common accessory phase associated with these felsic zones. The felsic phase shows a variation of contacts to the amphibole rich basaltic part with gradational contacts for banding or layering (Fig. 5.2a, c, e) and sharper contacts for small enclaves or ocelli. Further distinct felsic veins exist consisting almost entirely of plagioclase (Fig. 5.2c). For felsic layers or large blobs, the top part in cases exhibits a wavy horizon, indicating Rayleigh-Taylor instabilities between a mafic and a felsic melt phase.

5.5 Analytical Methods

Bulk Rock Geochemistry

After initial size reduction by a hydraulic press, all samples were first ground to a fine powder in an agate mill. Thereafter, an aliquot was heated to 1050°C in a furnace to determine the loss of ignition by mass difference. The fired product was then mixed with the appropriate amount of $Li_2B_4O_7$ (1.2121 : 6) and fused for five minutes in a Pt-crucible and subsequently poured in a Pt-casting dye and quenched to a glass. Major element compositions of whole rock samples were determined on glass beads by X-ray fluorescene (XRF), on a PANalytical Philips PW2400 spectrometer at the University of Lausanne. BHVO-1, NIM-N, NIM-G and SY-2 standards were used for quality control. Uncertainties of XRF analyses are in the range of 0.5 wt.% (2 sigma) for major components such as SiO_2 and 0.006% for a minor component such as NiO. The trace-element concentrations of bulk rocks were measured on the same XRF glass beads, with

a Geolas 200M 193 nm ArF excimer laser ablation system interfaced with an Elan 6100 DRC quadrupole spectrometer (LA-ICP-MS) at the Swiss Federal Institute of Technology, Zurich. The performance of the LA-ICP-MS was optimized with the NIST SRM 612 glass in order to improve the sensitivity (Mg $>$ 10000 cps and La $>$ 40000 cps). During this optimization doubly charged ions ($Ba^{++}/Ba^{+} < 2\%$) and oxide production rates (ThO^{+}/Th^{+}) were minimized. Three repeat measurements were performed on the glass beads with a laser pit size of 120μm, using a laser frequency of 10Hz and energy of 160mJ, which is equivalent to 12 J/cm2. Helium was used as a cell gas carrier. Background and ablation interval acquisition times were 70 and 30-35 seconds respectively. Dwell times for different isotopes range from 10 to 20ms, employing a peak hopping mode. Absolute trace-element concentrations were determined using CaO wt% (determined by XRF) as an internal standard and NIST 612 or NIST 610 as an external standard. The average elemental abundances are taken from Pearce et al. [1997] and data was reduced with SILLS software [Longerich et al., 1996, Guillong et al., 2008].

Mineral Chemistry

Major element compositions of minerals were measured by wavelength-dispersive analysis, using a JEOL JXA-8200 electron microprobe equipped with five spectrometers at the University of Lausanne. Samples were polished and carbon coated thin-sections; standards employed are natural minerals and synthetic glasses. Measurements were corrected with the PRZF method [Armstrong, 1995]. The beam current was set to 15nA with an acceleration voltage of 15keV and beam size was varied between 1μm and 4μm for feldspars (plagioclase, alkalifeldspar), amphibole, apatite and titanite. Major elements on the respective mineral phases were measured for 20s on peak and 10s on background on both sides of the peak. Minor-elements were measured for 30s on peak and 15s on background each side of the peak. For allanite, the acceleration voltage was 25kV and the beam current was set to 10nA. Potential interferences were avoided by checking EDS-spectra of natural allanite in the sample by choosing non interfering X-ray peaks for measurements. Counting times for major elements are the same as for the other phases whereas for trace elements counting times range from 30s to 100s for the peaks and 15s to 50s for backgrounds. Zr concentration measurements in rutile where performed with microprobe conditions of 200nA for the beam current and 15kV for the acceleration voltage. A counting time of 150s was applied on both sides of the peak on the background, whereas the counting time for the peak is 300s. Trace-element analysis was performed on the same polished thin-sections using an ELEMENT XR sector field ICP-MS, coupled with an UP193-FX ArF 193nm excimer laser ablation system at the University of Lausanne. The LA-ICP-MS system was optimized using NIST SRM 612 glass standard to maximize the sensibility ($La^{139+} > 3.5 \cdot 10^{6}$ cps and $Th^{232+} > 4.5 \cdot 10^{6}$ cps). At the same time, doubly charged ions ($Ba^{++}/Ba^{+} < 2\%$) and oxide production (ThO+/Th+ $< 0.05\%$) was minimized. Helium was used as cell gas (1.00 [l/min]) and Ar was used as sample gas (ranging from 0.700-0.730 [l/min]). The pit size during laser ablation was chosen according to grain size and mineral texture. Variations for different minerals are 20-25μm for amphibole, 50-75μm for titanite, 25-35μm for allanite, 10-20μm for rutile. The repetition rate and the laser energy was varied to achieve 5.22-5.98 J/cm^2 depending on the analyzed mineral phase. Reptition rate of the laser (frequency) was for amphibole 5Hz, titanite 10Hz, allanite 12Hz and rutile 7Hz. Acquisition times for background and ablation interval were 120s and 60s respectively, for each laser spot. According to expected

concentrations, dwell times for measured masses were varied between 20 to 40ms for amphibole, titanite and allanite. For rutile, dwell times are in the range of 20 to 80ms. Absolute trace-element concentrations were determined likewise for glass beads, using CaO wt% or alternatively Al_2O_3 (determined by EMPA) as internal standard and NIST 612 as an external standard. The data was reduced with LAMTRACE [Longerich et al., 1996, Jackson, 2008] and average elemental abundances for the NIST 612 standard were taken from Pearce et al. [1997].

X-ray Mapping

X-ray maps for zircon (Fig. 5.7) were acquired with the electron microprobe by wavelength dispersive spectrometry (WDS) under an acceleration voltage of 20kV and beam current of 400nA. The meshsize or pixel size of the X-ray maps is 0.5 by 0.5μm and for displaying, the elemental maps were further flattened or interpolated through image processing

5.6 Bulk Rock Geochemistry and Mineral Chemistry

Picro-Basaltic Dyke Profile

Ulmer [1986] collected in the immediate vicinity of the Lago della Vacca about 500m from the Rifugio Tita Secchi a profile of 11 samples (RC158/1A,RC158/1B, RC158/2-RC158/10) (Fig. 5.3) for bulk rock geochemical analysis. The outcrop was revisited and a schematic profile was recorded. The top of the profile shows an abundance of different felsic textures such as enclaves / ocellis and plagioclase rich layering. This top zone correlates with an increase in Al_2O_3 and incompatible elements such as Sr and Zr. On the other hand, MgO, Cr and Ni clearly decrease in this top zone. Particularly MgO and Ni demonstrate a compatible behaviour with regard to olivine and some of the smaller kinks in the profile can be related to accumulation of olivine phenocrysts. Incompatible element (Sr, Zr) concentrations increase within chilled margins on a small scale over the entire profile.

Felsic Lenses

Bulk geochemistry of two felsic enclaves (A, B) was determined by analyzing all the present major (plagioclase, amphibole) and accessory (alkalifeldspar, epidote/allanite, apatite, titanite) phases by the electron microprobe. The according bulk composition of the two felsic enclaves was calculated based on mineral phase modes (Tab. 5.3) obtained from backscatter image analysis (Fig. 5.4a, b). Thresholding the backscatter image yielded mineral modes of the felsic enclaves. Table 5.4 reports the major and minor element composition of all the phases in the two different enclaves. Plagioclase is zoned with an anorthite rich core ($\tilde{}An_{80}$) and albite rich rims ($\tilde{}An_{20}$). The core regions are partially replaced by sericite. Plagiclase composition was split into a core and rim domain. Measured plagioclase profiles were divided halfway between the two extremes in terms of the anorthite (An) number and averaged according to the two domains. For the bulk geochemical calculation of the enclaves (2/5) of plagioclase in figure 5.4b represent the plagioclase core domain whereas the other (3/5) represent the plagioclase rim domain.

Composition	**picro-basalt**	**picro-basalt**	**picro-basalt**	**picro-basalt**	**picro-basalt**	**picro-basalt**	**picro-basalt**	**picro-basalt**	**picro-basalt**	**picro-basalt**	**picro-basalt**
Sample	**RC158/1A [top]**	**RC158/1B**	**RC158/2**	**RC158/3**	**RC158/4**	**RC158/5**	**RC158/6**	**RC158/7**	**RC158/8**	**RC158/9**	**RC158/10 [base]**
Generation	**1B**	**1B**	**1B**	**1B**	**1B**	**1B**	**1B**	**1B**	**1B**	**1B**	**1B**
SiO2	46.95	47.31	45.19	44.95	45.08	45.12	45.25	45.46	45.51	45.39	46.86
TiO2	0.75	0.75	0.85	0.80	0.70	0.68	0.69	0.70	0.72	0.71	0.76
Al2O3	14.27	14.57	14.74	14.89	12.39	11.92	12.59	12.51	12.37	12.27	14.29
Fe2O3	3.18	3.80	5.29	4.94	3.16	3.30	3.19	3.41	3.43	3.55	4.69
MnO	0.15	0.16	0.14	0.13	0.16	0.17	0.16	0.17	0.18	0.17	0.15
MgO	13.14	13.01	12.68	12.03	14.47	16.89	15.68	16.04	16.45	16.29	13.56
CaO	9.88	10.13	9.42	9.69	10.31	9.55	9.85	9.92	10.15	10.09	9.96
Na2O	1.25	1.18	1.95	1.92	1.19	0.70	1.05	0.94	0.90	0.97	1.07
K2O	1.21	0.16	0.44	0.56	0.57	0.42	0.57	0.55	0.31	0.32	1.06
P2O5	0.13	0.13	0.11	0.12	0.10	0.10	0.10	0.10	0.09	0.09	0.13
Total	98.57	98.87	98.57	97.75	98.68	99.04	98.66	99.36	99.38	98.80	98.89
H2O	1.98	2.59	3.12	3.06	3.46	3.50	3.08	3.21	3.02	2.91	2.16
CO2	0.05	0.04	0.81	0.93	1.17	0.09	0.06	0.06	0.05	0.05	0.05
FeO	5.5	4.9	3.7	3.6	5.75	6.4	6.2	6.1	6	5.8	4

Table 5.1: Major elements from SiO_2 to P_2O_5 (all in [wt%]) were determined by XRF analysis.

Composition	picro-basalt	picro-basalt	picro-basalt	picro-basalt	picro-basalt	picro-basalt	picro-basalt	picro-basalt	picro-basalt	picro-basalt	picro-basalt
Sample	RC158/1A [top]	RC158/1B	RC158/2	RC158/3	RC158/4	RC158/5	RC158/6	RC158/7	RC158/8	RC158/9	RC158/10 [base]
Generation	1B	1B	1B	1B	1B	1B	1B	1B	1B	1B	1B
Sc	48.1	48.6	51.6	46.3	49.0	51.1	49.7	50.9	50.3	49.8	47.4
V	275	274	304	288	268	262	270	267	274	275	271
Co	45.2	44.6	44.5	41.7	45.9	53.5	52.1	50.4	53.8	52.1	46.0
Ni	244.3	234.8	222.8	198.4	255.5	326.3	296.6	303.9	324.2	309.6	235.5
Cu	181.3	350.0	3459.5	4281.9	155.8	13.4	12.5	15.4	22.2	27.7	478.4
Zn	37.6	35.7	33.0	30.5	32.7	38.9	37.1	37.2	38.6	38.0	35.8
Ga	12.1	12.7	11.7	12.1	10.7	10.7	10.8	10.7	10.8	10.6	11.6
Rb	41.3	3.4	12.4	16.1	18.6	13.2	16.6	15.9	7.3	7.2	34.0
Sr	272	265	331	344	220	133	172	163	149	150	253
Y	14.0	13.9	14.2	14.2	12.8	12.3	12.9	12.5	12.7	13.0	13.9
Zr	41	42	37	39	33	31	33	32	31	30	39
Nb	2.6	2.5	3.1	2.7	1.8	2.1	1.9	1.9	2.0	1.9	2.5
Cs	11.16	0.73	0.58	0.72	0.95	0.74	0.72	0.73	0.48	0.56	8.89
Ba	112	43	78	92	70	59	86	81	60	60	100
La	11.0	11.1	10.4	10.1	6.2	6.4	6.0	6.0	6.8	6.7	10.3
Ce	16.8	16.9	15.6	15.3	11.5	11.5	11.0	11.1	11.5	11.1	15.6
Pr	1.98	1.92	1.93	1.85	1.60	1.59	1.47	1.54	1.51	1.46	1.89
Nd	8.7	8.6	8.2	8.5	7.8	7.6	7.1	7.5	6.8	6.8	8.0
Sm	2.16	2.00	2.07	2.24	1.97	1.94	2.07	1.79	2.06	1.92	2.02
Eu	0.69	0.73	0.79	0.74	0.66	0.58	0.64	0.65	0.67	0.64	0.59
Gd	2.406	2.168	2.200	2.495	1.943	2.094	2.183	1.856	1.808	2.013	2.190
Tb	0.429	0.394	0.385	0.412	0.377	0.366	0.367	0.363	0.369	0.366	0.381
Dy	2.67	2.44	2.53	2.73	2.20	2.27	2.21	2.30	2.32	2.41	2.45
Ho	0.532	0.539	0.557	0.558	0.495	0.463	0.505	0.475	0.500	0.469	0.508
Er	1.38	1.57	1.51	1.54	1.29	1.28	1.29	1.32	1.23	1.26	1.42
Tm	0.213	3.427	0.209	0.199	0.200	0.178	0.197	0.194	0.170	0.173	0.183
Yb	1.64	3.43	1.44	1.44	1.38	1.35	1.41	1.22	1.29	1.27	1.63
Lu	0.233	0.220	0.185	0.202	0.178	0.193	0.171	0.203	0.205	0.189	0.192
Hf	1.07	1.17	1.14	1.14	0.95	0.95	0.99	0.98	0.99	0.94	1.10
Ta	0.19	0.18	0.15	0.16	0.11	0.12	0.14	0.14	0.13	0.11	0.17
Pb	0.93	0.93	1.78	1.93	1.45	1.40	1.17	1.10	1.21	0.74	0.95
Th	2.32	2.26	1.61	2.05	1.62	1.70	1.59	1.58	1.32	1.34	2.04
U	0.56	0.62	0.73	0.87	0.47	0.40	0.39	0.38	0.26	0.26	0.57

Table 5.2: Trace elements (all in [ppm]) were determined by LA-ICP-MS analysis. Internal standard for LA-ICP-MS data reduction in LAMTRACE is CaO wt% was taken form XRF analysis. External standard is the NIST SRM 612.

Likewise, amphibole exhibits an Al_2O_3rich core domain and a Al_2O_3 poorer rim domain. Amphibole cores in figure 5.4b build up (1/5) whereas rims build up (4/5).

The calculated bulk chemical compositions of the enclaves or lenses are generally basaltic-andesitic (SiO_2: 53.63-55.45 wt%). Table 5.4 reports further enrichment of Al_2O_3 (19.12-21.12 wt%) and Na_2O (4.09-4.85 wt%) with regard to the bulk rock composition of the Ol-tholeiite. Enrichment of Na_2O by

Phase	NHS1961LensA	NHS1961LensB
Modes	[%]	[%]
Amphibole	30.19	24.11
Plagioclase	66.15	74.47
AlkFsp	2.08	0.00
Apatite	0.40	0.63
Titanite	0.07	0.71
Epidote / Allanite	1.11	0.08

Table 5.3: Mineral modes for felsic lens A and lens B (NHS196-1), determined directly from a backscatter image that was thresholded for the different phases based on different intensity. The modal amounts in percents were calculated from different area proportions for the according phases, normalized to 100%.

more than a factor of two is related to the abundance of albitic plagioclase. On the other hand, MgO (3.85-4.09 wt%) and FeO (2.63-2.89 wt%) are depleted with regard to the ol-tholeiitic bulk composition, which is correlated with less abundant amphibole in the felsic enclaves.

Accessory Phases

For accessory allanite, major and minor elements together with trace elements such as SrO, P_2O_5, PbO, UO_2, Y_2O_3 and the light rare earth elements (LREE) from La_2O_3 to Dy_2O_3 (Tab. 5.5) were analyzed with the electron microprobe. Moreover, we report here representative allanite, titanite and amphibole analyses carried out with LA-ICP-MS (Tab. 5.7) covering a larger variation of trace elements. Chondrite normalized [McDonough and Sun, 1995] trace element patterns for allanite show a clear enrichment of LREE (La-Sm) (Fig. 5.5a), relative to titanite that exhibits flat chondrite normalized trace element patterns. Furthermore, allanite shows some preference for Th with regard to U. On the other hand, titanite exhibits some preference of U over Th. Total LREE apfu for allanite from the different samples analyzed by electron microprobe range from 0.41± 0.16 to 0.51 ± 0.17. Variation in LREE contents of allanite can be correlated with strong zoning, which is seen in back scatter images (Fig. 5.2d). Thus the observed epidote-group minerals lie halfway between the epidote and allanite endmember [Armbruster et al., 2006]. Exchange reactions for REE and U + Th in epidote are the following [Dollase, 1971, Armbruster et al., 2006]:

$$^{M3}(Mg,Fe)^{2+} +^{A2} REE^{3+} =^{M3} Al^{3+} +^{A2} Ca^{2+} \tag{5.1}$$

$$^{M3}(Mg,Fe)_2^{2+} +^{A2} (Th,U)^{4+} =^{M3} Al_2^{3+} +^{A2} Ca^{2+} \tag{5.2}$$

Non-stoichiometric allanites with $>$ 3 Si apfu on an 8 cation basis are excluded. For Armbruster et al. [2006], poor analysis notwithstanding, is among the most likely causes of partial non-stoichiometry and the presence of A-site vacancies, or substitution of O^{2-} by F^- on the O4-site (dollaseite substitution).

Chondrite normalized amphibole values of Th, U, Nb, Ta and REE appear completely flat with respect to the same trace element patterns for allanite. In some part this appears to be related to high LREE contents of allanite, which makes the same patterns for amphibole apparently uniform. Nevertheless amphibole exhibits the absence of a clear Eu-anomaly in the same normalized patterns which is either

Phase A	SiO2	TiO2	Cr2O3	Al2O3	FeO	MnO	MgO	NiO	CaO	Na2O	K2O	P2O5	F	Cl	Total	n
	[wt%]	[wt%]	[wt%]	[wt%]	[wt%]	[wt%]	[wt%]	[wt%]	[wt%]	[wt%]	[wt%]	[wt%]	[wt%]	[wt%]	[wt%]	
Am core	44.37	1.22	0.01	11.87	12.10	0.42	14.06	0.01	11.34	1.97	0.25	n.a.	<0.03	0.04	97.65	n=5
	(162)	(64)	(2)	(67)	(63)	(29)	(65)	(2)	(89)	(25)	(8)			(2)	(44)	
Am rim	53.80	0.15	0.05	4.04	9.27	0.22	17.64	0.03	12.93	0.44	0.13	n.a.	<0.03	0.01	98.69	n=5
	(167)	(5)	(2)	(102)	(36)	(6)	(71)	(2)	(13)	(11)	(5)			(1)	(136)	
Pl core	56.21	0.01	0.01	27.87	0.29	0.01	0.02	0.01	10.18	5.39	0.22	n.a.	<0.02	0.00	100.21	n=60
	(447)	(2)	(2)	(287)	(16)	(3)	(4)	(2)	(337)	(196)	(107)			(1)	(124)	
Pl rim	61.52	0.01	0.01	24.57	0.14	0.01	0.01	0.01	6.45	7.71	0.12	n.a.	0.00	0.01	100.55	n=56
	(326)	(1)	(2)	(173)	(11)	(2)	(4)	(2)	(212)	(131)	(4)		(0)	(3)	(171)	
Afs	66.75	0.00	0.00	18.25	0.15	0.01	0.03	0.00	0.03	0.47	14.69	n.a.	<0.02	0.00	100.37	n=16
	(100)	(0)	(2)	(31)	(17)	(3)	(15)	(1)	(3)	(21)	(26)			(1)	(122)	
Ap	0.23	0.00	n.a.	0.02	0.09	0.05	<0.03	n.a.	56.63	0.05	0.01	42.41	1.74	0.47	101.69	n=12
	(68)	(1)		(2)	(8)	(4)			(66)	(14)	(1)	(181)	(32)	(32)	(214)	
Ep	38.28	0.09	n.a.	23.79	11.22	0.09	0.02	n.a.	23.81	0.02	0.00	0.02	0.00	0.00	97.34	n=10
	(55)	(17)		(215)	(267)	(8)	(5)		(50)	(5)	(1)	(5)	(0)	(0)	(104)	
Ttn	30.76	38.47	n.a.	1.01	0.58	0.03	0.00	n.a.	28.76	0.03	0.01	0.31	0.01	0.00	99.98	n=11
	(68)	(91)		(39)	(29)	(5)	(1)		(68)	(3)	(2)	(65)	(6)	(1)	(164)	
Bulk lens A	53.65	0.12	0.01	19.12	2.63	0.07	4.09	0.01	8.80	4.68	0.45	0.17	0.01	0.01	93.82	
Bulk rock NHS011	47.05	0.79	0.09	15.16	8.28	0.17	11.10	0.02	10.05	1.67	0.99	0.17	n.a.	n.a.	99.23	

Phase B	SiO2	TiO2	Cr2O3	Al2O3	FeO	MnO	MgO	NiO	CaO	Na2O	K2O	P2O5	F	Cl	Total	n
	[wt%]	[wt%]	[wt%]	[wt%]	[wt%]	[wt%]	[wt%]	[wt%]	[wt%]	[wt%]	[wt%]	[wt%]	[wt%]	[wt%]	[wt%]	
Am core	46.24	0.79	0.00	10.12	12.77	0.46	14.04	0.01	11.46	1.70	0.29	n.a.	<0.03	0.04	97.93	n=4
	(255)	(42)	(1)	(587)	(259)	(37)	(106)	(1)	(115)	(136)	(12)			(3)	(170)	
Am rim	53.08	0.22	0.02	4.00	10.87	0.38	16.39	0.02	12.58	0.46	0.14	n.a.	<0.03	0.01	98.17	n=14
	(220)	(23)	(5)	(221)	(328)	(43)	(209)	(2)	(56)	(27)	(11)			(1)	(104)	
Pl core	53.35	0.01	0.00	29.14	0.38	0.01	0.03	0.01	12.32	4.43	0.12	n.a.	<0.02	0.00	99.80	n=28
	(273)	(1)	(1)	(161)	(13)	(3)	(5)	(2)	(186)	(107)	(16)			(1)	(240)	
Pl rim	59.39	0.00	0.00	25.38	0.14	0.01	0.01	0.01	7.46	7.21	0.15	n.a.	<0.02	0.00	100.31	n=54
	(318)	(1)	(1)	(152)	(13)	(3)	(2)	(2)	(185)	(106)	(4)			(1)	(113)	
Ap	0.08	0.00	n.a	0.02	0.15	0.02	0.00	n.a.	57.33	0.04	0.01	41.83	1.71	0.48	101.66	n=9
	(14)	(0)		(2)	(12)	(3)	(2)		(71)	(8)	(2)	(183)	(23)	(8)	(211)	
Ep	38.46	0.06	n.a	23.96	10.98	0.09	0.02	n.a.	23.77	0.02	0.00	n.a.	<0.02	0.00	97.41	n=3
	(97)	(3)		(88)	(38)	(5)	(3)		(30)	(4)	(1)			(1)	(190)	
Ttn	30.76	38.47	n.a	1.01	0.58	0.03	0.00	n.a.	28.76	0.03	0.01	0.31	0.01	0.00	99.98	n=11
	(68)	(91)		(39)	(29)	(5)	(1)		(68)	(3)	(2)	(65)	(6)	(1)	(164)	
Bulk lens B	55.45	0.36	0.01	21.12	2.89	0.10	3.85	0.01	10.33	4.85	0.14	0.27	0.01	0.01	99.66	

Table 5.4: All the mineral phases (Am, Pl, Afs, Ap, Ep (Aln), Ttn) in two felsic enclaves (A, B) that were analyzed by microprobe for major- and minor element oxides. The bulk rock analysis (NHS011) of the host Ol-tholeiite is shown for comparison in the table for lens A. n is the number of replicate microprobe analyses. In brackets two standard deviations of replicate analyses are reported in terms of the least unit cited. Thus 29.14 (161) represents 29.14 ± 1.61. Note that averages and variances are pooled over different crystals for each sample.

indicating high fO_2 conditions during crystallization of plagioclase beside amphibole or an early crystallization of amphibole and plagioclase later in sequence. Textural features favor an early crystallization of greenish amphibole followed by interstitial plagioclase.

Zr was analyzed as a trace element in rutile (Fig. 5.2f) with the electron microprobe. Values are reported in table 5.6 and for each sample, pooled mean value and standard deviation (in brackets) was calculated. The analytical details are described in the method section of this paper.

Sample Aln	**Aln002-1-11**	**Aln007-5-2**	**Aln011-3-2**	**Aln073-1-4**
	[wt%]	[wt%]	[wt%]	[wt%]
SiO2	35.74	35.78	36.63	36.04
TiO2	0.43	0.21	0.39	0.18
Al2O3	20.62	20.29	21.13	20.68
FeO	11.90	11.87	12.17	10.80
MnO	0.93	0.15	0.55	0.17
MgO	0.41	0.69	0.47	1.20
CaO	15.86	15.54	16.69	14.48
Na2O	0.08	b.l.d.	0.07	b.l.d.
K2O	0.01	b.l.d.	0.01	0.00
SrO	b.l.d.	b.l.d.	0.05	b.l.d.
P2O5	0.36	0.01	0.08	0.01
La2O3	4.64	4.22	5.22	5.21
Ce2O3	6.34	7.34	5.50	8.67
Pr2O3	0.45	0.64	0.26	0.64
Nd2O3	1.47	1.99	0.61	2.09
Sm2O3	0.07	0.20	0.05	0.14
Eu2O3	0.07	0.09	b.l.d.	0.10
Gd2O3	0.09	0.07	b.l.d.	0.06
Dy2O3	0.02	b.l.d.	b.l.d.	b.l.d.
Y2O3	0.17	0.04	0.01	0.05
PbO	0.03	0.01	0.02	b.l.d.
UO2	b.l.d.	b.l.d.	0.08	0.01
Total	99.98	100.14	100.33	101.54

Table 5.5: Representative allanite analyses for four different samples that were performed with the electron microprobe. Note that allanite appears strongly zoned in backscatter image (Fig. 5.2d), with variable concentrations of light rare earth elements (LREE). For analytical details see methods section.

5.7 Xenocrystic Zircon

Petrography and X-ray Mapping

At first glance, zircon crystals within these plagioclase rich felsic textures appear euhedral. Particular backscatter and cathodoluminescence imaging on a scanning electron microscope reveals further complexity. Zircon crystals are small and in the range of 10μm to 20μm. Polycrystalline zircon cores commonly exhibit pristine, regularly zoned overgrowths of only a few μm. A backscatter image in figure 5.7 presents

Phase	**Rt161-13**	**Rt161-11**	**Rt161-8**	**Rt161-5**	**Rt011-12**	**Rt011-10**	**Rt011-7**
Sample	**NHS161**	**NHS161**	**NHS161**	**NHS161**	**NHS011**	**NHS011**	**NHS011**
Al2O3 [wt%]	0.020	0.007	0.013	0.013	0.006	0.009	0.013
CaO [wt%]	0.152	<0.07	0.247	0.426	<0.09	<0.09	<0.02
V	1161	974	851	812	948	1097	1492
Cr	6.4	6.4	9.8	48.0	<7.3	53.8	9.4
Zr	11	93	14	15	22	17	21
Nb	1313.5	2858.9	2124.9	2026.1	1443.8	923.7	3151.3
Mo	2.42	3.13	2.62	2.71	2.90	2.47	3.08
Sn	12.7	16.7	19.0	9.8	6.1	12.9	14.6
Sb	16.14	16.43	14.16	13.16	33.55	15.02	6.91
Hf	0.40	3.27	0.49	0.36	0.66	0.37	0.62
Ta	110	189	141	109	108	62	249
W	4282	8974	1938	1563	2422	5880	12616
Pb	0.59	1.59	0.14	0.30	0.64	1.00	0.15
Th	1.85	3.15	1.83	1.80	1.37	3.40	1.19
U	16.72	27.27	18.80	14.22	7.59	17.51	14.42

Table 5.6: Rutile analyses carried out with LA-ICP-MS (all in [ppm] except CaO and Al_2O_3 in [wt%]). Major elements such as CaO were measured to check for accidental ablation of surrounding secondary titanite since rutile crystals have anhedral skeletal shapes.

Phase	**Ttn011-16**	**Ttn161-10**	**Aln002-3**	**Aln011-1**	**Am002-3**
Sample	**NHS011**	**NHS161**	**NHS002**	**NHS011**	**NHS002**
	[ppm]	[ppm]	[ppm]	[ppm]	[ppm]
Sc	20.2	8.0	112.7	24.6	35.4
V	1105	703	546	549	655
Rb	0.24	0.33	0.25	<0.10	23.88
Sr	17	29	691	224	230
Y	1658.2	2623.2	2025.7	150.2	31.4
Zr	535	564	46	1115	67
Nb	526.4	8263.1	0.1	1.5	4.2
Ba	0.14	0.18	27.57	4.09	117
La	312.0	84.9	24893	48806	5.5
Ce	1196.7	476.4	41929	58431	16.4
Pr	207.65	119.65	3994	4141	2.92
Nd	1031.0	818.9	13791	9187	16.7
Sm	295.08	323.25	1798	566	4.03
Eu	100.25	126.62	251	123	1.20
Gd	311.68	385.55	1116	148	5.90
Tb	49.27	65.06	122	12	0.78
Dy	326.06	468.75	579	45	5.74
Ho	66.54	91.90	80.65	5.83	1.21
Er	184.41	258.11	156.08	11.72	3.45
Tm	26.77	38.20	17.46	1.46	0.69
Yb	172.93	250.39	101.98	10.04	3.44
Lu	22.63	28.79	12.58	1.62	0.56
Hf	40.15	50.91	2.63	39.66	2.30
Ta	19.61	579.96	0.05	0.66	0.36
Pb	1.67	0.67	39.73	25.07	0.32
Th	326.03	37.93	2667.96	918.29	1.12
U	88.87	176.68	220.57	175.52	0.11

Table 5.7: Representative analyses of accessory titanite (Ttn) and allanite (Aln) acquired by LA-ICP-MS. Moreover, amphibole from the overall microgabbroic texture (Am) is reported for comparison. Internal standard for LA-ICP-MS data reduction in LAMTRACE is CaO wt% determined by electron microprobe. External standard is the NIST SRM 612.

a porous core with bright small phases that are different from zircon. The same image demonstrates again a later regular zircon overgrowth feature.

X-ray maps for Y and P demonstrate (Fig. 5.7) a homogeneous distribution over the whole analyzed zircon grain. Higher concentration of Th and U (Fig. 5.7) correspond with an abundance of bright separate phases of the porous core region. Porous texture of the zircon core indicates dissolution processes.

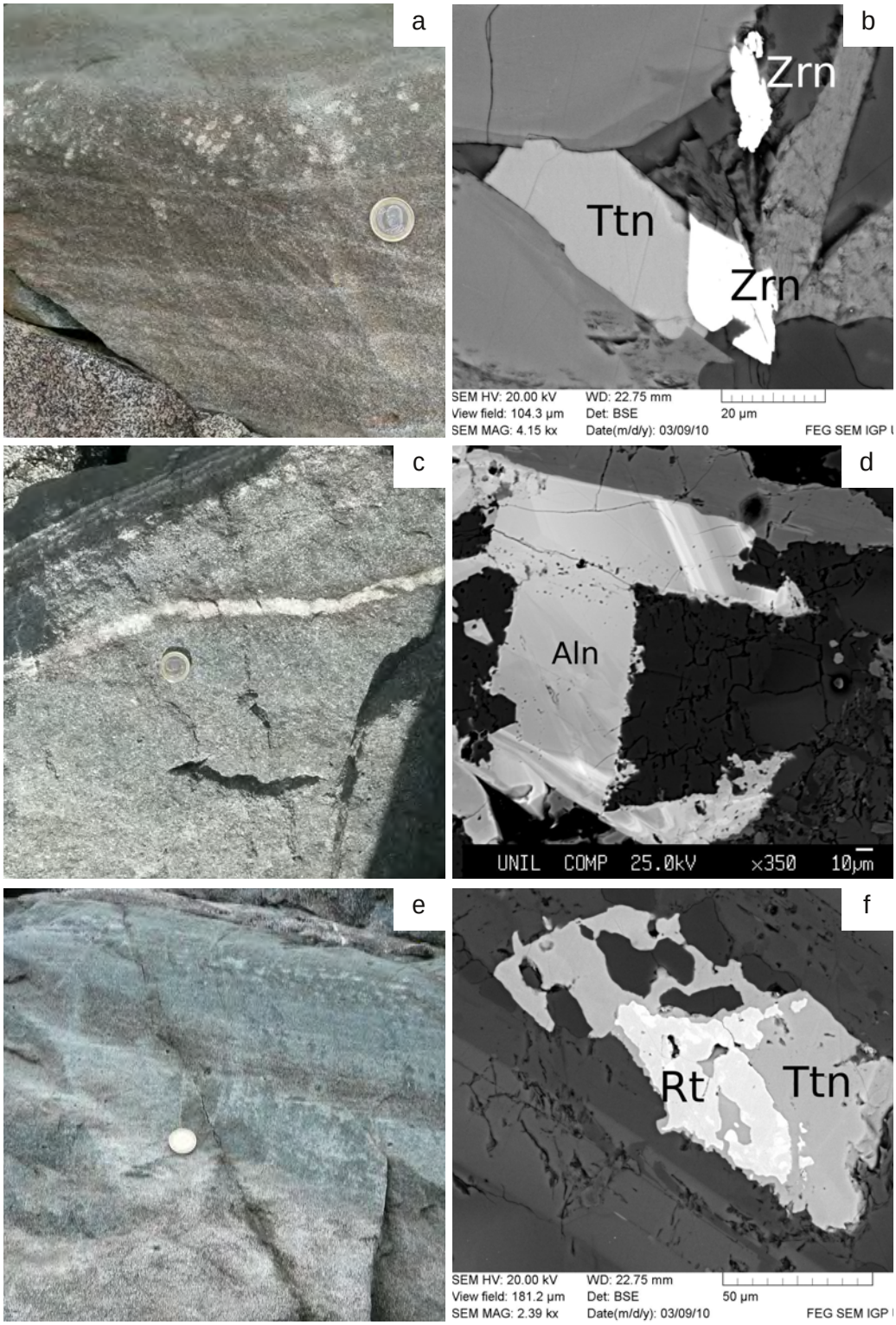

Figure 5.2: (a), (c) and (e) Subhorizontal picrobasaltic dykes (1B) with different forms of felsic plagioclase rich textures. (a) Concentration of felsic lenses at the top of the dyke. (c) Gradational plagioclase rich banding at the top of the dyke, together with a felsic channel crossing the central parts of the dyke. (e) Plagioclase rich micro-gabbroic texture within central parts of the dyke. (b), (d) and (f) Representative assemblage of accessory mineral phases concentrated within felsic part of picrobasalts (1B). (c) Both euhedral and subhedral zircon besides interstitial titanite. (d) Strongly zoned interstitial allanite that encloses plagioclase. (f) Rutile xenocryst that exhibits a reaction rim of titanite.

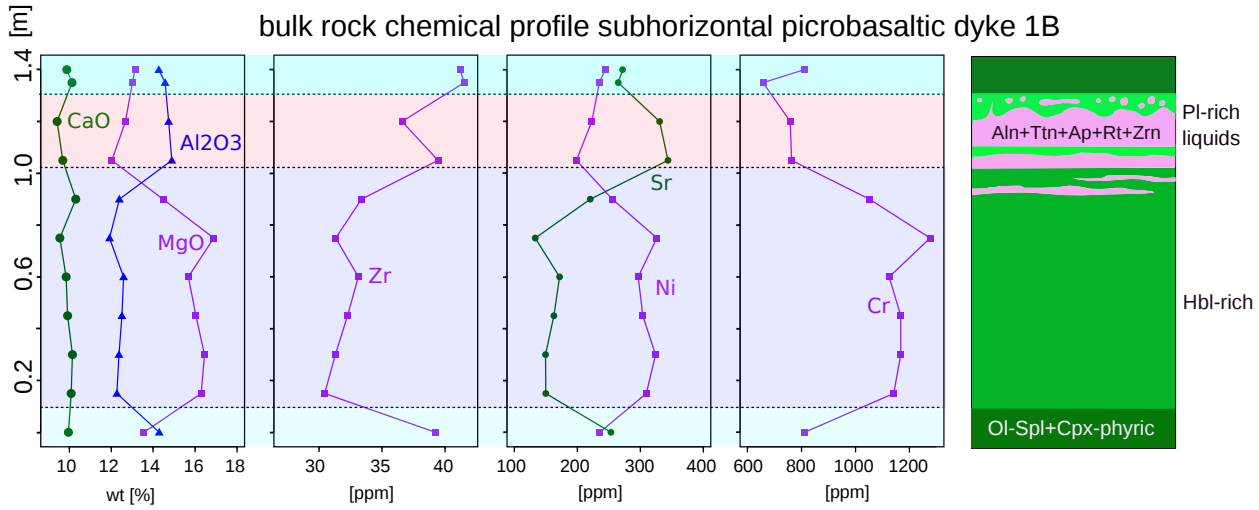

Figure 5.3: Bulk rock geochemical profile for picrobasalt for major elements CaO, Al_2O_3, MgO and trace elements Zr, Sr, Ni and Cr. Enrichment in incompatible elements such as Sr and Zr goes along with plagioclase rich zones at the dyke top, expressed by felsic bands and lenses. The same zone shows enrichment of Al_2O_3 and depletion of MgO, Ni and Cr. The top of such felsic layers shows wavy horizons. Boundaries between the mafic and the felsic magma phases range from very sharp to gradational.

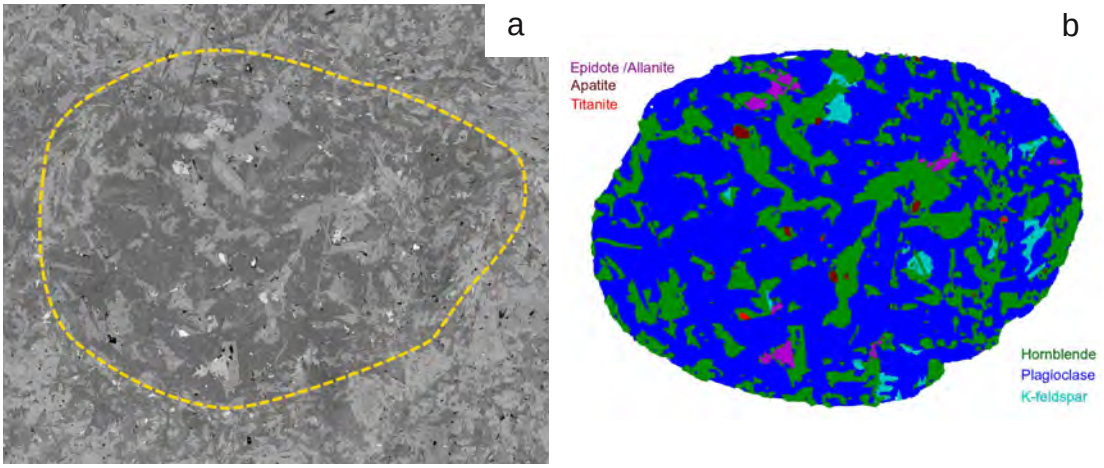

Figure 5.4: (a) Stiched backscatter image of a felsic enclave or ocelli occuring within picrobasalts and Ol-tholeiites (1B). The image shows the abundance of albite rich plagioclase together with an abundance of bright accessory phases. (b) Distinction of all different mineral phases (plagioclase: Pl; amphibole: Am; alkalifeldspar (Afs); epidote (Ep) and allanite (Aln); titanite (Ttn); apatite (Ap)) that are present in the felsic enclave of (a). Phase boundaries were determined by thresholding of the initial backscatter image.

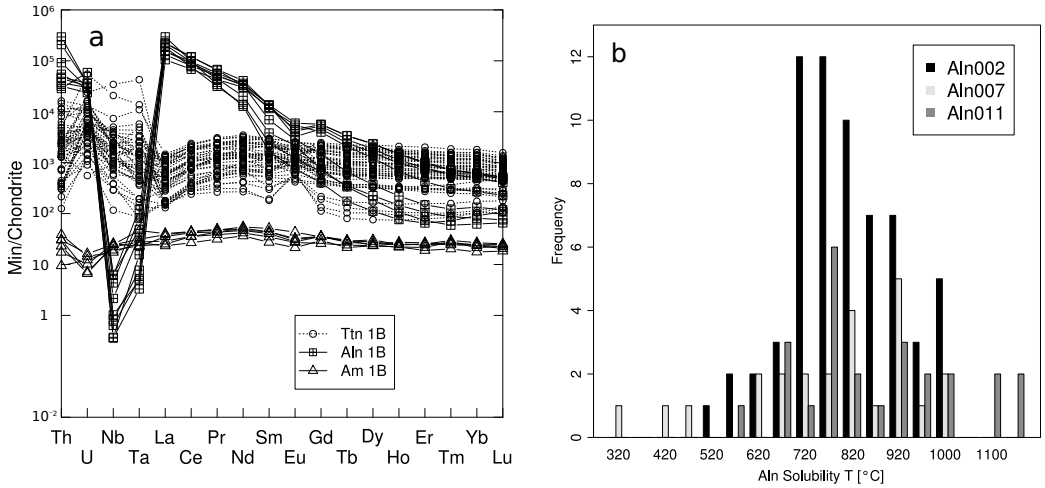

Figure 5.5: (a) Chondrite normalized [McDonough and Sun, 1995] rare earth element (REE) patterns of allanite (Aln) and titanite (Ttn) that are mainly concentrated in the felsic enclaves or ocellis. Amphibole (Am) in general of an Ol-tholeiite host for the enclaves is shown for comparison. (b) Allanite solubility temperatures for three different samples (NHS002, NHS007, NHS011) are displayed in the same histogram, with overall peak frequencies between 750°C and 920 °C. Solubility temperatures for allanite were calculated according to Klimm et al. [2008].

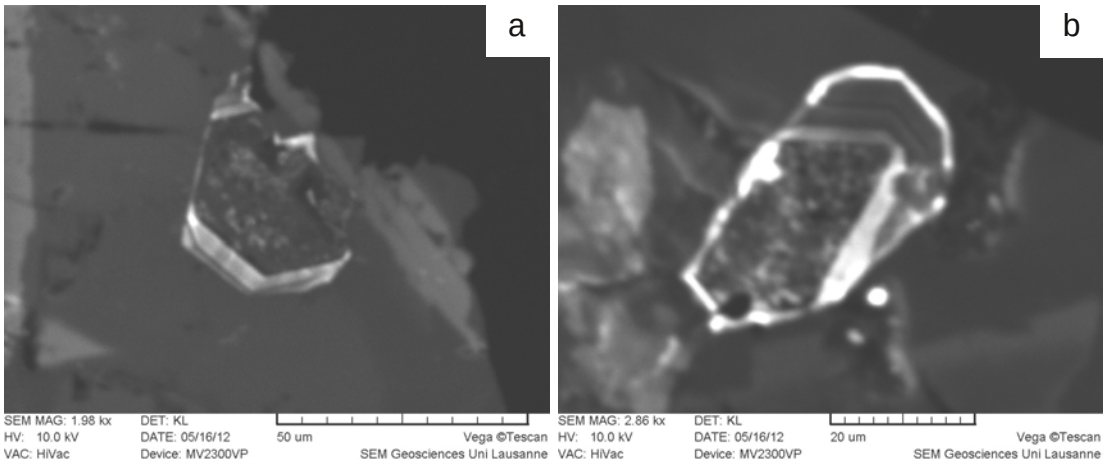

Figure 5.6: (a) and (b) Cathodoluminescence images of zircons from felsic zones of sample NHS011 and enclaves within picrobasalts that were acquired by a scanning electron microscope (SEM). Images exhibit a polycrystalline inhomogeneous core that at a later stage was overgrown by pristine regularly zoned zircon, resulting in an overall subhedral to euhedral shape of the single crystals.

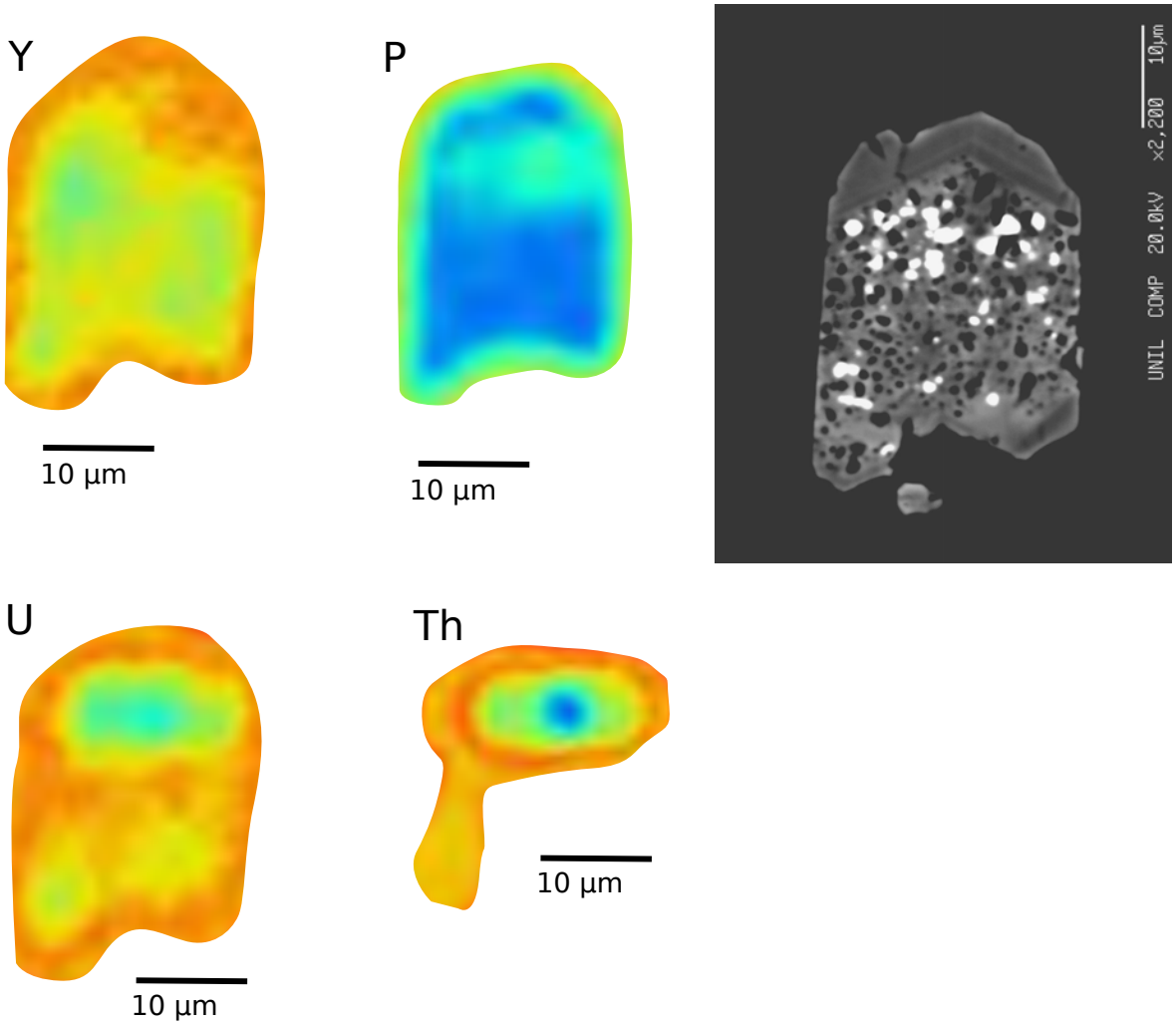

Figure 5.7: Different WDS X-ray (Y, P, U, Th) maps recorded with a electron microscope on a zircon from sample NHS011. Acquisition conditions of the four different elemental X-ray maps were carried out with an acceleration voltage of 20kV and with a beam current of 400nA. The mesh size or pixel size of the map is 0.5μm. Raw image was further flattened or interpolated through image processing. Blue (high) to orange-red (low) indicate concentration density of the different recorded elements. The upper right corner shows a backscatter image for the identical zircon grain. The backscatter image reveals an inhomogeneous porous core with very bright zones that are interpreted as phases different from zircon. Likewise as in cathodoluminescence images (Fig. 5.6a, b), the core is overgrown by pristine regularly zoned zircon. Bright phases in the porous core region correspond to higher concentrations of Th and to U to some extent, as indicated by the according X-ray maps.

Methods U-Pb Zircon Geochronology

Mineral separation started with crushing under a hydraulic press of 2-5cm sized precut blocks of the sample. The resulting gravel was then desintegrated with a tungsten carbide mill for short bursts of 12s. The product was sieved to a size fraction 125-250μm and a fraction of <125μm. The remaining coarser fraction was milled again until everthing passed through the sieve (<250μm). The two size fraction were then pre-panned to be processed afterwards through diiodomethane (3,2 g cm^{-3}) heavy liquid. Magnetite was removed from the heavy mineral separate by a Frantz magnetic separator. Individual zircon grains were hand picked under binocular microscope and inclusions within grains were avoided. A total of 5 zircons grains were analyzed for their U-Pb isotopic composition using high precision ID-TIMS techniques (see Broderick et al., in prep for analytical details) for three different samples. Zircons are chemically abraded after Mattinson [2005]. Titanite and zircon grains were spiked using the EARTHTIME (http://www.earth-time.org) ^{202}Pb-^{205}Pb-^{233}U-^{235}U-tracer solution and dissolved following procedures modified after Krogh [1973]. For zircons, all common Pb was assumed to be blank. All measurements were performed at the University of Geneva on a Thermo-Scientific TRITON thermal ionization mass spectrometer equipped with a MasCom discrete dynode electron multiplier operated in ion counting mode. The initial statistical analysis was done using the TRIPOLI program, followed by data reduction and age calculation using the U-Pb Redux software [Bowring et al., 2011], using the algorithms of McLean et al. [2011]. The data was corrected for mass fractionation with the ET2535 tracer composition using a ^{202}Pb/^{205}Pb ratio of 0.99924 and a ^{235}U/^{205}Pb ratio of 100.23. All uncertainties are reported at the two-sigma level. The uncertainties are propagated using the algorithms of Schmitz and Schoene [2007] and Crowley et al. [2007].

Zircon U-Pb Results

Zircon ^{206}Pb/^{238}U ages for a sample of a Ol-tholeiite (1B) (NHS011) crosscutting the layered gabbroic sequence on the NE face of the Cornone di Blumone indicate clearly a xenocrystic character. Zircons of the same sample are displayed in figure 5.6a, b and figure 5.7 where textures confirm their xenocryst origin. ^{206}Pb/^{238}U ages of five zircons from this sample are early Cretaceous and range from 139.50 ± 0.08 Ma to 140.65 ± 0.22 Ma (Tab. 5.8). These ages appear overall concordant in concordia plot (Fig. 5.8). Through dissolution of the single zircon grains, a mixing between a thin younger zircon overgrowth domain and a older core domain cannot excluded. A fixed discordia at 41.5 Ma ± 0.5, which is in the range of the titanite ages for the same sample (NHS011), leads to an upper intercept at 145 ± 0.3 (Fig. 5.8).

Sample	Wt. [mg]	U [ppm]	$\frac{Th}{U}$	Pb [ppm]	$\frac{Pb^*}{Pb_c}$	Pb_c [pg]	$\frac{206Pb}{204Pb}$	$\frac{207Pb}{206Pb}$	% err	$\frac{207Pb}{235U}$	% err	$\frac{206Pb}{238U}$	% err	corr. coef.	$\frac{207Pb}{204Pb}$	±	$\frac{207Pb}{235U}$	±	$\frac{206Pb}{238U}$	±
(a)	(b)	(c)	(d)	(c)	(e)	(e)	(f)	(g)	(h)	(g)	(h)	(g)	(h)		(i)	(h)	(i)	(h)	(i)	(h)
NHS011/z1	0.0010	17	0.90	0.52	4	0.98	256	0.04888	2.74	0.14794	2.84	0.021952	0.13	0.86	142.07	64.26	140.09	3.72	139.98	0.17
NHS011/z2	0.0010	31	1.16	0.90	13	0.64	687	0.04886	1.00	0.14738	1.04	0.021876	0.06	0.74	141.18	23.48	139.60	1.36	139.50	0.08
NHS011/z3	0.0010	20	1.14	0.60	7	0.76	373	0.04890	1.91	0.14768	1.99	0.021902	0.10	0.80	143.25	44.82	139.86	2.60	139.66	0.14
NHS011/z4	0.0010	7	0.88	0.27	2	0.94	122	0.04927	6.38	0.14934	6.63	0.021981	0.30	0.87	160.92	149.16	141.33	8.75	140.16	0.41
NHS011/z5	0.0020	41	1.09	1.43	3	3.33	190	0.04938	3.68	0.15019	3.82	0.022057	0.16	0.89	166.14	86.02	142.08	5.07	140.65	0.22

Table 5.8: (a) z1, z2 etc. and t1, t2 etc. are labels for single zircon grains or fragments. (b) Nominal weights measured (zircons are chemically abraded, after Mattinson [2005]. (c) Nominal U and total Pb concentrations subject to uncertainty in weighting zircons and titanites. (d) Model Th/U ratio calculated from radiogenic $^{208}Pb/^{206}Pb$ ratio and $^{207}Pb/^{235}U$ age. (e) Pb^* and Pb_c represent radiogenic and common Pb respectively; mol % $^{206}Pb^*$ with respect to radiogenic, blank and initial common Pb. (f) Measured ratio corrected for spike and fractionation only. Mass fractionation correction for Pb and U was applied using the EARTHIME ^{202}Pb-^{205}Pb-^{233}U-^{235}U tracer ($^{202}Pb/^{205}Pb = 0.999239$ and $^{235}U/^{205}Pb$=100.23). (g) Corrected for fractionation, spike and common Pb; All common Pb was assumed to be procedural blank in zircons. $^{206}Pb/^{238}U$ and $^{207}Pb/^{206}Pb$ ratios corrected for initial disequilibrium in $^{230}Th/^{238}U$ using Th/U [magma] = 4. (h) Errors are 2-sigma, propagated using the algorithms of Schmitz and Schoene et al. [2012] and Crowley et al. [2007].

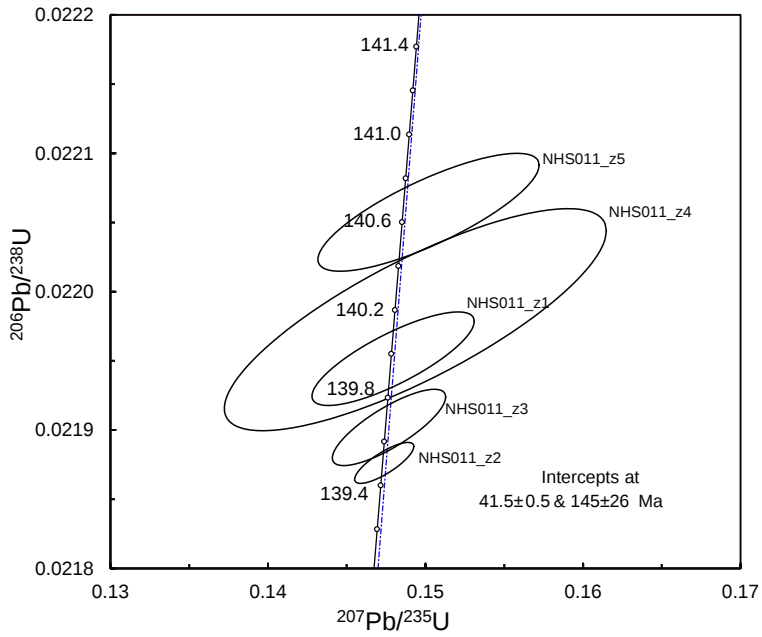

Figure 5.8: $^{206}Pb/^{238}U$ age of picrobasalt (1B) sample NHS011 in concordia plot for five different zircons. Detail U-Pb data of these zircons is reported in table 5.8. The error ellipses represent 2σ uncertainties, including uncertainty of tracer isotopic composition. A lower intercept was fixed on the concordia for a discordia in blue at 41.5 Ma, which is the range of titanite age [Hürlimann et al., in prep.b] for the same sample.

5.8 Discussion

Accessory Minerals and Temperature Constraints

Accessory minerals encompassing allanite, rutile and zircon present in felsic enclaves or ocellis and bands set in picrobasaltic to Ol-tholeiitic matrix are important hosts for various trace elements [e.g. Hermann, 2002, Spandler and Pirard, 2013]. The temperature dependent incorporation of Zr in rutile grown in equilibrium with quartz provides a single-mineral thermometer [Ferry and Watson, 2007, Tomkins et al., 2007, Zack et al., 2004, Watson et al., 2006]. Klimm et al. [2008] developed an allanite solubility model to constrain temperatures of dissolution in the context of melting of a H_2O saturated mid-ocean ridge basalt at high pressure (2.5 GPa), simulating the subduction conditions of oceanic crust.

Allanite is one of the key carriers of the light rare earth elements (LREE) for instance in deeply subducted eclogites and may contain >90% of REE of the bulk rock [Hermann, 2002, Regis et al., 2012, Tribuzio et al., 1996]. Redistribution and mobility of several trace elements (REE, Th, U and Y) is controlled by reactions involving allanite and other REE phases, together with several rock-forming minerals [Regis et al., 2012]. Residual allanite can control the LREE (La-Sm) of liquid chemistry and buffers these elements in liquids to relatively low levels while stable [Klimm et al., 2008]. Residual allanite is thereby produced (REE-poor Epidote = Allanite + Liquid) as well by incongruent melting. The increase of glass in

experiments during melting goes along with the total disappearance of amphibole and REE-poor epidote [Klimm et al., 2008]. Results of the applied allanite saturation thermometry of Klimm et al. [2008] are reported in table 5.9 and temperatures from pooled averages range from 791 ± 138 to 820 ± 68°C (Fig. 5.5b). Larger errors for each sample reported as one pooled standard deviation are explained by larger differences in LREE concentrations over small scale zoning (Fig. 5.2d) of allanite. From a textural view point, allanite is interstitial and precipitated after amphibole and most likely together with plagioclase due to the lack of a considerable Eu-anomaly. Given these relations and the fast cooling rates of these 1 to 2m thick, subhorizontal flat-lying dykes with chilled margins of several centimeters, these temperatures appear to lie close to the actual formation temperatures.

Rutile is a primary host for Ti, Nb and Ta in high temperature and high pressure metamorphic rocks [Deer et al., 1992, Hermann, 2002, Zack et al., 2002]. Zack et al. [2002] showed that rutile is the dominant carrier ($>$ 90% of whole rock content) for Ti, Nb, Sb, Ta and W, as well as an important carrier (5–45% of the whole rock content) for V, Cr, Mo and Sn. Within this context, the Zr-in-rutile thermometer [Zack et al., 2004, Watson et al., 2006, Ferry and Watson, 2007, Tomkins et al., 2007] has experienced great interest recently to determine temperature conditions of high-temperature and high-pressure metamorphic rocks. Moreover, in granulite facies rocks from the Ivrea-Verbano Zone at lower crustal level, Zr-in rutile thermometry can for instance robustly record peak temperatures that are otherwise not recorded by any other thermometer [Ewing et al., 2013]. Zr-in rutile thermometry in the present case records temperatures in the range of 465 ± 8 to 472 ± 57°C (Tab. 5.9), which is considerably lower than the allanite saturation temperatures determined in the same felsic enclaves or bands within the picrobasalts or Ol-tholeiites (1B). Furthermore, these temperatures are considerably lower than conditions of the primitive picrobasaltic host magma, with a liquidus temperature at 1375°C and emplacement conditions around 1200-1100°C [Hürlimann et al., in prep.a]. Overall, these are all indications that rutile retained metamorphic conditions of the assimilated material and did not requilibrate during the transfer within the hot picrobasaltic magma. Textural evidence implies that the reaction of rutile to secondary titanite (Fig. 5.2f) caused a thermochemical shield which lead to the preservation of these lower temperatures with regard to the host magma.

Allanite solubility			
Sample	$T[°C]$	±	**n**
Aln002	820	68	56
Aln007	803	129	24
Aln073	791	138	18
Zr in Rutile			
Sample	$T[C°]$	±	**n**
Rt161	472	57	4
Rt011	465	8	3

Table 5.9: Temperatures calculated from the allanite solubility model of Klimm et al. [2008]. Reported temperature values (T [°C]) for three samples (NHS002, NHS007, NHS011) are calculated from pooled averages and standard deviations for LREE values for allanite acquired by electron microprobe. Zr in rutile temperatures are calculated after the themometric calibration of Watson et al. [2006]. Zr concentrations in rutile determined by LA-ICP-MS for the thermometric calculations of the two samples (NHS011, NHS161) were taken from values as reported in table 5.6.

Observed zircon textures with porous polyphase cores indicate dissolution or recrystallization processes. Bright phases backscatter images, such as those shown in figure 5.7, are a strong indication of recrystallization processes that lead to a purification process of the zircon structure through the expulsion of less compatible trace elements and the formation of new minerals. These new minerals like thortveitite, yttrialite and xenotime-(Y) incorporate preferentially these trace elements [Spandler et al., 2004, Tomaschek et al., 2003]. Furthermore, a decrease of Th and light- to mid-REE for zircon affected by dissolution and reprecipitation processes has been shown by Rubatto et al. [2008]. These studies encompass a phengite-epidote-chlorite schist from the high-P belt of NE New Caledonia, representing a plagioclase rich mafic rock that has experienced previous low temperature seafloor alteration recorded in zircons [Spandler et al., 2004], a meta-plagiogranite from a high-pressure/low-temperature metamorphosed sequence from Syros [Tomaschek et al., 2003] and an eclogite facies (high-pressure/low-temperature) meta-plagiogranite from the Lanzo massif (Western Alps, Italy) [Rubatto et al., 2008]. All these cases have in common that textures of zircons are strikingly similar with observed textures in this case here. In the present case, zircons show a newly formed pristine regularly zoned overgrowth, which implies that after uptake within the picrobasaltic or Ol-tholeiitic magma, zircon saturation conditions were gained again in the travelling distinct unmixed felsic phase.

$^{206}Pb/^{238}U$ ages for a sample of a Ol-tholeiite (139.50 ± 0.08 to 140.65 ± 0.22 Ma), even though they are potentially a mixed age between a bulk part core age and minor rim age, are not in agreement with an inherited component of 469 ± 45 to 405 ± 54 Ma documented from tonalitic to granitic plutonic intrusives of the Southern Adamello [Schaltegger et al., 2009]. This much older inherited component appears to be associated with Ordovician metamorphism and magmatism in the Southalpine basement [Zurbriggen et al., 1997, Boriani et al., 1995] and is in the age range of a Rb–Sr isochron age of 460 Ma for the Edolo schists [Bigazzi et al., 1986]. The latter was used to model AFC processes for the Adamello intrusive rocks. Arguably xenocryst $^{206}Pb/^{238}U$ ages from the Ol-tholeiite do not relate to the Southalpine basement rocks and an alternative assimilant is proposed here. If the age is assumed to correspond to the titanite age range (41.5 Ma) for this Ol-tholeiite, then a mixed ratio between rim and core of 1:10 lead to a core age of 150 Ma whereas a mixing ratio of 1:5 lead to a core age of 160 Ma. The ratios of rim to core are rough estimates based on CL (Fig. 5.6) and BSE-images (Fig. 5.7).

Liquid Immiscibility of Assimilant

The felsic enclaves concentrated towards the chilled margins of these subhorizontal flat-lying picrobasaltic to Ol-tholeiitic dykes demonstrate two distinctively different phases that were not able to mix. Injection of mafic magma into partially solidified felsic magma leads to disaggregation of the mafic magma into enclaves [e.g. Caricchi et al. 2012, Turner and Campbell 1986, Hodge et al. 2012, Snyder and Tait 1995], which can be observed commonly in the field. The description of felsic enclaves or ocellis is widespread for Archean greenstone belts [Coltorti et al., 1987, Polat et al., 2007, 2008, Gelinas et al., 1976] and post Archean magmas [Philpotts, 1979, Freestone, 1978, Elthon et al., 1984, Mauger, 1988]. Appel et al. [2009] provided a model in which they compared dacitic ocelli in picrobasaltic lavas from the Isua greenstone belt (Greenland) with plagiogranites. The formation of plagiogranites was studied based on experiments and was associated with partial melting of altered oceanic crust (gabbros, basalts, sheeted

dykes) in the roof zone of magma chambers under spreading ridges [Koepke et al., 2007, Gillis and Coogan, 2002; and references theirein]. In their model [Appel et al., 2009], dacitic ocellis formed by partial melting of hydrated high-Mg crustal rocks (e.g. picrite volcanic rocks, sheeted dykes) that foundered into a magma chamber. During partial melting LREE are more soluble (mobile) than Th and HFSE (Nb, Ta, Zr, Hf, Y). Finally, lower density and higher viscosity dacitic melt droplets were entrained and transferred to the surface in denser basaltic (picritic) melts. The assimilation capacity of a picrobasalt flowing turbulently through the crust (Fig. 5.9b) were calculated by Huppert and Sparks [1985].

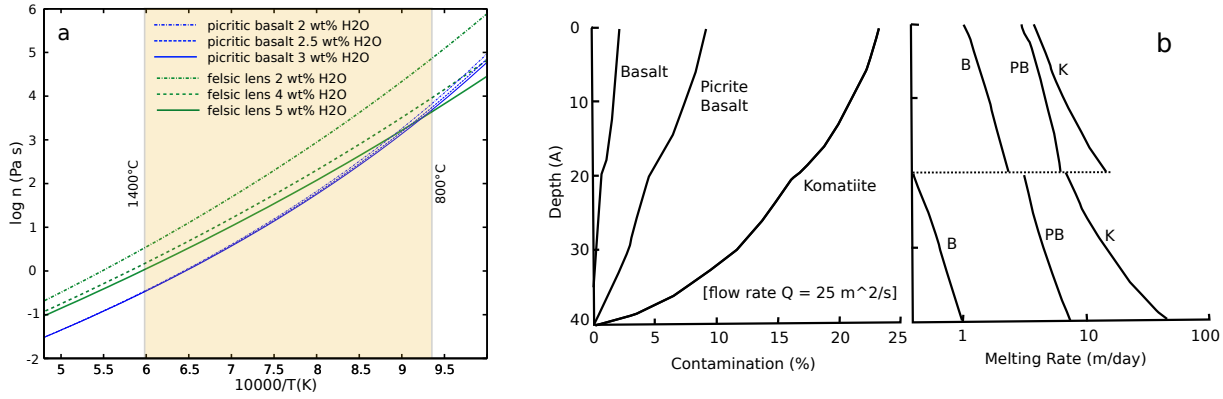

Figure 5.9: (a) Displayed are calculated non-Arrhenian Newtonian viscosity of silicate melts as a function of T and melt composition, including the rheologically important volatile constituents H_2O and F after Giordano et al. [2008] for a felsic phase (LensA; Tab. 5.4) (plagioclase rich enclaves or ocellis) and the host mafic phase (picrobasalt), each for different H_2O contents (felsic enclave/lens: 2, 4, 5 wt% H_2O; picrobasalt: 2, 2.5, 3 wt% H_2O). Liquidus temperature of picrobasalts is around 1375°C (~1400°C) and lower bound indicates saturation temperature (Tab. 5.9) around ~800°C of interstitial allanite in felsic enclaves/lenses that is interpreted as one of the last mineral phase to crystallize. Both the felsic and the mafic phase are taken entirely as silicate liquids under general temperatures conditions of >1100°C [Hürlimann et al., in prep.a] for the picrobasalt (1B) at time of emplacement. (b) Redrawn after Huppert and Sparks [1985] is shown the variation of contamination with depth for three magma types (komatiite, picrite basalt, basalt) for a flow rate of Q = 25 $\frac{m^2}{s}$ during the magma transfer through the crust. Right hand side shows the melting rates of the same three magma types as on the left.

In the field in the present case the felsic phase is commonly concentrated towards the top of the picrobasaltic to Ol-tholeiitic thin sills, which is interpreted as an effect of density between a lighter felsic phase and heavier mafic phase. Based on the silicate melt viscosity model of Giordano et al. [2008], this rheological property was calculated for the composition of a felsic enclave (Lens A, Tab. 5.4) or ocelli and a primitive picrobasaltic (1B) composition (Fig. 5.9a). In figure 5.9a, ~1400°C (1375°C) represents the liquidus temperature determined with MELTS of the picrobasalt at mantle separation conditions [Ulmer, 1988], whereas ~800°C corresponds to the allanite saturation temperature, one of the last phases crystallizing in felsic enclaves or ocellis. Based on interstitial allanite textures, these temperature conditions are close to solidification. The felsic and mafic phases were assumed to be completely liquid for calculations of the compositional and temperature dependent viscosity model [Giordano et al., 2008]. This assumption appears justified based on emplacement temperatures of >1100°C for the picrobasalt to Ol-tholeiites [Hürlimann et al., in prep.a]. At higher temperatures and different H_2O contents (2,4, 5 wt%) (Fig. 5.9a)

the felsic liquid is more viscous than the mafic picrobasaltic liquid (H_2O content wt%: 2, 3, 5). With lower temperatures and increasing H_2O concentrations the felsic liquid attains similar viscosity values like the mafic liquid. The mafic liquid is less susceptible to variations in H_2O concentrations than the felsic liquid according to the viscosity model [Giordano et al., 2008]. The differences in viscosity will have an effect on the capacity of mixing an assimilated felsic liquid in a picrobasaltic to Ol-tholeiitic liquid. Thus, in rapidly quenched chilled margins of the subhorizontal flat-lying dykes the felsic liquid remains unmixed in the form of enclaves or ocellis, whereas towards the central parts of these sill-like features, slower cooling down to lower temperatures allows some mixing of the felsic liquid with the mafic liquid. The latter can be observed with gradational contacts of layers or bands of the felsic plagioclase rich liquid with the mafic more amphibole rich liquid.

5.9 Conclusions

Primitive picrobasaltic to Ol-tholeiitic magmas assimilated felsic basaltic andesitic liquids during their transfer from mantle separation conditions through the crust. The felsic phase remains liquid and immiscible inside a mafic picrobasaltic to Ol-tholeiitic liquid up to rapid quenching, whereas mixing phenomena occur within parts of slower cooling.

Felsic enclaves or lenses and bands or layers crystallized abundant accessory phases such as interstitial titanite and allanite. Particularly allanite is the main carrier of LREE within these felsic phases whereas titanite holds another important part of REE. Allanite saturation temperature yields ~800°C.

The presence of zircon and rutile within the assimilated felsic phase provides a refractory residual archive and gives some indications of the type of assimilant. Zr-in-rutile thermometry yields around ~470°C and implies non re-equilibration of metamoprhic conditions of the assimilant. Zircon with its porous and polycrystalline multiphase core implies recrystallization and purification of zircon to trace element minerals such as thortveitite, yttrialite and xenotime-(Y). Similar textures and processes for zircon have been mainly observed for high-pressure/low-temperature metamorphic rocks associated with deeper subduction of oceanic crust. Furthermore, the inherited component of the $^{206}Pb/^{238}U$ ages (139.50 $\pm$ 0.08 to 140.65 $\pm$ 0.22 Ma) with an upper intercept at 145 $\pm$ 0.3 Ma does not imply assimilation of crustal material of documented Permian or Ordovician age. A potenial higher-pressure assimilant of Jurassic to early Cretacous age has never been described in the Central Southern Alps so far.

Chapter 6

Summary

The post-plutonic dyke swarm marks two phases in the plutonic assembly of the Re di Castello suite and U-Pb ages confirm the crosscutting relationships documented in the field. An early assemblage of plutonic rocks composing the southernmost part of the Adamello Batholith (Val Fredda, Alta Guardia, and Vacca tonalites and associated mafic intrusions) is terminated by the intrusion of the most primitive magmatic rocks found in the entire Adamello Batholith. A second phase is marked by a regional post-plutonic dyke swarm (2A, 2B, 2C, 3) that immediately succeeds a last voluminous phase of intermediate tonalitic intrusions (Monte Re di Castello tonalites). A prominent clear mode I crack extension direction can be linked with left lateral slip movements during emplacement, leading to a mixed mode I + II (shear mode) emplacement style of the dyke swarm. The formation of the dyke swarm preceeds the creation of cooling joints in the large plutonic bodies. The orientation of the dykes along the surfaces of dilatation is not entirely perpendicular to the least compressive stress σ_3 expressed by numerous en echelon arrays that indicate a rotation in the remote stress field by 7 to 10°. A gradient in the remote stress field along the surface of the fluid-dilated cracks can explain the two dimensional teardrop shape of some of the examined dykes. This is further an indication that dilatation surfaces of the magma filled cracks are not perfectly oriented perpendicular to the least compressive stress σ_3 of the regional stress field. In some cases, younger fault planes develop and nucleate along these post-plutonic dykes, which form a clear rheological contrast in an otherwise homogeneous tonalite. Moreover, regional valleys controlled by regional faults have the same lineaments as the regional dyke swarm and document the later erosion and drainage processes as a result of the tectonic uplift.

The largest compositional range of magma over the entire Batholith is documented by the present post-plutonic dyke suite. These dykes with their according composition can be approximated as an actual series of primitive to differentiated liquids produced through different stages of fractional crystallization. Peraluminous dacitic dykes are the result of extracted residual liquids of a fractional crystallization suite and do not need partial melting and assimilation of parts of the continental crust for their genesis. With the beginning of amphibole crystallization, the magma is driven towards these corundum normative compositions. Barometric constraints reinforce the importance of amphibole for the formation of andesitic and dacitic magmas out of hydrous mantle derived mantle magmas at middle to lower crustal depth. The composition of evolved andesitic and dacitic liquids are in very good correspondance with the evolution of the composition of the LLD of isobaric fractional crystallization experiments (7-10 kbar). Trace element signatures of andesitic and dacitic magmas are to a great extent acquired through fractional crystallization at middle to deep crustal level (20-40km). Such trace element signatures are calculated through a fractional crystallization model, taking into account the changing phase assemblage along the LLD and the variations of partition coefficients with changing mineral and melt composition. Different mantle source characteristics for the regional extent covered by the post-plutonic dyke swarm are not required to explain the trace element signature. Amphibole fractionation in these hydrous magmas is of great importance for a realistic model of evolution of the trace element concentration during differentiation to evolved dacitic composition, which are equivalent to plutonic tonalites and granodiorites. The hottest and most primitive picro-basalt demonstrates the most contaminated radiogenic isotope signature. Radiogenic isotope signatures demonstrate as well the thermal capabilities of different magmas with regard to assimilation. This contribution should help understand to what extent arc-tholeiitic to calc-alkaline magmas acquire

the geochemical characteristics in the middle to lower crust in continental margin or arc settings. This is of importance since in particular intermediate to more evolved magmas are building large volumes of batholiths, which are an important component of the continental crust.

Both selective and bulk assimilation are implied from partial melting textures of the tonalite host rock in immediate contact or vicinity of dykes within 10 to 15m wide swarms and the abundance of tonalitic host rock xenoliths. Amphibole xenocryst with a lower temperature (less Ti (apfu)) core and a high temperature overgrowths (higher Ti (apfu)) and plagioclase xenocrysts with inverse zoning, more albitic partially resorbed cores with fresh anorthite overgrowths underline the process of bulk assimilation. The tonalitic host rock assimilation source was identified based on bulk rock geochemical relations between the basaltic magma and the tonalite. In particular, trace elements such as Ni and Ba of basaltic hybrid (2B) dykes demonstrate a mixing relationship of more primitive basalts (2A) with Vacca tonalite end member in one case. The assimilation of Vacca tonalite through such a closely spaced basaltic hybrid dyke swarm is further reinforced by bulk radiogenic isotope ratios of $^{87}Sr/^{86}Sr$ and $^{143}Nd/^{144}Nd$. Amphibole microphenocrysts and the basaltic hybrid melt constrain the temperature to the high temperature stability (~1050°C) of amphibole within calc-alkaline magmas determined through trace element partitioning between the liquid (matrix) and microphenocrysts. These temperature constrains are based upon comparison with partition coefficients of amphibole from fractional crystallization experiments at 7 kbar [Nandedkar et al., in prep.]. Closely spaced, relatively thin dykes with a thickness for the bulk part of $<$0.5m show alternating coalescence to dykes of up to 5m in thickness and splitting again into less thick single dykes along the strike. Increased partial melting of the tonalite host rock, forming features like melt impregnated tonalite, basaltic intrusion breccias and back veining of the molten host tonalite into the basaltic hybrid (2B) dyke occurs with decreased spacing between single dykes in these swarms and with increasing coalescence. The contact surface to the tonalite host rock increases with numerous dykes in closely spaced swarm over 10 to 15m width in comparison with a single thicker dyke being the sum of the thicknesses of all the single dykes. This setting favors the heating effect of the host by the intrusion of the relatively hot primitive basaltic magma. Static heat conduction models, which are scaled to recorded dyke swarm cross sections, reproduce partial melting of the tonalite host rock based on the instantanenous intrusion of closely spaced single basaltic (2A) and basaltic hybrid (2B) dykes, as observed in the field. The host rock temperature has to be at least 500°C at the time of dyke intrusion in order to reproduce observed 1 to 2m wide basaltic intrusion breccias through a static thermal conduction model.

Primitive picrobasaltic to Ol-tholeiitic magmas assimilate immiscible felsic basaltic andesitic liquids during their transfer from mantle separation conditions through the crust. Immiscibility of the felsic phase inside a mafic picrobasaltic to Ol-tholeiitic liquid persists up to rapid quenching, whereas mixing phenomena occur within parts of slower cooling. Abundant accessory phases such as interstitial allanite and titanite crystallized within felsic enclaves or lenses and layers. Allanite saturation temperature yields ~800°C and the same phase is the main carrier of LREE within the felsic phase, whereas titanite holds another important part of REE. A refractory residual archive of the assimilated felsic material is provided by the presence of zircon and rutile, which gives indications of the type of the assimilant. Zr-in-rutile thermometry yields around ~470°C and implies non re-equilibration of metamorphic conditions of the assimilant in the hotter host magma. Porous and polycrystalline multiphase core textures of zircon imply

recrystallization and purification of the crystal lattice through the expulsion of trace elements forming separate minerals. High-pressure/low-temperatures metamorphic rocks associated with deeper subduction of oceanic crust exhibit similar textures and processes for zircon. An inherited component of the $^{206}Pb/^{238}U$ zircon ages (139.50 ± 0.08 to 140.65 ± 0.22 Ma) with an upper intercept at 145 ± 0.3 Ma does not document a lower crustal assimilant of Permian or Ordovician age. A potenial higher-pressure assimilant of Jurassic to early Cretacous age has never been described in the Central Southern Alps so far for Eocene to Oligocene magmatic rocks.

Chapter 7

Appendix

7.1 Sample Locations

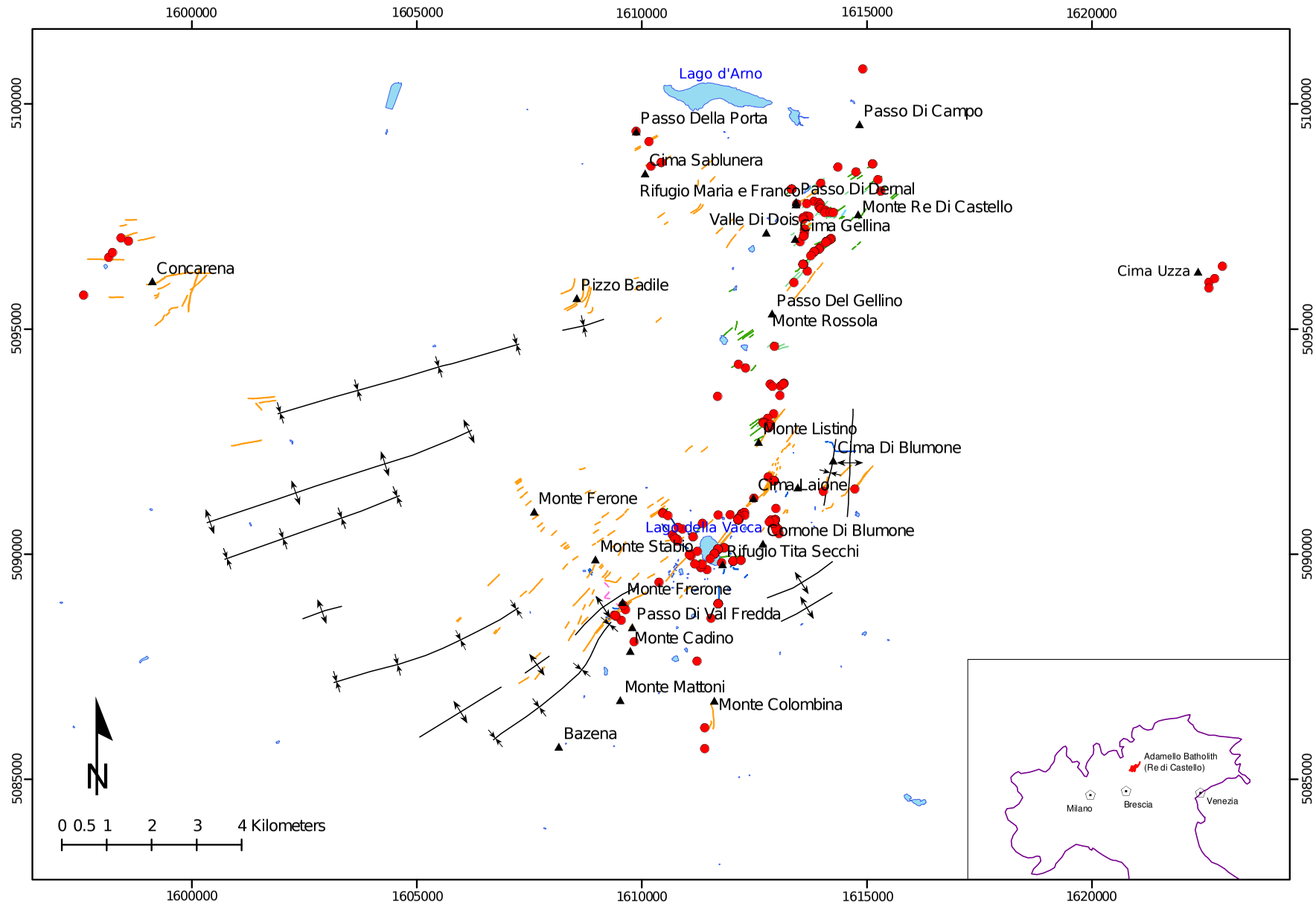

Figure 7.1: Map with all collected samples (2009-2012) and significant locations over the investigated area (Map datum: Monte Mario/Italy zone 1, Transverse Mercator Projection).

Sample Nr	x	y	z	Sample Nr	x	y	z
09NHS001	612866	5090759	2535	09NHS045	612277	5090929	2636
09NHS002	612025	5089846	2366	09NHS046	612282	5090864	2617
09NHS003	612024	5089845	2368	09NHS047	612132	5090767	2571
09NHS004	611307	5089698	2414	09NHS048	612142	5090768	2576
09NHS005	611312	5089725	2416	09NHS049	612148	5090762	2576
09NHS006	611339	5089774	2413	09NHS050	612145	5090762	2574
09NHS007	612954	5090638	2554	09NHS051	612172	5090822	2609
09NHS008	612917	5090688	2550	09NHS052	612136	5090790	2583
09NHS009	612918	5090690	2546	09NHS053	612135	5090771	2576
09NHS010	612944	5090662	2572	09NHS054	611960	5090873	2562
09NHS011	612861	5090712	2536	09NHS055	611691	5090869	2542
09NHS012	612919	5090689	2543	09NHS056	611345	5090686	2521
09NHS013	612925	5090728	2539	09NHS057	610899	5090558	2553
09NHS014	612928	5090723	2538	09NHS058	610469	5090919	2409
09NHS015	612930	5090710	2544	09NHS059	610462	5090906	2409
09NHS016	612931	5090724	2539	09NHS060	610576	5090856	2438
09NHS017	612927	5090728	2536	09NHS061	611091	5089959	2519
09NHS018	612975	5090598	2548	09NHS062	610807	5090598	2526
09NHS019	612974	5090601	2554	09NHS063	610679	5090428	2530
09NHS020	613049	5090459	2556	09NHS064	610793	5090289	2591
09NHS021	613018	5090553	2542	09NHS065	611053	5089995	2529
09NHS022	613024	5090560	2537	09NHS066	610715	5090375	2547
09NHS023	613022	5090558	2539	09NHS067	610783	5090327	2584
09NHS024	612991	5090521	2548	09NHS068	611233	5090061	2379
09NHS025	612487	5091246	2750	09NHS069	611135	5090385	2471
09NHS026	612979	5091012	2549	09NHS070	611135	5090385	2471
09NHS027	612200	5089863	2389	09NHS071	610738	5090342	2552
09NHS028	612198	5089864	2382	09NHS072	611173	5089780	2503
09NHS029	612965	5090765	2511	09NHS073	610378	5089374	2452
09NHS030	612963	5090766	2513	09NHS074	609825	5088055	2401
09NHS031	612960	5090769	2514	09NHS075	614727	5091445	2301
09NHS032	612969	5090580	2556	09NHS076	614030	5091397	2241
09NHS033	612923	5090686	2552	09NHS077	612139	5090764	2570
09NHS034	612936	5090739	2530	09NHS078	612138	5090759	2573
09NHS035	612833	5090718	2539	09NHS079	612172	5090822	2609
09NHS036	612933	5091631	2546	10NHS080	613580	5097473	2623
09NHS037	612927	5091633	2545	10NHS081	613584	5097435	2622
09NHS038	612933	5091633	2546	10NHS082	613600	5097067	2597
09NHS039	612937	5091634	2545	10NHS083	613591	5097070	2600
09NHS040	612928	5091640	2545	10NHS084	613516	5096941	2552
09NHS041	612924	5091635	2548	10NHS085	613818	5096700	2429
09NHS042	612221	5090897	2627	10NHS086	613677	5096286	2367
09NHS043	612217	5090885	2625	10NHS087	613154	5093795	2333
09NHS044	612222	5090890	2626	10NHS088	612938	5091623	2546

Sample Nr	x	y	z	Sample Nr	x	y	z
10NHS089	612024	5089848	2336	10NHS133	611682	5093503	2577
10NHS090	612224	5090898	2628	10NHS134	612690	5092932	2593
10NHS091	612274	5090924	2637	10NHS135	612690	5092932	2595
10NHS092	611396	5086146	1980	10NHS136	611834	5090140	2358
10NHS093	609386	5088649	2400	10NHS137	611824	5090148	2359
10NHS094	613376	5096031	2398	10NHS138A	611687	5090111	2359
10NHS095	612943	5094619	2601	10NHS138B	611687	5090111	2359
10NHS096	613617	5097219	2710	10NHS138C	611687	5090111	2359
10NHS097	610158	5099162	2359	10NHS138D	611687	5090111	2359
10NHS098	610431	5098701	2383	10NHS138E	611687	5090111	2359
10NHS099	610431	5098701	2385	10NHS138F	611687	5090111	2359
10NHS100	610201	5098617	2466	10NHS139	611697	5090108	2351
10NHS101	609874	5099391	2431	10NHS140	611696	5090106	2352
10NHS102	613821	5097837	2639	10NHS141	611537	5088578	2250
10NHS103	613661	5097789	2632	10NHS142	612813	5092813	2558
10NHS104	613930	5097814	2662	10NHS143	612809	5092809	2557
10NHS105	613962	5097769	2684	10NHS144	612808	5092810	2554
10NHS106	613963	5097765	2681	10NHS145	612811	5092821	2550
10NHS107	613937	5097712	2700	10NHS146	612734	5092919	2566
10NHS108	613961	5097681	2710	10NHS147	612733	5092917	2572
10NHS109	613977	5097677	2719	10NHS148	612805	5091715	2557
10NHS110	614077	5097637	2733	10NHS149	611223	5087621	2012
10NHS111	614112	5097599	2745	10NHS150	609539	5088532	2361
10NHS112	613438	5097781	2585	10NHS151	609425	5088623	2376
10NHS113	613649	5097510	2652	10NHS152	609405	5088641	2388
10NHS114	613716	5097498	2682	10NHS153	609635	5088765	2573
10NHS115	614198	5096998	2481	10NHS154	609581	5088866	2622
10NHS116	614166	5096981	2472	10NHS155	611444	5089657	2349
10NHS117	614097	5096950	2468	10NHS156	611696	5088898	2374
10NHS118	613964	5096813	2442	10NHS157	611697	5088899	2375
10NHS119	613933	5096777	2438	10NHS158	611697	5088899	2374
10NHS120	613930	5096778	2442	10NHS159	611697	5088899	2374
10NHS121	613833	5096726	2451	10NHS160	611697	5088899	2374
10NHS122	613823	5096716	2447	10NHS161	612028	5089839	2356
10NHS123	613754	5096628	2433	10NHS162	611772	5089811	2364
10NHS124	613596	5096442	2423	10NHS163	613081	5093735	2356
10NHS125	613610	5097146	2707	10NHS164	612702	5092911	2585
10NHS126	614066	5097591	2758	10NHS165	612807	5092829	2553
10NHS127	614184	5097596	2743	10NHS166	612845	5092883	2536
10NHS128	614252	5097587	2742	10NHS167	612847	5093777	2443
10NHS129	612927	5093115	2485	10NHS168	598150	5096591	2035
10NHS130	612790	5093013	2543	10NHS169	598232	5096697	2062
10NHS131	612303	5094134	2532	10NHS170	598590	5096955	2120
10NHS132	612147	5094217	2479	10NHS171	598425	5097024	2137

Table 7.1: Coordinates of collected samples (2009-2012) (Map datum: Monte Mario/Italy zone 1, Transverse Mercator Projection)

Sample Nr	x	y	z	Sample Nr	x	y	z
10NHS172	597595	5095754	1742	11NHS201	610666	5111016	2264
11NHS173	614354	5098597	2435	OMA001	611517	5089898	n.a.
11NHS174	614202	5097011	2476	PB784	611398	5085678	n.a.
11NHS175	614191	5097004	2476				
11NHS176	614180	5096987	2470				
11NHS177	614116	5096945	2461				
11NHS178	614087	5096928	2458				
11NHS179	613975	5098237	2509				
11NHS180A	615124	5098667	2418				
11NHS180B	615124	5098667	2418				
11NHS181	615310	5098065	2479				
11NHS182	615244	5098321	2492				
11NHS183	614756	5098494	2419				
11NHS184	612898	5093727	2427				
11NHS185	613149	5093789	2330				
11NHS186	613139	5093778	2333				
11NHS187	613067	5093525	2372				
11NHS188	612819	5092828	2552				
11NHS189	612820	5092829	2552				
11NHS190A	611611	5090011	2348				
11NHS190B	611611	5090011	2348				
11NHS190C	611611	5090011	2348				
11NHS190D	611611	5090011	2348				
11NHS191A	613327	5098111	2624				
11NHS191B	613327	5098111	2624				
11NHS191C	613327	5098111	2624				
11NHS191D	613327	5098111	2624				
11NHS191E	613327	5098111	2624				
11NHS191F	613327	5098111	2624				
11NHS191G	613327	5098111	2624				
11NHS192A	613581	5096442	2406				
11NHS192B	613581	5096442	2406				
11NHS192C	613581	5096442	2406				
11NHS192D	613581	5096442	2406				
11NHS192E	613581	5096442	2406				
11NHS192F	613581	5096442	2406				
11NHS193	616861	5102809	2382				
11NHS194	615734	5102019	2325				
11NHS195	614908	5100780	2412				
11NHS196	612869	5090712	2513				
11NHS197	612863	5090710	2521				
11NHS198	612860	5090713	2519				
11NHS199	610669	5111035	2259				
11NHS200	610670	5111039	2265				

Table 7.2: Coordinates of collected samples (2009-2012) (Map datum: Monte Mario/Italy zone 1, Transverse Mercator Projection)

7.2 Sample Description

SampleNr	SipDir	Orient	Dip	Orient	UpDown	Description	LithologyName	StratigraphyName	Photos
09NHS001	255		47		U	green d yke	basalt	basaltic dykes hybrids 2B	09NHS001
09NHS002	378		89		U	melanocratic amphibole-rich dyke	picrite - Ol-tholeiite	picrobasaltic dykes 1B	
09NHS003	0		75		U	melanocratic amphibole-rich dyke	picrite - Ol-tholeiite	picrobasaltic dykes 1B	
09NHS004	298		24		U	green dyke	basalt	basaltic dykes hybrids 2B	09NHS004
09NHS005	52		9		U	melanocratic amphibole-rich dyke	basalt	picrobasaltic dykes 1B	09NHS005
09NHS006						green dyke	basalt	basaltic dykes 2B	09NHS006
09NHS007						melanocratic amphibole-rich dyke, crosscuts Blumone gabbroic profile	picrite - Ol-tholeiite	picrobasaltic dykes 1B	09NHS007AB
09NHS008	221		45		U	phenocryst/crystal-rich grey dyke	andesite		09NHS008
09NHS009	43		83		U	fg grey dyke	andesite		
09NHS010	279		27		U	fg grey dyke	andesite		09NHS010
09NHS011						melanocratic amphibole-rich dyke, crosscuts Blumone gabbroic profile	picrite - Ol-tholeiite	picrobasaltic dykes 1B	09NHS011
09NHS012	268		87		U	metasediment sliver in a vortici gabbro	metacarbonate		09NHS012
09NHS013	40		67		U	fg grey dyke	andesite		09NHS013
09NHS014						desintegrated fg grey dyke (wallrock A Vortici)	andesite		09NHS014
09NHS015						fg grey dyke, back-veining of (wallrock A Vortici)	andesite		09NHS015
09NHS016	291		32		U	fg grey dyke in horn bridge structure (wallrock A Vortici)	andesite		09NHS016
09NHS017	13		30		U	fg grey dyke desintegrated into clasts surrounding leucosome (wallrock A Vortici)	andesite		09NHS017
09NHS018	163		20		U	melanocratic amphibole-rich dyke, crosscuts Blumone gabbroic profile	picrite - Ol-tholeiite	picrobasaltic dykes 1B	09NHS018&19
09NHS019						melanocratic amphibole-rich dyke, crosscuts Blumone gabbroic profile	picrite - Ol-tholeiite	picrobasaltic dykes 1B	09NHS020ABC
09NHS020	117		70		U	melanocratic amphibole-rich dyke, crosscuts Blumone gabbroic profile	picrite - Ol-tholeiite	picrobasaltic dykes 1B	09NHS021
09NHS021	196		71		U	ligther grey rather thick dioritic dyke	andesite		09NHS022
09NHS022						cummulitic hornblende&pyroxene gabbro (gradational)	hornblende gabbro		09NHS023
09NHS023						coarse grained hornblende&pyroxene gabbro	hornblende gabbro		09NHS024
09NHS024	51		69		U	fg grey dyke crosscuts cummulitic gabbro (hbl+pyx)	basaltic-andesite		
09NHS025	90					porphyritic dyke (Listino ring)	dacite		09NHS026
09NHS026	322		18		U	melanocratic pyroxene-rich dyke, crosscuts A Vortici and Spottey Dog	basalt		09NHS027AB
09NHS027	2		85		U	fg grey dyke within Spottey Dog	basaltic-andesite		09NHS028
09NHS028	269		19		U	phenocryst/crystal-rich grey dyke within Spottey Dog	basaltic-andesite		09NHS029
09NHS029						fg grey dyke grading into mafic enclaves, teared apart	basaltic-andesite		09NHS030
09NHS030	175		73		U	leucosome aplitic band within "spottey dog"	aplite		09NHS031
09NHS031						desintegrated fg grey dyke (A Vortici&Spottey Dog wallrock facies)	basaltic-andesite		09NHS032ABC
09NHS032						ligther grey rather thick dyke (dioritic), crosscuts Blumone gabbroic profile	diorite		09NHS033
09NHS033						Aplitic dyke crosscutting gabbroic wallrock	aplite		09NHS034
09NHS034						fg grey dyke with thicker coarse amphibole rims (wallrock A Vortici)	andesite		
09NHS035						phenocryst/crystal-rich grey dyke within A Vortici	basaltic-andesite		
09NHS036	171		58		U	foliated felsic dyke crosscutting gabbroic wallrock	aplite		
09NHS037	21		39		U	green dyke crosscutting gabbroic wallrock	basalt	basaltic dykes hybrids 2B	
09NHS038	20		63		U	green dyke crosscutting gabbroic wallrock	basalt	basaltic dykes hybrids 2B	
09NHS039	350		6		U	aplitic dyke crosscutting gabbroic wallrock	basalt	basaltic dykes hybrids 2B	
09NHS040						fg grey dyke crosscutting gabbroic wallrock	basalt	basaltic dykes hybrids 2B	
09NHS041						green dyke with xenoliths	basalt	basaltic dykes hybrids 2B	
09NHS042	139		84		U	green dyke with abundant crystal debris (xenocrysts) (wallrock Vacca tonalite)	basalt	basaltic dykes hybrids 2B	
09NHS043	296		65		U	green dyke with abundant crystal debris (xenocrysts) (wallrock Vacca tonalite)	basalt	basaltic dykes hybrids 2B	
09NHS044						green dyke with abundant crystal debris (xenocrysts) (wallrock Vacca tonalite)	basalt	basaltic dykes hybrids 2B	
09NHS045	208		83		U	green dyke, part of swarm with several off-splays and hornstructures (wallrock Vacca tonalite)	basalt	basaltic dykes hybrids 2B	09NHS045
09NHS046	271		26		U	green dyke, part of larger swarm (wallrock "vacca tonalite")	basalt	basaltic dykes hybrids 2B	09NHS046
09NHS047						green dyke, with abundant crystal debris (xenocrysts) and xenoliths (gabbroic, qtz-rich granodioritic, tonalitic?) (wallrock Vacca tonalite)	basalt	basaltic dykes hybrids 2B	09NHS047
09NHS048	214		47		U	green dyke, with abundant crystal debris (xenocrsyts) and xenoliths (gabbroic) (wallrock Vacca tonalite)	basalt	basaltic dykes hybrids 2B	09NHS048
09NHS049						green dyke, with inclusion of band of cooked wallrock (wallrock Vacca tonalite)	basalt	basaltic dykes hybrids 2B	
09NHS050	115		79		U	green dyke, crystal debris mainly qtz (xenocrysts) (wallrock Vacca tonalite)	basalt	basaltic dykes hybrids 2B	09NHS050
09NHS051	119		86		U	green dyke, complex array of several parallel small sheets dykes adjacent to each other, "sheet into sheet" (wallrock foliated Vacca tonalite)	basalt	basaltic dykes 2A	09NHS051ABC

Table 7.3: Field description for collected rock samples with indication if sample was oriented or not (DipDir Orient/Dip Orient) during collection.

SampleNr	DipDir Orient	Dip Orient	UpDown	Description	LithologyName	StratigraphyName	Photos
09NHS052				green dyke, large float block in vicinity to extensive green dyke swarm, wallrock-inclusion, reaction to of plag to epidote mainly?	basalt	basaltic dykes hybrids 2B	09NHS052
09NHS053				green dyke, some cystal debris mainly qtz (xenocrysts), closely jointed wallrock (Vacca tonalite) with several smaller dykes intruded along	basalt	basaltic dykes 2A	09NHS053AB
09NHS054	263	86	U	green dyke, some cystal debris mainly qtz (xenocrysts), bridge and horn structure, closer spaced dyke parallel jointing in vicinity (wallrock Vacca tonalite)	basalt	basaltic dykes hybrids 2B	09NHS054
09NHS055	324	72	U	green dyke, crystal debris in the form of qtz (xenocrysts), sulphides?, marginal Listino-Ring-Structure, variation in facies nearby,	basalt	basaltic dykes hybrids 2B	09NHS055AB
09NHS056	215	90	U	green dyke, crystal debris in the form of qtz (xenocrysts), (wallrock Vacca tonalite)	basalt	basaltic dykes hybrids 2B	09NHS056
09NHS057				melanocratic amphibole-rich dyke, clots of pseudomorphic olivine, (wallrock Galiner granodiorite)	basalt	basaltic dykes 1A	09NHS057AB
09NHS058				gabbro Mattoni-type, desintegration at margins into gabbroic enclaves	hornblende gabbro		09NHS058
09NHS059	160	70	U	green dyke, massive texture overall, brownish remanants of replaced phase (olivine?)	andesite	basaltic-andesitic andesitic dykes 2C	09NHS059
09NHS060				melanocratic amphibole-rich dyke, clots of pseudomorphic olivine, (wallrock Galiner granodiorite)	basalt	picrobasaltic dykes 1B	09NHS060AB
09NHS061	126	89	U	melanocratic amphibole-rich dyke, sparse ocelli	basalt	picrobasaltic dykes 1B	09NHS061AB
09NHS062	337	86	U	melanocratic amphibole-rich dyke, clots of pseudomorphic olivin within Galiner granodiorite, complex melt-pulse or migration textures	basalt	basaltic dykes 1A	09NHS062AB
09NHS063	230	51	U	melanocratic dyke, central parts very rich in coarse grained pyroxene-phenocrysts	basalt	picrobasaltic dykes 1B	09NHS063
09NHS064	137	36	U	melanocratic dyke, within Galiner granodiorite	basalt	basaltic dykes 1A	09NHS064
09NHS065	287	23	U	melanocratic dyke, larger clots of ol+amph, xenocrysts of qtz	basalt	picrobasaltic dykes 1B	09NHS065
09NHS066	221	34	U	melanocratic dyke, concentration of amphibole in central parts , xenocrysts of qtz, brownish phase as replacement product of olivine?	basalt	basaltic dykes 1A	09NHS066AB
09NHS067	16	75	U	green dyke, fine-grained mesocratic groundmass	basaltic-andesite	basaltic-andesitic andesitic dykes 2C	09NHS067
09NHS068	0	53	U	melanocratic dyke, brownish phase as replacement product of olivine?	basalt	picrobasaltic dykes 1B	09NHS068
09NHS069	245	65	U	melanocratic dyke, enrichment of pyx+amph phenocrysts in central parts of dyke, miralolitic cavities	basalt	basaltic dykes hybrids 2B	09NHS069NHS70A
09NHS070	48	56	U	tonalite (Vacca) in immediate vicinity to dyke which is part of swarm of several dykes	tonalite		09NHS069NHS70B
09NHS071	160	64	U	granodiorite (Galiner), wallrock in immediate vicinity to dyke which is part of a swarm of several dykes	granodiorite		09NHS071
09NHS072	97	31	U	green dyke, mesocratic fine-grained groundmass (wallrock Vacca tonalite)	basalt	basaltic dykes hybrids 2B	09NHS072
09NHS073				melanocratic pyroxene-rich dyke, felsic-bands of diggested wallrock	picrite - Ol-tholeiite	picrobasaltic dykes 1B	
09NHS074				green dyke, within Dolomia Principale	basalt	basaltic dykes hybrids 2B	
09NHS075	184	19	U	green dyke, within Bruffione Granodiorite, crosscutting aplitic-pegmatitic dykes	basalt	basaltic dykes hybrids 2B	09NHS075
09NHS076				melanocratic dyke within Buchenstein Fm	basalt		09NHS076
09NHS077				tonalite, (Vacca) wallrock to dyke swarm, dykes with lobate margins	tonalite		
09NHS078				green dyke, within dyke swarm with at least three generation, latest generation	basalt	basaltic dykes hybrids 2B	09NHS078
09NHS079				green dyke, several dykes sheets intruded into each other, sausage like texture, mainly pyroxene bearing	basalt	basaltic dykes 2A	
10NHS080	119	80	U	fg green melanocratic dyke	basalt	basaltic dykes 2A	10NHS080
10NHS081				pl-hbl-phyric green melanocratic dyke	andesite	basaltic-andesitic andesitic dykes 2C	
10NHS082				fg aplyric margin of melanocratic green dyke	basaltic-andesite	basaltic-andesitic andesitic dykes 2C	
10NHS083				am-pl-phyric green mesocratic dyke	dacite	dacitic dykes 3	
10NHS084	68	62	U	pl-am-phyric mesocratic to leucocratic grey-green dyke	dacite	dacitic dykes 3	10NHS084
10NHS085	119	30	U	am-pl-qz-phyric melanocratic green dyke	andesite	basaltic-andesitic andesitic dykes 2C	10NHS085AB
10NHS086	85	40	U	pl-phyric light green-grey dyke	dacite	dacitic dykes 3	10NHS086
10NHS087	149	86	U	am-phyric green melanocratic dyke	basalt	basaltic dykes 1A	
10NHS088				white-grey mg leucocratic granitic-tonalitic dyke	picrite - Ol-tholeiite	picrobasaltic dykes 1B	
10NHS089	102	32	U	stratified subhorizontal am-phyric picritic dyke	picrite - Ol-tholeiite	picrobasaltic dykes 1B	10NHS089
10NHS090	199	74	U	composite-multiple stage melanocratic ol-px-pl-qz-phyric dyke	basalt	basaltic dykes hybrids 2B	
10NHS091	210	86	U	composite multiple stage px-am-pl-phyric melanocratic dyke	basalt	basaltic dykes hybrids 2B	
10NHS092				equigranular microlitic melanocratic dyke (hbl-pl)	basalt	basaltic dykes hybrids 2B	10NHS092AB
10NHS093	189	53	U	px-am-qz-phyric mesocratic to melanocratic dyke	basalt	basaltic dykes hybrids 2B	10NHS093AB

Table 7.4: Field description for collected rock samples with indication if sample was oriented or not (DipDir Orient/Dip Orient) during collection.

SampleNr	DipDir Orient	Dip Orient	UpDown	Description	LithologyName	StratigraphyName	Photos
10NHS094	142	79	U	px-am-phyric melanocratic green dyke	basalt	basaltic dykes hybrids 2B	10NHS094AB
10NHS095	155	66	U	pl-am-phyric dyke	dacite	dacitic dykes 3	10NHS095
10NHS096				pl-am-phyric light-green-grey dyke	dacite	dacitic dykes 3	
10NHS097	61	33	U	multiple composite mesocratic to melanocratic green am-pl-qz-phyric dyke	basalt	basaltic dykes hybrids 2B	10NHS097
10NHS098	141	85	U	fg mesocratic to melanocratic dyke with microphenocryts am and xenocrysts qz	basalt	basaltic dykes hybrids 2B	10NHS098ABC
10NHS099	148	90	U	fg mesocratic px-am-qz-phyric green dyke	basalt	basaltic dykes hybrids 2B	10NHS099
10NHS100				grt-di skarn within esino-carbonates	metacarbonate		10NHS100
10NHS101	272	52	U	leucotonalite-granodiorite del Lago Boazzo, large incision, cataclasite, fault trace expressed by topography	tonalite		10NHS101AB
10NHS102				px-am-phyric melanocratic green dyke	basalt	basaltic dykes 2A	10NHS102
10NHS103	342	21	U	pl-am-phyric mesocratic grey-green dyke	andesite	basaltic-andesitic dykes 2C	andesitic 10NHS103AB
10NHS104	155	85	U	px-am melanocratic green dyke	basalt	basaltic dykes 2A	10NHS104
10NHS105	163	80	U	am-pl-phyric green mesocratic green dyke	andesite	basaltic-andesitic dykes 2C	andesitic 10NHS105106
10NHS106	270	90	U	am-pl-phyric green mesocratic green dyke	andesite	basaltic-andesitic dykes 2C	andesitic 10NHS105106
10NHS107	144	77	U	am-phyric green melanocratic dyke	andesite	basaltic-andesitic dykes 2C	andesitic
10NHS108	125	90	U	pl-phyric melanocratic green dyke	dacite	dacitic dykes 3	
10NHS109	124	88	U	am-pl-phyric mesocratic green dyke	dacite	dacitic dykes 3	10NHS109ABC
10NHS110	41	45	U	px-pl-phyric melanocratic green dyke	basalt	basaltic dykes hybrids 2B	10NHS110
10NHS111	323	65	U	am-pl mesocratic green dyke	andesite	basaltic-andesitic dykes 2C	andesitic 10NHS111
10NHS112	120	90	U	pl-am-phyric green melanocratic dyke with comb-layer like margins of am-pl	basalt	basaltic dykes hybrids 2B	
10NHS113	160	89	U	am-pl-phyric green mesocratic dyke	andesite	basaltic-andesitic dykes 2C	andesitic 10NHS113
10NHS114				am-pl-phyric green mesocratic dyke	andesite	basaltic-andesitic dykes 2C	andesitic
10NHS115	160	35	U	am-pl-phyric mesocratic grey dyke	andesite	basaltic-andesitic dykes 2C	andesitic 10NHS115
10NHS116	168	87	U	am-pl-phyric mesocratic grey dyke	andesite	basaltic-andesitic dykes 2C	andesitic 10NHS116
10NHS117	303	57	U	am-pl-phyric mesocratic green dyke	andesite	basaltic-andesitic dykes 2C	andesitic 10NHS117AB
10NHS118	311	90	U	am-pl-phyric mescoratic green dyke	basaltic-andesite	basaltic dykes hybrids 2B	
10NHS119	343	78	U	pl-phyric mesocratic green dyke, chilled margin of larger dyke 0.55m thick	basaltic-andesite	basaltic dykes hybrids 2B	
10NHS120	132	90	U	am-pl-phyric mesocratic green dyke	basaltic-andesite	basaltic dykes hybrids 2B	
10NHS121	310	70	U	pl-phyric grey-green mesocratic dyke	basaltic-andesite	basaltic dykes hybrids 2B	10NHS121
10NHS122	111	86	U	almost aphyric mesocratic to melanocratic green-grey dyke	basaltic-andesite	basaltic-andesitic dykes 2C	andesitic
10NHS123	129	88	U	slightly pl-phyric mesocratic green dyke	andesite	basaltic dykes hybrids 2B	
10NHS124	228	90	U	almost aphyric green mesocratic dyke	andesite	basaltic-andesitic dykes 2C	andesitic
10NHS125	205	87	U	pl-am-phyric mesocratic green dyke	dacite	dacitic dykes 3	10NHS125
10NHS126	282	71	U	pl-phyric grey-green mesocratic dyke	andesite	basaltic-andesitic dykes 2C	andesitic 10NHS126
10NHS127	170	86	U	pl-am-phyric green-grey mesocratic dyke	andesite	basaltic-andesitic dykes 2C	andesitic
10NHS128	329	67	U	am-phyric green-grey green mesocratic dyke	andesite	basaltic-andesitic dykes 2C	andesitic
10NHS129	325	80	U	pl-am-phyric green mesocratic dyke	dacite	dacitic dykes 3	
10NHS130	56	54	U	hbl-phyric mesocratic dyke to pipe structure cross-cutting Listino-structure and getting cross-cut by latest andesitic-basaltic dykes	dacite	dacitic dykes 3	
10NHS131	0	84	U	am-phyric green mesocratic dyke	dacite	dacitic dykes 3	10NHS131
10NHS132	177	84	U	pl-am-phyric mesocratic-andesitic green-grey dyke	andesite		
10NHS133	168	63	U	pl-qz-phyric grey mesocratic dyke	andesite	basaltic-andesitic dykes 2C	andesitic 10NHS133
10NHS134	61	90	U	am-pl-phyric mesocratic dyke, with composite structure at margin including comb-layers of am-pl	basaltic-andesite	basaltic-andesitic dykes 2C	andesitic

Table 7.5: Field description for collected rock samples with indication if sample was oriented or not (DipDir Orient/Dip Orient) during collection.

SampleNr	DipDir Orient	Dip Orient	UpDown	Description	LithologyName	StratigraphyName	Photos
10NHS135				am-pl-phyric mesocratic dyke, with composite structure at margin including comb-layers of am-pl	basaltic-andesite	basaltic-andesitic andesitic dykes 2C	
10NHS136	41	85	U	ol-px-am-phyric melanocratic dark-green picritic dyke, ol-pseudomorphs particular in the chilled margin	picrite - Ol-tholeiite	picrobasaltic dykes 1B	10NHS136
10NHS137	181	18	U	ol-px-am-phyric melanocratic dark-green picritic dyke, ol-pseudomorphs particular in the chilled margin	picrite - Ol-tholeiite	picrobasaltic dykes 1B	10NHS137
10NHS138A	130	90	U	px-am-pl-phyric, low-content of phenocrysts mesocratic green dyke	basalt	basaltic dykes hybrids 2B	10NHS138
10NHS138B	130	90	U	px-am-pl-phyric, low-content of phenocrysts mesocratic green dyke	basalt	basaltic dykes hybrids 2B	10NHS138
10NHS138C	130	90	U	px-am-pl-phyric, low-content of phenocrysts mesocratic green dyke	basalt	basaltic dykes hybrids 2B	10NHS138
10NHS138D	225	54	U	px-am-pl-phyric, low-content of phenocrysts mesocratic green dyke	basalt	basaltic dykes hybrids 2B	10NHS138
10NHS138E	18	81	U	px-am-pl-phyric, low-content of phenocrysts mesocratic green dyke	basalt	basaltic dykes hybrids 2B	10NHS138
10NHS138F	27	80	U	px-am-pl-phyric, low-content of phenocrysts mesocratic green dyke	basalt	basaltic dykes hybrids 2B	10NHS138
10NHS139	200	80	U	contact between am-bt-pl-phyric leucratic inner phase and pl-qz-phyric melanocratic darker green dyke	basalt	basaltic dykes hybrids 2B	10NHS139
10NHS140				pl-phyric inner light-green grey mesocratic dyke	andesite	basaltic dykes hybrids 2B	
10NHS141				am-pl-phyric mesocratic to melanocratic green groundmass	basalt	picrobasaltic dykes 1B	10NHS141
10NHS142	110	63	U	pl-am-px-phyric green mesocratic dyke, inner part broken up with felsic seggregation, actual brecciation	basaltic-andesite	basaltic dykes hybrids 2B	10NHS142
10NHS143	38	75	U	margin of composite multiple green to light-green melanocratic to mesocratic dyke, internal brecciation	basaltic-andesite	basaltic dykes hybrids 2B	10NHS143
10NHS144	100	33	U	green melanocratic dyke tip of same multiple dyke at 10NHS143 and 10NHS142	basalt	basaltic dykes hybrids 2B	10NHS144
10NHS145	85	56	U	pl-phyric mesocratic to almost leucocratic grey-green dyke	andesite	basaltic dykes hybrids 2B	
10NHS146	77	65	U	pl-am-phyric mesocratic green dyke	andesite	basaltic-andesitic andesitic dykes 2C	10NHS146
10NHS147	183	50	U	almost aphyric ocelli-bearing mesocratic dyke, ocelli originating from wallrock xenolith in cloud or trail?	andesite	basaltic-andesitic andesitic dykes 2C	
10NHS148	299	67	U	am-pl-qz-phyric green mesocratic dyke	basalt	basaltic dykes hybrids 2B	10NHS148
10NHS149	220	29	U	equigranular microlitic green-blue melanocratic dyke (hbl-pl)	basalt	picrobasaltic dykes 1B	
10NHS150	27	21	U	fg grey-blackish melanocratic dyke with few hbl-phenocrysts, slightly folded	picrite - Ol-tholeiite	picrobasaltic dykes 1B	
10NHS151	356	17	U	fg grey-blackish melanocratic dyke with few hbl-phenocrysts, slightly folded	picrite - Ol-tholeiite	picrobasaltic dykes 1B	
10NHS152	182	59	U	fg green mesocratic dyke with mainly qz-phenocrysts	andesite	basaltic dykes hybrids 2B	
10NHS153				fg melanocratic aphyric dyke	picrite - Ol-tholeiite	picrobasaltic dykes 1B	10NHS153
10NHS154	199	60	U	am-pl-qz-phyric mesocratic green dyke	andesite	basaltic-andesitic andesitic dykes 1C	
10NHS155	297	13	U	px-am-phyric dark green melanocratic dyke	picrite - Ol-tholeiite	picrobasaltic dykes 1B	10NHS155
10NHS156	213	88	U	upper margin of larger subhorizontal melanocratic dyke, ol-px-am-phyric chilled margin	picrite - Ol-tholeiite	picrobasaltic dykes 1B	10NHS156-160A
10NHS157	204	87	U	middle part of larger subhorizontal melanocratic dyke, equigranular am-pl, felsic pl-rich seggregations	picrite - Ol-tholeiite	picrobasaltic dykes 1B	10NHS156-160B
10NHS158	184	34	U	lower third of of larger subhorizontal melanocratic dyke, am-pl-equigranular txt, miralolitic cavities with carb-qz infills?	picrite - Ol-tholeiite	picrobasaltic dykes 1B	10NHS156-160B
10NHS159	297	23	U	lower third of of larger subhorizontal melanocratic dyke, am-pl-equigranular txt, adjacent chilled margin	picrite - Ol-tholeiite	picrobasaltic dykes 1B	10NHS156-160B
10NHS160	306	35	U	lowest part of larger subhorizontal melanocratic dyke, chilled margin pl-px-am-phyric	picrite - Ol-tholeiite	picrobasaltic dykes 1B	10NHS156-160B
10NHS161				subhorizontal picritc dyke, felsic band, seggregation	picrite - Ol-tholeiite	picrobasaltic dykes 1B	10NHS156-160B
10NHS162	23	60	U	px-ol-am-phyric dark-green melanocratic dyke	basalt	basaltic dykes 1A	
10NHS163	164	98	U	am-phyric green mesocratic dyke	basalt	basaltic dykes 1A	10NHS163ABC
10NHS164	116	90	U	pl-phyric grey-green mesocratic dyke	andesite	basaltic-andesitic andesitic dykes 2C	
10NHS165				pl-am-px-phyric green mesocratic dyke, inner part broken up with felsic seggregation, actual brecciation	basaltic-andesite	basaltic dykes hybrids 2B	10NHS165
10NHS166	125	90	U	am-phyric green mesocratic dyke	andesite	basaltic dykes hybrids 2B	10NHS166
10NHS167				am-px-phyric grey-green mesocratic dyke	basalt	basaltic dykes 1A	
10NHS168				fg green equigranular green mesocratic dyke	basalt	basaltic dykes hybrids 2B	
10NHS169	63	61	U	fg dark green-blueish mesocratic to melanocratic dyke	basalt	basaltic dykes hybrids 2B	

Table 7.6: Field description for collected rock samples with indication if sample was oriented or not (DipDir Orient/Dip Orient) during collection.

SampleNr	DipDir Orient	Dip Orient	UpDown	Description	LithologyName	StratigraphyName	Photos
10NHS170	145	51	U	fg green mesocratic dyke	andesite	basaltic dykes hybrids 2B	
10NHS171				fg mesocratic to melanocratic dyke with lietrally no phenocrysts	basalt	basaltic dykes hybrids 2B	
10NHS172				pl-am-phyric grey green mesocratic dyke	andesite		
11NHS173	290	80		melanocratic pl-hbl phyric greenish grey dyke	andesite	basaltic-andesitic dykes 2C	11NHS173
11NHS174	296	77		mesocratic hbl-pl-phyric greenish grey dyke	andesite	basaltic-andesitic dykes 2C	andesitic 11NHS174
11NHS175	189	99		mesocratic hbl-pl phyric greenish grey dyke	andesite	basaltic-andesitic dykes 2C	andesitic
11NHS176	348	86		mesocratic hbl-pl-phyric greenish grey dyke	andesite	basaltic-andesitic dykes 2C	andesitic 11NHS176
11NHS177	24	82		melanocratic aphyric greenish grey dyke, black very fine-grained chilled margin	andesite	basaltic-andesitic dykes 2C	andesitic 11NHS177
11NHS178	59	57		mesocratic aphyric green grey dyke	andesite	basaltic-andesitic dykes 2C	andesitic
11NHS179	222	77		melanocratic dark green aphyric dyke, microphenocrysts of hbl,px and pl	basalt	basaltic dykes hybrids 2B	
11NHS180A	309	80		mesocratic light green hbl-pl phyric dyke	andesite	basaltic-andesitic dykes 2C	andesitic 11NHS180
11NHS180B	130	70		mesocratic light green hbl-pl phyric dyke	andesite	basaltic-andesitic dykes 2C	andesitic 11NHS180
11NHS181				mesocratic hbl-pl-phyric greenish grey dyke	andesite	basaltic-andesitic dykes 2C	andesitic 11NHS181
11NHS182				mesocratic aphyric green grey dyke	andesite	basaltic-andesitic dykes 2C	andesitic
11NHS183	203	59		mesocratic strongly hbl-phyric greenish grey dyke, hbl shows pl inclusions	andesite	basaltic-andesitic dykes 2C	andesitic 11NHS183ABC
11NHS184	50	90		melanocratic pl-hbl phyric green dyke, pl partially as xenocrysts, resorbed cores	andesite	basaltic dykes 1A	11NHS184ABC
11NHS185				aplitic-granitic dyke	granite		
11NHS186				quartz veins, same orientation as dark green sheared dykes in vicinity	quartz dominant vein		11NHS186
11NHS187				melanocratic pl-hbl phyric green dyke	andesite	basaltic-andesitic dykes 2C	andesitic 11NHS187
11NHS188				mesocratic to melanocratic microgabbroic dyke	basalt	basaltic dykes hybrids 2B	
11NHS189	127	55		melanocratic pl-hbl-px phyric dark green dyke	basalt	basaltic dykes hybrids 2B	
11NHS190A	188	70		mesocratic hbl-phyric green dyke, groundmass equigranular hb and pl	basalt	basaltic dykes hybrids 2B	11NHS190A
11NHS190B	184	70		mesocratic hbl-phyric green dyke, groundmass equigranular hb and pl	basalt	basaltic dykes hybrids 2B	11NHS190B
11NHS190C	183	75		mesocratic hbl-phyric green dyke, groundmass equigranular hb and pl	basalt	basaltic dykes hybrids 2B	11NHS190C
11NHS190D	180	76		mesocratic hbl-phyric green dyke, groundmass equigranular hb and pl	basalt	basaltic dykes hybrids 2B	11NHS190D
11NHS191A	313	84		mesocratic pl-hbl phyric dyke, microphenocrysts together with phenocrysts, groundmass equigranular hbl and pl	andesite	basaltic-andesitic dykes 2C	andesitic 11NHS191A
11NHS191B	318	80		mesocratic pl-hbl phyric dyke, microphenocrysts together with phenocrysts, groundmass equigranular hbl and pl	andesite	basaltic-andesitic dykes 2C	andesitic 11NHS191B
11NHS191C	322	90		mesocratic pl-hbl phyric dyke, microphenocrysts together with phenocrysts, groundmass equigranular hbl and pl	andesite	basaltic-andesitic dykes 2C	andesitic
11NHS191D	313	87		mesocratic pl-hbl phyric dyke, microphenocrysts together with phenocrysts, groundmass equigranular hbl and pl	andesite	basaltic-andesitic dykes 2C	andesitic
11NHS191E	323	90		mesocratic pl-hbl phyric dyke, microphenocrysts together with phenocrysts, groundmass equigranular hbl and pl	andesite	basaltic-andesitic dykes 2C	andesitic
11NHS191F	323	90		mesocratic pl-hbl phyric dyke, microphenocrysts together with phenocrysts, groundmass equigranular hbl and pl	andesite	basaltic-andesitic dykes 2C	andesitic
11NHS191G				mesocratic pl-hbl phyric dyke, microphenocrysts together with phenocrysts, groundmass equigranular hbl and pl	andesite	basaltic-andesitic dykes 2C	andesitic
11NHS192A	206	85		mesocratic hbl-pl phyric greenish grey dyke, microphenocrysts mainly	andesite	basaltic-andesitic dykes 2C	andesitic 11NHS192A-192E
11NHS192B	117	41		mesocratic hbl-pl phyric greenish grey dyke, microphenocrysts mainly	andesite	basaltic-andesitic dykes 2C	andesitic 11NHS192A-192E
11NHS192C	132	20		mesocratic hbl-pl phyric greenish grey dyke, microphenocrysts mainly	andesite	basaltic-andesitic dykes 2C	andesitic 11NHS192A-192E
11NHS192D	125	17		mesocratic hbl-pl phyric greenish grey dyke, microphenocrysts mainly	andesite	basaltic-andesitic dykes 2C	andesitic 11NHS192A-192E

Table 7.7: Field description for collected rock samples with indication if sample was oriented or not (DipDir Orient/Dip Orient) during collection.

SampleNr	DipDir Orient	Dip Orient	UpDown	Description	LithologyName	StratigraphyName		Photos
11NHS192E	125	15		mesocratic hbl-pl phyric greenish grey dyke, microphenocrysts mainly	andesite	basaltic-andesitic dykes 2C	andesitic	11NHS192A-192E
11NHS193				mesocratic hbl-pl phyric green dyke, coarse-grained phenocrysts	andesite	basaltic-andesitic dykes 2C	andesitic	
11NHS194				mesocratic grey fine-grained dyke, some hbl pl microphenocrysts	andesite	basaltic-andesitic dykes 2C	andesitic	11NHS194ABC
11NHS195				mesocratic light grey pl-phyric dyke	andesite	basaltic-andesitic dykes 2C	andesitic	11NHS195ABC
11NHS196				melanocratic layered subhorizontal dyke with gradation in pl content besides green hbl	picrite - Ol-tholeiite	picrobasaltic dykes 1B		11NHS196A-196N
11NHS197				melanocratic layered subhorizontal dyke with gradation in pl content besides green hbl	picrite - Ol-tholeiite	picrobasaltic dykes 1B		11NHS197A-197E
11NHS198				melanocratic layered subhorizontal dyke with gradation in pl content besides green hbl	picrite - Ol-tholeiite	picrobasaltic dykes 1B		11NHS198
11NHS199				melanocratic blackish fine-grained dyke, blobs or lenses of felsic material (pl and carb)	picrite - Ol-tholeiite	picrobasaltic dykes 1B		11NHS199ABC
11NHS200				melanocratic blackish fine-grained dyke, blobs or lenses of felsic material (pl and carb)	picrite - Ol-tholeiite	picrobasaltic dykes 1B		11NHS200A-200E
11NHS201				melanocratic blackish fine-grained dyke, blobs or lenses of felsic material (pl and carb)	picrite - Ol-tholeiite	picrobasaltic dykes 1B		11NHS201A-201D
12NHS202				melanocratic grey-blueish dyke, ol-px phyric (ol-pseudomorphs), px with rosty inclusions, abundant different xenoliths (granitic, quarzite, mafic cumulates am+ol+px)	picrite - Ol-tholeiite			
12NHS203				melanocratic grey-blueish dyke, ol-px phyric (ol-pseudomorphs), px with rosty inclusions, abundant different xenoliths (granitic, quarzite, mafic cumulates am+ol+px)	picrite - Ol-tholeiite			
12NHS204				grey-green mesocratic basaltic-andesitic dyke am-pl phyric	basaltic-andesite			
12NHS205				massive mesocratic 5-6m thick am-pl phyric dyke with some very coarse grained am-autocrysts, xenoliths of deformed basement, am-rich enclaves that are often strecthed out in possible flow direction, altered carbonates, quarzite clasts	basaltic-andesite			12NHS205A-205I
OMA001				melanocratic Ol-tholeiitic dyke, some fresh Ol is preserved recognized by rusty parts	basalt	basaltic dykes 1A		
PB784				am-pl-phyric gre green mesocratic dyke	andesite	basaltic-andesitic dykes 1C	andesitic	

Table 7.8: Field description for collected rock samples with indication if sample was oriented or not (DipDir Orient/Dip Orient) during collection.

7.3 Whole Rock Data

Composition	Ol-tholeiite	Ol-tholeiite	Ol-tholeiite	Ol-tholeiite	Ol-tholeiite	Ol-tholeiite	Ol-tholeiite	Ol-tholeiite	Ol-tholeiite	Picro-basalt/Ol-thole.	Picro-basalt/Ol-thole.	Picro-basalt/Ol-thole.	Picro-basalt/Ol-thole.	Picro-basalt/Ol-thole.	Picro-basalt/Ol-thole.
Sample	NHS066	NHS066	NHS066	NHS066	NHS064	NHS064	NHS064	NHS057	NHS057	NHS162	NHS065	NHS065	NHS065	NHS065	NHS061	NHS061
Generation	1A	1A	1A	1A	1A	1A	1A	1A	1A	1A	1B	1B	1B	1B	1B	1B
SiO2	49.50	48.89	48.90	49.64	50.71	50.74	50.13	49.72	49.39	48.84	50.31	47.72	50.25	49.27	47.74	47.41	47.15	47.68	49.52	48.08
TiO2	0.60	0.55	0.56	0.64	0.70	0.68	0.67	0.67	0.63	0.61	0.72	1.39	0.84	0.80	0.80	0.82	0.82	0.77	0.90	0.83
Al2O3	14.68	13.09	13.34	15.67	17.87	17.09	16.62	16.32	15.27	14.64	17.87	15.56	18.85	17.93	17.24	17.15	16.62	15.47	19.91	17.90
Fe2O3	8.65	9.14	9.01	8.47	8.52	8.78	8.80	8.94	9.03	8.86	8.62	9.83	7.43	7.96	8.65	9.00	9.13	9.38	7.23	8.29
MnO	0.16	0.18	0.17	0.15	0.15	0.16	0.16	0.17	0.18	0.15	0.13	0.23	0.14	0.19	0.21	0.22	0.22	0.23	0.13	0.19
MgO	10.80	13.09	12.37	9.82	7.01	7.54	8.37	8.84	10.40	11.81	7.47	8.58	6.83	8.37	9.29	9.83	10.17	10.68	6.04	8.93
CaO	10.73	11.23	11.28	10.60	10.96	11.07	11.11	11.28	10.98	10.33	10.99	12.24	10.43	10.63	10.76	10.81	10.78	10.62	10.76	10.27
Na2O	1.71	1.16	1.28	1.95	2.14	2.07	1.96	1.95	1.70	1.48	2.55	2.18	2.54	2.13	1.87	1.80	1.71	1.56	2.76	1.92
K2O	0.73	0.66	0.62	0.73	0.68	0.58	0.60	0.49	0.64	1.35	0.35	0.59	0.92	1.11	1.19	1.26	1.27	1.21	0.90	1.62
P2O5	0.10	0.08	0.09	0.11	0.12	0.12	0.11	0.11	0.10	0.10	0.12	0.23	0.21	0.18	0.15	0.14	0.14	0.13	0.20	0.16
LOI	1.38	1.80	1.65	1.25	0.80	0.86	0.99	0.96	1.20	1.48	0.27	0.86	0.95	1.09	1.19	1.23	1.25	1.28	0.77	1.13
Cr2O3	0.07	0.10	0.10	0.06	0.03	0.04	0.05	0.05	0.06	0.09	0.04	0.04	0.03	0.05	0.06	0.06	0.06	0.10	0.01	0.05
NiO	0.02	0.02	0.02	0.01	0.01	0.01	0.01	0.02	0.02	0.02	0.01	0.01	0.01	0.01	0.01	0.02	0.02	0.02	0.01	0.01
Total	99.12	99.99	99.37	99.09	99.71	99.75	99.59	99.52	99.60	99.76	99.45	99.47	99.43	99.72	99.14	99.73	99.34	99.13	99.15	99.38
Sc	43.7	52.3	51.1	40.7	39.5	42.8	43.1	44.0	44.1	46.1	43.8	43.4	31.8	34.3	34.6	36.1	38.3	44.1	29.2	37.2
V	247	240	243	257	284	274	275	271	270	263	303	319	266	247	255	271	279	271	262	262
Cr	458	638	623	376	188	257	316	317	407	676	285	340	167	281	331	353	373	621	60	323
Co	39.6	45.5	43.1	37.3	32.2	34.4	34.7	34.7	41.9	46.9	59.1	36.9	28.1	30.8	31.3	33.0	34.3	35.3	23.8	31.2
Ni	123.5	157.6	146.0	113.7	55.1	47.0	74.5	68.7	121.0	167.6	108.0	97.1	69.8	103.9	96.5	129.8	131.1	137.7	41.9	121.3
Cu	116.9	21.9	18.8	287.0	55.3	16.6	13.8	15.0	14.5	13.2	12.6	5.6	697.0	112.2	26.5	22.3	27.4	19.1	8.8	8.5
Zn	124.5	150.4	154.7	122.4	170.8	127.8	148.6	115.8	125.3	128.7	111.9	191.7	131.1	163.6	126.3	166.2	167.8	167.5	124.8	149.4
Ga	13.4	13.1	12.7	14.2	15.8	15.4	14.7	14.7	14.3	14.2	16.6	17.4	16.4	15.8	15.8	15.9	15.8	15.2	16.7	14.8
Ge	2.1	2.4	2.0	1.0	2.2	1.2	2.3	2.0	2.5	2.2	2.0	3.8	2.3	1.2	2.1	2.8	2.8	3.0	1.6	2.3
As	1.4	1.6	1.7	0.8	1.0	1.0	1.3	1.1	0.0	0.0	0.0	1.6	1.5	1.3	0.8	1.9	0.0	1.3	1.1	1.1
Rb	16.8	16.7	15.0	18.6	14.3	8.8	10.2	8.0	13.1	40.5	6.9	6.0	33.5	39.4	42.3	47.5	47.7	47.1	28.8	61.0
Sr	401	317	345	448	456	446	433	417	387	372	546	461	398	351	328	314	308	282	443	325
Y	14.2	13.1	13.4	15.1	15.8	15.5	14.8	14.6	14.0	14.9	17.7	16.5	16.9	16.4	16.3	16.0	16.4	15.4	15.3	15.2
Zr	51	43	45	56	58	58	54	53	52	47	59	70	71	64	59	55	53	51	71	59
Nb	2.8	2.3	2.5	3.0	3.1	3.0	2.8	2.8	2.6	2.9	3.7	13.9	5.4	4.0	4.0	3.9	3.7	3.9	5.8	3.9
Mo	0.6	0.7	0.4	0.8	3.8	2.2	2.1	1.5	2.4	2.8	15.8	2.0	1.8	1.4	1.2	1.6	1.2	1.5	0.6	0.9
Cs	1.64	1.26	1.19	1.85	0.65	0.36	0.53	0.53	0.88	3.99	1.21	0.18	2.35	3.34	3.27	3.71	3.99	3.89	2.02	3.86
Ba	96	72	75	110	134	128	130	95	81	132	62	94	170	154	139	135	124	106	162	177
La	7.3	6.9	7.8	7.8	8.1	8.2	7.3	7.1	8.3	6.1	9.7	13.9	16.3	15.2	13.6	14.5	10.7	10.4	8.8	9.2
Ce	15.7	14.0	15.5	16.6	16.5	17.3	16.1	15.5	16.4	15.3	20.8	31.4	28.6	27.3	24.4	26.2	20.9	20.1	17.3	17.4
Pr	1.88	1.75	1.79	2.14	2.22	2.19	1.94	2.02	1.99	2.02	2.53	3.83	3.19	3.14	2.79	2.88	2.33	2.35	2.16	2.09
Nd	9.3	8.0	8.4	10.2	10.6	10.8	9.6	9.8	9.8	8.9	11.0	17.0	13.3	13.1	12.3	12.7	11.5	10.7	10.7	10.2
Sm	2.21	1.98	2.15	2.63	2.54	2.58	2.42	2.68	2.53	2.21	2.75	3.93	2.87	2.67	2.83	2.73	2.68	2.59	2.52	2.68
Eu	0.73	0.74	0.70	0.81	0.86	0.83	0.85	0.79	0.82	0.63	0.84	1.21	0.99	1.08	1.05	0.91	1.02	0.97	0.86	0.80
Gd	2.33	1.96	2.45	2.49	2.52	2.42	2.42	2.46	2.58	2.27	2.96	3.52	2.73	3.04	2.64	2.83	2.46	2.39	2.51	2.41
Tb	0.395	0.297	0.397	0.416	0.438	0.443	0.419	0.394	0.398	0.388	0.422	0.495	0.456	0.504	0.421	0.509	0.468	0.483	0.427	0.410
Dy	2.50	2.26	2.37	2.49	2.91	2.91	2.73	2.83	2.64	2.68	3.10	3.27	2.85	2.93	3.11	2.79	3.06	2.63	2.89	2.76
Ho	0.546	0.487	0.551	0.602	0.592	0.546	0.567	0.561	0.514	0.543	0.645	0.611	0.695	0.742	0.652	0.685	0.669	0.614	0.586	0.576
Er	1.51	1.33	1.44	1.69	1.71	1.64	1.59	1.60	1.58	1.62	1.92	1.78	1.77	1.78	1.72	1.78	1.70	1.65	1.77	1.67
Tm	0.226	0.200	0.229	0.248	0.237	0.240	0.228	0.238	0.232	0.237	0.283	0.242	0.256	0.323	0.315	0.289	0.303	0.262	0.292	0.232
Yb	1.57	1.38	1.46	1.71	1.84	1.79	1.68	1.54	1.64	1.58	2.07	1.65	1.88	2.03	1.92	1.83	1.67	1.72	1.82	1.75
Lu	0.215	0.207	0.216	0.260	0.284	0.232	0.227	0.251	0.240	0.232	0.315	0.239	0.313	0.308	0.276	0.301	0.293	0.297	0.293	0.281
Hf	1.45	1.19	1.26	1.56	1.58	1.43	1.47	1.48	1.31	1.35	1.68	1.93	1.54	1.64	1.55	1.56	1.52	1.54	1.68	1.62
Ta	0.22	0.14	0.23	0.26	0.36	0.20	0.20	0.19	0.20	0.18	0.20	0.80	0.37	0.31	0.28	0.32	0.33	0.32	0.43	0.24
W	1.91	1.29	1.69	2.42	1.15	1.00	0.70	2.43	0.93	0.00	0.00	0.00	1.10	0.79	0.56	0.68	0.58	0.71	3.48	1.64
Pb	1.26	1.01	1.01	1.33	1.01	0.92	0.96	0.81	0.78	1.32	2.10	4.09	1.73	1.48	1.20	1.33	1.05	1.12	2.61	1.29
Th	1.60	1.25	1.48	1.76	1.72	1.65	1.50	1.45	1.49	1.30	1.82	2.81	3.47	2.96	2.81	2.91	2.28	2.43	3.13	2.26
U	0.59	0.26	0.39	0.72	1.03	0.69	0.63	0.50	0.44	0.55	0.85	2.76	2.66	1.45	1.05	1.08	0.77	0.76	2.49	1.26

Table 7.9: Post-plutonic dyke rock suite of the Southern Adamello (Re di Castello superunit). Major elements from SiO_2 to NiO (all [wt%]) were determined by XRF analysis, all other elements were analyzed by LA-ICP-MS analysis (all [ppm]).

Composition	Picro-basalt/Ol-tholeiite	Picro-basalt/Ol-tholeiite	Picro-basalt/Ol-tholeiite	Picro-basalt/Ol-tholeiite	Picro-basalt/Ol-tholeiite	Picro-basalt/Ol-tholeiite	Picro-basalt/Ol-tholeiite	Picro-basalt/Ol-tholeiite	Picro-basalt/Ol-tholeiite	Picro-basalt/Ol-tholeiite	Picro-basalt/Ol-tholeiite	Picro-basalt/Ol-tholeiite	Picro-basalt/Ol-tholeiite	Picro-basalt/Ol-tholeiite
Sample	NHS061	NHS061	NHS061	NHS002	NHS003	NHS007	NHS011	NHS073	NHS011	NHS136	NHS160	NHS141	NHS157	NHS151	NHS137	NHS153
Generation	1B	1B	1B	1B	1B	1B	1B	1B	1B	1B	1B	1B	1B	1B	1B	1B
SiO2	48.59	49.18	49.75	47.68	46.84	45.77	47.05	48.31	47.13	45.94	49.10	45.83	46.97	47.16	48.83	46.40	46.33	46.49	47.55
TiO2	0.81	0.77	0.74	0.93	0.74	0.66	0.79	0.85	0.80	0.87	0.88	0.71	0.79	0.89	0.79	1.01	1.02	0.71	0.90
Al2O3	16.66	16.11	16.28	15.24	21.11	13.89	12.54	15.16	16.04	18.38	15.48	17.45	13.13	15.29	16.72	15.90	19.09	18.54	12.75	18.16
Fe2O3	8.79	8.74	8.39	8.70	6.65	9.67	11.29	9.20	8.63	7.67	9.54	6.78	9.80	9.24	8.11	7.08	9.61	9.70	9.63	8.38
MnO	0.22	0.23	0.22	0.24	0.08	0.18	0.21	0.17	0.15	0.13	0.17	0.11	0.17	0.16	0.12	0.11	0.11	0.10	0.17	0.13
MgO	9.74	9.91	9.51	10.00	6.69	13.22	14.24	11.10	10.31	9.13	12.14	8.52	15.38	12.00	10.49	10.61	6.02	5.96	15.26	8.34
CaO	10.31	10.35	10.32	10.25	9.94	8.87	9.84	10.05	9.95	11.36	11.40	10.04	10.01	9.48	9.67	9.83	11.77	11.85	10.02	11.19
Na2O	1.69	1.66	1.74	1.58	2.06	1.04	0.87	1.67	1.76	1.96	1.58	2.22	1.10	1.70	2.18	2.68	2.60	2.36	0.94	2.19
K2O	1.48	1.36	1.26	1.19	2.11	2.76	1.84	0.99	1.94	0.91	0.55	1.49	0.42	1.88	1.03	0.87	0.53	0.58	0.49	1.13
P2O5	0.15	0.14	0.15	0.14	0.16	0.17	0.15	0.17	0.21	0.16	0.13	0.20	0.09	0.18	0.15	0.18	0.23	0.22	0.09	0.18
LOI	1.22	1.20	1.21	1.28	1.88	1.80	1.97	2.77	1.45	2.12	2.16	2.29	2.57	1.62	3.17	2.16	2.14	2.90	2.60	1.14
Cr2O3	0.06	0.06	0.05	0.07	0.00	0.11	0.13	0.09	0.07	0.04	0.08	0.04	0.16	0.09	0.07	0.07	0.01	0.01	0.16	0.04
NiO	0.02	0.02	0.02	0.02	0.01	0.03	0.03	0.02	0.02	0.01	0.02	0.02	0.04	0.03	0.02	0.02	0.00	0.00	0.04	0.01
Total	99.74	99.74	99.64	99.01	99.30	99.30	99.53	99.23	99.69	99.80	100.04	99.13	99.40	99.42	99.77	99.14	99.51	99.58	99.34	99.34
Sc	38.5	38.4	36.3	38.1	23.5	44.2	45.7	41.7	39.8	33.5	51.7	39.4	52.8	45.6	41.2	42.4	34.8	37.6	56.8	41.8
V	268	265	253	259	231	233	272	276	290	268	325	264	291	267	315	292	338	324	297	296
Cr	414	407	353	433	39	676	781	662	521	283	620	396	1180	721	530	578	76	84	1172	315
Co	33.5	32.8	31.0	32.9	29.2	42.6	48.0	41.5	39.9	28.9	38.5	35.5	55.0	34.6	45.8	29.1	42.1	47.8	56.2	30.0
Ni	118.4	126.4	123.2	122.7	80.3	249.5	228.6	191.7	167.1	111.0	179.0	125.5	336.2	237.1	166.5	185.3	30.3	41.9	330.1	99.6
Cu	10.2	11.4	8.4	11.8	8.6	16.6	15.5	26.3	10.5	15.5	9.6	7.2	31.1	11.5	14.5	7.7	130.9	137.7	93.7	7.8
Zn	181.3	144.3	148.3	140.3	149.4	149.9	142.2	197.6	170.4	176.4	182.4	147.3	150.6	133.8	170.9	137.7	125.3	141.3	136.1	183.6
Ga	15.5	14.9	14.7	14.7	16.2	13.8	15.0	13.1	15.4	15.7	15.0	15.9	12.3	14.8	15.0	15.6	16.2	16.2	12.4	16.7
Ge	2.7	3.2	2.7	3.0	2.9	2.5	2.8	2.3	2.7	1.9	1.5	2.6	2.1	2.4	2.2	2.6	2.0	2.5	1.9	2.3
As	0.7	0.6	1.2	0.7	1.7	1.2	3.1	27.3	0.0	2.1	1.7	2.9	2.1	0.0	3.3	2.2	3.0	2.2	0.0	1.9
Rb	57.4	54.2	50.0	47.7	95.4	119.5	85.9	40.8	94.0	31.5	16.7	74.6	9.6	66.1	31.6	31.3	14.4	17.5	11.7	36.8
Sr	291	283	292	266	485	227	171	316	370	480	345	490	186	428	461	720	1054	1062	183	594
Y	15.5	15.4	14.9	15.1	13.9	14.0	12.7	13.9	15.6	17.8	15.8	20.3	13.1	15.5	17.1	15.2	20.4	20.5	13.7	18.0
Zr	54	54	55	51	53	54	46	43	56	55	47	60	33	57	51	55	48	49	35	57
Nb	4.0	3.8	3.7	3.7	9.2	5.2	5.3	4.5	4.4	7.3	3.5	6.4	2.3	6.2	5.3	5.9	2.6	2.7	2.6	4.7
Mo	0.6	0.4	0.4	0.7	1.1	0.7	1.1	2.2	1.7	1.9	2.1	2.1	2.5	2.6	1.7	2.1	2.7	4.1	2.7	3.1
Cs	3.50	3.05	2.63	2.58	3.44	9.38	5.04	0.98	6.40	0.95	1.29	3.15	1.16	5.63	0.88	0.58	1.15	1.25	2.79	3.40
Ba	147	127	118	107	300	250	147	261	347	127	105	294	62	201	245	142	75	76	68	133
La	14.3	9.9	13.0	11.3	15.8	15.9	13.5	10.9	21.7	13.4	8.9	22.4	6.5	17.8	16.0	21.9	8.7	9.4	7.2	13.9
Ce	25.3	19.1	23.7	21.9	26.0	26.3	23.3	22.0	36.3	26.5	18.5	38.3	13.6	30.2	29.5	37.8	21.2	22.4	14.9	27.8
Pr	2.80	2.25	2.63	2.53	2.85	2.90	2.71	2.43	3.69	3.10	2.29	4.23	1.73	3.25	3.34	3.88	2.84	2.98	1.81	3.20
Nd	12.9	11.1	12.0	11.5	13.5	12.7	11.9	10.8	14.4	13.1	10.1	18.2	8.0	13.5	13.9	15.3	13.0	14.0	8.2	13.6
Sm	2.72	2.54	2.69	2.77	2.78	2.74	2.54	2.45	2.95	3.12	2.26	3.63	2.12	2.93	2.98	3.00	3.19	3.45	1.99	2.69
Eu	0.83	0.91	0.84	0.96	1.14	0.86	0.82	0.76	0.81	0.89	0.78	1.24	0.66	0.81	0.96	0.95	1.03	1.09	0.64	1.01
Gd	2.61	2.79	2.31	2.56	2.49	2.52	2.28	2.58	2.96	3.18	2.65	3.87	1.97	2.73	3.03	2.71	3.61	3.60	2.51	3.09
Tb	0.391	0.406	0.427	0.390	0.404	0.421	0.351	0.396	0.426	0.466	0.370	0.489	0.363	0.423	0.469	0.391	0.559	0.547	0.354	0.476
Dy	2.82	2.70	2.92	2.65	2.56	2.43	2.38	2.61	2.62	3.17	2.83	3.90	2.60	2.96	3.04	2.67	3.79	3.64	2.31	3.43
Ho	0.590	0.594	0.542	0.565	0.522	0.593	0.517	0.505	0.533	0.637	0.600	0.784	0.506	0.575	0.653	0.551	0.726	0.753	0.513	0.635
Er	1.67	1.65	1.73	1.64	1.64	1.49	1.44	1.43	1.66	1.92	1.78	2.14	1.46	1.66	1.92	1.62	2.19	2.27	1.48	1.93
Tm	0.253	0.237	0.216	0.235	0.222	0.285	0.200	0.211	0.265	0.285	0.240	0.308	0.196	0.265	0.271	0.228	0.317	0.335	0.217	0.283
Yb	1.72	1.68	1.64	1.64	1.51	1.59	1.46	1.37	1.64	2.13	1.91	2.15	1.46	1.71	1.84	1.75	2.27	2.06	1.47	2.15
Lu	0.279	0.245	0.247	0.255	0.240	0.277	0.193	0.220	0.251	0.286	0.233	0.329	0.215	0.261	0.263	0.219	0.309	0.333	0.199	0.300
Hf	1.30	1.48	1.39	1.33	1.42	1.48	1.17	1.12	1.51	1.46	1.45	1.72	1.01	1.48	1.48	1.49	1.40	1.43	0.95	1.45
Ta	0.23	0.20	0.20	0.21	0.36	0.38	0.32	0.27	0.29	0.27	0.18	0.30	0.18	0.39	0.29	0.36	0.18	0.16	0.18	0.26
W	2.62	1.14	3.03	5.24	3.63	0.68	7.09	0.00	0.00	0.00	0.00	0.00	0.00	0.00	0.00	0.00	0.00	0.00	0.00	0.00
Pb	1.24	1.21	1.30	1.77	1.31	1.08	0.83	1.69	1.72	2.28	3.06	2.17	0.64	1.26	3.14	2.69	1.87	1.75	1.46	3.20
Th	2.79	1.98	2.38	2.10	4.16	5.21	4.02	2.32	2.52	1.94	6.12	1.74	6.12	4.29	5.85	1.13	1.13	1.89	1.89	2.85
U	0.90	0.71	0.78	0.64	1.24	1.65	0.49	0.55	1.06	0.73	1.44	0.28	1.44	0.35	1.87	1.11	1.80	0.29	0.41	0.70

Table 7.10: Post-plutonic dyke rock suite of the Southern Adamello (Re di Castello superunit). Major elements from SiO_2 to NiO (all [wt%]) were determined by XRF analysis, all other elements were analyzed by LA-ICP-MS analysis (all [ppm]).

Composition	Picro-basalt/Ol-thole.	Picro-basalt/Ol-thole.	Picro-basalt/Ol-thole.	Picro-basalt/Ol-thole.	Picro-basalt/Ol-thole.	Picro-basalt/Ol-thole.	Picro-basalt/Ol-thole.	Picro-basalt?Ol-thole.	Picro-basalt/Ol-thole.	Picro-basalt/Ol-thole.	basalt	basalt	basalt	basaltic hybrid	basaltic hybrid	basaltic hybrid	basaltic hybrid	basaltic hybrid	basaltic hybrid
Sample	NHS153	NHS153	NHS153	NHS153	NHS153	NHS156	NHS158	NHS159	NHS168	NHS168	NHS053	NHS079	NHS051	NHS045	NHS045	NHS045	NHS045	NHS045	NHS045	NHS045
Generation	1B	1B	1B	1B	1B	1B	1B	1B	1B	1B	2A	2A	2A	2B	2B	2B	2B	2B	2B	2B
SiO2	46.61	44.67	46.18	56.34	46.77	48.86	47.01	47.43	47.18	45.21	45.10	46.79	48.65	48.96	48.43	46.44	48.78	50.74	50.31	49.04
TiO2	0.84	0.93	0.81	0.57	0.85	0.92	0.77	0.71	0.78	0.86	0.79	0.79	0.83	0.84	0.98	0.95	0.98	1.03	0.96	0.92
Al2O3	16.63	12.57	15.47	18.40	17.17	19.19	14.49	13.67	14.54	15.45	15.36	15.20	15.94	16.25	17.25	17.44	17.48	17.61	17.17	16.81
Fe2O3	9.17	10.81	9.85	8.00	8.84	7.04	9.83	7.81	8.97	9.30	9.40	9.57	8.99	8.70	9.34	9.61	9.07	8.98	8.77	9.04
MnO	0.16	0.24	0.18	0.17	0.15	0.11	0.20	0.14	0.16	0.18	0.16	0.19	0.18	0.17	0.18	0.19	0.16	0.13	0.15	0.18
MgO	9.91	16.66	11.22	2.66	9.57	6.77	12.06	13.11	12.72	11.17	10.59	10.99	9.91	8.43	7.43	8.17	6.47	5.41	6.07	7.73
CaO	11.07	10.27	11.03	7.46	11.37	11.93	9.38	10.64	9.13	10.66	10.71	10.31	10.51	10.56	10.61	10.83	9.33	8.08	8.47	9.40
Na2O	1.78	1.01	1.55	3.18	1.82	2.67	1.73	1.86	1.73	1.90	1.55	1.40	1.57	1.76	2.39	1.96	3.10	3.78	3.53	2.86
K2O	1.28	0.44	1.36	1.16	1.23	0.71	1.42	0.74	2.02	0.38	1.33	0.82	0.94	0.78	0.60	1.00	1.84	2.30	2.18	1.23
P2O5	0.15	0.14	0.14	0.20	0.15	0.20	0.18	0.16	0.17	0.19	0.13	0.15	0.15	0.16	0.17	0.17	0.18	0.18	0.18	0.16
LOI	1.44	1.40	1.28	1.33	1.15	1.08	2.06	2.76	1.69	3.78	4.04	2.90	2.31	2.92	1.64	2.42	1.69	1.01	1.26	1.88
Cr2O3	0.06	0.18	0.08	0.00	0.06	0.02	0.11	0.11	0.09	0.11	0.07	0.10	0.09	0.07	0.06	0.08	0.05	0.03	0.04	0.06
NiO	0.02	0.04	0.02	0.00	0.02	0.01	0.03	0.03	0.02	0.02	0.02	0.02	0.01	0.01	0.01	0.01	0.01	0.00	0.00	0.01
Total	99.11	99.35	99.16	99.47	99.13	99.50	99.28	99.16	99.21	99.20	99.25	99.22	100.08	99.60	99.10	99.25	99.13	99.27	99.09	99.32
Sc	41.8	70.7	46.6	15.2	42.0	38.0	49.3	46.2	43.4	46.6	44.9	34.6	36.1	33.1	35.4	35.9	34.7	32.3	33.3	34.6
V	299	327	304	178	299	290	271	259	273	298	298	226	244	242	247	257	266	272	263	252
Cr	314	1357	603	58	445	198	828	832	740	791	559	647	668	549	390	479	305	195	266	399
Co	29.6	54.7	32.8	14.8	24.5	24.6	28.7	30.0	35.0	42.2	32.0	39.3	38.5	31.3	30.1	33.5	27.3	27.3	25.2	29.7
Ni	96.1	339.1	160.6	10.4	118.9	57.7	209.8	249.7	244.1	204.7	146.8	156.0	127.9	90.5	63.9	94.4	49.4	34.3	36.4	64.9
Cu	7.6	10.0	10.8	4.0	7.5	10.2	21.1	6.3	9.1	4.3	7.9	20.3	61.4	92.2	59.6	85.9	47.1	44.5	56.5	48.6
Zn	147.1	179.1	161.5	184.0	183.7	167.7	177.1	142.1	155.0	157.2	166.9	196.8	189.9	145.5	217.0	188.6	179.5	194.4	228.6	159.4
Ga	15.6	13.0	14.4	16.8	16.2	16.4	15.6	13.4	14.7	14.5	14.4	15.1	15.4	15.7	17.4	17.5	16.1	16.3	16.1	16.5
Ge	1.8	2.0	2.4	2.1	1.8	2.0	1.9	2.3	2.7	2.0	2.3	4.8	2.2	1.7	2.6	2.5	2.7	1.9	2.4	2.5
As	0.0	0.0	0.0	0.0	1.5	2.0	1.6	2.7	1.6	0.0	1.8	2.6	2.3	2.1	1.7	1.8	1.5	2.3	1.3	2.0
Rb	36.7	13.1	41.7	40.9	36.7	20.9	41.6	24.3	83.0	8.6	40.9	30.7	34.9	24.9	12.6	30.3	55.5	58.8	61.4	37.1
Sr	586	242	357	446	432	738	301	620	479	764	361	281	347	368	429	408	487	536	506	450
Y	18.2	15.1	16.1	21.0	17.2	19.9	15.7	14.3	15.1	17.7	15.9	14.7	15.4	15.3	18.5	18.1	19.3	19.6	18.2	17.8
Zr	56	40	46	96	53	64	53	47	47	51	46	77	75	73	84	88	89	94	90	83
Nb	4.7	6.1	3.9	4.7	3.7	6.4	6.0	4.7	5.0	6.2	3.8	5.2	5.5	5.5	5.7	5.6	5.8	5.9	5.7	5.2
Mo	3.0	2.1	2.7	2.9	3.0	2.9	1.9	2.3	1.8	1.6	2.9	0.3	1.9	2.2	1.5	1.4	1.4	3.1	1.5	0.7
Cs	3.34	0.66	4.03	1.08	3.25	1.64	3.74	0.75	6.20	0.27	4.09	0.49	0.62	0.29	0.48	0.65	0.95	0.82	0.94	0.76
Ba	132	81	108	261	142	129	251	120	162	196	118	118	209	168	199	270	432	598	531	320
La	13.8	11.4	9.9	19.3	12.3	13.2	16.7	18.0	16.0	17.2	10.3	14.9	15.0	15.4	16.3	16.2	17.3	17.4	17.7	15.9
Ce	27.4	24.1	21.1	35.4	24.4	26.6	28.8	31.0	28.7	31.1	21.2	28.8	31.1	31.4	31.6	31.4	33.5	34.1	33.8	30.4
Pr	3.26	2.75	2.63	3.89	2.97	3.15	3.13	3.31	3.31	3.67	2.55	3.27	3.73	3.65	3.87	3.65	3.96	3.97	3.96	3.52
Nd	13.5	11.8	10.9	15.5	12.7	13.6	12.8	12.6	13.5	15.0	11.4	15.1	14.5	15.0	16.5	15.7	17.1	17.2	16.6	16.1
Sm	2.95	2.71	2.70	3.44	2.85	2.97	2.84	2.69	2.81	2.94	2.68	3.13	3.05	3.16	3.68	3.33	3.69	3.89	3.58	3.48
Eu	0.98	0.84	0.81	1.08	1.01	1.11	0.79	0.84	0.70	0.86	0.82	0.94	0.85	0.95	1.08	1.07	1.14	1.06	1.10	1.01
Gd	2.96	2.75	2.58	3.19	2.82	3.61	3.23	2.59	2.91	3.29	2.53	2.82	2.85	2.85	3.19	3.27	3.29	3.49	3.30	3.36
Tb	0.500	0.446	0.425	0.536	0.456	0.569	0.377	0.382	0.399	0.476	0.389	0.505	0.450	0.406	0.524	0.469	0.553	0.577	0.539	0.487
Dy	3.30	3.05	2.93	3.81	3.16	3.41	3.07	2.41	2.69	3.13	2.72	2.53	2.88	2.83	3.15	3.21	3.40	3.53	3.34	3.09
Ho	0.649	0.584	0.585	0.778	0.624	0.700	0.580	0.548	0.535	0.643	0.586	0.566	0.553	0.566	0.719	0.654	0.724	0.735	0.698	0.671
Er	1.84	1.54	1.74	2.35	1.86	2.24	1.70	1.49	1.62	1.75	1.72	1.57	1.61	1.65	1.80	1.72	1.96	1.88	1.93	1.78
Tm	0.266	0.243	0.236	0.319	0.261	0.295	0.251	0.213	0.246	0.249	0.257	0.249	0.274	0.241	0.292	0.258	0.278	0.281	0.281	0.274
Yb	1.87	1.50	1.84	2.64	1.84	2.25	1.68	1.61	1.67	1.76	1.69	1.51	1.58	1.59	1.78	1.79	1.90	1.94	1.94	1.77
Lu	0.267	0.219	0.269	0.388	0.273	0.305	0.261	0.238	0.262	0.263	0.253	0.257	0.245	0.238	0.276	0.258	0.280	0.278	0.293	0.265
Hf	1.54	1.28	1.29	2.25	1.50	1.66	1.42	1.38	1.33	1.38	1.36	1.91	1.93	1.99	2.09	2.11	2.15	2.37	2.23	2.27
Ta	0.25	0.27	0.23	0.26	0.22	0.33	0.32	0.29	0.28	0.37	0.21	0.43	0.33	0.34	0.49	0.38	0.34	0.35	0.38	0.28
W	0.00	0.00	0.00	0.00	0.00	0.00	0.00	0.00	0.00	0.00	0.00	0.61	0.00	0.00	0.39	0.20	0.18	0.15	0.15	0.09
Pb	3.15	1.10	2.45	7.47	2.28	3.56	2.12	1.53	1.36	1.42	2.02	1.64	17.99	3.61	2.61	3.55	5.28	6.26	6.67	5.41
Th	2.73	1.83	2.08	5.62	2.49	3.18	5.52	4.70	4.63	3.45	2.15	2.90	3.13	3.11	3.25	3.24	3.50	3.51	3.41	3.16
U	0.68	0.17	0.28	1.25	0.49	0.91	1.62	1.52	0.82	0.62	0.33	0.66	0.77	0.76	0.67	0.62	0.59	0.63	0.59	0.56

Table 7.11: Post-plutonic dyke rock suite of the Southern Adamello (Re di Castello superunit). Major elements from SiO_2 to NiO (all [wt%]) were determined by XRF analysis, all other elements were analyzed by LA-ICP-MS analysis (all [ppm]).

Composition	basaltic hybrid	basaltic hybrid	basaltic hybrid	basaltic hybrid	basaltic hybrid	basaltic hybrid	basaltic hybrid	basaltic hybrid	basaltic hybrid	basaltic hybrid	basaltic hybrid	basaltic hybrid	basaltic hybrid	basaltic hybrid	basaltic hybrid	basaltic hybrid	basaltic hybrid
Sample	NHS053	NHS078	NHS078	NHS078	NHS042	NHS042	NHS042	NHS001	NHS041	NHS075	NHS093	NHS099	NHS094	NHS098	NHS118	NHS119	NHS123	NHS138A	NHS138B
Generation	2B	2B	2B	2B	2B	2B	2B	2B	2B	2B	2B	2B	2B	2B	2B	2B	2B	2B	2B
SiO2	48.00	49.84	50.10	50.32	47.92	46.02	47.21	46.51	48.33	47.03	50.75	48.92	46.54	49.02	49.21	49.35	51.04	48.76	48.33	47.76
TiO2	0.93	0.87	0.84	0.85	0.82	0.78	0.82	0.82	0.85	0.66	0.65	0.66	0.66	0.67	0.70	0.71	0.72	0.82	0.84	0.81
Al2O3	16.71	16.32	17.05	16.98	16.01	14.96	15.83	16.81	16.15	15.95	16.61	15.32	15.59	15.61	18.70	18.78	18.75	18.31	15.71	15.44
Fe2O3	9.41	8.50	8.15	8.07	8.99	9.47	9.05	9.45	8.84	8.75	8.22	8.93	9.39	9.17	9.63	9.81	10.00	10.11	9.10	8.55
MnO	0.18	0.15	0.14	0.14	0.18	0.21	0.18	0.17	0.16	0.17	0.16	0.17	0.18	0.17	0.19	0.22	0.19	0.20	0.17	0.18
MgO	8.50	6.96	6.75	6.72	10.26	11.69	10.36	9.65	8.98	10.57	8.03	8.84	10.74	8.78	3.97	3.80	3.82	5.64	9.43	8.61
CaO	9.93	8.25	7.47	7.41	9.92	10.42	10.06	11.37	9.93	10.72	9.38	9.78	10.06	9.35	9.92	9.33	7.98	9.44	9.96	9.50
Na2O	1.86	2.69	2.98	3.04	1.69	1.32	1.62	1.90	1.87	1.08	2.61	2.30	1.21	2.48	2.23	2.28	2.47	1.97	1.86	2.02
K2O	1.24	2.28	2.24	2.37	0.51	0.49	0.46	0.79	0.73	0.59	0.62	0.53	0.25	1.80	0.75	0.71	0.76	0.47	0.60	1.00
P2O5	0.16	0.15	0.17	0.17	0.15	0.12	0.15	0.11	0.15	0.12	0.14	0.10	0.10	0.10	0.15	0.15	0.15	0.12	0.15	0.16
LOI	2.16	3.12	3.21	3.12	3.34	4.27	3.49	2.11	3.60	4.18	2.82	4.41	5.14	2.68	4.21	4.33	3.51	3.92	3.41	5.38
Cr2O3	0.07	0.03	0.03	0.03	0.09	0.11	0.09	0.06	0.08	0.10	0.06	0.06	0.09	0.06	0.01	0.00	0.00	0.01	0.08	0.07
NiO	0.01	0.01	0.01	0.01	0.02	0.02	0.02	0.01	0.02	0.02	0.01	0.01	0.02	0.01	0.00	0.00	0.00	0.00	0.01	0.01
Total	99.15	99.18	99.15	99.23	99.91	99.88	99.36	99.76	99.69	99.95	100.05	100.03	99.97	99.89	99.68	99.47	99.41	99.76	99.65	99.49
Sc	33.9	32.3	29.4	29.5	31.9	35.6	35.6	54.4	33.0	38.7	36.6	47.0	41.6	50.3	26.6	24.6	23.6	47.4	38.1	33.2
V	250	242	220	218	224	239	239	312	248	239	255	286	270	304	280	285	282	361	250	240
Cr	429	198	179	169	552	684	684	430	599	697	460	449	704	458	84	70	58	127	607	563
Co	33.2	28.9	26.8	26.9	36.4	40.6	40.6	37.4	32.6	38.6	32.3	36.0	39.5	33.8	22.9	21.8	20.0	29.5	37.0	32.6
Ni	94.5	54.6	43.7	43.6	149.9	189.0	189.0	116.6	134.5	200.4	109.4	103.0	177.1	86.8	23.1	16.5	13.0	23.2	110.7	102.1
Cu	31.9	185.1	59.1	51.2	5.9	5.7	5.7	72.4	74.3	55.5	69.6	131.7	64.1	47.2	37.1	11.6	17.0	61.1	16.1	15.4
Zn	194.0	176.9	159.7	157.9	129.6	143.7	143.7	199.0	193.3	179.7	167.6	184.3	167.4	187.7	214.3	199.7	216.1	174.7	162.3	174.7
Ga	16.7	17.2	16.3	16.1	15.7	15.8	15.8	15.4	16.8	14.5	15.0	13.6	13.1	13.6	16.6	17.1	17.6	16.3	16.5	15.5
Ge	5.3	2.6	2.4	2.1	2.0	1.8	1.8	1.2	2.1	1.7	2.1	1.6	2.0	1.8	1.8	2.2	2.1	2.1	2.4	1.6
As	4.2	7.2	6.1	4.7	1.8	2.2	2.2	3.7	2.1	2.7	2.3	3.3	2.1	5.3	8.4	2.2	2.6	2.1	0.0	1.8
Rb	46.1	66.1	67.2	70.7	16.6	17.9	17.9	20.5	15.3	22.0	19.0	13.7	9.1	81.8	19.0	16.4	18.6	10.9	13.5	26.6
Sr	338	365	377	366	326	275	275	306	396	339	553	278	233	292	422	423	431	396	354	363
Y	18.9	18.4	18.0	18.4	16.6	15.3	15.3	16.1	16.7	15.1	15.4	16.0	14.7	14.7	19.8	19.8	20.7	19.2	16.0	15.7
Zr	79	101	108	108	83	70	70	44	80	47	53	40	38	38	59	61	65	50	76	76
Nb	5.2	6.6	7.1	7.2	6.1	4.4	4.4	2.9	6.1	3.1	3.5	2.6	2.0	2.6	3.0	3.1	3.3	2.5	5.8	5.8
Mo	0.7	1.2	1.0	0.4	0.9	0.9	0.9	1.8	1.9	1.7	2.5	2.8	2.2	2.0	5.0	1.8	2.1	1.9	1.8	2.0
Cs	0.46	0.56	0.49	0.52	0.43	0.60	0.60	0.41	0.27	0.67	0.73	0.47	1.30	1.43	0.70	0.63	0.58	0.33	0.31	0.61
Ba	174	506	488	516	134	102	102	189	238	137	213	185	94	579	151	156	160	104	184	258
La	16.5	23.7	24.0	24.1	16.0	15.0	15.0	8.3	18.8	11.1	13.7	10.9	7.6	9.8	11.3	11.2	11.9	8.9	15.6	15.9
Ce	31.4	42.4	45.0	44.8	31.9	28.1	28.1	17.3	37.1	21.9	26.5	19.2	14.8	18.0	22.6	22.2	24.0	18.7	31.9	32.2
Pr	3.77	4.73	4.78	4.81	3.58	3.12	3.12	2.16	4.09	2.66	3.03	2.18	1.73	2.07	2.69	2.80	2.85	2.31	3.72	3.78
Nd	16.3	19.2	20.0	20.5	15.8	13.2	13.2	9.3	16.6	11.2	12.1	9.5	7.7	9.0	11.7	11.3	12.6	10.3	15.8	15.4
Sm	3.64	4.15	3.93	3.85	3.26	2.86	2.86	2.35	3.37	2.41	2.61	2.38	2.04	2.14	2.85	2.57	2.77	2.49	3.16	3.13
Eu	1.23	1.17	1.09	1.08	1.00	0.94	0.94	0.69	0.95	0.88	0.84	0.78	0.62	0.71	0.88	0.94	0.95	0.82	0.99	0.93
Gd	3.29	3.38	3.71	3.28	2.74	2.65	2.65	2.58	3.27	2.60	2.60	2.55	2.06	2.24	3.07	2.87	2.98	2.68	2.77	3.01
Tb	0.591	0.536	0.583	0.561	0.472	0.466	0.466	0.390	0.466	0.376	0.405	0.401	0.361	0.364	0.476	0.467	0.577	0.466	0.469	0.438
Dy	3.28	3.30	3.29	3.20	3.05	2.69	2.69	2.75	3.11	2.58	2.74	2.82	2.68	2.57	3.53	3.60	3.56	3.63	3.94	3.90
Ho	0.743	0.754	0.676	0.716	0.615	0.573	0.573	0.686	0.644	0.555	0.532	0.611	0.536	0.559	0.742	0.744	0.795	0.758	0.599	0.581
Er	1.97	1.82	1.89	1.89	1.60	1.42	1.42	1.79	1.85	1.66	1.62	1.62	1.51	1.52	2.18	2.17	2.25	2.14	1.71	1.74
Tm	0.303	0.309	0.296	0.274	0.263	0.237	0.237	0.268	0.254	0.235	0.239	0.226	0.246	0.223	0.319	0.332	0.344	0.298	0.233	0.243
Yb	2.04	1.98	1.83	1.88	1.64	1.40	1.40	1.76	1.68	1.75	1.56	1.56	1.54	1.55	2.30	2.23	2.28	2.08	1.72	1.61
Lu	0.347	0.285	0.283	0.275	0.256	0.239	0.239	0.285	0.243	0.226	0.261	0.243	0.232	0.220	0.354	0.328	0.360	0.340	0.240	0.234
Hf	2.15	2.58	2.56	2.69	1.88	1.84	1.84	1.24	2.13	1.41	1.45	1.11	1.06	1.12	1.58	1.68	1.79	1.42	2.09	2.07
Ta	0.47	0.43	0.45	0.43	0.35	0.32	0.32	0.16	0.34	0.17	0.19	0.16	0.11	0.15	0.16	0.19	0.19	0.13	0.33	0.35
W	1.45	0.53	0.85	0.35	2.91	0.79	0.79	0.00	0.00	0.00	0.00	0.00	0.00	0.00	0.00	0.00	0.00	0.00	0.00	0.00
Pb	6.16	6.81	5.36	5.52	1.67	1.69	1.69	3.17	3.81	2.03	2.25	5.82	3.16	5.54	54.50	19.16	11.36	8.71	4.89	4.73
Th	3.47	5.13	5.80	5.69	4.09	3.35	3.35	1.65	4.27	2.97	4.04	3.15	2.34	3.09	3.35	3.30	3.63	2.59	3.18	3.13
U	0.69	0.95	0.97	0.94	0.69	0.68	0.68	0.32	0.70	0.62	0.81	0.79	0.47	0.94	0.81	0.84	0.87	0.63	0.81	0.82

Table 7.12: Post-plutonic dyke rock suite of the Southern Adamello (Re di Castello superunit). Major elements from SiO_2 to NiO (all [wt%]) were determined by XRF analysis, all other elements were analyzed by LA-ICP-MS analysis (all [ppm]).

Composition	basaltic hybrid	basaltic hybrid	basaltic hybrid	basaltic hybrid	basaltic hybrid	basaltic hybrid	basaltic hybrid	basaltic hybrid	basaltic hybrid	basaltic hybrid	basaltic-andesite andesite	basaltic-andesite andesite	basaltic-andesite andesite	basaltic-andesite andesite	basaltic-andesite andesite	basaltic-andesite andesite	basaltic-andesite andesite	basaltic-andesite andesite
Sample	NHS138C	NHS138D	NHS138E	NHS138F	NHS139	NHS140	NHS121	NHS120	NHS139	NHS170	NHS171	NHS085	NHS085	NHS103	NHS105	NHS106	NHS115	NHS117	NHS116	NHS122
Generation	2B	2B	2B	2B	2B	2B	2B	2B	2B	2B	2B	2C	2C	2C	2C	2C	2C	2C	2C	2C
SiO2	48.18	49.32	49.79	50.42	48.73	51.65	45.17	48.62	65.56	47.14	46.61	54.98	56.35	54.25	55.35	53.53	56.75	56.24	58.48	53.90
TiO2	0.81	0.83	0.84	0.85	0.94	0.90	0.82	0.82	0.40	0.85	1.35	0.55	0.54	0.61	0.63	0.75	0.57	0.61	0.57	0.57
Al2O3	15.59	15.70	16.03	16.51	16.91	17.61	15.73	18.18	16.39	17.23	14.78	18.91	17.97	18.62	18.56	18.29	17.62	17.76	17.97	18.35
Fe2O3	9.60	9.37	8.95	8.85	9.38	8.34	9.20	10.11	4.13	7.08	8.58	8.15	7.69	7.71	7.19	7.99	7.44	7.84	7.55	7.82
MnO	0.17	0.18	0.19	0.18	0.21	0.16	0.16	0.20	0.10	0.15	0.18	0.18	0.18	0.17	0.15	0.16	0.15	0.14	0.14	0.19
MgO	9.50	9.04	8.91	8.01	8.09	6.30	10.40	5.53	1.74	6.13	9.95	2.70	2.62	2.62	3.00	4.31	2.86	3.24	2.81	2.69
CaO	9.10	8.84	9.17	8.90	8.99	7.80	10.88	9.42	4.41	12.93	11.39	6.99	6.75	8.05	7.92	8.71	7.07	7.87	7.23	8.67
Na2O	1.88	1.90	1.96	1.85	2.58	2.30	1.58	1.93	3.16	1.49	3.05	2.73	2.91	2.90	2.80	2.68	2.85	2.65	2.93	2.73
K2O	1.01	1.17	1.01	1.00	1.26	1.40	1.31	0.47	2.19	1.51	0.56	1.91	1.48	1.09	1.21	0.75	1.10	1.15	0.92	0.91
P2O5	0.14	0.15	0.16	0.16	0.18	0.17	0.13	0.12	0.18	0.18	0.15	0.18	0.18	0.13	0.16	0.14	0.12	0.11	0.12	0.19
LOI	3.37	2.63	2.42	2.39	2.03	2.79	3.68	3.80	1.39	4.44	2.53	2.64	2.95	3.52	2.36	2.06	2.99	1.74	0.94	3.76
Cr2O3	0.08	0.08	0.07	0.07	0.06	0.02	0.07	0.01	0.00	0.04	0.08	0.00	0.00	0.00	0.00	0.01	0.00	0.00	0.00	0.00
NiO	0.01	0.01	0.01	0.01	0.01	0.00	0.02	0.00	0.00	0.01	0.02	0.00	0.00	0.00	0.00	0.00	0.00	0.00	0.00	0.00
Total	99.46	99.23	99.50	99.19	99.37	99.45	99.16	99.20	99.63	99.19	99.92	99.63	99.67	99.33	99.38	99.52	99.35	99.66	99.80	99.80
Sc	36.2	36.3	34.6	34.9	36.1	32.8	44.7	47.0	8.5	41.7	50.7	14.6	15.1	21.1	23.2	36.8	24.7	27.1	23.8	14.9
V	260	255	257	259	273	244	309	361	69	303	319	180	163	228	237	301	235	271	236	176
Cr	649	591	560	516	498	193	508	102	62	314	619	57	61	56	80	95	70	58	64	76
Co	36.4	35.2	34.6	32.3	34.7	26.7	31.6	29.9	8.2	25.5	38.2	14.5	13.5	18.3	16.1	21.1	18.7	21.6	19.2	14.2
Ni	117.9	119.9	100.4	84.8	96.5	35.3	147.2	18.3	15.1	56.9	143.0	16.0	10.1	12.3	18.6	20.1	18.2	17.5	18.0	13.7
Cu	17.2	16.9	20.5	24.0	21.4	35.0	6.9	58.5	26.2	5.5	45.2	12.9	5.2	39.3	45.4	49.4	36.8	60.2	50.8	24.4
Zn	185.0	221.6	185.7	194.4	186.1	195.8	127.5	168.3	208.1	133.5	160.8	246.9	190.5	205.6	207.2	195.5	164.7	245.6	169.8	212.2
Ga	16.2	16.6	16.9	17.3	17.6	19.3	15.2	16.7	19.6	17.7	17.5	17.5	16.9	17.0	16.3	16.9	16.0	16.1	16.4	18.4
Ge	2.7	2.6	2.5	2.5	2.6	2.2	2.2	1.7	3.6	2.3	3.0	2.0	1.7	2.4	2.2	2.5	1.9	2.1	2.3	2.6
As	0.0	0.0	0.0	1.4	1.8	2.5	0.0	0.0	2.3	0.0	2.8	3.0	2.0	2.2	0.0	0.0	0.0	2.7	2.0	0.0
Rb	31.1	37.6	27.4	25.8	38.4	44.5	40.8	10.9	60.2	78.1	9.3	74.7	51.0	27.5	31.4	15.0	25.2	43.1	23.1	29.6
Sr	343	338	366	395	388	447	380	398	448	506	269	460	450	498	607	596	500	499	508	473
Y	15.0	15.6	15.6	16.1	20.5	22.1	16.1	19.6	19.3	20.9	17.9	19.4	19.6	16.8	19.0	18.9	14.1	13.2	13.5	20.9
Zr	70	71	76	81	85	126	47	51	216	72	109	90	88	54	87	76	57	53	57	92
Nb	5.1	5.7	5.8	6.5	6.5	9.3	3.8	2.5	15.1	6.2	11.0	4.4	4.5	3.1	4.5	3.9	3.7	3.4	3.7	4.6
Mo	2.0	1.8	1.7	2.5	2.0	1.6	3.0	2.5	1.9	2.2	2.0	2.9	2.6	2.5	2.1	1.9	2.3	3.9	3.2	2.5
Cs	0.63	0.68	0.46	0.45	1.09	0.70	3.90	0.28	1.10	1.31	0.52	1.21	0.66	1.43	0.56	0.27	0.80	0.79	0.50	0.79
Ba	242	256	252	264	393	380	119	103	662	174	167	434	285	281	302	204	294	221	256	289
La	14.7	15.6	16.1	17.7	16.2	29.4	11.2	8.9	54.7	15.0	21.0	14.6	17.2	12.0	18.9	16.0	14.7	13.5	14.9	18.7
Ce	29.6	30.9	32.3	35.4	40.7	56.9	22.2	18.0	98.2	35.5	38.0	27.5	31.6	23.5	36.0	31.1	27.6	25.2	28.4	35.6
Pr	3.53	3.81	3.72	4.09	4.21	6.40	2.69	2.21	9.55	4.32	4.17	3.30	3.52	2.64	3.99	3.59	2.99	2.78	2.95	3.88
Nd	14.3	14.8	15.6	17.3	17.3	24.3	11.5	10.5	33.0	17.8	17.4	13.4	14.3	11.7	16.5	14.7	11.8	10.9	12.2	15.9
Sm	2.91	3.04	3.12	3.53	3.58	4.70	2.67	2.27	4.84	3.71	3.78	2.89	3.15	2.42	3.25	3.10	2.42	2.29	2.43	3.24
Eu	0.88	0.91	0.93	1.00	1.08	1.21	0.86	0.84	1.13	1.02	1.13	0.86	1.05	0.77	0.99	0.99	0.75	0.74	0.70	1.03
Gd	2.94	3.33	2.95	3.15	3.51	4.22	2.67	2.96	3.69	3.75	3.63	2.92	3.08	2.60	3.11	3.09	2.27	2.27	2.13	2.92
Tb	0.409	0.448	0.477	0.497	0.529	0.609	0.459	0.497	0.461	0.584	0.547	0.495	0.424	0.418	0.473	0.479	0.360	0.334	0.320	0.517
Dy	2.76	2.77	2.93	2.90	3.69	3.96	3.05	3.39	3.36	3.80	3.45	3.33	3.43	2.91	3.11	3.18	2.36	2.15	2.47	3.67
Ho	0.552	0.574	0.595	0.587	0.759	0.816	0.591	0.740	0.669	0.811	0.664	0.715	0.696	0.603	0.690	0.687	0.542	0.514	0.517	0.763
Er	1.61	1.63	1.70	1.64	2.34	2.31	1.80	2.25	1.94	2.23	1.90	2.14	2.27	1.69	1.94	1.92	1.51	1.40	1.44	2.17
Tm	0.229	0.224	0.225	0.247	0.334	0.348	0.244	0.329	0.312	0.333	0.252	0.338	0.340	0.282	0.304	0.292	0.242	0.200	0.217	0.336
Yb	1.57	1.57	1.58	1.67	2.27	2.37	1.62	2.08	2.40	2.15	1.73	2.38	2.51	1.80	2.21	2.02	1.67	1.56	1.55	2.33
Lu	0.226	0.222	0.238	0.235	0.353	0.358	0.264	0.341	0.373	0.334	0.247	0.381	0.379	0.291	0.321	0.330	0.257	0.239	0.249	0.362
Hf	1.84	1.96	2.08	2.14	2.43	3.16	1.40	1.40	4.92	1.96	3.16	2.25	2.12	1.57	2.15	1.86	1.69	1.61	1.60	2.28
Ta	0.33	0.33	0.41	0.38	0.54	0.20	0.14	0.95	0.41	0.82	0.28	0.25	0.22	0.22	0.24	0.21	0.24	0.23	0.25	0.30
W	0.00	0.00	0.00	0.00	0.00	0.00	0.00	0.00	0.00	0.00	0.00	0.00	0.00	0.00	0.00	0.00	0.00	0.00	0.00	0.00
Pb	10.20	32.10	17.53	8.90	5.07	5.59	2.11	9.08	10.78	1.01	1.34	11.17	11.36	6.25	5.24	4.86	9.63	8.18	7.98	10.49
Th	2.85	2.98	3.28	3.51	4.09	7.24	2.13	2.70	15.48	5.35	5.31	5.35	5.17	3.77	5.58	4.58	4.77	4.32	4.85	5.42
U	0.84	0.84	0.95	1.10	0.71	1.19	0.37	0.63	2.53	1.07	1.15	1.24	1.21	0.79	1.21	1.01	1.03	1.01	1.04	1.41

Table 7.13: Post-plutonic dyke rock suite of the Southern Adamello (Re di Castello superunit). Major elements from SiO_2 to NiO (all [wt%]) were determined by XRF analysis, all other elements were analyzed by LA-ICP-MS analysis (all [ppm]).

Composition	basaltic-andesite andesite	basaltic-andesite andesite	dacite	dacite
Sample	NHS122	NHS124	NHS083	NHS086
Generation	2C	2C	3	3
SiO2	55.55	54.86	65.70	64.45
TiO2	0.54	0.56	0.35	0.35
Al2O3	17.75	18.21	17.10	16.83
Fe2O3	7.46	7.96	3.80	3.81
MnO	0.18	0.20	0.15	0.11
MgO	2.54	2.71	1.45	1.24
CaO	8.10	7.93	5.03	5.23
Na2O	2.95	2.88	3.51	3.63
K2O	0.77	0.79	0.88	1.10
P2O5	0.17	0.18	0.18	0.14
LOI	3.68	3.02	1.24	2.62
Cr2O3	0.00	0.00	0.00	0.00
NiO	0.00	0.00	0.00	0.00
Total	99.70	99.30	99.38	99.50
Sc	14.7	15.5	6.0	8.2
V	164	172	66	80
Cr	65	35	64	76
Co	12.8	14.2	6.1	7.3
Ni	15.1	13.3	13.4	29.7
Cu	9.2	68.0	11.3	6.4
Zn	165.6	194.2	218.8	170.0
Ga	16.1	17.2	17.1	15.8
Ge	2.2	2.1	2.0	2.1
As	2.3	0.0	0.0	2.0
Rb	23.9	16.8	22.2	40.1
Sr	463	450	476	495
Y	19.6	21.0	12.3	13.9
Zr	87	92	92	114
Nb	4.2	4.7	6.1	7.2
Mo	2.4	2.8	2.3	2.2
Cs	0.60	0.39	0.44	0.78
Ba	227	349	346	407
La	15.9	18.3	24.6	29.1
Ce	30.0	34.0	43.1	48.4
Pr	3.36	3.88	4.54	4.83
Nd	14.9	16.3	16.1	16.6
Sm	3.15	3.01	2.62	2.49
Eu	0.94	0.94	0.85	0.75
Gd	2.87	3.28	2.36	2.27
Tb	0.499	0.518	0.272	0.377
Dy	3.46	3.63	2.28	2.27
Ho	0.720	0.735	0.396	0.488
Er	2.272	2.277	1.091	1.377
Tm	0.333	0.343	0.166	0.231
Yb	2.49	2.39	1.44	1.76
Lu	0.357	0.408	0.230	0.310
Hf	2.17	2.27	2.30	2.85
Ta	0.26	0.29	0.43	0.43
W	0.00	0.00	0.00	0.00
Pb	9.92	7.54	11.19	8.81
Th	5.25	5.49	7.96	10.29
U	1.16	1.16	1.78	2.14

Table 7.14: Post-plutonic dyke rock suite of the Southern Adamello (Re di Castello superunit). Major elements from SiO_2 to NiO (all [wt%]) were determined by XRF analysis, all other elements were analyzed by LA-ICP-MS analysis (all [ppm]).

7.4 References Partition Coefficients

Elements	Mg-tholeiite	Ol-tholeiite	Basalt	Basaltic-Andesite	Andesite	Dacite
REE+Y	**Ol:** McKenzie and O'Nions 1991 **Cpx:** Alonso-Perrez 2006	**Ol:** McKenzie and O'Nions 1991 **Cpx:** Alonso-Perrez 2006	**Ol:** McKenzie and O'Nions 1991 **Cpx:** Alonso-Perrez 2006	**Cpx:** Alonso-Perrez 2006 **Am:** Sisson 1994 **Pl:** Bédard 2006	**Am:** Alonso-Perrez 2006 **Pl:** Bédard 2006	**Am:** Alonso-Perrez 2006 **Pl:** Bédard 2006
HFSE: U,Th,Nb,Ti,Hf and Zr	**Ol:** McKenzie and O'Nions 1991 **Cpx:** Alonso-Perrez 2006; Hauri et al. 1994	**Ol:** McKenzie and O'Nions 1991 **Cpx:** Alonso-Perrez 2006; Hauri et al. 1994	**Ol:** McKenzie and O'Nions 1991 **Cpx:** Alonso-Perrez 2006; Hauri et al. 1994	**Cpx:** Alonso-Perrez 2006; Hauri et al. 1994 **Am:** La Tourette et al. 1995; Sisson 1994 **Pl:** Bédard 2006	**Am:** Alonso-Perrez 2006; La Tourette et al. 1995 **Pl:** Bédard 2006	**Am:** Alonso-Perrez 2006; La Tourette et al. 1995 **Pl:** Bédard 2006
LILE: Ba,Sr	**Ol:** McKenzie and O'Nions 1991 **Cpx:** Alonso-Perrez 2006	**Ol:** McKenzie and O'Nions 1991 **Cpx:** Alonso-Perrez 2006	**Ol:** McKenzie and O'Nions 1991 **Cpx:** Alonso-Perrez 2006	**Cpx:** Alonso-Perrez 2006 **Am:** La Tourette et al. 1995 **Pl:** Bédard 2006 **Pl:** Bédard 2006	**Am:** Alonso-Perrez 2006 **Pl:** Bédard 2006	**Am:** Alonso-Perrez 2006

Table 7.15: References for mineral/melt partition coefficients (Kd's) used in trace element model

7.5 Mineral Chemistry

Sample Rt	**SiO2**	**TiO2**	**ZrO2**	**Total**	**n**
	[wt%]	[wt%]	[wt%]	[wt%]	
Rt002	0.43 (40)	95.89 (144)	0.0363 (94)	96.35 (118)	18
Rt007	0.02 (1)	96.31 (220)	0.0542 (298)	96.38 (218)	4

Table 7.16: ZrO_2 analyses for rutile carried out with electron microprobe (EMPA).

Sample	Pl086-1	Pl086-1	Pl086-1	Pl086-1	Pl086-1	Pl086-1	Pl086-1	Pl086-1	Pl086-2	Pl086-2	Pl086-2	Pl086-2	Pl086-2
Rock Type	dacite	dacite	dacite	dacite	dacite	dacite	dacite	dacite	dacite	dacite	dacite	dacite	dacite
Generation	3	3	3	3	3	3	3	3	3	3	3	3	3
Rb	0.5	<0.352	<0.263	<0.333	0.3	<0.367	<0.291	<0.352	<0.297	<0.246	<0.287	<0.242	<0.299
Sr	1039	899	931	1305	873	909	950	921	923	903	738	676	686
Y	0.3	0.1	0.1	0.2	0.2	0.2	0.1	0.1	0.1	0.1	0.1	0.1	0.1
Zr	1.09	<0.371	<0.305	<0.343	<0.349	0.38	<0.337	<0.282	<0.350	<0.289	<0.275	<0.244	<0.333
Nb	<0.054	<0.033	0.034	<0.049	0.054	<0.048	0.048	0.040	<0.034	<0.032	<0.040	<0.029	<0.038
Ba	33	26	42	69	35	29	29	29	26	25	17	14	14
La	4.0	2.8	2.9	3.9	2.8	2.9	3.6	3.5	3.5	2.8	1.2	1.0	1.2
Ce	5.2	3.7	3.6	5.2	3.7	3.8	4.6	4.9	4.4	3.9	1.7	1.5	1.8
Pr	0.60	0.29	0.31	0.45	0.42	0.30	0.40	0.34	0.39	0.39	0.14	0.13	0.15
Nd	1.6	1.2	1.0	1.6	1.0	0.9	1.8	1.3	1.6	1.1	0.7	0.7	0.5
Sm	0.05	0.12	0.18	0.39	0.17	0.15	0.18	0.18	0.20	0.12	<0.025	0.10	0.08
Eu	0.45	0.38	0.39	0.55	0.43	0.35	0.39	0.40	0.37	0.38	0.28	0.20	0.30
Gd	<0.228	0.08	<0.127	<0.259	<0.052	<0.151	<0.112	<0.217	0.12	0.12	<0.093	0.11	<0.114
Tb	<0.005	<0.004	<0.018	<0.024	<0.014	<0.009	0.016	<0.020	0.010	<0.007	<0.017	<0.008	0.011
Dy	<0.064	0.12	<0.058	<0.111	0.04	0.04	<0.096	<0.068	0.07	<0.080	0.04	0.10	<0.063
Ho	0.015	0.003	0.019	0.017	0.016	<0.080	0.019	0.000	<0.019	<0.009	<0.019	<0.017	0.022
Er	<0.098	0.01	0.02	0.07	<0.069	0.02	<0.028	0.02	<0.013	0.02	<0.019	0.01	0.02
Tm	<0.020	0.000	<0.010	<0.014	<0.013	<0.007	<0.011	<0.011	<0.006	<0.009	<0.010	0.007	<0.007
Yb	0.06	0.01	0.00	<0.029	0.04	<0.023	<0.019	<0.040	<0.037	<0.013	<0.079	<0.035	0.02
Lu	<0.014	<0.008	<0.013	<0.006	<0.007	<0.009	<0.011	<0.005	<0.006	<0.013	<0.005	0.012	<0.009
Pb	1.85	1.24	1.09	1.54	1.22	1.25	1.53	1.75	1.39	1.22	0.68	0.59	0.66
Th	0.11	0.00	0.01	<0.009	0.05	0.03	<0.008	0.02	<0.010	<0.004	0.01	0.00	0.01
U	0.03	<0.005	0.01	0.01	0.01	0.01	<0.016	0.01	0.00	0.00	0.00	<0.004	0.00

Table 7.17: Trace element (all in [ppm]) profiles for a plagioclase phenocryst from dacites (3). Internal standard for data reduction in LAMTRACE is CaO wt% determined by electron microprobe. External standard is NIST SRM 612.

Sample	Pl106-4	Pl106-4	Pl106-4	Pl106-4	Pl106-1	Pl106-1	Pl106-1	Pl106-1	Pl106-1	Pl106-1	Pl106-1	Pl106-1	Pl106-1
Rock Type	basaltic-andesite	basaltic-andesite	basaltic-andesite	basaltic-andesite	basaltic-andesite	basaltic-andesite	basaltic-andesite	basaltic-andesite	basaltic-andesite	basaltic-andesite	basaltic-andesite	basaltic-andesite	basaltic-andesite
Generation	2C	2C	2C	2C	2C	2C	2C	2C	2C	2C	2C	2C	2C
Rb	<0.167	<0.172	0.1	1.2	<0.144	<0.101	<0.137	<0.110	<0.104	<0.132	<0.112	0.2	<0.114
Sr	970	1113	1054	1025	1024	865	1110	1131	1161	1046	953	1140	1048
Y	0.2	0.1	0.1	0.2	0.1	0.1	0.1	0.2	0.1	0.1	0.1	0.2	0.1
Zr	<0.144	<0.162	<0.033	0.34	<0.075	<0.067	<0.105	0.12	<0.090	<0.094	<0.093	0.32	<0.121
Nb	<0.023	<0.035	<0.004	0.031	<0.019	<0.014	<0.021	0.015	<0.018	<0.013	<0.021	0.022	<0.020
Ba	17	23	25	34	19	12	17	20	23	19	15	21	15
La	1.2	1.4	1.6	1.6	0.9	0.6	1.0	1.3	1.3	0.9	0.8	1.3	0.8
Ce	1.8	2.1	2.4	2.4	1.4	0.9	1.6	1.9	1.8	1.3	1.3	2.0	1.2
Pr	0.19	0.22	0.23	0.22	0.11	0.10	0.17	0.19	0.17	0.13	0.13	0.21	0.13
Nd	0.6	0.9	0.7	0.8	0.6	0.3	0.5	0.6	0.7	0.5	0.5	0.8	0.5
Sm	0.10	0.12	0.13	0.09	0.16	0.08	0.05	0.11	0.09	0.08	0.09	0.09	0.10
Eu	0.29	0.28	0.26	0.24	0.23	0.17	0.18	0.27	0.23	0.17	0.17	0.22	0.17
Gd	<0.060	<0.060	0.06	0.06	0.04	<0.035	0.08	0.05	0.07	0.04	<0.038	<0.040	0.05
Tb	0.008	0.014	0.010	0.010	0.008	<0.004	<0.003	0.005	<0.003	0.005	<0.006	0.007	0.005
Dy	0.04	0.07	0.03	0.04	0.05	0.02	0.04	0.05	0.06	0.02	<0.014	<0.019	0.03
Ho	<0.014	0.010	0.005	0.007	0.015	<0.002	0.008	0.002	0.007	0.007	<0.007	0.005	0.003
Er	<0.014	0.01	0.01	0.03	0.02	0.01	0.01	<0.005	0.01	0.02	<0.007	0.02	0.03
Tm	<0.006	<0.006	<0.002	0.003	<0.002	<0.002	0.002	0.002	<0.003	0.003	<0.003	0.002	0.004
Yb	0.01	0.00	0.01	0.02	<0.009	0.01	0.01	0.02	0.01	<0.008	<0.007	0.01	0.00
Lu	<0.005	<0.003	<0.001	<0.004	<0.004	<0.003	<0.005	<0.004	<0.002	<0.003	<0.002	<0.002	<0.003
Pb	0.55	0.75	0.62	1.07	0.48	0.29	0.51	0.70	0.66	0.42	0.43	0.83	0.70
Th	<0.005	<0.011	0.00	0.15	0.01	<0.004	<0.003	0.04	0.01	0.01	0.01	0.04	0.01
U	<0.004	<0.009	0.00	0.01	0.00	<0.002	0.01	0.01	<0.002	0.00	0.00	0.01	0.00

Table 7.18: Trace element (all in [ppm]) profiles for a plagioclase phenocryst from basaltic-andesite (2C). Internal standard for data reduction in LAMTRACE is CaO wt% determined by electron microprobe. External standard is NIST SRM 612.

Sample	Pl105-11	Pl105-11	Pl105-11	Pl106-4	Pl106-4	Pl106-4	Pl106-4	Pl106-4	Pl106-4	Pl106-4	Pl106-4	Pl106-4	Pl106-4
Rock Type	basaltic-andesite	basaltic-andesite	basaltic-andesite	basaltic-andesite	basaltic-andesite	basaltic-andesite	basaltic-andesite	basaltic-andesite	basaltic-andesite	basaltic-andesite	basaltic-andesite	basaltic-andesite	basaltic-andesite
Generation	2C	2C	2C	2C	2C	2C	2C	2C	2C	2C	2C	2C	2C
Rb	0.4	0.4	0.9	2.0	<0.151	0.4	1.1	<0.138	<0.157	0.3	6.6	<0.125	<0.125
Sr	1200	932	959	1104	1172	1156	1129	1107	1112	1121	1108	992	1051
Y	0.1	0.1	0.1	0.2	0.1	0.1	0.2	0.2	0.1	0.2	0.2	0.1	0.1
Zr	0.36	0.13	0.19	1.03	<0.167	<0.134	<0.148	<0.159	<0.144	<0.139	<0.153	<0.159	<0.143
Nb	0.009	0.021	0.554	<0.026	<0.019	<0.031	<0.032	<0.021	<0.028	<0.016	<0.024	<0.023	<0.026
Ba	27	18	17	41	27	30	27	27	26	33	31	20	21
La	1.8	0.8	0.8	1.8	2.2	1.9	2.0	1.8	1.7	1.7	1.8	1.4	1.6
Ce	2.7	1.4	1.4	2.7	3.2	2.8	3.0	2.7	2.5	2.6	2.6	2.1	2.2
Pr	0.25	0.12	0.13	0.24	0.30	0.25	0.29	0.23	0.27	0.21	0.25	0.18	0.20
Nd	0.8	0.5	0.6	1.0	0.7	0.8	1.1	1.0	0.7	0.8	0.9	0.8	0.9
Sm	0.11	0.09	0.14	0.15	0.14	0.20	0.11	0.10	0.15	0.16	0.13	0.15	0.20
Eu	0.30	0.16	0.19	0.41	0.35	0.41	0.38	0.35	0.32	0.30	0.23	0.25	0.26
Gd	0.04	0.04	0.09	0.19	<0.124	0.07	<0.059	0.08	0.08	<0.059	0.07	0.20	<0.078
Tb	0.005	0.003	0.008	<0.009	0.010	0.009	0.009	<0.009	<0.006	<0.006	<0.010	<0.009	<0.006
Dy	0.03	0.03	0.06	<0.081	<0.032	<0.060	<0.052	0.05	<0.045	<0.061	<0.061	0.07	<0.052
Ho	0.006	0.004	0.007	0.017	<0.008	0.008	<0.009	0.016	0.011	0.011	0.006	0.009	0.002
Er	0.01	0.01	0.02	0.02	0.01	0.01	0.01	0.01	0.01	0.01	0.02	<0.013	0.02
Tm	0.001	0.002	0.003	<0.012	<0.010	<0.006	0.013	0.008	<0.006	<0.006	0.009	0.004	<0.008
Yb	0.01	0.01	0.02	<0.031	<0.035	<0.009	0.02	0.03	0.01	0.03	<0.026	<0.019	<0.024
Lu	<0.002	0.001	0.002	0.005	<0.009	0.007	<0.005	<0.008	<0.013	<0.004	<0.007	0.000	<0.012
Pb	0.76	0.39	0.47	1.06	0.86	1.02	1.14	0.89	0.82	0.92	1.55	1.47	0.75
Th	0.05	0.06	0.04	0.05	<0.007	0.01	0.03	0.06	0.02	0.07	0.12	0.02	0.01
U	0.01	0.03	0.05	0.02	<0.005	0.00	0.00	<0.005	<0.003	0.00	0.02	<0.006	<0.005

Table 7.19: Trace element (all in [ppm]) profiles for a plagioclase phenocryst from basaltic-andesite (2C). Internal standard for data reduction in LAMTRACE is CaO wt% determined by electron microprobe. External standard is NIST SRM 612.

Sample	Pl105-4	Pl105-4	Pl105-4	Pl105-4	Pl105-4	Pl105-4	Pl105-12	Pl105-12	Pl105-12	Pl105-12	Pl105-11	Pl105-11	Pl105-11
Rock Type	basaltic-andesite	basaltic-andesite	basaltic-andesite	basaltic-andesite	basaltic-andesite	basaltic-andesite	basaltic-andesite	basaltic-andesite	basaltic-andesite	basaltic-andesite	basaltic-andesite	basaltic-andesite	basaltic-andesite
Generation	2C	2C	2C	2C	2C	2C	2C	2C	2C	2C	2C	2C	2C
Rb	0.2	25.6	38.2	2.6	0.7	0.5	1.0	2.2	0.9	1.9	1.5	0.2	0.4
Sr	1132	1112	1177	997	914	1332	1252	1379	1629	1613	1038	1249	1189
Y	0.2	0.2	0.3	0.1	0.1	0.2	0.3	0.4	0.5	0.3	0.5	0.2	0.2
Zr	0.04	0.28	0.51	0.10	0.26	0.15	0.86	0.76	4.50	1.15	7.34	0.41	1.84
Nb	0.008	0.247	0.058	<0.011	<0.009	0.011	0.042	0.033	0.129	0.152	0.022	<0.012	<0.010
Ba	39	68	40	24	18	51	51	70	72	66	32	28	29
La	1.9	1.0	1.6	0.9	0.7	2.3	2.4	2.7	3.1	3.1	0.9	1.8	1.8
Ce	2.9	1.7	3.2	1.4	1.1	3.3	3.5	3.7	4.6	4.5	1.6	2.7	2.7
Pr	0.28	0.17	0.24	0.14	0.12	0.31	0.31	0.37	0.45	0.43	0.17	0.25	0.26
Nd	0.9	0.7	0.9	0.5	0.4	1.0	1.1	1.3	1.5	1.5	0.5	0.8	1.0
Sm	0.13	0.06	0.13	0.05	0.06	0.09	0.14	0.23	0.18	0.25	0.06	0.14	0.07
Eu	0.32	0.23	0.20	0.20	0.16	0.36	0.33	0.38	0.47	0.46	0.19	0.34	0.31
Gd	0.10	<0.041	0.07	0.06	0.04	0.06	0.09	0.18	0.10	0.07	0.06	0.09	0.07
Tb	0.009	0.007	0.012	0.006	0.004	0.007	0.014	0.021	0.013	0.015	0.010	0.009	0.010
Dy	0.06	0.05	0.07	0.02	0.04	0.05	0.05	0.11	0.10	0.11	0.07	0.05	0.05
Ho	0.009	0.010	0.009	0.007	<0.003	0.007	0.009	0.017	0.031	0.016	0.015	0.007	0.008
Er	0.02	0.03	0.04	0.01	0.01	0.02	0.03	0.04	0.07	0.03	0.04	0.02	0.03
Tm	0.002	<0.003	0.009	0.003	0.003	0.002	<0.003	0.005	0.013	<0.008	<0.007	0.003	0.005
Yb	0.01	0.03	0.04	<0.008	0.01	0.02	0.02	0.05	0.09	0.04	0.14	0.01	0.03
Lu	0.003	0.004	0.008	<0.002	<0.002	<0.002	<0.004	0.005	0.016	0.007	0.018	0.002	0.005
Pb	0.85	2.36	4.19	1.15	0.65	1.10	1.06	1.09	1.86	1.75	0.55	0.78	0.74
Th	0.05	0.24	0.25	0.04	0.04	0.03	0.05	0.25	0.69	0.10	0.34	0.03	0.11
U	0.01	0.09	0.24	0.04	0.04	0.02	0.01	0.03	0.23	0.07	0.12	0.01	0.04

Table 7.20: Trace element (all in [ppm]) profiles for a plagioclase phenocryst from basaltic-andesite (2C). Internal standard for data reduction in LAMTRACE is CaO wt% determined by electron microprobe. External standard is NIST SRM 612.

7.6 Diffusion Spinel Picrobasalts (1B)

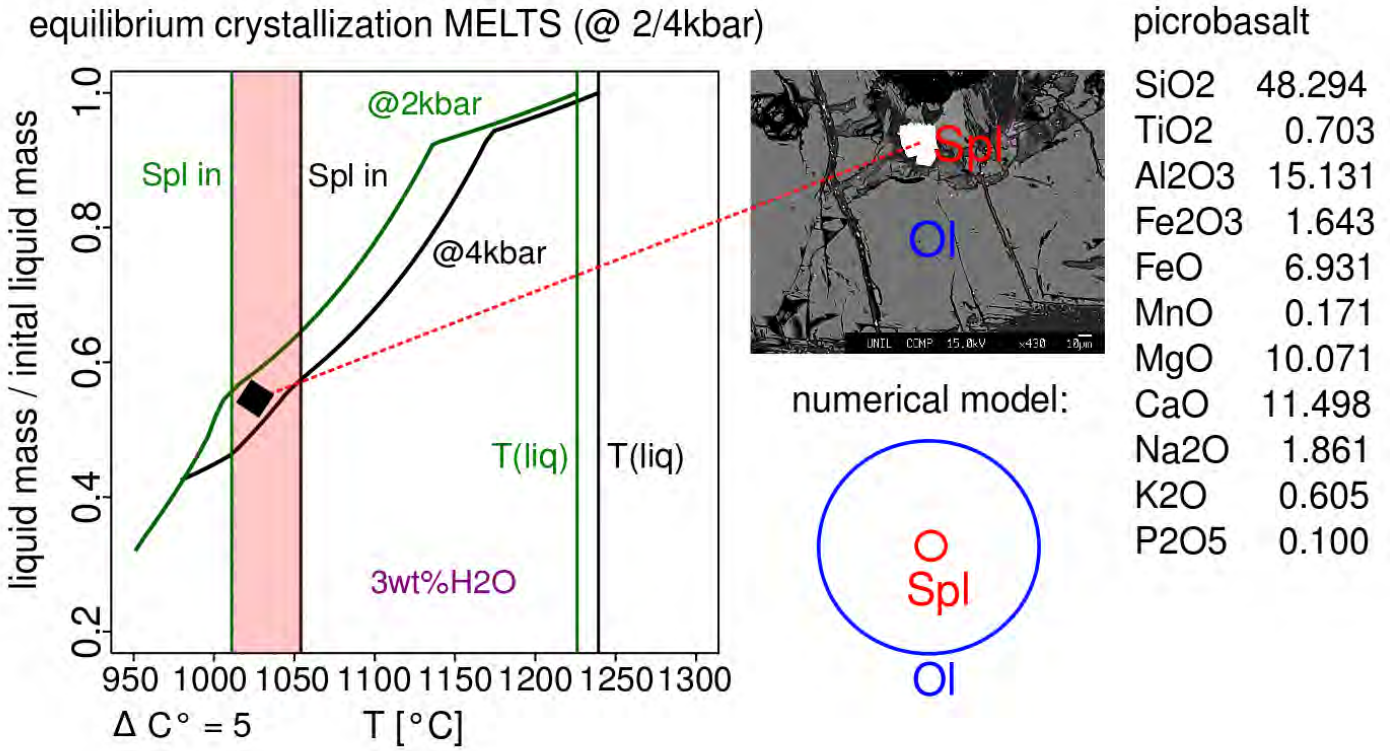

Figure 7.2: Equilibrium crystallization calculations of MELTS for incoming spinel crystallization at 2kbar and 4kbar. Starting compositions corresponds to start material for fractional crystallization experiments of Nandekar [2013].

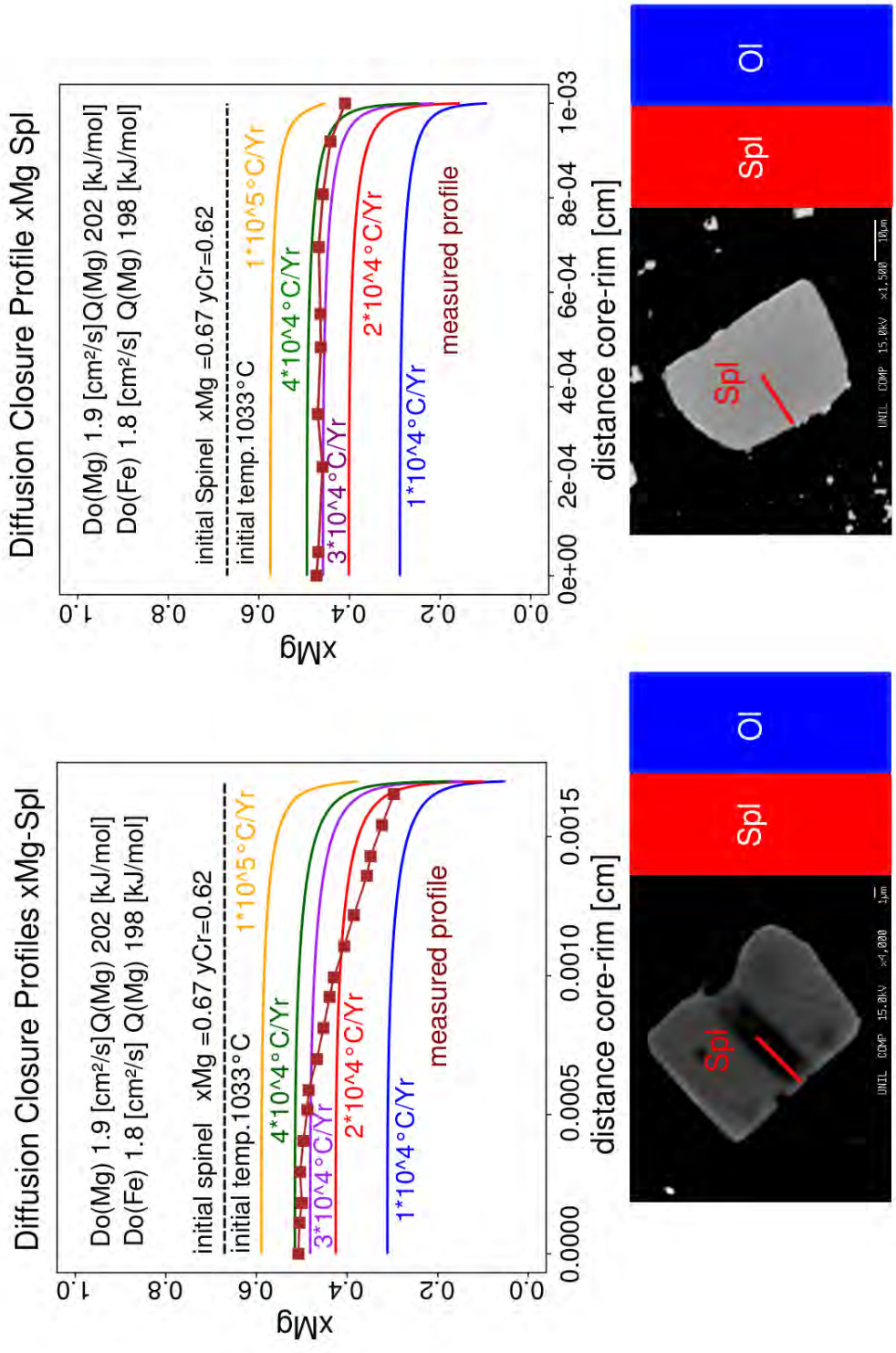

Figure 7.3: Fe-Mg diffusion calculations for spinel inclusions in olivine. Numerical methods are after Robl et al. [2007]

7.7 Diffusion Plagioclase Basaltic-Andesites / Andesites (2C)

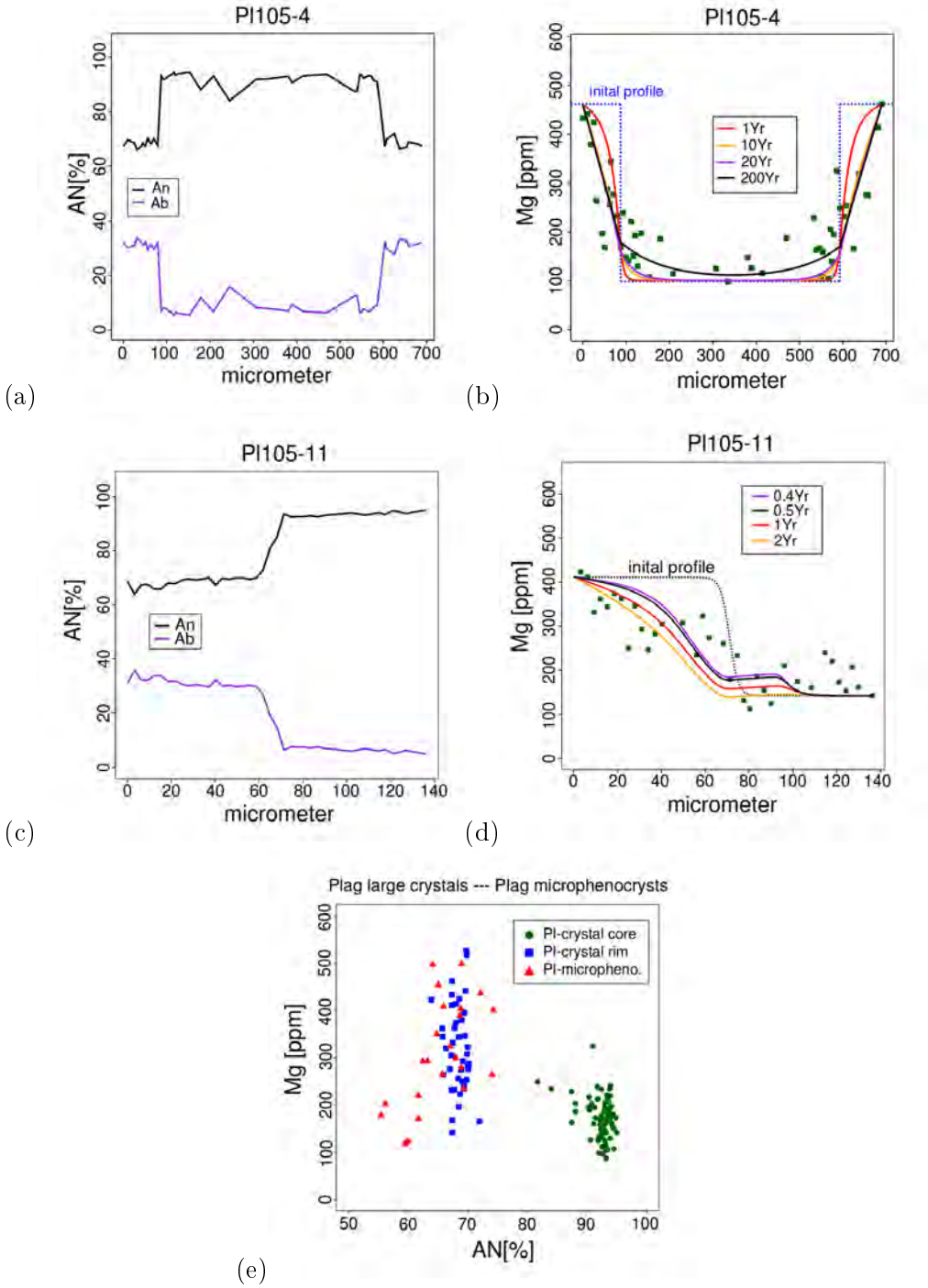

Figure 7.4: (a) and (c) represent profiles measured across plagioclase for anorthite-albite content. (b) and (d) show Mg-diffusion calculations performed after Costa et al. [2003]. (e) Comparison of Mg [ppm] and anorthite content (all measured by EMPA) between plagioclase phenocryst-cores and -rims and plagioclase microphenocrysts in the matrix of basaltic-andesites / andesites 2C.

Bibliography

B. Alastair. The geometry of en-echelon vein arrays. *Tectonophysics*, 28(4):245–263, 1975.

R. Alonso-Perez. *The role of garnet in the evolution of hydrous, calcalkaline magmas: An experimental study at 0.8 - 1.5 GPa*. PhD thesis, Swiss Federal Institute of Technology Zurich, ETHZ, 2006.

R. Alonso-Perez, O. Muntener, and P. Ulmer. Igneous garnet and amphibole fractionation in the roots of island arcs: experimental constraints on andesitic liquids. *Contributions to Mineralogy and Petrology*, 157:541–558, 2009.

A.T. Anderson. Significance of hornblende in calc-alkaline andesites and basalts. *American Mineralogist*, 65(9-10):837–851, 1980.

E.M. Anderson. The dynamics of sheet intrusions. *Proceedings of the Royal Society of Edinburgh*, 58: 242–251, 1938.

E.M. Anderson. *The Dynamics of Faulting and Dyke Formation with Applications to Britain*. Oliver and Boyd Ltd, Edinburgh, 1951.

C. Annen and R.S.J. Sparks. Effects of repetitive emplacement of basaltic intrusions on thermal evolution and melt generation in the crust. *Earth and Planetary Science Letters*, 203(3-4):937 – 955, 2002.

C. Annen, J.D. Blundy, and R.S.J. Sparks. The genesis of intermediate and silicic magmas in deep crustal hot zones. *Journal of Petrology*, 47(3):505–539, 2006.

P.W.U. Appel, A. Polat, and R. Frei. Dacitic ocelli in mafic lavas, $3.8 - 3.7$ *ga* isua greenstone belt, west greenland: Geochemical evidence for partial melting of oceanic crust and magma mixing. *Chemical Geology*, 258(3-4):105–124, 2009.

R.J. Arculus. Oxidation status of the mantle: Past and present. *Annual Review of Earth and Planetary Sciences*, 13(1):75–95, 1985.

R.J. Arculus, R.W. Johnson, B.W. Chappell, C.O. McKee, and H. Sakai. Ophiolite-contaminated andesites, trachybasalts, and cognate inclusions of mount lamington, papua new guinea: anhydrite-amphibole-bearing lavas and the 1951 cumulodome. *Journal of Volcanology and Geothermal Research*, 18(1-4):215–247, 1983.

R. Arevalo and W.F. McDonough. Chemical variations and regional diversity observed in morb. *Chemical Geology*, 271(1-2):70–85, 2010.

E. Argand. Sur l'arc des alpes occidentales. *Eclogae Geologicae Helvetiae*, 14:145–191, 1916.

T. Armbruster, P. Bonazzu, M. Akasaka, V. Bermanec, C. Chopin, R. Gieré, S. Heuss-Assbichler, A. Liebscher, S. Menchetti, Y. Pan, and M. Pasero. Recommended nomenclature of epidote-group minerals. *European Journal of Mineralogy*, 18(5):551–567, 2006.

J. Armstrong. *CITZAF-a package of correction programs for the quantitative electron microbeam X-ray analysis of thick polished materials, thin-films and particles.* Number 4. 1995.

A. Arzi. Critical phenomena in the rheology of partially melted rocks. *Tectonophysics*, 44:173 – 184, 1978.

P.D. Asimow and M.S. Ghiorso. Algorithmic modifications extending melts to calculate subsolidus phase relations. *American Mineralogist*, 83(9-10):1127–1132, 1998.

O. Bachmann, M.A. Dungan, and P.W. Lipman. The fish canyon magma body, san juan volcanic field, colorado: rejuvenation and eruption of an upper-crustal batholith. *Journal of Petrology*, 43(8):1469–1503, 2002.

S.A. Barboza and G.W. Bergantz. Dynamic model of dehydration melting motivated by a natural analogue: applications to the ivrea-verbano zone, northern italy. *Geological Society of America Special Papers*, 315:23–31, 1996.

S. Barth, F. Oberli, and M. Meier. U-th-pb systematics of morphologically characterized zircon and allanite: a high-resolution isotopic study of the alpine rensen pluton (northern italy). *Earth and Planetary Science Letters*, 95(3-4):235–254, 1989.

J.H. Bédard. Trace element partitioning in plagioclase feldspar. *Geochimica et Cosmochimica Acta*, 70 (14):3717–3742, 2006.

D. Bercovici and Y. Ricard. Energetics of a two-phase model of lithospheric damage, shear localization and plate-boundary formation. *Geophysical Journal International*, 152(3):581–596, 2003.

D. Bercovici, Y. Ricard, and G. Schubert. A two-phase model for compaction and damage: 1. general theory. *Journal of Geophysical Research: Solid Earth*, 106(B5):8887–8906, 2001.

G.W. Bergantz. Underplating and partial melting: Implications for melt generation and extraction. *Science*, 245(4922):1093–1095, 1989.

S. Bergbauer and S.J. Martel. Formation of joints in cooling plutons. *Journal of Structural Geology*, 21 (7):821–835, 1999. ISSN 0191-8141.

A. Berger, C. Rosenberg, and S. Schmid. Ascent, emplacement and exhumation of the bergell pluton within the southern steep belt of the central alps. *Schweizerische mineralogische und petrographische Mitteilungen*, 76:357–382, 1996.

A. Bianchi and G. Dal Piaz. Ii settore meridionale del massiccio del 1'adamello. relazioni sul rilevamento e studi preliminari della zona compresa fra la valle stabio e l'alta valle del caffaro. *Boll. Uff. Geol. Ital.*, 62:1–87, 1937.

G. Bigazzi, A. Moro, and P. Macera. A quantitative approach to trace element and sr isotope evolution in the adamello batholith (northern italy). *Contributions to Mineralogy and Petrology*, 94:46–53, 1986.

G. Bigi. *Structural Model of Italy and Gravity Map*. Quaderni de la Ricerca scientifica. Consiglio nazionale delle ricerche, 1990.

F. Blanckenburg and J.H. Davies. Slab breakoff: A model for syncollisional magmatism and tectonics in the alps. *Tectonics*, 14(1):120–131, 1995.

J. Blichert-Toft, C.E. Lesher, and M.T. Rosing. Selectively contaminated magmas of the tertiary east greenland macrodike complex. *Contributions to Mineralogy and Petrology*, 110(2-3):154–172, 1992.

J. Blundy, K. Cashman, and M. Humphreys. Magma heating by decompression-driven crystallization beneath andesite volcanoes. *Nature*, 443(7107):76–80, 2006.

J.D. Blundy. *The geology of the southern Adamello Massif, Italy*. PhD thesis, Cambridge, England, University of Cambridge, 1989.

J.D Blundy and N. Shimizu. Trace element evidence for plagioclase recycling in calc-alkaline magmas. *Earth and Planetary Science Letters*, 102(2):178–197, 1991.

J.D. Blundy and R.S.J. Sparks. Petrogenesis of mafic inclusions in granitoids of the adamello massif, italy. *Journal of Petrology*, 33(5):1039–1104, 1992.

J.D. Blundy and B.J. Wood. Crystal-chemical controls on the partitioning of sr and ba between plagioclase feldspar, silicate melts, and hydrothermal solutions. *Geochimica et Cosmochimica Acta*, 55(1):193–209, 1991.

J.D. Blundy and B.J. Wood. Prediction of crystal-melt partition coefficients from elastic moduli. *Nature*, 372(6505):452–454, 1994.

W.A. Bohrson. Insight into subvolcanic magma plumbing systems. *Geology*, 35(8):767–768, 2007.

A. Boriani, E.G. Origoni, and L. Pinarelli. Paleozoic evolution of southern alpine crust (northern italy) as indicated by contrasting granitoid suites. *Lithos*, 35(1-2):47–63, 1995.

L. Borsi, U. Schärer, L. Gaggero, and L. Crispini. Age, origin and geodynamic significance of plagiogranites in lherzolites and gabbros of the piedmont-ligurian ocean basin. *Earth and Planetary Science Letters*, 140(1-4):227–241, 1996.

J. F. Bowring, N. M. McLean, and S. A. Bowring. Engineering cyber infrastructure for u-pb geochronology: Tripoli and u-pb redux. *Geochemistry, Geophysics, Geosystems*, 12(6):n/a–n/a, 2011.

P. Brack. Structures in the southwestern border of the adamello intrusion (alpi bresciane, italy). *Schweizerische mineralogische und petrographische Mitteilungen*, 61:37–49, 1981.

P. Brack. Multiple intrusions-examples from the adamello batholith (italy) and their significance on the mechanisms of intrusion. *Memorie della Società Geologica Italiana*, 26:145–157, 1983.

P. Brack. *Geologie der Intrusiva und Rahmengesteine des Suedwest-Adamello*. PhD thesis, Swiss Federal Institute of Technology Zurich, ETHZ, 1984.

M. Brearley and C.M. Scarfe. Dissolution rates of upper mantle minerals in an alkali basalt melt at high pressure: An experimental study and implications for ultramafic xenolith survival. *Journal of Petrology*, 27(5):1157–1182, 1986.

C. Breitkreuz, L. Cortesogno, and L. Gaggero. Crystal-rich mass flow deposits related to the eruption of a sublacustrine silicic cryptodome (early permian collio basin, italian alps). *Journal of Volcanology and Geothermal Research*, 114:373–390, 2002.

J.C. Brice. Some thermodynamic aspects of the growth of strained crystals. *Journal of Crystal Growth*, 28(2):249 – 253, 1975.

W.B. Bryan, L.W. Finger, and F. Chayes. Estimating proportions in petrographic mixing equations by least-squares approximation. *Science*, 163(3870):926–927, 1969.

W.R. Buck, P. Einarsson, and B. Brandsdóttir. Tectonic stress and magma chamber size as controls on dike propagation: Constraints from the 1975-1984 krafla rifting episode. *Journal of Geophysical Research: Solid Earth*, 111:n/a–n/a, 2006.

J.-P. Burg, L. Arbaret, N.M. Chaudhry, H. Dawood, S. Hussain, and G. Zeilinger. Shear strain localization from the upper mantle to the middle crust of the kohistan arc (pakistan). *Geological Society, London, Special Publications*, 245(1):25–38, 2005.

R. Bürgmann, D.D. Pollard, and S.J. Martel. Slip distributions on faults: effects of stress gradients, inelastic deformation, heterogeneous host-rock stiffness, and fault interaction. *Journal of Structural Geology*, 16(12):1675–1690, 1994.

E. Callegari. Geological and pertrological aspects of the magmatic activity at adamello (northern italy). *Memorie della Società Geologica Italiana*, 26:83–103, 1983.

E. Callegari and P. Brack. Geological map of the tertiary adamello batholith (northern italy)-explanatory notes and legend. *Memorie di Scienze Geologiche*, 54:19–49, 2002.

A.J. Calvert. Seismic evidence for a magma chamber beneath the slow-spreading mid-atlantic. *Nature*, 377(6548):410–414, 1995.

L. Caricchi, C. Annen, A. Rust, and J. Blundy. Insights into the mechanisms and timescales of pluton assembly from deformation patterns of mafic enclaves. *J. Geophys. Res.*, 117(B11):B11206–, 2012.

I.S.E. Carmichael. The redox states of basic and silicic magmas: a reflection of their source regions? *Contributions to Mineralogy and Petrology*, 106:129–141, 1991.

E. Carminati and G.B. Siletto. The effects of brittle-plastic transitions in basement-involved foreland belts: the central southern alps case (n italy). *Tectonophysics*, 280(1-2):107–123, 1997.

E. Carminati, G.B. Siletto, and D. Battaglia. Thrust kinematics and internal deformation in basement-involved fold and thrust belts: The eastern orobic alps case (central southern alps, northern italy). *Tectonics*, 16(2):259–271, 1997.

E. Carminati, D. Cavazza, D. Scrocca, R. Fantoni, P. Scotti, and C. Doglioni. Thermal and tectonic evolution of the southern alps (northern italy) rifting: Coupled organic matter maturity analysis and thermokinematic modeling. *AAPG Bulletin*, 94(3):369–397, 2010.

G. Cassinis and A. Castellarin. Il significato delle linee della gallinera e delle giudicarie sud nella geologia dell'adamello e zone circonstati. *Atti Ticinensi di Scienze della Terra*, 31(5):446–462, 1988.

G. Cassinis, L. Cortesogno, L. Gaggero, C. Perotti, and A. Ronchi. Volcanic products from early permian collio basin (southern alps) and their geodynamic implications. *Periodico di Mineralogia*, 76:25–47, 2007.

A. Castellarin and L. Cantelli. Neo-alpine evolution of the southern eastern alps. *Journal of Geodynamics*, 30(1-2):251–274, 2000.

A. Castellarin, A.M. Fesce, V. Picotti, G.A. Pini, G. Prosser, R. Sartori, L. Selli, L. Cantelli, and R. Ricci. Structural and kinematic analysis of the giudicarie deformation belt. implications for compressional tectonics southern alps. *Mineralogica et Petrographica Acta*, 30:287–310, 1987.

A. Castellarin, S. Piccioni, G. Prosser, E. Sanguinetti, R. Sartori, and L. Selli. Mesozoic continental rifting and neogene inversion along the south giudicarie line (northwestern brenta dolomites). *Memorie della Società Geologica Italiana*, 49:125–144, 1993.

A. Castellarin, G.B. Vai, and L. Cantelli. The alpine evolution of the southern alps around the giudicarie faults: A late cretaceous to early eocene transfer zone. *Tectonophysics*, 414:203–223, 2006.

R. G. Cawthorn and M. J. O'Hara. Amphibole fractionation in calc-alkaline magma genesis. *American Journal of Science*, 276(3):309–329, 1976.

R.G. Cawthorn and P.A. Brown. A model for the formation and crystallization of corundum-normative calc-alkaline magmas through amphibole fractionation. *The Journal of Geology*, 84(4):467–476, 1976.

R.G. Cawthorn, D.F. Strong, and P.A. Brown. Origin of corundum-normative intrusive and extrusive magmas. *Nature*, 259(5539):102–104, January 1976.

Z. Chen, Z.-H. Jin, and S. E. Johnson. A perturbation solution for dyke propagation in an elastic medium with graded density. *Geophysical Journal International*, 169(1):348–356, 2007.

M. Chiaradia. Adakite-like magmas from fractional crystallization and melting-assimilation of mafic lower crust (eocene macuchi arc, western cordillera, ecuador). *Chemical Geology*, 265(4):468–487, 2009.

M. Chiaradia, O. Müntener, and B. Beate. Enriched basaltic andesites from mid-crustal fractional crystallization, recharge, and assimilation (pilavo volcano, western cordillera of ecuador). *Journal of Petrology*, 52(6):1107–1141, 2011.

P.P. Christiansen and D.D. Pollard. Nucleation, growth and structural development of mylonitic shear zones in granitic rock. *Journal of Structural Geology*, 19(9):1159–1172, 1997.

J.D. Clemens and G. Stevens. What controls chemical variation in granitic magmas? *Lithos*, 134-135: 317–329, 2012.

J.D. Clemens, G. Stevens, and F. Farina. The enigmatic sources of i-type granites: The peritectic connexion. *Lithos*, 126:174–181, 2011.

D.S. Coleman, B.S. Carl, A.F. Glazner, and J.M. Bartley. Cretaceous dikes within the jurassic independence dike swarm in eastern california. *Geological Society of America Bulletin*, 112:504–511, 2000.

D.S. Coleman, W. Gray, and A.F. Glazner. Rethinking the emplacement and evolution of zoned plutons: Geochronologic evidence for incremental assembly of the tuolumne intrusive suite, california. *Geology*, 32:433–436, 2004.

M. Coltorti, A.V. Vicente, V.A.V. Girardi, and J.H.D Schorscher. Liquid immiscibility in the archean greenstone belt of piumhi (minais gerais, brazil). *Lithos*, 20(1):77–91, 1987.

H.P. Cornelius. Zur altersbestimmung der adamello- und bergeller intrusion. *Sitzungberichte der Österreichischen Akademie der Mathematischen Naturwissenschaftlichen Klasse*, 137:451–562, 1924.

G. Cortecci, A. Moro, G. Leone, and G.C. Pardini. Correlation between strontium and oxygen isotopic compositions of rocks from the adamello massif (northern italy). *Contributions to Mineralogy and Petrology*, 68:421–427, 1979.

F. Costa, S. Chakraborty, and R. Dohmen. Diffusion coupling between trace and major elements and a model for calculation of magma residence times using plagioclase. *Geochimica et Cosmochimica Acta*, 67(12):2189 – 2200, 2003. ISSN 0016-7037. doi: 10.1016/S0016-7037(02)01345-5. URL `http://www.sciencedirect.com/science/article/pii/S0016703702013455`.

S. Couch, R.S J. Sparks, and M.R. Carroll. Mineral disequilibrium in lavas explained by convective self-mixing in open magma chambers. *Nature*, 411(6841):1037–1039, 2001.

C. Creixell, M.A. Parada, D. Morata, P. Roperch, and C. Arriagada. The genetic relationship between mafic dike swarms and plutonic reservoirs in the mesozoic of central chile (30°-33°45's): insights from ams and geochemistry. *International Journal of Earth Sciences*, 98(1):177–201, 2009.

J.A. Crisp. Rates of magma emplacement and volcanic output. *Journal of Volcanology and Geothermal Research*, 20(3-4):177 – 211, 1984.

J.L. Crowley, B. Schoene, and S.A. Bowring. U-pb dating of zircon in the bishop tuff at the millennial scale. *Geology*, 35(12):1123–1126, 2007.

G.L. Cumming, V. Köppel, and A. Ferrario. A lead isotope study of the northeastern ivrea zone and the adjoining ceneri zone (n-italy): evidence for a contaminated subcontinental mantle. *Contributions to Mineralogy and Petrology*, 97:19–30, 1987.

K.L. Currie and J. Ferguson. The mechanism of intrusion of lamprophyre dikes indicated by offsetting of dikes. *Tectonophysics*, 9(6):525–535, 1970.

P. D'Adda, A. Zanchi, M. Bergomi, F. Berra, M. Malusà, A. Tunesi, and S. Zanchetta. Polyphase thrusting and dyke emplacement in the central southern alps (northern italy). *International Journal of Earth Sciences*, 100:1095–1113, 2011.

M. D'Alessio and S.J. Martel. Development of strike-slip faults from dikes, sequoia national park, california. *Journal of Structural Geology*, 27(1):35–49, 2005.

R.A. Daly. *Igneous Rocks and the Depths of the Earth*. Hafner Publishing Company, 1933.

J.D. Dana, E.S. Dana, C. Palache, H. Berman, and C. Frondel. *The System of Mineralogy of J.D. Dana and E.S. Dana*. Wiley, 1944.

K.A. Daniels, J.L. Kavanagh, T. Menand, and R.S.J. Sparks. The shapes of dikes: Evidence for the influence of cooling and inelastic deformation. *Geological Society of America Bulletin*, 23, 2012.

N. Dauphas, P.R. Craddock, P.D. Asimow, V.C. Bennett, A.P. Nutman, and D. Ohnenstetter. Iron isotopes may reveal the redox conditions of mantle melting from archean to present. *Earth and Planetary Science Letters*, 288(1-2):255–267, 2009.

G. De Lucchi. Il giacimento del contatto di q. 2591 del m. farinas del frerone. *Atti Ist. Venet. Sci. Lett. Art., Cl. Mat. Nat.*, 48, 1938/39.

V. De Michele and U. Zezza. Manifestazioni ipoabissali quarzodioritiche di età alpina nelle prealpi bergamasche (alpi meridionali). *Atti della Società italiana di Scienze naturali e del Museo Civico di Storia naturale di Milano*, 114:181, 1979.

V. De Michele, M. Oddone, and U. Zezza. La porfirite di costa di belloro-premolo nel quadro delle manifestazioni ipoabissali di etÃ alpina nelle prealpi bergamasche. *Memorie della Società Geologica Italiana*, 26:69–81, 1983.

L.U. De Sitter and C.M. De Sitter-Koomans. *The geology of the Bergamasc Alps Lombardia, Italy*. Contributions to the Geology of the Bergamasc Alps. 1949.

S.M. DeBari and R.G. Coleman. Examination of the deep levels of an island arc: Evidence from the tonsina ultramafic-mafic assemblage, tonsina, alaska. *Journal of Geophysical Research: Solid Earth*, 94 (B4):4373–4391, 1989.

W.A. Deer, R.A. Howie, and J. Zussmann. *An Introduction to Rock-Forming Minerals*. Longmans Scientific and Technical, 1992.

A. Del Moro, G.C. Pardini, C. Quercioli, I. M. Villa, and E. Callegari. Rb/sr and k/ar chronology of adamello granitoids, southern alps. *Memorie della Società Geologica Italiana*, 26:285–299, 1985.

P.T. Delaney and D.D. Pollard. Deformation of host rocks and flow of magma during growth of minette dykes and breccia-bearing intrusions near ship rock, new mexico. *U.S. Geological Survey Professional Paper*, 1202:61, 1981.

P.T. Delaney, D.D. Pollard, J.I. Ziony, and E.H. McKee. Field relations between dikes and joints; emplacement processes and paleostress analysis. *Journal of Geophysical Research*, 91(B5):4920–4938, 1986.

D.J. DePaolo. Trace element and isotopic effects of combined wallrock assimilation and fractional crystallization. *Earth and Planetary Science Letters*, 53(2):189 – 202, 1981.

M. Dessimoz, O. Müntener, and P. Ulmer. A case for hornblende dominated fractionation of arc magmas: the chelan complex (washington cascades). *Contributions to Mineralogy and Petrology*, 163:567–589, 2012.

G. Di Toro and G. Pennacchioni. Superheated friction-induced melts in zoned pseudotachylytes within the adamello tonalites (italian southern alps). *Journal of Structural Geology*, 26:1783–1801, 2004.

G. Di Toro and G. Pennacchioni. Fault plane processes and mesoscopic structure of a strong-type seismogenic fault in tonalites (adamello batholith, southern alps). *Tectonophysics*, 402:55–80, 2005.

G. Di Toro, S. Nielsen, and G. Pennacchioni. Earthquake rupture dynamics frozen in exhumed ancient faults. *Nature*, 436(7053):1009–1012, 2005a.

G. Di Toro, G. Pennacchioni, and G. Teza. Can pseudotachylytes be used to infer earthquake source parameters? an example of limitations in the study of exhumed faults. *Tectonophysics*, 402:3–20, 2005b.

A. Dini, D.S. Westerman, F. Innocenti, and S. Rocchi. Magma emplacement in a transfer zone: the miocene mafic orano dyke swarm of elba island, tuscany, italy. *Geological Society, London, Special Publications*, 302(1):131–148, 2008.

F. Dobran. *Volcanic Processes: Mechanisms in Material Transport*. Springer London, Limited, 2012.

B.R. Doe, P.W. Lipman, C.E. Hedge, and H. Kurasawa. Primitive and contaminated basalts from the southern rocky mountains, u.s.a. *Contributions to Mineralogy and Petrology*, 21(2):142–156, 1969.

W.A. Dollase. Refinement of the crystal structures of epidote, allanite and hancockite. *American Min*, 53:1882–1898, 1971.

C.H. Donaldson. The rates of dissolution of olivine, plagioclase and quartz in a basalt melt. *Mineralogical Magazine*, 49:683–693, 1985.

C.H. Donaldson. Forsterite dissolution in superheated basaltic, andesitic and rhyolitic melts. *Mineralogical Magazine*, 54:67–74, 1990.

B.R. Edwards and J.K. Russell. A review and analysis of silicate mineral dissolution experiments in natural silicate melts. *Chemical Geology*, 130(3-4):233 – 245, 1996a.

B.R. Edwards and J.K. Russell. Influence of magmatic assimilation on mineral growth and zoning. *The Canadian Mineralogist*, 34(6):1149–1162, 1996b.

D. Elthon, R. Hanson, R. Allen, and H. Vergara. Unusual ocellar textures in diabases from the sarmiento ophiolite complex, chile. *Canadian Journal of Earth Sciences*, 21(3):376–378, 1984.

T.A. Ewing, J. Hermann, and D. Rubatto. The robustness of the zr-in-rutile and ti-in-zircon thermometers during high-temperature metamorphism (ivrea-verbano zone, northern italy). *Contributions to Mineralogy and Petrology*, 165(4):757–779, 2013.

J.M. Ferry and E.B. Watson. New thermodynamic models and revised calibrations for the ti-in-zircon and zr-in-rutile thermometers. *Contributions to Mineralogy and Petrology*, 154(4):429–437, 2007.

R. J. Finch and J.M. Hanchar. Structure and chemistry of zircon and zircon-group minerals. *Reviews in Mineralogy and Geochemistry*, 53(1):1–25, 2003.

M.R. Fisk. Basalt magma interaction with harzburgite and the formation of high-magnesium andesites. *Geophysical Research Letters*, 13(5):467–470, 1986.

J.D. Foden and D.H. Green. Possible role of amphibole in the origin of andesite: some experimental and natural evidence. *Contributions to Mineralogy and Petrology*, 109(4):479–493, 1992.

L. Fodor, I. Gerdes, A.and Dunkl, B. Koroknai, Z. Pécskay, M. Trajanova, P. Horváth, M. Vrabec, B. Jelen, K. Balogh, and W. Frisch. Miocene emplacement and rapid cooling of the pohorje pluton at the alpine-pannonian-dinaridic junction, slovenia. *Swiss Journal of Geosciences*, 101(1):255–271, 2008.

F. Forcella. Assetto strutturale delle orobie orientali tra la val seriana e la val camonica. *Rendiconti della Società Geologica Italiana*, 11:269–278, 1988.

A.D. Fowler, L.S. Jensen, and S.A. Peloquin. Varioles in archean basalts; products of spherulitic crystallization. *Canadian Mineralogist*, 25:275–289, 1987.

A.D. Fowler, B. Berger, M. Shore, M.I. Jones, and J. Ropchan. Supercooled rocks: development and significance of varioles, spherulites, dendrites and spinifex in archaean volcanic rocks, abitibi greenstone belt, canada. *Precambrian Research*, 115(1-4):311–328, 2002. ISSN 0301-9268.

I.C. Freestone. Liquid immiscibility in alkali-rich magmas. *Chemical Geology*, 23(1-4):115–123, 1978.

W. Frisch, J. Kuhlemann, I. Dunkl, and A. Brúgel. Palinspastic reconstruction and topographic evolution of the eastern alps during late tertiary tectonic extrusion. *Tectonophysics*, 297:1–15, 1998.

N. Froitzheim, P. Conti, and M. van Daalen. Late cretaceous, synorogenic, low-angle normal faulting along the schlinig fault (switzerland, italy, austria) and its significance for the tectonics of the eastern alps. *Tectonophysics*, 280(3):267–293, 1997.

B. Fügenschuh. *Thermal and Kinematic History of the Brenner Area (Eastern Alps, Tyrol)*. 1995.

M. Gaetani and F. Jadoul. The structure of the bergamasc alps. *Atti Accademia Nazionale dei Lincei*, 66: 411–416, 1979.

L. Gelinas, C. Brooks, and W.E. Trzcienski Jr. Archean variolites-quenched immiscible liquids. *Canadian Journal of Earth Sciences*, 13(2):210–230, 1976.

D.C. Gerlach and T.L. Grove. Petrology of medicine lake highland volcanics: Characterization of end-members of magma mixing. *Contributions to Mineralogy and Petrology*, 80(2):147–159, 1982.

N. Geshi, S. Kusumoto, and A. Gudmundsson. Geometric difference between non-feeder and feeder dikes. *Geology*, 38(3):195–198, 2010.

M.S. Ghiorso and R.O. Sack. Chemical mass transfer in magmatic processes iv. a revised and internally consistent thermodynamic model for the interpolation and extrapolation of liquid-solid equilibria in magmatic systems at elevated temperatures and pressures. *Contributions to Mineralogy and Petrology*, 119:197–212, 1995.

J.B. Gill. *Orogenic andesites and plate tectonics*. Minerals and rocks. Springer-Verlag, 1981.

K.M. Gillis and L.A. Coogan. Anatectic migmatites from the roof of an ocean ridge magma chamber. *Journal of Petrology*, 43(11):2075–2095, 2002.

D. Giordano, J.K. Russell, and D.B. Dingwell. Viscosity of magmatic liquids: A model. *Earth and Planetary Science Letters*, 271(1-4):123–134, 2008.

A.F. Glazner, J.M. Bartley, and B.S. Carl. Oblique opening and noncoaxial emplacement of the jurassic independence dike swarm, california. *Journal of Structural Geology*, 21(10):1275–1283, 1999.

A.F. Glazner, B.S. Carl, D.S. Coleman, J.S. Miller, and J.M. Bartley. Chemical variability and the composite nature of dikes from the jurassic independence dike swarm, eastern california. *Geological Society of America Special Papers*, 438:455–480, 2008.

D.H. Green and A.E. Ringwood. The genesis of basaltic magmas. *Contributions to Mineralogy and Petrology*, 15(2):103–190, 1967.

N.L. Green. Mechanism for middle to upper crustal contamination: Evidence from continental-margin magmas. *Geology*, 22(3):231–234, 1994.

A.R. Greene, S.M. DeBariI, P.B. Kelemen, J. Blusztajn, and P.D. Clift. A detailed geochemical study of island arc crust: the talkeetna arc section, south-central alaska. *Journal of Petrology*, 47(6):1051–1093, 2006.

C.H. Grohmann. Morphometric analysis in geographic information systems: applications of free software {GRASS} and r. *Computers & Geosciences*, 30:1055–1067, 2004.

T. Grove, S. Parman, S. Bowring, R. Price, and M. Baker. The role of an h2o-rich fluid component in the generation of primitive basaltic andesites and andesites from the mt. shasta region, n california. *Contributions to Mineralogy and Petrology*, 142(4):375–396, 2002.

T.L. Grove. Corrections to expressions for calculating mineral components in 'origin of calc-alkaline series lavas at medicine lake volcano by fractionation, assimilation and mixing' and 'experimental petrology of normal morb near the kane fracture zone: 22-25n, mid-atlantic ridge'. *Contributions to Mineralogy and Petrology*, 114:422–424, 1993.

T.L. Grove, D.C. Gerlach, and T.W. Sando. Origin of calc-alkaline series lavas at medicine lake volcano by fractionation, assimilation and mixing. *Contributions to Mineralogy and Petrology*, 80:160–182, 1982.

T.L. Grove, D.C. Gerlach, T.W. Sando, and M.B. Baker. Origin of calc-alkaline series lavas at medicine lake volcano by fractionation, assimilation and mixing: Corrections and clarifications. *Contributions to Mineralogy and Petrology*, 82:407–408, 1983.

T.L. Grove, L.T. Elkins-Tanton, S.W. Parman, N. Chatterjee, O. Müntener, and G.A. Gaetani. Fractional crystallization and mantle-melting controls on calc-alkaline differentiation trends. *Contributions to Mineralogy and Petrology*, 145:515–533, 2003.

A. Gudmundsson, L.B. Marinoni, and J. Marti. Injection and arrest of dykes: implications for volcanic hazards. *Journal of Volcanology and Geothermal Research*, 88(1-2):1–13, 1999.

J.M. Guilbert and C.F. Park. *The geology of ore deposits*. Waveland Press, 2007.

M. Guillong, D.L. Meier, M.M. Allan, C.A. Heinrich, and B.W.D. Yardley. *SILLS: A matlab-based program for the reduction of laser ablation icp-ms data of homogeneous materials and inclusions*. Mineralogical Association of Canada, 2008.

P.L. Hancock. The analysis of en-échelon veins. *Geological Magazine*, 109:269–276, 4 1972.

E. Hanski, S. Mertanen, T. Rämö, and J. Vuollo. *Dyke Swarms - Time Markers of Crustal Evolution: Selected Papers of the Fifth International Dyke Conference in Finland, Rovaniemi, Finland, 31 July-3 Aug 2005 & Fourth International Dyke Conference, Kwazulu-Natal, South Africa 26-29 June 2001*. Balkema - Proceedings and Monographs in Engineering, Water and Earth Sciences. Taylor & Francis, 2010.

W. Hansmann. *U-Pb Datierungen an Zirkonen und Thoriten aus einer magmatischen Gesteinssuite am Beispiel des südlichen Adamello (Norditalien)*. PhD thesis, Swiss Federal Institute of Technology Zurich, ETHZ, 1986.

W. Hansmann and F. Oberli. Zircon inheritance in an igneous rock suite from the southern adamello batholith (italian alps). *Contributions to Mineralogy and Petrology*, 107:501–518, 1991.

F.C. Hawthorne. The crystal chemistry of amphiboles. *Canadian Mineralogist*, 21:173–480, 1983.

F.C. Hawthorne and R. Oberti. Amphiboles: Crystal chemistry. *Reviews in Mineralogy and Geochemistry*, 67(1):1–54, 2007.

J. Hermann. Allanite: thorium and light rare earth element carrier in subducted crust. *Chemical Geology*, 192(3-4):289–306, 2002.

J. Hermann, D. Rubatto, A. Korsakov, and V.S. Shatsky. Multiple zircon growth during fast exhumation of diamondiferous, deeply subducted continental crust (kokchetav massif, kazakhstan). *Contributions to Mineralogy and Petrology*, 141(1):66–82, 2001.

W. Hildreth and St. Moorbath. Crustal contributions to arc magmatism in the andes of central chile. *Contributions to Mineralogy and Petrology*, 98(4):455–489, 1988.

K.F. Hodge, G. Carazzo, and A.M. Jellinek. Experimental constraints on the deformation and breakup of injected magma. *Earth and Planetary Science Letters*, 325-326:52–62, 2012.

J.D. Hoek. *Physics and Chemistry of Dykes*, chapter Dyke propagation and arrest in Proterozoic tholeiitic dyke swarms, Vestfold Hills, Antarctica, pages 79–93. 1995.

J. Hofierka, H. Mitasova, and M. Neteler. Chapter 17 geomorphometry in {GRASS} {GIS}. In Tomislav Hengl and Hannes I. Reuter, editors, *Geomorphometry Concepts, Software, Applications*, volume 33 of *Developments in Soil Science*, pages 387 – 410. Elsevier, 2009.

T. Holland and J. Blundy. Non-ideal interactions in calcic amphiboles and their bearing on amphibole-plagioclase thermometry. *Contributions to Mineralogy and Petrology*, 116:433–447, 1994.

L.S. Hollister and R.B. Hargarves. *Compositional zoning and its significance in pyroxenes from two coarse grained Apollo 11 samples*, volume Geochimica et Cosmochimica Acta Supplement, Volume 1. Proceedings of the Apollo 11 Lunar Science Conference held 5-8 January, 1970 in Houston, TX. Volume 1: Mineraolgy and Petrology. Pergammon Press, 1970.

L.S. Hollister, Jr. Trzcienski, W.E., R.B. Hargraves, and C.G. Kulick. *Petrogenetic significance of pyroxenes in two Apollo 12 samples*, volume 2. Proceedings of the Lunar Science Conference, 1971.

J. Hunziker and A. Zingg. Lower paleozoic amphibolite to granulite facies metamorphism in the ivrea zone. *Schweiz Mineralogische Petrografische Mitteilungen*, 62:483–486, 1980.

H.E. Huppert and R.S.J. Sparks. Cooling and contamination of mafic and ultramafic magmas during ascent through continental crust. *Earth and Planetary Science Letters*, 74(4):371–386, 1985.

H.E. Huppert and R.S.J. Sparks. The generation of granitic magmas by intrusion of basalt into continental crust. *Journal of Petrology*, 29(3):599–624, 1988.

N. Hürlimann, O. Muntener, P. Ulmer, and M. Chiaradia. Fractionation of primitive arc-tholeiitic magmas in middle to deep crustal level and implications on the trace element signature of andesites. *Journal of Petrology*, in prep.a.

N. Hürlimann, Muntener O. Ovtcharova, M., and P. Ulmer. Dyke magmatism suceeding large volume plutonic activity as stress marker. an example from the southern adamello n-italy. *American Journal of Science*, in prep.b.

D. Insergueix-Filippi, L. Dupeyrat, L.A. Dimo-Lahitte, P. Vergély, and J. Bébien. Albanian ophiolites; ii, model of subduction zone infancy at a mid-ocean ridge. *Ofioliti*, 25:47–53, 2000.

H.M. Iyer. Geophysical evidence for the locations, shapes and sizes, and internal structures of magma chambers beneath regions of quaternary volcanism. *Philosophical Transactions of the Royal Society of London. Series A, Mathematical and Physical Sciences*, 310(1514):473–510, 1984.

S. Jackson. *Lametrace data reduction software for LA-ICP-MS, laser ablation-ICP-MS in the earth sciences: current practices and outstanding issues.* Mineralogical Association of Canada, 2008.

S.B. Jacobsen and G.J. Wasserburg. Sm-nd isotopic evolution of chondrites. *Earth and Planetary Science Letters*, 50(1):139–155, 1980.

O. Jagoutz. Construction of the granitoid crust of an island arc. part ii: a quantitative petrogenetic model. *Contributions to Mineralogy and Petrology*, 160:359–381, 2010.

M.Q. Jan and R.A. Howie. The mineralogy and geochemistry of the metamorphosed basic and ultrabasic rocks of the jijal complex, kohistan, nw pakistan. *Journal of Petrology*, 22(1):85–126, 1981.

C. Jaupart and C.J. Allègre. Gas content, eruption rate and instabilities of eruption regime in silicic volcanoes. *Earth and Planetary Science Letters*, 102:413 – 429, 1991.

A.M. Jellinek and D.J. DePaolo. A model for the origin of large silicic magma chambers: precursors of caldera-forming eruptions. *Bulletin of Volcanology*, 65(5):363–381, 2003.

F.E. Jenner, H.ST.C. O'Neill, R.J. Arculus, and J.A. Mavrogenes. The magnetite crisis in the evolution of arc-related magmas and the initial concentration of au, ag and cu. *Journal of Petrology*, 51(12): 2445–2464, 2010.

W. Johannes and F. Holtz. *Petrogenes and Experimental Pertology of Granitic Rocks.* Springer, 1996.

B.E. John and J. D. Blundy. Emplacement-related deformation of granitoid magmas, southern adamello massif, italy. *Geological Society of America Bulletin*, 105(12):1517–1541, 1993.

R.J.H. Jolly and D.J. Sanderson. Variation in the form and distribution of dykes in the mull swarm, scotland. *Journal of Structural Geology*, 17(11):1543 – 1557, 1995.

S.M. Kaczor, G.N. Hanson, and Z.E. Peterman. Disequilibrium melting of granite at the contact with a basic plug - a geochemcial and petrographic study. *Journal of Geology*, 96:61–78, 1988.

H. Kagami, P. Ulmer, W. Hansmann, V. Dietrich, and R.H. Steiger. Nd-sr isotopic and geochemical characteristics of the southern adamello (northern italy) intrusives: Implications for crustal versus mantle origin. *Journal of Geophysical Research*, 96(B9):14331–14346, 1991.

R. Kägi. *The liquid line of descent of hydrous primary, calc-alkaline magmas under elevated pressure. An experimental approach.* PhD thesis, Swiss Federal Institute of Technology Zurich, ETHZ, 2000.

L. Karlstrom, J. Dufek, and M. Manga. Organization of volcanic plumbing through magmatic lensing by magma chambers and volcanic loads. *Journal of Geophysical Research: Solid Earth*, 114(B10):n/a–n/a, 2009.

I. Katayama, S. Maruyama, C.D. Parkinson, K. Terada, and Y. Sano. Ion micro-probe u-pb zircon geochronology of peak and retrograde stages of ultrahigh-pressure metamorphic rocks from the kokchetav massif, northern kazakhstan. *Earth and Planetary Science Letters*, 188(1-2):185–198, 2001.

J.L. Kavanagh and R.S.J. Sparks. Insights of dyke emplacement mechanics from detailed 3d dyke thickness datasets. *Journal of the Geological Society*, 168:965–978, 2011.

R.W. Kay. Aleutian magnesian andesites: Melts from subducted pacific ocean crust. *Journal of Volcanology and Geothermal Research*, 4(1-2):117–132, 1978.

S.M. Kay and R.W. Kay. Role of crystal cumulates and the oceanic crust in the formation of the lower crust of the aleutian arc. *Geology*, 13(7):461–464, 1985.

P.B. Kelemen. Assimilation of ultramafic rock in subduction-related magmatic arcs. *The Journal of Geology*, 94(6):829–843, 1986.

P.B. Kelemen. Reaction between ultramafic rock and fractionating basaltic magma i. phase relations, the origin of calc-alkaline magma series, and the formation of discordant dunite. *Journal of Petrology*, 31 (1):51–98, 1990.

P.B. Kelemen. Genesis of high mg andesites and the continental crust. *Contributions to Mineralogy and Petrology*, 120:1–19, 1995.

P.B. Kelemen, D.B. Joyce, J.D. Webster, and J.R. Holloway. Reaction between ultramafic rock and fractionating basaltic magma ii. experimental investigation of reaction between olivine tholeiite and harzburgite at 1150-1050c and 5 kb. *Journal of Petrology*, 31(1):99–134, 1990.

P.B. Kelemen, H.J.B. Dick, and J.E. Quick. Formation of harzburgite by pervasive melt/rock reaction in the upper mantle. *Nature*, 358(6388):635–641, 1992.

P.B. Kelemen, K. Hanghøj, and A.R. Greene. One view of the geochemistry of subduction-related magmatic arcs, with an emphasis on primitive andesite and lower crust. *Treatise on Geochemistry*, 3:593–659, 2003.

K.A. Kelley and E. Cottrell. Water and the oxidation state of subduction zone magmas. *Science*, 325 (5940):605–607, 2009.

K.A. Kelley, T. Plank, T.L. Grove, E.M. Stolper, S. Newman, and E. Hauri. Mantle melting as a function of water content beneath back-arc basins. *Journal of Geophysical Research: Solid Earth*, 111(B9):n/a–n/a, 2006.

R.J. Kinzler, T.L. Grove, and S.I. Recca. An experimental study on the effect of temperature and melt composition on the partitioning of nickel between olivine and silicate melt. *Geochimica et Cosmochimica Acta*, 54(5):1255–1265, 1990.

D.E. Kitchen. The disequilibrium partial melting and assimilation of caledonian granite by tertiary basalt at barnesmore, co. donegal. *Geological Magazine*, 126(4):397–405, 1989.

K. Klimm, J.D. Blundy, and T.H. Green. Trace element partitioning and accessory phase saturation during h2o-saturated melting of basalt with implications for subduction zone chemical fluxes. *Journal of Petrology*, 49(3):523–553, 2008.

K.M. Knesel and J.P. Davidson. Isotopic disequilibrium during melting of granite and implications for crustal contamination of magmas. *Geology*, 24(3):243–246, 1996.

S. Kodaira, N. Noguchi, N. Takahashi, O. Ishizuka, and Y. Kaneda. Evolution from fore-arc oceanic crust to island arc crust: A seismic study along the izu-bonin fore arc. *J. Geophys. Res.*, 115(B9):B09102–, 2010.

J. Koepke, J. Berndt, S.T. Feig, and F. Holtz. The formation of sio2-rich melts within the deep oceanic crust by hydrous partial melting of gabbros. *Contributions to Mineralogy and Petrology*, 153(1):67–84, 2007.

V. Köppel. Isotopic u-pb ages of monazites and zircons from the crust-mantle transition and adjacent units of the ivrea and ceneri zones (southern alps, italy). *Contributions to Mineralogy and Petrology*, 43:55–70, 1974.

M. Krawczynski, T.L. Grove, and H. Behrens. Amphibole stability in primitive arc magmas: effects of temperature, h2o content, and oxygen fugacity. *Contributions to Mineralogy and Petrology*, 164(2): 317–339, 2012.

T.E. Krogh. A low-contamination method for hydrothermal decomposition of zircon and extraction of u and pb for isotopic age determinations. *Geochimica et Cosmochimica Acta*, 37:485–494, 1973.

I. Kushiro. Effect of water on the composition of magmas formed at high pressures. *Journal of Petrology*, 13(2):311–334, 1972.

J. Larocque and D. Canil. The role of amphibole in the evolution of arc magmas and crust: the case from the jurassic bonanza arc section, vancouver island, canada. *Contributions to Mineralogy and Petrology*, 159:475–492, 2010.

H.P. Laubscher. Das alpen-dinariden-problem und die palinspastik der südlichen tethys. *Geologische Rundschau*, 60(3):813–833, 1971.

H.P. Laubscher. The late alpine (periadriatic) intrusions and the insubric line. *Memorie della Società Geologica Italiana*, 26:21–30, 1983.

H.P. Laubscher. Large-scale, thin-skinned thrusting in the southern alps: Kinematic models. *Geological Society of America Bulletin*, 96(6):710–718, 1985.

H.P. Laubscher. The problem of the deep structure of the southern alps: 3-d material balance considerations and regional consequences. *Tectonophysics*, 176(1-2):103–121, 1990a.

H.P. Laubscher. Material balance in alpine orogeny. *Geological Society of America Special Papers*, 253: 189–204, 1990b.

M.J. Le Bas, R.W. Le Maitre, A. Streckeisen, B. Zanettin, and IUGS Subcommission on the Systematics of Igneous Rocks. A chemical classification of volcanic rocks based on the total alkali-silica diagram. *Journal of Petrology*, 27(3):745–750, 1986.

B.E. Leake, A.R. Woolley, C.E.S. Arps, W.D. Birch, M.C Gilbert, J.D. Grice, F.C. Hawthorne, A. Kato, H.J. Kisch, V.G. Krivovichev, K. Linthout, J. Laird, J.A. Mandarino, W.V. Maresch, E.H. Nickel, N.M.S. Rock, J.C. Schumacher, D.C. Smith, N.C.N. Stephenson, L. Ungaretti, E.J.W. Whittaker, and Guo Y. Nomenclature of amphiboles; report of the subcommittee on amphiboles of the international mineralogical association, commission on new minerals and mineral names. *American Mineralogist*, 82 (9-10):1019–1037, 1997.

C.-T.A. Lee, P. Luffi, V. Le Roux, R. Dasgupta, F. Albarede, and W.P. Leeman. The redox state of arc mantle using zn/fe systematics. *Nature*, 468(7324):681–685, 2010. ISSN 0028-0836.

C.-T.A. Lee, P. Luffi, E.J. Chin, R. Bouchet, R. Dasgupta, D.M. Morton, V. Le Roux, Q. Yin, and D. Jin. Copper systematics in arc magmas and implications for crust-mantle differentiation. *Science*, 336(6077): 64–68, 2012.

C.-Ty A. Lee, W.P. Leeman, D. Canil, and Z.-X.A. Li. Similar v/sc systematics in morb and arc basalts: Implications for the oxygen fugacities of their mantle source regions. *Journal of Petrology*, 46(11): 2313–2336, November 2005.

W. Leng and M. Gurnis. Dynamics of subduction initiation with different evolutionary pathways. *Geochemistry, Geophysics, Geosystems*, 12(12):n/a–n/a, 2011.

H.-P. Liermann and J. Ganguly. Diffusion kinetics of fe2+ and mg in aluminous spinel: experimental determination and applications. *Geochimica et Cosmochimica Acta*, 66(16):2903 – 2913, 2002.

D.H. Lindsley and D.J. Andersen. A two-pyroxene thermometer. *Journal of Geophysical Research: Solid Earth*, 88(S02):A887–A906, 1983.

J.R. Lister and R.C. Kerr. Fluid-mechanical models of crack propagation and their application to magma transport in dykes. *Journal of Geophysical Research: Solid Earth*, 96(B6):10049–10077, 1991.

H.P. Longerich, S.E. Jackson, and D. Gunther. Inter-laboratory note. laser ablation inductively coupled plasma mass spectrometric transient signal data acquisition and analyte concentration calculation. *J. Anal. At. Spectrom.*, 11:899–904, 1996.

F. Maccaferri, M. Bonafede, and E. Rivalta. A numerical model of dyke propagation in layered elastic media. *Geophysical Journal International*, 180(3):1107–1123, 2010.

I.D. MacGregor and C.H. Smith. The use of chrome spinels in petrographic studies of ultramafic intrusions. *The Canadian Mineralogist*, 7(3):403–412, 1963.

K.I. Mahon, T.M. Harrison, and D.A. Drew. Ascent of a granitoid diapir in a temperature varying medium. *Journal of Geophysical Research: Solid Earth*, 93(B2):1174–1188, 1988.

N.S. Mancktelow. Neogene lateral extension during convergence in the central alps: Evidence from interrelated faulting and backfolding around the simplonpass (switzerland). *Tectonophysics*, 215:295–317, 1992.

N.S. Mancktelow and G. Pennacchioni. The control of precursor brittle fracture and fluid-rock interaction on the development of single and paired ductile shear zones. *Journal of Structural Geology*, 27(4): 645–661, 2005.

N.S. Mancktelow, D.F. Stöckli, B. Grollimund, W. Müller, B. Fügenschuh, G. Viola, D. Seward, and I.M. Villa. The dav and periadriatic fault systems in the eastern alps south of the tauern window. *International Journal of Earth Sciences*, 90(3):593–622, 2001.

B.B. Mandelbrot and A. Blumen. Fractal geometry: What is it, and what does it do? [and discussion]. *Proceedings of the Royal Society of London. A. Mathematical and Physical Sciences*, 423:3–16, 1989.

W. Marian. Shuttle radar topography mission (srtm) mission overview. *Frequenz*, 55:75–79, 2001.

B.D. Marsh. On the mechanics of igneous diapirism, stoping and zone-melting. *American Journal of Science*, 282(6):808–855, 1982.

J.M. Mattinson. Zircon u-pb chemical abrasion (ca-tims) method: Combined annealing and multi-step partial dissolution analysis for improved precision and accuracy of zircon ages. *Chemical Geology*, 220 (1-2):47–66, 2005.

R. L. Mauger. Ocelli; transient disequilibrium features in a lower carboniferous minette near concord, north carolina. *The Canadian Mineralogist*, 26(1):117–131, 1988.

M.T. McCulloch and J.A. Gamble. Geochemical and geodynamical constraints on subduction zone magmatism. *Earth and Planetary Science Letters*, 102(3-4):358–374, 1991.

W.F. McDonough and S.-s. Sun. The composition of the earth. *Chemical Geology*, 120(3-4):223–253, 1995.

D. McKenzie. The generation and compaction of partially molten rock. *Journal of Petrology*, 25(3): 713–765, 1984.

D. McKenzie and R.K. O'Nions. Partial melt distributions from inversion of rare earth element concentrations. *Journal of Petrology*, 32(5):1021–1091, 1991.

N. M. McLean, J. F. Bowring, and S. A. Bowring. An algorithm for u-pb isotope dilution data reduction and uncertainty propagation. *Geochemistry, Geophysics, Geosystems*, 12(6), 2011.

P. McLeod and S. Tait. The growth of dykes from magma chambers. *Journal of Volcanology and Geothermal Research*, 92(3-4):231–245, 1999.

T. Menand. Dyke propagation and spatial distribution in dyke swarms. page F7, 2010.

T. Menand. Physical controls and depth of emplacement of igneous bodies: A review. *Tectonophysics*, 500:11–19, 2011.

T. Menand and S.R. Tait. The propagation of a buoyant liquid-filled fissure from a source under constant pressure: An experimental approach. *J. Geophys. Res.*, 107(B11):2306–, 2002.

T. Menand, K.A. Daniels, and P. Benghiat. Dyke propagation and sill formation in a compressive tectonic environment. *J. Geophys. Res.*, 115(B8):B08201–, August 2010.

J.S. Miller, J.E.P. Matzel, C.F. Miller, S.D. Burgess, and R.B. Miller. Zircon growth and recycling during the assembly of large, composite arc plutons. *Journal of Volcanology and Geothermal Research*, 167: 282–299, 2007.

A. Miyashiro. Volcanic rock series in island arcs and active continental margins. *American Journal of Science*, 274(4):321–355, 1974.

I. Molen and M.S. Paterson. Experimental deformation of partially-melted granite. *Contributions to Mineralogy and Petrology*, 70(3):299–318, 1979.

A. Monese. I lamprofiri del lago della vacca (adamello meridionale). *Mem. Accad. Patav. Sc. L. A.*, 80: 165–187, 1968.

A. Montrasio, R. Bersezio, F. Forcella, F. Jadoul, and E. Sciesa. Geological interpretation of the profile crop - central alps (passo spluga - bergamo). *Quad. Geodin. Alpina Quat.*, 2:171–186, 1994.

S. Morgante. Le valli palobbia, paghera, dois, di braone, di cobello, del re e di fa nell'adamello sud-occidentale. *Memorie di Scienze Geologiche*, 29:30, 1972.

J.R. Muller, G. Ito, and S.J. Martel. Effects of volcano loading on dike propagation in an elastic half-space. *Journal of Geophysical Research: Solid Earth*, 106:11101–11113, 2001.

O.H. Muller and D.D. Pollard. The stress state near spanish peaks, colorado determined from a dike pattern. *Pure and Applied Geophysics*, 115:69–86, 1977.

W. Müller, N.S. Mancktelow, and M. Meier. Rb-sr microchrons of synkinematic mica in mylonites: an example from the dav fault of the eastern alps. *Earth and Planetary Science Letters*, 180(3-4):385–397, 2000.

W. Müller, G. Prosser, N.S. Mancktelow, I.M. Villa, S.P. Kelley, G. Viola, and F. Oberli. Geochronological constraints on the evolution of the periadriatic fault system (alps). *International Journal of Earth Sciences*, 90(3):623–653, 2001.

J.E. Mungall. Roasting the mantle: Slab melting and the genesis of major au and au-rich cu deposits. *Geology*, 30(10):915–918, 2002.

O. Müntener and P. Ulmer. Experimentally derived high-pressure cumulates from hydrous arc magmas and consequences for the seismic velocity structure of lower arc crust. *Geophysical Research Letters*, 33 (21):L21308–, 2006.

O. Müntener, P. Kelemen, and T. Grove. The role of h2o during crystallization of primitive arc magmas under uppermost mantle conditions and genesis of igneous pyroxenites: an experimental study. *Contributions to Mineralogy and Petrology*, 141:643–658, 2001.

S.A.F. Murrell. The theory of the propagation of elliptical griffith cracks under various conditions of plane strain or plane stress: Part i. *British Journal of Applied Physics*, 15(10):1195, 1964.

J.D. Myers, B.D. Marsh, and A.K. Sinha. Strontium isotopic and selected trace element variations between two aleutian volcanic centers (adak and atka): implications for the development of arc volcanic plumbing systems. *Contributions to Mineralogy and Petrology*, 91(3):221–234, 1985.

R.H. Nandedkar, N. Hurlimann, P. Ulmer, and O. Muntener. Trace element partitioning between andesitic to rhyolite liquids and pargasitic to cummingtonitic amphibole. in prep.

R. Nandekar. *Petrological constraints on calcalkaline batholith formation (Adamello, Italy): An experimental approach.* PhD thesis, Swiss Federal Institute of Technology, ETHZ, 2013.

F. Neubauer and G. Genser. Architektur und kinematik der östlichen zentralalpen-eine übersicht. *Mitteilungen des Naturwissenschaftlichen Vereins Steiermark*, 120:274–283, 1990.

R. Nicholson and D.D. Pollard. Dilation and linkage of echelon cracks. *Journal of Structural Geology*, 7 (5):583–590, 1985.

F. Oberli, M. Meier, A. Berger, C.L. Rosenberg, and R. Gieré. U-th-pb and 230th/238u disequilibrium isotope systematics: Precise accessory mineral chronology and melt evolution tracing in the alpine bergell intrusion. *Geochimica et Cosmochimica Acta*, 68(11):2543–2560, 2004.

E.F. Osborn. Role of oxygen pressure in the crystallization and differentiation of basaltic magma. *American Journal of Science*, 257(9):609–647, 1959.

K. Ozawa. Evaluation of olivine-spinel geothermometry as an indicator of thermal history for peridotites. *Contributions to Mineralogy and Petrology*, 82:52–65, 1983.

K. Ozawa. Olivine-spinel geospeedometry: Analysis of diffusion-controlled mg-fe2+ exchange. *Geochimica et Cosmochimica Acta*, 48(12):2597 – 2611, 1984.

J.A. Pearce and R.J. Stern. Origin of back-arc basin magmas: Trace element and isotope perspectives. In *Geophys. Monogr. Ser.*, volume 166, pages 63–86. AGU, Washington, DC, 2006.

N.J.G. Pearce, W.T. Perkins, J.A. Westgate, M.P. Gorton, S.E. Jackson, C.R. Neal, and S.P. Chenery. A compilation of new and published major and trace element data for nist srm 610 and nist srm 612 glass reference materials. *Geostandards Newsletter*, 21(1):115–144, 1997.

G. Pennacchioni. Control of the geometry of precursor brittle structures on the type of ductile shear zone in the adamello tonalites, southern alps (italy). *Journal of Structural Geology*, 27(4):627–644, 2005.

G. Pennacchioni, G. Di Toro, P. Brack, L. Menegon, and I.M. Villa. Brittle-ductile-brittle deformation during cooling of tonalite (adamello, southern italian alps). *Tectonophysics*, 427:171–197, 2006.

H. L. Petcovic and A. L. Grunder. Textural and thermal history of partial melting in tonalitic wallrock at the margin of a basalt dike, wallowa mountains, oregon. *Journal of Petrology*, 44(12):2287–2312, 2003.

A. R. Philpotts. Silicate liquid immiscibility in tholeiitic basalts. *Journal of Petrology*, 20(1):99–118, 1979.

A.R. Philpotts and P.M. Asher. Wallrock melting and reaction effects along the higganum diabase dike in connecticut: Contamination of a continental flood basalt feeder. *Journal of Petrology*, 34(5):1029–1058, 1993.

V. Picotti, Prosser G., and Castellarin A. Structures and kinematics of the giudicarie-val trompia fold and thrust belt (central southern alps, northern italy). *Memorie della Società Geologica Italiana*, 47: 95–109, 1995.

M. Pieri, G. Groppi, Progetto Finalizzato Geodinamica. Sottoprogetto "Modello Strutturale.", and Consiglio nazionale delle ricerche. *Subsurface Geological Structure of the Po Plain, Italy*. Consiglio Nazionale delle Ricerche, 1981.

C. Pin. *Granulites and crustal evolution*, chapter Evolution of the lower crust in the Ivrea Zone: a model based on isotopic and geochemical data, pages 87–110. 1990.

C. Pin, D. Briot, C. Bassin, and F. Poitrasson. Concomitant separation of strontium and samarium-neodymium for isotopic analysis in silicate samples, based on specific extraction chromatography. *Analytica Chimica Acta*, 298(2):209–21, 1994.

L. Pinarelli, A. Boriani, and A. Del Moro. The pb isotopic systematics during crustal contamination of subcrustal magmas: the hercynian magmatism in the serie dei laghi (southern alps, italy). *Lithos*, 31 (1-2):51–61, 1993.

A. J. Piwinskii. Experimental studies of igneous rock series central sierra nevada batholith, california. *The Journal of Geology*, 76(5):548–570, 1968.

A. J. Piwinskii and P. J. Wyllie. Experimental studies of igneous rock series: A zoned pluton in the wallowa batholith, oregon. *The Journal of Geology*, 76(2):205–234, 1968.

T. Plank. Constraints from thorium/lanthanum on sediment recycling at subduction zones and the evolution of the continents. *Journal of Petrology*, 46(5):921–944, 2005.

M. Poland, W. Moats, and J. Fink. A model for radial dike emplacement in composite cones based on observations from summer coon volcano, colorado, usa. *Bulletin of Volcanology*, 70:861–875, 2008.

A. Polat, P.W.U Appel, R. Frei, Y. Y. Pan, J.C. Dilek, Juan C. Ordonez-Caldeeron, B. Fryer, J.A. Hollis, and J.G. Raith. Field and geochemical characteristics of the mesoarchean (ca. 3075 ma) ivisaartoq greenstone belt, southern west greenland: Evidence for seafloor hydrothermal alteration in supra-subduction oceanic crust. *Gondwana Research*, 11(1-2):69–91, 2007.

A. Polat, R. Frei, P.W.U Appel, Y. Dilek, B. Fryer, J.C. Ordonez-Caldeeron, and Z. Yang. The origin and compositions of mesoarchean oceanic crust: Evidence from the 3075 ma ivisaartoq greenstone belt, sw-greenland. *Lithos*, 100(1-4):293–321, 2008.

D.D. Pollard. *Elementary Fracture Mechanics Applied to the Structural Interpretation of Dykes*, chapter 1, pages 5–24. Geological Association of Canada Special Paper, 1987.

D.D. Pollard and O.H. Muller. The effects of gradients om regional stress and magma pressure on the form of sheet intrusions in cross section. *Journal of Geophysical Research*, 81(5):975–984, 1976.

D.D. Pollard, P. Segall, and P.T. Delaney. Formation and interpretation of dilatant echelon cracks. *Geological Society of America Bulletin*, 93(12):1291–1303, 1982.

H. Pomella, U. Klötzli, R. Scholger, M. Stipp, and B. Fügenschuh. The northern giudicarie and the meran-mauls fault (alps, northern italy) in the light of new paleomagnetic and geochronological data from boudinaged eo-/oligocene tonalite. *International Journal of Earth Sciences*, 100(8):1827–1850, 2011.

G. Prosser. Strike-slip movements and thrusting along a transpressive fault zone: The north giudicarie line (insubric line, northern italy). *Tectonics*, 17(6):921–937, 1998.

G. Prosser. The development of the north giudicarie fault zone (insubric line, northern italy). *Journal of Geodynamics*, 30:229–250, 2000.

G. Proteau and B. Scaillet. Experimental constraints on the origin of the 1991 pinatubo dacite. *Journal of Petrology*, 44(12):2203–2241, 2003.

J.E. Quick. The origin and significance of large, tabular dunite bodies in the trinity peridotite, northern california. *Contributions to Mineralogy and Petrology*, 78(4):413–422, 1982.

M. Rabinowicz, Y. Ricard, and M. Grégoire. Compaction in a mantle with a very small melt concentration: Implications for the generation of carbonatitic and carbonate-bearing high alkaline mafic melt impregnations. *Earth and Planetary Science Letters*, 203(1):205–220, 2002.

B. Rabus, M. Eineder, A. Roth, and R. Bamler. The shuttle radar topography mission-a new class of digital elevation models acquired by spaceborne radar. *Journal of Photogrammetry and Remote Sensing*, 57:241–262, 2003.

F. Raia and F.J. Spera. Simulations of crustal anatexis: Implications for the growth and differentiation of continental crust. *Journal of Geophysical Research: Solid Earth*, 102(B10):22629–22648, 1997.

E. Rampone, A.W. Hofmann, and I. Raczek. Isotopic contrasts within the internal liguride ophiolite (n. italy): the lack of a genetic mantle-crust link. *Earth and Planetary Science Letters*, 163:175–189, 1998.

J.G. Ramsay. Shear zone geometry: A review. *Journal of Structural Geology*, 2(1-2):83–99, 1980.

vom G. Rath. Beitraege zur kenntnis der eruptiven gesteine der alpen. 1- ueber das gestein des adamellogebriges. *Zeitschrift der geologischen Geselschaft*, 16:249–266, 1864.

L. Ratschbacher, W. Frisch, H.-G. Linzer, and O. Merle. Lateral extrusion in the eastern alps, part 2: Structural analysis. *Tectonics*, 10(2):257–271, 1991.

Z. Reches and J. Fink. The mechanism of intrusion of the inyo dike, long valley caldera, california. *Journal of Geophys*, 93:4321–4334, 1988.

D. Regis, B. Cenki-Tok, J. Darling, and M. Engi. Redistribution of ree, y, th, and u at high pressure: Allanite-forming reactions in impure meta-quartzites (sesia zone, western italian alps). *American Mineralogist*, 97(2-3):315–328, 2012.

M. Rehkämper and A.W. Hofmann. Recycled ocean crust and sediment in indian ocean {MORB}. *Earth and Planetary Science Letters*, 147(1-4):93–106, 1997.

P.W. Reiners, B.K. Nelson, and M.S. Ghiorso. Assimilation of felsic crust by basaltic magma: Thermal limits and extents of crustal contamination of mantle-derived magmas. *Geology*, 23(6):563–566, 1995.

C. Riccomini and A.P. Cróstal. Análise preliminar de lineamentos em imagens de sensores remotos aplicada à prospeccõo mineral na area dos granitóides mandira, sp. *Bol. IG-USP, Sér. Cient.*, 19:23–37, 1988.

F. Ridolfi, A. Renzulli, and M. Puerini. Stability and chemical equilibrium of amphibole in calc-alkaline magmas: an overview, new thermobarometric formulations and application to subduction-related volcanoes. *Contributions to Mineralogy and Petrology*, 160:45–66, 2010.

E. Rivalta and T. Dahm. Dyke emplacement in fractured media: application to the 2000 intrusion at izu islands, japan. *Geophysical Journal International*, 157(1):283–292, 2004.

S. Robl, J.and Hergarten, K. Stüwe, and C. Hauzenberger. Thermal history: A new software to interpret diffusive zoning profiles in garnet. *Computers & Geosciences*, 33(6):760–772, 2007.

D. Roeder. Thrusting and wedge growth, southern alps of lombardia (italy). *Tectonophysics*, 207(1-2): 199–243, 1992.

C. L. Rosenberg. Shear zones and magma ascent: A model based on a review of the tertiary magmatism in the alps. *Tectonics*, 23(3):n/a–n/a, 2004.

C. L. Rosenberg and M. R. Handy. Experimental deformation of partially melted granite revisited: implications for the continental crust. *Journal of Metamorphic Geology*, 23(1):19–28, 2005.

U.E. Rösli. Geologie und petrographie des südlichen adamello: Vii valle del caffaro. Master's thesis, Swiss Federal Institute of Technology Zurich, ETHZ, 1982.

D. Rubatto, O. Müntener, A. Barnhoorn, and C. Gregory. Dissolution-reprecipitation of zircon at low-temperature, high-pressure conditions (lanzo massif, italy). *American Mineralogist*, 93(10):1519–1529, 2008.

A.M. Rubin. Dikes vs. diapirs in viscoelastic rock. *Earth and Planetary Science Letters*, 117(3-4):653 – 670, 1993a.

A.M. Rubin. Tensile fracture of rock at high confining pressure: Implications for dike propagation. *Journal of Geophysical Research: Solid Earth*, 98(B9):15919–15935, 1993b.

A.M. Rubin. Propagation of magma-filled cracks. *Annual Review of Earth and Planetary Sciences*, 23(1): 287–336, 1995.

R.L. Rudnick. Making continental crust. *Nature*, 378(6557):571–578, 1995.

R.L. Rudnick and S. Gao. Composition of the continental crust. *Treatise on Geochemistry*, 3:1–64, 2003.

E. H. Rutter and D. H. K. Neumann. Experimental deformation of partially molten westerly granite under fluid-absent conditions, with implications for the extraction of granitic magmas. *Journal of Geophysical Research: Solid Earth*, 100(B8):15697–15715, 1995.

V. Rzevskij, G. Novik, A. K. Chatterjee, and A. A. Beknazarov. *The physics of rocks*. Mir, 1971.

W. Salomon. Die adamellogruppe. *Abhandlungen der geologischen Reichanstalt*, 1/2, 1908.

E.W. Sawyer, B. Cesare, and M. Brown. When the continental crust melts. *Elements*, 7(4):229–234, 2011.

U. Schaltegger, L. Desmurs, G. Manatschal, O. Müntener, M. Meier, M. Frank, and D. Bernoulli. The transition from rifting to sea-floor spreading within a magma-poor rifted margin: field and isotopic constraints. *Terra Nova*, 14(3):156–162, 2002.

U. Schaltegger, P. Brack, M. Ovtcharova, I. Peytcheva, B. Schoene, A. Stracke, M. Marocchi, and G.M. Bargossi. Zircon and titanite recording 1.5 million years of magma accretion, crystallization and initial cooling in a composite pluton (southern adamello batholith, northern italy). *Earth and Planetary Science Letters*, 286:208–218, 2009.

R. Schmid. Are the metapelites of the ivrea-verbano zone restites? *Memorie di Scienze Geologiche Universita Padova*, 33:67–69, 1978/79.

R. Schmid and B.J. Wood. Phase relationships in granulitic metapelites from the ivrea-verbano zone (northern italy). *Contributions to Mineralogy and Petrology*, 54:255–279, 1976.

S. M. Schmid, H. R. Aebli, F. Heller, and A. Zingg. The role of the periadriatic line in the tectonic evolution of the alps. *Geological Society, London, Special Publications*, 45(1):153–171, 1989.

S.M. Schmid, O.A. Pfiffner, N. Froitzheim, G. Schönborn, and E. Kissling. Geophysical-geological transect and tectonic evolution of the swiss-italian alps. *Tectonics*, 15(5):1036–1064, 1996.

S.M. Schmid, B. Fügenschuh, E. Kissling, and R. Schuster. Tectonic map and overall architecture of the alpine orogen. *Eclogae Geologicae Helvetiae*, 97(1):93–117, 2004.

M.D. Schmitz and B. Schoene. Derivation of isotope ratios, errors, and error correlations for u-pb geochronology using 205pb-235u-(233u)-spiked isotope dilution thermal ionization mass spectrometric data. *Geochemistry, Geophysics, Geosystems*, 8:n/a–n/a, 2007.

B. Schoene, U. Schaltegger, P. Brack, C. Latkoczy, A. Stracke, and D. Günther. Rates of magma differentiation and emplacement in a ballooning pluton recorded by u-pb tims-tea, adamello batholith, italy. *Earth and Planetary Science Letters*, 355-356:162 – 173, 2012.

G Schönborn. A kinematic model of the western ber alps, southern alps, italy. *Eclogae Geologicae Helvetiae*, 83(3):665–682, 1990.

G. Schönborn. Alpine tectonics and kinematic models of the central southern alps. *Memorie di*, 44: 229–393, 1992.

G. Schönborn. Balancing cross sections with kinematic constraints: The dolomites (northern italy). *Tectonics*, 18(3):527–545, 1999.

R.A. Schultz. Brittle strength of basaltic rock masses with applications to venus. *Journal of Geophysical Research: Planets*, 98(E6):10883–10895, 1993.

C.S. Schwandt and G.A. McKay. Minor- and trace-element sector zoning in synthetic enstatite. *American Mineralogist*, 91(10):1607–1615, 2006.

P. Segall and D.D. Pollard. Joint formation in granitic rock of the sierra nevada. *Geological Society of America Bulletin*, 94(5):563–575, 1983.

P. Segall, E.H. McKee, S.J. Martel, and B.D. Turrin. Late cretaceous age of fractures in the sierra nevada batholith, california. *Geology*, 18(12):1248–1251, 1990.

G.P. Sighinolfi and C. Gorgoni. Chemical evolution of high-grade metamorphic rocks-anatexis and remotion of material from granulite terrains. *Chemical Geology*, 22:157 – 176, 1978.

T.W. Sisson. Hornblende-melt trace-element partitioning measured by ion microprobe. *Chemical Geology*, 117:331–344, 1994.

T.W. Sisson and T.L. Grove. Temperatures and h_2o contents of low-mgo high-alumina basalts. *Contributions to Mineralogy and Petrology*, 113:167–184, 1993a.

T.W. Sisson and T.L. Grove. Experimental investigations of the role of h2o in calc-alkaline differentiation and subduction zone magmatism. *Contributions to Mineralogy and Petrology*, 113:143–166, 1993b.

T.W. Sisson, T.L. Grove, and D.S. Coleman. Hornblende gabbro sill complex at onion valley, california, and a mixing origin for the sierra nevada batholith. *Contributions to Mineralogy and Petrology*, 126 (1-2):81–108, 1996.

T.W. Sisson, K. Ratajeski, W.B. Hankins, and A.F. Glazner. Voluminous granitic magmas from common basaltic sources. *Contributions to Mineralogy and Petrology*, 148:635–661, 2005.

N.H. Sleep. Segregation of magma from a mostly crystalline mush. *Geological Society of America Bulletin*, 85(8):1225–1232, 1974.

N.H. Sleep. Tapping of melt by veins and dikes. *Journal of Geophysical Research: Solid Earth*, 93(B9): 10255–10272, 1988.

R.L. Smith. Ash-flow magmatism. *Geological Society of America Special Papers*, 180:5–28, 1979.

D. Snyder and S. Tait. Replenishment of magma chambers: comparison of fluid-mechanic experiments with field relations. *Contributions to Mineralogy and Petrology*, 122(3):230–240, 1995.

C. Spandler and C. Pirard. Element recycling from subducting slabs to arc crust: A review. *Lithos*, 170-171:208 – 223, 2013.

C. Spandler, J. Hermann, and D. Rubatto. Exsolution of thortveitite, yttrialite, and xenotime during low-temperature recrystallization of zircon from new caledonia, and their significance for trace element incorporation in zircon. *American Mineralogist*, 89(11-12):1795–1806, 2004.

R.S.J. Sparks and L.A. Marshall. Thermal and mechanical constraints on mixing between mafic and silicic magmas. *Journal of Volcanology and Geothermal Research*, 29:99–124, 1986.

D.A. Spence and D.L. Turcotte. Magma-driven propagation of cracks. *Journal of Geophysical Research*, 90(B1):575–580, 1985.

F.J. Spera and W.A. Bohrson. Energy-constrained open-system magmatic processes 3. energy-constrained recharge, assimilation, and fractional crystallization (ec-rafc). *Geochemistry Geophysics Geosystems*, 3: 1–20, 2002.

M. Spiegelman. Flow in deformable porous media. part 1 simple analysis. *Journal of Fluid Mechanics*, 247:17–38, 1993a.

M. Spiegelman. Flow in deformable porous media. part 2 numerical analysis - the relationship between shock waves and solitary waves. *Journal of Fluid Mechanics*, 247:39–63, 1993b.

M. Stipp, H. Stünitz, R. Heilbronner, and S.M. Schmid. The eastern tonale fault zone: a natural laboratory for crystal plastic deformation of quartz over a temperature range from 250 to 700°c. *Journal of Structural Geology*, 24(12):1861–1884, 2002.

M. Stipp, B. Fügenschuh, L.P. Gromet, H. Stünitz, and S.M. Schmid. Contemporaneous plutonism and strike-slip faulting: A case study from the tonale fault zone north of the adamello pluton (italian alps). *Tectonics*, 23(3):n/a–n/a, 2004.

B. Taisne and C. Jaupart. Dike propagation through layered rocks. *Journal of Geophyscial Research*, 114 (B9):B09203, 2009.

A. Takada. Experimental study on propagation of liquid-filled crack in gelatin: Shape and velocity in hydrostatic stress condition. *Journal of Geophysical Research: Solid Earth*, 95(B6):8471–8481, 1990.

N. Takahashi, S. Kodaira, S.L. Klemperer, Y. Tatsumi, Y. Kaneda, and K. Suyehiro. Crustal structure and evolution of the mariana intra-oceanic island arc. *Geology*, 35:203–206, 2007.

T. Tanaka, S. Togashi, H. Kamioka, H. Amakawa, H. Kagami, T. Hamamoto, M. Yuhara, Y. Orihashi, S. Yoneda, H. Shimizu, T. Kunimaru, K. Takahashi, T. Yanagi, T. Nakano, H. Fujimaki, R. Shinjo, Y. Asahara, M. Tanimizu, and C. Dragusanu. Jndi-1: a neodymium isotopic reference in consistency with lajolla neodymium. *Chemical Geology*, 168(3-4):279–281, 2000.

Y. Tatsumi. Continental crust formation by crustal delamination in subduction zones and complementary accumulation of the enriched mantle i component in the mantle. *Geochemistry Geophysics Geosystems*, 1(12):–, 2000.

Y. Tatsumi. The subduction factory: how it operates in the evolving earth. *GSA Today*, 15:4–10, 2005.

G.K. Taylor and D.E. Randall. Structural analysis of dyke emplacement directions as an aid to palaeomagnetic studies: an example from northern chile. *Geophysical Journal International*, 141(1):252–258, 2000.

S.R. Taylor and S.M. McLennan. *The Continental Crust*. Geoscience Texts. Wiley, 1985.

S.R. Taylor, S.M. McLennan, R.L. Armstrong, and J. Tarney. The composition and evolution of the continental crust: Rare earth element evidence from sedimentary rocks [and discussion]. *Philosophical Transactions of the Royal Society of London. Series A, Mathematical and Physical Sciences*, 301(1461): 381–399, 1981.

B.A. Thompson, L. Matile, and P. Ulmer. Some thermal constraints on crustal assimilation during fractionation of hydrous, mantle derived magmas with examples from central alpine batholith. *Journal of Petrology*, 43(3):403–422, 2002.

M. Tiepolo, R. Tribuzio, and A. Langone. High-mg andesite petrogenesis by amphibole crystallization and ultramafic crust assimilation: Evidence from adamello hornblendites (central alps, italy). *Journal of Petrology*, 52(5):1011–1045, 2011.

W. Todt, R.A. Cliff, A. Hanser, and A. W. Hofmann. *Earth Processes: Reading the Isotopic Code*, volume 95. AGU, Washington, DC, 1996.

A.K. Tokarski. *Dyke swarms as stress indicators: two constraints, in Mafic Dykes and Emplacement Mechanisms*. Balkema, Rotterdam, 1990.

F. Tomaschek, A. K. Kennedy, I. M. Villa, M. Lagos, and C. Ballhaus. Zircons from syros, cyclades, greece-recrystallization and mobilization of zircon during high-pressure metamorphism. *Journal of Petrology*, 44(11):1977–2002, 2003.

H. S. Tomkins, R. Powell, and D. J. Ellis. The pressure dependence of the zirconium-in-rutile thermometer. *Journal of Metamorphic Geology*, 25(6):703–713, 2007.

D.R. Tormey, T.L. Grove, and W.B. Bryan. Experimental petrology of normal morb near the kane fracture zone: 22-25 n, mid-atlantic ridge. *Contributions to Mineralogy and Petrology*, 96:121–139, 1987.

Y.S. Touloukian, W.R. Judd, and R.F. Roy. *Physical properties of rocks and minerals*. McGraw-Hill, 1981.

L. Trevisan. Il gruppo di brenta (trentino occidentale). *Memorie di Scienze Geologiche*, 13:1–128, 1939.

R. Tribuzio, B. Messiga, R. Vannucci, and P. Bottazzi. Rare earth element redistribution during high-pressure-low-temperature metamorphism in ophiolitic fe-gabbros (liguria, northwestern italy): Implications for light ree mobility in subduction zones. *Geology*, 24(8):711–714, 1996.

J.S. Turner and I.H. Campbell. Convection and mixing in magma chambers. *Earth-Science Reviews*, 23 (4):255–352, 1986.

Ulmer. Geologie und petrographie des südlichen adamello: Viii. valle de caffaro. Master's thesis, Swiss Federal Institute of Technology Zurich, ETHZ, 1982.

P. Ulmer. *Basische und ultrabasische Gesteine des Adamello.* Phd thesis, Swiss Federal Institute of Technology Zurich, ETHZ, 1986.

P. Ulmer. High pressure phase equilibria of a calc-alkaline picro-basalt: Implications for the genesis of calc-alkaline magmas. *Carnegie Institution of Washington Yearbook, Annual Report of the Director of the Geophysical Laboratory*, 88:28–35, 1988.

P. Ulmer. Differentiation of mantle-derived calc-alkaline magmas at mid to lower crustal levels: experimental and petrologic constraints. *Periodico di Mineralogia*, 76:309–325, 2007.

P. Ulmer, E. Callegari, and U.C. Sonderegger. Genesis of the mafic rocks and their genetical relations to the tonalitic-trondhjemitic granitoids of the southern part of the adamello batholith (northern-italy). *Memorie della Società Geologica Italiana*, 26:171–222, 1983.

G.A. Valentine and K.E.C. Krogh. Emplacement of shallow dikes and sills beneath a small basaltic volcanic center - the role of pre-existing structure (paiute ridge, southern nevada, usa). *Earth and Planetary Science Letters*, 246(3-4):217–230, 2006.

G. Viola. *Kinematics and timing of the periadriatic fault system in the Giudicarie region (central-eastern Alps).* PhD thesis, Swiss Federal Institute of Technology Zurich, ETHZ, 2000.

G. Viola, N.S. Mancktelow, and D. Seward. Late oligocene-neogene evolution of europe-adria collision: New structural and geochronological evidence from the giudicarie fault system (italian eastern alps). *Tectonics*, 20(6):999–1020, 2001.

F. von Blackenburg. Combined high-precision chronometry and geochemical tracing using accessory minerals: applied to the central-alpine bergell intrusion (central europe). *Chemical Geology*, 100(1-2):19–40, 1992.

H. Voshage, J.C. Hunziker, A.W. Hofmann, and A. Zingg. A nd and sr isotopic study of the ivrea zone, southern alps, n-italy. *Contributions to Mineralogy and Petrology*, 97:31–42, 1987.

H. Voshage, A. W. Hofmann, M. Mazzucchelli, G. Rivalenti, S. Sinigoi, I. Raczek, and G. Demarchi. Isotopic evidence from the ivrea zone for a hybrid lower crust formed by magmatic underplating. *Nature*, 347(6295):731–736, 1990.

Walker, P.R. G.P.L Eyre, S.R. Spengler, M.D. Knight, and K. Kennedy. *Congruent Dyke-Widths in Large Basaltic Volcanoes, Physics and Chemistry of Dykes, Physics and Chemistry of Dyke*. Balkema, Rotterdam, 1995.

G. P. L. Walker. Koolau dike complex, oahu: Intensity and origin of a sheeted-dike complex high in a hawaiian volcanic edifice. *Geology*, 14(4):310–313, 1986.

T. Watanabe, T. Masuyama, K. Nagaoka, and T. Tahara. Analog experiments on magma-filled cracks: Competition between external stresses and internal pressure. *Earth, Planets and Space*, 54:1247–1261, 2002.

E. Watson, D. Wark, and J. Thomas. Crystallization thermometers for zircon and rutile. *Contributions to Mineralogy and Petrology*, 151(4):413–433, 2006.

E.B. Watson. Basalt contamination by continental crust: Some experiments and models. *Contributions to Mineralogy and Petrology*, 80(1):73–87, 1982.

B.L. Weaver and J. Tarney. Empirical approach to estimating the composition of the continental crust. *Nature*, 310(5978):575–577, August 1984.

J. Weertman. Theory of water-filled crevasses in glaciers applied to vertical magma transport beneath oceanic ridges. *Journal of Geophysical Research*, 76(5):1171–1183, 1971. ISSN 2156-2202. doi: 10.1029/JB076i005p01171. URL `http://dx.doi.org/10.1029/JB076i005p01171`.

J.H.L. Wennekkers. *The Structure of the Bergamo Alps Compared with that of the North-west Highlands of Scotland*. Number Bd. 8,Teil 1 in Bijdrage tot de geologie der Bergamakser Alpen. N.v. boeken steendrukkerij E. Ijdo, 1932.

E. Werling. *Tonale-, Pejo- und Judicarien-Linie: Kinematik, Mikrostrukturen und Metamorphose von Tektoniten aus räumlich interferierenden aber verschiedenaltrigen Verwerfungszonen*. PhD thesis, Swiss Federal Institute of Technology, Zurich, 1992.

M. Wiedenbeck. Structural and isotopic age profile across the insubric line, mello, valtellina, n. italy. *Schweiz Mineralogische Petrografische Mitteilungen*, 66:211–227, 1986.

C.A. Williams, C. Connors, F.A. Dahlen, E.J. Price, and J. Suppe. Effect of the brittle-ductile transition on the topography of compressive mountain belts on earth and venus. *Journal of Geophysical Research: Solid Earth*, 99(B10):19947–19974, 1994.

B. J. A. Willigers, F. C. Mengel, D. Bridgwater, J. R. Wijbrans, and J. A. M. van Gool. Mafic dike swarms as absolute time markers in high-grade terranes: 40ar/39ar geochronological constraints on the kangâmiut dikes, west greenland. *Geology*, 27(9):775–778, 1999.

B.J. Wood and S. Banno. Garnet-orthopyroxene and orthopyroxene-clinopyroxene relationships in simple and complex systems. *Contributions to Mineralogy and Petrology*, 42:109–124, 1973.

B.J. Wood and J. D. Blundy. A predictive model for rare earth element partitioning between clinopyroxene and anhydrous silicate melt. *Contributions to Mineralogy and Petrology*, 129:166–181, 1997.

R.K. Workman and S.R. Hart. Major and trace element composition of the depleted {MORB} mantle (dmm). *Earth and Planetary Science Letters*, 231(1-2):53–72, 2005.

J.E. Wright and J.W. Shervais. Emplacement age of balmuccia lherzolite massif, nw italy. *International Congress, 26th Paris, Abstracts*, 2:804, 1980.

T. Zack and T. John. An evaluation of reactive fluid flow and trace element mobility in subducting slabs. *Chemical Geology*, 239:199 – 216, 2007.

T. Zack, A. A Kronz, S.F. Foley, and T. Rivers. Trace element abundances in rutiles from eclogites and associated garnet mica schists. *Chemical Geology*, 184(1-2):97–122, 2002.

T. Zack, R. Moraes, and A. Kronz. Temperature dependence of zr in rutile: empirical calibration of a rutile thermometer. *Contributions to Mineralogy and Petrology*, 148(4):471–488, 2004.

R.E. Zartman and B.R. Doe. Plumbotectonics-the model. *Tectonophysics*, 75(1-2):135–162, 1981.

M.M. Zimmer, T. Plank, E.H. Hauri, G.M. Yogodzinski, P. Stelling, J. Larsen, B. Singer, B. Jicha, C. Mandeville, and C.J. Nye. The role of water in generating the calc-alkaline trend: New volatile data for aleutian magmas and a new tholeiitic index. *Journal of Petrology*, 51(12):2411–2444, 2010.

R. Zurbriggen, L. Franz, and M.R. Handy. Pre-variscan deformation, metamorphism and magmatism in the strona-ceneri zone (southern alps of northern italy and southern switzerland). *Schweizerische Mineralogische und Petrografische Mitteilungen*, 77:361–380, 1997.